23rd SEACOMP & 16th TMPS

"Inspiring the next generation of Medical Physicists"

23-26 January 2025

Chiang Rai, Thailand

Proceedings

The 23rd South-East Asian Congress of Medical Physics (SEACOMP)

The 16th Annual Meeting of Thai Medical Physicist Society (TMPS)


23rd South-East Asian Congress of Medical Physics (SEACOMP)

and

16th Annual Meeting of Thai Medical Physicist Society (TMPS)

“Inspiring the next generation of Medical Physicists”

23-26 January 2025

Chiang Rai

Thailand

Welcome Message from SEAFOMP President

Dear Colleagues,

It is with great enthusiasm that I invite you to join us for SEACOMP 2025, which will be held from January 23-26, 2025, at The Heritage Hotel and Convention in Chiang Rai, Thailand. This upcoming Congress promises to be an exceptional event, bringing together the brightest minds and leaders in medical physics from across Southeast Asia and beyond.

Hosted by TMPS Local Host, SEACOMP 2025 will offer a unique opportunity to engage in cutting-edge discussions, share research findings, and collaborate with fellow professionals. The conference will feature a diverse program, including keynote lectures, scientific sessions, and interactive workshops, all designed to advance our collective knowledge and foster innovation in the field of medical physics.

I encourage all members and participants to take advantage of this invaluable experience. Your participation will not only contribute to the success of the Congress but also enhance your professional development and expand your network within our vibrant community.

We look forward to welcoming you to Chiang Rai for what promises to be an inspiring and productive Congress.

Thank you for your continued support and commitment to advancing medical physics.

Warm regards,

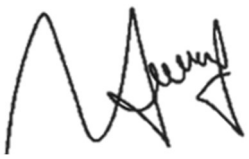

Prof. Dr. Chai Hong Yeong
SEAFOMP President

Welcome Message from Thai Medical Physicist Society

Dear Colleagues,

Welcome to the 23rd Southeast Asian Congress of Medical Physics and the 16th Annual Scientific Meeting of Thai Medical Physicist Society held on January 23-26, 2025 at The Heritage Chiang Rai Convention and Hotel, Chiang Rai, Thailand. The Theme of the Conference is ***'Inspiring the Next Generation of Medical Physicists'***

Chiang Rai is one of Thailand's seventy-seven provinces, which lies in upper northern Thailand and is Thailand's northernmost province. It is bordered by the Shan State of Myanmar to the north, Bokeo province of Laos to the east, Phayao to the south, Lampang to the southwest, and Chiang Mai to the west. The Fourth Thai–Lao Friendship Bridge that spans the Mekong links the provinces to Houayxay Laos.

Chiang Rai was founded in 1262. Populations have dwelled in Chiang Rai since the 7th century and it became the center of the Lanna Kingdom during the 13th century. The region, rich in natural resources, was occupied by the Burmese until 1786. Chiang Rai province's golden triangle bordering Laos and Burma was once the hub of opium production. Chiang Rai became a province in 1910, after being part of the Lanna Kingdom for centuries. After Lanna was incorporated into Thailand, it remained an autonomous region and thus the Chiang Rai area was administered from Chiang Mai. The majority of the population are ethnic Thai who speak Kham Muang among themselves, but 12.5% are of hill tribes origin, a sizeable minority in the north provinces. A smaller number are of Chinese descent, mainly descendants of the Kuomintang soldiers who settled in the region, notably in Santikhiri.

The seal of the province shows a white elephant, the royal symbol, recalling that Chiang Rai was founded by King Mengrai, according to legend because his elephant liked the place. The former provincial slogan was , 'Northernmost of Siam, beautiful Doi Tung, repository of culture, most delicious rice, sweet and fragrant lychee, beautiful ladies, the finest flavored tea, pineapple from Nang Lae, source of the giant catfish.

Chiang Rai is known for its beautiful landscapes, cultural heritage, and unique attractions. The city attracts a large number of tourists every year who come to explore its temples, markets, museums, and its natural beauty.

One of the most popular attractions is the Wat Rong Khun, another attraction is the Golden Triangle, which is the meeting point of Thailand, Laos, and Myanmar and offers views of the Mekong River and the surrounding mountains. Other popular

attractions in Chiang Rai include the Doi Tung Royal Villa, Baan Dam Museum, the Hill Tribe Museum and Education Center, and the Khun Korn Waterfall. Chiang Rai is also a popular base for exploring the surrounding areas, including the Mae Sai border town, the Chiang Saen historical city, and the Doi Mae Salong tea plantations.

The Congress scientific program will be started with Pre Congress Workshops on January 23rd, followed by the three day Congress of the ASEAN College of Medical Physics (ACOMP), John Cameron Memorial Lecture. Proposed topics for the Congress are: RT: Innovations in Radiation Therapy Delivery and Planning, Dosimetry and Quality Assurance in radiation therapy, Advances in Machine Learning and AI for Medical Physics, MI : Photon Counting Detection: Theory, Practical Considerations, and Applications, Remote Interpretation of Medical Images and Physics: Approaches, Challenges, and the Future, Patient and Fetal Dose in Diagnostic Imaging, QUAADRIL, NM: QC Performance Updates of ACR NM & PET QC Manuals: What, When, and How? PET/MR - Research Opportunities and Clinical Potential, Dosimetry for theranostic etc. Gala Khan Tok dinner is organized on 24th January evening with the announcement of the SEAFOMP Young Leader Awards. Proffered papers from medical physics graduated students will be set in the afternoon of 25th January for 3 fields. Lunch Symposium /Vendor talks of advance development, Commercial Exhibition are available at the Congress. Last but not least, the credit hour for member to renew the MP National License will certainly be prepared for you. See you all in January 23-26, 2025 in Chiang Rai, Thailand!

Anchali Krisanachinda, Ph.D., FIOMP, FIUPESM
President, TMPS
August 1, 2024

SEAFOMP Executive Committee

President	Chai Hong Yeong
Vice President	Taweap Sanghangthum
Officers & Committee Members	Delmar Arzabal
	Kitiwat Khamwan
	Lukmanda Evan Lubis
	Aik Hao Ng
	Supriyanto Pawiro
	Hafiz Zin
	Vanyat Ath
	Melvin Chew
Advisors	Anchali Krisanachinda
	Agnette Peralta
	Freddy Haryanto
	Kwan Hoong Ng
	James Lee
	Djarwani Soejoko

Organizing Committee

President	Anchali Krisanachinda
Vice President, Treasurer	Tanawat Sontrapornpol
Scientific	Puangpen Tangboonduangjit
	Chirapha Tannanonta
	Chumpot Kakanaporn
	Sawwanee Asavaphatiboon
	Napapong Pongnapang
	Nauljun Stansook
	Suphalak Khachonkham
	Taratip Narawong
	Chirasak Khamfongkhruea
Registration	Paranee Sahachjesdakul
	Lakkana Apipanyasopon
Commercial Exhibition	Sivalee Suriyapee
	Panya Pasawang
Social and Audiovisual	Kitiwat Khamwan
Social and Transportation	Amporn Funsian
International Cooperation	Thitithip Tippayamontri
Webmaster	Tawatchai Chaiwatanarat
Secretary General and Audiovisual	Taweap Sanghangthum

Theme: Inspiring the Next Generation of Medical Physicists @ The Heritage Chiang Rai Hotel, Chiang Rai, Thailand

Time	23/1/2025 (pre-congress)			24/01/2025			25/01/2025			26/01/2025		
	Lanna 2	Lanna 4	Lanna 5	Radiotherapy (Grand Ballroom)	Diagnostic Imagiing (Heritage 1)	NM Imaging (Heritage 2)	Radiotherapy (Grand Ballroom)	Diagnostic Imagiing (Heritage 1)	NM Imaging (Heritage 2)	Radiotherapy (Grand Ballroom)	Diagnostic Imagiing (Heritage 1)	NM Imaging (Heritage 2)
08:00-08:30	**Registration** **Pre-congress Workshop**			**Registration**			**Fundamental Principles of AI Relevant to Medical Physicists** *Chanon Puttanawarut*				**Radiation Protection Equipment in Diagnostic and Interventional Radiology** *Kosuke Matsubara*	
08:30-09:00				**Opening Ceremony** *Vanchai Sirichana, Chai Hong Yeong, Anchali Krisanachinda*			**Medical Physics in THAI-QUATRO** *Chumpot Kakanaporn*	**CT Technology and Dosimetry** *Katsumi Tsujioka*	**New Trends in PET/CT Technology** *Krisanat Chuamsaamarkkee*	**Flash Proton Therapy** *Martin Handschin Grossmann*	**Establishing a Comprehensive MR Safety Program in Clinical Environment** *Anzi Zhou*	**Administering Targeted Radionuclide Therapy - Safety and Quality Management** *Somanesan S.*
09:00-09:30	**IAEA Regional Project: Integrating AI-Driven Bridge in Postgraduate Medical Physics Education and Training:** *Anchali Krisanachinda, Chirasak Khamfongkhruea, Puangpen Tangboonduangjit, Suphalak Khachonkham, Massoud Malek* **Lanna 2**			**John Cameron Memorial Lecture** **Smart Ideas Are Not Enough – The Role of Technological Innovations in Physics Applications for Medicine** *Martin Handschin Grossmann*			**Development of End-to-End 3D Dosimetry Audit for Advanced Radiotherapy** *Ahmad Taufek Abdul Rahman*	**3D C-arms with Volumetric Imaging Capability for Fluoroscopically-guided Interventions** *Lukmanda Evan Lubis*	**Implementation of population PK modeling in molecular radiotherapy** *Deni Hardiansyah*	**TRS492 on Brachytherapy Dosimetry and the updated TRS398** *Sakchai Buppaungkul*	**Reproduction of Processing Steps of EPI Image Reconstruction by MRI Simulation** *Noriyuki Tawara*	**Advancements in Evaluating Terbium-161 vs Lutetium-171 for Enhanced Theranostic Application** *Shuichi Shiratori*
09:30-10:00				**Opening Commercial Exhibition & Coffee Break**			**MRGRT: Clinical Implementation and Challenges** *Chanida Sathitwathanawirot*	**Patient Dosimetry in Pedriatic CT** *Kosuke Matsubara*	**Radionuclide Imaging and Therapy in Oncology** *Ponlawat Angsulajit*	**Evolution and Applications of SGRT** *Anirut Watcharawipha/ Sithiphong Suphaphong*	**Photon Counting CT: Principles and Applications** Picha Shunhavanich	**Exploring Novel Combined Therapeutic Strategies: EBRT & Targeted Radionuclide Therapy** *Thititip Tippayamontri*
10:00-10:30							**Coffee Break**			**Coffee Break**		
10:30-11:00	**Workshop for Measuring the MTF of CT Scanners** *Katsumi Tsujioka* **Lanna 2**			**Pradub Atthakorn Memorial Lecture** **Reviewing Your High Dose Rate Brachytherapy Quality Assurance Program: Back to the Basics** *Allan Wilkinson*			**Gel Dosimetry for Radiotherapy** *Akihiro Takemura*	**AI in Breast Cancer Screening** *Todsaporn Fuangrod*	**Quantitative Theranostic Nuclear Medicine: How Far Are We From Personalised Dosimetry?** *Chai Hong Yeong*	**New generation long-axis PET system NEMA performance and clinical validation** *Haiqiong Zhang*		
11:00-11:30				**The current and emerging revolution in ultrasound imaging technology** John Owen Gibson			**AAPM TG 267: Brachytherapy** *Pitchayut Nakkrasae*	**3D Cellular Arrangement Modeling: Trend for the Future** *Arunothai Wanta* *Harit Boonyaputthikul*	**New Trends for Lu-177 Personalized Dosimetry using a Ring-shaped CZT-based Camera: the Game Changes?** *Kitiwat Khamwan*	**Medical Physics and AI: Where Do We Start?** *Daniel Carrion*		
11:30-12:00				**Beyond Boundaries: Inspiring the Next Generation of Medical Physicists** *Kwan Hoong Ng*			**TMPS-Varian RapidPlan Project** *Taweap Sanghangthum*		**Implementation of Dosimetry for Molecular Radiotherapy in SEA Region: Current Status** *Nur Rahmah Hidayati*	**Beyond Language Barriers: Generative AI in Patient Communication** *Mohamed Badawy*		
12:00-12:30	**Lunch**			**Lunch Symposium (GE)** **Imaging in Radiotherapy** *Taweap Sanghangthum*			**Lunch Symposium (Saint Med)** **On-line Adaptive RT bases on CT-linac** *Wenzhao Sun*			**The Current IOMP Efforts for International Certification of Medical Physicists** *Allan Wilkinson*		
12:30-13:00										**Closing Ceremony & Awards**		
13:00-13:30	**ACOMP-ASEAN DRL** *Vannyat Ath (CAM), Rini Shintawati (IND), Nurmazaina Ariffin (MAL), Thinn Thinn Myint (MYM), Agnette Peralta (PHI), Somanesan S (SIN), Anchali Krisanachinda (THA), Shiwani Shayal (FIJ), Ikunanoa Tohotoa (TON), Amos Toka (VAN)* **Lanna 2**	**Automation in Medical Physics Task** *Nat Siriruttbunkajorn* *Wisawa Phongprapan* *Todsaporn Fuangrod* **Lanna 4**	**Point of Care Ultrasound (POCUS) Workshop** *John Owen Gibson* *Mae Fah Luang* **Lanna 5**	**Vendor Talk (Siemens): Optimizing Radiotherapy Outcomes with PET/CT and Artificial Intelligence** *Ferdinand Lipps*			**Physics of Proton Therapy and Future Direction** *Wei Yang Calvin KOH*	**AAPM TG 368: Methodology for Establishing Exam-Specific Target Exposure Indices in General Radiography** *Anzi Zhou*	**AI in medical imaging and NM** *Yothin Rakvongthai*	**Lunch**		
13:30-13:50				**3-Year Experience in Proton Therapy in Thailand** *Chonlakiet Khorpresert* *Napapat Amornwichet*			**Proffered Papers in Radiation Oncology - non-AI @ Ballroom 1 - AI, MC, Proton @ Ballroom 2**	**Proffered Papers in Diagnostic Imaging**	**Proffered Papers in NM Imaging & Others**			
13:50-14:10												
14:10-14:30				**Vendor Talk (Business Alignment): RapidArc Dynamic – A Turning Point of Arc Therapy** *Roman Wicha*								
14:30-15:00	**Women in MP** *Rini Shintawati (IND), Chai Hong Yeong (MAL), Agnette Peralta(PHI), Anchali Krisanachinda (THA)* **Lanna 2**			**Vendor Talk (Med-I): Unlocking the Potential of Astatine-211 as a Promising Alternative to Actinium-225 in Theranostics** *Shuichi Shiratori*			**Coffee Break**				**1/25/2025**	**Lanna 2**
15:00-15:30				**Coffee Break**			**Proffered Papers in Radiation Oncology**	**Proffered Papers in Diagnostic Imaging**	**Proffered Papers in NM Imaging & Others**		**12:00-12:30**	**Ex-com Meeting**
15:30-16:00				**Proton Therapy in Breast Cancer** *Kanjana Shotelersuk*	**Implementing a QM System in Diagnostic Radiology: The Roles of Clinical Medical Physicists** *Napapong Pongnapang*	**Trends in AI for MRI: An Introduction to the Latest Technologies** *Yasuo Takatsu*					**12:30-13:00**	**Council Meeting**
16:00-16:30				**Dose Verification in Organ Motion Radiotherapy** *Supriyanto Pawiro*	**Applied Physics in Thai Biomedical Inventions** *Sittiporn Punyanitya*	**Risk Control: Role of a Medical Physcist Not Only Optimization in Diagnostic Medical Activities** *Franco Milano*						
16:30-17:00				**TMPS Bussiness Meeting (Heritage 1)**								
18:00-21:00	**Presidential Dinner (Commiittee & Invited Speakers): Sponsor by United Imaging (Heritage 1)**			**Gala Dinner: Sponsor by Med-I (Grand Ballroom)**								

Mae Fah Luang ACOMP

Southeast Asia Federation of Organizations for Medical Physics

Thai Medical Physicist Society & Mae Fa Luang University

The 23rd SEACOMP & 16th TMPS Annual Scientific Meeting,

23 -26 January 2025

The Heritage Chiang Rai Hotel and Convention, Chiang Rai, Thailand

Theme: "Inspiring the Next Generation of Medical Physicists"

Room *Grand Ballroom (Opening & Radiotherapy)*

Heritage 1 (Diagnostic Imaging, Business Meeting)

Heritage 2 (Nuclear Medicine)

Lanna 2 (SEAFOMP EXCOM Meeting, Council Meeting),

In front of Grand Ballroom (Commercial Exhibition & Coffee Break)

MEETING PROGRAM

THURSDAY, 23 JANUARY 2025

08:00-09:00 **REGISTRATION – Pre-congress Workshop**

Room *Lanna 2*

Chair: *Anchali Krisanachinda*

09:00-10:30 **IAEA Regional Project: Integrating AI-Driven Bridge in Postgraduate Medical Physics Education and Training**

Anchali Krisanachinda, Chirasak Khamfongkhruea, Puangpen Tangboonduangjit, Suphalak Khachonkham, Massoud Malek

Room *Lanna 2*

Chair: *Kitiwat Khamwan*

10:30-12:00 **Hands-on experience with the latest CT technology**

-Performance Evaluation and New Research Trends-

Katsumi Tsujioka

12:00-13:00 **LUNCH**

Room *Lanna 2*

Chair: *Kosuke Matsubara*

13:00-14:30 **ACOMP-ASEAN Dose Reference Level**

Vannyat Ath (CAM), Rini Shintawati (IND), Nurmazaina Ariffin (MAL), Thinn Thinn Myint (MYM), Agnette Peralta (PHI), Somanesan S (SIN), Anchali Krisanachinda (THA), Shiwani Shayal (FIJ), Ikunanoa Tohotoa (TON), Amos Toka (VAN)

Chair:	*Chai Hong Yeong*
14:30-16:00	**Women in Medical Physics**
	Rini Shintawati (IND), Chai Hong Yeong (MAL), Agnette Peralta (PHI), Anchali Krisanachinda (THA)
Room	*Lanna 4*
Chair:	*Chirasak Khamfongkhruea*
13:00-14:30	**Automation in Medical Physics Task**
	Nat Sirirutbunkajorn, Wisawa Phongprapan, Todsaporn Fuangrod
Room	*Lanna 5*
Chair:	*Keerakarn Somsuan*
13:00-16:00	**Point of Care Ultrasound (POCUS) Workshop**
	John Owen Gibson
Room	*Heritage 1*
18:00-21:00	**PRESIDENTIAL DINNER (for invited speaker and committee)**
	Sponsor by United Imaging

FRIDAY, 24 JANUARY 2025

08:00-08:30	REGISTRATION
Room	*Grand Ballroom*
MC:	*Kitiwat Khamwan, Thititip Tippayamontri*
08:30-09:00	OPENING CEREMONY
	Vanchai Sirichana, Chai Hong Yeong, Anchali Krisanachinda
09:00-09:30	**John Cameron Memorial Lecture**
	Smart Ideas Are Not Enough – The Role of Technological Innovations in Physics Applications for Medicine
	Martin Handschin Grossmann
09:30-10:30	OPENING COMMERCIAL EXHIBITION & COFFEE BREAK

Room	*Grand Ballroom*
Chair:	*Anchali Krisanachinda*
10:30-11:00	**Pradub Atthakorn Memorial Lecture** **Reviewing Your High Dose Rate Brachytherapy Quality Assurance Program: Back to the Basics** *Allan Wilkinson*
11:00-11:30	**The current and emerging revolution in ultrasound imaging technology** *John Owen Gibson*
11:30-12:00	**Beyond Boundaries: Inspiring the Next Generation of Medical Physicists** Kwan Hoong Ng
Chair:	***Puangpen Tangboonduangjit***
12:00-13:00	**GE LUNCH SYMPOSIUM: Imaging in Radiotherapy** *Taweap Sanghangthum*

Room	*Grand Ballroom*
Chair:	*Sivalee Suriyapee*
13:00-13:30	**Vendor Talk (Siemens): Optimizing Radiotherapy Outcomes with PET/CT and Artificial Intelligence** *Ferdinand Lipps*
13:30-14:10	**3-Year Experience in Proton Therapy in Thailand** *Chonlakiet Khorprasert, Napapat Amornwichet*
Chair:	*Puangpen Tangboonduangjit*
14:10-14:30	**Vendor Talk (Business Alignment):** **RapidArc Dynamic – A Turning Point of Arc Therapy** *Roman Wicha*
14:30-15:00	**Vendor Talk (Med-I):** **Unlocking the Potential of Astatine-211 as a Promising Alternative to Actinium-225 in Theranostics** *Shuichi Shiratori*
15:00-15:30	COFFEE BREAK

Room	*Grand Ballroom*
Chair:	*Chonlakiet Khorprasert*
15:30-16:00	**Proton Therapy in Breast Cancer** *Kanjana Shotelersuk*

16:00-16:30 **Dose Verification in Organ Motion Radiotherapy**

Supriyanto Pawiro

Room Heritage 1

Chair: ***Kitiwat Khamwan***

15:30-16:00 **Implementing a QM System in Diagnostic Radiology: The Roles of Clinical Medical Physicists**

Napapong Pongnapang

16:00-16:30 **Applied Physics in Thai Biomedical Inventions**

Sittiporn Punyanitya

Room ***Heritage 2***

Chair: ***Anchali Krisanachinda***

15:30-16:00 **Trends in AI for MRI: An Introduction to the Latest Technologies**

Yasuo Takatsu

16:00-16:30 **Risk Control: Role of a Medical Physicist Not Only Optimization in Diagnostic Medical Activities**

Franco Milano

Room ***Heritage 1***

16:30-17:00 **TMPS BUSINESS MEETING**

Room ***Grand Ballroom***

18:00-21:00 **GALA DINNER – Sponsor by Med-I**

SATURDAY 25 JANUARY 2025

Room ***Grand Ballroom***

Chair: ***Wannapha Nobnop***

08:00-08:30 **Fundamental Principles of AI Relevant to Medical Physicists**

Chanon Puttanawarut

08:30-09:00 **Medical Physics in THAI-QUATRO**

Chumpot Kakanaporn

09:00-09:30 **Development of End-to-End 3D Dosimetry Audit for Advanced Radiotherapy**

Ahmad Taufek Abdul Rahman

09:30-10:00 **MRGRT: Clinical Implementation and Challenges**

Chanida Sathitwathanawirot

Room	***Heritage 1***
Chair:	**Lukmanda Evan Lubis**
08:30-09:00	**CT Technology and Dosimetry** *Katsumi Tsujioka*
09:00-09:30	**3D C-arms with Volumetric Imaging Capability for Fluoroscopically-guided Interventions** *Lukmanda Evan Lubis*
09:30-10:00	**Patient Dosimetry in Pedriatic CT** *Kosuke Matsubara*

Room	***Heritage 2***
Chair:	***Chai Hong Yeong***
08:30-09:00	**Emerging Trends and Technologies in Nuclear Medicine Imaging: What Medical Physicists Must Know?** *Krisanat Chuamsaamarkkee*
09:00-09:30	**Implementation of population PK modeling in molecular radiotherapy** *Deni Hardiansyah*
09:30-10:00	**Radionuclide Imaging and Therapy in Oncology** *Polawat Angsulajit*
10:00-10:30	COFFEE BREAK

Room	***Grand Ballroom***
Chair:	***Supriyanto Pawiro***
10:30-11:00	**Gel Dosimetry for Radiotherapy** *Akihiro Takemura*
11:00-11:30	**AAPM TG 267: A Joint AAPM GEC-ESTRO Report on Biophysical Models and Tools for the Planning and Evaluation of Brachytherapy** *Pitchayut Nakkrasae*
11:30-12:00	**TMPS-Varian RapidPlan Project** *Taweap Sanghangthum*

Room	***Heritage 1***
Chair:	***Thititip Tippayamontri***
10:30-11:00	**AI in Breast Cancer Screening** *Todsaporn Fuangrod*

11:00-12:00 **3D Cellular Arrangement Modeling: Trend for the Future**

Arunothai Wanta, Harit Boonyaputthikul

Room ***Heritage 2***

Chair: ***Anchali Krisanachinda***

10:30-11:00 **Personalised Dosimetry in Theranostic Nuclear Medicine: Lessons Learnt**

Chai Hong Yeong

11:00-11:30 **New Trends for Lu-177 Personalized Dosimetry using a Ring-shaped CZT-based Camera: the Game Changes?**

Kitiwat Khamwan

11:30-12:00 **Implementation Dosimetry for Molecular Radiotherapy in SE Asia Region: What Are We Up To?**

Nur Rahmah Hidayati

Room ***Grand Ballroom***

Chair: ***Thititip Tippayamontri***

12:00-13:00 **Saint Med LUNCH SYMPOSIUM**

On-line Adaptive RT bases on CT-linac

Wenzhao Sun

Room ***Grand Ballroom 1***

Chair: ***Lakkana Apipanyasopon***

13:00-13:30 **Physics of Proton Therapy and Future Direction**

Wei Yang Calvin KOH

Room ***Heritage 1***

Chair: ***Picha Shunhavanich***

13:00-13:30 **AAPM TG 368: Methodology for Establishing Exam-Specific Target Exposure Indices in General Radiography**

Anzi Zhao

Room ***Heritage 2***

Chair: ***Somanesan S.***

13:00-13:30 **AI in medical imaging and NM**

Yothin Rakvongthai

Proffered Paper in Radiotherapy (non-AI): **Grand Ballroom 1**

Proffered Paper in Radiotherapy (AI, MC, Proton, and Other): **Grand Ballroom 2**

Proffered Paper in Diagnostic Radiology: **Heritage 1**

Proffered Paper in Nuclear Medicine & Others: **Heritage 2**

Proffered Paper in Radiotherapy (non-AI)

Room *Grand Ballroom 1*

Chair: *Puangpen Tangboonduangjit*

Co-Chair: *Taweap Sanghangthum*

13:30-13:40 **RT 1_Development and characterization of customizable carrageenan bolus for superficial radiation therapy**
Cruzet Rhodesa, Calma J, Dadol G

13:40-13:50 **RT 2_Measurement of photoneutron dose rate from high energy photon beams in medical linear accelerator using a neutron survey meter**
Hmwe Aye T, Damrongkijudom N, Kakanaporn C, Ekjeen T, Suwannarat A, Kittipayak S

13:50-14:00 **RT 3_Determination of neutrons in a photon radiotherapy treatment room using CR-39 dosimeters**
Rattanarungruangchai Natch, Suwanbut P, Thongsawad S, Liamsuwan T

14:00-14:10 **RT 4_Sensitivity of error detection in EPID for patient-specific QA in head and neck VMAT plans**
Thaiwattana Chanchakorn, Udee N, Khamfongkhruea C, Donmoon T, Yabsantia S

14:10-14:20 **RT 5_Implementation of an EPID for patient-specific VMAT quality assurance: Experience at Surin Hospital**
Pischom Narueporn, Songsri S, Tangboonduangjit P, Khachonkham S

14:20-14:30 **RT 6_Investigation of in vivo EPID-based software for detecting dosimetric errors: A phantom studies**
Suksawang Penpisuth, Limpichotikul N, Sahachjesdakul P, Kakanaporn C, Khachonkham S

14:30-15:00 COFFEE BREAK

Proffered Paper in Radiotherapy (non-AI) (Cont.)

Room *Grand Ballroom 1*

Chair: *Supriyanto Pawiro*

Co-Chair: *Anirut Watcharawipha*

15:00-15:10 **RT 7_Investigated radiation dose at surrounding area in real-time motion tracking system of tomotherapy: A phantom study**

Kititharakun Phairot, Watcharawipha A, Nopnob W, Kongsa A

15:10-15:20 **RT 8_Investigated performance of real-time motion tracking system in tomotherapy**

Messuwan Jiraphat, Watcharawipha A, Nopnob W, Kongsa A

15:20-15:30 **RT 9_Comparison of normal tissue integral dose between VMAT and helical tomotherapy for post-mastectomy radiation therapy with regional nodal irradiation**

Tananchai Kamonwan, Watcharawipha A, Onchan W, Nobnop W

15:30-15:40 **RT 10_Assessment of imaging dose delivered to patients throughout the treatment course in tomotherapy systems**

Hompeng Pratchayakan, Nobnop W, Donmoon T, Chusin T

15:40-15:50 **RT 11_Dosimetric comparison between images with and without contrast agent using intensity modulated arc therapy in head and neck cancer**

Wantongsuk Wilasinee, Watcharawipha A, Nopnob W, Chakrabandhu S, Thongsuk W

15:50-16:00 **RT 12_Dosimetric comparison between the original and revised TRS-398 code of practice for photon beam reference dosimetry**

Kyaw WLL, Sanghangthum T, Lin SS, Huq MS

Proffered Paper in Radiotherapy (non-AI) (Cont.)

Room *Grand Ballroom 1*

Chair: *Chumpot Kakanaporn*

Co-Chair: *Tanawat Tawonwong*

16:00-16:10 **RT 13_Evaluating dosimetric accuracy of AAA and AXB algorithms in free-breath and deep inspiration breath hold DIBH for lung SBRT**

Htet May Thu, Tawonwong T, Sanghangthum T

16:10-16:20 **RT 14_Interfraction motion and dosimetric comparison between wing board and breast board immobilization devices during postmastectomy 3D-CRT for breast cancer**
Coronel Michael Ben Joseph, Zerrudo JI, Caballar RC, Balete MJ, Mones E, Cereno RE

16:20-16:30 **RT 15_Impact of multi-leaf collimator (MLC) width and normal tissue objective (NTO) on radiation dose distributions in stereotactic radiosurgery using hyperarc for single brain lesions**
Oh Se An, Kim SY, Park JW, Yea JW, Park J, Jo YJ

16:30-16:40 **RT 16_Evaluation of patient-specific quality assurance for beam-matching in SRS/SRT**
Boujamrat Thanuch, Oonsiri S, Oonsiri P, Kingkaew S, Vimolnoch M, Plangpleng N, Chatchumnan N, Yabsantia S

16:40-16:50 **RT 17_Dosimetric comparison between volumetric modulated arc therapy on TrueBeam and Halcyon of total body irradiation**
Jaihow Wanwanut, Tawonwong T, Sanghangthum T

16:50-17:00 **RT_18 Design and fabrication of a dedicated phantom for geometric verification in single-isocenter multiple-target (SIMT) stereotactic radiosurgery**
Montreemanorom Warisara, Khamfongkhruea C, Mundee T, Chanpanya T, Suwanbut P, Polee C, Wonglee S, Thongsawad S

17:00-17:10 **RT_19 Eclipse scripting application programming interface validation for breast cancer in flattening filter free photon beams**
Tansangworn Prasit, Chatchumnan N, Saksornchai K, Kingkaew S, Vimolnoch M, Oonsiri P, Oonsiri S

17:10-17:20 **RT_20 Assessment of Bladder and Rectal Dose Distributions Using Three-Channel Vaginal Applicators in HDR Electronic Brachytherapy**
Md Mokhlesur Rahman, Rahman Md H, Nath NK

Proffered Paper in Radiotherapy (AI, MC, Proton, and Other)

Room *Grand Ballroom 2 (AI)*

Chair: *Chirasak Khamfongkhruea*

Co-Chair: *Suphalak Khachonkham*

13:00-13:10 **RT 21_ Development of deep learning-based auto-segmentation on CT images for prostate radiotherapy**
Pranee Chanaphat, Kummanee P, Deeharing A, Fuangrod T, Khamfongkhruea C

13:10-13:20 **RT 22_The effect of constructing CT images from multiple MR sequences in the treatment planning of a brain tumor**
Pisut Duanghatai, Auethavekiat S, Oonsiri S

13:20-13:30 **RT 23_Machine learning model for predicting radiation-induced xerostomia from head and neck cancer radiotherapy**
Chantarak Kiattiyot, Suntiwong S, Chamchod S, Liamsuwan T

13:30-13:40 **RT 24_Artificial intelligence-based dose prediction for optimizing treatment plans in locally advanced cervical cancer radiation therapy**
Yooyen Nattawut, Thongsawad S, Chamchod S, Kummanee P, Intanin P, Nimjaroen K, Chaipanya T, Khamfongkhruea C

13:40-13:50 **RT 25_Dose Prediction for Cervical Cancer Brachytherapy using Deep Learning**
Rinjan Nawarat, Khamfongkrue C, Chanpanya T, Kummanee, Tannanonta C, Tharavichitkul E, Thongsawad S

13:50-14:00 **RT 26_Auto-segmentation for cervical cancer brachytherapy using deep learning**
Wattanagul Nuttapol, Khamfongkruea C, Kummanee P, Tannanonta C, Tharavichitkul E, Thongsawad S

14:00-14:10 **RT 27_Failed-tolerance detection of EPID in vivo dosimetry using machine learning**
Saiyo Nipon, Kojima H, Noto K, Isomura N, Tsukamoto K, Segawa Y, Yamaguchi S, Kohigashi J, Takemura A

14:10-14:20 **RT 28_Tumor prognosis in nasopharyngeal carcinoma using deep transfer learning with RadImageNet from CT images**
Petiraksakul Parida, Prayongrat A, Kitpanit S, Kannarunimit D, Chakkabat C, Lertbutsayanukul C, Sriswasdi S, Khongwirotphan S, Rakvongthai Y

14:20-14:30 **RT 29_Deep learning for radiation dose distribution prediction in VMAT breast cancer irradiation**
Sukha Thanakorn, Puttanawarut C, Sirirutbunkajorn N, Changkaew P, Stansook N, Khachonkham S

14:30-14:40 **RT 30_Comparative analysis of convolution neural networks (CNNs) for automated organ-at-risk delineation in prostate cancer computed tomography images**
Khuadpudsa Wanitchaya, Kaewlek T

14:40-14:50 **RT 31_Prediction of radiation pneumonitis using artificial intelligence in non-small cell lung cancer patients undergoing volumetric modulated arc therapy**
Chevajarassakul Wasin, Chamchod S, Phonlakrai M, Kummanee P, Masa-nga W, Nimjaroen K, Chaipanya T, Khamfongkhruea C

14:50-15:00 **RT 32_Evaluation of Knowledge-Based Planning Model in Head and Neck Cancer Using Volumetric Modulated Arc Therapy**
Plangpleng Nattha, Suriyapee S, Tawonwong T, Raungchan S, Kanphet J, Sanghangthum T

15:00-15:30 **COFFEE BREAK**

Proffered Paper in Radiotherapy (AI, MC, Proton, and Other) (Cont.)

Room ***Grand Ballroom 2 (Proton)***

Chair: ***Wei Yang Calvin KOH***

Co-Chair: ***Mintra Keawsamur***

15:30-15:40 **RT 33_Investigation of collimator effects on secondary Bragg peak formation in proton beams based on Monte Carlo simulation**
Azimah Alfia Faizatul, Haryanto F, Widita R, Arif I

15:40-15:50 **RT 34_Comparative dosimetric analysis between volumetric modulated arc therapy and intensity-modulated proton therapy for craniospinal irradiation plans**
Buranavanitvong Nalinpun, Plangpleng N, Ruangchan S, Sanghangthum T

15:50-16:00 **RT 35_Proton beam characteristics through dental materials**
Yamram Nattaporn, Sanghangthum T, Saikaew P, Phaisangittisakul N, Prayongrat A, Israngkul Na Ayuthaya I, Tawonwong T, Ruangchan S

16:00-16:10 **RT 36_Assessing the efficacy of independent calculation-based methods for patient-specific quality assurance in Intensity-Modulated Proton Therapy**
Chatchumnan Nichakan, Suriyapee S, Sanghangthum T

16:10-16:20 **RT 37_Range comparison of Monte Carlo and pencil beam algorithms in treatment planning system for proton therapy**
Monkongsubsin Wiroon, Israngkul Na Ayuthaya I, Sanghangthum T, Keawsamur M

16:20-16:30 **RT 38_Comparison of kinetic repair models for protons induced DNA damage**
Tikamol Natthawat, Nantajit D, Liamsuwan T

Proffered Paper in Radiotherapy (AI, MC, Proton, and Other) (Cont.)

Room *Grand Ballroom 2 (MC & Others)*

Chair: *Wannapha Nobnop*

Co-Chair: *Suphalak Khachonkham*

16:30-16:40 **RT 39_The evaluation of radiotherapy plan complexity using root mean square error based on IMRT linac log-files**
Azzi Akbar, Habyb FE, Ryangga D

16:40-16:50 **RT 40_Dosimetric study of a Co-60 HDR brachytherapy source using PHITS**
Aquino Patrick Vincent

16:50-17:00 **RT 41_ Uncertainty of radiophotoluminescence glass dosimeter in low energy photon beams**
Jittrakool Kantida, Kingkaew S, Chatchumnan N, Oonsiri P, Oonsiri S, Vimolnoch M

17:00-17:10 **RT 42_Unlocking the potential of 3D optical dosimetry in polyvinyl alcohol dosimeters enhanced with silver bromide and zinc oxide nanoparticles for radiotherapy dosimetry applications**
Adenan Mohd Zulfadli, Mahat MM, Jamalludin Z, Min UN, Yaakub NH, Ahmad Taufek Abdul Rahman

17:10-17:20 **RT_43 SafeRT: software for quantitative QA evaluation of IG-IMRT linac performance and treatment delivery**
Zin HM, Lim SY, Abubakar A, Sakaria K, Midi NS, Zamri NAM, Uwais F, Rosli NF

Proffered Paper in Diagnostic Radiology

Room *Heritage 1*

Chair: *Lukmanda Evan Lubis*

Co-Chair: *Kitiwat Khamwan*

13:00-13:10 **Dx 1_Image quality evaluation of ACR CT accreditation phantom using IndoQCT Software**
Chakrapong Apawadee, Krisanachinda A

13:10-13:20 **Dx 2_Optimization of clinical indication DRL of CT protocols**
Kanyakham Kannikar, Kriengkrai I, Krisanachinda A

13:20-13:30 **Dx 3_Real-time staff radiation dose monitoring from neuro-interventional procedures at KCMH**
Prajamchuea Kornkamol, Krisanachinda A

13:30-13:40 **Dx 4_Dosimetry and image quality studies between grid and non-grid fluoroscopy during catheterization in pediatric protocol: a phantom study**

Netprasert Sa-angtip, Krisanachinda A

13:40-13:50 **Dx 5_Comparison of the image quality and dose by using the ACR DM and small ACR mammography phantoms from FFDM systems**

Ruenjit Sakultala, Krisanachinda A

13:50-14:00 **Dx 6_Comparison of Image Quality and Apparent Diffusion Coefficient value in Upper Abdominal MRI: Calculated vs. Acquired Diffusion-Weighted Imaging at high b-value**

Lowong Thanatchaya, Pisuchpen N, Satja M, Krisanachinda A

14:00-14:10 **Dx 7_A breast phantom study for mean glandular dose estimation from full field digital mammography and digital breast tomosynthesis**

Thupsuri Suphawat, Singkavongs A, Tuiduang S

14:10-14:20 **Dx 8_Organ absorbed dose estimation for abdomen-pelvis CT based on measurement and Monte Carlo simulation: phantom study**

Nuntue Chatnapa, Matsubara K, Watanabe S

14:20-14:30 **Dx 9_PHITS modelling and simulation of a D-D neutron generator facility for radiation safety assessment**

Dulohan Christine, Egwolf B, Asuncion-Astronomo A

14:30-15:00 COFFEE BREAK

Proffered Paper in Diagnostic Radiology (Cont.)

Room ***Heritage 1***

Chair: ***Yothin Rakvongthai***

Co-Chair: ***Picha Shunhavanich***

15:00-15:10 **Dx 10_Assessment of patient and occupational radiation dose during angiography procedures in interventional radiology**

Muhammad Roslan Abdul Gani, Widya Apriyani S, Endah P

15:10-15:20 **Dx 11_AI-augmented assessment of quantitative parameters in a 3.0 tesla MRI machine at Songklanagarind Hospital**

Chanchayanon Thanakrit, Sakjirapapong S, Wanai A, Saengsurichai S, Ina N, Rojchanaumpawan T, Cheewakul J

15:20-15:30 **Dx 12_Dose mapping of a deuterium-tritium (D-T) neutron generator laboratory using Monte Carlo transport code PHITS**

Alipio Andrea, Egwolf B, Asuncion-Astronomo A

15:30-15:40 **Dx 13_Optimization of energy thresholds in photon counting CT for characterizing renal stone composition: A simulation study**

Wongsirinanon Sangsirin, Shunhavanich P

15:40-15:50 **Dx 14_Organ dose mapping in AP pelvic radiography: Phantom study**

Sayed Inayatullah Shah, Muhamad Jamil NN, Rohayzaad NIA, Kamzaiman AA

15:50-16:00 **Dx 15_A new simulation method for reproducing semiempirical model-based X-ray spectra considering heel effect**

Santo Taiki, Matsubara K

16:00-16:10 **Dx 16_Image quality comparison in computed tomography system using different image reconstruction methods: a phantom study**

Pangsai Teerapong, Sangruang-orn S, Sodkokkruad P, Chaknam K, Asavaphatiboon S

16:10-16:20 **Dx 17_MRI-Based Radiomics model from mesorectal fat to predict pathologic extramural vascular invasion in locally advanced rectal cancer patients**

Swaengdee Yaniga, Khongwirotphan, Lasode J, Kuecharoen P, Phetvilay P, Boonsirikamchai P, Rakvongthai Y

16:20-16:30 **MPED1_ Academic qualifications of medical physicists in Malaysia: Looking back and moving forward**

Zin M Hafiz, Suardi N, Wong JHD, Azlan CA, Yeong CH, Ng AH, Abdul Rahman AT

Proffered Paper in Nuclear Medicine

Room *Heritage 2*

Chair: *Taratip Narawong*

Co-Chair: *Panya Pasawang*

13:30-13:40 **NM 1_Voxel-based dosimetry of ^{177}Lu-DOTATATE peptide receptor radionuclide therapy using SPECT/CT imaging with RT-PHITS simulations**

Tantiwetchayanon Khajonsak, Matsubara K, Wakabayashi H, Konishi T

13:40-13:50 **NM 2_ Proficiency testing program for ^{131}I and ^{99m}Tc radiopharmaceuticals using radionuclide calibrators in Thailand**

Saejia Korawee, Dachviriyakij T, Thongdeelert N, Luansri K, Pungkun V

13:50-14:00 **NM 3_Evaluation of total counts in SIMIND Monte Carlo simulation for SPECT/CT systems using PyTomography**

Ohnishi Haruki, Matsubara K, Fujiwara K, Tantiwetchayanon K

14:00-14:10 **NM 4_Feasibility of total-body fast SPECT imaging for optimized image quality and voxel-based dosimetry in ^{177}Lu molecular radiotherapy using ring-shaped CZT SPECT/CT**

Handayani Wuri, Chantadisai M, Pasawang P, Noipinit N, Phromphao B, Damthongsen P, Khamwan K

14:10-14:20 **NM 5_Radiation dose reduction in CT-related radiation exposure for NPC protocols in PET/CT imaging at UMMC**
Mohd Zain Azleen, Ahmad F, Md Shah MN, Jasa MJ

14:20-14:30 **NM 6_Comparing image quality characteristics of different post-filtered Iodine-131 SPECT: A phantom study**
Rattanamongkonkul Pattaravarin, Chuamsaamarkkee K, Krisanachinda A

14:30-15:00 COFFEE BREAK

15:00-15:10 **NM 7_Optimization of shortening acquisition for quantitative 99mTc bone SPECT imaging with ordered subset conjugate gradient minimizer reconstruction: A phantom study**
Songprakhon Rangsee, Chuamsaamarkkee K, Krisanachinda A

15:10-15:20 **NM 8_Estimation of 18F-FDG PET/CT effective dose associated with three different calculating methods**
Myint Thinn Thinn, Krisanachinda A

15:20-15:30 **NM 9_Local DRL at nuclear medicine centers in Thailand and Myanmar**
Aye Yin Moe, Krisanachinda A, Thein MPZ

SUNDAY 26 JANUARY 2025

Room ***Grand Ballroom***

Chair: ***Chirapha Tannanonta***

08:30-09:00 **Commissioning of a clinical pencil beam scanning proton therapy unit for ultra-high dose rates (FLASH)**
Martin Handschin Grossmann

09:00-09:30 **TRS492 on Brachytherapy Dosimetry and the updated TRS398**
Sakchai Buppaungkul

09:30-10:00 **Evolution and Applications of SGRT**
Anirut Watcharawipha, Sithiphong Suphaphong

Room ***Heritage 1***

Chair: ***Anchali Krisanachinda***

08:00-08:30 **Radiation Protection Equipment in Diagnostic and Interventional Radiology**
Kosuke Matsubara

08:30-09:00 **Establishing a Comprehensive MR Safety Program in Clinical Environment**
Anzi Zhao

09:00-09:30 **Reproduction of Processing Steps of EPI Image Reconstruction by MRI Simulation**
Noriyuki Tawara

09:30-10:00 **Photon Counting CT: Principles and Applications**
Picha Shunhavanich

Room ***Heritage 2***
Chair: ***Kitiwat Khamwan***

08:30-09:00 **Administering Targeted Radionuclide Therapy - Safety and Quality Management**
Somanesan S

09:00-09:30 **Advancements in Evaluating Terbium-161 vs Lutetium-171 for Enhanced Theranostic Application**
Shuichi Shiratori

09:30-10:00 **Exploring Novel Combined Therapeutic Strategies: EBRT & Targeted Radionuclide Therapy**
Thititip Tippayamontri

10:00-10:30 COFFEE BREAK

Room ***Grand Ballroom***
Chair: ***Chirasak Khamfongkhruea***

10:30-11:00 **New Generation Long-axis PET System NEMA Performance and Clinical Validation**
Haiqiong Zhang

11:00-11:30 **Medical Physics and AI: Where Do We Start?**
Daniel Carrion

11:30-12:00 **Beyond Language Barriers: Generative AI in Patient Communication**
Mohamed Badawy

12:00-12:30 **The Current IOMP Efforts for International Certification of Medical Physicists**
Allan Wilkinson

12:30-13:00 **PRESENTATION AWARDS AND CLOSING**

13:00-14:00 LUNCH

Contents

Abstract: Invited

23 January 2025

Lanna 2

Lanna 5

24 January 2025

Grand Ballroom 1

Heritage 1

Heritage 2

25 January 2025

Grand Ballroom

Heritage 1

Heritage 2

26 January 2025

Grand Ballroom

Abstract: Proffered Papers

25 January 2025

Proffered Paper in Radiotherapy (non-AI)
Grand Ballroom 1: 13:30 – 17:20

Proffered Paper in Radiotherapy (AI, MC, Proton, and Other)
Grand Ballroom 2 (AI): 13:30 – 15:00

Grand Ballroom 2 (Proton): 15:30 – 16:30

Grand Ballroom 2 (MC and Others): 16:30 – 17:20

Proffered Paper in Diagnostic Radiology

Heritage 1: 13:00 – 16:30

Proffered Paper in Nuclear Medicine

Heritage 2: 13:30 – 15:30

Full Paper

Diagnostic Imaging

Nuclear Medicine

Radiotherapy

Abstract:
Invited

IAEA Regional Project: Integrating AI-driven bridge in postgraduate medical physics education and training

Krisanachinda Anchali[1*], Tangboonduangjit P[2], Sanghangthum T[1], Khamfongkhruea C[3], Khachonkham S[2], Malek M[4].

1 Department of Radiology, Faculty of Medicine Chulalongkorn University, Bangkok, Thailand
2 Department of Diagnostic and therapeutic Radiology, Division of Radiation Oncology, Faculty of Medicine Ramathibodi Hospital, Mahidol University, Bangkok, Thailand
3 Princess Srisavangavadhana College of Medicine, Chulabhorn Royal Academy, Bangkok, Thailand
4 International Atomic Energy Agency, Vienna, Austria
**anchali.kris@gmail.com*

The shortage of medical physicists is a recognized problem worldwide, especially in developing countries. Over the last decade, the demand for medical physicists in the Asia and Pacific region has increased tremendously with the increased emphasis on innovative technology for healthcare, particularly implementing the Artificial Intelligence (AI) bridge to utilize existing resources for optimizing education and training for postgraduate medical physics. In response, the counterparts propose this regional project to address tailored education and training needs based on analytical assessments. This project aims to improve patient care by integrating AI for postgraduate medical physics education and training to enhance the capacity and capability of medical physicists in the region. In achieving this goal, the focus will be given to establishing databases for postgraduate medical physics education and training programmes, utilizing AI-driven bridges for medical physics education, training, and research, creating learning paths, as well as capacity building through tailored training programmes based on user's learning experience, feedback and performance analysis (personalized learning). This current project will lead to the efficient delivery of postgraduate medical physics education and training to facilitate personalized learning experiences. It is expected that the successful implementation of this project will ultimately improve patient care outcomes in radiation medicine.

Keywords: Artificial Intelligence, medical physics education and training, International Atomic Energy Agency.

CT workshop and lecture

Katsumi Tsujioka

School of Medical Sciences,
Fujita Health University. Toyoake, Aichi, JAPAN
tsujioka@fujita-hu.ac.jp

Hands-on experience with the latest CT technology
-Performance Evaluation and New Research Trends-

Performance evaluation of CT equipment is essential for better CT examinations. CT performance includes spatial resolution, contrast resolution, and time resolution. This lecture aims to acquire basic knowledge about CT spatial resolution, practice using software, and acquire the latest knowledge.

1. Understanding MTF in CT spatial resolution
Spatial resolution in CT evaluates how small objects can be distinguished and displayed. Modulation transfer function (MTF) is an important technology for evaluating spatial resolution. In the lecture, the principle of MTF, its calculation method, and how to read MTF graphs will be lectured.

2. Practice of MTF calculation using PC
Traditionally, MTF was calculated manually. Recently, software that automatically calculates this technique has been developed. In this lecture, ha
CT-measure created by the Japanese society of CT technology (JSCT) will be introduced, and a demonstration and hands-on will be conducted.
If participants bring their own Windows PC, they will be able to calculate MTF and other parameters on the spot.

3. Latest knowledge on imaging of small objects and creating 3D images
Recent CTs have made it possible to improve spatial resolution. These include high-resolution CT devices and photon counting CT. It has become clear that there are problems with evaluating the imaging of small blood vessels with these latest CTs in the same way as with conventional CTs. In this lecture, we will present problems with the evaluation of the spatial resolution of CT devices and discuss ways to improve them.

Participants should bring their own Windows PC. Software and images for evaluation will be distributed at the venue.

Update on Indonesia's Diagnostic Reference Level

Shintawati Rini[3,7], Lubis LE[1,2,3*], Anam C[4,3], Kunarsih E[5], Putra Pratama IBG[5], Pawiro SA[1,3], Haryanto F [6,3]

1 Dept. of Physics, FMIPA, Universitas Indonesia
2 Radiology Unit, Universitas Indonesia Hospital
3 Indonesian Association of Physicists in Medicine
4 Dept. of Physics, FSM, Diponegoro University
5 Indonesian Nuclear Energy Regulatory Agency
6 FMIPA, Bandung Institute of Technology
7 Nuclear Medicine Department, Hasan Sadikin Hospital
**lukmanda.evan@sci.ui.ac.id*

The Diagnostic Reference Level (DRL) serves as an investigative indicator to help optimize patient radiation protection from medical exposure. The principle of optimization in this context involves efforts to maintain the patient's dose as low as possible while still achieving adequate image quality for diagnosing the patient.

The DRL is a level expressed in terms of radiation dose or the activity of radiopharmaceuticals administered to the patient in diagnostic and interventional radiology examinations as well as diagnostic nuclear medicine, functioning as one of the indicators for implementing radiation protection optimization and safety for patients.

The DRL is driven by the Nuclear Energy Regulatory Agency (Bapeten), by collecting dose data since 2015, involving the Ministry of Health and other health organizations. This technical guideline aims to provide comprehensive guidance in implementing diagnostic reference levels as part of optimization efforts for medical exposure, particularly in the fields of diagnostic and interventional radiology and diagnostic nuclear medicine. The existence of the DRL guideline can support the national DRL values, update data, and serve as a comparison with relevant SEA RDRL values.

Keywords: Diagnostic Reference level, Optimization, medical exposure

ASEAN COLLEGE OF MEDICAL PHYSICS
Establishing NDRL for FFDM and DBT in Malaysia

Ariffin MN[1], Mohd Imran S[2*], Ismail Z[3], Borhan N[4], Md Non NH[5], Mohd Razak PA[6], Mohamed A[7], Mohamed R[8], Mohd Noor R[9], Mohd Zain NR[10]

1 Medical Radiation Surveillance Division, Ministry of Health Malaysia, Putrajaya, Malaysia.
2 Hospital Ampang, Selangor, Malaysia.
3 Hospital Putrajaya, Putrajaya, Malaysia.
4 Selangor State Health Department, Selangor, Malaysia.
5 Pahang State Health Department, Pahang, Malaysia.
6 Hospital Melaka, Melaka, Malaysia.
7 University Malaya Medical Centre, Kuala Lumpur, Malaysia.
8 Hospital Canselor Tuanku Muhriz UKM, Kuala Lumpur, Malaysia.
9 Hospital Kuala Lumpur, Malaysia.
10 Institut Kanser Negara, Putrajaya, Malaysia.
**nzaina23@gmail.com*

Introduction: Establishing national diagnostic reference level (NDRL) for digital mammography is essential for optimising patient safety and ensuring consistent image quality. This study aims to establish a new NDRL value in full-field digital mammography (FFDM) and digital breast tomosynthesis (DBT) in Malaysia.

Methods: A one-year nationwide survey was conducted from 2022 to 2023. Data were collected from 40 health facilities with FFDM and/or DBT units in Malaysia. NDRLs were set as the third quartile of the distribution of the median values of the mean glandular dose (MGD) obtained from each healthcare facility. Patient demographic information including MGD were recorded. Data were analyzed based on descriptive statistics using Excel statistical software. The DRLs based on MGD were established and compared with other countries.

Results: 1,882 cases were collected from 42 unit of FFDM and DBT systems. The proposed FFDM NDRL for CC and MLO views were 1.6 and 1.8 mGy, respectively. Meanwhile, DBT NDRL for CC and MLO view were 1.9 and 2.3 mGy, respectively.

Discussion: FFDM generally shows lower radiation doses compared to DBT for both CC and MLO views. This is due to different technology and techniques such as multiple projections at different angles. MGD value for DBT MLO view were 28% higher than FFDM, supporting the necessity to develop facility DRL for improvement. Overall, the comparison among countries shows significant variations depending on the type of examination and different practices in the various countries, thus reflecting differences in breast thickness, composition and technological standards.

Conclusion: By applying the proposed NDRLs, healthcare profession can avoid unnecessary radiation exposure, protecting patients from potential radiation-related health risks while still achieving high quality images. This can contribute to better diagnostic accuracy while enhance patient safety.

Keywords:-National diagnostic reference level, FFDM, digital breast tomosynthesis

Establishing diagnostic reference levels for radiological examinations in Singapore: A current overview

S Somanesan[1], Samuel Meng-En Lian[2], Tay Young Soon[1], Joel Low En Zuo[1,3], Laurentcia Arlany[4], Chia Koon Liang[5]

1 Department of Nuclear Medicine and Molecular Imaging, Singapore General Hospital, Singapore
2 Department of Radiography, Changi General Hospital, Singapore
3 Division of Radiological Science, Singapore General Hospital, Singapore
4 Department of Radiology, Sengkang General Hospital, Singapore
5 Department of Diagnostic Imaging, National University Hospital, Singapore
Email: somanesan@sgh.com.sg

Introduction: Singapore currently lacks national diagnostic reference levels (DRLs) for radiological examinations. This study aims to assess the progress in establishing local DRLs, compare them with international standards, and identify challenges and future directions in optimising radiation doses.

Methods: Data were collected from multiple institutions in Singapore, including Singapore Health Services (SingHealth) cluster hospitals and National University Hospital, for computed tomography (CT) and general X-ray examinations from 2015 to 2020. Both manual and automated data collection methods were employed, utilising systems such as DoseMonitor^{TM} and DoseWatch^{TM}. Typical values (50th percentile) and local DRLs (75th percentile) were derived for various examinations.

Results: The study included 17,646 CT examinations (1,706 manual, 15,940 automated) for typical values, 2,413 CT examinations for local DRLs, and 109 general X-ray examinations. Typical values for 14 common general X-ray examinations ranged from 0.02 to 1.12 Gy·cm^2. Local DRLs were established for common CT examinations including brain, chest, kidney-ureter-bladder, abdomen pelvis, and pulmonary angiography.

Discussion: Comparisons between typical values and local DRLs revealed slight differences, attributed to factors such as dose reduction algorithms, patient weight variations, and equipment upgrades. Comparisons with international standards suggest lower radiation doses in Singapore for most examinations. The implementation of automated dose management systems has improved data collection efficiency and real-time monitoring capabilities.

Conclusion: While significant progress has been made in establishing local DRLs and typical values, challenges remain. Future efforts should focus on expanding data collection to include interventional procedures, conducting regular reviews of DRLs, and participating in regional harmonization initiatives.

Keywords: Diagnostic reference levels, computed tomography, X-ray, radiation dose, dose optimisation, medical imaging

ASEAN College of Medical Physics (ACOMP) ASEAN Diagnostic Reference Level, Local Clinical Indication DRLs VS Anatomical-Based National DRLs: Which is appropriate for CT?

Krisanachinda Anchali[1*], Suksancharoen W[2]

1 Department of Radiology, Faculty of Medicine, Chulalongkorn University, Bangkok, Thailand.
2 Department of Radiology, King Chulalongkorn Memorial Hospital, Bangkok, Thailand
**anchali.kris@gmail.com*

Diagnostic reference level (DRL) is the term for the investigation level used for optimization of protection in the medical exposure of patients. DRLs are initially defined for an anatomical location, with lacking information on the clinical indication and on the procedure. A CT scan is used for numerous clinical indications depending on the organs to evaluate. Indications for obtaining a CT scan are to help the physician diagnose, narrow the differential diagnosis, and confirm the doctor's suspicions. CT can also be used for cancer screening, staging, and follow-up, helps to perform biopsies adequately and to assist during a surgical procedure**.** The definition of clinical indication-based, cDRLs, should be a combination of disease and symptoms, anatomical location and of the used technique. CT scans provide information as close to real-time that allows for the proper management of multiple diseases.

The purpose of this presentation to identify the appropriateness of clinical indication LDRL for CT scan in relation to the benefit of anatomical-based from national DRL of CT scan.

Workshop: Point of Care Ultrasound

Gibson, John

Department of Community Health, Mae Fah Luang University, School of Medicine
Chiang Rai, Thailand
john.gib@mfu.ac.th

Point of Care Ultrasound skills have now become an essential skill for virtually all clinicians who diagnose and see patients. We will demonstrate the skills in a variety of clinical situations on normal model patients and then allow the participants a chance to practice the manual skills of the Point of Care Ultrasound exam in the following systems: Cardiac, Liver and Gall Bladder, Renal and Bladder, Aorta and Carotid, Thyroid and small parts and leg venous ultrasound. We discuss and demonstate the role of Ultrasound in medical education to augment the learning of anatomy and clinical decision-making skills of the student clinician. Target Participants: Physicians, radiology technicians, and medical technologist and engineers engaged in design and implementation of medical devices. Workshop format: 2 hours per group, Up to 25 learners per group. Short presentations by Powerpoint followed by participant practice.

Keywords: POCUS; Manual, Medical Education

Reviewing your high dose rate brachytherapy quality assurance program: back to the basics

Wilkinson D Allan, Kost, S

Department of Radiation Oncology, Cleveland Clinic, Cleveland, Ohio, USA

Introduction: With changes in delivery equipment, planning software, regulations, and task group reports, periodic reviews of HDR quality assurance (QA) programs must be performed. The review should focus on the basic elements of the QA program: source dwell time, position, source strength and safety.

Methods: Annual reports from the U.S.NRC and reports from the IAEA were used to identify incidents resulting from the medical application of radionuclides. Additionally, examples from our own practice, including clinical incidents and near misses, will be presented and examined.

Results: There were 8147 nuclear material events listed in the U.S.NRC database for the years 2007 to 2023. Of these, 832 were medical events which can be subdivided into diagnostic (nuclear medicine) and therapeutic (HDR and low dose rate infusions and implants). HDR incidents totaled 90; 72 were planner/physician based; 11 involved equipment failures, and 7 were a result of patient movement. The IAEA Safron database appears to take data from the NRC. Two cases of improper treatment planning from our institution will be discussed in the context of these data.

Discussion: Examination of the historical reporting of medical events involving radioactive materials shows that certain types of errors occur more frequently and therefore should be of particular interest in designing and updating QA procedures. By comparing these examples to our own clinical experience, improvements to the QA program were implemented.

Conclusion: Proactive use of regulatory data can help guide HDR brachytherapy QA program review and modification to increase robustness and preventative detection of errors.

Key Words: Quality assurance, HDR brachytherapy

The current and emerging revolution in ultrasound imaging technology

Gibson John

Department of Community Health, Mae Fah Luang University, School of Medicine
Chiang Rai, Thailand
john.gib@mfu.ac.th

While medical diagnostic ultrasound has been in common use since the 1950s, the last 10 to 20 years has seen an explosion in the development of imaging devices in ever smaller and less expensive packages with advanced image quality and resolution. The emergence of Point of Care Ultrasound (POCUS) performed by the clinician has moved ultrasound equipment out of the domain of the radiology department and into virtually every medical discipline and department. Addition of color doppler, 3D/4D real time imaging along with Tissue harmonic technology has improve scanning fidelity and enabled more accurate diagnoses from OB/GYN to Cardiac to ER and every outpatient setting. Probes in an array of variable sizes and frequencies now can be used to image virtually every part of the body. Emergence of hand held devices along with simplified storage, review capabilities with AI enabled tools have now enabled primary care clinicians to have powerful beside tools that fit into their pocket to take to any location for to better care for their patients. We will review cutting edge advances in elastography, transcranial imaging, holographic projections and new technology in types of ultrasound probes that will further revolutionize the use of ultrasound in the medical world. In addition, we will discuss the role of Ultrasound in medical education to augment the learning of anatomy and clinical decision-making skills.

Keywords: POCUS; AI, Medical Education

Unlocking the Potential of Astatine-211 as a Promising Alternative to Actinium-225 in Theranostics.

Shiratori Shuichi[1*]

1 Department of Radiology, Faculty of Medicine Siriraj Hospital, Mahidol University, Bangkok, Thailand
**shuichi.shi@mahidol.ac.th*

The rise of targeted alpha therapy (TAT) has revolutionized cancer treatment, with Actinium-225 (Ac-225) at the forefront. However, the global demand for Ac-225 has highlighted the need for alternative alpha-emitters. Astatine-211 (At-211) emerges as a promising candidate due to its favorable half-life (7.2 hours) and high linear energy transfer (LET), enabling precise tumor cell destruction with minimal damage to surrounding healthy tissue. Unlike Ac-225, At-211 undergoes a direct alpha decay, eliminating the risk of long-lived daughter isotopes contributing to unnecessary radiation exposure.

The production of At-211 is achieved via cyclotron irradiation of bismuth-209 using alpha particles, offering a scalable and regionally sustainable supply chain. Advances in targetry and separation chemistry have enhanced its availability, paving the way for broader clinical applications.

Efficient labeling methods for At-211 have been developed, leveraging its unique chemistry. Astatination via electrophilic or nucleophilic substitution allows for stable conjugation with biomolecules such as monoclonal antibodies and peptides, maintaining their biological activity and targeting specificity.

Ongoing research explores At-211's efficacy across various malignancies, including glioblastomas, hematological cancers, and metastatic tumors. Preclinical and early-phase clinical trials have demonstrated promising results, with favorable safety and biodistribution profiles.

This symposium will delve into the rationale for adopting At-211 in theranostics, the advancements in its production and radiolabeling, and the translational research efforts underway to position At-211 as a viable alternative to Ac-225, ushering in a new era of precision oncology.

Keywords: Astatine-211, Actinium-225, linear energy transfer, Cyclotron-produced α emitter

Dose verification in organ motion radiotherapy

Pawiro Supriyanto Ardjo*

Department of Physics, Faculty of Mathematics and Natural Sciences, Universitas Indonesia, Depok, Indonesia, 16424
**Supriyanto.p@sci.ui.ac.id*

Organ Motion is a challenge during dose delivery in radiotherapy. In order to evaluate the accuracy of dose delivery, several methods have been developed for dose point measurement and planar dose measurement. In this paper, we will describe the methodology of dose verification in organ motion radiotherapy from the point of view of phantom development and dose measurement in various clinical settings in radiotherapy.

Keywords: Dose verification, organ motion, radiotherapy

Applied physics in Thai biomedical inventions

Punyanitya Sittiporn S[1*], Raksanti A[2], Chankachang P[3,] Koonawoot R[4]

1 Innovative Biomaterials and Medical Device Research Group, School of Medicine, Mae Fah Luang University, Muang, Chiang Rai 57100, Thailand
2 Multidisciplinary Research Institute, Muang, Chiang Mai 50200, Thailand
3 Faculty of Management Science, Sakon Nakhon University, Sakon Nakhon 50200, Thailand
4 Boonyapanit Company Limited, Muang, Chiang Mai 50200, Thailand
** sittiporn.pun@mfu.ac.th*

Our research team aims to enhance the value of Thai natural resources by developing novel inventions from agricultural raw materials and transforming them into midstream and downstream products that offer economic and social benefits, particularly in the fields of biomaterials and medical devices. Many of these innovations are grounded in fundamental principles of applied physics, such as nanotechnology and materials science and engineering. Examples of Thai biomedical inventions include 1. Fresh Rubber Latex Preservation: A new technology that uses hot wet boiling at near-sterilization temperatures (97°C) with non-toxic chemicals like sodium hydroxide, sodium lauryl sulfate, sodium chloride, and sodium bicarbonate, enabling the final solution to be preserved for over four years. 2. Biodegradable Cellulose Fibrils: Fibrils, 500 nanometers long, prepared from medical-grade cotton fiber through the chemical breakage of beta 1,4 glycosidic bonds using strong sulfuric acid. 3. Ready-to-Use Artificial Skull Cap: Designed for skull defect repair, this cap is prepared from micro-sized hydroxyapatite powder with bioactive properties, kept in medical packaging, and sterilized using gamma radiation. 4. Rice Gel for Medical Ultrasonic Signals: Made from medical-grade rice starch of organic origin, this gel serves as a medium for medical ultrasonic signals. Each invention has been prototyped and undergone basic laboratory characterization. All are based on Thai technology, developed by Thai scientists, manufactured in Thailand, and registered for patents. These products are superior and more affordable than those currently available in the Thai market. In addition, the research team is actively developing other medical inventions, such as hot compress cassava gel, medical fibroin from cocoons, and capsaicin from Thai chili peppers, with the goal of producing medical innovations from Thai agricultural raw materials.

Keywords: Natural materials, Agricultural, Biomedical, Medical devices, Innovation.

Trends in AI for MRI: An introduction to the latest technologies

Takatsu Yasuo

Fujita Health University, Department of Molecular Imaging, Clinical Collaboration Unit, School of Medical Sciences, Toyoake, Aichi, and Japan.
yasuo.takatsu@fujita-hu.ac.jp

In MRI, there is a well-known trade-off between resolution and acquisition time, as well as between signal-to-noise ratio (SNR) and acquisition time. Recently, methods leveraging artificial intelligence (AI) have been developed to address this issue by simultaneously reducing acquisition time and performing noise reduction. These techniques denoise high-frequency components and combine them with the original low-frequency components, preserving contrast while achieving a high SNR.

Additionally, technologies have emerged that enable the conversion of relatively low-resolution images into high-resolution images in the k-space domain. Conventional methods, such as zero-filling, which add zeros to the high-frequency region of k-space to enhance apparent resolution, often result in blurring and ringing artifacts. The proposed method applies deep learning to correct these artifacts, enabling the generation of high-resolution images. The neural network used in this approach is trained with fully sampled high-resolution images as reference data, specifically designed to address the limitations of zero-filling. Moreover, this technique incorporates denoising capabilities, allowing for the reconstruction of low-SNR, low-resolution images into high-SNR, high-resolution images.

Another critical factor affecting image quality is motion. AI-powered motion correction techniques have been developed to address both rigid and non-rigid motion, incorporating shot rejection and motion estimation processes. These methods model the effects of motion on echo signals and images in k-space using conjugate gradient methods for efficient estimation and correction. For cases where model-based approaches are insufficient due to significant motion, AI trained to differentiate between motion-affected and unaffected data is employed for correction.

This presentation will provide an overview and explanation of AI-driven noise reduction techniques, high-resolution imaging methods, and advanced motion correction technologies in MRI.

Keywords: magnetic resonance imaging, artificial intelligence, denoise, high-resolution, motion correction.

Risk control: role of a medical physicist not only optimization in diagnostic medical activities

Franco Milano

University of Florence,Italy

The future role of a medical physicist is likely to shift more toward **risk control** rather than focusing solely on **optimization** in diagnostic and therapeutic activities due to the following key developments:

Increased Complexity of Technologies

- **Artificial Intelligence (AI) and Deep Learning (DL)**: The integration of AI and Deep Learning algorithms in medical imaging and radiation therapy is significantly increasing the complexity of these processes. While these technologies promise improved diagnostic accuracy and treatment outcomes, they also introduce **new risks** related to errors in data interpretation, algorithm biases, and system failures. Medical physicists will need to manage these risks, ensuring that the AI tools work as intended and do not introduce harm.
- **Automation**: With more automated systems in medical diagnostics and therapy, there is less human intervention, increasing the potential for **automated errors**. Medical physicists will play a critical role in overseeing these processes and mitigating risks.

Patient Data Management

- **Big Data and Personalized Medicine**: As patient data management becomes more crucial with the advent of personalized medicine, medical physicists will need to ensure that AI models are handling large volumes of data safely. They must oversee data quality, privacy, and security, given that **flaws in data** can lead to inappropriate diagnoses or treatment decisions.
- **Ethical and Privacy Concerns**: The management and security of sensitive patient data is essential in the age of AI. Medical Physicists will need to control the risks associated with data breaches, unauthorized access, and the ethical use of patient data in AI models, ensuring compliance with health regulations.

Regulatory Compliance and Safety Standards

- **New Risks with AI**: AI tools, especially Deep Learning systems, can behave in unpredictable ways due to their "black box" nature. Medical physicists will be tasked with evaluating and controlling the risks posed by AI systems, ensuring that they meet safety and efficacy standards required by national regulatory bodies.
- **Radiation Safety and Dosimetry**: In the therapeutic context, AI-guided radiotherapy systems may optimize dose delivery, but misconfigurations could increase patient exposure to harmful radiation. Controlling this risk becomes essential as technology advances.

Dynamic Adaptation in Clinical Practice

Evolving AI Systems: AI models can change and adapt based on new data inputs over time. Medical Physicists will need to ensure continuous monitoring of AI tools to avoid any unintended negative effects on patient outcomes and avoid risks arising from model drift, where the performance of AI models declines as new data changes the system's behavior.

Quality Assurance and Risk Mitigation Frameworks

- **Proactive Role in Risk Management**: While optimization has been the traditional focus of Medical Physicists—ensuring that medical imaging systems or radiotherapy equipment deliver the best possible results—the future will involve creating robust **risk control frameworks**. These will involve systematic quality assurance protocols, failure mode analysis, and real-time monitoring of AI systems to avoid and mitigate risks before they occur.

Conclusion

With AI, Deep Learning, and Data Management becoming central to healthcare, the **uncertainties and risks** associated with these technologies will grow. Medical Physicists will transition from primarily optimizing workflows and equipment to ensuring the **safe and reliable** application of these advanced tools. Risk control in this context involves **anticipating, identifying, and mitigating potential threats**, making it a central focus of their future role in clinical practice.

Fundamental Principles of AI Relevant to Medical Physicists

Chanon Puttanawarut[1,2*] Nat Sirirutbunkajorn[3].

1. *Chakri Naruebodindra Medical Institute, Faculty of Medicine, Ramathibodi Hospital, Mahidol University, Samut Prakan, Thailand*
2. *Department of Clinical Epidemiology and Biostatistics, Faculty of Medicine, Ramathibodi Hospital, Mahidol University, Bangkok, Thailand*
3. *Department of Diagnostic and Therapeutic Radiology, Faculty of Medicine, Ramathibodi Hospital, Mahidol University, Bangkok, Thailand*

**chanonp@protonmail.com*

Artificial Intelligence (AI), particularly machine learning (ML) and deep learning (DL), has the potential to revolutionize medical physics by automating tasks, improving diagnostic accuracy, and optimizing treatment plans. For medical physicists, understanding the foundational principles of AI is important to leveraging its potential in practice. However, it also poses risks if applied incorrectly, including the potential to harm patients due to unreliable or poorly validated models. This underscores the critical need for medical physicists to understand not only the concept of AI development but also how to ensure its reliability. This introduction will provide a basic knowledge of AI, including its subset, machine learning (ML) and deep learning (DL), with a focus on their relevance to medical physics. This presentation will provide a concise overview of AI, ML, and DL concepts, focusing on their relevance to medical physics applications. We will explore a typical AI pipeline, including data acquisition, preprocessing, feature engineering, model training, and evaluation. Furthermore, to ensure the reliability and safety of AI-driven solutions, we will discuss the importance of trustworthy AI. This includes addressing challenges like out-of-distribution generalization, uncertainty quantification, and model interpretability. Attendees will gain insights into the opportunities and risks associated with AI in medical physics. This knowledge will support them to make informed decisions and contribute to the development and deployment of AI solutions that enhance patient care and improve clinical outcomes.

Keywords: Artificial Intelligence, Machine learning, Deep learning, Trustworthy, Medical physics.

The role of medical physicist in THAI QUATRO

Kakanaporn, C*

**Division of Radiation Oncology, Faculty of Medicine Siriraj Hospital, Mahidol University, Bangkok, THAILAND*
**kakanaporn@yahoo.com*

Nowadays, radiation therapy technology has been rapidly developed to escalate high radiation dose to the tumor and rapid steep dose gradient to the normal structure close by. As a result, the standard of radiotherapy for the treatment of selected cases of several cancers is Intensity Modulated Radiation Therapy (IMRT)/ Volumetric Modulated Arc Therapy (VMAT). As part of a comprehensive approach to quality assurance (QA) in the radiation therapy, an independent external audit is important to assess adequate quality of practice and delivery of treatment. Quality audits can be of various types and levels, either reviewing specific critical parts of the radiation therapy process, partial audit or comprehensive audit. Whole process audit methodology has been developed by IAEA through a series of workshops, with the input of numerous experts from various parts of the world. It is called “QUATRO, Quality Assurance Team for Radiation Oncology. A tool for quality improvement.”

In Thailand, we have decided to use the existing IAEA QUATRO methodology and audit tool in order to carry out peer-reviewed clinical audits of our radiotherapy departments since 2023. With the help of IAEA and Thai Office of Atoms for Peace (OAP), Thai Association of Radiation Oncology (THASTRO) has proposed the project to set up National QUATRO project aims to continually maintain the National auditing system of radiation therapy treatment established in overall radiation therapy facilities in Thailand and it is called “ T QUATRO”.

Setting up T QUATRO audit: THASTRO together with Thai medical physicist society, Thai society of radiological technologists, National cancer institute, Department of medical services, and OAP is setting up the system.

For medical physicist task in T QUATRO

- Obtains the necessary Pre-Audit information from the clinic
- Patient related procedures
- Machine related procedures
- Radiation safety
- Physical measurement in the program

Physical measurements within the program

Development of End-to-End 3D Dosimetry Audit for Advanced Radiotherapy

Ahmad Taufek Abdul Rahman[* 1, 2], Muhammad Zamir Mohyedin[1,3], Hafiz Mohd Zin[4]

1 School of Physics and Material Studies, Faculty of Applied Sciences, Universiti Teknologi MARA, 40450 Shah Alam, Selangor, MALAYSIA.
2 Centre for Astronomy and Applied Radiation, Institute of Science, Universiti Teknologi MARA, 40450 Shah Alam, Selangor, MALAYSIA.
3 Institute for Mathematical Research (INSPEM), Universiti Putra Malaysia, Serdang 43400, Selangor, Malaysia
4 Advanced Medical and Dental Institute (IPPT), Universiti Sains Malaysia, Penang, Malaysia

The increasing complexity of modern radiotherapy techniques poses challenges to both dosimetric and geometric accuracy in dose delivery. To ensure precision, it is essential to verify the dose distribution using a dosimetry system that accounts for variations in human tissue, thereby more accurately reflecting patient-specific conditions. Commercial phantoms, often composed of homogeneous water-equivalent materials, lack the ability to measure dose distribution in three dimensions (3D). Level III dosimetry audits require verification within an anthropomorphic phantom to better simulate clinical scenarios. With the steep dose gradients inherent in advanced radiotherapy techniques such as intensity-modulated radiotherapy (IMRT) and volumetric-modulated arc therapy (VMAT), 3D dosimetry is increasingly necessary to capture these variations. In this study, we developed an end-to-end 3D radiotherapy dose audit system using the MAX-HD anthropomorphic head and neck phantom (IMT, Troy, New York) with a customized intracranial insert for the PRESAGE® dosimeter. The phantom features a removable, four-part radiochromic film insert that forms a cubic shape within the intracranial region, which was adapted to accommodate the PRESAGE® dosimeter. Both IMRT and VMAT treatment plans were applied to a 20- mm spherical target in the brain region of the phantom. The first irradiation utilized the PRESAGE® insert, while the second employed the radiochromic films in both the coronal and axial planes. Dose distributions were measured using an in-house optical computed tomography (OCT) imaging system, which employs a CMOS Active Pixel Sensor and lens to capture projection images of the rotating PRESAGE® dosimeter. These images were reconstructed into 3D volumetric data using a filtered backprojection algorithm in MATLAB (MathWorks, Natick, MA, USA). The 3D dose distribution measured with PRESAGE® showed strong agreement with both radiochromic film measurements and treatment plan predictions, with a maximum difference of less than 3% for both IMRT and VMAT treatments. Discrepancies observed were largely attributed to limitations in the dosimetry system, such as ring artefacts in OCT imaging due to light scattering and refractive index mismatches between the matching liquid and the PRESAGE® material. Despite these artefacts, the 3D volumetric data obtained through the OCT system provided a valuable means of compensating for these errors. Gamma analysis comparing PRESAGE® measurements to EBT film and the Monaco treatment planning system (TPS) showed pass rates exceeding 95% for the 3% dose difference and 3 mm distance-toagreement criteria. This study demonstrates the feasibility of using the PRESAGE® dosimeter, the MAX-HD phantom, and the OCT imaging system for comprehensive 3D dose distribution measurement, supporting the advancement of Level III dosimetry audits in radiotherapy.

MRGRT: Clinical Implementation and Challenges

Sathitwatthanawirot Chanida*

Department of Radiology, Division of Radiation Oncology, Faculty of Medicine Siriraj Hospital, Mahidol University, Bangkok, Thailand
**chanida.cs7@gmail.com*

Imaging plays an important role in radiotherapy. To improve the accuracy of treatment, in-room imaging is necessary to verify the patient's position before starting treatment delivery, a process known as image-guided radiotherapy (IGRT). Nowadays, the technology used for in-room imaging has improved to enhance image quality. Magnetic Resonance Imaging (MRI) provides superior soft tissue contrast and is recommended for target delineation. As a result, there have been developments to integrate MRI with the linear accelerator (Linac), creating the MR-Linac machine.

Siriraj Hospital began using the MR-Linac for clinical treatments in 2021. Since then, over 500 patients have been treated with the MR-Linac, totaling more than 3,000 treatment fractions. The most common cases treated are prostate cancer, followed by liver cancer, lymph node metastasis, pancreatic cancer, cervical cancer, bladder cancer, and others.

The advantages of the MR-Linac include the absence of radiation during image acquisition, meaning MRI can be performed at any time. It also features 2D-cine imaging, which allows real-time monitoring of the target during beam delivery. Additionally, the MR-Linac can perform adaptive radiotherapy (ART) both online and offline, allowing for the adaptation of treatment plans based on the daily position and shape of the tumor.

Although the MR-Linac has many advantages, it still has some limitations. The process of online adaptive planning is time-consuming due to contouring and planning steps. However, MRI can still be used to verify the patient’s position before beam delivery. Furthermore, treatment planning is limited to step and shoot IMRT (Intensity-Modulated Radiation Therapy), and the dose rate of the MR-Linac machine is relatively low due to the long source-to-axis distance, which results in longer treatment times compared to conventional Linac machines. Therefore, it may not be suitable for patients who are in poor condition or unable to lie still for extended periods.

In summary, while the MR-Linac offers many benefits, it also has limitations. Thus, a careful trade-off must be made when deciding on adaptive planning techniques and selecting patients in good condition for treatment.

Keywords: MR-Linac, image-guided radiotherapy, adaptive radiotherapy

Gel dosimeter for radiotherapy

Akihiro Takemura*

Faculty of Health Sciences, Institute of Medical, Pharmaceutical and Health Sciences, Kanazawa University. Kanazawa, Ishikawa, Japan
**at@mhs.mp.kanazawa-u.ac.jp*

Nowadays, highly precise dose delivery techniques such as volumetric modulated arc therapy and stereotactic radiation therapy are commonly used in radiotherapy treatment. These techniques require complex leaf motion or precise leaf positioning for small fields. Therefore, it is crucial to assure accurate dose delivery before the initial treatment. However, these dose distributions cannot be directly measured in three dimensions. Instead, they are typically checked in two dimensions or reconstructed from a few two-dimensional dose planes.

Gel dosimeters offer the potential to directly measure three-dimensional dose distributions. Gel dosimeters are a type of chemical dosimeter. There are several types of gel dosimeters, including polymer gel dosimeters and dye gel dosimeters. Each type has a different composition and responds differently to radiation. They are soft and jelly-like, allowing for flexible shaping and enabling three-dimensional dosimetry. However, they also have advantages and disadvantages.

In this lecture, I will discuss the following topics:

- What is a Gel Dosimeter?
- Chemical Reactions
- Contributions by Japanese Researchers

These topics will cover the types of gel dosimeters, the chemical reactions involved in each type, and examples of research using gel dosimeters in radiotherapy, including our own research.

Keywords: Gel dosimeter, Radiotherapy, 3D dose distribution

Physics of Proton Therapy and Future Directions

Koh Wei Yang, Calvin

National Cancer Centre Singapore, Division of Radiation Oncology
calvin.koh.w.y@nccs.com.sg

The accurate delivery of proton therapy relies fundamentally on the understanding of proton beam physics and dosimetry, which directly impacts the commissioning of treatment planning systems (TPS). This session will begin with essential proton beam physics, focusing on stopping power relationships, range uncertainties, and the characteristics of the pristine and spread-out Bragg peak. We will explore the reference and absolute dosimetry parameters including integral depth dose measurements, lateral beam profiles, and spot characteristics in pencil beam scanning systems. The session will detail key commissioning measurements required for TPS configuration, including absolute dose calibration, monitor unit verification, and biological measurements. Particular emphasis will be placed on the relationship between measured beam data and TPS beam modelling parameters, highlighting how measurement uncertainties propagate through the commissioning process. Looking toward the future, the presentation concludes emerging trends including hardware miniaturization, proton imaging developments, LET optimization strategies, FLASH therapy, adaptive treatment approaches, artificial intelligence applications, and the potential of proton arc therapy. This comprehensive overview aims to connect fundamental principles with practical clinical implementation while providing insight into innovations shaping the field's future.

CT workshop and lecture

Tsujioka Katsumi

School of Medical Sciences,
Fujita Health University. Toyoake, Aichi, JAPAN
tsujioka@fujita-hu.ac.jp

Latest CT Technology -Performance Evaluation and New Research Trends

CT workshop

1) Lecture (Measurement principle)
   - Performance evaluation in CT
   - Spatial resolution (MTF, TTF)
   - Contrast resolution (SD, NPS)
   - Temporal resolution (TSP)
   - Artifact
2) Hands-on seminar
   Practical training using CT measure software provided by JSCT
   CTmeasure, http://www.jsct-tech.org/, 2012-2014.
   - MTF
   - NPS
   - CT number measurement

CT lecture

1) Latest CT Technology
   - Photon counting CT
   - High spatial resolution CT
   - Deep learning reconstruction
   - Others
2) Latest CT Research Trends
   - Contrast enhancement technology
   - Special clinical techniques

Cross-sectional dose distribution of 3D C-arms with volumetric imaging capability for fluoroscopically-guided interventions: challenges and opportunities for medical physicists

Azzi Akbar[1,2], Sulistyani A[1], Rachman ND[1], Satrio MC[2], Raharja HDR[4], Gani MRA[5], Lubis LE[1,2,3,*]

1. *Department of Physics, Faculty of Mathematics and Natural Sciences, Universitas Indonesia, Depok 16424, Indonesia*
2. *Center for Medical Physics and Biophysics, Institute for Applied Sciences, Faculty of Mathematics and Natural Sciences, Universitas Indonesia, Depok 16424, Indonesia*
3. *Radiology Unit, Universitas Indonesia Hospital, Depok 16424, Indonesia*
4. *Radiology Department, MRCCC Siloam Hospitals Semanggi, Jakarta 12930, Indonesia*
5. *Radiodiagnostic Department, Dharmais National Cancer Center, Jakarta 11420, Indonesia*

**lukmanda.evan@sci.ui.ac.id*

Introduction: 3Dimension C-arm systems with volumetric imaging capabilities are essential for fluoroscopically-guided interventions, yet dose distribution assessment remains crucial for patient and staff safety, especially in non-360-degree rotation imaging like 3D rotational angiography (3DRA). This study investigates cross-sectional dose distribution using Monte Carlo simulations alongside thermoluminescent dosimeters (TLDs) and radiochromic film in an in-house phantom.

Methods: An in-house phantom was designed to simulate clinical conditions, capturing dose distribution during 3DRA imaging in two angiography devices. TLDs and radiochromic film were strategically placed within the phantom to record dose values across different cross-sectional planes. Monte Carlo simulations were developed to model the 3D C-arm setup and imaging protocol. The measured dose maps were then visually compared with simulation results to evaluate alignment.

Results: Both TLD and radiochromic film measurements demonstrated strong visual agreement with Monte Carlo simulation results, indicating accuracy in capturing dose distribution profiles for partial-rotation 3D imaging. This alignment supports the combined use of simulation and measurement for reliable dose assessment in 3DRA.

Discussion: The concordance between TLD, film measurements, and simulations suggests that this approach effectively captures complex dose patterns in non-360-degree imaging protocols. Using both simulations and physical measurements can provide comprehensive insight into dose distribution, which is critical for effective dose management in 3D C-arm procedures.

Conclusion: This study demonstrates that combining Monte Carlo simulations with TLD and radiochromic film measurements is an effective dosimetry method for 3D C-arm systems with non-360-degree rotation, like 3DRA. These findings establish a basis for selecting dosimetry methods suitable for partial-rotation volumetric imaging, supporting dose optimization strategies in clinical practice.

Keywords: 3DRA, Dose distribution, Monte Carlo simulation, TLD.

Patient Dosimetry in Pediatric CT

Matsubara Kosuke[1*]

1 Department of Quantum Medical Technology, Faculty of Health Sciences, Institute of Medical, Pharmaceutical and Health Sciences, Kanazawa University, Kanazawa, Japan
**matsuk@mhs.mp.kanazawa-u.ac.jp*

Children are at higher risk of developing radiation-induced cancers because they are younger at the time of exposure and many tissues are more sensitive to radiation than adults. They may receive a higher radiation dose than necessary if CT scan parameters are not adjusted for their body size.

From the measurement results using a 1-year-old phantom and radiophotoluminescence glass dosimeters, various information can be obtained for optimizing scanning parameters in pediatric CT. In head CT, there was a large difference in the absorbed dose depending on the position in the body axis direction. The absorbed doses at the eye lenses were higher than at other positions, and the absorbed dose within the cross section was relatively uniform. In neck CT, the difference in absorbed dose within the cross section was small, and the absorbed dose at the thyroid location tended to be higher than at other locations. In chest CT, the absorbed doses to lung tissue were slightly lower than those to soft tissue in all cross sections that included the lungs. In abdominal CT, the variation in absorbed dose in the body axis direction was small, and the difference in absorbed dose within the cross section was also small. Additionally, the distribution of absorbed dose differed depending on the tube voltage even if the output radiation dose was almost the same.

When determining the optimal scanning parameters including tube voltage, consideration should be given not only to the image quality, such as contrast-to-noise ratio, but also to the absorbed dose distribution.

Keywords: Pediatric CT, dosimetry, radiophotoluminescence glass dosimeter

3D cellular arrange modeling trend for the future

Wanta Arunothai[1*], Boonyaputthikul H[2*]

1 Cancer and Immunology Research Unit (CIRU), School of Medicine, Mae Fah Luang University, Chiang Rai, Thailand
2 Histocenter (Thailand), Co., Ltd., Bangkok, Thailand
**arunothai.wan@mfu.ac.th,*Harit@histocenter.com*

The traditional two-dimensional (2D) arrangement of cells and tissues, typically observed on a flat plane, often fails to fully capture the intricate structure and organization of biological samples. In contrast, three-dimensional (3D) reconstruction offers a more accurate and realistic depiction, revealing the complete architecture of biological structures. Examining tissues in 3D enables researchers to understand spatial relationships, such as cellular interactions with their environment, which is essential for analyzing complex structures like tumors, organs, and neural networks. 3D studies provide more realistic observations of cellular behaviors, including migration, proliferation, and differentiation, compared to conventional 2D cultures. This is particularly critical for understanding diseases such as cancer, where alterations in the 3D structure of tissues significantly influence disease progression and therapeutic strategies. Advanced imaging technologies, including live cell imaging systems, confocal microscopes, and scanning electron microscopes (SEM), have transformed the study of cells and tissues in 3D by offering high-resolution images and detailed analyses. Techniques such as time-lapse imaging, Z-stack acquisition, and electron beam scanning are pivotal in producing 3D reconstructions. Moreover, numerous third-party companies now leverage artificial intelligence (AI) to generate high-quality 3D images of biological structures, thereby enhancing diagnostics, research, and education in medical science.

As 3D reconstruction continues to trend and advance rapidly, it provides a more comprehensive understanding of cellular and tissue structures, leading to deeper insights into their functions, behaviors, and interactions.

Keywords: 3D reconstruction, Cell, Tissue, AI

Establishing target exposure index in digital radiography – preliminary experience from AAPM Task Group 368

Zhao Anzi.*[1]

1 Department of Radiology, *Northwestern University, Northwestern Medicine, Chicago, IL, USA.*
*anzi.zhao@nm.org

Introduction: In digital radiography (DR), the exposure index (EI) is a metric used to estimate exposure to the image detector and hence to evaluate the exposure levels of radiographic exams. EI helps optimize clinical practice in DR by reducing dose creep and electronic noise. The target exposure index (TEI) represents the optimal exposure for a radiographic exam, while the deviation index (DI) indicates deviations from this target, providing immediate feedback to technologists. The AAPM Task Group (TG) 368 is dedicated to developing a methodology for appropriately establishing TEI in DR.

Methods: Two workflows, A and B, have been developed to establish TEI for common radiographic exams. Workflow A is designed for radiological technologists to retrospectively analyze EI data to adjust TEI accordingly. Workflow B is designed for facilities with medical physicists, who can prospectively normalize clinically reported EI values to a TEI that accurately reflects detector exposure from the Automatic Exposure Control (AEC) system. A methodology was developed to estimate TEI, accounting for variability related to X-ray tube potential and AEC density. Clinical EI data were collected from seven DR manufacturers, categorized by bucky type, anatomical region, imaging view, and AEC parameters, focusing on eight common protocols across seven anatomical regions.

Results: Over 37,000 images acquired from 25 X-ray systems were analyzed, revealing significant variability ($p<0.05$) in the clinical EI based on anatomical region, imaging view, and the manufacturer. Both workflows have provided systematic methodologies designed to assist end users in establishing their TEI.

Discussion: The findings underscore the necessity of appropriately establishing TEI values. It was found that variabilities in the calculation of clinical EI among different manufacturers represent a significant factor impacting clinical EI values.

Conclusion: A methodology for establishing TEI has been developed for DR, offering potential for enhanced practice in the acquisition of radiographic imaging.

Keywords: digital radiography, exposure index, target exposure index, automatic exposure control.

Implementation of population PK modeling in molecular radiotherapy

Hardiansyah Deni*

Medical Physics and Biophysics Research Group, Physics Department, Faculty of Mathematics and Natural Sciences (FMIPA), Universitas Indonesia, 16424 Indonesia.
**denihardiansyah@ui.ac.id*

Individualized calculation of radiation absorbed doses is desirable for optimizing molecular radiotherapy in theragnostic. Population pharmacokinetic (PK) modeling, particularly through non-linear mixed-effects (NLME) approaches, has emerged as a robust tool for achieving this goal. These advanced techniques surpass traditional individual fitting and widely used single-time-point (STP) dosimetry methods by delivering higher accuracy in radiation dose estimation.

NLME modeling not only enhances accuracy but also provides critical insights into the inter- and intra-individual variability of radiation dose distribution within a population, enabling more personalized and effective treatment planning. These capabilities contribute to improved dosimetry in clinical applications.

This presentation will discuss the theoretical principles, practical implementation, and recent developments in population PK modeling using NLME techniques for molecular radiotherapy dosimetry. It will highlight their transformative role in advancing treatment accuracy, optimizing patient care, and shaping the future of dosimetry in theragnostic.

Keywords: Population PK, NLME, STP, theragnostic, dosimetry.

Radionuclide imaging and therapy in oncology

Angsulajit Polawat [1, 2*]

1 Medical Oncology Unit, Department of Medicine, Mae Fah Luang University medical center hospital, Mueang Chiang Rai District, Thailand.

2 Cancer and Immunology Research Unit (CIRU), Mae Fah Luang University, Chiang Rai 57100, Thailand

**polawat.ang@mfu.ac.th*

The role of nuclear medicine in the personalized management of oncology patients is rapidly growing, offering effective and low-risk approaches for both diagnostics and internal radioactive isotope therapy. Compared to traditional anatomic imaging techniques, radionuclide imaging techniques, such as positron emission tomography (PET), provide in-depth insights into tumor metabolism and molecular processes, with significantly greater sensitivity and ability to enable early detection, precise staging, therapy selection, effective treatment planning, as well as monitoring therapy response and follow-up. Concurrently, radionuclide therapy has emerged as a transformative approach in oncology, using radioactive isotopes to deliver targeted radiation directly to cancer cells. This therapeutic modality specifically binds to cancer cells, delivering localized radiation while sparing adjacent healthy tissues. The dual approach of nuclear medicine is not only improving patient outcomes by personalizing treatment strategies but also advancing our understanding of cancer biology and therapeutic targeting.

This presentation introduces the significance and current state of radionuclide imaging and therapy in oncology, highlighting their potential to further revolutionize cancer treatment paradigms.

Personalised dosimetry in theranostic nuclear medicine: lessons learnt

YEONG Chai Hong

School of Medicine, Faculty of Health and Medical Sciences, Taylor's University, 47500 Subang Jaya, Malaysia
yeongchaihong@gmail.com

Theranostic nuclear medicine, an innovative approach merging therapeutic and diagnostic principles in nuclear medicine, has garnered significant attention in the realm of precision medicine. Personalised dosimetry plays a vital role in achieving optimum treatment outcomes. This lecture shares the current practice of theranostic nuclear medicine, focusing on the journey towards personalized dosimetry, which holds immense promise in optimizing therapeutic outcomes while minimizing adverse effects on the patients. The essence of personalised dosimetry lies in its ability to tailor treatments to individual patients based on precise assessments of disease characteristics and therapeutic response. However, the realization of personalized dosimetry in nuclear medicine remains a frontier yet to be fully traversed. Lessons learnt from clinical practice highlight the complexity of integrating personalised dosimetry into workflows, requiring precise imaging, multi-time point protocols, and dedicated software. A key challenge is the lack of standardization in dosimetry practices, leading to variability in treatment planning and reporting. Successful implementation has shown that collaboration across disciplines, i.e. nuclear medicine, medical physics, radiology, and computational science, is essential for overcoming technical and clinical barriers. Additionally, advances in data accuracy, software usability, and patient-specific modelling are vital for improving dosimetry precision, though limitations in data interoperability remain. Regulatory and ethical considerations, including ensuring equitable access to technology, must also evolve in tandem with these advancements. Looking ahead, the future of personalised dosimetry in theranostic nuclear medicine depends on continued technological development, standardized practices, and stronger global research collaborations to turn theoretical concepts into practical, patient-centered solutions, maximizing the potential of precision cancer treatments.

New Trends for Lu-177 Personalized Dosimetry using a Ring-shaped CZT-based Camera: the Game Changes?

Khamwan Kitiwat*

Department of Radiology, Division of Nuclear Medicine, Faculty of Medicine, Chulalongkorn University, Bangkok, Thailand
**kitiwat.k@chula.ac.th*

Molecular radiotherapy (MRT) has emerged as a promising targeted approach for treating various cancers by delivering radiation directly to cancer cells. Lutetium-177 (^{177}Lu)-labelled radiopharmaceuticals are increasingly used in therapeutic applications, particularly for treating metastatic neuroendocrine tumors with somatostatin receptor ligands and prostate adenocarcinoma with PSMA-targeting ligands. As interest in targeted radionuclide therapies for personalized medicine grows, MRT dosimetry is becoming increasingly important. Accurate, patient-specific dose estimation is crucial for optimizing clinical outcomes while minimizing the risk of radiation-induced toxicity, especially in rapidly developing cancer therapies where the risk–benefit ratio must be carefully evaluated. The current Medical Internal Radiation Dose (MIRD) formalism, based on organ-level dosimetry using time-integrated activity and radionuclide S-values, provides the mean absorbed dose to a target organ per radioactive decay in a source organ. However, this organ-based schema assumes a uniform activity distribution within each organ, which is not always the case. To overcome this limitation, voxel-based dosimetry techniques that consider heterogeneous activity distributions including the dose point kernel and voxel S-value (VSV) approaches have been proposed, which offers more accurate dosimetry at the voxel level. The recent introduction of a ring-shaped 12-swiveling CZT-based digital detectors SPECT/CT, has revolutionized the state-of-the-art imaging technology in the field. This system offers higher sensitivity, improved count rate performance, reduced acquisition time and total activity, and better spatial resolution compared to conventional cameras. By enabling fully digital tomographic exams, it captures photons more effectively, resulting in enhanced image contrast and lesion detection, thus providing more accurate dosimetry for radiopharmaceutical therapies. This presentation delves into a cutting-edge approach on the personalized dosimetry for Lu-177 molecular radiotherapy utilizing a ring-shaped 12-swiveling CZT-based digital detectors SPECT/CT including its advanced imaging techniques, representing a novel and potentially transformative approach for theranostic dosimetry in nuclear medicine.

Keywords: Lu-177 therapy, theranostic dosimetry, ring-shaped CZT SPECT/CT, molecular radiotherapy, voxel-based dosimetry

Implementation of Dosimetry for Molecular Radiotherapy in South East Asia Region: Current Status

Hidayati, NR[1,2*], Nuraeni N[1], Ardjopawiro, S[2], Hardiansyah, D[2]

1 Research Center for Safety, Metrology, and Nuclear Quality Technology, National Research and Innovation Agency(BRIN), KST BJ Habibie, Tangerang Selatan, Indonesia.
2 Department of Physics, Faculty of Mathematics and Natural Sciences. Universitas Indonesia. Depok Campus, Indonesia.
**Email: nurr001@brin.go.id.*

Introduction: Molecular radiotherapy (MRT) is a rapidly advancing cancer treatment that relies on accurate dosimetry to ensure effective and safe therapy. Dosimetry is highly desirable in personalized treatment planning, dose verification, and minimizing harm to non-target tissues. This talk aims to highlight the current state of dosimetry in Southeast Asia, its critical importance in radionuclide therapy, and practical approaches for improvement. By fostering collaboration and commitment among regional stakeholders, Southeast Asia can advance dosimetry implementation, ensuring equitable access to safer and more effective MRT across the region.

Methods: This presentation draws insights from the European experience with MRT dosimetry, focusing on data from surveys, guidelines, and implementation strategies. Recommendations are tailored to the Southeast Asian context, emphasizing the need for assessing current MRT capabilities, establishing regional guidelines, training medical physicists, prioritizing QA protocols, and expanding access to dosimetry tools.

Results: Key findings suggest that while MRT is increasingly adopted in the region, the implementation of dosimetry might vary significantly. Regions with limited dosimetry practices face risks such as suboptimal dosing and reduced patient safety.

Discussion: The European approach highlights the importance of regional collaboration, training, and standardized practices to enhance dosimetry. For Southeast Asia, addressing gaps in staffing, infrastructure, and QA can help overcome barriers. Leveraging international support and fostering regional partnerships are key to advancing dosimetry implementation.

Conclusion: Improving dosimetry practices in Southeast Asia is critical for enhancing the safety and efficacy of MRT. By adopting tailored strategies, the region can ensure equitable access to advanced radionuclide therapies and better align with international standards. Regular evaluations and collaboration will be essential to sustain progress

Keywords: Dosimetry Molecular Radionuclide Therapy, South East Asia Region, Patient Safety

AI in Medical Imaging and Nuclear Medicine

Rakvongthai Yothin[1,2*]

1 Division of Nuclear Medicine, Department of Radiology, Faculty of Medicine, Chulalongkorn University, Bangkok, Thailand.
2 Chulalongkorn University Biomedical Imaging Group, Department of Radiology, Faculty of Medicine, Chulalongkorn University, Bangkok, Thailand.
**yothin.r@chula.ac.th*

Artificial intelligence (AI) is revolutionizing the field of medical imaging and nuclear medicine, offering the potential to improve diagnostic accuracy, treatment planning, and patient outcomes. This session will delve into the current state of AI, focusing on its applications in image reconstruction, image analysis, and clinical decision support. Moreover, we will explore the challenges and limitations of AI in medical imaging and nuclear medicine.

Keywords: Artificial intelligence, Medical imaging, Nuclear medicine, Image analysis

Commissioning of a clinical pencil beam scanning proton therapy unit for ultra-high dose rates (FLASH)

Grossmann Handschin Martin*

Paul Scherrer Institut, WBBB/006, Forschungsstrasse 111, 5232 Villigen PSI, Switzerland
**martin.grossmann@psi.ch*

After the end of clinical operation at PSI Gantry 1 in December 2018 we worked to convert it into a flexible platform for FLASH research with protons by adapting a former clinical pencil beam scanning gantry to irradiations with ultra-high dose rates. We optimized the beamline parameters to transport the 250 MeV beam extracted from the PSI COMET accelerator to the treatment room, maximizing the transmission of beam intensity to the sample. We characterized a dose monitor on the gantry to ensure good control of the dose, delivered in spot-scanning mode. We characterized the beam for different dose rates and field sizes for transmission irradiations. We explored scanning possibilities in order to enable conformal irradiations or transmission irradiations of large targets (with transverse scanning).

TRS492 on Brachytherapy Dosimetry and the updated TRS398

Buppaungkul Sakchai*

Department of Medical Sciences, Ministry of Public Healths, Nonthaburi, Thailand
**sakchai.b@dmsc.mail.go.th*

The technology in radiotherapy has rapidly change therefore reference protocols have to be updated. The IAEA TECDOC-1274 has been used for calibration of photon and beta ray sources used in brachytherapy in Thailand however IAEA has published new reference protocol for brachytherapy TRS-492 in 2023. New parameters such as source data and source model correction factors are added in this new protocol. For external beam radiotherapy, IAEA TRS-398 has been updated and replaced old version. IAEA TRS-398 v.1 changes reference protocols for dosimetry measurement. Because of increasing the use of experimental data and simulated calculation, the correction factors have been changed in order to get the accuracy for determination of absorbed dose to water measurement. Specifications and characteristics for reference equipment are added in the chapter 4. For high energy photon beams, k_{vol} and k_q value can be calculated by $TPR_{20,10}$ follow the equation 22 and 34 respectively. Plane parallel ionization chamber used for low energy x-ray dosimetry has to add additional buildup 0.2 mm thick PMMA for tube voltage above 40 kV. Reference conditions for determination of absorbed dose in high energy electron and medium energy x-ray are clearly defined in Table 19 and 31 respectively. For proton beam dosimetry, the reference ionization chambers calibrated in Co-60 can be used however cross calibration is recommended in this version.

TRS492 on Brachytherapy Dosimetry and the updated TRS398 have been published by IAEA. The change of correction factors and reference conditions affect to the absorbed dose measurement. Therefore, medical physicists have to update their data in order to get the accuracy dose for treatment.

Keywords: reference protocol, correction factor, cross calibration,

Evolutions and applications of surface guided radiotherapy

Watcharawipha Anirut[1], Suphaphong S[2]

1 Department of Radiology, Division of Radiation Oncology, Faculty of Medicine, Chiang Mai University, Chiang Mai, Thailand.

2 Department of Diagnostic and Therapeutic Radiology, Division of Radiation Therapy, Faculty of Medicine Ramathibodi Hospital, Mahidol University, Bangkok, Thailand.

Surface Guided Radiotherapy (SGRT) is one of the image-guided radiotherapy equipment. This system provides images of surface objects using optical light. The technique utilizes 3-Dimension image capture that locates the surface coordinates using triangulated calculation. The displacements of the position are calculated using image registration, both Rigid Image Registration (RIR) and Deformable Image Registration (DIR). Recently, another dimension has been combined in the SGRT system, which is the object temperature. This dimension can provide the benefit of uphill and downhill of the object surface. However, these system require an acceptance test procedure (ATP) and commissioning to be implemented in the clinic, as recommended by the American Association of Physicists in Medicine Task Group report 302 (AAPM TG-302). The guideline also recommends the workflows for each treatment region and considerations in the application of SGRT, such as the effect of the reference surface and region of interest, assessing the impact of image quality, and the impact of camera occlusion. Finally, most clinical applications using SGRT are applied to position verification, motion monitoring, and deep inspiration breath hold (DIBH).

Medical Physics and AI: Where Do We Start?

Carrion Daniel[1*], Badawy MK[1,2]

1 Monash Imaging, Monash Health, Clayton, Australia
2 Department of Medical Imaging and Radiation Sciences, Monash University, Melbourne, Australia
**daniel.carrion@monashhealth.org*

Artificial intelligence (AI) is transforming medical physics, enhancing diagnostics, optimising workflows, and improving patient care. However, for many medical physicists, getting started can feel daunting. This presentation offers a practical introduction to AI, focusing on core concepts, accessible tools, and real-world applications to help attendees take their first steps.

We'll begin by demystifying machine learning and neural networks, followed by an exploration of practical frameworks and open-source resources that simplify AI implementation. These tools empower medical physicists to quickly gain hands-on experience and reduce barriers to adoption.

The presentation includes real-world applications of AI, such as using machine learning to identify suboptimal chest X-rays and applying CycleGANs in wrist imaging for cast suppression. These examples showcase AI's potential to address challenges in medical imaging and will be discussed to highlight practical lessons and outcomes.

Finally, the presentation provides a quick look at setting up essential infrastructure for AI projects. Attendees will get an overview of how to use Orthanc to set up a separate PACS server for research and AI purposes, keeping clinical systems untouched while enabling secure access to imaging data for model training.

Designed to benefit medical physicists across all expertise levels, this presentation provides concrete steps and practical knowledge to begin incorporating AI into medical physics work.

Keywords: Medical Physics, Medical Imaging, Quality Control, Infrastructure, AI, Governance

Beyond Language Barriers: Generative AI in Patient Communication

Badawy MK[1,2]

1 Monash Imaging, Monash Health, Clayton, Australia
2 Department of Medical Imaging and Radiation Sciences, Monash University, Melbourne, Australia
mohamed.badawy@monashhealth.org

Effective communication of radiation safety information is essential for empowering patients to make informed decisions, alleviating anxiety, and fostering trust in healthcare systems. Yet, traditional patient education materials often fail to engage diverse patient populations, particularly those facing literacy or language barriers. The rapid advancements in generative artificial intelligence (GenAI) technology offer an unprecedented opportunity to transform how we communicate radiation-related information, tailoring content to individual linguistic, cultural, and educational needs.

This talk will explore the emerging landscape of GenAI applications in patient-facing radiation safety communication. We will begin by examining the fundamental principles of GenAI, including large-language models and multimodal synthesis, to understand their capability to deliver accessible, accurate, and context-sensitive health education content. This presentation will highlight findings from a recent pilot project utilising HeyGen, a generative AI platform, to create personalised, Thai-language patient education videos on common radiation imaging procedures in nuclear medicine and radiology.

Beyond this case study, the talk will discuss the broader implications and future directions of GenAI in healthcare communication: improving natural language output, ensuring culturally aligned content, and integrating feedback loops to refine and personalise patient education materials continuously. Attendees will gain insight into the practical considerations, ethical implications, and collaborative opportunities that lie ahead as GenAI continues to evolve, ultimately enabling more effective and inclusive communication around radiation safety and patient care.

The Current IOMP Efforts for International Certification of Medical Physicists

Wilkinson DA*

Committee member of the IMPCB
**wilkinson44106@gmail.com*

The International Medical Physics Certification Board (IMPCB) was established in 2010 under the aegis of the International Organization of Medical Physics. Its mission is to support the practice of medical physics through a certification program in accordance with IOMP guidelines. There are three aspects to this mission. One is to establish the infrastructure, requirements and examination procedures for the certification of medical physicists in accordance with the requirements of IOMP guidelines; two is to establish the infrastructure, requirements and assessment procedures for the accreditation of medical physics certification programs in accordance with the requirements of IOMP guidelines; and three is to establish the requirements for continuing education and professional development for certified medical physicists.

As of November 2024, there are 73 diplomates of the certification program from 27 different countries. There are currently 78 candidates for Part I and 48 for Part II. Accreditation of the Hong Kong Medical Physics Certification Board, the Korean Medical Physics Certification Board, and the Chinese (Taipei) Medical Physics Certification Board has been completed. A committee to develop and maintain continuing professional development for certified physicists has recently been established.

Radiation Protective Equipment in Diagnostic and Interventional Radiology

Matsubara Kosuke*

Department of Quantum Medical Technology, Faculty of Health Sciences, Institute of Medical, Pharmaceutical and Health Sciences, Kanazawa University, Kanazawa, Japan
**matsuk@mhs.mp.kanazawa-u.ac.jp*

The three principles of external radiation protection are "distance", "shielding", and "time," and when it is difficult to keep the "distance" from the scattered x-ray source and shorten the "time" of the procedure, it is important to make effective use of radiation protective equipment ("shielding"). There are two types of radiation protective equipment: those that are attached to rooms or equipment, and those that are worn by workers themselves. The former includes such as ceiling- or equipment-mounted radiation protection shields. The latter includes such as radiation protective aprons, gloves, and glasses.

A novel detachable lead arm support (DLAS) consists of L-shaped acrylic plate and a detachable waterproof cover encasing the 0.5-, 0.75-, or 1.0-mm lead. It can be placed right next to the patient to effectively reduce X-ray scattering around the worker's position. At a height of 160 cm (assuming the height of the lens), mean dose reduction rate for 10 typical working angles in percutaneous coronary intervention using DLAS with 0.5-, 0.75-, and 1.0-mm leads was 43.0%. The combination of DLAS with 0.5-mm lead and radiation protective curtain (0.5 mmPb) could increase dose reduction rate to 47.1%.

Radiation protective aprons are standardly used in radiation protection, but lead-free aprons, which are made using alternative metals and composite materials such as bismuth, tungsten, and antimony, are increasingly becoming a popular alternative. Even for lead-free aprons that satisfy 0.25 mmPb or more at 100 kV, some of them were below 0.25 mmPb at tube voltages above and below 100 kV.

There are various types of radiation protective glasses with different lead equivalents and shapes, and they should be used depending on the purpose. Those for staff assisting patients during CT examinations should have high lead equivalents and no gaps around the nose and under the anterior lens.

Keywords: Radiation protective equipment, DLAS, lead-free apron, radiation protective glasses

Establishing a comprehensive MR safety program in clinical environment

Zhao Anzi[*1], Diller E.[2]

1 Department of Radiology, Northwestern University, Northwestern Medicine, Chicago, IL, USA.
2 Department of Radiology, University of New Mexico, Albuquerque, NM, USA
**anzi.zhao@nm.org*

Introduction: Magnetic Resonance Imaging serves as a highly effective diagnostic tool but poses numerous safety risks, including projectile hazards and radiofrequency burns. This study outlines a structured approach to implementing a comprehensive magnetic resonance (MR) safety program in a large clinical setting, emphasizing the importance of safety protocols to minimize MR associated risks.

Methods: The program initiated by reviewing past MR safety events and integrating best practices derived from current regulatory requirements and standards. A MR Safety Committee (MRSC) was established to oversee activities including analyzing MR safety events, creating and implementing MR safety training modules, as well as creating patient screening protocols, particularly for those with implants and medical devices. The program also included assessing compliance gaps and establishing a risk assessment framework for identifying potential risks related to patient scans.

Results: The implementation of the MR safety program led to significant improvements in safety compliance among staff. There was a 64% reduction in adverse events, whereas early detection incidents experienced a 73% increase following one year of implementation. Furthermore, enhanced communication among radiologists, technologists and medical physicists contributed to improved safety protocols during MR procedures.

Discussion: Our findings indicate that a structured MR safety program positively impacts patient safety by reducing adverse events and fostering heightened safety awareness. Implementing such a program is essential for addressing evolving technological and clinical challenges. Furthermore, tailoring the program to the unique requirements and risks of the clinical setting optimizes its overall efficacy.

Conclusion: Establishing a comprehensive MR safety program is vital to ensure patient safety in clinical MR environment. Our study highlights the importance of a collaborative strategy that includes ongoing training, safety review, risk assessment, and effective communication. This model can serve as a blueprint for other institutions aimed at establishing or enhancing their MR safety programs.

Keywords: MR safety, risk, patient safety, quality.

Reproduction of the processing steps of echo planar imaging (EPI) image reconstruction by MRI simulation

Tawara Noriyuki *

Department of Medical Radiological Technology, Faculty of Health Sciences and Graduate School of Health Sciences, Kyorin University, Mitaka City, Tokyo, Japan.
**noriyuki-tawara@ks.kyorin-u.ac.jp*

Introduction: EPI, one of the k-space filling methods in MRI, is now one of the indispensable methods. On the other hand, unlike cartesian sampling, which is the usual k-space filling method, EPI's description of k-space filling is limited to illustrating the trajectory of k-space filling by traversing k-space in a “zig-zag” trajectory. In addition, ordinary medical physicists currently cannot perform validation using k-space data from diagnostic MRI systems. The purpose of this study was to reproduce the k-space data processing obtained on an MRI simulator to educate the image processing of EPI from data acquisition to image reconstruction.

Methods: MRI simulations were implemented by BlochSolver (MRIsimulations Inc., Tokyo, Japan), and Cylindrical phantom, which comes with the software, was used for the numerical phantom. The pulse sequence used was Gradient Echo (GrE)-EPI. Data processing acquired by MRI simulations was performed using Interactive Data Language (IDL; Geospatial Solutions KK, Boulder, CO, USA).

Results: Raw data, which is data obtained by an MRI simulator, is filled in the usual Cartesian method, so a zig-zag filling process was necessary when expanding it to k-space data. Since the k-space trajectory of EPI is a zig-zag trajectory, the sampling point is shifted by one point when the read direction is reversed plus or minus for each row. It was confirmed that a correction for this is also necessary.

Discussion: It is suggested that the reproduction of the image reconstruction procedure facilitates our understanding of the EPI image reconstruction procedure because it allowed us to reproduce the reasons regarding why the k-trajectory in EPI went from a mere zig-zag to a blipped.

Conclusion: This study were able to reproduce the procedure of EPI image reconstruction including expansion from raw data obtained by the MRI simulator to k-space.

Keywords: MRI simulation, echo planar imaging (EPI), k-trajectory.

Photon Counting CT: Principles and Applications

Shunhavanich Picha

Department of Radiology, Faculty of Medicine, Chulalongkorn University, Bangkok, Thailand
** picha.s@chula.ac.th*

Photon-counting-detector CT (PCD CT) with new detector technology has many advantages over conventional, energy-integrating-detector CT, including elimination of electronic noise, increased spatial resolution, improved contrast-to-noise ratio, and constant availability of spectral information. In this review, the principles and benefits of PCDs are described. We also discuss different applications and possible nonidealities of the system and mention different implementations of PCD CT.

Keywords: Computed Tomography, Photon-counting detectors, Spectral CT

Administering Targeted Radionuclide Therapy - Safety and Quality Management

S Somanesan

Department of Nuclear Medicine and Molecular Imaging, Singapore General Hospital, Singapore
**somanesan@sgh.com.sg*

Introduction: Theranostics in a growing arm of Nuclear Medicine that has had a resurgence in the last few decades due in part to the number of diagnostic and therapeutic radiopharmaceutical agents available for radionuclide therapies.

Methods: The radiation safety and quality management programs in the delivery of theranostic service are significant as the radioactivity involved is generally high and no place for error and wastage. There is a great need to ensure radiation safety and quality management procedures for staff, patient, general public and the environment especially with the new emerging theranostic with the use of alpha particles, which pose a significant challenge.

Results: Another key component of theranostic service delivery is the sustained radiation safety and quality improvement training not just for the staff of the department of Nuclear Medicine and Molecular Imaging but also to the other non-radiation hospital staff such as inpatient ward nurses. The results of overseeing of this training and supervision of personnel, in radiation safety and quality management aspects such as decontamination techniques in the event of a radioactive spill have to be consistent and sustainable will be shown in this presentation.

Discussion: Another key component of theranostic service delivery is the sustained radiation safety and quality improvement training not just for the staff of the department of Nuclear Medicine and Molecular Imaging but also to the other non-radiation hospital staff such as inpatient ward nurses. The overseeing of this training and supervision of personnel, in radiation safety and quality management aspects such as decontamination techniques in the event of a radioactive spill have to be consistent and sustainable.

Conclusion: The overseeing of Nuclear Medicine therapy patient discharge based on local legislation and international best practice, instructions to patients and their care-givers and mitigation of any incidents and accidents including management of untimely death of patient with radionuclides besides the monitoring of staff personal exposure to ensure no breach of dose limits will be discussed. The guidance contained in this presentation will assist radiation safety and quality management professionals in the implementation of safe, practical, reproducible and effective radionuclide therapy programs, even at small sites with limited to no experience in radionuclide therapies.

Keywords: Theranostics, Radionuclide Therapy, Radiation safety, Quality Management

Advancements in evaluating Terbium-161 vs Lutetium-171 for enhanced theranostic application

Shiratori Shuichi*

Department of Radiology, Faculty of Medicine Siriraj Hospital, Mahidol University, Bangkok, Thailand
**shuichi.shi@mahidol.ac.th*

Terbium-161 (Tb-161) is gaining attention as a next-generation radionuclide for theranostic applications, offering potential advantages over the widely used Lutetium-177 (Lu-177). Tb-161 combines beta emission with a high proportion of conversion and Auger electrons, resulting in higher linear energy transfer (LET). This unique characteristic enables superior tumor cell killing efficiency, especially in micrometastases and disseminated tumor clusters, where traditional beta emitters may be less effective.

The production of Tb-161 involves neutron irradiation of enriched gadolinium-160 in a nuclear reactor, followed by chemical separation to achieve high-purity formulations. Advances in radiochemistry have optimized the yield and quality of Tb-161, ensuring its suitability for clinical applications.

Efficient labeling methods have been developed to conjugate Tb-161 with peptides, antibodies, and small molecules, ensuring stability and targeting specificity. These methods are compatible with well-established theranostic ligands used for Lu-177, allowing a seamless transition to Tb-161-based therapies while offering enhanced therapeutic efficacy.

Preclinical studies have demonstrated the potential of Tb-161 to outperform Lu-177 in eradicating micrometastases and improving overall therapeutic outcomes. Early-phase clinical trials are underway to validate its safety, biodistribution, and efficacy in various cancers.

The potential of Tb-161 as a radionuclide for theranostics will be discussed, emphasizing its high LET properties, superior efficacy in treating micrometastatic disease, production methods, labeling techniques, and the ongoing translational research efforts that are shaping its clinical potential.

Keywords: Terbium-161, Lutetium-177, Linear energy transfer, Micrometastases, Auger electron.

Exploring novel combined therapeutic strategies: external beam radiotherapy and targeted radionuclide therapy

Tippayamontri Thititip*

Department of Radiological Technology and Medical Physics, Faculty of Allied Health Sciences, Chulalongkorn University, Bangkok, Thailand
**Thititip.T@chula.ac.th*

The integration of External Beam Radiotherapy (EBRT) with Targeted Radionuclide Therapy (TRT) represents an innovative approach in cancer treatment, leveraging the complementary mechanisms of these modalities to enhance therapeutic outcomes. EBRT delivers high-energy radiation precisely to tumor sites, offering excellent control of localized disease, while TRT utilizes radiolabeled agents to target and irradiate metastatic or systemic malignancies selectively. The synergistic potential of combining these therapies lies in their ability to maximize tumor cell eradication while minimizing damage to healthy tissues. Preclinical and early clinical studies are investigating this approach in various cancers, including prostate cancer, neuroendocrine tumors, and bone metastases. The integration of EBRT and TRT may offer potential strategies to improve tumor control, reduce treatment resistance, and provide personalized therapeutic options tailored to tumor characteristics and patient profiles. However, the successful implementation of this combination requires careful planning and optimization. Challenges include optimizing dosing schedules, managing toxicity, and addressing logistical considerations for clinical application. Exploring the underlying biological principles, technological advancements, and clinical applications of EBRT and TRT combinations is crucial to realizing their full potential. Ultimately, combining EBRT and TRT may redefine the landscape of multimodal cancer therapy, offering transformative opportunities to improve survival and quality of life for patients with complex oncological conditions.

Keywords: Combination; external beam radiotherapy; targeted radionuclide therapy

Abstract:
Proffered Papers

Development and characterization of customizable carrageenan bolus for superficial radiation therapy

Cruzet Rhodesa[1,2*], Calma J[2], Dadol G[2,3]

1 Cebu Doctors' University Hospital Radiation Therapy Center, Cebu City, Philippines.
2 Medical Biophysics Group, University of San Carlos, Cebu City, Philippines
3 Department of Chemical Engineering, University of San Carlos, Cebu City, Philippines
**rhodesacruzet@gmail.com*

Introduction: In radiation therapy, bolus is a tissue-equivalent material used to alter the radiation dose distribution and resolve the skin-sparing effect of megavoltage x-ray energies. Commonly used bolus materials are non-customizable and usually result in air gaps making the bolus less effective. This project aims to develop prototypes of customizable bolus made from kappa carrageenan for superficial radiation therapy and then compared with commercial gel-type bolus sheets using specific tests for characterization of physical, mechanical, radiation attenuation, and radiation dosimetric properties that satisfy the criteria of a good radiotherapy bolus.

Methods: Semi-refined kappa-carrageenan was processed, combined with other polymers and additives, and molded into 0.5cm and 1.0cm sheets. Characterization tests were performed for commercial and carrageenan boluses to determine the: optical transmittance, conformity to curved surfaces with air gap estimation, CT numbers, relative depth doses, gel strength, and viscoelastic properties. The carrageenan gel mixture was also subjected to rheological tests to assess its potential for customized shape applications.

Results: The carrageenan bolus has better optical transmittance and shape conformity than the commercial type. CT scan images indicate the tissue equivalence of both bolus types with the carrageenan bolus closer to water. The relative depth doses of the boluses indicated the shift of d_{max} to shallower depths. The different additives had an effect on the mechanical and viscoelastic properties of carrageenan bolus based on indentation and rheology tests.

Discussion: The versatility and tunability of kappa carrageenan make it suitable for use as a bolus in radiotherapy and agree with other previous studies that use kappa carrageenan in combination with other additives in tissue-mimicking applications.

Conclusion: The developed carrageenan bolus satisfies the specific characteristics and criteria of a radiotherapy bolus.

Keywords: customized bolus, carrageenan, hydrogel, radiation therapy, dosimetry

Measurement of photoneutron dose rate from high energy photon beams in medical linear accelerator using neutron survey meter

Hmwe Aye T[1*], Damrongkijudom N[1], Kakanaporn C[2], Ekjeen T[1], Suwannarat A[1], Kittipayak S[3]

1 Department of Radiological Technology, Faculty of Medical Technology, Mahidol University, Salaya, Nakhon Pathom, Thailand
2 Department of Radiation Oncology, Faculty of Medicine, Siriraj Hospital, Mahidol University, Bangkok-Noi, Bangkok, Thailand
3 Faculty of Health Science Technology, HRH Princess Chulabhorn College of Medical Science, Chulabhorn Royal Academy, Bangkok, Thailand
**ayethiri.hmw@student.mahidol.edu*

Introduction: Undesirable photoneutrons can be produced from a linear accelerator (LINAC) operating above 10 MV photon beam and contribute extra doses to treated patients and staff. This study aimed to measure photoneutron dose rate produced by Elekta Versa HD LINAC with different photon energies.

Methods: Photoneutron dose rates of LINAC delivering 6 MV, 10 MV, 15 MV, 6 MV FFF (flattening filter free), and 10 MV FFF were measured using a Ludlum Model 12-4 survey meter with a He-3 neutron detector. The measurement was performed at various locations in the treatment room, and outside the front door with open and closed doors, respectively.

Results: The highest photoneutron dose rates from LINAC operated at 6 MV, 10 MV, 15 MV, 6 MV FFF and 10 MV FFF with 10 x 10 cm^2 field size were 3.00±0.00 mSv/h, 27.80±0.45 mSv/h, 48.00±0.00 mSv/h, 1.74±0.09 mSv/h and 10.00±0.00 mSv/h respectively at radiation therapist working spot beside the patient couch. When delivered doses were higher than 600 MU/min, the highest photoneutron dose rates produced from 6 MV FFF and 10 MV FFF were 3.12±0.11 mSv/h and 30.00±0.00 mSv/h respectively at the same location. For 15 MV photon beam, the photoneutron dose rate measured outside the front door was 0.02±0.00 mSv/h with the door opened, and unable to detect with the door closed.

Discussion: The photoneutron dose rate increases with increasing energies of photon beam and decreases with increasing distance from the isocenter. Moreover, the photon beam with flattening filter free reduces the production of photoneutron, however, the potential neutron dose rate still rise when higher delivered dose rate (MU/min) were applied.

Conclusion: The information of the photoneutron dose rates from this study is beneficial for the clinical practice in optimizing of radiation safety for the patient and radiation therapist during the procedures.

Keywords: Photoneutron, Neutron dose rate, Linear accelerator, Survey Meter

Determination of neutrons in a photon radiotherapy treatment room using CR-39 dosimeters

Rattanarungruangchai Natch[1*], Suwanbut P[2], Thongsawad S[1, 2], Liamsuwan T[1]

1 Princess Srisavangavadhana College of Medicine, Chulabhorn Royal Academy, Bangkok, Thailand

2 Radiation Oncology Department, Chulabhorn Hospital, Chulabhorn Royal Academy, Bangkok, Thailand

**natch.rat@edu.cra.ac.th*

Introduction: Neutrons are undesired products in high-energy photon beam radiotherapy caused by interactions between photons and treatment head components. Neutron measurement is essential to evaluate out-of-field dose in patients and treatment room design for radiation protection purposes. This study aimed to determine neutron ambient dose equivalent, $H^*(10)$, at different locations of the 10 MV linear accelerator treatment room for different field sizes shaped by multi-leaf collimators (MLCs).

Methods: CR-39 dosimeters were placed at 100 cm and 200 cm from the isocenter, maze junction, maze, and entrance during irradiation with 10 MV flattened photon beams from the TrueBeam machine with the field sizes of 1×1 cm^2, 2×2 cm^2, 5×5 cm^2, 10×10 cm^2, and 20×20 cm^2 for 1,800 monitor units. The CR-39 dosimeters have been calibrated free in air with ^{252}Cf for fast neutrons and ^{241}Am-Be moderated with graphite blocks for thermal neutrons.

Results: $H^*(10)$ was highest at 100 cm from the isocenter and decreased with increasing distance from the isocenter. $H^*(10)$ at the maze and entrance were lower than neutrons at the maze junction. The different field sizes shaped by MLC affected $H^*(10)$ with decreased $H^*(10)$ as the field size was increased.

Discussion: $H^*(10)$ at 100 cm and 200 cm from the isocenter obtained in this study were 6-31% lower than those obtained by a similar study, which determined $H^*(10)$ by a neutron spectrometer. This could suggest that standard source calibration coefficients may not be adequate for accurate neutron dose determination

Conclusion: Neutron ambient dose equivalent decreased with the increased distance from the isocenter and increased field size. To determine accurate neutron dose, dosimeters should be calibrated in a reference neutron field that has a similar energy spectrum as the neutron field of interest.

Keywords: CR-39 dosimeter, neutron dosimetry, photon radiotherapy, 10 MV

Sensitivity of error detection in electronic portal imaging devices for patient-specific QA in head and neck VMAT plans

Thaiwattana Chanchakorn[1*], Udee N[1], Khamfongkhruea C[2], Donmoon T[3], Yabsantia S[1]

1 Department of Radiological Technology, Medical physics Program, Faculty of Allied Health Sciences, Naresuan University, Phitsanulok, Thailand
2 Princess Srisavangavadhana College of Medicine, Chulabhorn Royal Academy, Bangkok, Thailand
3 Mahavajiralongkorn Thanyaburi Hospital, Pathum Thani, Thailand
**Chanchakornt66@nu.ac.th*

Introduction: Head and neck cancers often occur near organs at risk, requiring advanced radiation techniques for effective treatment. These techniques demand patient-specific quality assurance (PSQA) to verify treatment plan accuracy before clinical use. Dosimetry devices used in PSQA vary in their ability to detect errors. At the institution conducting this study, the newly installed equipment has not yet been evaluated for its error detection sensitivity. Therefore, this research aims to assess the sensitivity of the electronic portal imaging device (EPID) for error detection.

Methods: Five treatment plans for head and neck cancers were intentionally modified using a MATLAB program to introduce delivery errors related to the multileaf collimator (MLC) with an error of ± 1, ± 3, and ± 5 mm. PSQA for both error and non-error plans were performed using portal dosimetry and analyzed with EPI beam software. Each plan was evaluated using a gamma-index criterion of 3%/2 mm. Plans with a gamma passing rate (GPR) above 95% were considered acceptable. The sensitivity of MLC error detection was then assessed.

Results: Lower GPR values were observed with higher MLC errors. All original plans had a GPR greater than 95%. Error plans with a 1 mm MLC displacement also maintained a GPR above 95%. However, plans with MLC displacements greater than 2 mm failed to meet the GPR criteria, with values falling below 95%.

Conclusion: The modified treatment plans with introduced errors demonstrated the device's effectiveness in detecting delivery errors. Portal dosimetry is an effective tool for PSQA, capable of detecting MLC displacements of at least 2 mm. This ability to identify errors during the quality assurance process enhances the accuracy and precision of treatment plans, contributing to improve patient care.

Keywords: Electronic Portal Imaging Device, Error Detection, Head and Neck Cancer, Patient-Specific QA, Volumetric modulated arc therapy (VMAT)

Implementation of an EPID for patient-specific VMAT quality assurance: Experience at Surin Hospital

Pischom Narueporn[1*], Songsri S[1], Tangboonduangjit P[2], Khachonkham S[2]

1 Department of Radiology, Division of Radiation Oncology, Surin hospital, Surin, Thailand
2 Department of Diagnostic and Therapeutic Radiology, Faculty of Medicine, Ramathibodi Hospital, Mahidol University, Bangkok, Thailand
**Narueporn.pis@yahoo.com*

Introduction: Patient-specific quality assurance (PSQA) is crucial for ensuring the accuracy of Volumetric Modulated Arc Therapy (VMAT) treatments. Electronic portal imaging devices (EPID) has been increasingly utilized for PSQA due to its high spatial resolution and low volume averaging. In this study, we implemented EPIbeam, an EPID-based portal dosimetry software, for clinical applications and evaluated its performance by comparing it with the PTW1500 detector based on gamma criteria.

Methods: The EPIbeam configuration was performed according to the manufacturer's recommended procedure, using a gamma criterion of 2%/2mm for implementation. To validate the VMAT PSQA, we assessed 20 different VMAT plans for the head and neck, brain, and pelvic organs using gamma criteria of 3%/3mm and 3%/2mm, respectively. Additionally, the gamma passing rates for all patient plans were compared with the results obtained using the PTW1500 array detector inserted in PTW Octavius 4D phantom.

Results: The clinical implementation of the commercial procedure achieved a gamma passing rate of over 99%. When compared with the PTW1500 and EPIbeam, the average gamma passing rate at 3%/3mm was 97.12% and 99.72%, respectively. At 3%/2mm, the average gamma passing rate was 92.86% and 99.28%, respectively.

Discussion: The EPIbeam commissioning was successful, confirming its suitability for PSQA. In terms of clinical gamma passing rates, EPIbeam outperforms the PTW1500 across all criteria. The lowest gamma passing rate was observed in head and neck cases, primarily due to the large PTV volume and field size. Additionally, various factors, such as control points and fluence, influence VMAT planning and can affect the results.

Conclusion: This study implements EPIbeam for clinical use, and the results demonstrate that the gamma passing rate from EPIbeam is higher than that of the PTW1500, with agreement across all criteria. From the result, we consider EPIbeam a reliable alternative for patient-specific quality assurance.

Keywords: Radiotherapy, Electronic portal imaging device (EPID), patient specific quality assurance (PSQA),

Investigation of in vivo EPID-based software for detecting dosimetric errors: A phantom studies

Suksawang Penpisuth[1*], Limpichotikul N[1], Sahachjesdakul P[1], Kakanaporn C[2], Khachonkham S[3]

1 Department of Radiology, Division of Radiation Oncology, MedPark Hospital, Bangkok 10110, Thailand
2 Faculty of Medicine Siriraj Hospital, Mahidol University, Division of Radiation Oncology, Bangkok 10700, Thailand
3 Department of Diagnostic and therapeutic Radiology, Division of Radiation Oncology, Faculty of Medicine Ramathibodi Hospital, Mahidol University, Bangkok 10400, Thailand
**penpisuth.suk@gmail.com*

Introduction: Changes in a patient's external contour can lead to dosimetric errors, compromising treatment accuracy. In vivo dosimetry systems, such as Dosisoft EPIgray with iView^{TM}EPID, enabling the detection of patient depth errors. This study aims to evaluate the capability of EPIgray in identifying dosimetric error resulting from changes in the patient's external contour.

Methods: This study generated reference plans for Head and Neck and Prostate cases following the TG-119 guidelines and using the Volumetric Modulated Arc Therapy (VMAT) technique. Intentional depth errors from 0.5cm to 5 cm were introduced in a solid water phantom which insert the PTW Semiflex 0.125cc, irradiated according to the reference plans. It then compares dose distributions and point doses for the target and organs at risk between a planned dose, measurements, and EPIgray calculation.

Results: The results showed that a 1 cm change in depth resulted in dose errors in target and organ at risk ranging from 1.6% to 3.2%. Additionally, the dose errors increase as the thickness of phantom decrease. Furthermore, this study demonstrated good agreement in the detection of dose distribution errors and point dose between the planned dose, measurements and EPIgray calculations, with discrepancies remaining within 2% across all depths.

Discussion: The dosimetric errors resulting from a 1 cm change in depth are consistent with the others finding. Furthermore, comparisons between EPIgray, planned dose, and measurements data highlight the EPIgray's effectiveness in detecting dosimetric errors cause by changes in the patient's external contour. However, further studies are needed to investigate EPIgray's sensitivity to other factors that may affect dosimetric accuracy.

Conclusion: Dosisoft EPIgray software, in conjunction with iView^{TM}EPID, is effective in detecting dosimetric errors caused by changes in the patient's external contour. However, results from phantom studies revealed certain limitations of the system.

Keywords: In vivo dosimetry, Electronic portal imager (EPID), EPIgray

Investigated radiation dose at surrounding area in real time motion tracking system of tomotherapy: A phantom study

Kititharakun Phairot[1,2], Watcharawipha A[2], NopNob W[2], Kongsa A[2]

1 Department of Radiology, Medical Physics program, Faculty of Medicine, Chiang Mai University, Chiang Mai, Thailand.

2 Department of Radiology, Division of Radiation Oncology, Faculty of Medicine, Chiang Mai University, Chiang Mai, Thailand.

** phairotkititharakun@gmail.com*

Introduction: Real time motion tracking (RTMT) is the method that delivers radiation to the moving target. The system tracks the target movement and adapts the radiation aperture corresponding to the target position. During the target movement, the surrounding organs remain in a permanent location. The organ dose may increase due to the returning target position. This study investigated the dose difference at the surrounding area in a phantom study.

Methods: Five breathing cycles were acquired from patients diagnosed with thoracic cancer. Three treatment plans of stereotactic body radiotherapy were recruited and matched to these breathing cycles. The radiation dose was measured using ArcCHECK® with a synthetic moving target. A 0.13cm^3 ionization chamber (IC) was simulated as the target driven by dynamic platforms CIRS®. The dose difference between the static and moving target was observed and compared.

Results: The Gamma passing rates evaluated for static target measurements were 99.6 ± 0.4% and 99.1 ± 0.9% for Gamma criteria of 3%/3mm and 3%/2mm, respectively.

The percentage of detectors with percent dose difference levels within 5%, 10%, 15%, 20%, 25%, 30% and more than 30% were 46.4 ± 16.6%, 21.3 ± 6%, 9.2 ± 3.4%, 5.3 ± 2.3%, 4.1 ± 1.9%, 2.9 ± 2.2% and, 10.9 ± 12.3%, respectively, compared to the static target measurement.

Discussion: The study confirmed an increase in dose in the surrounding area using the RTMT method, consistent with previous findings.

Conclusion: Using the RTMT method can increase the surrounding dose when these organs are static. The dose can be increased by up to 10% of the treatment planning dose. However, a dose difference of more than 10% appeared at the area of low dose.

Keyword: Real time motion tracking, Tomotherapy, Gamma passing rate, surrounding dose.

Investigated performance of real-time motion tracking system in tomotherapy

Messuwan Jiraphat[1,2*], Watcharawipha A[2], Nopnob W[2], Kongsa A[2]

1 Department of Radiology, Medical Physics program, Faculty of Medicine, Chiang Mai University, Chiang Mai, Thailand.

2 Department of Radiology, Division of Radiation Oncology, Faculty of Medicine, Chiang Mai University, Chiang Mai, Thailand.

** Jiraphat_me@cmu.ac.th, First33@outlook.com*

Introduction: Real-time motion tracking (RTMT) is an advanced radiotherapy technique where treatment machines deliver radiation by tracking target motion. The machine is equipped with a kV imaging system and an optical positioner to generate motion cycles. However, the transition between the acquired signal and beam adaptation may affect delivery accuracy. This study assessed the performance of the RTMT system in Tomotherapy using clinical breathing cycles.

Methods: A surface detector (SentinelTM) captured 15 breathing cycles from a patient with thoracic cancer. Six treatment plans for stereotactic body radiotherapy in lung cancer were randomly matched to these breathing cycles. Sixty pairs of measurements were taken using MapCHECK® on the Dynamic platform CIRS® and compared between static and moving targets using a potential difference (PD) of 3. An analysis of the Gamma passing rate (GPR) assessed the performance of RTMT with Gamma criteria of 3%/2mm, 3%/1mm, 2%/3mm, 2%/2mm, and 2%/1mm.

Result: The results illustrated that the mean PTV size, traveling distance and frequency were 10.2 ± 7.8 cm^3, 7.5 ± 2.3 mm and 22.6 ± 6.0 cycles/min, respectively. The mean GPR value of 3%/2mm, 3%/1mm, 2%/3mm, 2%/2mm, and 2%/1mm for a static target revealed 100 ± 0.0%, 100 ± 0.0%, 100 ± 0.0%, 99.8 ± 0.4% and 99.5 ± 1.2% whereas a moving target showed 100 ± 0.2%, 99.9 ± 0.6%, 99.6 ± 0.6%, 99.2 ± 1.1% and 97.9 ± 2.4% respectively. However, results demonstrated no significant correlation among GPR and travel distance and breathing frequency.

Discussion: The recommended setup parameter of PD was ensured for clinical practice. Using this PD, the accuracy of RTMT still achieved a GPR value above 97.0% with a 1 mm distance-to-agreement (DTA).

Conclusion: The performance of the Tomotherapy tracking system showed a high accuracy with a DTA value as low as 1 mm for both 2% and 3% dose differences.

Keywords: Tomotherapy, Real-time motion tracking, Motion management, Gamma passing rate.

Comparison of normal tissue integral dose between volumetric modulated arc therapy and helical tomotherapy for post-mastectomy radiation therapy with regional nodal irradiation

Tananchai Kamonwan[1*], Watcharawipha A[2], Onchan W[2], Nobnop W[2]

1 Department of Radiology, Medical Physics Program, Faculty of Medicine, Chiang Mai University, Chiang Mai, Thailand.

2 Department of Radiology, Division of Radiation Oncology, Faculty of Medicine, Chiang Mai University, Chiang Mai, Thailand.

**Kamonwan.tanan@gmail.com, Kamonwan_tanan@cmu.ac.th*

Introduction: The Volumetric Modulated Arc Therapy (VMAT) and Helical Tomotherapy (HT) techniques are widely used in breast cancer treatment. However, these techniques may increase the normal tissue integral dose (NTID), potentially leading to complications and secondary cancers. Therefore, this study aims to compare the NTID between VMAT and HT for post-mastectomy radiotherapy (PMRT).

Methods: Thirty patients treated using VMAT were enrolled in the study. Each patient was replanned using the HT plan, with and without an L-shaped (LB) directional block. The conformity index (CI), homogeneity index (HI), integral dose (ID), ID to OARs, NTID, V_{5Gy}, and nontarget tissue receiving 10% to 75% of prescription dose were analyzed.

Results: The HTLB plan showed significantly better CI and HI compared to VMAT, but there was no significant difference between HTLB and HT. The ID for VMAT, HT, and HTLB were 152.9+/-5.9, 162.0+/-6.5, and 152.9+/-5.8 Gy·L, respectively. The NTID values were 120.5+/-4.0, 129.9+/-4.7, and 120.0+/-4.0 Gy·L, respectively. The heart ID was 3.4+/-0.3, 3.5+/-0.2, and 3.4+/-0.2 Gy·L; the ipsilateral lung ID was 16.7+/-0.9, 16.9+/-1.0, and 16.8+/-0.9 Gy·L; the contralateral lung ID was 2.9+/-0.2, 3.8+/-0.3, and 3.5+/-0.2 Gy·L; and the contralateral breast ID was 4.2+/-0.4, 3.9+/-0.3, and 3.8+/-0.4 Gy·L, respectively. The V_{5Gy} for HTLB was not significantly different from VMAT. Additionally, HTLB showed better sparing of nontarget tissue at high doses, while VMAT performed better in sparing at low to moderate doses.

Discussion: The HTLB plan utilized a directional block to limit the entrance dose to the OARs, resulting in significantly better ID and NTID compared to HT, with no significant difference from VMAT. Additionally, HTLB demonstrated better sparing of the contralateral breast, attributed to the highly modulated dose delivery at each helical slice.

Conclusion: The NTID showed no significant difference between VMAT and HTLB, but there were significant differences compared to HT.

Keywords: Integral Dose, VMAT, Helical Tomotherapy, PMRT.

Assessment of imaging dose delivered to patients throughout the treatment course in tomotherapy systems

Hompeng Pratchayakan[1*], Nobnop W[2], Donmoon T[3], Chusin T[4]

1 Department of Radiological Technology, Faculty of Allied Health Sciences, Naresuan University, Phitsanulok, Thailand
2 Division of Radiation Oncology, Department of Radiology, Faculty of Medicine, Chiang Mai University, Chiang Mai, Thailand
3 Maha Vajiralongkorn Thanyaburi Hospital, Department of Medical Services, Ministry of Public Health, Thailand
4 Department of Radiological Technology, Faculty of Allied Health Sciences, Naresuan University, Phitsanulok, Thailand
** pratchayakan.h@gmail.com*

Introduction: The American Association of Physicists in Medicine (AAPM) Task Group 180 Report recommends that the imaging dose should be included in the prescription dose (PD) if the imaging dose exceeds 5% of the prescription dose. The purpose of this study was to evaluate whether the cumulative imaging dose administered to patients throughout the treatment course in Tomotherapy systems exceeds 5% threshold or not.

Methods: The volumetric computed tomography dose index ($CTDI_{Vol}$), and the number of imaging series were retrospectively collected from two centers for 30 breast cancer and 30 prostate cancer patients from July 2023 to September 2024. Center A utilized kilovoltage computed tomography (kVCT) for imaging. Imaging modes included "fine" and "normal," with tube currents between 80–160 mA and tube potentials between 120–140 kVp. Center B utilized megavoltage computed tomography (MVCT) for imaging. All imaging was performed in coarse mode with a 3.5 MeV beam.

Results: The mean cumulative $CTDI_{Vol}$ values for kVCT were 25.0 ± 9.8 cGy (0.56% of mean PD) for breast cancer and 40.3 ± 17.8 cGy (0.66% of mean PD) for prostate cancer. For MVCT, mean cumulative $CTDI_{Vol}$ values were 21.3 ± 4.7 cGy (0.45% of mean PD) for breast cancer and 24.8 ± 6.7 cGy (0.37% of mean PD) for prostate cancer. The number of imaging series ranged from 17 to 40 for breast cancer and 23 to 58 for prostate cancer with kVCT, and from 16 to 28 for breast cancer and 20 to 40 for prostate cancer with MVCT.

Discussion: The cumulative imaging dose for kVCT was higher than that of MVCT, primarily due to the increased number of imaging series in Center A.

Conclusion: The cumulative imaging doses delivered to patients throughout the treatment course remained below 5% of the prescription doses for both kVCT and MVCT imaging.

Keywords: Tomotherapy systems, Imaging Radiation Dose, kVCT, MVCT

Dosimetric comparison between images with and without contrast agent using intensity modulated arc therapy in head and neck cancer

Wantongsuk Wilasinee[1,2*], Watcharawipha A[2], Nopnob W[2], Chakrabandhu S[2], Thongsuk W[2]

1 Department of Radiology, Medical Physics program, Faculty of Medicine, Chiang Mai University, Chiang Mai, Thailand.

2 Department of Radiology, Division of Radiation Oncology, Faculty of Medicine, Chiang Mai University, Chiang Mai, Thailand.

** wilasinee.wantongsuk@gmail.com, wilasinee_wa@cmu.ac.th*

Introduction: Intensity Modulated Arc Therapy (IMAT) is a widely used technique for targeted radiotherapy. Accurately identifying the target's shape and location is essential for effective treatment. The use of a contrast agent is necessary to define the target during this process. However, the increased intensity in the image can impact dose calculations, especially with precise algorithms. This study aims to evaluate the impact of contrast enhancement on dose calculations and compare different dose calculation algorithms.

Methods: This study included twenty head and neck treatment plans using Volumetric Modulated Arc Therapy (VMAT) and Helical Tomotherapy (HT) based on CT image series without contrast agent. The treatment geometry was recalculated on contrast-enhanced images, and the plans were transferred for replanning on a different treatment planning system. The doses to targets and organs at risk were analyzed and compared.

Result: The study found that the percentage dose difference (%DD) between images with and without contrast was minimal. The doses on Planning Target Volume of 70.0 Gy, 59.4 Gy, and 54.0 Gy showed %DD 0.49%, 0.67%, and 0.75%, respectively. The doses of OARs ranged from 0.16% to 1.02%. The target dose had a lower %DD on VMAT than HT, while HT resulted in higher doses to OARs.

Discussion: Several publications have shown that the accuracy of dose calculation algorithms can be affected by contrast enhancement in images, leading to significant dose differences. However, this study found different results, possibly due to variations in the grid size used for dose calculation.

Conclusion: Contrast agent can be used in the images for IMAT treatment planning, despite the dose calculation being performed with a high-accuracy algorithm. The %DD between with and without contrast images was within 1.1%. The more precise dose calculation algorithm led to a reduced impact of radiation dose on the target and OARs.

Keywords: Contrast agent, Head and Neck cancer, Volumetric modulated arc therapy, Helical Tomotherapy, Dose calculation algorithm.

Dosimetric comparison between the original and revised TRS 398 code of practice for photon beam reference dosimetry

Kyaw WLL[1*], Sanghangthum T[2], Lin SS[3], Huq MS[3]

1 Department of Radiation Oncology, Pinlon Cancer Center, Yangon, Myanmar.
2 Department of Radiology, Medical physics Program, Faculty of Medicine, Chulalongkorn University, Bangkok, Thailand.
3 Department of Radiation Oncology, University of Pittsburgh School of Medicine and UPMC Hillman Cancer Center, Pittsburgh, PA, USA.
**wllk.plgh@gmail.com*

Introduction: The IAEA recently revised TRS-398 Code of Practice (CoP), presenting updated data that differ from the original version. These changes could impact the determination of absorbed-dose-to-water under reference conditions in high-energy photon beams. This study aims to compare absorbed-dose-to-water results using both original and revised TRS-398 CoP in radiotherapy.

Methods: A PTW 30013 Farmer reference class ionization chamber measured dose with four photon beam energies (6 MV, 10 MV, 6X FFF, and 10X FFF) on a Varian TrueBeam™ linear accelerator at Pinlon Hospital, Myanmar. Measurements for flattening filter free (FFF) beams were repeated using a small volume cross-calibrated PTW 31016 Pinpoint 3D chamber. The data were analyzed following the recommendations given in both the original and revised versions of TRS-398 CoP. Since the methods for determining influence quantities are the same in both CoPs, the differences in absorbed-dose-to-water between the two CoPs are solely due to the differences in the k_Q values given in the two CoPs.

Results: The results show that k_Q values for both chambers in the revised CoP range from 0.9753 to 1.0047; this in the original CoP, range from 0.9800 to 1.0055 across all beam energies. This indicates a reduction of up to 0.48% in the values of k_Q and a corresponding reduction in the determination of absorbed-dose-to water following the recommendations given in the revised CoP.

Discussion: In this study, revised TRS-398 CoP k_Q values are lower than the original for all chambers and beam energies, resulting in reduced absorbed-dose-to-water.

Conclusion: Absorbed doses determined using the revised TRS-398 CoP will yield a smaller (< 0.5%) value than those determined using the original CoP for the chambers and beam energies investigated in this study. These differences are within the uncertainties quoted in the Codes of Practice.

Keywords: Revised TRS-398 CoP, Absorbed dose determination, photon beam.

Acknowledgment: The idea of this project was conceived at the Global Medical Physics mentorship program that occurs every Saturday and includes medical physicists from all over the world.

Evaluating dosimetric accuracy of AAA and AXB algorithms in free-breath and deep inspiration breath hold DIBH for lung SBRT

Htet May Thu[1*], Tawonwong T[2], Sanghangthum T[3]

1 Department of Radiology, Medical Physics Program, Faculty of Medicine, Chulalongkorn University, Bangkok, Thailand
2 Department of Radiology, King Chulalongkorn Memorial Hospital, Thai Red Cross Society, Bangkok, Thailand
3 Department of Radiology, Faculty of Medicine, Chulalongkorn University, Bangkok, Thailand
**mth.plgh@gmail.com*

Introduction: The accuracy of dose calculation in heterogeneous media is strongly influenced by the dose calculation algorithm. This study aims to evaluate the dosimetric differences among analytical anisotropic algorithm (AAA) , Acuros (AXB) and Monte Carlo (MC) algorithm in lung SBRT.

Methods: Twenty-four lung cancer patients were selected for SBRT planning. Patients were separated into two groups: DIBH and free-breath. The Eclipse treatment planning system was used to generate the 6 MV, FFF, VMAT plan with prescribed dose of 50 Gy in 5 fractions. Initially, plans were calculated with AXB, normalized the prescribed dose to cover 95% of PTV, then re-calculated using AAA with fixed MUs and exported the plan to ray station TPS then re-calculated with MC to investigate the impact of various algorithms.

Results: D95% and D2% showed a significant difference for PTV, where AAA yielded a higher value (51.9Gy) (55.6Gy) for free-breath and (58.2Gy) (62.7Gy) for DIBH than AXB. However, Dmax, D98%, and D50% for free breath showed no significant differences. There were noticeable differences for every parameter in the DIBH approach. Dmax result from AXB was higher than AAA. Dmean for lung and Dmax for heart showed no significant differences, while HI, V5Gy for lung, D15cc and D5cc for heart, D0.35cc showed significant differences between two algorithms in both respiratory motion managements.

Discussion: In this study, AAA and AXB agree well in Dmax, D98%. D50%, for both respiratory motion managements and CI in free-breath and GI in DIBH for PTV. The results also agree with Tsuruta et al.

Conclusion: A comparative analysis of dose volumetric data with AXB demonstrated that AAA provides higher D2% and dose to OAR. Dose is more conform, homogeneous dose and steep dose gradient without optimizing and normalizing but spend longer computation time.

Keywords: SBRT, Lung cancer, AAA, AXB

Interfraction motion and dosimetric comparison between wing board and breast board immobilization devices during postmastectomy 3D-CRT for breast cancer

Coronel Michael Ben Joseph[1,2*], Zerrudo JI[3], Caballar RC[1,4], Balete MJ[2], Mones E[2], Cereno RE[2,5,6]

1 The Graduate School, University of Santo Tomas, Manila 1008, Philippines
2 Radiation Oncology Center, Global Care Cancer Institute Inc., Bay, Laguna 4033, Philippines
3 Department of Radiation Oncology, Batangas Medical Center, Batangas City, Batangas 4200, Philippines
4 Department of Mathematics and Physics, College of Science, University of Santo Tomas, Manila 1008, Philippines
5 College of Medicine, University of the Philippines Manila, Manila 1000, Philippines
6 Department of Radiology, Division of Radiation Oncology, University of the Philippines – Philippine General Hospital, Manila 1000, Philippines
**michaelben.coronel.gs@ust.edu.ph*

Introduction: Postmastectomy radiotherapy includes the chest wall, axilla, and supraclavicular fossa as targets. Immobilization devices such as wingboards (WB) and breastboards (BB) are crucial to ensure precise dose delivery. The study aims to compare setup errors, target volume dose coverage, and doses received by organs-at-risk (OARs) between WB and BB setups during three-dimensional conformal radiation therapy (3D-CRT) for breast cancer.

Methods: Twenty WB setups and 22 BB setups were utilized for this study. Setup errors were derived by recording the lateral, longitudinal, and vertical couch shifts. These were used to calculate the clinical target volume (CTV) to planning treatment volume (PTV) margins. Doses to the target volumes and OARs were compared for the WB and BB setups in the original and shifted plans.

Results: Interfraction setup errors were higher in the WB setup. The computed CTV-PTV margins were 2.75 mm (lateral), 2.15 mm (longitudinal), and 3.97 mm (vertical) for the WB setup, and were 2.08 mm, 1.96 mm, and 2.16 mm for the BB setup. There was better dose coverage in WB setup for the chestwall (CTV $V_{90\%}$=91.07% vs 89.05%; CTV $V_{95\%}$=85.46% vs 81.38%) and supraclavicular fossa (CTV $V_{90\%}$=96.31% vs 95.11%; CTV $V_{95\%}$=94.10% vs 90.55%). Doses received by the heart (V_{17Gy} WB=1.50%, BB=3.82%), ipsilateral lung (V_{17Gy} WB=33.41%, BB=37.32%), and spinal cord (D_{max} WB=13.02 Gy, BB=22.74 Gy) were lower in the WB setup.

Discussion: Although interfraction setup errors were higher in the WB compared to the BB setup, there was better target dose coverage and lower doses to the OARs in the former in the original plans. Nonetheless, these setup errors were lower than the prescribed 5 mm margin in the institution.

Conclusion: Based on the findings, the WB can be used as an alternative immobilization device during 3D-CRT for breast cancer. Further validation in a larger sample size is recommended.

Keywords: radiotherapy, 3D-CRT, offline review, breast cancer, wing board, breast board

Impact of multi-leaf collimator (MLC) width and normal tissue objective (NTO) on radiation dose distributions in stereotactic radiosurgery using hyperarc for single brain lesions

Oh Se An[1, 2*], Kim SY[1], Park JW[1, 2], Yea JW [1, 2], Park J[1, 2], Jo YJ[1, 2]

1 Department of Radiation Oncology, Yeungnam University Medical Center, Daegu, Korea
2 Department of Radiation Oncology, Yeungnam University College of Medicine, Daegu, Korea
**sean.oh5235@gmail.com*

Introduction: HyperArc has been widely used for SRS treatment in the brain. Therefore, this study retrospectively investigated the impact of SRS NTO and MLC width on radiation dose distribution when treated patients with single brain metastasis using HyperArc.

Methods: This study includes 21 consecutively patients treated with HyperArc of TrueBeam linear accelerator for SRS from November 2022 to June 2024. All patients received radiotherapy with HA_{SH} planned with SRS NTO and HD MLC, and HA_{AH} (HyperArc combined by the Auto NTO and HD MLC) and HA_{AM} (HyperArc combined by the Auto NTO and Millenium MLC) were generated and compared respectively. The MU, CI(Conformity Index), rDHI(radical Dose Homogeneity Index), mDHI(moderate Dose Homogeneity Index), and GI(Gradient Index) were analyzed as target factors, and V_2(Gy), V_{10}(Gy), V_{12}(Gy), V_{18}(Gy), V_{10}(cc), V_{12}(cc) were analyzed as normal brain factors.

Results: Dosimetric comparisons were performed between HA_{SH}, HA_{AH}, and HA_{AM} in terms of Target and normal brain. Between HA_{SH} and HA_{AH}, averaged MU was 7206 and 5798, which was statistically significant ($P<0.001$). The MU of HA_{AM} is 5835. Between HA_{SH}, HA_{AH}, and HA_{AM}, CI and mDHI were not statistically significant, but there were significant differences in rDHI, GI, and normal brain.

Discussion: For treating a single brain region using HyperArc, SRS NTO can be seen to have a significant effect on the dose to MU, GI, and normal brain, and the width of MLC has an effect on the dose to rDHI, GI, and normal brain.

Conclusion: In HyperArc, SRS NTO and MLC width have a significant effect on the radiation dose to the target and brain.

Keywords: HyperArc, SRS NTO, MLC width

Evaluation of patient-specific quality assurance for beam-matching in stereotactic radiosurgery and stereotactic radiotherapy (SRS/SRT)

Boujamrat Thanuch[1*], Oonsiri S[2], Oonsiri P[2], Kingkaew S[2], Vimolnoch M[2], Plangpleng N[2], Chatchumnan N[2], Yabsantia S[3]

1 Department of Radiological Technology, Faculty of Allied Health Sciences, Naresuan University, Muang District, Phitsanulok, Thailand
2 Department of Radiology, Division of Radiation Oncology, King Chulalongkorn Memorial Hospital, The Thai Red Cross Society, Bangkok, Thailand
3 Department of Radiological Technology, Faculty of Allied Health Sciences, Naresuan University, Muang District, Phitsanulok, Thailand
**Thanuch3110@gmail.com*

Introduction: Beam-matching in institutions with multiple linacs ensures consistent radiation beam characteristics across the treatment planning system (TPS). This allows for patient transfers between linacs without the need for replanning. To ensure accuracy when switching machines, especially for complex techniques like Stereotactic Radiosurgery (SRS) and Stereotactic Radiotherapy (SRT), it is essential to evaluate patient-specific quality assurance (PSQA) to verify the consistency of radiation delivery across linacs. Therefore, the objective is to assess the quality assurance of treatment plans for beam-matched linacs in SRS and SRT.

Methods: We evaluated 50 SRS and SRT treatment plans using 6 MV flattening filter-free (FFF) beams and volumetric modulated arc therapy (VMAT) technique on two beam-matched linacs (TrueBeam 1 and TrueBeam 2). Treatment plans were created on TrueBeam 1 and assessed on both linacs. PSQA was conducted using portal dosimetry, with gamma passing rates compared at criteria of 3%/2 mm, 2%/1 mm, and 1%/1 mm.

Results: The mean gamma passing rate of TrueBeam 1 and 2 were 99.0 ± 1.3% and 99.1 ± 1.3% for the 3%/2 mm, were 94.3 ± 5.2% and 93.4 ± 6.0% for the 2%/1 mm and were 91.7 ± 6.5% and 90.7 ± 7.1% for the 1%/1 mm criteria. The average differences between TrueBeam 1 and 2 were within 0.6%, 2.6%, and 3.1% for the 3%/2 mm, 2%/1 mm, and 1%/1 mm criteria, respectively. All differences were statistically insignificant ($P > 0.05$, paired-sample t-test), indicating consistent performance between the two linacs.

Conclusion: The mean gamma passing rate of TrueBeam 1 and 2 decreased as the criteria became tighter. The differences between the beam-matched linacs were not statistically significant, allowing for patient transfer between linacs without replanning in SRS and SRT using VMAT. This confirms the feasibility of delivering complex treatment plans across beam-matched linacs.

Keywords: Beam-matching, Stereotactic Radiosurgery, Stereotactic Radiotherapy, portal dosimetry, patient-specific quality assurance

Dosimetric comparison between volumetric modulated arc therapy on TrueBeam and Halcyon of total body irradiation

Jaihow Wanwanut [1*], Tawonwong T [2], Sanghangthum T[3]

1 Department of Radiology, Medical Physics Program, Faculty of Medicine, Chulalongkorn University, Bangkok, Thailand
2 Department of Radiology, Division of Radiation Oncology, King Chulalongkorn Memorial Hospital, Thai Red Cross Society, Bangkok, Thailand
3 Department of Radiology, Division of Radiation Oncology, Faculty of Medicine, Chulalongkorn University, Bangkok, Thailand
**rotty1920@gmail.com*

Introduction Total Body Irradiation (TBI) is a special treatment technique with the aim of immunosuppression. The purpose of this study was to compare the dosimetric results of volumetric modulated arc therapy (VMAT) plans of TBI treatment between TrueBeam and Halcyon treatment machines.

Methods: Eight TBI patients were planned by 6 MV of two lateral opposing with extended source-to-axis distance (SAD) technique to 5 meters to receive the prescribed dose of 1200 cGy in 6 fractions at head and legs. A single fraction was added as a boost dose on ranging from shoulder to mid-thigh. Plans were optimized and calculated in Eclipse treatment planning system using VMAT by TrueBeam (6 isocenters) and Halcyon (4 isocenters) machines based on dose from the original opposing plan. The prescribed dose was normalized at $D_{50\%}$.

Results: The results showed that $D_{98\%}$, $D_{95\%}$, and $D_{2\%}$ of PTV were 954.2±42.3 cGy, 997.1±17.5 cGy, and 1359.5±16.6 cGy for TrueBeam and 928.2±25.4 cGy, 962.8±12.4 cGy, and 1386.8±36.7 cGy for Halcyon, respectively. The D_{mean} of lungs and kidneys were 992.5±24.0 cGy and 979.1±17.8 cGy for TrueBeam and 1004.9±27.7 cGy and 977.8±13.9 cGy for Halcyon, respectively. The monitor unit (MU) of TrueBeam was 7655.1±483.4 MU and Halcyon was 7439.6±283.7 MU. The Homogeneity Index (HI) of TrueBeam was 0.34±0.02, and Halcyon was 0.38±0.04. The gamma passing rate of TrueBeam and Halcyon were 99.99±0.04 and 99.78±0.27, respectively.

Discussion: There were no significant differences between the two groups in terms of $D_{98\%}$, $D_{2\%}$, and MU ($p=0.11$, 0.07, and 0.24). However, $D_{95\%}$ and HI showed significant differences ($p=0.02$ and 0.02), and the gamma passing rate of both machines passed the tolerance.

Conclusion: Both plans pass the clinical goals except for the mean lungs dose. TrueBeam plans are slightly better in both PTV coverage and OAR dose sparing.

Keywords: Total Body Irradiation (TBI), Volumetric modulated arc therapy (VMAT), TrueBeam, Halcyon

Design and fabrication of a dedicated phantom for geometric verification in single-isocenter multiple-target (SIMT) stereotactic radiosurgery

Montreemanorom Warisara [1*], Khamfongkhruea C[1,2], Mundee T[2], Chanpanya T[2], Suwanbut P[2], Polee C[3], Wonglee S[3], Thongsawad S[1,2]

1 Princess Srisavangavadhana College of Medicine, Chulabhorn Royal Academy, Bangkok, Thailand
2 Radiation Oncology Department, Chulabhorn Hospital, Chulabhorn Royal Academy, Bangkok, Thailand
3 Nuclear Research and Developments, Thailand Institute of Nuclear Technology, Bangkok, Thailand
**warisara.mon@edu.cra.ac.th*

Introduction: The Single-Isocenter Multiple-Target (SIMT) stereotactic radiosurgery technique streamlines treatment by eliminating the need for separate isocenter setups for each target, resulting in reduced setup and treatment time. However, accurate alignment across multiple targets is essential, and a single Winston-Lutz test is inadequate for complete geometric verification. This study develops a dedicated phantom with multiple metallic markers to accurately identify and verify radiation isocenters for multiple targets.

Methods: A cubic phantom dimension of 16×15×16 cm^3 was constructed from polymethyl methacrylate (PMMA) and embedded with thirteen stainless steel ball markers to define both isocenter and off-isocenter positions. A geometric verification plan for SIMT was developed, which involved shaping the multileaf collimator (MLC) around the markers at gantry angles of 0°, 45°, 90°, 135°, 180°, 225°, 270°, and 315°, across five separate tests. The plan was implemented on a TrueBeam linear accelerator, with the Electronic Portal Imaging Device (EPID) capturing images to assess the accuracy of isocenter and off-isocenter alignments. Positioning accuracy was evaluated by calculating the centroid deviation between the markers and the radiation beam.

Results: The geometric verification indicates increased beam uncertainty at positions further from the isocenter. At the isocenter, the beam positioning errors range from 0.02 cm to 0.06 cm, with the largest error at a gantry angle of 135°, measuring 0.06±0.02 cm. At the off-isocenter, the beam positioning errors increase, ranging from 0.05 cm to 0.13 cm, with the maximum error at a gantry angle of 180°, measuring 0.13±0.02 cm.

Discussion: The results of this study suggest that additional margins should be considered for targets located farther from the isocenter to account for the increased uncertainty.

Conclusion: This phantom is well-suited for verifying the geometric accuracy of the SIMT technique, offering a cost-effective and user-friendly solution. Integrating MATLAB script code for analysis can further streamline SIMT geometric verification workflows.

Keywords: Single-isocenter multiple-target stereotactic radiosurgery, stereotactic radiosurgery, and geometric verification.

Eclipse scripting application programming interface validation for breast cancer in flattening filter free photon beams

Tansangworn Prasit[1*], Chatchumnan N[2], Saksornchai K[2], Kingkaew S[2], Vimolnoch M[2], Oonsiri P[2], Oonsiri S[2]

1 Department of Radiology, Medical Physics Program, Faculty of Medicine, Chulalongkorn University, Bangkok, Thailand
2 Department of Radiology, Division of Radiation Oncology, King Chulalongkorn Memorial Hospital, Bangkok, Thailand
**6670059730@student.chula.ac.th*

Introduction: Automated treatment planning has become increasingly important in treatment planning systems, not only by saving time but also by improving plan quality. EZFluence is one of automated treatment planning tools used in three-dimensional conformal radiation therapy. This study aims to validate the EZFluence software for left-sided breast cancer treatment using flattening filter-free photon beams.

Methods: Seventy left-sided breast cancer patients without locoregional node involvement were treated with a prescribed dose of 42.4 Gy in 16 fractions. Treatment plans were generated using electronic compensators and automated treatment planning. Portal dosimetry with 3%/2mm criteria and Mobius with 3%/3mm and 5%/3mm criteria were used to validate the treatment plans.

Results: The gamma passing rate for portal dosimetry with 3%/2mm criteria exceeded 99.0% for both two techniques, with no statistically significant difference (p-value = 0.60). Using Mobius with 3%/3mm criteria, automated treatment planning demonstrated a gamma passing rate of 88.5±4.3% which was significantly lower than the 92.2±3.7% achieved by the electronic compensator technique (p-value <0.05). However, when using Mobius with 5%/3mm criteria, automated treatment planning exhibited a significantly higher gamma passing rate of 98.3±1.8% compared to 97.6±2.1% for electronic compensator technique (p-value <0.05).

Discussion: In portal dosimetry, no significant difference was observed between the two techniques, consistent with finding reported (Yoder 2019). Using Mobius with 3%/3mm criteria, both plans yielding gamma passing rate below 95%. In contrast, with 5%/3mm criteria, both plans exceeded 95%. This discrepancy can be attributed to the fact that Mobius with 3%/3mm is typically utilized for measurements in homogeneous conditions; however, breast cancer case is inherently inhomogeneous, resulting in lower measured values. When the criteria were increased to 5%/3mm which is more appropriate for inhomogeneous situations, the values exceeded 95%.

Conclusion: Automated treatment planning has demonstrated accuracy in generating treatment plans and could be effectively utilized in the treatment planning for left-sided breast cancer.

Keywords: Automated treatment planning, Electronic compensator, Left-side breast cancer.

Assessment of bladder and rectal dose distributions using three-channel vaginal applicators in HDR electronic brachytherapy

Rahman Md. Mokhlesur[1*], Rahman MH[2], Nath NK[3]

1 Department of Medical Physics and Biomedical Engineering, Gono Bishwabidyalay

2 Gazi Cancer Center, Dhaka

3 Gonoshasthaya Community based cancer hospital and research Centre

**hsmaklesur553@gmail.com*

Introduction: High-Dose-Rate (HDR) electronic brachytherapy (Isotope-free, only used E-50KV) is utilized for treating gynecological cancers in Bangladesh. Vaginal applicators play a critical role in delivering targeted radiation to tumors while aiming to minimize exposure to nearby organs such as the bladder and rectum. However, dose distribution challenges persist, especially with three-channel applicators. This study analyzes and compares dose distributions to the vagina, bladder, and rectum, assessing adherence to prescribed dose constraints and identifying opportunities for optimizing treatment planning.

Methods: A Study was conducted using three-channel vaginal applicators in HDR electronic brachytherapy. The dose levels received by the vagina, bladder, and rectum were recorded and evaluated against prescribed dose limits. Key metrics, including the maximum dose (Dmax) and specific dose volumes (e.g., D2 cm^3, D0.1 cm^3), were analyzed to identify deviations from the intended constraints.

Results: The three-channel applicator approach demonstrated dose escalations, with critical thresholds for the bladder and rectum consistently exceeded, raising safety concerns.

Discussion: This study shows challenges in using three-channel vaginal applicators for HDR electronic brachytherapy, with bladder and rectum doses often exceeding safe limits. These findings highlight the need for better treatment planning to reduce risks to nearby organs.

Conclusion: This study highlights substantial deviations from prescribed dose constraints in HDR electronic brachytherapy using three-channel vaginal applicators. The findings underscore the need for enhanced treatment planning and dose optimization to mitigate risks to the bladder and rectum. Refinements in HDR brachytherapy techniques are essential to ensure safer and more effective treatments for gynecological cancers.

Keywords: High-Dose-Rate, Electronic brachytherapy, Three-channel applicators and Bladder

Development of deep learning-based auto-segmentation on CT images for prostate radiotherapy

Pranee Chanaphat[1*], Kummanee P[1], Deeharing A[2], Fuangrod T[1], Khamfongkhruea C[1,2]

1 Princess Srisavangavadhana College of Medicine, Chulabhorn Royal Academy, Bangkok, Thailand.

2 Radiation Oncology Department, Chulabhorn Hospital, Chulabhorn Royal Academy, Bangkok, Thailand.

**Chanaphat.pra@edu.cra.ac.th*

Introduction: Accurately delineating organ at risk (OAR) volumes and clinical target volume (CTV) is a vital process in radiotherapy, requiring considerable time and expertise. Manual delineation is time-consuming, labor-intensive, and inconsistent due to inter-observer variability. Therefore, this study focuses on developing deep learning-based CTV and OAR prediction models for prostate radiotherapy.

Methods: Treatment plans, treatment structures, and computed tomography (CT) scans of 53 prostate Volumetric Modulated Arc Therapy (VMAT) cases were randomly retrieved from Chulabhorn Hospital. The dataset was split into two subsets: 80% for training deep learning models using U-Next architecture and 20% for testing the model's performance. The models were built for specific CTV and OARs including the bladder, rectum, bowel, sigmoid, and left and right femurs. The model's performance was evaluated for the auto-segmentation of the CTV and OARs using Boundary F-1 Score (BFScore).

Results: The BFScore of CTV was 0.84641. In addition, the BFScores of OARs of bladder, rectum, bowel, left femur, and right femur were 0.92643, 0.67716, 0.58189, 0.75234, and 0.72514, respectively.

Discussion: The models demonstrated varied performance in prostate radiotherapy auto-segmentation. Bladder segmentation showed a high BFScore of 0.92643 from high contrast from other tissues, while the bowel and rectum presented challenges (BFScores of 0.58189 and 0.67716, respectively) due to similar tissue contrast. However, CTV segmentation showed good results and femoral heads were moderately well-segmented.

Conclusion: These findings suggest that the deep learning-based auto-segmentation shows potential to assist the radiotherapy planning process in prostate radiotherapy.

Keywords: Deep learning, Auto-segmentation, CT image, prostate cancer.

The effect of constructing CT images from multiple MR sequences in the treatment planning of a brain tumor

Pisut Duanghatai [1*], Auethavekiat S[2], Oonsiri S[3]

1 Department of Biomedical Engineering, Faculty of Engineering, Chulalongkorn University, Bangkok, Thailand
2 Department of Electrical Engineering, Faculty of Engineering, Chulalongkorn University, Bangkok, Thailand
3 Department of Radiology, Division of Radiology, King Chulalongkorn Memorial Hospital, Bangkok, Thailand
6572026921@student.chula.ac.th

Introduction: The information from CT and MR imaging are different. Thus, the translation of a MR image to a CT image is not perfect. In most studies, a CT image is constructed from a single MR sequence. However, brain tumor patients take three MR sequences: T1W, T2W and FLAIR. Multiple MR sequences contain more information and should lead to better construction of the CT image. The effect of using multiple MR sequences to generate CT brain image was investigated.

Methods: In this study, the MR and CT images were manually registered. Pix2Pix was used to translate an MR image to a CT image. Three Pix2Pix networks were constructed and had different types of inputs: (1) T1W image only, (2) the combination of T1W and T2W images and (3) the combination of T1W, T2W and FLAIR images. Different MR sequences were combined by putting them into different color channels. Only the slices above the eyes were used. The training set consisted of 377, 371 and 372 slices for the translation from T1W image only, the combination of T1W and T2W images and the combination of T1W, T2W and FLAIR images, respectively. 10 slices from the patient not used in the training were used to evaluate the translation efficiency.

Results: The construction of CT images from multiple MR sequences was better. The ventricle was more complete. However, the effect of the additional FLAIR sequence was not distinct.

Discussion: Though the translation was improved, there were not enough slices containing brain tumors to make a conclusion about the accuracy of translating the tumor from MR to CT images.

Conclusion: Compared to the translation from a single sequence, the translation from multiple MR sequences produced more detailed CT images. More data was necessary to evaluate whether multiple MR sequences led to better tumor translation.

Keywords: Image translation, MR to CT images translation, Multiple MR sequences

Machine learning model for predicting radiation-induced xerostomia from head and neck cancer radiotherapy

Chantarak Kiattiyot[1*], Suntiwong S[2], Chamchod S[1,2], Liamsuwan T[1]

1 Princess Srisavangavadhana College of Medicine, Chulabhorn Royal Academy, Bangkok, Thailand
2 Radiation Oncology Department, Chulabhorn Hospital, Chulabhorn Royal Academy, Bangkok, Thailand
**kiattiyot.cha@edu.cra.ac.th*

Introduction: This study aimed to develop a machine learning (ML) model for predicting radiation-induced xerostomia in head and neck cancer (HNC) patients treated with intensity-modulated radiation therapy (IMRT) and volumetric-modulated radiation therapy (VMAT), using clinical, radiomic, and dosimetric features.

Methods: 85 HNC patients underwent IMRT and VMAT were included. Radiomic features were extracted from the patients' computed tomography (CT) images, while dosimetric features were obtained from the dose-volume histograms (DVHs). A total of 121 features were initially considered. The endpoint of interest was grade ≥2 xerostomia at 6 months after treatment. The patients were randomly split into the training (n = 68) and test (n = 17) datasets. Machine learning (ML) models, including Random Forest (RF), Support Vector Machine (SVM), Naïve Bayes (NB), and Logistic Regression (LR) were investigated using Orange software. For these models, five-fold cross-validation was conducted with the training dataset. Feature selection on training set was achieved by ReliefF. Finally, the model performance was assessed with the test dataset using the area under precision-recall curve (AUC-PR).

Results: ReliefF selected 2, 10, and 5 clinical, radiomics, and dosimetric features, respectively. Three models achieved the AUC-PRs above 0.60, namely RF and SVM with radiomic features (AUC-PR = 0.67 and 0.64, respectively) and RF with dosimetric features (AUC-PR = 0.60).

Discussion: RF with only radiomics features provided the highest AUC-PR. The use of only radiomics features based on patients' CT images was proved to be capable of predicting radiation-induced xerostomia.

Conclusion: Using only radiomics features, the ML models could acceptably predict grade ≥2 xerostomia, allowing for prediction of this toxicity before dose calculation in the treatment planning process.

Keywords: Radiation-induced xerostomia, head and neck cancer, radiomics, machine learning, predictive model

Artificial intelligence-based dose prediction for optimizing treatment plans in locally advanced cervical cancer radiation therapy

Yooyen Nattawut[1*], Thongsawad S[1, 2], Chamchod S[1, 2], Kummanee P[1], Intanin P[2], Nimjaroen K[2], Chaipanya T[1,3], Khamfongkhruea C[1, 2]

1 Princess Srisavangavadhana College of Medicine, Chulabhorn Royal Academy, Bangkok, Thailand.
2 Radiation Oncology Department, Chulabhorn Hospital, Chulabhorn Royal Academy, Bangkok, Thailand.
3 Division of Radiation Oncology, Lopburi Cancer Hospital, Lopburi, Thailand.
**Nattawut.Yoo@edu.cra.ac.th*

Introduction: Intensity-modulated radiation therapy (IMRT) is essential for locally advanced cervical cancer, delivering precise tumor doses while sparing healthy organs. However, its complex planning relies heavily on the planner's experience, causing variability that impacts outcomes. This study aims to develop an artificial intelligence (AI)-based dose prediction model to assist planners in achieving optimal treatment planning, thereby improving plan quality and reducing workload.

Methods: This study utilized computed tomography (CT) images from 48 locally advanced cervical cancer patients treated with IMRT. 535 radiomic features were extracted from the images and reduced to 54 significant features using the F-test algorithm. The dataset was divided into 80% training and 20% testing for machine learning in MATLAB. Five models—support vector machine (SVM), decision tree, Gaussian process regression, kernel, and ensemble—were trained to predict dose metrics, including maximum dose (D_{max}) and organ volumes receiving 50 Gy (V_{50}), 45 Gy (V_{45}) and 40 Gy (V_{40}). Model performance was evaluated using mean absolute error (MAE), accuracy, sensitivity, and specificity.

Results: Among the models tested, the SVM model showed the best performance, achieving the lowest MAE values. For the bladder, MAE was 1.23(D_{max}), 14.21(V_{50}), and 11.01(V_{45}). For the rectum, it was 1.29(D_{max}) and 12.92(V_{40}). For the small bowel, MAE was 1.16(D_{max}) and 8.53 (V_{40}). Binary classification accuracy ranged from 0.50 to 0.90, with specificity between 0.67 and 1.00, and sensitivity between 0.44 and 1.00.

Discussion: The proposed model shows potential for improving IMRT dose planning. However, higher MAE in certain parameters highlights the need for further refinements such as increasing sample data and integrating advanced deep learning models, which could enhance consistency and better support clinical decision-making.

Conclusion: The AI-based dose prediction model improves IMRT planning by providing accurate dose forecasts, reducing variability, and supporting more precise treatment decisions, helping to outcomes for cervical cancer patients.

Keywords: Dose prediction, cervical cancer, artificial intelligence, intensity-modulated radiation therapy, brachytherapy, radiomics

Dose Prediction for Cervical Cancer Brachytherapy using Deep Learning

Rinjan Nawarat[1*], Khamfongkrue C.[1,2], Chanpanya T.[2], Kummanee P.[1], Tannanonta C.[2], Tharavichitkul E. [3], Thongsawad S.[1,2]

1 Princess Srisavangavadhana College of Medicine, Chulabhorn Royal Academy, Bangkok, Thailand
2 Radiation Oncology Department, Chulabhorn Hospital, Chulabhorn Royal Academy, Thailand
3 Department of Radiology, Division of Radiation Oncology, Faculty of Medicine, Chiang Mai University
**nawarat.rin@edu.cra.ac.th*

Introduction: Dose distribution in brachytherapy planning depends on the dwell time of the radioactive source and the positioning of targets and organs at risk (OARs). Manual dwell time optimization, while robust, is prone to variation based on the planner's expertise and is often time-consuming. To address these challenges, a deep learning model was developed to predict dose distribution in brachytherapy, with the goal of providing guidance for more efficient and standardized treatment planning in the future.

Methods: Data from 54 cervical cancer patients who underwent brachytherapy with different applicators -Tandem ovoids (15 patients), tandem rings (22 patients), and tandem cylindrical (17 patients) was analyzed. The dataset included computed tomography images, radiation dose distributions, and organ-at-risk positions. Data processing was conducted using Python, and the dataset was divided into 80% for training, 10% for validation, and 10% for testing. A Cascade 3D U-Net deep learning model was employed for dose prediction. Model performance was evaluated using Mean Absolute Error (MAE) in Gy.

Results: The deep learning model showed the correlation between predicted and actual radiation doses. The MAE values for tandem ovoids, tandem rings, and tandem cylindrical were approximately 0.301 Gy, 0.234 Gy, and 0.272 Gy, respectively.

Discussion: The results demonstrate the efficiency of the deep learning model in predicting radiation doses. The MAE values for each applicator show that the model can predict dose distributions, although some errors still occur, likely due to multiple factors. This suggests that while the model does not generate complete treatment plans, it can assist planners by providing dose distribution predictions, helping to improve the accuracy and consistency of the planning process, and potentially reducing human error.

Conclusion: These findings highlight the potential of the deep learning model to improve the accuracy of dose predictions, although some errors persist. Further refinement is needed, including expanding the dataset and validating the model in clinical trials to ensure its reliability in treatment delivery.

Keywords: Deep learning, dose prediction, brachytherapy, needle insertion, cervical cancer

Auto-segmentation for cervical cancer brachytherapy using deep learning

Wattanagul Nuttapol[1*], Khamfongkruea C[1,2] , Kummanee P[1], Tannanonta C[2], Tharavichitkul E [3], Thongsawad S[1,2]

1 Princess Srisavangavadhana College of Medicine, Chulabhorn Royal Academy, Bangkok, Thailand
2 Radiation Oncology Department, Chulabhorn Hospital, Chulabhorn Royal Academy, Bangkok, Thailand
3 Department of Radiology, Faculty of Medicine, Chiang Mai University, Chiang Mai, Thailand
**nuttapol.wat@edu.cra.ac.th*

Introduction: Manually delineating organs at risk (OARs) in cervical cancer brachytherapy treatment planning is a time-intensive and laborious process, requiring precision to ensure effective treatment. Deep learning provides a promising avenue to automate and accelerate this critical task. This study aims to develop and validate a deep learning-based model to automatically segment OARs in cervical cancer patients from computed tomography (CT) images, thereby enhancing the efficiency of treatment planning and potentially improving clinical outcomes.

Methods: A deeply supervised UNet 3+ architecture, was implemented on dataset consisting of 60 cervical cancer cases. The dataset was split into 48 cases for training (80%), 6 cases for validation (10%), and 6 cases for independent testing (10%). The model was designed to segment the bladder, rectum, sigmoid, and bowel from CT images. Model performance was evaluated using the Dice Similarity Coefficient (DSC).

Results: The mean DSC values for the segmentation of the bladder, rectum, sigmoid, and bowel were 0.843, 0.848, 0.752, and 0.721, respectively. These findings indicate strong performance in delineating the bladder and rectum, with moderate accuracy for the sigmoid and bowel.

Discussion: Future efforts should prioritize data augmentation and robust cross-validation to improve model generalization.

Conclusion: A supervised UNet 3+ model demonstrates that deep learning can effectively automate the segmentation of OARs in cervical cancer brachytherapy, achieving high accuracy, particularly for the bladder and rectum. This model can assist radiation oncologists by reducing the workload and time required for contouring in brachytherapy.

Keywords: Deep learning, auto-segmentation, cervical cancer, brachytherapy, UNet 3+, organs at risk (OARs), computed tomography (CT), Dice similarity coefficient (DSC)

Failed-tolerance detection of EPID in vivo dosimetry using machine learning

Saiyo Nipon[1*], Kojima H[2], Noto K[2], Isomura N[2], Tsukamoto K[2], Segawa Y[1], Yamaguchi S[1], Kohigashi J[1], Takemura A[3]

1 Department of Quantum Medical Technology, Division of Health Sciences, Graduate School of Medical Sciences, Kanazawa University, Kanazawa, Ishikawa, Japan
2 Department of Radiology, Kanazawa University Hospital, Kanazawa, Ishikawa, Japan
3 Faculty of Health Sciences, Institute of Medical, Pharmaceutical, and Health Sciences, Kanazawa University, Kanazawa, Ishikawa, Japan
nipon.saiyo@outlook.com

Introduction: EPIgray™ in vivo dosimetry software shows results as the dose deviation between the treatment planning system (TPS) dose and the electronic portal dosimetry (EPID) reconstructed dose in 53 points of interest within 5%. In cases of failed tolerance, the failed cause should be evaluated. The aim of this study is to develop a machine learning (ML) model to classify the cause of failed tolerance for EPIgray™ results.

Methods: 23 prostate volumetric modulated arc therapy (VMAT) plans were used to recalculate the dose distribution on the intensity modulated radiation therapy (IMRT) phantom images as no error (NE) plans. Three errors were simulated, - a randomized multileaf collimator (RMLC) error, monitor unit (MU) errors, and patient position errors. NE and all errors were delivered via IMRT phantom and measured by EPID. RMLC error plans used 23 VMAT plans for editing MLC position with an average error of 0.5 mm. Additionally, MU and position errors used NE plans for measurement with varying MU (±5%) and shifting phantom position in lateral (±2 mm), pitch (±2 degree), and roll (±2 degree) directions. All EPIgray™ results were used to create the ML model by support vector machine (SVM) for each error type. The F1 score and the percent accuracy were used to evaluate the performance for all ML models.

Results: The F1 score was 0.99, 0.91, 0.66, 0.65, and 0.67, the percent accuracy was 99.3, 91.2, 66.1, 65.2, and 66.8 for 5 errors, respectively.

Discussion: SVM model can classify the cause of failed analysis for EPIgray™ results, especially MLC and MU errors, which have a high F1 score and percent accuracy. However, SVM is an appropriate performance for the classification of all position errors.

Conclusion: ML model can classify the cause of failed tolerance for three variations of EPIgray™ in vivo dosimetry.

Keywords: Failed-tolerance detection, EPIgray™ in vivo dosimetry, machine learning model

Tumor prognosis in nasopharyngeal carcinoma using deep transfer learning with RadImageNet from CT images

Petiraksakul Parida[1,2*], Prayongrat A[3], Kitpanit S[3], Kannarunimit D[4], Chakkabat C[4], Lertbutsayanukul C[4], Sriswasdi S[5,6], Khongwirotphan S[2,7], & Rakvongthai Y[2,8]

1 Department of Radiology, Medical Physics Program, Faculty of Medicine, Chulalongkorn University, Bangkok, Thailand
2 Department of Radiology, Chulalongkorn University Biomedical Imaging Group, Faculty of Medicine, Chulalongkorn University, Bangkok, Thailand
3 Department of Radiology, Division of Radiation Oncology, King Chulalongkorn Memorial Hospital, Bangkok, Thailand
4 Department of Radiology, Division of Radiation Oncology, Faculty of Medicine, Chulalongkorn University, Bangkok, Thailand
5 Center for Artificial Intelligence in Medicine, Research Affairs, Faculty of Medicine, Chulalongkorn University, Bangkok, Thailand
6 Center of Excellence in Computational Molecular Biology, Chulalongkorn University, Bangkok, Thailand
7 Department of Radiological Technology and Medical Physics, Faculty of Allied Health Sciences, Chulalongkorn University, Bangkok, Thailand
8 Division of Nuclear Medicine, Department of Radiology, Faculty of Medicine, Chulalongkorn University, Bangkok, Thailand
**6670077030@student.chula.ac.th*

Introduction: Nasopharyngeal cancer (NPC), which is prevalent in Southeast Asia, poses a challenge due to its high incidence and unique clinical characteristics. Recent advancements in deep learning, particularly convolutional neural networks (CNNs), have enhancing the detection and diagnosis of cancers. Transfer learning (TL), leveraging pretrained models like those based on ImageNet, has shown promising results in various medical applications. The introduction of RadImageNet, a dataset designed for medical imaging, offers new opportunities for TL in clinical practice. This study aimed to assess the efficacy of TL models using RadImageNet pretrained weights to predict NPC prognosis based on CT imaging, with a focus on key outcomes including 3-year overall survival (OS), progression-free survival (PFS), and distant metastasis-free survival (DMFS).

Methods: The dataset included CT images from 197 NPC patients treated at King Chulalongkorn Memorial Hospital from October 2010 to January 2019. Four commonly-used CNN architectures (ResNet50, Inception-ResNet-v2 [IRV2], DensNet121, InceptionV3) for image classification were trained and validated with RadImageNet and ImageNet pretrained weights to predict 3-year OS, PFS, and DMFS. Performance was assessed using the area under the receiver operating characteristic curve (AUC).

Results: In the validation set, the best-performing models using ImageNet weights were IRV2 for OS (AUC = 0.805±0.106), ResNet50 for PFS (AUC = 0.858±0.092), and IRV2 for DMFS (AUC = 0.786±0.087). Using RadImageNet weights, InceptionV3 outperformed other models. It achieved AUC values of 0.885±0.062 for OS, 0.888±0.06 for PFS, and 0.883±0.056 for DMFS. RadImageNet showed AUC improvements of 5.1%, 5.8%, and 4.1% for OS, PFS, and DMFS, respectively, as compared to ImageNet ($p < 0.05$).

Discussion: RadImageNet, specifically developed for medical imaging, provides a better learning set for the CT images, allowing the models to more effectively capture the key features related to NPC prognosis.

Conclusion: Deep learning models with RadImageNet show great promise in the NPC prognosis by significantly improving model performance.

Keywords: Nasopharyngeal carcinoma, Prognosis prediction, CT Image, Deep Learning, RadImageNet, ImageNet

Deep learning for radiation dose distribution prediction in VMAT breast cancer irradiation

Sukha Thanakorn[1*], Puttanawarut C[2], Sirirutbunkajorn N[1], Changkaew P[1], Stansook N[1], Khachonkham S[1]

1 Department of Diagnostic and Therapeutic Radiology, Faculty of Medicine Ramathibodi Hospital, Mahidol University, Bangkok, Thailand.
2 Chakri Naruebodindra Medical Institute, Faculty of Medicine Ramathibodi Hospital, Mahidol University, Samut Prakan, Thailand.
**thanakorn.su2@student.mahidol.ac.th*

Introduction: Volumetric modulated arc therapy (VMAT) planning requires more time and expertise due to its complexity and need for repeated optimization. To address this, a deep learning (DL) model for dose prediction was developed. This study assesses the feasibility and reliability of the DL model's predictions for VMAT breast irradiation.

Methods: A 6-channel U-Net-based network was trained and tested using data from 53 breast cancer VMAT plans. Input data included CT images, binary masks of the planning target volume (PTV), and organs at risk (OARs). The clinically accepted dose distribution served as the target for the predicted dose. Model predictions were evaluated using metrics such as mean absolute error (MAE), gamma passing rate (GPR) and dosimetric indices comparison.

Results: Data from 8 plans were used for model testing. MAE for the PTV ranged from 1.7% to 2.6%, with an average of 2.0 ± 0.3%, while for the heart and lungs, MAE was 2.7 ± 1.0% and 3.4 ± 0.7%, respectively. The GPR at 3%/3mm ranged from 74.40% to 89.68%, with an average of 84.47 ± 0.07%. For PTV, $D_{99\%}$, $D_{98\%}$, and $D_{2\%}$ differences were 0.26 ± 0.68, 0.05 ± 0.27, and 0.05 ± 0.42 Gy, respectively.

Discussion: The developed DL model can be used for dose prediction in VMAT breast treatment, with an average GPR of 84.47%. The largest difference between the clinical and predicted values is observed in OARs, particularly in low-dose regions, where the MAE value is high. Model performance may be improved by increasing the size and variability of the training dataset

Conclusion: The results show the potential of DL models in enhancing the efficiency and accuracy of VMAT dose planning, supporting advancements in personalized radiation therapy for breast cancer patients.

Keywords: Deep learning, Dose prediction, VMAT, Breast Cancer

Comparative analysis of convolution neural networks (CNNs) for automated organ-at-risk delineation in prostate cancer computed tomography images

Khuadpudsa Wanitchaya[1,*], Kaewlek T[1,2,3]

1 Department of Radiological Technology,Medical Physics Program, Faculty of Allied Health Sciences, Naresuan University, Phitsanulok Province, Thailand.
2 Department of Radiological Technology, Faculty of Allied Health Sciences, Naresuan University, Phitsanulok Province, Thailand.
3 Interdisciplinary Health and Data Sciences Research Unit, Faculty of Allied Health Sciences, Naresuan University, Phitsanulok Province, Thailand.
wanitchayakh66@nu.ac.th

Introduction: Prostate cancer is the fourth most common cancer worldwide and the second most common among men, according to the World Cancer Research Fund International. In treatment planning, the accurate delineation of organs at risk (OARs) is crucial for optimizing treatment plans, making the process faster and more efficient. Recent advancements in artificial intelligence (AI) have become a significant tool in medicine, helping to reduce delays and streamline treatment workflows. U-Net was selected for its simplicity and effectiveness as a widely used foundational model in medical image segmentation, while Dense V-Net, represents an evolution of segmentation architectures, improve feature propagation and minimize information loss. This study aims to investigate and compare the performance of deep learning models for the automatic delineation of OARs in CT images of prostate cancer patients.

Methods: 300 CT images from the prostate-anatomical-edge-cases dataset were used to test the U-Net and Dense V-Net models under identical parameters for the automatic delineation of the bladder and rectum. The models' performances were evaluated using Dice Similarity Coefficient (DSC), 95th percentile Hausdorff Distance (95HD), and Mean Surface Distance (MSD).

Results: The Dense V-Net model achieved the best performance, with DSC, 95HD, and MSD values for the bladder of 0.99, 0.003, and 0.012, respectively. and 0.98, 0.01, and 0.02 for the rectum, respectively, under the same number of epochs.

Discussion: Dense V-Net consistently outperformed U-Net across all metrics, achieving superior DSC, 95HD, and MSD values. Although the type of GPU used did not significantly affect performance, Dense V-Net required 10 times more training time and memory compared to U-Net.

Conclusion: Dense V-Net demonstrated the highest accuracy in delineation tasks but required substantially greater computational resources and training time compared to U-Net when evaluated under the same batch size and number of epochs.

Keywords: Deep Learning, CT, Auto-Delineation, Prostate cancer

Prediction of radiation pneumonitis using artificial intelligence in non-small cell lung cancer patients undergoing volumetric modulated arc therapy

Chevajarassakul Wasin [1*], Chamchod S[1,2], Phonlakrai M[3], Kummanee P[1], Masa-nga W[2], Nimjaroen K[2], Chaipanya T[1,4], Khamfongkhruea C[1,2]

1 Princess Srisavangavadhana College of Medicine, Chulabhorn Royal Academy, Bangkok, Thailand
2 Radiation Oncology Department, Chulabhorn Hospital, Chulabhorn Royal Academy, Bangkok, Thailand
3 Faculty of Health Science Technology, HRH Princess Chulabhorn College of Medical Science, Chulabhorn Royal Academy, Bangkok, Thailand
4 Division of Radiation Therapy, Lopburi Cancer Hospital, Lopburi, Thailand
**Wasin.Che@edu.cra.ac.th*

Introduction: Volumetric modulated arc therapy (VMAT) has advanced outcomes for non-small cell lung cancer (NSCLC) patients, but radiation pneumonitis (RP) remains a critical complication. Current RP prediction models often overlook lung function variability, reducing precision. This study aims to improve RP prediction by combining artificial intelligence (AI) with four-dimensional computed tomography (4DCT) ventilation and perfusion imaging to capture detailed functional variability in lung regions, enhancing model accuracy for refining treatment planning.

Methods: This study analyzed 4DCT data from 56 NSCLC patients treated with VMAT, classifying patients by RP severity as either grade < 2 and grade ≥ 2 based on evalautions by experienced radiation oncologists. MATLAB was used for dataset preprocessing, with an 80% and 20% split for training and testing. From 535 radiomic features, the chi-square algorithm selected 54 relevant features for RP prediction. Five machine learning models—support vector machines (SVM), Naive Bayes, logistic regression, linear SVM, and k-nearest neighbors (KNN)—were trained and optimized via 5-fold cross-validation on the training set. Model performance was assessed using specificity, sensitivity, precision, accuracy, and area under the precision-recall curve (AUPRC).

Results: The SVM model was the most accurate in predicting RP, achieving an accuracy of 0.67, sensitivity of 0.60, specificity of 0.71, and precision of 0.60. The model also attained an AUPRC of 0.20.

Discussion: The AI-based RP prediction model holds potential for improving treatment planning in radiotherapy. While promising, the model performance could be enhanced with a larger dataset. Future studies should focus on increasing data size and exploring advanced AI methods, such as deep learning, to further improve model performance.

Conclusion: Integrating AI into RP prediction offers a valuable approach for optimizing treatment planning, paving the way for personalized care and minimizing risks of radiotherapy complications.

Keywords: Artificial intelligence (AI), Machine learning (ML), Radiation pneumonitis (RP), Non-small cell lung cancer (NSCLC), Volumetric modulated arc therapy (VMAT).

Evaluation of knowledge-based planning model in head and neck cancer using volumetric modulated arc therapy

Plangpleng Nattha[1*], Suriyapee S[2], Tawonwong T[1], Raungchan S[1], Kanphet J[1], Sanghangthum T[2].

1 Department of Radiology, King Chulalongkorn Memorial Hospital, The Thai Red Cross Society, Bangkok, Thailand.
2 Department of Radiology, Faculty of Medicine, Chulalongkorn University, Bangkok, Thailand
**nattha27682l@gmail.com*

Introduction: Volumetric modulated arc therapy (VMAT) is commonly used in head and neck treatment due to its ability to deliver high conformal dose distributions. However, the planning process remains complex, especially in balancing target coverage with the organs at risk (OARs) sparing. Knowledge-based planning optimization engine, RapidPlan, was utilized to potentially reduce organs at risk doses and decrease optimization times. This work aimed to compare the dosimetric difference between plans generated using RapidPlan and manually optimized plans for head and neck cancer.

Methods: RapidPlan model was created using dosimetric and geometric data from 60 patients with head and neck cancer. All plans were clinically approved and had been used in previous treatments with 6MV photon energy, three targets at dose levels of 54, 60, and 70 Gy in 33 fractions from 2-3 arcs. Dosimetric outcomes and planning efficiency of VMAT plans produced with RapidPlan (RP plans) were compared to manually optimized plans (manual plans).

Results: The results showed that RP plans significantly reduced the mean dose to parallel organs compared to manual plans, while the maximum dose to serial organs did not increase significantly. The average time required to generate the RP plans with single optimization and manual plans was 24 and 45 minutes, respectively.

Discussion: Overlapping between target and OARs had a greater impact on serial organs than parallel organs. The RP plans were effective in reducing the maximum dose to serial organs by incorporating the manual objective constraints to target and OARs. Additionally, the average time to generate an acceptable plan decreased with the experience of the planner.

Conclusion: The RapidPlan model with single optimization is comparable to manually optimized plans for head and neck cancer. Moreover, the RapidPlan model can reduce the parallel organ doses and optimization times.

Keywords: Knowledge-based planning, RapidPlan, Head and neck cancer, VMAT.

Investigation of collimator effects on secondary Bragg peak formation in proton beams based on Monte Carlo simulation

Azimah Alfia Faizatul*, Haryanto F, Widita R, Arif I*

Nuclear Physics and Biophysics Research Division, Faculty Mathematics and Natural Sciences, Institut Teknologi Bandung, Jalan Ganesha 10, Bandung, West Java 40132, Indonesia.
**alfiafaizaazimah@gmail.com , idam@itb.ac.id*

Introduction: The interaction between high-energy proton beams and beamline components, particularly the patient assembly collimator, significantly impacts beam characteristics by generating secondary particles such as protons and neutrons. This study investigated proton beam characteristics after interacting with brass, copper (^{63}Cu), nickel (^{58}Ni), and iron (^{55}Fe) collimators.

Methods: TOPAS MC code was used to simulate the 15625 protons source with the energy range of 130 MeV-140 MeV (2 MeV interval) in a passive scattering system. The brass, copper, nickel, and iron collimators were modeled as plates and tubes, with varying thicknesses of the plate (5 mm, 10 mm, 15 mm) and tube lengths (37.5 mm, 50 mm, 62.5 mm). The collimator opening diameters were 10 mm, 12.5 mm, and 15 mm. The phase space after the beamline exit and dose distribution in a 15×15×15 cm^3 water phantom was analyzed.

Result: A dual-energy beam was observed in the phase space of the 140 MeV proton beam after passing through the collimators. Secondary protons energy of 43 MeV (brass), 37 MeV (copper), 28 MeV (nickel), and 49 MeV (iron) were observed. The 140 MeV dose distribution showed a Bragg peak at 12.85 cm, while secondary protons produced by brass, copper, nickel, and iron collimators resulted in secondary Bragg peaks at 1.4 cm, 0.9 cm, 0.4 cm, and 1.9 cm, respectively.

Discussion: The thicker plate and longer tube reduced the number of secondary particles, contrasting with smaller collimator openings. The material cross-section played a crucial role in the secondary proton generation mechanism.

Conclusion: The secondary proton is responsible for the dual-Bragg-peak. The collimator material and geometry influence the formation of secondary proton, with iron and brass producing higher energy secondary protons, while nickel reduces the energy of secondary protons.

Keywords: Proton Beam, Secondary Proton, Bragg-Peak, Monte Carlo

Comparative dosimetric analysis between volumetric modulated arc therapy and intensity-modulated proton therapy for craniospinal irradiation plans

Buranavanitvong Nalinpun[1*], Plangpleng N[2], Ruangchan S[2], Sanghangthum T[3]

1 Department of Radiology, Medical Physics Program, Faculty of Medicine, Chulalongkorn University, Bangkok, Thailand
2 Department of Radiology, Division of Radiation Oncology, King Chulalongkorn Memorial Hospital, Thai Red Cross Society, Bangkok, Thailand
3 Department of Radiology, Division of Radiation Oncology, Faculty of Medicine, Chulalongkorn University, Bangkok, Thailand
**nalinpun.b@gmail.com*

Introduction: Craniospinal irradiation (CSI) is the treatment for posterior fossa tumors. This study aimed to compare dosimetric differences in CSI volumetric modulated arc therapy (VMAT) plans between TrueBeam, Halcyon, and intensity-modulated proton therapy (IMPT) from ProBeam.

Methods: Ten CSI cases were optimized for the prescription dose at 2340 cGy in 13 fractions. The clinical target volume (CTV) and organs at risk (OARs) doses, conformity index (CI), homogeneity index (HI), total normal tissue volume (TNTV) dose, and total monitor units (MUs) were used to evaluate the results.

Results: All plans met clinical goals. A paired samples t-test and repeated measures ANOVA were conducted. Analysis showed no significant differences in $D_{95\%}$, $D_{50\%}$, and $D_{2\%}$ in the CTV, with similar CI between TrueBeam and Halcyon plans, however, Halcyon plans exhibited a better HI ($p = 0.03$). Compared to ProBeam, ProBeam plans demonstrated superior CI ($p < 0.01$) and the best %TNTV doses, followed by Halcyon and TrueBeam ($p < 0.01$). The 10 of 16 OARs in ProBeam received lower doses than other plans, while 11 OARs in TrueBeam had lower doses than Halcyon, with five showing significant differences. Total MUs were 1367.6 ± 113.8 for TrueBeam, 1451.4 ± 348.2 for Halcyon, and 157130.6 ± 23005.4 for ProBeam.

Discussion: The properties of protons lead to lower %TNTV and OAR doses in ProBeam plans. In contrast, Halcyon's dual-layer stacked MLC configuration enhances TNTV doses. Halcyon plans require more total MUs than TrueBeam plans due to additional isocenters from field size limitations.

Conclusion: ProBeam plans are better in CI, %TNTV, and OARs dose than the others. TrueBeam plans show superior OAR sparing, and have lower total MUs than Halcyon plans. Conversely, Halcyon plans perform better in %TNTV dose.

Keywords: Craniospinal irradiation (CSI), Volumetric Modulated Arc Therapy (VMAT), Intensity Modulated Proton Therapy (IMPT), TrueBeam, Halcyon.

Proton beam characteristics through dental materials

Yamram Nattaporn[1*], Sanghangthum T[2,3], Saikaew P[4], Phaisangittisakul N[5], Prayongrat A[2,6], Israngkul Na Ayuthaya I[2,6], Tawonwong T[2,6], Ruangchan S[2,6]

1 Department of Radiology, Medical Physics Program, Faculty of Medicine, Chulalongkorn University, Bangkok, Thailand
2 Her Royal Highness Princess Maha Chakri Sirindhorn Proton Center, Bangkok, Thailand
3 Department of Radiology, Division of Radiation Oncology, Faculty of Medicine, Chulalongkorn University, Bangkok, Thailand
4 Department of Operative and Endodontics, Faculty of Dentistry, Mahidol University, Bangkok, Thailand
5 Department of Physics, Faculty of Science, Chulalongkorn University, Bangkok, Thailand
6 Department of Radiology, Division of Radiation Oncology, King Chulalongkorn Memorial Hospital, The Thai Red Cross Society, Bangkok, Thailand
**nattaporn.ym@gmail.com*

Introduction: Dental materials present challenges in head and neck proton therapy due to the CT image artifacts. The study of stopping power ratio **(**SPR) and the effects of dental materials on proton beams remains limited and requires further investigation. This research aims to determine the correlation between SPR and CT numbers of these materials and explore their overall impact.

Methods: Proton beam parameters in FLUKA Monte Carlo (MC) simulation for 4 energies (80, 100, 150, and 200 MeV) were investigated. The SPR values of 5 dental materials were validated through simulation and measurement. A table correlating SPR with CT numbers was generated based on the CT calibration curve in the proton treatment planning system (TPS). Dose distribution and proton characteristics regarding spot shadowing and profile were investigated and compared across simulation and measurement.

Results: The simulation parameters for 4 energies were determined, proton range and spot size were compared with the measurement and results were within the acceptable range following TG-224 guidelines. The simulation SPR of dental materials agreed well with the measurement, while the maximum deviation of the SPR at 0.6 from amalgam was observed. A table correlating SPR and CT numbers was generated for 5 dental materials. The simulated proton beam characteristics aligned with measurements, confirming dose fill-in phenomena for both high and low proton energies.

Discussion: The SPR difference between simulation and measurement may be caused by uncertainties in material compositions. However, the correlation between SPR and CT number is generated by using measured SPR. Dental material with high density presents a larger impact on the proton beam characteristics by producing more scatter and leading to dose shadowing.

Conclusion: A correlation table between SPR and CT numbers was generated, and proton beam characteristics aligned well with measurements, confirming the impact of dental materials on dose distribution.

Keywords: Dental materials, Therapeutic proton beam, Monte Carlo simulation

Assessing the efficacy of independent calculation-based methods for patient-specific quality assurance in Intensity-Modulated Proton Therapy

Chatchumnan Nichakan[1*], Suriyapee S[2], Sanghangthum T[2].

1 Department of Radiology, King Chulalongkorn Memorial Hospital, Bangkok, Thailand.
2 Department of Radiology, Faculty of Medicine, Chulalongkorn University, Bangkok, Thailand.
** nichamush_fern@hotmail.com*

Introduction: In proton therapy, secondary independent calculation-based dose verification for patient-specific quality assurance (PSQA) is essential to ensure patient safety and treatment efficacy. This study aims to evaluate the performance of an independent calculation software based on Monte Carlo simulations for PSQA in Intensity-Modulated Proton Therapy (IMPT).

Methods: The myQAiON independent dose calculation software was used to calculate point doses and compared with measurement by a chamber in the Varian ProBeam system. The simple plans were evaluated in homogeneous and heterogeneous phantoms. Sixty IMPT treatment plans, covering five regions, were created on the Eclipse Treatment Planning System. These plans were recalculated on myQAiON software and compared using 3%/3mm gamma criteria. Additionally, the confidence limits were determined to ensure the accuracy and reliability of dose calculation.

Results: The point dose differences between the myQAiON software and measurements were within 1%. For simple plan results, the gamma passing rate was 97.5±4.4% in homogeneous phantom and 86.9±3.9% in heterogeneous phantom. For the IMPT treatment plans, average gamma passing rates were 95.4±1.9%, 95.8±1.2%, 94.6±2.5%, 95.2±2.4%, 98.5±2.4% for head-and-neck, breast, chest, abdomen, and pelvis, respectively. The confidence limit for clinical plans was 90.6%.

Discussion: The lower gamma passing rate was found in inhomogeneous phantom due to different algorithms for dose calculation that high impact on the heterogeneous area. In clinical situations, the chest IMPT plan exhibited the lowest gamma pass, while pelvis region had the highest. This discrepancy highlights the challenges of dose calculation in lungs. The variability in gamma passing rates across different treatment sites underscores the importance of establishing confidence limits for site-specific adjustments to ensure accurate dose delivery.

Conclusion: The myQAiON independent dose calculation software, Monte Carlo-based, is reliable for verifying IMPT plans. The high confidence limit underscores its effectiveness in enhancing the PSQA in proton therapy.

Keywords: Patient-specific quality assurance, independent calculation-based, Intensity-Modulated Proton Therapy, Monte Carlo.

Range comparison of Monte Carlo and pencil beam algorithms in treatment planning system for proton therapy

Monkongsubsin Wiroon[1*], Israngkul Na Ayuthaya I[2], Sanghangthum T[3], Keawsamur M[3]

1 Department of Radiology, Medical Physics program, Faculty of Medicine, Chulalongkorn University, Bangkok, Thailand
2 Department of Radiology, King Chulalongkorn Memorial Hospital, Bangkok, Thailand
3 Department of Radiology, Faculty of Medicine, Chulalongkorn University, Bangkok, Thailand
** wiroonmon@gmail.com*

Introduction: The pencil beam (PB) scanning technique has expanded rapidly due to its precision in targeting tumors using Bragg peak while minimizing exit dose to surrounding tissues. Proton range is determined by the energy, and reducing range uncertainties is crucial in clinical applications. Monte Carlo (MC) algorithm has demonstrated an accuracy in proton dose calculations, especially in heterogeneous tissues. This study aims to compare the proton range differences between MC and pencil beam algorithms using experimental measurements across various tissue types.

Methods: A Gammex 467 tissue characterization phantom with 11 insertion rods was used to study the proton range in different human tissues. The range calculations were performed in RayStation Treatment planning system using both MC and PB algorithms for a single proton spot with 150 MeV passing through each rod. The range measurements were conducted using an IBA Multi-plane parallel ionization chamber (Giraffe) with a Varian ProBeam system, and the ranges were compared with the calculated ranges.

Results: The proton range was determined at R_{80} (the depth at the distal 80% of the prescribed dose). The differences between the calculated and measured ranges of each rods were analyzed. The mean range differences were 1.4 mm ± 2.0%, and 1.7 mm ± 2.1% for MC and PB, respectively. The Wilcoxon signed-rank test indicated a statistically significant difference with a *p*-value of 0.003.

Discussion: PB demonstrated the least agreement with measured range, particularly in bone-like material, which was improved with MC.

Conclusion: The limitations of the pencil beam algorithm in calculating dose for bone-like materials should be noted and considered in clinical practice.

Keywords: Monte Carlo algorithm, Pencil beam algorithm, Treatment planning system, Proton therapy.

Comparison of kinetic repair models for protons induced DNA damage

Tikamol Natthawat[1*], Nantajit D[1], Liamsuwan T[1]

1 Princess Srisavangavadhana College of Medicine, Chulabhorn Royal Academy, Bangkok, Thailand
**natthawat.tik@edu.cra.ac.th*

Introduction: Proton therapy provides benefits over photon therapy due to its accurate dose targeting, which can spare healthy tissues. In clinical practice, the relative biological effectiveness (RBE) of protons of 1.1 is used throughout the beam path. However, cell experiments showed that the RBE varied close to the end of the proton path. Therefore, mechanistic modeling of DNA damage and repair specific for proton therapy could help to quantify the accurate RBE of protons. In this work, existing DNA repair models were systematically evaluated for therapeutic proton beams.

Methods: The DNA double-strand break (DSB) repair models proposed by Belov (Model A), Taleei and Nikjoo (Model B) were investigated. Both models consisted of a set of partial differential equations with repair kinetic constants specific to the mechanistic pathways proposed by each model. Initial DNA damage yields and damage complexity obtained from Monte Carlo track structure simulations were used as inputs for estimating residual DSBs over time, which was validated against experimental data. Re-optimization of the repair kinetic constants was also performed.

Results: The root mean square (RMS) errors of Models A and B ranged from 6.35–33.74% and 21.52–29.00% respectively. After re-optimization, the RMS errors were 2.73–13.67% and 0.19 – 13.76% respectively.

Discussion: Model A was more accurate because it considered repair kinetics across all cell cycle phases, while Model B only focused on the G1 and early S phases. Moreover, the rate constants used in Model A were derived from both low and high LET experiments, while Model B was based on X-ray irradiation.

Conclusion: Model A was more suitable for predicting DNA repair kinetics for proton therapy than Model B.

Keywords: DNA double-strand break (DSB), DSB repair kinetics, proton therapy, mechanistic modeling

The evaluation of radiotherapy plan complexity using root mean square error based on IMRT linac log-files

Azzi Akbar[1*], Habyb FE[1], Ryangga D[2]

1 Department of Physics, Faculty of Mathematics and Natural Sciences, Universitas Indonesia, Depok, West Java, Indonesia
2 Department of Radiotherapy, Pasar Minggu General Region Hospital, South Jakarta, Jakarta, Indonesia
**akbar.azzi@sci.ui.ac.id*

Introduction: This study aims to evaluate the complexity of planning in log-file-based IMRT cases using the root mean square error (RMSE) method. Therefore, it is expected that there is a threshold of complexity in radiotherapy treatment planning that must be considered in conducting log-file-based PSQA.

Methods: The study involved forty patients, ten patients per case, for head and neck, breast, bone, and brain cancer cases. All patients were irradiated with Varian Trilogy Linac machine. The RMSE evaluation was applied for five fractions for each patient while complexity was evaluated by using the modulation complexity score (MCS) from the radiation treatment planning. The relationship between RMSE and MCS was evaluated using Pearson correlation. In addition, gamma index measurements are carried out using portal dosimetry.

Results: For breast cancer cases, the correlation (r value) was -0.317; for head and neck cases, it was -0.711; for bone cases, it was 0.194, and for brain cases, it was 0.298. Head and neck, breast, and brain cancer cases can be categorized as having moderate correlation ($0.2 < r < 0.7$), while bone cancer cases exhibited weak correlation ($r < 0.2$). The average global gamma passing rate with criteria 3%/3mm and 10% threshold for head and neck, breast, bone, and brain cancer cases were 91.17%, 94.63%, 93.42%, and 91.8%.

Discussion: The findings of this study indicate that the complexity of planning in IMRT cases, as evaluated by RMSE and MCS, varies across different cancer types. The moderate correlation observed in head and neck, breast, and brain cancer cases suggest that the complexity of these plans may influence the accuracy of dose delivery, as indicated by the higher RMSE values.

Conclusion: This study highlights the importance of considering plan complexity in log-file-based PSQA for IMRT treatments. The moderate correlation between RMSE and MCS in certain cancer types underscores the need for observing the quality of linac treatment during a complex treatment plan.

Keywords: log-file, root mean square error, plan complexity.

Dosimetric study of a Co-60 HDR brachytherapy source using PHITS

Aquino Patrick Vincent*

Radiation Oncology Section, Batangas Regional Cancer Center, Batangas Medical Center, Batangas City, Batangas, Philippines
**pvgaquino@gmail.com*

Introduction: In brachytherapy, consensus dosimetry datasets serve as a standard reference for dose distribution calculations in treatment planning. The availability of these datasets promotes consistency in dosimetry practices and reduces variability across different practitioners and planning systems. These dosimetric datasets are developed through a comprehensive and rigorous process that integrates experimental measurements with results from Monte Carlo simulations. This study examines the dose distribution parameters of a Co-60 brachytherapy source obtained using the Particle and Heavy Ion Transport System (PHITS) code and compares them against consensus datasets.

Methods: The BEBIG Co-60 source type Co0.A86 was modeled using PHITS version 3.34. A T-Deposit tally was employed to score dose distributions up to a distance of 10 cm surrounding the source, with a total of 10^9 particle histories simulated. Relative doses were obtained at different distances to calculate the radial dose function, $g_L(r)$, and 2D anisotropy function, $F(r,\theta)$, based on the TG-43U1 formalism.

Results: The relative differences between the calculated values for $g_L(r)$ and the TG-43 consensus data are all within 2%. Similarly, the relative difference for $F(r,\theta)$ fall within 2% for$10 < \theta < 170$, but increases significantly outside this range. These angles correspond to the direction of the source tip ($\theta < 10$) and the direction along the wire opposite the tip ($\theta > 170$). The relatively high difference at these angles can be attributed to larger statistical uncertainty on this direction due to more attenuation at the tip and the wire. This can be improved in future studies by increasing the number of simulation histories.

Conclusion: The derived values for $g_L(r)$ and $F(r,\theta)$ align closely with the consensus dataset established for the Co0.A86 source type. The developed model can serve as a reliable basis for future PHITS-based Monte Carlo studies involving brachytherapy sources.

Keywords: brachytherapy, PHITS, Monte Carlo, TG-43

Uncertainty of radiophotoluminescence glass dosimeter in low energy photon beams

Jittrakool Kantida [1*], Kingkaew S[2], Chatchumnan N [2], Oonsiri P[2], Oonsiri S[2], Vimolnoch M[2]

1 Department of Radiology, Medical Physics Program, Faculty of Medicine, Chulalongkorn University, Bangkok, Thailand
2 Department of Radiology, Division of Radiation Oncology, King Chulalongkorn Memorial Hospital, Bangkok, Thailand
**kantida.jit@gmail.com*

Introduction: The uncertainty is a critical factor in low energy photon beams due to the inherent characteristics of the detectors. This study aims to estimate the uncertainty associated with radiophotoluminescent glass dosimeters (RPLGD) in low energy photon beams.

Methods: To estimate the uncertainty of the RPLGD model GD-352M in low-energy photon beams, the RPLGD was calibrated against a Radcal 10X6-6 ionization chamber and an Accu-Pro electrometer (Radcal Corporation, Monrovia, CA, USA) using the substitution method, as guideline in the International Atomic Energy Agency Technical Reports Series No. 457. The uncertainties associated with the RPLGD, including uniformity, reproducibility, reader reproducibility, magazine position reproducibility, linearity, accuracy, energy dependence, and minimum detectable dose, were estimated for doses ranging from 0.05 to 80 mGy.

Results: The uncertainties estimation of the RPLGD model GD-352M, including uniformity, reproducibility, reader reproducibility, magazine position reproducibility, linearity, accuracy, and energy dependence, were estimated to be 0.07%, 0.70%, 1.06%, 0.03%, 0.00%, 0.02%, and 0.02%, respectively. The combined uncertainty was 4.56% (k = 2), and the minimum detectable dose was 12.41 ± 0.87 μGy.

Discussion: The coefficient of variation for uniformity was 2.11%, consistent with the manufacturer's specifications. The RPLGD demonstrated good linearity, and its energy dependence indicated that the GD-352M model is suitable for use with X-rays in this energy range, in agreement with Kim et al. The reproducibility of the reader showed stable readouts and high precision. Additionally, the magazine position did not affect the readout values, aligning with the results of Oonsiri et al. The minimum detectable dose was 12.41 ± 0.87 μGy, which is comparable to the manufacturer's specifications. Overall uncertainty presented good outcomes as previously mentioned by Kim et al.

Conclusion: This study indicates that the uncertainty estimation of RPLGD model GD-352M is suitable for measuring low-energy photon beams.

Keywords: Uncertainty, Radiophotoluminescent glass dosimeter, Low energy photon beams

Unlocking the potential of 3D optical dosimetry in polyvinyl alcohol dosimeters enhanced with silver bromide and zinc oxide nanoparticles for radiotherapy dosimetry applications

Adenan Mohd Zulfadli [1,2,3*], Mahat MM[1], Jamalludin Z[4], Min UN[4], Yaakub NH[5], Ahmad Taufek Abdul Rahman[1,2*]

1 School of Physics and Material Studies, Faculty of Applied Sciences, Universiti Teknologi MARA, Shah Alam 40450, Selangor, Malaysia
2 Centre of Astrophysics & Applied Radiation, Institute of Science, Universiti Teknologi MARA, Shah Alam 40450, Selangor, Malaysia
3 Centre of Medical Imaging, Faculty of Health Sciences, Universiti Teknologi MARA Cawangan Selangor Campus of Puncak Alam, Puncak Alam 42300, Selangor, Malaysia
4 Clinical Oncology Unit, Faculty of Medicine, Universiti Malaya, 50603, Kuala Lumpur, Malaysia
5 Clinical Oncology and Radiotherapy Department, Pantai Hospital Kuala Lumpur, 59100, Kuala Lumpur, Malaysia
**ahmadtaufek@uitm.edu.my, mohdzulfadli@uitm.edu.my*

Introduction: In recent years, a novel radiochromic gel dosimeter using polyvinyl alcohol (PVA) as its primary component has emerged as a promising candidate for 3D dosimetry in radiotherapy applications. This study aims to explore the potential of integrating silver bromide (AgBr) and zinc oxide (ZnO) nanoparticles into PVA to create a high-performance 3D dosimeter suitable for clinical radiotherapy systems.

Methods: Laboratory-based PVA-AgBr dosimeters with varying concentrations of AgBr were fabricated and irradiated using a medical linear accelerator at photon energies of 6 MV and 10 MV, with doses ranging from 0 Gy to 30 Gy. Following irradiation, dosimeter samples were refrigerated for 24 hours before being characterized using UV-Vis spectroscopy to assess dosimetric properties and dose response. ZnO nanoparticles were also incorporated to evaluate their influence on dosimeter sensitivity and dose enhancement.

Results: Upon irradiation, PVA-AgBr dosimeter samples displayed a colour change from colourless to varying shades of grey, indicating dose response. Analysis demonstrated a strong linear correlation in dose response (R^2 better than 0.9955) and a sensitivity of 0.00805. The incorporation of ZnO nanoparticles further enhanced the linearity of dose response, with increasing concentrations of AgBr and ZnO yielding greater dose enhancement as the radiation dose increased.

Discussion: Findings indicate that the addition of high atomic number (Z) materials such as AgBr and ZnO significantly enhances X-ray photon absorption, leading to improved dose response and sensitivity in the PVA-based dosimeter. This enhancement supports the suitability of the PVA-AgBr-ZnO formulation as a viable option for advanced dosimetry in radiotherapy.

Conclusion: The PVA-based dosimeter with AgBr and ZnO nanoparticles exhibits strong potential for use in 3D radiation dosimetry, showing consistent dose response and enhanced sensitivity, making it promising for clinical and audit applications.

Keywords: polyvinyl alcohol, silver bromide, zinc oxide, 3D dosimetry, radiotherapy

SafeRT: software for quantitative QA evaluation of IG-IMRT linac performance and treatment delivery

Zin HM*, Lim SY, Abubakar A, Sakaria K, Midi NS, Zamri NAM, Uwais F, Rosli NF

Advanced Medical & Dental Institute, Universiti Sains Malaysia, 13200 Bertam, Penang, Malaysia
**hafiz.zin@physics.org*

Introduction: Image guided-intensity modulated radiotherapy (IG-IMRT) requires a systematic quality assurance (QA) programme to ensure the accurate delivery of highly conformal beam. Periodical performance tests (daily, weekly and monthly) of various linac components (AAPM TG 142) and patient-specific QA (AAPM TG 218) are performed to identify and rectify any inaccuracies.

Methods: An in-house MATLAB-based software package was developed, comprising algorithms to streamline the QA processes of IG-IMRT linac and treatment delivery. It performs statistical process control (SPC) analysis of daily dose outputs, automated images analysis of the MLC picket-fence test and CBCT imaging quality metrics, and automated calculation of setup uncertainties and patient-specific QA using log data. The algorithms were tested at the radiotherapy unit of USM Bertam Medical Centre, Advanced Medical and Dental Institute, Penang, Malaysia.

Results: The dosimetry analysis provided energy-specific daily dose output visualisation with points selection for linac recalibration and SPC analysis. MLC analysis integrated both EPID-based tracking and log file tracking errors. CBCT image analysis calculated various quantitative quality metrics. The IGRT module calculated systematic and random errors, PTV margins, and scatter plots for NAL/eNAL protocols. All results were exportable in Word or Excel formats, streamlining workflows and complying with the specifications recommended by the manufacturers, TG 142 and TG 218.

Discussion: SafeRT offers a comprehensive and effective quantitative analysis of IG-IMRT linac performance across different QA components and test frequencies, including patient-specific QA. The rapid system reduces the time spent for QA and allows more efficient use of resources while ensuring patient safety.

Conclusion: The in-house developed software suite may improve the efficacy of QA assessments and reduce measurement variations caused by subjective errors. Software trials are available upon request: https://rti2research.com/safert-software/

Keywords: IG-IMRT, QA, Patient Specific QA, TG 142, TG 218.

Image quality evaluation of ACR CT accreditation phantom using IndoQCT Software

Chakrapong Apawadee[1*], Krisanachinda A[2]

1 Department of Radiology, King Chulalongkorn Memorial Hospital, Thai Red Cross Society, Bangkok, Thailand
2 Department of Radiology, Faculty of Medicine, Chulalongkorn University, Bangkok, Thailand
**apawadee16@gmail.com*

Introduction: Quality control program of CT is required to ensure the accurate and reliable diagnostic information at acceptable patient radiation dose. IndoQCT software is an automated software for CT image quality evaluation. The objective of this study is to evaluate image quality parameters using American College of Radiology CT accreditation phantom (ACR CTAP) images from three different CT scanners analyzed by IndoQCT software.

Method: The ACR CTAP was scanned by 3 CT scanners using 4 clinical protocols of adult head, pediatric head, adult abdomen, and pediatric abdomen. Image quality parameters evaluated by IndoQCT software include CT number uniformity, CT numbers of different materials, CNR, spatial resolution, and slice thickness. The results were compared to ACR tolerance level.

Results: CT number uniformity shows the variation of CT number between peripheral and central ROIs within 5 HU. The CT number of different materials was within the tolerance level except Teflon (bone) and polyethylene of pediatric head and abdomen protocols. The CNR of adult and pediatric head protocols was 2.48, 1.21, 1.61 and 1.16, 1.16 and 1.05 respectively. The CNR of adult and pediatric abdomen protocols was 1.56, 0.81, 0.94, and 1.11, 0.55, 0.39 respectively. The spatial resolution of 5 line pair.cm^{-1} was detectable for all protocols. The slice thickness was within tolerance level at 1.5 mm.

Conclusion: The acceptable image quality parameters were CT number uniformity, spatial resolution and slice thickness of all protocols from 3 scanners. For pediatric head and abdomen protocol, the CT number of Teflon (bone) and polyethylene were not acceptable. The CNR of adult head and pediatric head from 3 scanners met the ACR standards. The annual CT image quality performed and evaluated by qualified medical physicist using ACR CTAP and analyzed by IndoQCT software is very important for the accuracy and reliable of diagnostic information.

Keywords: Image quality, Computed tomography, IndoQCT software, ACR CT phantom

Optimization of clinical indication DRL of CT protocols

Kanyakham Kannikar[1*], Kriengkrai I[1], Krisanachinda A[2]

1 Imaging Center, Phyathai 2 Hospital, Bangkok, Thailand
2 Department of Radiology, Faculty of Medicine, Chulalongkorn University, Bangkok, Thailand.
**kanni.pp@gmail.com*

Introduction: The Diagnostic Reference Level (DRL) is an indication for the optimization of the patient dose. The objective of this study is to establish the local clinical indication DRL (LcDRL) of CT protocols with optimization.

Methods: The clinical indication based diagnostic reference level (cDRL) of CT protocols include the number of phases, scan and reconstruction techniques, protocol details and reference phantom size. Dose monitor software was used to collect data on $CTDI_{vol}$, DLP, and scan length. Patient size was selected based on BMI, ranging from 19-29 kg/m². CTDIvol and DLP were compared to the national DRL, NDRLs Thailand 2023. Optimization was performed after radiation dose reduction and image quality assessment.

Results: The clinical indication DRL of CT protocols consist of brain (trauma): $CTDI_{vol}$ and DLP(before/after optimization). $CTDI_{vol}$ 48.3/48.3 mGy, DLP 1042.5/ 970.15 mGy.cm, DLP decreased 6.94%. Chest (Thrombus detection) $CTDI_{vol}$ were 13.6/11.9 mGy, DLP 592.50/500.4 mGy.cm, percent decreased CTDI/DLP were 12.50/15.54. Cardiac (Calcium score NC) $CTDI_{vol}$ 7/5.5 mGy, DLP 90.4/74.65 mGy.cm, percent decrease 0.5/15.08. Sinus (Sinusitis) $CTDI_{vol}$ 34.65/20.80 mGy, DLP 649.75/437.80 mGy.cm, percent decreased 39.97/32.62. Abdomen/ Pelvis (Detection of Stones) $CTDI_{vol}$ 10.1/10 mGy, DLP 477.2/472.2 mGy.cm, percent decrease 0.5/ 15.08.
The LcDRL of CT protocol is compared to NDRL 2023 of anatomical based. The result shows the NDRL/LcDRL as Brain $CTDI_{vol}$ 62/48.3mGy, DLP 1028/970 mGy.cm. Chest $CTDI_{vol}$ 18/11.9 mGy DLP 665/500 mGy.cm. Cardiac (Calcium score NC) $CTDI_{vol}$ 6.2/5.5 mGy, DLP 85/74.6 mGy.cm. Sinus (Sinusitis) $CTDI_{vol}$ 34.3/20.8 mGy, DLP 548/437 mGy.cm. Abdomen/ Pelvis (Detection of Stones) $CTDI_{vol}$ 13.6/10 mGy, DLP 548/472.2 mGy.cm. All LcDRL are lower than NDRLs 2023.

Discussion & Conclusion: The limitation in dose reduction in LcDRL is the variation in scan length per patient. The optimization of LcDRL for CT protocols result in the patient dose reduction when compared to NDRL2023.

Keywords: Clinical CT protocols, NcDRLs, CTDIvol, DLP

Real-time staff radiation dose monitoring from neuro-interventional procedures at King Chulalongkorn Memorial Hospital

Prajamchuea Kornkamol[1*], Krisanachinda A[2]

1 Department of Radiology, King Chulalongkorn Memorial Hospital, Bangkok 10330, Thailand
2 Department of Radiology, Faculty of Medicine, Chulalongkorn University, Bangkok 10330, Thailand
**kornploy7@gmail.com*

Introduction: A real-time radiation dosimeter is helpful for monitoring staff dose during the neuro-interventional procedures which were performed by biplane angiography system. This study is the first real-time staff radiation dose report of the neuro-interventional radiology procedures in Thailand. The objective of this study is to monitor, report the real-time radiation dose of medical staff team and determine the affecting parameters to staff radiation dose during the procedures.

Methods: The research methodology is the prospective descriptive study. It starts from the collection of the real-time radiation dose of medical staff team consisting of neuro-interventionist, fellow, scrub radiographer, medical physicist and anaesthesiologist during the procedures using RaySafe i3 dosimeter. Analyze dose rate and related parameters using descriptive statistics and report the real-time staff radiation dose with the affecting parameters.

Results: The average real-time radiation dose per case of the neuro-interventionist, fellow, scrub radiographer and medical physicist are 0.01, 0.03, 0.01 and 1.03 mSv, respectively. There is no radiation dose of the anesthesiologist. The affecting parameters are the position of lead barrier, the source-staff distance, X-ray tube angle, the exposure technique, source-image receptor distance (SID), and the total procedure time among the staff.

Discussion: As the anaesthesiologist works behind the lead barrier during the procedure, there is no radiation dose report in this study. Therefore, the medical staff should use the radiation protection equipment and stay behind the lead barrier.

Conclusion: The real-time radiation dose of medical staff team has been monitored and reported. The radiation protection management is the most important for this neuro-interventional procedure. The affecting parameters to occupational radiation dose are the position of the medical staff team, the application of the real-time radiation dosimeter, and the lead barrier during the procedures.

Keywords: real-time staff radiation dose, real-time radiation dosimeter, neuro-interventional procedures.

Dosimetry and image quality studies between grid and non-grid fluoroscopy during catheterization in pediatric protocol: a phantom study

Netprasert Sa-angtip[1*], Krisanachinda A[2]

1 Department of Radiology, King Chulalongkorn Memorial Hospital, Bangkok, Thailand.
2 Department of Radiology, Faculty of Medicine, Chulalongkorn University, Bangkok, Thailand.
**n.saangtip@gmail.com*

Introduction: Since fluoroscopic radiography is beneficial during interventional radiological procedures, the pulsed fluoroscopic imaging offered the high patient dose especially in children. The removing of an anti-scatter grid has been recommended. The purpose of this research is to study the dosimetry and image quality between using grid and non-grid fluoroscopy for a pediatric catheterization protocol.

Methods: As an X-ray tube is under the table, PMMA slabs of 16 cm thickness represent pediatric is placed on an X-ray table. TOR 18FG is placed between the slabs and a solid-state detector is placed on the table and under the PMMA slab, for dosimetry studies. The fluoroscopic system will be set as a routine paediatric clinical procedure. Both fluoroscopic mode and single mode were exposed with and without grid, repeat the exposures 5 times to obtain the average dose and the image quality in each mode.

Results: For with and without grid, the dose rate of fluoroscopic mode was 23.69 mGy/sec, and 10.27 mGy/sec (p-value <0.05). The dose rate of single mode was 39.18 and 36.23 mGy/sec (p-value = 0.02) respectively. The spatial resolution was 1.25 and 0.9 line pair/mm for fluoroscopic mode and 2.5 and 1.8 lp/mm for single mode. The contrast was 5.3 and 8.8 percent for fluoroscopic mode and no change on the single mode.

Discussion: At without grid, the dose rate reduction was 56.6% for fluoroscopic mode and 7.5 % for single mode. The spatial resolution reduced 28% for both modes. The contrast reduced by 40% for fluoroscopic mode and 0% for single mode.

Conclusion: Even though the grid had improved the image quality of both modes in the catheterization protocol of paediatric, the radiation dose rate increased by 56.6%. The use of fluoroscopy without grid during the paediatric procedure is encouraged.

Keywords: Grid, Non-grid, Paediatric interventional fluoroscopy, Dosimetry, Image quality.

Comparison of the image quality and dose by using the American College of Radiology (ACR) digital mammography (DM) and small ACR mammography phantoms from full-field digital mammography (FFDM) systems

Ruenjit Sakultala[1*], Krisanachinda A[2]

1 Department of Radiology, King Chulalongkorn Memorial Hospital, Bangkok, Thailand.
2 Department of Radiology, Faculty of Medicine, Chulalongkorn University, Bangkok, Thailand.
**Sakultala.ruen.rad@gmail.com*

Introduction: The new ACR DM phantom for 2D and digital breast tomosynthesis (DBT) in FFDM systems is introduced to test objects visibility with finer lesion and smaller object sizes than the small ACR phantom. The purpose of this study is to compare the image quality and mean glandular dose (MGD) using the ACR DM versus small ACR phantoms in FFDM systems.

Methods: The ACR DM and small ACR mammography phantoms were scanned in 2D and DBT modes by 3 FFDM systems using the AEC techniques. MGD, SNR, CNR and visibility of objects in each phantom image were assessed. A qualified medical physicist scored visible objects with the images under optimal viewing conditions on acquisition workstation monitor and then calculated the visible scores using weighted indexes and drew a square-shaped ROI in the 2D images only that the mean value of the cavity and background and the SD of background were automatically provided for SNR and CNR calculations.

Results: The mean MGD of DM phantom for 3 systems in 2D and DBT mode were 1.12±0.14 mGy and 1.66±0.32 mGy, respectively. The mean MGD of the small ACR phantom were 1.15±0.22 mGy and 1.84±0.49 mGy, respectively. The mean SNR and CNR of the DM phantom were 47.43±5.85 and 2.71±0.09, respectively. The mean SNR and CNR of the small ACR phantom were 53.57±10.06 and 10.76±1.39, respectively. The visible score of phantom objects were much higher in the ACR DM phantom than those in the small ACR phantom ($p < 0.05$).

Discussion & Conclusion: The ACR DM phantom is superior to the small ACR phantom in terms of MGD and visibility of phantom objects but the SNR & CNR were lower. Thus, ACR DM phantom appears to be satisfactory for assessing the qualitative image quality in FFDM.

Keywords: Full-field digital mammography (FFDM), American College of Radiology (ACR), Digital Mammography (DM), Phantom image quality, Mean Glandular Dose (MGD).

Comparison of Image Quality and Apparent Diffusion Coefficient value in Upper Abdominal MRI: Calculated vs. Acquired Diffusion-Weighted Imaging at high b-value

Lowong Thanatchaya[1*], Pisuchpen N[1,2], Satja M[1,2], Krisanachinda A[2]

1 Department of Radiology, King Chulalongkorn Memorial Hospital, Thai Red Cross Society, Bangkok, 10330, Thailand.
2 Department of Radiology, Faculty of Medicine, Chulalongkorn University, Bangkok 10330, Thailand
** thanatchaya.l@chulahospital.org*

Introduction: Diffusion-weighted imaging (DWI) is an MRI technique that uses tissue diffusion properties to detect and characterize lesions. This study compares the image quality of upper abdominal MRI obtained through calculated DWI (cDWI) and acquired DWI (aDWI) at high b-values.

Methods: The patients age over 18 years old, underwent upper abdominal MRI with DWI, using four b-values of 50, 500, 1000, 1500 s/mm² from August to September 2024. Calculated DWI at b = 1500 s/mm² was automatically generated using software. Both cDWI and aDWI values at b = 1500 s/mm² were measured for the liver, spleen, pancreatic body, and renal cortices. Apparent diffusion coefficient (ADC) values were calculated using the mono-exponential model. Intraclass correlation coefficients (ICCs) were determined to assess the reliability of the measured DWI and ADC values for both cDWI and aDWI.

Results: Twenty patients (13 of males and 7 of females) were included. The mean signal intensity ranged from 107.70±7.00 to 413.24±17.14 for aDWI images and from 100.41±12.64 to 414.93±22.30 for cDWI images. The average ADC values of the acquired (aADC) and calculated (cADC) images ranged from 0.67±0.16 to 1.58±0.07 (10^{-3} mm²/s) and 0.64±0.09 to 1.71±0.06 (10^{-3} mm²/s), respectively. The ICC values between aDWI and cDWI for the liver, spleen, pancreatic body, and both renal cortices ranged from 0.653 to 0.964. For aADC and cADC values, the range was 0.441 to 0.696 across these same organs. The overall agreement between the two observers, measured by Cohen's kappa coefficient, was 0.577 for aDWI and 0.459 for cDWI images.

Discussion and Conclusion: The ICCs demonstrate moderate to excellent reliability between aDWI and cDWI in the liver, spleen, pancreatic body, and renal cortices. While ADC values showed moderate consistency, inter-observer agreement was moderate for both techniques, supporting cDWI as a potential alternative to aDWI for high b-value imaging.

Keywords: Computed diffusion-weighted imaging, high b-value, apparent diffusion coefficient,

A breast phantom study for mean glandular dose estimation from full field digital mammography and digital breast tomosynthesis

Thupsuri Suphawat*, Singkavongs A, Tuiduang S

Department of Medical Sciences, Bureau of Radiation and Medical Devices, Ministry of Public Health, Nontaburi, Thailand
**Suphawat.t@dmsc.mail.go.th*

Introduction: In mammography, the radiation sensitive breast tissue is glandular. This study determines the mean glandular dose (MGD), displayed on the operator's console in digital systems. In order to verify the MGD, the incident air kerma is an essential parameter to measure. A breast phantom of various thickness is used to estimate the MGD. This phantom study leads to the establishment of the national diagnostic reference levels (NDRLs) in full field digital mammography (FFDM) and digital breast tomosynthesis (DBT) from the craniocaudally (CC) and medio-lateral oblique (MLO) views of 192 digital mammography systems from 358 health facilities in Thailand.

Methods: A polymethyl methacrylate (PMMA) breast phantom with compression device was acquired by the FFDM and DBT systems for CC and MLO views. The MGD across various compressed breast thickness (CBT) of 20, 30, 40, 45, 50, 60, and 70 mm were recorded. The 75th percentile of the median values of MGD were estimated for both FFDM and DBT systems.

Results: The MGD at CBT of 20, 30, 40, 45, 50, 60, and 70 mm were 0.6, 0.8, 1.1, 1.2, 1.6, 2.4, and 3.1 mGy for FFDM and 0.9, 1.1, 1.4, 1.6, 1.8, 2.4, and 3.2 mGy for DBT system.

Discussion: The MGD of FFDM and DBT were compared to the acceptable and achievable AGD recommended by IAEA Human Health Series 49. All values were within the limits of all breast thicknesses.

Conclusion: The NDRLs of FFDM and DBT systems should be established for the purpose of radiation protection of the patients and the risk of breast cancer in Thailand. The phantom study is a part of quality control of the FFDM and DBT systems and the MGD verification.

Keywords: Diagnostic reference levels (DRLs), average glandular dose (AGD), full field Digital Mammography(FFDM), digital breast tomosynthesis (DBT), compressed breast thickness(CBT)

Organ absorbed dose estimation for abdomen-pelvis CT based on measurement and Monte Carlo simulation: phantom study

Nuntue Chatnapa[1,3*], Matsubara K[2], Watanabe S[1]

1 Department of Quantum Medical Technology, Division of Health Sciences, Graduate School of Medical Sciences, Kanazawa University, Kanazawa, Japan
2 Department of Quantum Medical Technology, Faculty of Health Sciences, Institute of Medical, Pharmaceutical and Health Sciences, Kanazawa University, Kanazawa, Japan
3 Department of Radiological Technology, Faculty of Allied Health Sciences, Thammasat University, Pathumthani, Thailand
**Chatnapa@stu.kanazawa-u.ac.jp*

Introduction: The absorbed dose in an organ from CT exposure is complex for the direct measurement. Monte Carlo simulation is one of the methods that can be used to estimate the absorbed doses from CT in patients. This study aimed to determine organ absorbed doses by measurement and Monte Carlo simulation in abdomen-pelvis phantom.

Methods: The $CTDI_{vol}$ measurements were performed with PMMA body phantom. The female abdomen-pelvis phantom (RAN-110) was scanned by 256-MDCT. The organ absorbed doses were measured using radiophotoluminescence glass dosimeters (GD-302M) inserted at various organ positions in the phantom. The radiophotoluminescence glass dosimeters were calibrated against an ionization chamber and applied a correction factor for energy dependence. For simulation, the voxelized model of the phantom was generated based on CT images. The geometry of a CT scanner and scanning parameters were reproduced on the Particle Heavy Ion Transport code System (PHITS) as Monte Carlo simulation code, similar to the measurements, to obtain the dose distribution.

Results: The percent of relative difference between $CTDI_{vol}$ measurements and simulation were within 10%. The absorbed dose demonstrated a range between 20.99 ± 0.71 and 37.24 ± 0.20 mGy. The dose distribution simulation was uniform in all regions of abdominal and pelvis. However, the bone showed a slightly higher dose than other organs.

Discussion: The $CTDI_{vol}$ measurement and simulation were in good agreement, which indicates that the PHITS simulation accurately reflects the dose distribution in the phantom. The energy dependence of glass dosimeters in various anatomical locations was affected the absorbed dose measurement. The bone's high X-ray absorption rate affected the dose distribution when compared to other organs.

Conclusion: The measurements and Monte Carlo simulations enable the estimation of organ absorbed dose. PHITS could be useful as a simulation code for dose estimation, while direct measurements could not be performed easily in the patients.

Keywords: Monte Carlo simulation, abdominal computed tomography, voxel phantoms, organ absorbed dose

PHITS modelling and simulation of a D-D neutron generator facility for radiation safety assessment

Dulohan Christine[1*], Egwolf B[2], Asuncion-Astronomo A[3]

1 The Graduate School, University of Santo Tomas, Manila, Philippines
2 Department of Mathematics and Physics, College of Science, University of Santo Tomas, Manila, Philippines,
3 DOST-Philippine Nuclear Research Institute, Quezon City, Philippines
**christine.dulohan.gs@ust.edu.ph*

Introduction: Deuterium-deuterium (DD) neutron generators (NG) are considered a promising alternative neutron source for various applications. However, effective shielding for neutrons and photons is essential to protect workers in facilities with DD NG. This study aims to develop a simulation model to evaluate the radiological safety of the future DD NG facility in the Philippines, ensuring compliance with prescribed dose limits.

Methods: The Monte Carlo-based Particle Heavy Ion Transport Code System (PHITS) was used to model a DD NG facility with a 2.48 MeV source and 10^8 n/s yield. The ambient dose equivalent rates at 30 spherical air detectors positioned around the NG were calculated using PHITS region tally together with ICRP 74 flux-to-dose conversion factors. Optimal radiation protection was determined by analyzing various high-density polyethylene (HDPE) moderator configurations.

Results: The west-oriented NG yielded the lowest doses, making it the optimal position. With a fully shielded configuration, the highest dose rates calculated are 979 µSv/h for neutrons and 22 µSv/h for photons, while average dose rates near the NG, in the working area, and the control room were 131, 0.476, and 0.0005 µSv/h, respectively. As expected, higher dose rates were obtained for NG configurations with reduced shielding.

Discussion: Full shielding reduced dose rates to below the ICRP 60 recommended limit of 5 µSv/h for most locations, except at detectors located close to the HDPE moderator. Establishing safety boundaries near the source is recommended. Doses in work areas will not exceed the annual limit of 20 mSv even with full operating time.

Conclusion: A fully shielded, west-oriented NG ensures that dose rates are below occupational limits. Workers can safely operate the NG even with full operating time in a year. This study provides a reference for radiation safety assessment of the future DD NG facility in the Philippines.

Keywords: DD neutron generator, radiation safety, dose, Monte Carlo simulation, PHITS

Assessment of patient and occupational radiation dose during angiography procedures in interventional radiology

Muhammad Roslan Abdul Gani*, Widya Apriyani S, Endah P

Department Radiology, Dharmais National Cancer Center Hospital, Jakarta 11420, Indonesia
**mroslanagani@gmail.com*

Introduction: The angiographic procedure uses real-time X-ray imaging to visualize blood vessels. While angiography offers valuable diagnostic and therapeutic benefits, the assessment of both patient and occupational radiation doses during interventional radiology procedures is essential. This helps ensure the safety and health of the patients and medical staff.

Methods: The data from angiographic procedures, patient's dose-area product (DAP), and fluoroscopy time, conducted from 2022 to 2023, was collected and assessed. Personal digital dosimeters were placed on the chest area inside the lead apron to monitor the interventional radiologists, technologists, and nurses in a unit of mSv. The occupational dose data were displayed and recorded after the examination.

Results: 184 DSA procedures were performed in 2022 and increased to 365 procedures in 2023**.** The average DAP decreased from 66.96 (0.02 - 566.61) Gy.cm^2 in 2022 to 59.27 (0.02 - 471.30) Gy.cm^2 in 2023, respectively. The personal digital dosimeter ranged from 0.07 to 0.15 mSv/year for interventional radiologists, 0.01 to 0.07 mSv/year for technologists, and 0.01 to 0.04 mSv/year for nurses.

Discussion: Optimizing protection in interventional radiology procedures with the use of CARE mode, lower frame rate, and short exposure time to an average of 9.96 minutes significantly reduces patients' radiation exposure. All medical staff safely received radiation doses below the annual occupational dose limit.

Conclusion: Patient exposure during interventional radiology is assessed by using the DAP meter. The interventional radiologists who received the highest annual doses, followed by technologists and nurses, all were under the annual dose limit.

Keywords: Angiography, Interventional radiology, Occupational exposure

AI-augmented assessment of quantitative parameters in a 3.0 tesla magnetic resonance imaging machine at Songklanagarind Hospital

Chanchayanon Thanakrit, Sakjirapapong S, Wanai A, Saengsurichai S, Ina N,
Rojchanaumpawan T, Cheewakul J*

Department of Radiology, Faculty of Medicine, Prince of Songkla University, Songkhla, Thailand.
** jongwatcheewakul@gmail.com*

Introduction: Quantitative assessment is vital for evaluating Magnetic Resonance Imaging machine performance. Traditional quantitative tests include geometric accuracy, signal-to-noise ratio (SNR), high-contrast spatial resolution, slice-thickness accuracy, slice-position accuracy, percentage intensity uniformity (PIU), percent-signal ghosting (PSG), and low-contrast object detectability. With advancements in artificial intelligence, Large Language Models (LLMs) can now automate and enhance these assessments. This study compares the performance of a 3.0 Tesla MRI scanner using conventional methods and AI-powered LLM analysis, focusing on efficiency and accuracy.

Methods: An ACR MRI phantom was scanned in axial and sagittal planes using head coils on a 3.0 Tesla Philips Achieva dStream MR System at Songklanagarind Hospital, Thailand, in October 2024. Traditional analysis utilized the Synapse DICOM viewer to measure SNR, PIU, and percentage ghosting ratio (PGR) across eight exams, following ACR standards. The same datasets were analyzed using a pre-trained LLM integrated with custom algorithms for automated parameter extraction and compliance evaluation.

Results: Traditional analysis yielded: geometric accuracy: -0.67 to +0.53 mm, slice thickness: 4.73 and 5.04 mm, PIU: 85.38% and 86.49%, ghosting ratios: 0.147 and 0.128, low-contrast detectability: 40 spokes. LLM analysis showed <0.5% deviation from manual values, detected outliers with 99% sensitivity, and generated compliance reports in under 30 seconds, compared to 20 minutes manually.

Discussion: This study highlight the potential of leveraging LLMs for enhancing the efficiency and reliability of MRI performance evaluations. Traditional methods, while robust and validated by long-standing standards such as those of the ACR, can be time-intensive and prone to variability due to manual processes. By integrating LLMs into the analysis workflow, significant improvements in speed and consistency were observed.

Conclusion: LLMs effectively augment traditional assessments, providing fast, reliable, and standardized evaluations. This approach aligns with ACR guidelines, supporting efficient clinical workflows and predictive maintenance insights.

Keywords: Quantitative assessment, ACR MRI phantom, Large Language Models, AI analysis

Dose mapping of a deuterium-tritium (D-T) neutron generator laboratory using Monte Carlo transport code PHITS

Alipio Andrea[1*], Egwolf B[2], Asuncion-Astronomo A[3]

1 The Graduate School, University of Santo Tomas, Manila, Philippines
2 Department of Mathematics and Physics, College of Science, University of Santo Tomas, Manila, Philippines
3 Philippine Nuclear Research Institute, Quezon City, Philippines
**andrea.alipio.gs@ust.edu.ph*

Introduction: Neutron and secondary photon radiation exposure to staff working around a deuterium-tritium (D-T) neutron generator (NG) can be assessed using Monte Carlo methods. Particle and Heavy Ion Transport code System (PHITS), a Monte Carlo-based program, was used to calculate the dose distributions for different NG configurations and to evaluate if the doses meet radiation protection standards.

Methods: An isotropic, monoenergetic 14.1 MeV D-T neutron source was defined with an intensity of 5×10^9 neutrons/second. The D-T NG was modelled together with a high-density polyethylene moderator assembly and the facility layout. Simulations were performed using mesh tallies along the xy, yz, and xz planes with 30 spherical region tallies serving as air detectors in strategic locations. The NG orientation that resulted in the lower set of doses was determined and used as a reference scenario for other configurations.

Results: Higher doses were calculated for for the east-oriented NG versus the west. The highest dose rate in the counting room was 0.14 μSv/h, while the work area obtained 689.90 μSv/h. Compared to a fully shielded configuration, partially shielded and unshielded configurations resulted in a 62% and 378% increase in average total dose, respectively.

Discussion: The west-facing NG is the optimal position during operation. For a 500-hour annual operating time, the counting room doses are acceptable with respect to occupational dose limits. However, additional shielding is necessary to lessen doses in the work area. ICRP 74 coefficients that yield ambient dose equivalent rates were found to provide a practical and conservative estimate for dose-limiting values.

Conclusion: A computational model developed in PHITS provided a preliminary assessment of the neutron and secondary photon doses in a D-T NG facility. As a pioneer study on NG technology in the Philippines, the findings will offer a reference for the safe and reliable installation and operation of a D-T NG.

Keywords: radiation protection, radiation dosimetry, neutron generators, D-T fusion

Optimization of energy thresholds in photon counting CT for characterizing renal stone composition: A simulation study

Wongsirinanon Sangsirin[1*], Shunhavanich P[2]

1 Department of Radiology, Medical Physics Program, Faculty of Medicine, Chulalongkorn University, Bangkok, Thailand.
2 Department of Radiology, Faculty of Medicine, Chulalongkorn University, Bangkok, Thailand.
sangsirin.dear@gmail.com

Introduction: Photon-counting detector CT (PCD-CT) systems offer advanced imaging capabilities for renal stones ≤ 3 mm. These systems can differentiate between uric acid (UA) and non-uric acid (NUA) stones and between different NUA subtypes, aiding in effective treatment selection. The aim of this study is to optimize PCD energy thresholds for characterizing renal stone composition.

Methods: A 30x20-cm elliptical water phantom with six 3-mm-diameter inserts of different stone types (uric acid (UA), cystine (CYS), calcium oxalate dihydrate (COD), calcium oxalate monohydrate (COM), brushite (BRU), and apatite (APA)) was used. 350 noisy PCD data sets were generated using Photon Counting Toolkit (PcTK) version 3.2 with four energy thresholds (25 keV, and three selected from 35 to 95 keV at 10 keV intervals) and dual-energy thresholds of 25 and 75 keV. Simulated images were reconstructed using filtered backprojection. CT number ratios (CTRs) for each stone type were calculated as the ratio of energy bin 1 to bins 2, 3, or 4. For each energy threshold setting, the area under the receiver operating characteristic curve (AUC) was calculated for distinguishing between stone types (UA vs. CYS, CYS vs. COM, COM vs. APA, COM vs. BRU, and COM vs. COD), using the CTRs, and the average AUC for all stone pairs as the evaluation metric.

Results: The energy-threshold setting of 25, 65, 75, and 95 keV showed the highest average AUC of 0.94, with the CTR of energy bins 1 to 4.

Discussion: Using four energy thresholds in PCD could be more effective in discriminating stone types than dual-energy thresholds, especially with the CTR from energy bin 1 to bin 4.

Conclusion: The energy thresholds of 25, 65, 75, and 95 keV could potentially be optimal in PCD for discriminating renal stone composition.

Keywords: photon-counting CT, PcTK, kidney stones, simulation

Organ dose mapping in anteroposterior (AP) pelvic radiography: Phantom study

Sayed Inayatullah Shah[1*], Muhamad Jamil N N[1], Rohayzaad N I A[1], Kamzaiman A A[1]

1 Department of Diagnostic Imaging and Radiotherapy, Kulliyyah of Allied Health Sciences, International Islamic University Malaysia, Kuantan Campus, 25200 Kuantan, Pahang, Malaysia
**inayatullah@iium.edu.my*

Introduction: X-ray imaging equipment often exhibits non-uniform radiation intensity across the imaging field. This non-uniformity presents challenges in accurately determining the radiation dose absorbed by organs. Current dosimetry methods lack the precision needed for accurate, organ-specific dose measurements, which limits advancements in patient safety and optimization of medical imaging practices. Our research focuses on radiation dose mapping within pelvic cavity organs using optically stimulated luminescent dosimeters (OSLD), aiming to enhance dose accuracy and improve patient care quality in diagnostic imaging.

Methods: A Kyoto Kagaku phantom positioned supine on the table bucky in an anteroposterior (AP) orientation. The source-to-image distance was set at 100 cm. Exposure parameters included kVp settings of 70, 75, and 79 kVp, with corresponding mAs values of 10, 12.5, and 16. To measure the entrance skin dose (ESD), multiple nanoDot OSLDs were placed on the surface of the phantom at locations corresponding to the sacrum, urinary bladder, male gonads and ovaries.

Results: The average ESD in mGy at selected exposure settings was measured for key pelvic organs. Results for specific organs are as follows: sacrum 0.85, 1.65, and 2.54 mGy; bladder 0.73, 1.43, and 2.15 mGy; male gonads 0.52, 1.02, and 1.63 mGy; and ovaries 0.83, 1.64, and 2.47 mGy.

Discussion: This study highlights the significant variations in ESD across pelvic organs during X-ray imaging, attributed to the non-uniform radiation intensity of the equipment. Measurements indicated that the sacrum and ovaries received higher ESDs compared to the bladder and male gonads, demonstrating the impact of organ positioning and exposure settings.

Conclusion: Organ-specific dose mapping can effectively capture variations in radiation dose across pelvic organs, providing a more accurate and reliable method for dosimetry in diagnostic imaging. This precision is essential for reducing radiation exposure to sensitive organs and enhancing patient safety. Implementing this technique can improve patient care by refining imaging protocols and managing radiation doses more effectively.

Keywords: Organ dose mapping, Diagnostic imaging, Pelvic radiography, Radiation protection, Patients' safety.

A new simulation method for reproducing semiempirical model-based X-ray spectra considering heel effect

Santo Taiki[1*], Matsubara K[2]

1 Department of Quantum Medical Technology, Division of Health Sciences, Graduate School of Medical Sciences, Kanazawa University, Kanazawa, Japan
2 Department of Quantum Medical Technology, Faculty of Health Sciences, Institute of Medical, Pharmaceutical and Health Sciences, Kanazawa University, Kanazawa, Japan
** santo310@stu.kanazawa-u.ac.jp*

Introduction: Recently Monte Carlo simulations have been widely applied to radiation dose calculation in the diagnostic field. Semiempirical models are commonly used for generating X-ray spectra. However, the simulation studies that used these models did not reproduce X-ray spectra considering heel effect. The aim of this study is to develop a method to reproduce semiempirical model-based X-ray spectra considering heel effect in simulations.

Methods: The Monte Carlo simulation code PHITS Ver.3.32 was used for this study. A specialized filter made of the same material as the anode of X-ray tube was created to reproduce semiempirical-model-based X-ray spectra considering heel effect. From the semiempirical model, the X-ray spectrum at 10 degrees on the cathode side was obtained. Then, the specialized filter was placed around an X-ray source that irradiated X-rays with the obtained X-ray spectrum. To confirm the reproduction of X-ray spectra considering heel effect, X-ray spectra were obtained every 2 degrees from 10 degrees on the cathode side to 10 degrees on the anode side in both the simulation and the semiempirical models.

Results: At all angles, the shapes of X-ray spectra that calculated by the simulations agreed well with those calculated by the semiempirical models. However, at most angles, the intensity of the K characteristic X-rays tended to be higher in the simulation than in the semiempirical models.

Discussion: The results suggested that the X-ray spectrum considering the heel effect can be mostly reproduced by applying the specialized filter and the X-ray spectrum at 10 degrees on the cathode side that was obtained from the semiempirical model. Regarding the intensity of characteristic X-rays, the difference was due to the different calculation theory between PHITS and semiempirical models.

Conclusion: Through comparing the spectral shapes, it was confirmed that heel effect can be almost reproduced under simulation by using this method.

Keywords: Monte Carlo simulation, heel effect, x-ray spectrum

Image quality comparison in computed tomography system using different image reconstruction methods: a phantom study

Pangsai Teerapong[1], Sangruang-orn S[2], Sodkokkruad P[3], Chaknam K[3], Asavaphatiboon S[3*].

1 Department of Radiology, Master of Science Program in Medical Physics, Faculty of Medicine Ramathibodi Hospital, Mahidol University, Bangkok, Thailand.
2 Department of Radiology, Phramongkutklao Hospital, Bangkok, Thailand.
3 Department of Radiology, Division of Diagnostic Radiology, Faculty of Medicine Ramathibodi Hospital, Mahidol University, Bangkok, Thailand.
**sawwanee.medphy@gmail.com*

Introduction: Deep learning-based reconstruction is an advanced technique in CT image reconstruction that enhances image quality and corrects noise texture variations associated with iterative reconstruction methods. This study aimed to compare the image quality across different reconstruction techniques and to evaluate the impact of image dose reduction in relation to these techniques in brain CT protocol at Phramongkulklao Hospital.

Methods: A Catphan®600 phantom was acquired using a CT scanner (Aquilion ONE PRISM Edition, Canon Medical Systems) at four levels of dose reduction (SURE Exp.3D). The raw data were reconstructed using four techniques: filtered-back projection (FBP), iterative reconstruction (AIDR 3D and FIRST), and as deep learning reconstruction (AiCE). Image quality was evaluated based on noise magnitude, noise texture, high contrast resolution, and low contrast detectability using various software tools.

Results: The study found that noise in iterative and deep learning reconstructions differed significantly from FBP. All three image reconstruction techniques exhibited a decrease in noise from low to high at mild, standard, and strong noise reduction levels. The FIRST technique showed the least noise distribution. High contrast resolution results (lp/cm) showed no significant differences across methods. Regarding low contrast detectability, at both 0.5% and 1% contrast levels, the FIRST technique at high-quality SURE Exp.3D demonstrated superior detection of smaller objects compared to FBP.

Discussion: All reconstruction techniques demonstrated superior image quality compared to FBP, with the FIRST technique showing the most notable improvement. Additionally, at the high-quality dose reduction level, each reconstruction at the strong setting provided the best image quality. However, it was observed that increased noise reduction resulted in smoother images.

Conclusion: Iterative and deep learning reconstructions are essential for image noise reduction and improved image quality. Caution is required in clinical practice, as the resulting images may exhibit increased smoothness, potentially reducing the ability to detect subtle differences.

Keywords: Deep learning reconstruction, iterative reconstruction, high contrast resolution, low contrast detectability

MRI-Based Radiomics model from mesorectal fat to predict pathologic extramural vascular invasion in locally advanced rectal cancer patients

Swaengdee Yaniga[1,2 *], Khongwirotphan S[2,3], Lasode J[4], Kuecharoen P[5], Phetvilay P[5], Boonsirikamchai P[5], Rakvongthai Y[2,6]

1 Department of Radiology, Medical Physics Program, Faculty of Medicine, Chulalongkorn University, Bangkok, Thailand
2 Department of Radiology, Chulalongkorn Biomedical Imaging Group, Faculty of Medicine, Chulalongkorn University, Bangkok, Thailand
3 Department of Radiological Technology and Medical Physics, Faculty of Allied Health Sciences, Chulalongkorn University, Bangkok, Thailand
4 Department of Radiology, Division of Diagnostic Radiology,King Chulalongkorn Memorial Hospital, Bangkok, Thailand.
5 Department of Radiology, Division of Diagnostic Radiology, Faculty of Medicine, Chulalongkorn University, Bangkok, Thailand.
6 Department of Radiology, Division of Nuclear Medicine, Faculty of Medicine, Chulalongkorn University, Bangkok, Thailand
**Yaniga.Swaengdee@gmail.com*

Introduction: Extramural vascular invasion (EMVI) is a critical biomarker associated with a poor prognosis in colorectal cancer. Magnetic resonance imaging (MRI) is the standard imaging modality for primary staging of rectal cancer, particularly in locally advanced rectal cancer (LARC) patients. However, the sensitivity and specificity of MRI in detection of EMVI (mrEMVI) are still moderate. Radiomics, a non-invasive technique that extracts quantitative features from medical images, has shown potential in predicting tumor prognosis. The purpose of this study is to build and evaluate the performance of a radiomic model from mesorectal fat regions in MRI to predict pathologic EMVI in LARC patients.

Methods: 219 LARC patient data and MR images were retrospectively collected, mesorectal fat was the region of interest (ROI). Three radiologists delineated the ROI for 30 datasets to calculate intraclass correlation coefficients (ICC), with the acceptable ICC was greater than 0.5. 1,288 radiomic features were extracted from each ROI using PyRadiomics version 3.1.0. The data were split into training and validation sets using 5-fold cross-validation. Feature selection was performed using univariate analysis, ICC, and recursive feature elimination. Three models: logistic regression (LR), random forest (RF), and support vector machine (SVM), were built and evaluated with statistical analysis conducted using a sign test.

Results: The fine-tuned LR model achieved an AUC of 0.851±0.017 in the training set and 0.776±0.073 in the validation set. While RF and SVM models performed better in the training set (AUCs: 0.991±0.004 and 0.882±0.016), their performance dropped significantly in the validation set (AUCs: 0.685±0.075 and 0.711±0.073). Only the LR model maintained its performance in the validation set, showing statistically significant differences compared to SVM and RF ($P < 0.05$).

Discussion: The results showed that radiomic features of mesorectal fat can predict EMVI, potentially determining prognosis of LARC patients.

Conclusion: MR-based radiomics from mesorectal fat effectively predicts EMVI in LARC patients.

Keywords: Radiomics, Mesorectal fat, locally advanced rectal cancer, Extramural venous invasion

Academic qualifications of medical physicists in Malaysia: Looking back and moving forward

Zin M Hafiz[1*], Suardi N[2], Wong JHD[3], Azlan CA[3], Yeong CH[4], Ng AH[5], Abdul Rahman AT[6,7]

1 Advanced Medical & Dental Institute, Universiti Sains Malaysia, 13200 Bertam, Penang, Malaysia
2 School of Physics, Universiti Sains Malaysia, Penang, Malaysia
3 Department of Biomedical Imaging, Faculty of Medicine, University of Malaya, 50603 Kuala Lumpur, Malaysia
4 School of Medicine, Faculty of Health & Medical Sciences, Taylor's University,47500 Subang Jaya, Selangor, Malaysia
5 Department of Clinical Oncology, Faculty of Medicine, University of Malaya, 50603 Kuala Lumpur, Malaysia
6 Faculty of Applied Sciences, Universiti Teknologi MARA, 40450 Shah Alam, Selangor Malaysia
7 Centre of Astrophysics & Applied Radiation, Institute of Science, Universiti Teknologi MARA, 40450 Shah Alam, Selangor, Malaysia
**hafiz.zin@physics.org*

Introduction: The education and training of the medical physics workforce are critical to healthcare delivery and the advancement of research. This study evaluates the education of the current workforce in Malaysia and identifies the gaps in comparison with international standards.

Methods: An analysis of academic qualifications was conducted by examining the degree programmes of medical physicists in Malaysia. Data were collected on the degree qualifications of the largest group of the current workforce. The curriculum content was analysed for alignment with the IAEA recommendations in TCS-56 Rev 1.

Results: The analysis of 188 recorded workforce members from the public sector revealed significant variations in the undergraduate education. The majority graduated from nuclear science programme (26%), followed by the health physics (20%), pure physics (18%), medical physics (14%), medical radiation (11%) and applied physics programmes (4%). 47% hold postgraduate qualification, of which 23% of the total workforce have a master's degree in medical physics.

Discussion: One-third of the workforce has an undergraduate education containing less than one semester's equivalent of physics and mathematics but includes larger components of subjects in medical physics or other applied nuclear/radiation sciences topics. These candidates may be perceived as more competent for hospital-based medical physicist roles during hiring, despite their lack of a strong foundation in physics and mathematics. This issue is particularly common in countries without formal recognition of the medical physicist profession and accreditation of academic programmes to train the professional.

Conclusion: There is a pressing need to harmonise and standardise the education of future medical physicist, by establishing an improved academic qualification framework for the profession. Additionally, continuous training programmes should be developed to address the mismatch in academic qualifications within the existing workforce.

Keywords: Medical Physicist, Profession, Academic Qualification

Voxel-based dosimetry of ^{177}Lu-DOTATATE peptide receptor radionuclide therapy using SPECT/CT imaging with RT-PHITS simulations

Tantiwetchayanon Khajonsak[1*], Matsubara K[2], Wakabayashi H[3], Konishi T[4]

1 Department of Quantum Medical Technology, Division of Health Sciences, Graduate School of Medical Sciences, Kanazawa University, Kodatsuno, Kanazawa, Ishikawa, Japan
2 Department of Quantum Medical Technology, Faculty of Health Sciences, Institute of Medical, Pharmaceutical and Health Sciences, Kanazawa University, Kodatsuno, Kanazawa, Ishikawa, Japan
3 Department of Nuclear Medicine, Kanazawa University Hospital, Takara-machi, Kanazawa, Ishikawa, Japan
4 Department of Radiological Technology, Kanazawa University Hospital, Takara-machi, Kanazawa, Ishikawa, Japan
**khajta@stu.kanazawa-u.ac.jp*

Introduction: The Particle and Heavy Ion Transport code System has developed a radiotherapy package, RT-PHITS, which facilitates Monte Carlo-based dose calculations for radionuclide therapies, including post-therapeutic ^{177}Lu-DOTATATE. The purpose of this study is to evaluate the effectiveness of RT-PHITS for voxel-based dosimetry in patients undergoing ^{177}Lu-DOTATATE therapy.

Methods: ^{177}Lu-DOTATATE SPECT/CT images from five patients had been acquired at four different time points post-therapy. Semi-automatic organ and tumor segmentation were performed. Rigid registration was applied, followed by Elastix registration. Time-integrated activity (TIA) maps were created using mono-exponential and bi-exponential functions, which were used in RT-PHITS. Patient-specific phantoms, derived from CT images, enabled RT-PHITS to calculate dose maps which were compared to doses calculated using IDAC-Dose software.

Results: The mono-exponential function resulted in higher average time-integrated activity coefficients (TIACs) across all organs and tumors were compared to the bi-exponential function and IDAC-Dose. The differences between IDAC-Dose and the bi-exponential function were less than 10% for organs but reached 17% for the tumor. RT-PHITS calculations using bi-exponential function exhibited slight deviations from IDAC-Dose for kidneys and liver, while larger differences in the spleen and tumor.

Discussion: The voxel-based dosimetry using RT-PHITS, particularly with the bi-exponential function, showed strong agreement with IDAC-Dose for most organs. However, notable differences were observed in tumor dose calculations. This discrepancy is likely due to IDAC-Dose employing a spherical model for tumor dose, while RT-PHITS utilizes voxel-specific methods, accounting for patient-specific anatomy and source distribution heterogeneity. Furthermore, organs adjacent to tumors exhibited higher absorbed doses in the RT-PHITS calculations. These factors contribute to the significant differences between the patient-specific voxel-based method and the phantom-based approach, especially in cases where tumors are located near target organs.

Conclusion: RT-PHITS has the potential for calculating absorbed doses in ^{177}Lu-DOTATATE therapy through patient-specific voxel-based dosimetry, which incorporates individual anatomy and radionuclide distribution.

Keywords: RT-PHITS, ^{177}Lu-DOTATATE, voxel-based dosimetry, Monte Carlo simulation

Proficiency testing program for ^{131}I and ^{99m}Tc radiopharmaceuticals using radionuclide calibrators in Thailand

Saejia Korawee[1,*], Dachviriyakij T[1,2], Thongdeelert N[1], Luansri K[1], Pungkun V[1]

1 Ionizing Radiation Metrology Section, Office of Atomic for Peace, Ministry of Higher Education, Science, Research and Innovation, Bangkok 10900, Thailand.
2 The Korea Research Institute of Standards and Science (KRISS), Daejeon 34113, Republic of Korea.
**korawee.s@oap.go.th*

Introduction: The Office of Atoms for Peace (OAP), the regulatory authority for radiation and nuclear energy safety in Thailand, has implemented an Interlaboratory Proficiency Testing (IPT) Program for laboratories performing activity measurements. This comparative research aims to compare the measured activity through a proficiency testing program using radionuclide calibrators across nuclear medicine facilities in Thailand.

Methods: An IPT program includes 21 laboratories in Thailand for ^{131}I testing and 11 laboratories in Bangkok and vicinity for ^{99m}Tc testing. Two sessions were conducted from 2023 to 2024. 3 cc for ^{131}I activity 6-12 mCi and 3.6 cc for ^{99m}Tc activity 15-25 mCi were prepared as reference materials (RMs) in 5 cc glass ampoules. The reference values were measured by the re-entrant ionization chambers with gas filled chamber and high voltage supply. RMs and calibration reports were sent to laboratories for activity measurement.

Results: The results were analyzed in the percent accuracy and normalized error (E_n). The measured activity from 31 radionuclide calibrators across 21 laboratories for ^{131}I and 18 radionuclide calibrators from 11 laboratories for ^{99m}Tc were compared with the OAP reference values. It was found that 96.77% of ^{131}I measured activity and 83.33% of ^{99m}Tc measured activity were within ±5% of the reference values (6-12 mCi for ^{131}I and 15-25 mCi for ^{99m}Tc). The normalized error, E_n was 96.77% for ^{131}I and 100% of ^{99m}Tc, which were accurate for uncertainty estimation.

Discussion: The OAP proficiency testing program showed the satisfactory performance of radionuclide calibrators, in particular to less than 20% deviation from the OAP reference values.

Conclusion: Over 80% of the radionuclide calibrators were accurate within ± 5% of the OAP reference values. Only one ^{131}I radionuclide calibrator (3.2%) required recalibration against the reference standard solution to ensure the accurate activity.

Keywords: Proficiency testing, Radionuclide calibrator, ^{131}I, ^{99m}Tc, Radiopharmaceutical

Evaluation of total counts in SIMIND Monte Carlo simulation for SPECT/CT systems using PyTomography

Ohnishi Haruki[1*], Matsubara K[2], Fujiwara K[3], Tantiwetchayanon K[1]

1 Department of Quantum Media Technology, Division of Health Sciences, Graduate School of Medical Sciences, Kanazawa University, Kodatsuno, Kanazawa, Ishikawa, Japan
2 Department of Quantum Media Technology, Faculty of Health Sciences, Institute of Medical Pharmaceutical and Health Sciences, Kanazawa University, Kodatsuno, Kanazawa, Ishikawa, Japan
3 Department of Radiology, Kanazawa University Hospital, Takara-machi, Kanazawa, Ishikawa, Japan
**tnmhy0312@stu.kanazawa-u.ac.jp*

Introduction: In nuclear medicine, phantom experiments are often complicated in terms of handling radiopharmaceuticals and the preparation of phantoms. Therefore, Monte Carlo (MC) simulations are expected to predict results without phantom experiments. This study aimed to evaluate the accuracy of SIMIND MC simulation by comparing phantom experiments in various single-photon emission computed tomography/computed tomography (SPECT/CT) systems.

Methods: The SIMIND MC simulation ver.8.0 and PyTomography ver.3.2.3, a Python library for image reconstruction, were used. Phantom experiments were performed by the following SPECT/CT systems: Symbia-Intevo.Bold (Siemens) and Discovery NM/CT 670 Pro (GE Healthcare). The simulated and measured data for SPECT imaging was acquired from a uniform cylindrical phantom (JIS Z4922) filled with water and ^{99m}Tc at 60 views for 10 s/view, circular orbit with a radius of rotation of 24 cm. Both simulated and measured images were reconstructed using ordered subset expectation maximization (OSEM) with the attenuation and scatter corrections, and the resolution recovery to compare the total counts in the projection and reconstruction data.

Results: The total count differences for measurement against simulation were -4.2% and -5.0% for Symbia and Discovery, respectively, in the projection data, -98.7% and -99.9% for Symbia and Discovery, respectively, in the reconstruction data.

Discussion: In the comparison of total counts, the lower simulation values were attributed to the lack of backscatter from the opposite detector. The simulations did not consider this effect because it was a single detector system, unlike the measurement with dual detector system. Although there was relatively good agreement in the projection data, there were large differences in the reconstruction data. The reconstruction process of each system is often undisclosed and difficult to reproduce strictly.

Conclusion: The SIMIND MC simulation could easily reproduce the phantom experiment. However, the large discrepancy in the total counts after reconstruction requires further study.

Keywords: SIMIND, Monte Carlo simulation, PyTomography, SPECT.

Feasibility of total-body fast SPECT imaging for optimized image quality and voxel-based dosimetry in ^{177}Lu molecular radiotherapy using ring-shaped CZT SPECT/CT

Handayani Wuri[1*], Chantadisai M[3], Pasawang P[3], Noipinit N[3], Phromphao B[3], Damthongsen P[1], Khamwan K[1,2,4]

1 Department of Radiology, Medical Physics Program, Faculty of Medicine, Chulalongkorn University, Bangkok 10330, Thailand
2 Department of Radiology, Division of Nuclear Medicine, Faculty of Medicine, Chulalongkorn University, Bangkok 10330, Thailand
3 Department of Radiology, Division of Nuclear Medicine, King Chulalongkorn Memorial Hospital, The Thai Red Cross Society, Bangkok 10330, Thailand
4 Department of Radiology, Chulalongkorn University Biomedical Imaging Group, Faculty of Medicine, Chulalongkorn University, Bangkok 10330, Thailand
**wuri.handayani92@gmail.com*

Introduction: Molecular radiotherapy dosimetry requires 3D SPECT scans for accurate absorbed dose calculation, which can be time-consuming and impacting patient comfort. This study evaluated the feasibility of ^{177}Lu therapy dosimetry and image quality based on fast-imaging protocol.

Methods: The NEMA/IEC body phantom with six fillable spheres filled with ^{177}Lu solution at a 10:1 target-to-background ratio, was scanned for 30 min by SPECT/CT Veriton-CT 200 (Spectrum Dynamics Medical) with energy window of 113 keV±10%. Simulated acquisition time of 15, 10, 5, and 2 min were performed to assess the quantification accuracy. The signal-to-noise ratio (SNR) was determined by measuring the activity concentration (Bq/cc) in spheres and background. The recovery coefficient (RC) was computed as quotient of the estimated and actual activity concentration in the sphere. Retrospectively, total-body SPECT/CT image of eight ^{177}Lu therapy patients scanned for 28 min at ~4, 24, and 48-72 h post-injection were analyzed. The fast-imaging protocols were simulated by reducing acquisition time to 25-, 22-, 19-, and 16-min. The patient absorbed doses in kidneys, liver, spleen, salivary glands, and tumors were calculated using MIM voxel-based dosimetry software. Image quality and absorbed dose difference were compared between protocols.

Results: The phantom study demonstrated declining RC and SNR as acquisition times decreased. The difference between calculated and measured activity concentrations increased up to 38% in the largest sphere. Patient absorbed dose calculations revealed relative percentage differences (RPD) <10% in the liver, 13-26% in the salivary gland, spleen, and kidney, and up to 40% in tumors.

Discussion: Shortened acquisition times increased image noise and absorbed dose differences due to reduced counts.

Conclusion: These results indicate that fast imaging protocol improves patient workflow, however anticipated optimization in image quality and personalized dosimetry were not fully achieved.

Keywords: ^{177}Lu, Molecular Radiotherapy Dosimetry, Shortened Acquisition Time, Ring-shaped SPECT/CT.

Radiation dose reduction in CT-related radiation exposure for nasopharyngeal carcinoma (NPC) protocols in positron emission tomography / computed tomography (PET/CT) imaging, University Malaya Medical Centre (UMMC).

Mohd Zain Azleen[1*], Ahmad F[1], Md Shah MN[2], Jasa MJ[2]

1 Medical Physics Department, UMMC

2 Nuclear Medicine Unit, Bio-medical Imaging Department, UMMC

Email: *azleen@ummc.edu.my

Introduction: Technologic advances in CT have generated a dramatic increase in the radiation dose. It is necessary to optimize CT imaging protocols and apply radiation dose reduction techniques to ensure the best images with the lowest radiation dose. This project is to provide a radiation dose reduction for patients undergoing PET/CT Philips Ingenuity TF installed in 2016, utilizing a dedicated diagnostic, contrast-enhanced Head-Neck protocol. The goal of dose reduction is the optimization level with preservation of appropriate image quality in clinical practice.

Methods: Investigation was focused on Head-Neck CT protocol ^{18}F-Fluorodeoxyglucose (FDG) PET/CT examinations for NPC patient. The Head-Neck PET/CT was done separately from the thorax, abdomen, and pelvis in the same sitting. Retrospective data was taken from 150 PET/CT examinations, comprising fifty (50) pre- , fifty (50) 1st post- , and fifty (50) 2nd post-protocol-optimisation scans. Radiation dose parameters of CT scans were obtained from the PACS. Volumetric CT dose index ($CTDI_{vol}$), scan length, and dose length product (DLP) values were recorded. Effective dose (ED) was calculated and parameters such as CT tube potential (kVp), tube current (mA), rotation speed, scan pitch, and slice thickness, were recorded.

Results: Compared to the pre-optimised scans, the optimised head and neck CT component of the scan showed a 57% reduction in the CT-related radiation exposure, based on the $CTDI_{vol}$ and DLP. The median calculated ED of the Head-Neck CT was brought down to 2.55mSv.

Conclusion: Overall radiation dose parameters obtained in this study points out the need for optimization of head CT examinations in our institution. The dosimetry concepts provide a valuable tool for the optimization of ^{18}F-FDG PET/CT protocols. Further reduction of dose can be achieved by having a team consists of medical physicists, radiologists and radiographers, to be compliance to diagnostic reference levels (DRLs), while maintaining agreed-upon diagnostic image quality.

Key Words: CT, Head and Neck, Dose Reduction, Protocols, Optimization.

Comparing image quality characteristics of different post-filtered Iodine-131 SPECT: A phantom study

Rattanamongkonkul Pattaravarin[1*], Chuamsaamarkkee K[2], Krisanachinda A[3].

1 Department of Radiology, Maha Vajiralongkorn Thanyaburi Hospital, Pathumthani, Thailand.
2 Department of Diagnostic and Therapeutic Radiology, Faculty of Medicine, Ramathibodi Hospital, Mahidol University, Thailand.
3 Department of Radiology, Faculty of Medicine, Chulalongkorn University, Bangkok, Thailand.
**Pattaravarin_rl@outlook.com*

Introduction: Single photon emission computed tomography (SPECT) Iodine-131 (131I) imaging is a nuclear medicine technique that has become an important tool for diagnostic of thyroid cancer and accurately localizing treatment outcomes after high-dose thyroid ablation. However, the SPECT image quality is limited by the reconstructed images' finite spatial resolution and noise. Typically, the post-processing filter is the common method that is applied after SPECT reconstruction to suppress noise and improve the image quality. Hence, this study aims to evaluate the effect of post-filter on ^{131}I SPECT/CT using three types of filters: Butterworth, Hann, and Gaussian.

Methods: The NEMA/IEC phantom was filled with an aqueous solution of ^{131}I with a sphere-to-background ratio of 10:1 (activity concentration in the sphere of 740 kBq/mL, background of 74 kBq/mL) acquired by the dual-head SPECT/CT GE 870 DR. The OSEM reconstruction technique (4 iterations, 8 subsets) was employed as a clinical routine, followed by the application of three post-filters: Butterworth, Hann, and Gaussian with different parameter settings after reconstruction. For image quality analysis, the contrast-to-noise ratio (CNR) and relative noise were evaluated and compared.

Results and Discussion: The CNR of all spheres increased with the increasing cutoff frequency of Butterworth filter. Similarly, the CNR generally increased with the increasing cutoff frequency of the Hann filter, except at the smallest sphere diameter showed a decreased CNR at higher cutoff frequencies. For the Gaussian filter, the CNR results showed a decrease with increasing the filter size in sphere size from 13 mm to 37 mm. The smallest sphere showed the opposite result. In terms of noise, the noise decreased as the decreasing of cutoff frequency of Butterworth filter and Hann filter. While, the Gaussian filter shows the decreased noise when the FWHM increased.

Conclusion: These findings highlight the importance of optimizing filter parameters to balance image quality. Post-filtering impacts the image quality and could influence lesion detectability, especially in the smallest sphere of ^{131}I SPECT for clinical thyroid imaging.

Keywords: Butterworth filter, Hann filter, Gaussian filter, SPECT, I-131.

Optimization of shortening acquisition for quantitative 99mTc bone SPECT imaging with ordered subset conjugate gradient minimizer reconstruction: A phantom study

Songprakhon Rangsee[1*], Chuamsaamarkkee K[2], Krisanachinda A.[3]

1 Radiology Department, Division of Nuclear Medicine, Surin Hospital, Muang Surin, Surin, Thailand.
2 Department of Diagnostic and Therapeutic Radiology, Faculty of Medicine, Ramathibodi Hospital, Mahidol University, Bangkok, Thailand
3 Department of Radiology, Faculty of Medicine, Chulalongkorn University, Bangkok, Thailand
**Blaosvse@gmail.com*

Introduction: Bone Single Photon Emission Computed Tomography (SPECT) imaging with Ordered Subset Conjugate Gradient Minimizer (OSCGM) reconstruction is a modern technique to improve the image quality and quantitative accuracy of SPECT images for the diagnosis and evaluation of various skeletal disorders. However, standard protocol often suffers from long acquisition times. This study aimed to optimize protocol of shortening acquisition for quantitative bone SPECT with OSCGM using the ACR PET phantom.

Methods: The hot cylinders of ACR PET phantom were filled with a bone-equivalent solution and technetium-99m (99mTc). This phantom was acquired by SPECT system using step-and-shoot mode with time per view at 5, 8, 10, 15, 20, 25, and 30 seconds, respectively. SPECT images were reconstructed using OSCGM. The volume of interests (VOIs) placed at the center of each hot cylinders for measuring the set of standard uptake values (SUV), the activity concentration (AC), the percent coefficient of variation (%CV), and the recovery coefficient (RC).

Results: The SUVmax, SUVpeak, and SUVmean were similar among each protocol. There was no reduction of the %CV for each acquisition time. However, the AC and RC of time per view below 10 seconds showed the percent differences exceeding 15% and 10%, respectively.

Discussion: The increased percent differences of AC and RC at time per view below 10 seconds result from the low counting statistics, which leading to the increased noise, the partial volume effects, and the potential reconstruction artifacts.

Conclusion: The shortened acquisition time per view at 10 seconds can be set when using the step and shoot mode for quantitative 99mTc bone SPECT imaging with OSCGM reconstruction.

Keywords: Quantitative, Bone SPECT, OSCGM

Estimation of 18F-FDG PET/CT effective dose associated with three different calculating methods

Myint Thinn Thinn

Department of Nuclear Medicine, PET/CT and Cyclotron Center Yangon General Hospital, Yangon, Myanmar
** thinnthinnmyint@gmail.com*

Introduction: The aim of present study is to estimate the effective dose of positron emission computed tomography (PET/CT) in patient with three different calculating methods.

Methods: This is a retrospective study involved 90 patients (43 male, 47 female, aged 55±15 years) underwent whole body ^{18}F-FDG PET/CT in 2024. Patient's demographic data, scan protocols and radiation dose quantities were collected. The standard protocol region was vertex to mid-thigh used for PET/CT scan in this hospital. The prescribed ^{18}F-FDG dose of 0.12mCi per kg of patient weight administered via intravenous infusion. For CT parameters, 120-140 kVp and 90-150 mAs were used upon body mass index (BMI) 19-30 kg m^{-2}. The effective dose was calculated for each patient using algorithm adapted from ICRP Publication 106, modified for patient weight and patient blood volume with three different methods. The CT effective doses were evaluated by dose length product DLP (mGy.cm) and coefficient k ($mSv.mGy^{-1}cm^{-1}$).

Results: The mean and standard deviation of CT effective dose is 11.36, 3.65 mSv based on BMI 25.17, 4.56 $kg.m^{-2}$and ^{18}F-FDG PET effective dose is 6.84, 1.24 mSv. Therefore, the mean and standard deviation of total effective dose of ^{18}F-FDG PET/CT is approximately 18.19, 4.05 mSv, 19.06, 3.72 mSv and 19.29, 3.85 mSv by ICRP method, body weight method and blood volume method for standard protocol respectively. The effective dose increases as the patient weight increases.

Conclusion: The effective dose of PET/CT in present study is not significantly difference for each effective dose calculation methods. According to the patient's weight and BMI that highly influences total effective dose due to increase injection activity. A significant association between body weights, BMI, scan length and effective dose is reported in present study notice in achieving radiation dose as low as reasonably achievable.

Keywords: effective dose, PET/CT, dosimetry, DLP

Local diagnostic reference level at nuclear medicine centers in Thailand and Myanmar

Aye Yin Moe[1*], Krisanachinda A[2], Thein MPZ[3]

1 Department of Radiology, Medical Physics Program, Faculty of Medicine, Chulalongkorn University, Bangkok, Thailand.
2 Department of Radiology, Faculty of Medicine, Chulalongkorn University, Bangkok, Thailand.
3 Department of Nuclear Medicine, Pinlon Hospital, Yangon, Myanmar.
**yinmoeaye2277@gmail.com*

Introduction: Due to the advanced technology in nuclear medicine, clinical examinations have increased over the past decades. Diagnostic reference level (DRL) plays an important role in the optimization of protection in the medical exposure of patients. Local DRL represents the median value, or 50th percentile of the quantity distribution of common examinations. This study aims to establish LDRL at NM centers in Thailand and Myanmar.

Methods: Between January 2023 and July 2024**,** the demographic data of adult patients of 45-75 kg at least 20 cases per examination, radiation metric parameters including radiopharmaceutical administered activity (MBq), volumetric CT dose index (CTDIvol, mGy), and dose length product (DLP, mGy.cm) were retrospectively collected at King Chulalongkorn Memorial Hospital (KCMH) in Thailand and Pinlon Hospital (PL) in Myanmar. LDRL was estimated and compared to NDRL Thailand of the 75th percentile of the median distribution.

Results: At KCMH and PL, LDRL of administered activity of bone scan were 640 and 679 MBq, thyroid scan were 155 and 144 MBq and renal scan were 96 and 153 MBq respectively. NDRL Thailand of bone, thyroid, and renal scans were 800MBq, 200MBq, and 200MBq respectively. For ^{18}F-FDG whole-body PET/CT scan, LDRL of administered activity at KCMH and PL were 255 and 185MBq while NDRL Thailand was 400MBq. CTDIvol and DLP of ^{18}F-FDG WB PET/CT scan at KCMH were 4.34 mGy and 424.6 mGy.cm and NDRL Thailand were 11.28mGy and 500mGy.cm.

Discussion: LDRL at both centers were lower than the NDRL Thailand. At PL, LDRL of some studies could not be established according to number of cases were lower than 20.

Conclusion: The LDRL for common NM examinations of adult patients at two centers were established. LDRL should be consistently estimated together with the image quality for the optimization in radiation protection of patients.

Keywords: Diagnostic reference level, administered activity, CTDIvol, DLP

Full Papers

Image Quality Evaluation of ACR CT Accreditation Phantom using IndoQCT Software

Chakrapong Apawadee[1], Krisanachinda Anchali[2*]

1 Department of Radiology, King Chulalongkorn Memorial Hospital, Thai Red Cross Society, Bangkok, Thailand
*2 Department of Radiology, Faculty of Medicine, Chulalongkorn University, Bangkok, Thailand, (*Corresponding author: anchali.kris@gmail.com)*

Abstract — **Introduction:** Quality control program of CT is required to ensure the accurate and reliable diagnostic information at acceptable patient radiation dose. IndoQCT software is an automated software for CT image quality evaluation. The objective of this study is to evaluate image quality parameters using American College of Radiology CT accreditation phantom (ACR CTAP) images from three different CT scanners analyzed by IndoQCT software. **Methods:** The ACR CTAP was scanned by 3 CT scanners using 4 clinical protocols of adult head, pediatric head, adult abdomen, and pediatric abdomen. Image quality parameters evaluated by IndoQCT software include CT number uniformity, CT numbers of different materials, CNR, spatial resolution, and slice thickness. The results were compared to ACR tolerance level. **Results:** CT number uniformity shows the variation of CT number between peripheral and central ROIs within 5 HU. The CT number of different materials was within the tolerance level for adult head and abdomen protocol. The CNR of adult and pediatric head protocols was 2.48, 1.21, 1.61 and 1.16, 1.16 and 1.05 respectively. The CNR of adult and pediatric abdomen protocols was 1.56, 0.81, 0.94, and 1.11, 0.55, 0.39 respectively. The spatial resolution of 5 line pair.cm^{-1} was detectable for all protocols. The slice thickness was within tolerance level at 1.5 mm. **Conclusion:** The acceptable image quality parameters were CT number uniformity, spatial resolution and slice thickness of all protocols from 3 scanners. The CT number of different materials were acceptable. The CNR of adult head and pediatric head from 3 scanners met the ACR standards. The annual CT image quality performed and evaluated by qualified medical physicist using ACR CTAP and analyzed by IndoQCT software is very important for the accuracy and reliable of diagnostic information.

Keywords — Image quality, Computed tomography, IndoQCT software, ACR CT phantom

I. INTRODUCTION

Computed tomography (CT) images are widely used in healthcare facilities. Almost 400 million CT scans are annually performed worldwide [1]. In comparison to other radiological examinations, the patient radiation dose from CT scans are higher. The rapid development and advanced CT technology offer better image quality, scan speed, and patient dose reduction [2]. Good imaging performance in CT scans means that the images quality should be sufficient to meet clinical requirements [3]. Quality control program of CT is required to ensure the accurate and reliable diagnostic information at acceptable patient radiation dose. IndoQCT software is an automated software for CT image quality evaluation [4]. The objective of this study is to evaluate image quality parameters using American College of Radiology CT accreditation phantom (ACR CTAP) images from 3 different CT scanners analyzed by IndoQCT software.

II. MATERIALS AND METHODS

A. Materials

1. Three CT scanners include GE Revolution Apex 256 slice CT, Siemens Somatom Force 192 slice and Philips Incisive 64 slice.

2. IndoQCT software version 24b is a freeware developed by Anam C et al. It has been used to evaluate CT image quality from various types of phantoms such as ACR CTAP, American Association of Physicists in Medicine (AAPM) CT performance phantom, Catphan phantom and other commercial phantom. This software can be used to analyze DICOM CT images from every manufacturer.

3. The ACR CTAP is a cylindrical image quality phantom and is used for ACR CT accreditation testing. It contains four distinct modules. Each module is 4 cm in depth and 20 cm in diameter and can be used for testing various aspects of image quality. Module 1 measures alignment, CT number accuracy and slice thickness. Module 2 measures low contrast

resolution. Module 3 measures uniformity, noise and slice sensitivity profile (SSP). Module 4 measures high contrast resolution.

B. Methods

The ACR CTAP was scanned by 3 CT scanners using 4 clinical protocols such as adult head, pediatric head, adult abdomen and pediatric abdomen as shown in table 1, 2, 3 and 4 respectively. All image quality evaluation was automatically performed on IndoQCT software including CT number uniformity, CT numbers of different materials, Contrast-to-Noise Ratio (CNR), spatial resolution, and slice thickness. The result was compared to ACR tolerance limit.

Table 1. *Adult head protocol parameters*

Parameter	Scanner 1	Scanner 2	Scanner 3
Manufacturer	GE Revolution APEX	Siemens Somatom Force	Philips Incisive
Scan mode	Helical	Helical	Helical
Rotation time (sec)	0.5	1	0.5
Pitch	0.516:1	0.55	0.4
Slice Thickness (mm)	5	5	5
kV	120	120	120
mA	330	240	280
Reconstruction	DL-M	SAFIRE 3	iDose 2

Table 2. *Pediatric head protocol parameters*

Parameter	Scanner 1	Scanner 2	Scanner 3
Manufacturer	GE Revolution APEX	Siemens Somatom Force	Philips Incisive
Scan mode	Helical	Helical	Helical
Rotation time (sec)	0.5	1	0.5
Pitch	-	0.8	0.4
Slice Thickness (mm)	5	5	5
kV	120	100	100
mA	335	145	255
Reconstruction	DL-M	SAFIRE 3	iDose 2

Table 3. *Adult abdomen protocol parameters*

Parameter	Scanner 1	Scanner 2	Scanner 3
Manufacturer	GE Revolution APEX	Siemens Somatom Force	Philips Incisive
Scan mode	Helical	Helical	Helical
Rotation time (sec)	0.5	0.5	0.75
Pitch	0.992:1	0.6	1
Slice Thickness (mm)	2.5	2.5	2.5
kV	120	120	120
mA	505	228	387
Reconstruction	DL-L	SAFIRE 3	iDose 3

Table 4. *Pediatric abdomen protocol parameters*

Parameter	Scanner 1	Scanner 2	Scanner 3
Manufacturer	GE Revolution APEX	Siemens Somatom Force	Philips Incisive
Scan mode	Helical	Helical	Helical
Rotation time (sec)	0.5	0.5	0.5
Pitch	0.984:1	1.4	1
Slice Thickness (mm)	2.5	2	2
kV	100	100	100
mA	160	350	160
Reconstruction	DL-L	SAFIRE 3	iDose 3

III. RESULTS

The result of the ACR CTAP image quality evaluation of adult head, pediatric head, adult abdomen and pediatric abdomen protocols from 3 CT scanners are presented in Table 5, 6, 7 and 8 respectively. For adult head protocol, all test results were within ACR standard.

Table 5. *Results of image quality evaluation of adult head protocol from 3 CT scanners*

Parameter	Scanner 1	Scanner 2	Scanner 3	ACR standard
CT no. uniformity (HU)	3.05	0.95	0.43	≤ 5
CT no. of materials (HU)				
- Water	2.75	-0.77	0.66	-7 to +7
- Air	-995.05	-994.12	-1000.84	-970 to -1005
- Teflon (Bone)	908.09	920.32	879.8	850 to 970
- Polyethylene	-98.02	-96.24	-95.8	-107 to -84
- Acrylic	122.2	125.4	125.12	110 to 135
CNR	1.21	2.48	1.61	≥ 1
Spatial resolution (lp/cm)	6	5	5	5
Slice thickness(mm) / Difference (mm)	6.25 / 1.25	5.25 / 0.25	5.25 / 0.25	± 1.5

Table 6 shows the results of image quality evaluation of pediatric head protocol from 3 CT scanners. The CT number of Teflon (Bone) and

polyethylene were out of the ACR standard range for scanner 2 and 3. They were above the upper range for Teflon (Bone) and under the lower range for polyethylene.

Table 6. *Results of image quality evaluation of pediatric head protocol from 3 CT scanners*

Parameter	Scanner 1	Scanner 2	Scanner 3	ACR standard
CT no. uniformity (HU)	3.64	0.63	0.81	≤ 5
CT no. of materials (HU)				
- Water	-6.33	-1.06	-0.05	-7 to +7
- Air	-996.45	-993.02	-1001.56	-970 to -1005
- Teflon (Bone)	930.27	1035.35	997.55	850 to 970
- Polyethylene	-104.6	-107.51	-107.38	-107 to -84
- Acrylic	117.39	117.41	117.60	110 to 135
CNR	1.16	1.16	1.05	≥ 0.7
Spatial resolution (lp/cm)	6	6	5	5
Slice thickness(mm) / Difference (mm)	6 / 1	5 / 0	5.5 / 0.5	± 1.5

Table 7 shows the results of image quality evaluation of adult abdomen protocol. The CNR of scanner 1 and 3 did not meet the ACR standard. They were 0.81 and 0.94 respectively. The criteria CNR of adult protocol was equal to or greater than 1.

Table 7. *Results of image quality evaluation of adult abdomen protocol from 3 CT scanners*

Parameter	Scanner 1	Scanner 2	Scanner 3	ACR standard
CT no. uniformity (HU)	1.78	0.59	1.19	≤ 5
CT no. of materials (HU)				
- Water	3.66	1.12	1.93	-7 to +7
- Air	-991.70	-1002.9	-993.67	-970 to -1005
- Teflon (Bone)	900.71	911.35	909.78	850 to 970
- Polyethylene	-96.33	-95.82	-94.23	-107 to -84
- Acrylic	123.42	126.61	126.34	110 to 135
CNR	0.81	1.56	0.94	≥ 1
Spatial resolution (lp/cm)	6	5	6	5
Slice thickness(mm) / Difference (mm)	3.5 / 1	2.25 / 0.25	2.25 / 0.25	± 1.5

Table 8 shows the result of the image quality evaluation of pediatric abdomen protocol from 3 CT scanners. The CT number of Teflon (Bone) were higher than the acceptable range for all scanners. The CT number of polyethylene of scanner 2 was lower than the acceptable range. The CNR of scanner 3 was 0.39 that was not accepted. The ACR proposed the criteria of CNR for pediatric abdomen at be equal to or greater 0.4.

Table 8. *Results of image quality evaluation of pediatric abdomen protocol from 3 CT scanners*

Parameter	Scanner 1	Scanner 2	Scanner 3	ACR standard
CT no. uniformity (HU)	3.85	1.24	2.36	≤ 5
CT no. of materials (HU)				
- Water	2.38	0.78	1.43	-7 to +7
- Air	-996.56	-999.82	-989.34	-970 to -1005
- Teflon (Bone)	1136.16	1013.6	1016.76	850 to 970
- Polyethylene	-109.38	-104.45	-105.71	-107 to -84
- Acrylic	116.59	118.54	116.88	110 to 135
CNR	0.55	1.11	0.39	≥ 0.4
Spatial resolution (lp/cm)	6	5	6	5
Slice thickness(mm) / Difference (mm)	3.5 / 1	2.5 / 0.5	2.5 / 0.5	± 1.5

IV. DISCUSSION

In this study, ACR CTAP image quality were automatically evaluated by IndoQCT software. CT number uniformity shows the variation of CT number between peripheral and central ROIs within 5 HU for all scanners. The spatial resolution of 5 line pair.cm^{-1} was detectable for all protocols. The measured slice thickness of all protocols were within tolerance value at 1.5 mm.

According to ACR guideline, the CT number of different materials of ACR phantom should meet the standard for 120 kV. For other kV settings and phantoms, the water and air values must be met [5]. In our study, the tube voltage at 120 kV was used for adult head and abdomen protocol. The CT number of all materials of adult protocol was within the acceptable range for all scanners. The tube voltage at 100 kV was used for pediatric abdomen protocol for all scanners and pediatric head protocol for scanner 2 and 3. The CT numbers of water and air of these pediatric protocol were within the range of the ACR criteria. Therefore, the CT number of materials were accepted.

The CNR criteria for adult head and abdomen were ≥ 1, pediatric head ≥ 0.7 and pediatric abdomen ≥ 0.4. Our CNR result were within the criteria for adult and pediatric head protocol. For adult abdomen protocol, scanner 1 and 3 were

not accepted. For pediatric abdomen, scanner 3 was not accepted. Currently iterative reconstruction (IR) and deep learning reconstruction (DLR) were used to improve image quality by decreasing noise with reduced radiation dose [6, 7]. According to An AAPM task-group report, TG-233, recommends using task-based metrics to properly characterize image quality in CT [8]. The performance of IR and DLR are not adequately quantified using classical image quality metrics such as noise, contrast-to-noise ratio, and signal-to-noise ratio. More advanced metrics such as the noise power spectrum (NPS), the task-based modulation transfer function, and model observer metrics are required.

V. CONCLUSION

The acceptable image quality parameters were CT number uniformity, spatial resolution and slice thickness of all protocols from 3 scanners. The CT number of different materials were acceptable. The CNR of adult head and pediatric head from 3 scanners met the ACR standards. The annual CT image quality performed and evaluated by qualified medical physicist using ACR CTAP and analyzed by IndoQCT software is very important for the accuracy and reliable of diagnostic information.

ACKNOWLEDGEMENTS

The authors would like to acknowledge with thanks to Dr.Choirul Anam, Department of Physics, Faculty of Science and Mathematics, Diponegoro University, Indonesia for his kind support on the IndoQCT software in this study.

REFERENCES

[1] UNSCEAR Sources and Effects of Ionizing Radiation. Volume I: Sources: Report to the General Assembly, Scientific Annexes A. UNSCEAR 2020/2021 Report. United Nations Scientific Committee on the Effects of Atomic Radiation. United Nations sales publication E.22.XI.1. United Nations, New York, 2022.

[2] Roa AM, Andersen HK, Martinsen AC. CT image quality over time: comparison of image quality for six different CT scanners over a six-year period. Journal of applied clinical medical physics. 2015 Mar;16(2):350-65.

[3] Mansour Z, Mokhtar A, Sarhan A, Ahmed MT, El-Diasty T. Quality control of CT image using American College of Radiology (ACR) phantom. The Egyptian journal of Radiology and nuclear medicine. 2016 Dec 1;47(4):1665-71.

[4] Anam C, Naufal A, Budi WS, Sutanto H, Haryanto F, Dougherty G. IndoQCT: A platform for automated CT image quality assessment. MEDICAL PHYSICS. 2023;11(2).

[5] Chad D, William B, Jessica C. Computed tomography quality control manual 2017. American College of Radiology. 2017;1-86.

[6] Greffier J, Frandon J, Larbi A, Beregi JP, Pereira F. CT iterative reconstruction algorithms: a task-based image quality assessment. European radiology. 2020 Jan;30:487-500.

[7] Higaki T, Nakamura Y, Zhou J, Yu Z, Nemoto T, Tatsugami F, Awai K. Deep learning reconstruction at CT: phantom study of the image characteristics. Academic radiology. 2020 Jan 1;27(1):82-7.

[8] Samei E, Bakalyar D, Boedeker KL, Brady S, Fan J, Leng S, Myers KJ, Popescu LM, Ramirez Giraldo JC, Ranallo F, Solomon J. Performance evaluation of computed tomography systems: summary of AAPM Task Group 233. Medical physics. 2019 Nov;46(11):e735-56.

Contacts of the corresponding author:
Author: Dr.Anchali Krisanachinda
Institute: Chulalongkorn University
Street: Rama IV Road
City: Bangkok
Country: Thailand
Email: Anchali.kris@gmail.com

Optimization of clinical indication DRL of CT protocols

Kanyakham Kannikar[1], Iemsawatdikul Kriengkrai[2], Loungwutiwong Jakapat[3], Suwanjutah Thouantosaporn[4], Nitipongpun Pradit[5], Viwatborvornwong Darunee[6], Phasuk Sukpachart[7], Thongnuem Julaluck[8], Krisanachinda Anchali[9*]

1,2,3 Imaging Center, Phyathai 2 Hospital, Bangkok, Thailand
4 Phyathai Medical campus, Phyathai 2 Hospital, Bangkok, Thailand
5 Imaging Center, Phyathai 1 Hospital, Bangkok, Thailand
6 Imaging Center, Phyathai Phaholyothin Hospital, Bangkok, Thailand
7 Imaging Center, Phyathai 3 Hospital, Bangkok, Thailand
8 Imaging Center, Phyathai Nawamin Hospital, Bangkok, Thailand
9 Department of Radiology, Faculty of Medicine, Chulalongkorn University, Bangkok, Thailand.
*(*Corresponding author: anchali.kris@gmail.com)*

Abstract — **Introduction:** The Diagnostic Reference Level (DRL) is an indication for the optimization of the patient dose. The objective of this study is to establish the local clinical indication DRL (LcDRL) of CT protocols with optimization. **Methods:** The clinical indication based diagnostic reference level (cDRL) of CT protocols include the number of phases, scan and reconstruction techniques, protocol details and reference phantom size. Dose monitoring software was used to collect data on CTDIvol, DLP, and scan length. Patient size was selected based on BMI, ranging from 19-29 kg/m². CTDIvol and DLP were compared to the national DRL, NDRLs Thailand 2023. Optimization was performed after radiation dose reduction and image quality assessment. **Results**: The median value of radiation metric, CTDIvol and DLP, was selected for LcDRL, the 75th percentile was selected for NDRL .The cDRL of CT protocols consist of brain (trauma): CTDIvol and DLP, before/after optimization were 49.2/48.3 mGy, and 1107/1012 mGy.cm, CTDI/DLP decreased in percentage 1.83/8.58, Chest (Thrombus detection) CTDIvol were 13.26/11.5 mGy, DLP 533.78/455 mGy.cm, percent decreased CTDI/DLP were 13.24/0.15. Cardiac (Calcium score) CTDIvol 6.64/5.7 mGy, DLP 88.78/82.2 mGy.cm, percent decrease 14.09/0.07. Sinus (Sinusitis) CTDIvol 27.08/20.80 mGy, DLP 551.05/440.35 mGy.cm, percent decreased 23.19/0.24. Abdomen/Pelvis (Detection of Stones) CTDIvol 11.90/11.10 mGy, DLP 546.70/512.2 mGy.cm, percent decrease 6.72/6.31.
The LcDRL of CT protocol is compared to NDRL 2023 of anatomical based. The result shows the NDRL/LcDRL as Brain (trauma) CTDIvol 62/48.3mGy, DLP 1028/1012 mGy.cm. Chest (Thrombus detection) CTDIvol 12.7/11.5 mGy DLP 495/455 mGy.cm. Cardiac (Calcium score NC) CTDIvol 6.2/5.7 mGy, DLP 85/82.2 mGy.cm. Sinus (Sinusitis) CTDIvol 34.3/20.8 mGy, DLP 548/420.35 mGy.cm. Abdomen/ Pelvis (Detection of Stones) CTDIvol 13.6/11.1 mGy, DLP 625/512.2 mGy.cm. All LcDRL are lower than NDRLs 2023.**Conclusion:** The optimization of LcDRL for CT protocols results in the patient dose reduction when compared to NDRL2023.
Keywords — Clinical CT protocols, NcDRLs, CTDIvol, DLP

I. INTRODUCTION

Computed Tomography (CT) is a widely used imaging modality that provides detailed cross-sectional images for diagnostic and interventional purposes. However, the relatively high radiation doses associated with CT scans highlight the need for dose optimization to ensure patient safety. The principles of justification and optimization, as emphasized by the International Atomic Energy Agency (IAEA) and the International Commission on Radiological Protection (ICRP), are essential for balancing image quality with radiation protection. Diagnostic Reference Levels (DRLs) are a critical radiation protection tool designed to guide dose optimization in medical imaging. Specifically, clinical indication-specific DRLs (LcDRLs) enable precise dose management tailored to different examinations and clinical needs. Implementing LcDRLs not only enhances patient safety but also improves diagnostic outcomes and supports compliance with quality assurance programs and regulatory standards [1,2]. The objective of this study is to establish local clinical indication LcDRLs for CT protocols, then optimize to ensure the efficient dose management while maintaining diagnostic image quality.

II. MATERIALS AND METHODS

The study involved CT scanners from five Phyathai group hospitals, each equipped with a

CT scanner: Phyathai 1 Hospital: IQon Spectral CT (Philips), Phyathai 2 Hospital: Brilliance iCT 256 slices (Philips), Phyathai 3 Hospital: Brilliance iCT 256 slices (Philips), Phyathai Phaholyothin Hospital: Incisive max mA667 (Philips), Phyathai Nawamin Hospital: Incisive max mA667 (Philips). The clinical indication based diagnostic reference level (cDRL) of CT protocols include the number of phases, scan and reconstruction techniques, protocol details and reference phantom size. Data were collected using dose monitoring software, which recorded volume CT dose index (CTDIvol), dose-length product (DLP), and scan length. The number of cases for each procedure was 50 patients. Patient size was categorized based on body mass index (BMI), specifically selecting patients within the range of 19–29 kg/m² to ensure consistent body size representation. The hospital statistics identify five clinical indication examinations, and the highest frequency CT examinations performed as follows: brain (trauma), chest (thrombus detection), cardiac (calcium score non contrast), sinus (sinusitis), and abdomen/pelvis (detection of stones). Calculated LcDRL of CTDIvol and DLP values were compared to the national diagnostic reference levels (NDRLs) Thailand in 2023. Optimization of the protocols was performed following radiation dose reduction and image quality assessment. [3] The process aimed to achieve a balance between minimizing radiation exposure and maintaining sufficient diagnostic image quality.

Statistics analysis

Data were organized in Microsoft Excel, with each procedure recorded in a separate worksheet. Key metrics (CTDIvol, DLP, patient weight, and BMI) were analyzed for minimum, maximum, standard deviation, and quartiles (25th, 50th/median, 75th). Local DRLs were established using the median (P50), compared to Thailand's 2023 NDRL of third quartile (P75) values.

Ethical approval

Ethical approval for the study was obtained from the Phyathai-Paolo Hospital Group Institutional Review Board.

III. RESULTS

All the CT scanners in this study were manufactured by Philips. Table 1 shows the scanner models, number of detectors, kVp, mAs, rotation time, and dose modulation capabilities. All machines were installed between 2018 and 2024. Before data collection, all CT scanners were calibrated to ensure accurate measurements of parameters such as CTDIvol, mAs, DLP, kVp, slice thickness, and CTDIw.

Table 1. *Scanner information including scanner model, number of the detector, kVp, mAs, dose modulation, and rotation time*

Model	Slices	No. of scanner	No. of detectors	kVp (min–max)	mAs (min–max)	Dose modulation	Rotation time (sec)
Brilliance iCT	256	2	128	80-140	10-1000	iDoseRight	Up to 0.27
Incisive max mA667	128	1	64	70-140	10-1000	iDoseRight	Up to 0.27
Incisive max mA667	128	1	64	70-140	10-1000	iDoseRight	Up to 0.27
Qiong Spectral CT	256	1	64	80-140	10-1000	iDoseRight	Up to 0.27

A. Patient characteristics

Data were collected from a total of 1,700 patient procedures. Before optimization, 850 patient procedures were analyzed, representing clinical indication CT protocols for the brain (trauma), chest (thrombus detection), cardiac (non-contrast calcium scoring), sinus (sinusitis), and abdomen/pelvis (stone detection). After optimization, data from an additional 850 patient procedures were collected using the optimized protocols.

The patient body weight ranged from 45.0 to 75 kg, BMI 19 to 29 kg/m². The median distribution of weight in different scanners ranged from 48.5 to 75 kg, and BMI 22.76 to 28 kg/m².

B. Patient dose indices

A statistical analysis of the radiation dose indices in terms of CTDIvol per sequence and DLP per examination. The median values of CTDIvol and DLP represent typical clinical DRL. The table also includes the mean, median, and first and third quartile values for both

CTDIvol and DLP (Table 2).The results of the optimization process for clinical indication DRLs of various CT protocols are presented in Table 3. The comparison includes the CTDIvol (mGy) and DLP (mGy.cm) values before and after optimization, along with their corresponding percentage reductions.The cDRL of CT protocols consist of (1) brain (trauma) : $CTDI_{vol}$: 49.20→48.30mGy (1.83%decrease.), DLP:1107→970.15mGy·cm (8.58% decrease), (2) Chest (Thrombus detection): $CTDI_{vol}$:13.26 →11.50mGy(13.27%decrease), DLP:533.78 → 455 mGy·cm (14.76%decrease), (3) Cardiac (CalciumScore):$CTDI_{vol}$: 6.64 →5.70 mGy (14.09%decrease), DLP:88.78→82.20mGy.cm (7.41%decrease), (4) Sinus (Sinusitis): $CTDI_{vol}$ 27.08→20.80 mGy(23.19%decrease), DLP: 551.05→420.35 mGy·cm (23.72%decrease), (5) Abdomen/Pelvis (Detection of Stones): CTDIvol 11.90→11.10 mGy (6.72% decrease), DLP:546.70→512.20mGy·cm(6.31% decrease)

The LcDRL of CT protocol is compared to NDRL 2023 of anatomical based as shown in Table 4. The result shows the NDRL/LcDRL as Brain (trauma) CTDIvol 62/48.3mGy, DLP 1028/1012mGy.cm.Chest (Thrombus detection) CTDIvol 12.7/11.5 mGy DLP 495/455 mGy.cm. Cardiac (Calcium score NC) CTDIvol 6.2/5.7 mGy, DLP 85/82.2 mGy.cm. Sinus (Sinusitis) CTDIvol 34.3/20.8 mGy, DLP 548/420.35mGy.cm. Abdomen/Pelvis (Detection of Stones) CTDIvol 13.6/11.1 mGy, DLP 625/512.2 mGy.cm. All LcDRL are lower than NDRLs 2023.

Table 2 *LcDRL of CTDIvol per sequence and DLP per series, for distribution of median values*

CT protocol	CTDIvol (mGy)				DLP (mGy.cm)			
	P25	P50	Mean	P75	P25	P50	Mean	P75
Brain (trauma)	48.30	48.30	48.96	49.20	1001.54	1012.00	1018.88	1047.50
Chest (Thrombus detection)	11.37	11.50	10.81	11.90	445.83	455.00	428.05	500.40
Cardiac (Calcium score)	5.65	5.70	5.91	6.20	75.21	82.20	83.73	89.14
Sinus (Sinusitis)	19.41	20.80	22.77	22.98	349.20	420.35	422.19	495.48
Abdomen/Pelvis (Detection of Stones)	10.54	11.10	10.72	12.80	485.48	512.20	478.11	578.60

Table 3 *Comparison between before and after optimization CT protocol*

CT protocols	Before		After		Percent (%)decreased	
	CTDIvol (mGy)	DLP (mGy.cm)	CTDIvol (mGy)	DLP (mGy.cm)	CTDIvol (mGy)	DLP (mGy.cm)
Brain (trauma)	49.20	1107.00	48.30	1012.00	1.83	8.58
Chest (Thrombus detection)	13.26	533.78	11.50	455.00	13.27	14.76
Cardiac (Calcium score)	6.64	88.78	5.70	82.20	14.09	7.41
Sinus (Sinusitis)	27.08	551.05	20.80	420.35	23.19	23.72
Abdomen/Pelvis (Detection of Stones)	11.90	546.70	11.10	512.20	6.72	6.31

Table 4 *Comparison between local DRL and NDRLs Thailand 2023*

CT protocol	CTDIvol (mGy)		DLP (mGy.cm)	
	LcDRL	NDRLs 2023	LcDRL	NDRLs 2023
Brain (trauma)	48.30	62.00	1012.00	1028.00
Chest (Thrombus detection)	11.50	12.70	455.00	495.00
Cardiac (Calcium score)	5.70	6.20	82.20	85.00
Sinus (Sinusitis)	20.80	34.30	420.35	548.00
Abdomen/Pelvis (Detection of Stones)	11.10	13.60	512.20	625.00

IV. DISCUSSION

This study analyzed CT radiation dose indices (CTDIvol and DLP) for various clinical indications across multiple scanners within Phyathai Group hospitals. By establishing local diagnostic reference levels (LcDRLs), the

research highlights effective dose management practices, as all LcDRLs were lower than the 2023 national DRLs (NDRLs). [6] These findings emphasize the importance of dose optimization techniques, such as protocol customization and advanced reconstruction algorithms, in minimizing radiation exposure while maintaining diagnostic accuracy.

The study demonstrates the value of LcDRLs as benchmarks for quality assurance, enabling the identification of high-dose protocols for further optimization. Monitoring dose indices and aligning local practices with international standards contribute to continuous improvement in radiation protection and patient safety.

However, variability in doses due to scanner technology, protocol settings, patient size, and clinical requirements was observed. Differences in scan length may also influence DLP reductions, requiring further analysis to isolate this factor. Standardizing equipment and conducting ongoing audits and staff training remain essential for consistent dose optimization. Limitations of this study are differences in scanner models and technologies across facilities may have contributed to the variability in dose reductions. Standardizing equipment or incorporating more consistent scanner technology could enhance optimization outcomes and scan length variability. The reduction in DLP for some protocols may be partially attributed to variations in scan length rather than pure protocol optimization. A detailed analysis of scan length standardization is required to isolate this factor. [4,6]

V. CONCLUSION

All LcDRLs derived in this study are lower than the NDRLs 2023, reflecting effective dose optimization practices. The most significant dose reductions were observed in the sinus protocol, with a 23.19% decrease in CTDIvol and a 23.72% decrease in DLP.

ACKNOWLEDGEMENTS

The authors sincerely thank the radiology team, including managers, radiologists, and CT technologists, for their invaluable support and contributions to this study.

REFERENCES

[1] International Atomic Energy Agency (IAEA). Radiation Protection and Safety in Medical Uses of Ionizing Radiation, IAEA Safety Standards Series No. SSG-46, IAEA, Vienna (2018).

[2] Vañó E, Miller D, Martin C, Rehani M, Kang K, Rosenstein M, et al. ICRP publication 135: diagnostic reference levels in medical imaging. Annals of the ICRP. 2017;46(1):1-144.

[3] American Association of Physicists in Medicine (AAPM). Quality control in diagnostic radiology. Report of Task Group #12 Diagnostic X-ray Imaging Committee. AAPM Report No. 74.

[4] AAPM, Madison, 2002. [4] Elshami W, Abuzaid M, Joseph DZ, Tekin HO, Ghonim H. Development of acceptable quality radiation dose levels for common computed tomography examinations: A focused multicenter study in United Arab Emirates. Frontiers in Public Health. 2022; 10:964104.

[5] MOPH. National Diagnostic Reference Levels in Thailand 2023. 2003:6-7.

[6] Abuzaid MM, Elshami W, Tekin HO, Ghonim H, Shawki M, Salama DH. Computed tomography radiation doses for common computed tomography examinations: a nationwide dose survey in United Arab Emirates. Insights into Imaging. 2020; 11:1-6.

Contacts of the corresponding author:
Author: Anchali Krisanachinda
Institute: Department of Radiology, Faculty of Medicine, Chulalongkorn University
Street: Phayathai Road
City: Bangkok
Country: Thailand
Email: Anchali.kris@gmail.com

Real-Time Staff Radiation Dose Monitoring from Neuro-Interventional Procedures, King Chulalongkorn Memorial Hospital

Prajamchuea Kornkamol [1], Krisanachinda Anchali [2*]

1 Department of Radiology, King Chulalongkorn Memorial Hospital, Bangkok 10330, Thailand,
2 Department of Radiology, Faculty of Medicine, Chulalongkorn University, Bangkok 10330, Thailand
**Corresponding author: anchali.kris@gmail.com*

Abstract — **Introduction:** A real-time radiation dosimeter is helpful for monitoring staff dose during the procedures. The neuro-interventional procedures are performed under biplane angiography. This study is the first real-time staff radiation dose report of the neuro-interventional radiology procedures in Thailand. The objective of this study is to monitor, report the real-time radiation dose of medical staff team and determine the affecting parameters to staff radiation dose during the procedures. **Methods:** The research methodology is the prospective descriptive study. It starts from the collection of the real-time radiation dose of medical staff team consisting of neuro-interventionist, fellow, scrub radiographer, medical physicist and anesthesiologist during the procedures using RaySafe i3 dosimeter. Analyze dose rate and related parameters using descriptive statistics and report the real-time staff radiation dose with the affecting parameters. **Results:** The mean real-time radiation dose per case of the neuro-interventionist, fellow, scrub radiographer, medical physicist and anesthesiologist are 0.012, 0.047, 0.001, 0.347 and 0.004 mSv, respectively. The affecting parameters are the position of lead barrier, the source-staff distance, X-ray tube angle, the exposure technique, source-image receptor distance (SID), and the total procedure time among the staff. **Conclusion:** The real-time radiation dose of medical staff team has been monitored and reported. The radiation protection management is the most important for this neuro-interventional procedure. The most affecting parameters to occupational radiation dose are the position of the medical staff team, the application of the real-time radiation dosimeter, and the position of lead barrier during the procedures.

Keywords — real-time staff radiation dose, real-time radiation dosimeter, neuro-interventional procedures, occupational exposure monitoring and reporting.

I. INTRODUCTION

The number of diagnostic and therapeutic of neuro-interventional procedures are increasingly performed under Biplane Angiography system. During the procedures, both the patient and medical staff team received high radiation dose.

The annual occupational exposure dose limit for radiation workers is 20 mSv, averaged over 5 years, in planned exposure situations recommended by The International Commission on Radiological Protection (ICRP). Generally, the cumulative exposure dose recorded by an Optically Stimulated Luminescence Dosimeter (OSLD) has been monitored every 3 months by Department of Medical Sciences, Ministry of Public Health. However, it would be better for the interventional team to monitor the exposure dose in real time during the procedure, especially for a higher operating dose procedure. Therefore, a real-time radiation dosimeter is helpful for monitoring Interventional procedure staff dose.

In the past, there was no real-time staff radiation dose report at the unit of vascular and interventional radiology, King Chulalongkorn Memorial Hospital. The objective of this study is to monitor, report the real-time radiation dose of medical staff team and to determine the parameters affecting staff radiation dose during the procedures for the radiation protection management of the facilities.

II. MATERIALS AND METHODS

The Institutional Review Board of Faculty of Medicine, Chulalongkorn University approved the research proposal and required the informed consent from medical staffs. This prospective descriptive study includes the collection of the real-time radiation dose of medical staff team of neuro-interventionist, fellow, scrub radiographer, medical physicist and anesthesiologist using 30 RaySafe i3 dosimeters for 3 months.

The 39 neuro-interventional procedures were performed under Biplane Angiography system, Philips Allura Clarity Xper FD20/15. For the measurement of the personal real-time dose, the RaySafe i3 was placed on a lead apron at chest level as shown in Figure 1.

Figure1. *Real time dose, RaySafe i3*

As there is a limited number of the anesthesiologist, who rotated to the neuro-interventional procedures and moved on to other procedures, the real-time dosimeter for the anesthesiologist was fixed behind the lead barrier. The real-time radiation dose of medical staff team during neuro-interventional procedures were collected and analyzed using statistical descriptive such as mean, minimum, maximum, standard deviation, median and the interquartile range, IQR. The medical physicist reviewed the patient radiation dose summary report and related parameters such as cumulative fluoroscopic time (minute), cumulative Air KERMA at reference point dose (mGy), cumulative KERMA area product (mGy.cm^2), pulse rate (p/s), frame rate (f/s) and X-ray tube angle. The affecting parameters such as the position of lead barrier, the source-staff distance, X-ray tube angle, the exposure technique, source-image receptor distance (SID), and the total procedure time. The real-time staff radiation dose report of neuro-interventional procedures was prepared and compared the real-time radiation dose among the medical staff team.

III. RESULTS

The average number of neuro-interventional cases under general anesthesia per month was 13. The average fluoroscopic time of neuro-interventional procedures for 3 months was 36 minutes. The mean ± SD of the real-time radiation dose per case of the neuro-interventionist, fellow, scrub radiographer, medical physicist and anesthesiologist was 0.012± 0.013, 0.047±0.039, 0.001 ±0.003, 0.347 ±0.802 and 0.004±0.015 mSv, respectively as shown in Figure 2. The estimated average annual occupational exposure was 1.80, 7.36, 0.12, 54.08, and 0.60 mSv respectively as shown in Figure 3. The maximum real-time radiation dose per case of the neuro-interventionist, fellow, scrub radiographer, medical physicist and anesthesiologist was 0.050, 0.170, 0.010, 3.310 and 0.080 mSv, respectively. The estimate maximum annual occupation exposure was 7.80, 26.52, 1.56, 516.36 and 12.48 mSv respectively. Minimum real-time radiation dose per case of all staffs was 0 mSv.

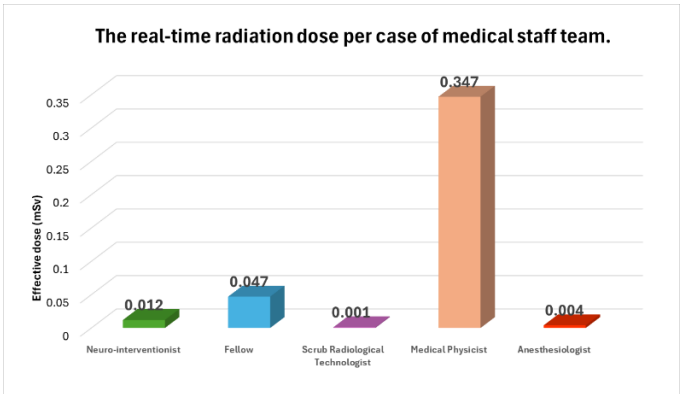

Figure 2. *The bar chart of real-time radiation dose per case of medical staff team.*

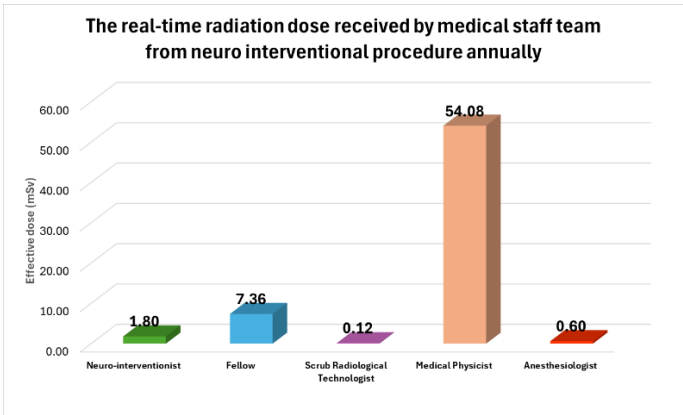

Figure 3. *The bar chart of estimated real-time radiation dose received by medical staff team from neuro interventional procedure annually.*

There are two positions of lead barrier. The first position was behind the lateral X-ray tube to protect the neuro-interventionist or fellow who did the procedure. The second position was to protect the anesthesiologist team. The neuro-interventionist or fellow is mostly close to the X-ray tube and the patient. During some cases, the scrub radiographer controlled the X-ray tube at different angles of cerebral vessels imaging using the exposure technique 'Cerebral 3fps 50%' in general. The source-image receptor distance (SID) at more than 80 cm depends on

the height of the neuro-interventionist or fellow. The average procedure time per case is 2.33 hours.

IV. DISCUSSION

Not only monitored the real-time staff radiation dose and patient radiation dose but the medical physicist also performed a radiographer job without a lead barrier. Thus, the medical physicist received the average real-time radiation dose at 54.08 mSv/year and highest among the medical staff. From the real time radiation dose, the maximum occupational exposure obtained by the medical physicist was 516.36 mSv/year which measured outside the lead apron at chest level. The scrub radiographer received lowest real-time radiation dose at 0.12 mSv/ year, because they were quite a distance from an X-ray tube and next to the neuro-interventionist and fellow during the procedure. Fellow interventional radiologist received the real-time radiation dose higher than the neuro-interventionist because he needs more practice to improve his skill under supervision of the neuro-interventionist. Even though the anesthesiologist stand close to an X-ray tube, the real-time radiation dose is not high because she/he was always behind the lead barrier.

V. CONCLUSION

The real-time radiation dose of medical staff team has been monitored and reported. Medical physicist received the highest real-time radiation dose. The radiation protection management should be planned and processed to reduce the occupational exposure for the medical physicist. The amount of whole body dose, Hp (10) from personal dosimeter, OSLD, should be compared to the real time radiation dose from all medical staff to obtain the relation between both dosimeters. The affecting parameters to occupational radiation dose are the position of the medical staff team in relation to the radiation source, the application of the real-time radiation dosimeter, the optimization of exposure technique, the total fluoroscopic time and the position of the lead barrier during the procedures.

RECOMMENDATIONS

In order to reduce the occupational exposure, the guidelines to manage radiation dose exposure

Follow ALARA Guidelines

• Time – Minimize radiation exposure time

• Distance – Maximize distance from radiation source

• Shielding

– Use shielding best practices

– Use lead aprons, thyroid collars, radiation glasses and moveable shields to absorb radiation

– Wear dosimeters to monitor radiation exposure.

ACKNOWLEDGEMENTS

Special thanks to all staffs of division of quality assurance and medical physics and the unit of vascular and interventional radiology, for their cooperation, encouragement during the research.

REFERENCES

[1] The 2007 recommendations of the International Commission on Radiological Protection. ICRP publication 103. Ann ICRP. 2007; 37: 1-332.

[2] Fluke Biomedical. Real-time staff dose radiation monitoring: Immediate and long-term solutions for reducing medical radiation risks. Specifications subject to change without notice. September 2018; 6011406a-en.

[3] Kim T, Kwon O-Ki, et.al., A Phantom Menace to Medical Personnel During Endovascular Treatment of Cerebral Aneurysms: Real-Time Measurement of Radiation Exposure During Procedures. World Neurosurgery. 2019; Vol. 125: e289-e296.

[4] Vitali K, Lena C., Leon D. G., et.al., Reduction of Radiation Dose Using Real-Time Visual Feedback Dosimetry During Angiographic Interventions. Journal of Applied Clinical Medical Physics. 2023; 24: e13860.

Contacts of the corresponding author:
Author: Anchali Krisanachinda
Institute: Faculty of Medicine,
Chulalongkorn University
Street: Rama IV Road
City: Bangkok
Country: Thailand
Email: anchali.kris@gmail.com

Dosimetry and image quality studies between grid and non-grid fluoroscopy during catheterization in pediatric protocol: a phantom study

Netprasert Sa-angtip[1], Krisanachinda Anchali[2*]

1 Department of Radiology, King Chulalongkorn Memorial Hospital, Bangkok, Thailand
2 Department of Radiology, Faculty of Medicine, Chulalongkorn University, Bangkok, Thailand
**anchali.kris@gmail.com*

Abstract — **Introduction:** Since fluoroscopic radiography is beneficial during interventional radiological procedures, the pulsed fluoroscopic imaging offered the high patient dose especially in children. The removing of an anti-scatter grid has been recommended. The purpose of this research is to study the dosimetry and image quality between using grid and non-grid fluoroscopy for a pediatric catheterization protocol. **Methods:** As an X-ray tube is under the table, CIRS 903 phantom represents pediatric is placed on an X-ray table. TOR 18FG is placed between the CIRS phantom and a solid-state detector is placed on the table and under the CIRS 903 phantom, for dosimetry studies. The fluoroscopic system will be set as a routine paediatric clinical procedure. Both fluoroscopic mode and single mode were exposed with and without grid, repeat the exposures 5 times to obtain the average dose and the image quality in each mode. **Results:** For with and without grid, the dose rate of fluoroscopic mode was 23.69 mGy/sec, and 10.27 mGy/sec (p-value <0.05). The dose of single mode was 573.50 and 236.54 µGy respectively (p-value = 0.02). The spatial resolution was 1.25 and 0.9 line pair/mm for fluoroscopic mode and 2.5 and 1.8 lp/mm for single mode. The contrast was 5.3 and 8.8 percent for fluoroscopic mode and no change on the single mode. **Conclusion:** Even though the grid had improved the image quality of both modes in the catheterization protocol of paediatric, the radiation dose rate increased by 56.6%. The use of fluoroscopy without grid during the paediatric procedure is encouraged.
Keywords — Grid, Non-grid, Paediatric interventional fluoroscopy, Dosimetry, Image quality

I. INTRODUCTION

Since fluoroscopic radiography is beneficial for real-time imaging during interventional radiological procedures, the fluoroscopy machine is clinically used for diagnostic and treatment purposes. However, there is a disadvantage of using pulsed fluoroscopic imaging which is a high radiation dose exposure to patients. According to the statement of International Commission on Radiological Protection (ICRP) publication 121, that radiation dose increases the probability of stochastic effect attribution, and the probability of such effects is increased when ionizing radiation is used in medical therapeutic or interventional procedures. Although a single radiological examination leads to a slightly increase in the probability of cancer risk in patient, but some populations may undergo several examination or procedure because of their health status which increase the cumulated radiation dose. Therefore, some groups of the population are more sensitive to radiation such as fetus, embryo or children, which probably result in an early cancer in the young (1).

Since the radiation dose from an Interventional procedure are higher compared to some radiation examination. Moreover, most patients including pediatrics may undergo interventional procedure more than one time during their admission which cause to the higher accumulate radiation dose. So, the National Council of Radiation Protection and Measurements (NCRP) published the NCRP Report No. 168 title Radiation Dose Management for Fluoroscopically-Guided Interventional Medical Procedures (2). This report provides a guideline for radiation dose management for patients and medical staff during the use of fluoroscopic systems for image guided diagnostic and therapeutic procedures. One of the recommendations to reduce the dose for pediatric patients is removing the anti-scatter grid that is attached to the front of image receptor. Since grid is benefit for removing the radiation scatter from the patient, but also increases the radiation dose to the patient to maintain the image quality. However, the proportion of scattered radiation is depending on the patient size; the larger patient the more scatter occurs. So the anti-scatter grid is unnecessary in pediatric patients which have low scattered radiation.

In consideration of the radiation dose and the image quality assessment of grid using and grid removing for the acquisition of the fluoroscopic

system with catheterization protocol is important to encourage radiological technicians to follow the recommendation especially the radiation dose obtained by the pediatric patients.

II. MATERIALS AND METHODS

This study is a phantom study. Single plane fluoroscopic system Siemens Artis Q ceiling tube was used in this study. CIRS 903 phantom represents the paediatric patient and TOR 18FG was used for image quality assessment. Solid state detector was used for dosimetry.

A. Protocol selection

Central line insertion protocol was selected since this procedure is the most frequently performed in pediatrics patient at Vascular and Interventional Radiology, Department of Radiology at King Chulalongkorn Memorial Hospital.

B. Phantom settings and examination

Set position of each equipment in the procedure condition. CIRS 903 phantom were used to represent pediatrics patient and the TOR 18FG were put between the slabs to represent the detailed that will be assessed for image quality aspect. For dosimetry aspect, solid state detector was placed on table and the other equipment was in the same condition of the TOR 18FG.

Exam in both with and without grid and exam in both fluoroscopic mode with 5 seconds exposed and in a single shot of radiograph mode with an AEC. Repeat all modes 5 times with result recorded.

C. Dose and Image assessment

Image quality was evaluated according to the TOR 18FG assessment manual. For the statistic, paired t-test will be used to compare all the radiation dose of with and without grid.

III. RESULTS

A. Dosimetry

In fluoroscopic mode, the mean dose rate of exposure with grid was 23.66 µGy/sec, and 10.04 µGy/sec with grid removal with p-value was <0.05 as shown in Figure 1. In single shot of radiograph mode, mean dose was 573.50 and 236.54 µGy with grid and grid removal respectively, p-value was <0.05 as shown in Figure 2.

B. Image quality

The spatial resolution of grid insertion was 1.25 lp/mm and without grid was 0.9 lp/mm for fluoroscopic mode. For single shot of radiograph mode was 2.5 and 1.8 lp/mm of with grid and grid removal respectively. The contrast was 5.3 and 8.8 percent for fluoroscopic mode and no change on the single mode.

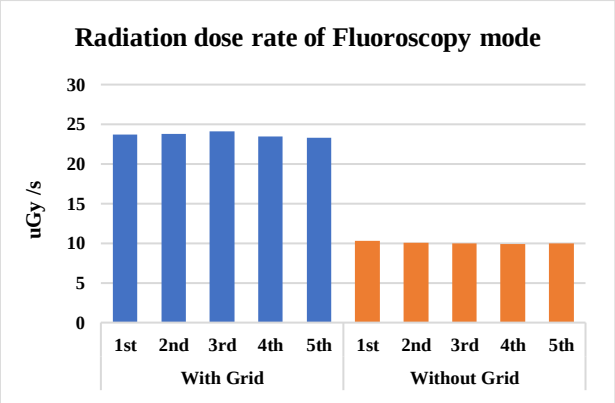

Figure 1. *Box plot of the 5-time repeated radiation dose rate of Fluoroscopic mode of with and without grid.*

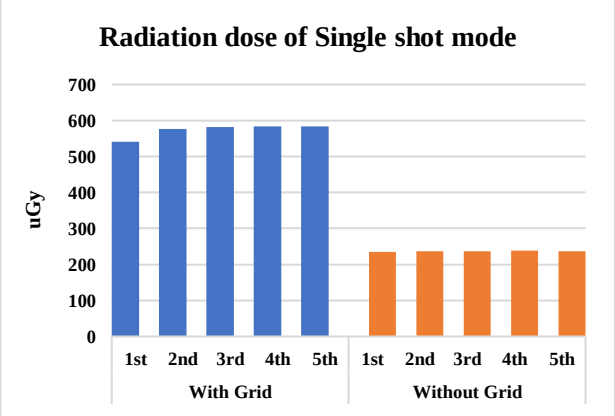

Figure 2. *Box plot of the 5-time repeated radiation dose of Radiographic mode of with and without grid.*

IV. DISCUSSION

At without grid, the dose rate reduction was 56.6% for fluoroscopic mode and 58.76% for single mode. Likewise, the spatial resolution reduced 28% for both modes. The contrast reduced by 40% for fluoroscopic mode but remained the same for single mode.

From the image quality assessment using TOR18FG with grid and without grid, figure 3 shows the line pair pattern for the spatial resolution of fluoroscopic image with grid insertion was 1.25 line pair/mm (Fig 3a) and 0.40 mm and without grid is 0.56 mm (fig 3b).

a. b. c. d.

Figure 3. *TOR 18FG of (a.) with grid and (b.) without grid from Fluoroscopic mode and (c.) with grid and (d.) without grid from single shot mode.*

Spatial resolution of single shot image with grid and without grid is 0.2 and 0.28 mm respectively. Since a 0.018-inch guidewire was commonly used for guiding and vessel selection during paediatric transvenous catheterization, the guidewire might not be clearly seen in the fluoroscopic image without a grid during the procedure. However, the contrast between guidewire is well distinguished in the thoracic area since there is a big difference contrast.

For the contrast assessment, the contrast was greatly reduced after grid removal in fluoroscopic mode but remained the same in radiographic mode. Therefore, grid removal technique should be considered according to the body region of the procedure which the contrast between area of interest and the radiopaque interventional equipment is highly displayed. If the procedure is performed in the thoracic area, grid should be detached during the examination.

In clinical, almost paediatric patients tend to repeat this central line insertion procedure more than one time during the admission. Therefore, grid removal during the procedure of paediatric is recommended according to the NCRP Report No. 168. Not only the dose of non-grid technique is less than a half of the grid technique, but the cumulated dose of the paediatric patient during the admission will also decrease significantly. As a result, the risk from radiation in children is also reduced.

However, there is a limitation of this study. Because of phantom thickness, only 20 cm. of PMMA material phantom (CIRS 903) was performed to represent the child. This thickness cannot represent all sizes of the paediatric patients of a wide range of age and patient size. Varying the phantom thickness should be performed in a further study to investigate the impact of patient size on grid and non-grid fluoroscopy during catheterization in pediatric protocol.

V. CONCLUSION

In conclusion, although the anti-scatter grid had improved the image quality of both modes in the trans-venous catheterization protocol of paediatric, the radiation dose rate increased by double in both modes. Therefore, the use of fluoroscopy without grid during the paediatric procedure is encouraged.

ACKNOWLEDGEMENTS

The authors would like to thank Assoc. Prof. Anchali Krisanachinda from Department of Radiology, Faculty of Medicine, Chulalongkorn University for her help and valuable advices.

REFERENCES

[1] Khong P, Ringertz H, Donoghue V, Frush D, Rehani M, Appelgate K, et al. ICRP publication 121: radiological protection in paediatric diagnostic and interventional radiology. Annals of the ICRP. 2013;42(2):1-63.

[2] Protection NCoR, Measurements, editors. NCRP Report2001: National Council on Radiation Protection and Measurements.

[3] Ubeda C, Vano E, Gonzalez L, Miranda P. Influence of the antiscatter grid on dose and image quality in pediatric interventional cardiology X-ray systems. Catheterization and Cardiovascular Interventions. 2013;82(1):51-7.

[4] Cortis K, Miraglia R, Maruzzelli L, Gerasia R, Tafaro C, Luca A. Removal of the antiscatter grid during routine biliary interventional procedures performed in a flat-panel interventional suite: preliminary data on image quality and patient radiation exposure. Cardiovascular and interventional radiology. 2014; 37:1078-82.

Contacts of the corresponding author
Author: Anchali Krisanachinda
Institute: Faculty of Medicine, Chulalongkorn University
Street: Rama IV Road
City: Bangkok
Country: Thailand
Email: anchali.kris@gmail.com

Comparison of the image quality and dose by using the American College of Radiology (ACR) digital mammography (DM) and small ACR mammography phantoms from full-field digital mammography (FFDM) systems

Ruenjit Sakultala[1], Krisanachinda Anchali[2*]

1 Department of Radiology, King Chulalongkorn Memorial Hospital, Bangkok, Thailand,
2 Department of Radiology, Faculty of Medicine, Chulalongkorn University, Bangkok, Thailand.
**Anchali.kris@gmail.com*

Abstract — **Introduction:** The new ACR DM phantom for 2D and digital breast tomosynthesis (DBT) of FFDM systems is introduced for the test objects visibility with finer lesion and smaller object sizes than the small ACR phantom. The purpose of this study is to compare the image quality and mean glandular dose (MGD) using the ACR DM phantom versus small ACR phantom for the FFDM systems. **Methods:** The ACR DM and small ACR mammography phantoms were scanned in 2D and DBT modes by 3 FFDM systems using the AEC techniques. The MGD, SNR, CNR and visibility of objects in each phantom image were calculated and analyzed. A qualified medical physicist scored visible objects with the images under optimal viewing conditions on acquisition workstation monitor and then calculated the visible scores using weighted indexes and drew a square-shaped ROI on the 2D images only that the mean value of the cavity and background and the SD of background were automatically provided for SNR and CNR calculations. **Results:** The mean MGD in 2D and DBT modes using DM phantom for 3 systems were 1.06±0.10 mGy and 1.44±0.08 mGy, respectively. The mean MGD using the small ACR phantom were 1.13±0.22 mGy and 1.53±0.11 mGy, respectively. The mean SNR and CNR of the DM phantom were 47.46±3.98 and 2.76±0.10, respectively. The mean SNR and CNR of the small ACR phantom were 54.17±7.19 and 10.80±0.98, respectively. The visible score of phantom objects were much higher in the ACR DM phantom than those in the small ACR phantom, especially for specks in DBT ($p < 0.05$). **Conclusion:** The ACR DM phantom is superior to the small ACR phantom in terms of MGD and visibility of phantom objects but the SNR & CNR were lower. Thus, ACR DM phantom appears to be satisfactory for assessing the qualitative image quality in FFDM.

Keywords — Full-field digital mammography (FFDM), small ACR mammography phantom, ACR DM phantom, image quality, mean glandular dose.

I. INTRODUCTION

The small ACR mammography phantom was earlier designed to simulate human breast tissue. The breast phantom including micro-calcifications, masses, and fibers was scanned by the screen-film mammography (SFM) system to evaluate the glandular dose and the image quality taken. Nowadays, this phantom is still in use at several centers including the Breast Imaging unit, King Chulalongkorn Memorial Hospital (KCMH) equipped with the FFDM systems.

The FFDM innovation of different technologies to improve imaging processes has been compared to SFM systems. FFDM has greater accuracy for the diagnosis of breast cancer in women under 50 years of age, women with dense breasts, and premenopausal or perimenopausal women. There are several unsatisfactory studies on the quality of small ACR phantom images using digital mammography. (1-5) Therefore, the ACR introduced a new DM phantom for two-dimensional (2D) and digital breast tomosynthesis (DBT) systems as the test objects with finer lesion and smaller sizes than the small phantom to evaluate the artifact of entire detector (6). This study compared the image quality in terms of the signal to noise ratio (SNR), the contrast to noise ratio (CNR), the visibility of phantom objects and MGD using the ACR DM and small ACR phantoms in FFDM systems.

II. MATERIALS AND METHODS

The small ACR mammography and ACR DM phantoms were scanned in 2D and DBT modes by 3 FFDM systems using the AEC techniques for assessing image quality and MGD. FFDM systems for each manufacturer and model are listed in Table 1.

Table 1. *Three FFDM systems for clinical study with manufacturer and model at KCMH.*

Manufacturer	Model	Number
Hologic	Selenia Dimensions	1
Hologic	3Dimensions	2

A. The small ACR and ACR DM phantoms

The small ACR phantom sized 10.2 × 10.8 ×4.5 cm^3 was designed for the ACR accreditation program of SFM systems. The phantom simulates a 4.2 cm compressed 50–50 breast thickness, with six fibers, five speck groups, and five masses. The ACR DM phantom was designed for the performance test of DM systems based on the ACR DM QC manual (6). It also simulates a 4.2 cm compressed 50-50 glandularity breast with a larger dimension of 31×19×4.1 cm^3. The finer grade test objects phantom has smaller size with six fibers, six speck groups and six masses.

B. Mean Glandular Dose, MGD

The MGDs of both small ACR and ACR DM phantoms automatically displayed on a monitor. They were verified by the measured breast entrance exposures using a calibrated multimeter for several mammographic X-ray beam energies. (Piranha model 657, RTI Electronics, Sweden). The corresponding conversion factors calculated by Dance (7) was multiplied by the measured breast entrance exposures to obtain the MGD.

C. Image quality

The small ACR phantom (Gammex, Inc, Sun Nuclear Company; Model 156) is displayed in Figure 1, ACR DM phantom (Gammex, Inc, a Sun Nuclear company; Model Mammo FFDM) in Figure 2, and ACR DM phantom (Pro-Project, Diagnomatic; Model Pro-MAM Accreditation FF) in Figure 3 were scanned by 2D and DBT modes using Auto-filter technique.

The image quality in terms of SNR, CNR and visibility of objects was evaluated for each phantom image. A qualified medical physicist scored of 1, 0.5, or 0 according to their visibility for each type of detail (fiber, specks, and mass) as shown in Figure 1-3 based on the ACR scoring protocol (6) with the images under optimal viewing conditions on acquisition workstation monitor.

The size of visible objects to weighted indexes were transferred as shown in Table 2 to compare the image quality using the small ACR and ACR DM phantoms directly. The number and size of each object on the small ACR and the ACR DM Phantoms were different. Weighted indexes were calculated using a modified version of Gennaro G et al.'s weighting method, which is intended to increase the quantization levels of phantom scores by weighting details by their size (5). The weighted index total score was also calculated as the sum of the weighted index scores of fibers, specks, and masses.

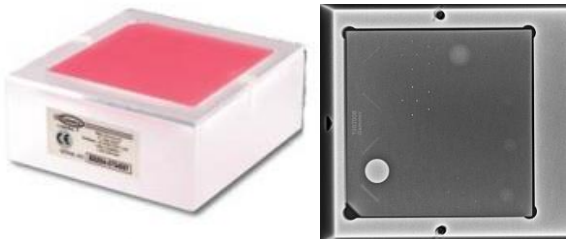

Figure 1. Small ACR mammography phantom and phantom image (Gammex, Inc, Sun Nuclear Company; Model 156)

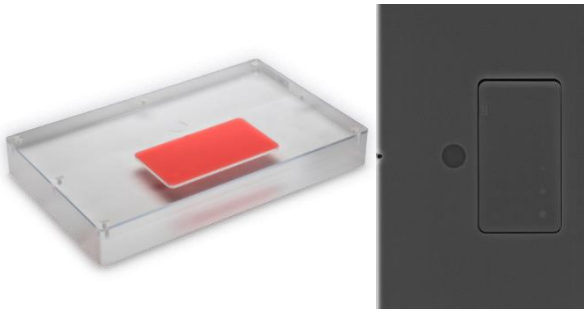

Figure 2. ACR DM phantom and phantom image (Gammex, Inc, a Sun Nuclear company; Model Mammo FFDM)

Figure 3. ACR DM phantom and phantom image (Pro-Project, Diagnomatic; Model Pro-MAM Accreditation FF)

A qualified medical physicist drew a square-shaped ROI in the 2D images only that the mean value of the cavity and background and the SD of background were automatically provided for SNR and CNR calculations, following equation (1) and (2).

$$SNR = [Mean_{bg} - DC\ offset]/Std_{bg} \quad (1)$$

$$CNR = [Mean_{bg} - Mean_{disk}]/Std_{bg} \quad (2)$$

Table 2. *Weighted indexes for each size of phantom objects for the small ACR and ACR DM phantoms*

Phantom			Detail size of each group					
			1	2	3	4	5	6
Small ACR	Fiber	Size (mm)	1.56 *	1.12	0.89	0.75	0.54	0.4
		index	1.00	1.39	1.75	2.08	2.89	3.9
	Speck	Size (mm)	0.54 *	0.4	0.32	0.24	0.16	
		index	1.00	1.35	1.69	2.25	3.38	
	Mass	Size (mm)	2*	1	0.75	0.5	0.25	
		index	1.00	2.00	2.67	4.00	8.00	
ACR DM	Fiber	Size (mm)	0.89	0.75	0.61	0.54	0.4	0.3
		index	1.75	2.08	2.56	2.89	3.90	5.20
	Speck	Size (mm)	0.33	0.28	0.23	0.2	0.17	0.14
		index	1.64	1.93	2.35	2.7	3.18	3.86
	Mass	Size (mm)	1	0.75	0.5	0.38	0.25	0.2
		index	2.00	2.67	4.00	5.26	8.00	10.0

**Largest size of each object as reference size (Smallest weighted index)*

B. Statistical analysis

All data were reported as mean ± standard deviation (SD), maximum and minimum. Differences in MGDs, SNR, CNR and weighted index scores between the small ACR and ACR DM phantoms were compared using the paired t-test. Differences were considered significant at $p < 0.05$.

III. RESULTS

Table 3. *Mean, SD, maximum and minimum of MGD (mGy), SNR, CNR of different phantoms in FFDM systems*

Phantom	MGD (mGy) in 2D	MGD (mGy) in DBT	SNR	CNR
Small ACR	1.13±0.22 (0.91-1.35)	1.53±0.11 (1.46-1.65)	54.17±7.19 (46.46-60.69)	10.80±0.98 (9.78-11.75)
ACR DM (Gammex)	1.06±0.12 (0.96-1.19)	1.44±0.10 (1.35-1.54)	47.90±4.21 (43.30-51.57)	2.71±0.07 (2.64-2.78)
ACR DM (Pro project)	1.05±0.12 (0.95-1.18)	1.43±0.09 (1.35-1.53)	47.03±4.62 (41.95-50.98)	2.82±0.12 (2.74-2.95)

A. MGD

As shown in Table 3, MGD of small ACR phantom was slightly higher than ACR DM phantoms both of 2D and DBT. This difference was not statistically significant (p value ≥ 0.05)

B. Visible scores and Weighted index scores

Table 4. *Visible scores and Weighted index scores of different phantoms in FFDM systems*

Phantom	Objects	2D	DBT
Small ACR	Fiber	5.33±0.58(3.22)	5.67±0.58(3.56)
	Specks	4.00±0.00(2.25)	4.00±0.00(2.25)
	Mass	4.83±0.29(7.33)	4.00±0.00(4.00)
	Total	**14.2±0.76 (12.80)**	**13.7±0.58(9.80)**
ACR DM (Gammex)	Fiber	4.83±1.04(3.83)	4.33±0.58(3.23)
	Specks	3.83±0.58(2.67)	3.83±0.29(2.64)
	Mass	4.67±0.58(7.09)	4.33±0.58(6.17)
	Total	**13.3±1.04(13.58)**	**12.5±0.87(12.04)**
ACR DM (Pro project)	Fiber	4.33±0.58(3.23)	4.67±0.58(3.56)
	Specks	4.00±0.00(2.70)	3.83±0.29(2.64)
	Mass	5.33±0.76(8.54)	4.83±0.58(7.42)
	Total	**13.7±1.04 (14.47)**	**13.3±1.04(13.63)**

Values are Mean±SD of visible scores (Weighted index scores)

Each weighted index score of fibers, specks, masses, and overall weighted index scores on the small ACR Phantom and ACR DM Phantoms were also compared as shown in Table 4. The ACR DM phantoms were superior to the small ACR phantom both of 2 modes; these differences were statistically significant for specks in DBT mode (p value < 0.05).

C. SNR and CNR

SNR of the small ACR, ACR DM (Gammex) and ACR DM (Pro project) were 54.17±7.19, 47.90±4.21, 47.03±4.62, respectively. CNR of the small ACR, ACR DM (Gammex) and ACR DM (Pro project) were 10.80±0.98, 2.71±0.07, 2.82±0.12, respectively. The SNR and CNR of small ACR phantom were higher than ACR DM phantoms. This difference was statistically significant (p value < 0.05).

IV. DISCUSSION

A. MGD

Both the small ACR and ACR DM phantoms simulate a 4.2-cm compressed averaged breast thickness at different dimensions and thickness. This difference may result in an uneven

compressed thickness, which may cause the systems to be exposed differently to these phantoms, according to the AEC technique employed. However, in this study, no statistical significantly difference was observed between the MGDs using the small ACR phantom and those using the ACR DM phantoms.

B. Visible scores and Weighted index scores

According to ACR passing criteria, the passing rate still reached 100% for those phantoms. In this study, the weighted index scores were derived from the visible scores by considering the size of each detail. The higher weighted index score for the ACR DM phantoms, especially for specks in DBT mode that were significant difference may result from the smaller size visualized or finer gradient of the details. Therefore, the ACR DM phantom provides better discrimination for digital systems with a small difference of image quality in detecting architectural distortions (fibers), microcalcifications (specks) and masses. Better discrimination for smaller specks is important because FFDM systems are intrinsically superior in detecting microcalcifications than SFM systems. ACR also applied the DM phantom for DBT QC in 2018 (6). DBT should provide better visualization of objects.

C. SNR and CNR

The results demonstrated the mean values of both SNR and CNR of the small ACR Phantom were significantly superior to the ACR DM Phantoms. In this study, AEC technique was used that provided mAs automatically. The mean mAs and MGD of the small ACR phantom were higher than ACR DM phantoms. Therefore, the small ACR Phantom can provide better SNR and CNR than the ACR DM Phantoms.

V. CONCLUSION

The ACR DM phantom is superior to the small ACR phantom in terms of assessing MGD and visibility of phantom objects, but the SNR & CNR were lower. Thus, ACR DM phantom appears to be satisfactory for assessing performance of FFDM systems in terms of the qualitative image quality.

ACKNOWLEDGEMENTS

The authors acknowledge the Breast imaging center, Division of Diagnostic Radiology, King Chulalongkorn Memorial Hospital for supporting the facility.

REFERENCES

[1] Huda W, Sajewicz A.M, Ogden K.M, Scalzetti E.M, Dance D.R, et al. How good is the ACR accreditation phantom for assessing image quality in digital mammography? Acad. Radiol. 2002;9: 764–772.

[2] Pisano ED, Gatsonis C, Hendrick E, Yaffe M, Baum JK, Acharyya S, et al. Diagnostic performance of digital versus film mammography for breast-cancer screening. N Engl J Med. 2005;353:1773-1783.

[3] Song S.E, Seo B.K, Yie A, Ku B.K, Kim H.Y, Cho K.R, et al. Which phantom is better for assessing the image quality in full-field digital mammography?: American College of Radiology Accreditation phantom versus digital mammography accreditation phantom. Korean J. Radiol. 2012;13:776–783.

[4] Krug K.B, Stützer H, Girnus R, Zähringer M, Goßmann A, Winnekendonk G, et al. Image quality of digital direct flat-panel mammography versus an analog screen-film technique using a phantom model. AJR Am. J. Roentgenol. 2007;188:399–407.

[5] Gennaro G, Katz L, Souchay H, Alberelli C, Maggio C, et al. Are phantoms useful for predicting the potential of dose reduction in full-field digital mammography? Phys. Med. Biol. 2005;50:1851–1870.

[6] Berns E.A, Pfeiffer D.E, Butler P.F, et al. Digital Mammography Quality Control Manual. American College of Radiology, Reston, Va. 2018.

[7] Dance D.R, Young K.C, Engen R.E, et al. Further factors for the estimation of mean glandular dose using the United Kingdom, European and IAEA breast dosimetry protocols. Phys. Med. Biol. 2009; 54: 4361–4372.

Contacts of the corresponding author:
Author: Anchali Krisanachinda, PhD
Institute: Faculty of Medicine, Chulalongkorn University
Street: Rama IV Road
City: Bangkok
Country: Thailand
Email: Anchali.kris@gmail.com

Comparison of Image Quality and Apparent Diffusion Coefficient value in Upper Abdominal MRI: Calculated vs. Acquired Diffusion-Weighted Imaging at high b-value

Lowong Thanatchaya[1], Pisuchpen Nisanard[1,2], Satja Minchanat[1,2], Krisanachinda Anchali[2*]

[1] *Department of Radiology, King Chulalongkorn Memorial Hospital, Thai Red Cross Society, Bangkok, 10330, Thailand.*
[2] *Department of Radiology, Faculty of Medicine, Chulalongkorn University, Bangkok 10330, Thailand (*Corresponding author: anchali.kris@gmail.com)*

Abstract — **Introduction:** Diffusion-weighted imaging (DWI) is an MRI technique that uses tissue diffusion properties to detect and characterize lesions. This study compares the image quality of upper abdominal MRI obtained through calculated DWI (cDWI) and acquired DWI (aDWI) at high b-values. **Methods:** The patients age over 18 years old, underwent upper abdominal MRI with DWI, using five b-values of 0, 50, 500, 1000 and 1500 s/mm² from August to September 2024. Calculated DWI at b = 1500 s/mm² was automatically generated using software. Both cDWI and aDWI values at b = 1500 s/mm² were measured for the liver, spleen, pancreatic body, and renal cortices. Apparent diffusion coefficient (ADC) values were calculated using the mono-exponential model. Intraclass correlation coefficients (ICCs) were determined to assess the reliability of the measured DWI and ADC values for both cDWI and aDWI. **Results:** Twenty patients (13 of males and 7 of females) were included. The mean signal intensity ranged from 117.94±6.58 to 507.99±19.81 for aDWI images and from 113.17±11.69 to 502.63±25.30 for cDWI images. The average aADC values of the acquired (aADC) and calculated (cADC) images ranged from 0.65±0.11 to 1.76±0.13 (10^{-3} mm²/s) and 0.65±0.13 to 1.59±0.09 (10^{-3} mm²/s), respectively. The ICC values between aDWI and cDWI for the liver, spleen, pancreatic body, and both renal cortices ranged from 0.756 to 0.979. For aADC and cADC values, the range was 0.648 to 0.868 across these same organs. The overall agreement between the two observers, measured by Cohen's kappa coefficient, was 0.577 for aDWI and 0.459 for cDWI images. **Conclusion:** The ICCs demonstrate moderate to excellent reliability between aDWI and cDWI in the liver, spleen, pancreatic body, and renal cortices. While ADC values showed good consistency, inter-observer agreement was moderate for both techniques, supporting cDWI as a potential alternative to aDWI for high b-value imaging.

Keywords — Calculated diffusion-weighted imaging, High b-value, Apparent diffusion coefficient

I. INTRODUCTION

Diffusion-weighted imaging (DWI) is a Magnetic Resonance Imaging (MRI) technique used to detect and characterize lesions by assessing water molecule motion.[1] High b-values (>1,000 s/mm²) are particularly valuable for distinguishing diseased tissues in the breast, prostate, and brain.[2-5] However, the use of high b-values often leads to challenges, such as reduced signal-to-noise ratio (SNR), compromised image quality, and extended acquisition times.

Recent developments include calculated DWI (cDWI) with high b-values, generated mathematically from acquired DWI (aDWI) images using a mono-exponential diffusion model.[6] This method, utilizing at least two different low b-values, has shown effectiveness in tissue differentiation with reduced scan times compared to standard acquired DWI.

Despite significant advancements, the application of cDWI in adult upper abdominal MRI remains relatively underexplored. This study aims to compare calculated and acquired high b-value DWI in upper abdominal MRI by assessing image quality and the reproducibility of Apparent Diffusion Coefficient (ADC) values.

II. MATERIALS AND METHODS

The Institutional Review Board approved this prospective study, which included patients over 18 years old who underwent upper abdominal MRI with DWI, using b-values of 0, 50, 500, 1000, and 1500 s/mm² from August to September 2024 at King Chulalongkorn Memorial Hospital. Patients with severe motion or susceptibility artifacts and diffuse abnormalities in the liver, spleen, pancreas, or kidneys, preventing the placement of regions of interest (ROIs) in normal parenchyma, were excluded.

MRI was performed on a 3-Tesla system (SIGNA™ Premier, GE Healthcare, USA) using a free-breathing 2D spin echo echo-planar

imaging (SE-EPI) DWI sequence with five b-values. The MRI parameters were as follows: TR 12,600 ms, TE 90 ms, matrix size 112 × 144, section thickness 5 mm, flip angle 90°, and a total acquisition time of approximately 5 minutes, depending on the patient's breathing.

To generate calculated high b-value images, the acquired DWI sequence was processed using MAGiC DWI software (GE Healthcare). Two blinded radiologists assessed image quality using a 5-point Likert scale, based on overall quality, including tissue details and resolution.[7]

For quantitative analysis, one radiologist manually drew circular ROIs (three 100-pixel ROIs per organ, two for each renal cortex) on the liver, spleen, pancreatic body, and renal cortices. The mean DWI values within each ROI were recorded. ADC values were calculated using the mono-exponential model:[6]

$$ADC = -\ln(Sb/S0)/b$$

where Sb is the signal intensity of DWI at a specific b-value, S0 is the signal intensity at b = 0 s/mm², and b is the degree of diffusion weighting.

Descriptive parameters were presented as mean and standard deviation. Cohen's kappa coefficient was used to measure inter-rater reliability for qualitative items.[8] Bland-Altman plots were used to compare ADC values of the liver, spleen, pancreatic body, and both renal cortices.[9] Intraclass correlation coefficients (ICCs) were calculated to assess the reliability of DWI and ADC values for both calculated and acquired DWI. The two-way mixed model was applied to evaluate absolute agreement between these values. ICC results were interpreted with a 95% confidence interval (CI) as follows: poor (ICC < 0.50), moderate (0.50 < ICC < 0.75), good (0.75 < ICC < 0.90), and excellent (ICC > 0.90).[10]

III. RESULTS

A total of 20 patients (13 males and 7 females) were included in the study. The mean signal intensity ranged from 117.94 ± 6.58 to 507.99 ± 19.81 for aDWI images and from 113.17 ± 11.69 to 502.63 ± 25.30 for cDWI images. The mean ADC values derived from aDWI (aADC) and cDWI (cADC) images ranged from 0.65 ± 0.11 to 1.76 ± 0.13 (10^{-3} mm²/s) and 0.65 ± 0.13 to 1.59 ± 0.09 (10^{-3} mm²/s), respectively. Bland Altman plots of the ADC values are presented in Fig 2. The ICC values between aDWI and cDWI for the liver, spleen, pancreatic body, and both renal cortices were 0.962, 0.979, 0.756, and 0.915, respectively. For aADC and cADC values, the ICC values were 0.648, 0.723, 0.766, and 0.868 across the same organs. The overall agreement between the two observers, as measured by Cohen's kappa coefficient, was 0.577 for aDWI and 0.459 for cDWI images.

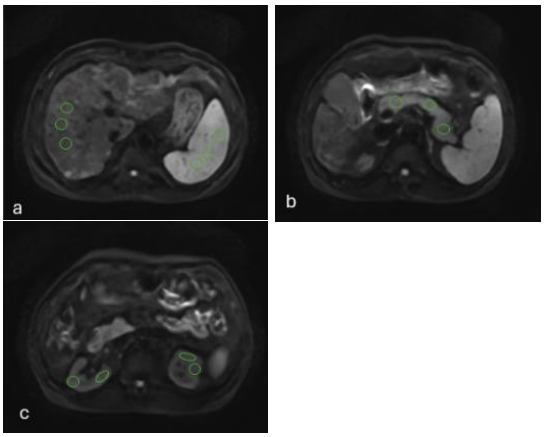

Figure 1. *Three circular regions of interest (ROIs, circles) of approximately 100 pixels were placed within the right hepatic lobe, spleen, and pancreatic body, and two circular ROIs within the left and right kidneys, on the DWI image.*

IV. DISCUSSION

The signal intensities of aDWI and cDWI images showed minimal differences, with overlapping ranges and acceptable variability. The ability of cDWI to achieve comparable signal quality demonstrates the effectiveness of interpolation algorithms for generating synthetic diffusion-weighted images. Although minor discrepancies in interobserver agreement were observed (Cohen's kappa: 0.577 for aDWI vs. 0.459 for cDWI), both methods provided sufficient diagnostic reliability. This aligns with previous studies reporting that cDWI can achieve image quality comparable to that of aDWI across various anatomical regions. [6,11]

The ADC values derived from aDWI (aADC) and cDWI (cADC) were closely aligned, with ICC values ranging from 0.648 to 0.868 across the liver, spleen, pancreas, and renal cortices. While slight underestimation of cADC was noted at higher ranges, this variation was within clinically acceptable limits. Such findings are

Table 1 *Measured DWI and ADC values for acquired and calculated images using b = 1,500 s/mm.*[2]

	DWI (b = 0 s/mm^2)	aDWI (b = 1,500 s/mm^2)	cDWI (b = 1,500 s/mm^2)	aADC (10^{-3} mm^2/s)	cADC (10^{-3} mm^2/s)
Liver	450.88±34.56	117.94±6.58	118.02±11.23	0.88±0.09	0.88±0.11
Spleen	1323.98±63.54	507.99±19.81	502.63±25.30	0.65±0.11	0.65±0.13
Pancreas	1048.30±95.37	259.08±21.06	244.15±31.61	0.92±0.12	0.97±0.13
Kidneys	1559.09±125.38	259.08±21.06	113.17±11.69	1.76±0.13	1.59±0.09

Values are presented as means and standard deviations

Table 2 *ICC values (95% confidence interval) between acquired and calculated images using b = 1,500 s/mm.*[2]

	aDWI and cDWI	aADC and cADC
Liver	0.962	0.648
Spleen	0.979	0.723
Pancreas	0.756	0.766
Kidneys	0.915	0.868

consistent with previous research demonstrating the reliability of synthetic ADC values for both qualitative and quantitative evaluations. [3,4]

The comparability between aDWI and cDWI offers significant clinical benefits. cDWI allows for faster acquisition times by reducing the need for high b-value scans, minimizing patient discomfort, and decreasing motion-related artifacts. This advantage is particularly relevant in pediatric or uncooperative patients, as highlighted in recent studies. [11]

Moreover, the ability of cDWI to provide reliable diffusion metrics suggests it can be used as an alternative to aDWI in routine abdominal imaging, without compromising diagnostic accuracy. For applications such as liver fibrosis staging, lesion characterization, or monitoring response to therapy, cDWI may offer a practical and efficient option.

There were several limitations to the present study. First, the small sample size of 20 patients limits the statistical power and generalizability of the findings. Second, the study focused on comparing image quality and ADC values without correlating these metrics with clinical outcomes or pathology. Larger and more diverse studies are needed to validate these results and evaluate the diagnostic accuracy of acquired and calculated DWI in detecting specific pathologies.

V. CONCLUSION

The ICCs demonstrate moderate to excellent reliability between aDWI and cDWI in the liver,

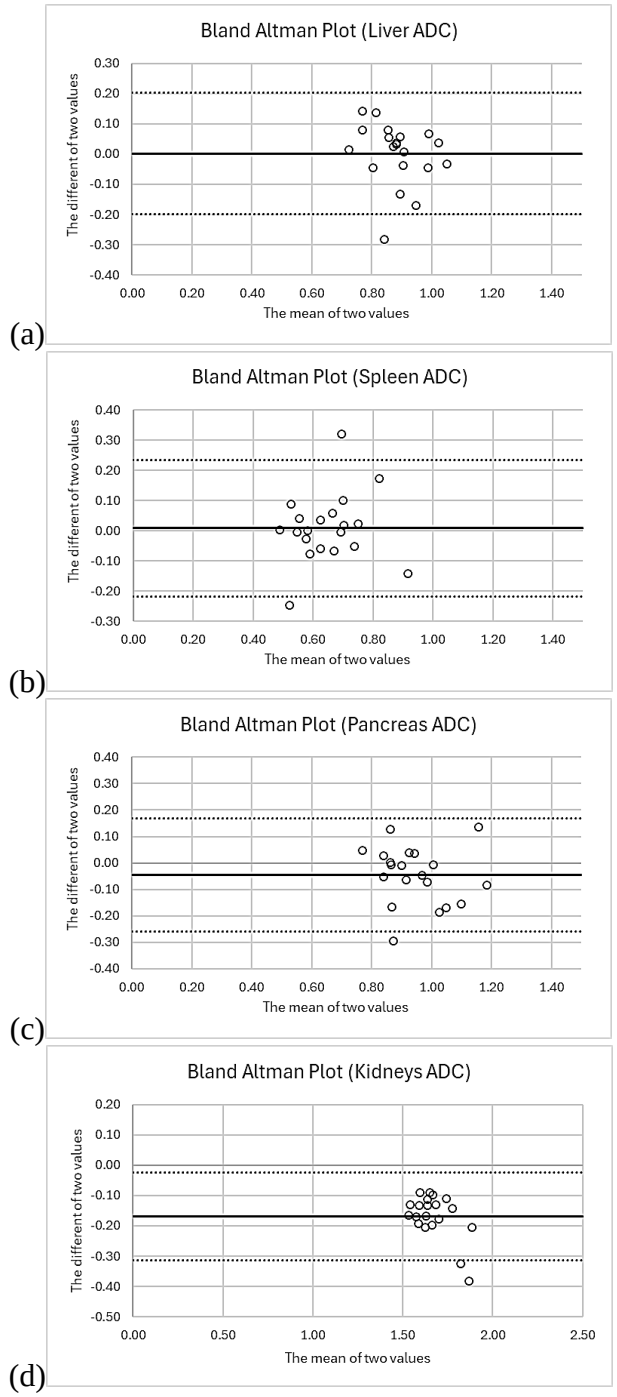

Figure 2. *Bland-Altman plot of acquired and calculated ADC values using b = 1,500 s/mm*^{2} *for the (a) liver, (b) spleen, (c) pancreas, and (d) kidneys.*

spleen, pancreatic body, and renal cortices. Additionally, while ADC values demonstrated moderate to good consistency, inter-observer agreement remained moderate for both techniques. These findings support cDWI as a viable alternative to aDWI for high b-value imaging.

ACKNOWLEDGEMENTS

The authors sincere thank technologists and clinical staff at Unit of Magnetic Resonance Imaging, Department of Radiology, King Chulalongkorn Memorial Hospital, Bangkok, Thailand for their kind support in this study.

REFERENCES

[1] Malayeri AA, El Khouli RH, Zaheer A, Jacobs MA, Corona-Villalobos CP, Kamel IR, et al. Principles and applications of diffusion-weighted imaging in cancer detection, staging, and treatment follow-up. Radiographics. 2011;31(6):1773-91.

[2] Bickel H, Polanec SH, Wengert G, Pinker K, Bogner W, Helbich TH, et al. Diffusion-weighted MRI of breast cancer: Improved lesion visibility and image quality using synthetic b-values. Journal of Magnetic Resonance Imaging. 2019;50(6):1754-61.

[3] Sahoo P, Rockne RC, Jung A, Gupta PK, Rathore RK, Gupta RK. Synthetic Apparent Diffusion Coefficient for High b-Value Diffusion-Weighted MRI in Prostate. Prostate Cancer. 2020;2020(1):5091218.

[4] Cha SY, Kim E, Park SY. Why is a b-value range of 1500–2000 s/mm2 optimal for evaluating prostatic index lesions on synthetic diffusion-weighted imaging? Korean Journal of Radiology. 2021;22(6):922.

[5] Sartoretti T, Sartoretti E, Wyss M, Mannil M, van Smoorenburg L, Eichenberger B, et al. Diffusion-weighted MRI of ischemic stroke at 3T: Value of synthetic b-values. The British Journal of Radiology. 2021;94(1121):20200869.

[6] Higaki T, Nakamura Y, Tatsugami F, Kaichi Y, Akagi M, Akiyama Y, et al. Introduction to the technical aspects of computed diffusion-weighted imaging for radiologists. Radiographics. 2018;38(4):1131-44.

[7] Rosenkrantz AB, Oei M, Babb JS, Niver BE, Taouli B. Diffusion-weighted imaging of the abdomen at 3.0 Tesla: Image quality and apparent diffusion coefficient reproducibility compared with 1.5 Tesla. Journal of Magnetic Resonance Imaging. 2011;33(1):128-35.

[8] McHugh ML. Interrater reliability: the kappa statistic. Biochemia medica. 2012;22(3):276-82.

[9] Bland JM, Altman D. Statistical methods for assessing agreement between two methods of clinical measurement. The lancet. 1986;327(8476):307-10.

[10] Koo T, Li M. A guideline of selecting and reporting intraclass correlation coefficients for reliability research. J Chiropr Med. 2016; 15 (2): 155–63. 2000.

[11] Shin H, Son N-H, Hwang S, Song K. Reliability of synthetic diffusion-weighted imaging with a high b-value for paediatric abdominal MRI. Clinical Radiology. 2023.

Contacts of the corresponding author:
Author: Anchali Krisanachinda
Institute: Department of Radiology, Faculty of Medicine, Chulalongkorn University
Street: Rama IV Road
City: Bangkok
Country: Thailand
Email: anchali.kris@gmail.com

Optimization of energy thresholds in photon counting CT for characterizing renal stone composition: A simulation study

Wongsirinanon Sangsirin[1], Shunhavanich Picha [2,*]

1 Department of Radiology, Medical Physics Program, Faculty of Medicine, Chulalongkorn University, Bangkok, Thailand.
2 Department of Radiology, Faculty of Medicine, Chulalongkorn University, Bangkok, Thailand.
*(*picha.shunhavanich@gmail.com)*

Abstract — **Introduction:** Photon-counting detector CT (PCD-CT) systems offer advanced imaging capabilities for renal stones ≤ 3 mm. These systems can differentiate between uric acid (UA) and non-uric acid (NUA) stones and between different NUA subtypes, aiding in effective treatment selection. The aim of this study is to optimize PCD energy thresholds for characterizing renal stone composition. **Methods:** A 30x20-cm elliptical water phantom with six 3-mm-diameter inserts of different stone types (uric acid (UA), cystine (CYS), calcium oxalate dihydrate (COD), calcium oxalate monohydrate (COM), brushite (BRU), and apatite (APA)) was used. 700 noisy PCD data sets were generated using Photon Counting Toolkit (PcTK) version 3.2 with four energy thresholds (25 keV, and three selected from 35 to 95 keV at 10 keV intervals) and dual-energy thresholds of 25 and 75 keV. Simulated images were reconstructed using filtered backprojection. CT number ratios (CTRs) for each stone type were calculated as the ratio of energy bin 1 to bins 2, 3, or 4. For each energy threshold setting, the area under the receiver operating characteristic curve (AUC) was calculated for distinguishing between stone types (UA vs. CYS, CYS vs. COM, COM vs. APA, COM vs. BRU, and COM vs. COD), using the CTRs, and the average AUC for all stone pairs was the evaluation metric. **Results:** The energy-threshold setting of 25, 65, 75, and 95 keV had the highest average AUC of 0.94, with the CTR of energy bins 1 to 4. The average AUC for the dual-energy threshold setting was 0.83. **Conclusion:** The energy thresholds of 25, 65, 75, and 95 keV could potentially be optimal in PCD for discriminating renal stone composition.

Keywords — photon-counting CT, PcTK, kidney stones, simulation

I. INTRODUCTION

Renal stones have been associated with an increased risk of several health conditions such as chronic kidney disease (CKD), and end-stage renal failure (ESRF) [1]. The type of renal stones is crucial for determining the appropriate treatment, as each type requires a specific management approach. Therefore, the ability to diagnose the type and early-stage stones plays an important role in treatment options.

The main types of renal stones are classified into two terms uric acid (UA) stones and non-uric acid (NUA) stones. The subtypes of NUA stone are classified as calcium oxalate (CaOx) which is the most common stone [2], calcium phosphate, struvite, and Cystine stones (CYS). Each type is managed differently. For example, UA stones are managed with urine alkalinization, which facilitates their dissolution [3]. Calcium oxalate stones may require management through supplementation with magnesium potassium citrate, along with sodium restriction, while cystine-binding agents may be used for CYS stones [4].

Dual-energy CT (DECT) technologies enable the ability to accurately determine stone composition at standard and low-dose acquisitions with performance varied among different models based on the scanner parameters, DECT technique, and stone type. However, the distinction of subtypes of NUA stones is a limitation [5,6]. Clinical CT scanners currently use conventional Energy-Integrating Detectors (EIDs), in which the output signal is proportional to the total energy deposited over a measurement interval, in contrast with Photon Counting Detectors (PCDs), which count individual photons and discriminate them into multiple energy bins [7,8].

Several studies have investigated the ability of PCD-CT systems to distinguish between renal stone types [9-10]. Ferrero et al. [9] found that using CT number ratios (CTRs), a research PCD-CT scanner is not inferior to a corresponding DECT in detecting and characterizing UA and NUA stones ex vivo. Marcus et al. [10] reported a similar finding in human participants, while also found PCD-CT

to be particularly better than DECT in characterizing small renal stones (≤ 3 mm), which are the source of emerging and recurring stones related to patients with chronic nephrolithiasis [11]. Kirkbride et al. [12] used linear attenuation coefficient in each energy bin of a PCD micro-CT system with four energy thresholds to discriminate between APA and CaOx stones of different concentrations and found the selection of energy thresholds to be more significant than tube voltage. However, optimal energy thresholds for distinguishing renal stone composition have not been investigated.

This study aims to optimize the energy thresholds for characterizing kidney stone subtypes in PCD-CT in simulation, which could lead to more accurate diagnosis of renal stones.

II. MATERIALS AND METHODS

This study was an experimental study by a simulation study to characterize renal stone composition.

A. Phantom

A 30x20-cm elliptical water phantom with six 3-mm-diameter inserts of different stone types (Table 1), assuming a 0.225 mm slice thickness for a total thickness of approximately 3 mm, was modelled in MATLAB 2024a, as shown in Figure 1.

Table 1. *Specific information for each type of renal stone*

Stone type	Subtype	Chemical formula	Density (g/cm^3)
Uric acid (UA)	-	$C_5H_4N_4O_3$	1.89
Non-Uric acid (UA)	Calcium oxalate monohydrate (COM)	$CaC_2O_4.H_2O$	2.12
	Calcium oxalate dihydrate (COD)	$CaC_2O_4.2H_2O$	2.02
	Apatite (APA)	$Ca_{10}(PO_4)_6.(OH)_2$	3.10
	Brushite (BRU)	$CaHPO_4.2H_2O$	2.33
	Cystine (CYS)	$(SCH_2CH(NH_2)CO_2H)_2$	1.68

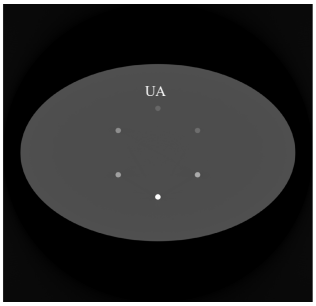

Figure 1*. A 30x20-cm elliptical water phantom with six 3-mm-diameter inserts of different stone types.*

The mass attenuation coefficient of each stone was calculated using a function in SPEKTR 3.0 [13], following Equation 1, based on the known chemical composition of the stone,

$$\left(\frac{\mu}{\rho}\right)_{eff}(E) = \frac{\sum_{i=1}^{M} N_i AW_i \left(\frac{\mu}{\rho}\right)_i (E)}{MW} \quad (1)$$

where, $\left(\frac{\mu}{\rho}\right)_i$ is the mass attenuation coefficient of each element in the compound, M is the number of elements in the compound, AW is the atomic weight of each element, and MW is the molecular weight of the stone. For calculation of linear attenuation coefficient, the stone density as presented in Table 1 was assumed, and each stone was assumed to comprise of 50% water.

B. PCD data generation and reconstruction

The workflow of phantom data is shown in Figure 2. Phantom sinogram was generated using analytical forward projection. Noisy PCD data sets were generated using Photon-Counting toolkit (PcTK) version 3.2 [14] at 140 kVp with four energy thresholds. We tested 35 energy threshold combinations, chosen from fixing the lowest threshold at 25 keV and selecting three threshold energy values from a set of 7 (ranging from 35 to 95 keV at 10 keV intervals). Additionally, dual-energy thresholds of 25 and 75 keV was tested for performance comparison. For each energy threshold setting, 20 noise realizations were generated. The PCD was assumed to have a detector size of 225 μm, thickness of 1.6 mm, and density of 5.85 g/cm^3 CdTe. The initial x-ray spectrum was generated from SpekPy ver 2.0 [15]. Simulated images were reconstructed using filtered back projection (FBP) with 2000 projections per rotation and 1501 detector channels.

C. Characterization and evaluation

Characterization was performed by ROIs 2 mm at the center of each stone. CT number ratios (CTRs) for each stone type were calculated as the ratio of CT number in energy bin 1 to bins 2, 3, or 4 following equation (2).

$$\text{CTR} = \frac{\text{HU of Bin 1}}{\text{HU of Bin 2,3, or 4}} \quad (2)$$

For each energy threshold setting, three CTR combinations were considered: For each energy threshold setting, three CTR combinations were considered: CTR from bin 1 to bin 2, CTR from bin 1 to bin 3, and CTR from bin 1 to bin 4. Each

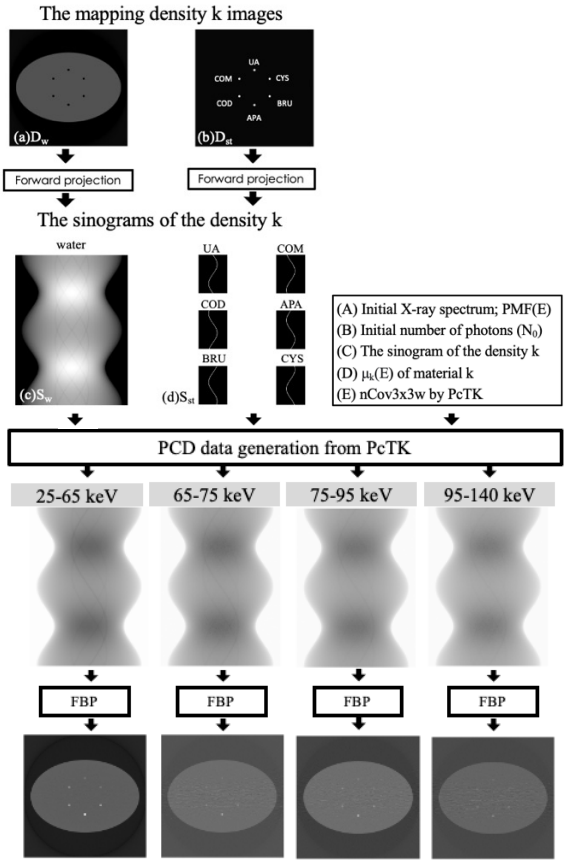

Figure 2. *Workflow for PCD data generation. (a–b) The density maps of water;D_w (a) and stones;D_{st} (b). (c–d) The sinograms of water;S_w(c) and stones:S_{st} (d) were generated from (a) and (b), respectively, through forward projection (FPJ). (e–h) Noisy PCD projection data with cross-talk and spectral response effects of the four energy windows, generated using a random number generator with other input data(A)-(E). (i–l) CT images reconstructed from each of the PCD data (e)–(h) independently using filtered back projection (FBP).*

energy threshold and CTR setting, the area under the receiver operating characteristic curve (AUC) was calculated for distinguishing between stone types (UA vs. CYS, CYS vs. COM, COM vs. APA, COM vs. BRU, and COM vs. COD), The optimal energy threshold and CTR settings were selected based on the highest average AUC of all stone pairs as the evaluation metric.

III. RESULTS

Table 2 shows the best energy threshold setting (with average AUC over 5 stone pairs being highest across 35 threshold combinations) and its corresponding average AUC for each CTR combination. For CTR combination of bin 1 to bin 2, the energy threshold set of 25, 55, 85, and 95 keV had the highest average AUC of 0.87. For CTR combination of bin 1 to bin 3, the energy threshold set of 25, 55, 75, and 95 keV had the highest average AUC of 0.92. For CTR combination of bin 1 to bin 4, the energy threshold set of 25, 65, 75, and 95 keV had the highest average AUC of 0.94.

Comparing among the three CTR combinations, the CTR of energy bins 1 to 4 provide the highest AUC, which was also higher than when using dual-energy threshold, with an average AUC of 0.83. The comparison of the performance in discriminating each stone pair between dual-energy threshold settings of 25 and 75 keV and energy threshold settings of 25,65,75, and 95 keV with the CTR of energy bins 1 to 4, is shown in Figure 3.

Figure 4 illustrates the boxplot of the CTR of bin 1 to bin 4 with the optimal threshold setting for each stone type. It can be seen that the CTR for different stone types were relatively well separated, except for BRU, COD, and COM. Moreover, the ability to discriminate COM vs. BRU and COM vs. COD with CTR of bins 1 to 4 at 25, 65, 75, and 95 keV was superior to CTR at 25 and 75 keV.

Table 2. *The energy threshold set that has the highest average AUC among the 35 sets for each CTR combination.*

CTR combination	The threshold set (the highest average AUC over 35 threshold set)	UA vs CYS	COM vs CYS	COM vs APA	COM vs BRU	COM vs COD	Average AUC (All stone pairs)
CTR (Bin1/Bin2)	25/55/85/95	1	1	0.97	0.59	0.79	0.87
CTR (Bin1/Bin3)	25/55/75/95	1	1	1	0.83	0.77	0.92
CTR (Bin1/Bin4)	25/65/75/95	1	0.94	1	0.87	0.91	0.94
CTR (Bin1/Bin2)	25/75	1	1	1	0.51	0.64	0.83

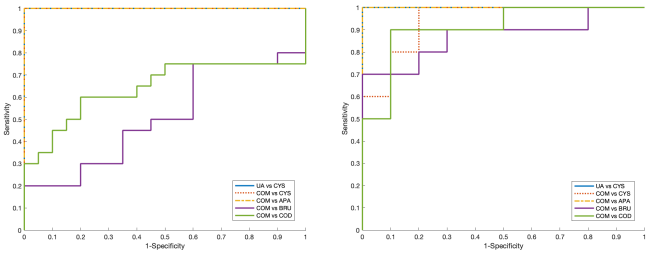

Figure 3. *The ROC curve of each stone pair of (left)dual energy threshold settings of 25 and 75 keV had the highest average AUC of 0.87,(right) energy threshold settings of 25,65,75, and 95 keV had the highest average AUC of 0.94, with the CTR of energy bins 1 to 4.*

IV. DISCUSSION

In this study, we optimized the energy thresholds for characterizing kidney stone types using PCD-CT simulations (PcTK) by varying 4 energy thresholds. We evaluated results using the CTR value in 3 combinations and selected

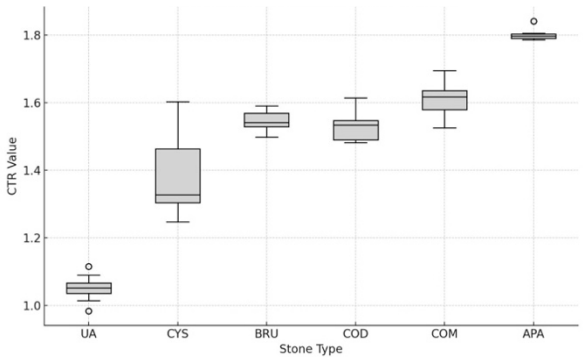

Figure 4. *The CTR from Bin 1/ Bin 4 of 6 stone types at the optimal energy threshold of 25,65,75and 95 keV.*

the energy threshold set that exhibited the best performance based on the highest average AUC across all 5 stone pairs. It demonstrated that the energy-threshold setting of 25, 65, 75, and 95 keV, with the CTR of energy bins 1 to 4, had the highest average AUC, making it the optimal energy threshold for characterizing kidney stone types. At the optimal energy threshold set, the distinction between UA and CYS stones gave the same results as using dual threshold at 25 and 75 keV. Furthermore, the characterization of other stone pairs at the optimal energy threshold is superior to the dual-energy threshold especially COM from BRU and COM from COD stones.

Our results are consistent with Gutjahr et al. [16] and Ferrero et al. [17] in discrimination between UA and CYS stones, even though they tested in ex vivo study using the same dual-energy threshold. However, the results of discrimination between COM and CYS, COM and APA at energy thresholds of 25 and 75 keV from this simulation study were slightly higher AUC than their studies. This study has limitations. Firstly, the photon counting toolkit (PcTK) version 3.2 has not included Compton scattering and pulse pileups. Secondly, the phantoms are only basic simple models, and each renal stone is assumed to be composed of only one type (no mixed stone). Thirdly, this study assumed the ideal detector response and parallel rays. Lastly, this test was only performed in simulation.

V. CONCLUSION

The energy thresholds of 25, 65, 75, and 95 keV could potentially be optimal in PCD for discriminating renal stone composition, especially with the CTR of energy bins 1 to 4.

ACKNOWLEDGEMENTS

We thank Katsuyuki Taguchi et al., from Johns Hopkins University for providing the Spatio-energetic crosstalk in photon counting detectors: Numerical detector model (PcTK) code.

REFERENCES

[1] Sigurjonsdottir VK, Runolfsdottir HL, Indridason OS, Palsson R, Edvardsson VO. Impact of nephrolithiasis on kidney function. BMC Nephrol. 2015; 16:149.

[2] Alelign T, Petros B. Kidney Stone Disease: An Update on Current Concepts. Adv Urol. 2018;2018:3068365.

[3] Avinash R. Kambadakone BHE, Onofrio Antonio Catalano, Dushyant V. Sahani,. New and Evolving Concepts in the Imaging and Management of Urolithiasis: Urologists' Perspective. RSNA. 2010;30.

[4] Frassetto L, Kohlstadt I. Treatment and prevention of kidney stones: an update. Am Fam Physician. 2011;84(11):1234-42.

[5] Pourvaziri A, Parakh A, Cao J, Locascio J, Eisner B, Sahani D, et al. Comparison of Four Dual-Energy CT Scanner Technologies for Determining Renal Stone Composition: A Phantom Approach. Radiology. 2022;304(3):580-9.

[6] Euler A, Wullschleger S, Sartoretti T, Müller D, Keller EX, Lavrek D, et al. Dual-energy CT kidney stone characterization can diagnostic accuracy be achieved at low radiation dose? European Radiology. 2023;33(9):6238-44.

[7] Willemink MJ, Persson M, Pourmorteza A, Pelc NJ, Fleischmann D. Photon-counting CT: Technical Principles and Clinical Prospects. Radiology. 2018;289(2):293-312.

[8] Leng S, Bruesewitz M, Tao S, Rajendran K, Halaweish AF, Campeau NG, et al. Photon-counting Detector CT: System Design and Clinical Applications of an Emerging Technology. Radiographics. 2019;39(3):729-43.

[9] Ferrero A, Gutjahr R, Halaweish AF, Leng S, McCollough CH. Characterization of Urinary Stone Composition by Use of Whole-body, Photon-counting Detector CT. Acad Radiol. 2018;25(10):1270-6.

[10] Marcus RP, Fletcher JG, Ferrero A, Leng S, Halaweish AF, Gutjahr R, et al. Detection and Characterization of Renal Stones by Using Photon-Counting-based CT. Radiology. 2018;289(2):436-42.

[11] A. Skolarikos HJ, A. Neisius, A. Petřík, B. Somani, T. Tailly, G. Gambaro AU Guidelines on Urolithiasis. European Association of Urology 2023.

[12] Kirkbride TER, Aamir Y. Müller, Kristin Bateman, Christopher J. Becce, Fabio Anderson, Nigel G. Discrimination Between Calcium Hydroxyapatite and Calcium Oxalate Using Multienergy Spectral Photon-Counting CT. American Journal of Roentgenology. 2017;209(5):1088-92.

[13] Punnoose J, Xu J, Sisniega A, Zbijewski W, Siewerdsen JH. Technical Note: Spektr 3.0-A computational tool for x-ray spectrum modeling and analysis. Med Phys. 2016;43(8):4711.

[14] Taguchi K, Stierstorfer K, Polster C, Lee O, Kappler S. Spatio-energetic cross-talk in photon counting detectors: Numerical detector model (PcTK) and workflow for CT image quality assessment. Med Phys. 2018;45(5):1985-98.

[15] Poludniowski G, Omar A, Bujila R, Andreo P. Technical Note: SpekPy v2.0-a software toolkit for modeling x-ray tube spectra. Med Phys. 2021;48(7):3630-7.

[16] Gutjahr R, Polster C, Henning A, Kappler S, Leng S, McCollough CH, et al. Dual Energy CT Kidney Stone Differentiation in Photon Counting Computed Tomography. Proc SPIE Int Soc Opt Eng. 2017;10132.

[17] Ferrero A, Gutjahr R, Henning A, Kappler S, Halaweish A, Abdurakhimova D, et al. Renal Stone Characterization using High Resolution Imaging Mode on a Photon Counting Detector CT System. Proc SPIE Int Soc Opt Eng. 2017;10132.

Contacts of the corresponding author:
Author: Picha Shunhavanich
Institute: Department of Radiology, Faculty of Medicine, Chulalongkorn University
Street: Pathumwan
City: Bangkok
Country: Thailand
Email: picha.shunhavanich@gmail.com

Image quality comparison in computed tomography system using different image reconstruction methods: a phantom study

Pangsai Teerapong[1], Sangruang-orn Supakajee[2], Sodkokkruad Prapa [3], Chaknam Korawig [3], Asavaphatiboon Sawwanee[3*].

[1]*Department of Radiology, Master of Science Program in Medical Physics, Faculty of Medicine Ramathibodi Hospital, Mahidol University, Bangkok, Thailand.*
[2]*Department of Radiology, Phramongkutklao Hospital, Bangkok, Thailand.*
[3]*Department of Radiology, Division of Diagnostic Radiology, Faculty of Medicine Ramathibodi Hospital, Mahidol University, Bangkok, Thailand.*
*sawwanee.medphy@gmail.com

Abstract — **Introduction:** Deep learning-based reconstruction is an advanced technique in CT image reconstruction that enhances image quality and corrects noise texture variations associated with iterative reconstruction methods. This study aimed to compare the image quality across different reconstruction techniques and to evaluate the impact of image dose reduction in relation to these techniques in brain CT protocol at Phramongkulklao Hospital. **Methods:** A Catphan®600 phantom was acquired using a CT scanner (Aquilion ONE PRISM Edition, Canon Medical Systems) at four levels of dose reduction (SURE Exp.3D). The raw data were reconstructed using four techniques: filtered-back projection (FBP), iterative reconstruction (AIDR 3D and FIRST), and as deep learning reconstruction (AiCE). Image quality was evaluated based on noise magnitude, noise texture, high contrast resolution, and low contrast detectability using various software tools. **Results:** The study found that noise in iterative and deep learning reconstructions differed significantly from FBP. All three image reconstruction techniques exhibited a decrease in noise from low to high at mild, standard, and strong noise reduction levels. The FIRST technique showed the least noise reduction. High contrast resolution results (lp/cm) showed no significant differences across methods. Regarding low contrast detectability, at both 0.5% and 1% contrast levels, the FIRST technique at high-quality SURE Exp.3D demonstrated superior detection of smaller objects compared to FBP. **Discussion:** All reconstruction techniques demonstrated superior image quality compared to FBP, with the FIRST technique showing the most notable improvement. Additionally, at the high-quality dose reduction level, each reconstruction at the strong setting provided the best image quality. However, it was observed that increased noise reduction resulted in smoother images. **Conclusion:** Iterative and deep learning reconstructions are essential for image noise reduction and improved image quality. Caution is required in clinical practice, as the resulting images may exhibit increased smoothness, potentially reducing the ability to detect subtle differences.

Keywords: Deep learning reconstruction, iterative reconstruction, high contrast resolution, low contrast detectability, noise

I. INTRODUCTION

Currently, CT scanners are widely used in medical diagnostics, driving continuous advancements in both hardware and software. Notably, image reconstruction techniques have evolved to improve image quality.

The Iterative Reconstruction (IR) method, first introduced in the 1970s, overcame the computational limitations of the previously used filtered back projection (FBP) technique, which had been in use for nearly four decades. While FBP offers acceptable image quality, its application at lower radiation doses increases noise and artifacts. In the 2000s, two powerful IR techniques—hybrid iterative reconstruction (HIR) and model-based iterative reconstruction (MBIR) (1), —were developed, significantly reducing noise and artifacts, resulting in superior image quality, particularly in low-dose protocols. However, these methods still face challenges related to noise texture and reconstruction time. With the rise of artificial intelligence (AI), a novel image reconstruction technique, deep learning reconstruction (DLR), has emerged. DLR further enhances image quality by reducing noise and artifacts while maintaining the natural noise texture of images (2).

The researcher aims to evaluate and compare the image quality of various CT image reconstruction methods currently in use, including FBP, IR, and DLR, at Phramongkutklao Hospital using a phantom model. The primary objective of this study is to assess the image quality of these reconstruction techniques and to investigate the impact of image dose reduction on image quality in the brain CT examination protocol.

II. MATERIALS AND METHODS

A. Image acquisition and reconstruction

Images of the Catphan®600 phantom (The Phantom Laboratory, NY, USA) were acquired using a CT scanner (Aquilion ONE PRISM Edition, Canon Medical Systems) with a brain CT protocol at different SURE Exposure 3D (SURE Exp. 3D) levels. Table 1 outlines the main acquisition and reconstruction parameters**.** Each acquisition was repeated three times using the same settings.

Table 1 *Protocol acquisition and reconstruction parameters adopted in this study.*

Body part examined	Brain
Acquisition mode	Helical
Tube voltage (kV)	120
Tube current (mA)	400, 310, 230, 250
SURE Exp.3D	High quality, Standard, Low dose, Off
$CTDI_{vol}$ (mGy)	94.6, 77.1, 56.7, 58.5
Rotation time (s)	1
Collimation (mm)	0.5 x 40
Pitch	0.625
D-FOV (mm)	250
Slice thickness (mm)	3
Slice interval (mm)	3
Reconstruction techniques	FBP AIDR 3D (mild, standard, and strong levels) FIRST (mild, standard, and strong levels) AiCE (mild, standard, and strong levels)

The images were reconstructed using various techniques: filtered-back projection (FBP), iterative reconstruction methods (Adaptive Iterative Dose Reconstruction 3D [AIDR 3D] and Forward-Projected Model-Based Iterative Reconstruction Solution [FIRST]), and deep learning reconstruction (Advanced Intelligent Clear IQ Engine [AiCE]). AIDR 3D, FIRST, and AiCE each offer three levels of intensity: mild, standard, and strong.

B. Data analysis

The image quality evaluation followed the American Association of Physicists in Medicine (AAPM) Task Group report 39 and 233 guidelines for testing CT systems. The analysis used various software, including WEASIS Medical Viewer v4.2.1, IQWork v0.7.2, and ImQuest (Duke University, USA) v7.3.01.

C. Statistical analysis

All assessments were presented as mean and/or standard deviation (SD). Noise magnitude was evaluated with the One-way ANOVA to determine differences within each SURE Exp.3D, with a significance level set at $p < 0.05$.

III. RESULTS

A. Noise magnitude

AiCE exhibits lower noise compared to AIDR 3D and FBP, but higher noise than FIRST across all SURE Exp.3D levels, as presented in **Table 2**. When comparing iterative and deep learning reconstruction techniques to FBP, the noise reduction (NR) values for AiCE range from 30% to 63%, FIRST ranges from 39% to 76%, and AIDR 3D ranges from 12% to 32%. These results indicated that both FIRST and AiCE demonstrated statistically significant noise reduction, with a significance level of $p < 0.05$.

B. Noise texture

The Noise Power Spectrum (NPS) curve exhibited distinct trends depending on the reconstruction technique. Specifically, the FBP technique displayed a curve with a more prominent peak compared to other techniques. the peak frequency (fP) and average frequency (fA) of FIRST and AiCE were significantly lower than those of AIDR 3D and FBP across all levels of SURE Exp.3D. These lower frequencies contributed to smoother images, as shown in **Table 3**.

C. High contrast resolution

From **Table 4**, the line pair per centimeter (lp/cm) values for AiCE at standard and high levels were lower than those for AIDR 3D and FBP across all SURE Exp.3D levels. For low-dose and off SURE Exp.3D settings, the high contrast resolution of AiCE and FIRST was 6 lp/cm lower than that of AIDR 3D and FBP, except at the mild level, where FIRST, AIDR 3D, and FBP exhibit lp/cm of 7.

D. Low contrast detectability

As shown in **Table 5**, the AiCE technique demonstrated superior low contrast detectability compared to other techniques for supra-slice target diameter at 1% contrast level across all SURE Exp. 3D levels. However, when the contrast level was reduced to 0.5%, the low contrast detectability of AiCE became comparable to that of the other techniques.

IV. DISCUSSION

According to noise magnitude and NPS results (as shown in **Table 2**), the study found that image reconstruction using AIDR 3D, FIRST, and AiCE exhibited lower noise magnitude values and narrower NPS patterns compared to the FBP method. The results also demonstrated the highest level of reconstruction, and SURE Exp.3D had the lowest mean noise magnitude and narrowest NPS pattern. The noise magnitude is related to different reconstruction techniques, with AiCE having a better noise magnitude than AIDR 3D and FBP but worse than FIRST at all levels. These findings were consistent with the findings of Tomasi et al. in 2023 (3), which indicated that DLR technique effectively reduces noise magnitude compared to HIR and FBP

techniques. Additionally, these results aligned with Cozzi et al.'s study (2023) (4) which reported that AIDR 3D reconstruction exhibited higher average noise and broader noise patterns than the DLR method. The assessment of noise texture was evaluated through NPS calculation. The position of the average frequency tended to shift towards lower frequencies from the mild to the strong level in each image reconstruction technique, indicating smoother image texture. Additionally, the average frequency increased as the SURE Exp.3D level decreased from high quality to low dose. Thus, the granularity of the noise texture appeared similar. This study aligned with the findings of Oostveen et al. in 2021 (5), who reported that the AiCE technique had smoother noise texture than the AIDR 3D and FIRST techniques. These findings found the same results at the low dose and off levels of SURE Exp.3D, while FIRST demonstrated smoother noise texture than AiCE at high quality and standard levels. They also noted that DLR (Canon Medical Systems Corporation) aims to decrease noise and artifacts to the same extent as MBIR, but with only a slight increase in reconstruction time compared to Hybrid-IR techniques. Moreover, DLR results in a more natural, and less plastic-like appearance compared to MBIR.

For high contrast resolution, AiCE cannot provide a higher resolution or better quality than other imaging reconstruction techniques, and it also has lower lp/cm values than the AIDR and FBP systems, as shown in **Table 4**. According to AAPM No. 39 (6), it indicates that what affects high spatial resolution is blurring. The reason is that the noise texture in the AiCE image has a lower average frequency value, making the image smoother than the other images. For low contrast detectability (LCD), it was found that AiCE had better LCD values than other reconstruction techniques at a supra-slice diameter at 1% and 0.5% contrast levels. According to AAPM No. 39 (6), the factor affecting LCD is image noise. If the image has more noise, the LCD will have worse values, meaning higher values. From the noise measurement results, it was found that AiCE had lower noise magnitude values than AIDR 3D and FBP, resulting in better LCD values than both

Table 2 *Noise magnitude (SD) and percentage noise reduction (%NR) were obtained from images of the CTP486 module.*

SURE Exp.3D		High quality			Standard			Low dose			Off		
Reconstruction techniques		SD	%NR	p-value	SD	%NR	p-value	SD	%NR	p-value	SD	%NR	p-value
FBP		**3.93 ± 0.04**	-		**4.00 ± 0.02**	-		**4.70 ± 0.07**	-		**4.54 ± 0.10**	-	
	Mild	3.08 ± 0.02	21.78	<0.001	3.48 ± 0.03	12.93	<0.001	4.06 ± 0.10	13.61	0.014	4.00 ± 0.13	11.89	0.002
AIDR 3D	Standard	2.69 ± 0.05	31.69	<0.001	3.01 ± 0.01	24.77	<0.001	3.49 ± 0.09	25.80	<0.001	3.46 ± 0.14	23.84	<0.001
	Strong	2.71 ± 0.01	31.10	<0.001	3.03 ± 0.02	24.10	<0.001	3.36 ± 0.07	28.49	<0.001	3.36 ± 0.12	26.05	<0.001
	Mild	1.84 ± 0.09	53.14	<0.001	2.16 ± 0.10	45.87	<0.001	2.85 ± 0.18	39.40	<0.001	2.68 ± 0.14	41.01	<0.001
FIRST	Standard	1.21 ± 0.07	69.32	<0.001	1.46 ± 0.11	63.47	<0.001	2.00 ± 0.14	57.41	<0.001	2.09 ± 0.10	53.93	<0.001
	Strong	0.96 ± 0.09	75.68	<0.001	1.13 ± 0.08	71.64	<0.001	1.53 ± 0.12	67.40	<0.001	1.68 ± 0.09	64.78	<0.001
	Mild	2.75 ± 0.07	30.00	<0.001	2.86 ± 0.06	28.52	<0.001	3.23 ± 0.12	31.35	<0.001	3.12 ± 0.09	31.25	<0.001
AiCE	Standard	1.83 ± 0.07	53.47	<0.001	1.83 ± 0.05	54.21	<0.001	1.93 ± 0.09	58.89	<0.001	1.91 ± 0.04	57.96	<0.001
	Strong	1.66 ± 0.07	57.88	<0.001	1.65 ± 0.06	58.72	<0.001	1.75 ± 0.13	62.79	<0.001	1.74 ± 0.08	61.63	<0.001

Table 3 *The peak frequency (f_p)and average frequency (f_A) in mm^{-1} of the measured NPS.*

Image reconstruction techniques		Peak frequency (mm^{-1})				Average frequency (mm^{-1})			
		SURE Exp.3D				SURE Exp.3D			
		High quality	Standard	Low dose	Off	High quality	Standard	Low dose	Off
FBP		**0.22**	**0.20**	**0.25**	**0.25**	**0.33**	**0.34**	**0.34**	**0.34**
	Mild	0.20	0.20	0.24	0.24	0.29	0.29	0.30	0.29
AIDR 3D	Standard	0.20	0.19	0.20	0.24	0.26	0.27	0.28	0.27
	Strong	0.20	0.19	0.20	0.24	0.27	0.27	0.26	0.26
	Mild	0.08	0.08	0.08	0.08	0.14	0.15	0.17	0.17
FIRST	Standard	0.08	0.08	0.08	0.08	0.11	0.12	0.14	0.13
	Strong	0.06	0.08	0.08	0.08	0.10	0.12	0.12	0.12
	Mild	0.08	0.08	0.08	0.08	0.22	0.22	0.23	0.22
AiCE	Standard	0.08	0.08	0.08	0.08	0.14	0.14	0.15	0.14
	Strong	0.08	0.08	0.08	0.08	0.12	0.12	0.12	0.11

techniques. The experimental results demonstrate that image reconstruction using the IR and DLR techniques can effectively reduce noise, enabling the reduction of radiation dose. In cases of low-dose imaging to minimize radiation exposure to patients, among the methods evaluated, AiCE and FIRST were more effective at reducing noise than AIDR 3D, but they produced smoother images, which may impair the visibility of both high- and low-contrast areas compared to AIDR 3D. These findings align with the recommendations provided by the manufacturer, which suggests using the AIDR 3D image reconstruction technique for CT brain imaging.

Table 4 *Line pair per centimeter (lp/cm) value from CTP528 module*

Image reconstruction techniques		SURE Exposure 3D			
		High quality	Standard	Low dose	Off
FBP		**7**	**7**	**7**	**7**
AIDR 3D	Mild	7	7	7	7
	Standard	7	7	7	7
	Strong	7	7	7	7
FIRST	Mild	7	7	7	7
	Standard	7	6	6	6
	Strong	6	6	6	6
AiCE	Mild	7	7	6	6
	Standard	6	6	6	6
	Strong	6	6	6	6

Table 5 *Low contrast detectability of supra-slice target diameter (1% and 0.5% contrast level).*

Supra-slice target diameter		1% contrast level				0.5% contrast level			
Image reconstruction techniques		SURE Exp.3D				SURE Exp.3D			
		High quality	Standard	Low dose	Off	High quality	Standard	Low dose	Off
FBP		**7**	**7**	**7**	**7**	**8**	**8**	**15**	15
AIDR 3D	Mild	6	7	7	7	7	8	15	15
	Standard	6	7	7	7	7	8	15	15
	Strong	6	7	7	7	7	8	15	15
FIRST	Mild	6	7	7	7	8	9	15	15
	Standard	6	7	7	7	8	9	15	15
	Strong	5	7	7	7	7	9	15	15
AiCE	Mild	5	6	6	6	8	8	9	9
	Standard	5	6	6	6	7	8	15	15
	Strong	5	6	6	6	8	9	15	15

V. CONCLUSION

In summary, hybrid and model-based IR techniques, and DLR, effectively reduce noise and improve image quality compared to FBP technique, allowing for a reduction in radiation dose during CT imaging. However, caution must be exercised when using these techniques, as the reduction in image noise may result in a loss of visibility of high- and low-contrast areas, potentially affecting the ability to diagnose lesions accurately.

ACKNOWLEDGEMENTS

I would like to acknowledge with thanks Asst. Prof. Sawwanee Asavaphatiboon, D.Eng., Assoc. Prof. Supakajee Saengruang-Orn, Ph.D., and all teachers for knowledge and suggestion, Department of Radiology, Faculty of Medicine Ramathibodi Hospital, Mahidol University, and Department of Radiology, Phramongkutklao Hospital for the permission of data and facilities in this study.

REFERENCES

[1] Willemink MJ, de Jong PA, Leiner T, de Heer LM, Nievelstein RA, Budde RP, et al. Iterative reconstruction techniques for CT Part 1: technical principles. Eur Radiol. 2013;23(6):1623-31.

[2] Nagayama Y, Sakabe D, Goto M, Emoto T, Oda S, Nakaura T, et al. Deep Learning-based Reconstruction for Lower-Dose Pediatric CT: Technical Principles, Image Characteristics, and Clinical Implementations. 2021;41(7):1936-53.

[3] Tomasi S, Szilagyi KE, Barca P, Bisello F, Spagnoli L, Domenichelli S, et al. A CT deep learning reconstruction algorithm: Image quality evaluation for brain protocol at decreasing dose indexes in comparison with FBP and statistical iterative reconstruction. Phys Med. 2024;119:103319.

[4] Cozzi A, Cè M, De Padova G, Libri D, Caldarelli N, Zucconi F, et al. Deep Learning-Based Versus Iterative Image Reconstruction for Unenhanced Brain CT: A Quantitative Comparison of Image Quality. Tomography. 2023;9(5):1629-37.

[5] Oostveen LJ, Meijer FJA, de Lange F, Smit EJ, Pegge SA, Steens SCA, et al. Deep learning-based reconstruction may improve non-contrast cerebral CT imaging compared to other current reconstruction algorithms. Eur Radiol. 2021;31(8):5498-506.

[6] AAPM Report 39 - CT Acceptance Testing (1993).pdf.

Contacts of the corresponding author:
Author: Sawwanee Asavaphatiboon
Institute: Faculty of Medicine Ramathibodi Hospital, Mahidol University
Street: Rama 6
City: Bangkok
Country: Thailand
Email: sawwanee.medphy@gmail.com

MRI-Based Radiomics model from mesorectal fat to predict pathologic extramural vascular invasion in locally advanced rectal cancer patients

Swaengdee Yaniga[1,2], Khongwirotphan Sararas[2,3], Lasode Jaravee[4], Kuecharoen Phakakarn[5], Phetvilay Phathayphout[5], Boonsirikamchai, Piyaporn[5], Rakvongthai, Yothin[2,6 *]

1 Department of Radiology, Medical Physics Program, Faculty of Medicine, Chulalongkorn University, Bangkok, Thailand
2 Department of Radiology, Chulalongkorn Biomedical Imaging Group, Faculty of Medicine, Chulalongkorn University, Bangkok, Thailand
3 Department of Radiological Technology and Medical Physics, Faculty of Allied Health Sciences, Chulalongkorn University, Bangkok, Thailand
4 Department of Radiology, Division of Diagnostic Radiology,King Chulalongkorn Memorial Hospital, Bangkok, Thailand.
5 Department of Radiology, Division of Diagnostic Radiology, Faculty of Medicine, Chulalongkorn University, Bangkok, Thailand.
6 Department of Radiology, Division of Nuclear Medicine, Faculty of Medicine, Chulalongkorn University, Bangkok, Thailand
**Yothin.R@chula.ac.th*

Abstract — **Introduction:** Extramural vascular invasion (EMVI) is a critical biomarker associated with a poor prognosis in colorectal cancer. Magnetic resonance imaging (MRI) is the standard imaging modality for primary staging of rectal cancer, particularly in locally advanced rectal cancer (LARC) patients. However, the sensitivity and specificity of MRI in detection of EMVI (mrEMVI) are still moderate. Radiomics, a non-invasive technique that extracts quantitative features from medical images, has shown potential in predicting tumor prognosis. Therefore, this study aimed to build and evaluate the performance of a radiomic model from mesorectal fat regions in MRI to predict pathologic EMVI in LARC patients. **Methods:** Data from 219 LARC patients and MR images were retrospectively collected, mesorectal fat was the region of interest (ROI). Three radiologists delineated the ROI for 30 datasets to calculate intraclass correlation coefficients (ICC), with ICC > 0.5 was acceptable. 1,288 radiomic features were extracted from each ROI using PyRadiomics version 3.1.0. The data were split into training and validation sets using 5-fold cross-validation. Feature selection was performed using univariate analysis, ICC, and recursive feature elimination. We built and evaluated three models: logistic regression (LR), random forest (RF), and support vector machine (SVM), with statistical analysis conducted using a sign test. **Results:** The fine-tuned LR model achieved an AUC of 0.851±0.017 in the training set and 0.776±0.073 in the validation set. While RF and SVM models performed better in the training set (AUCs: 0.991±0.004 and 0.882±0.016), their performance dropped significantly in the validation set (AUCs: 0.685±0.075 and 0.711±0.073). **Conclusion:** MR-based radiomics from mesorectal fat effectively predicts EMVI in LARC patients.

Keywords — Radiomics, Mesorectal fat, Locally advanced rectal cancer, Extramural venous invasion

I. INTRODUCTION

Colorectal cancer (CRC), which is the third most common malignancy worldwide, is rapidly increasing in Southeast Asia, partly due to cultural factors (1). Extramural venous invasion (EMVI), a significant predictor of poor prognosis in CRC patients, is traditionally diagnosed through mesorectal excision (2). While mesorectal excision, which includes the removal of mesorectal fat, remains the gold standard for diagnosing EMVI, it can also be detected using magnetic resonance imaging (MRI) plays a vital role in tumor staging and guiding treatment decisions for CRC patients, particularly in locally advanced rectal cancer (LARC). However, the sensitivity and specificity of EMVI detection from MRI images are moderate and subject to observer variability. Radiomics, the process of extracting quantitative features from medical images, has shown promise in predicting tumor prognosis. Therefore, this study aimed to develop and validate a radiomics model based on mesorectal fat regions in MRI to predict pathological EMVI in LARC patients.

II. MATERIALS AND METHODS

A. Patient enrollment

This retrospective study was conducted on a single cohort, comprising 219 patients with LARC treated at King Chulalongkorn Memorial Hospital between 2013 and 2021. The inclusion criteria for the study were: (a) patients with LARC, as staged by pre-neoadjuvant chemoradiotherapy MRI; (b) patients who completed neoadjuvant chemoradiotherapy, with chemotherapy administered prior to radiation therapy; and (c) patients with high-spatial-resolution T2-weighted MRI of adequate quality for analysis.

B. Segmentation and feature extraction

The mesorectal fat was drawn as the region of interest (ROI) for this study. Using '3D Slicer' version 5.0.3, a board-certified radiologist manually delineated the ROI on high-spatial-resolution T2-weighted MRI images in the axial oblique plane. To assess the repeatability and inter-operator variability of the radiomic features, three radiologists with 13, 4, and 3 years of experience, respectively, independently contoured thirty examples from the study. Following image segmentation, the MRI images were resampled to a voxel size of 0.5 x 0.5 x 0.5 cm^3. Radiomic features were extracted from the resampled images using the ROI mask, employing 'PyRadiomics' version 3.1.0 within Jupyter Notebook version 7.0.7, with Python version 3.12.1. In total, 1,288 radiomic features were extracted.

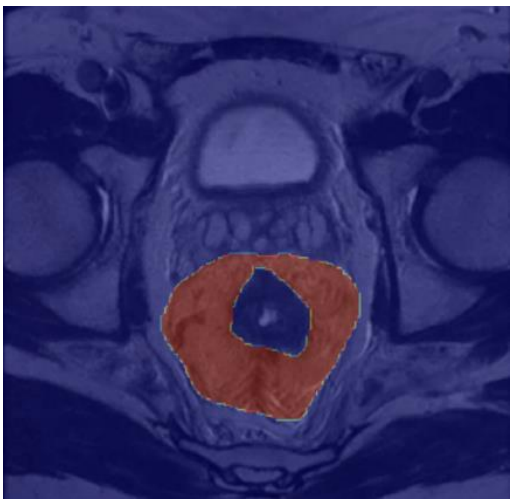

Figure 1. *Example of mesorectal fat MRI image segmentation (orange color area demonstrated mesorectal fat region)*

C. Feature selection

The feature selection process consisted of two steps:

1. The intraclass correlation coefficient (ICC) was applied to evaluate the reproducibility of radiomic features. ICC values were computed from 30 independently delineated cases by three radiologists. Radiomic features with an ICC above 0.5 were considered acceptable.

2. Univariate logistic regression was applied to the radiomic features to evaluate their relevance to pathological status. Recursive feature elimination with cross-validation (RFECV) was performed to minimize the number of features while maximizing the performance of the univariate analysis, as determined by the area under the receiver operating characteristic curve (AUC). The optimized set of radiomic features was selected for model building.

D. Model building and statistical analysis

The data were divided into training set and validation sets using 5-fold cross-validation. Three models were built and evaluated: (a) logistic regression (LR), (b) Random Forest classifier (RF), and (c) support vector machine (SVM). Afterward, fine-tuning will be performed for each model to optimize performance. The best-performing version of each model were used to compare differences in EMVI prediction accuracy, with statistical significance assessed using the sign test and Benjamin-Hochberg were employed to evaluate p-value of the models. All statistical analyses were conducted on Python.

III. RESULTS

A. Model performance

Following model development and evaluation, the LR model achieved an AUC of 0.851 ± 0.017 on the training set and 0.776 ± 0.073 on the validation set. The RF model, although performing exceptionally well on the training set with an AUC of 0.991 ± 0.004, exhibited a notable drop in performance on the validation set with an AUC of 0.685 ± 0.075, suggesting potential overfitting. The SVM model demonstrated an AUC of 0.882 ± 0.016 on the training set and 0.711 ± 0.073 on the validation set.

Model	Train (mean ± sd)	Validation (mean ± sd)	Features
Logistic Regression	0.851 ± 0.017	0.776 ± 0.073	17
Support Vector Machine	0.822 ± 0.016	0.711 ± 0.073	16
Random Forest Classifier	0.991 ± 0.004	0.685 ± 0.075	18

Table 1 *Model performances (Mean values of AUC ± Standard deviation*

B. Model performance Comparison

A statistical sign-test was performed to compare the models. In the training set, the Logistic Regression (LR) model demonstrated statistically significant superior performance compared to the Random Forest (RF) and Support Vector Machine (SVM) models (p-value < 0.05). Similar results were observed in the validation set, where the LR model consistently outperformed the RF and SVM models with statistically significant differences (p-value < 0.05).

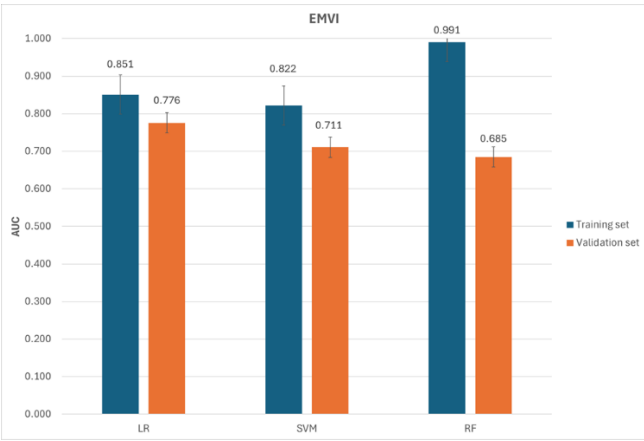

Figure 2. *Overview of model performance*

IV. DISCUSSION

Our findings demonstrate that MRI-based radiomics models derived from mesorectal fat can effectively predict EMVI status in LARC patients. The best-performing model in our study achieved a sensitivity of 0.76 for EMVI detection. In comparison, a literature review by Kim Tae-Hyung. et al.(3) reported an average sensitivity of 0.61 for EMVI detection by radiologists. This indicates that our radiomics model has the potential to be an effective tool for the screening and detection of EMVI.

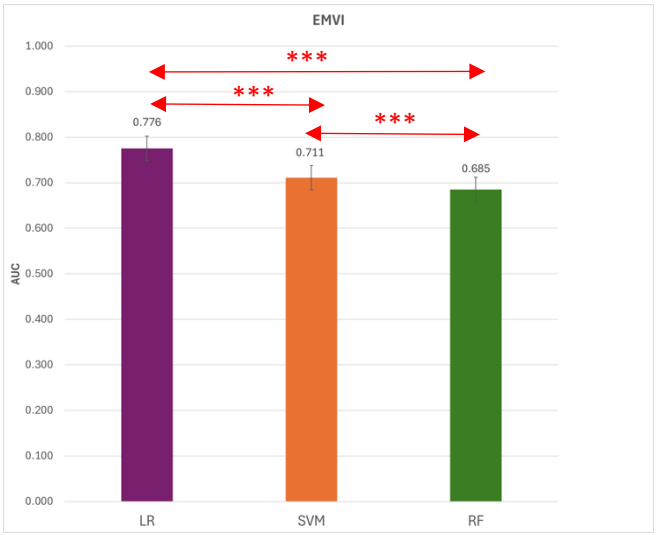

Figure 3 *Model performance comparison *** indicates statistically significant (p-value <0.05)*

Furthermore, when comparing our results to those of Lin et al. (4), who developed and evaluated three MRI-based radiomic models of tumor (LR, SVM, and RF), their best model was the SVM, which attained an AUC of 0.981 on the training set and 0.861 on the validation set. In contrast, the best-performing model in our study was LR model, which achieved an AUC of 0.851 ± 0.017 on the training set and 0.776 ± 0.073 on the validation set. This highlights the potential of MRI-based radiomic models, particularly from mesorectal fat regions, to predict EMVI status. Interestingly, only two radiomic features were consistently selected by all three models: (a) wavelet-HHH_firstorder_Mean and (b) log_sigma-4-0-mm_3D_firstorder_90Percentile. These features were likely to be strongly associated with EMVI status in LARC patients. However, our study had some limitations. As a single-cohort study,

it included a relatively small number of EMVI-positive patients, which might affect the generalizability of the results. Additionally, variations in MRI scanners may influence the radiomic feature properties. Nonetheless, image resampling was performed to mitigate these effects as much as possible.

V. CONCLUSION

Our results indicate that MRI-based radiomic models derived from mesorectal fat can effectively predict EMVI status in LARC patients, regardless of the specific model used. This approach holds potential as an alternative method for personalized treatment planning in LARC patients, offering a non-invasive tool to aid in prognosis and treatment decisions.

ETHICAL CONSIDERATION

This study was approved by Institutional Review Board, Faculty of Medicine, Chulalonkorn University, Bangkok, Thailand

REFERENCES

[1] Pardamean CI, Sudigyo D, Budiarto A, Mahesworo B, Hidayat AA, Baurley JW, Pardamean B. Changing Colorectal Cancer Trends in Asians: Epidemiology and Risk Factors. Oncology Reviews. 2023;17.

[2] Mc Entee PD, Shokuhi P, Rogers AC, Mehigan BJ, McCormick PH, Gillham CM, et al. Extramural venous invasion (EMVI) in colorectal cancer is associated with increased cancer recurrence and cancer-related death. Eur J Surg Oncol. 2022;48(7):1638-42.

[3] Kim TH, Woo S, Han S, Suh CH, Vargas HA. The Diagnostic Performance of MRI for Detection of Extramural Venous Invasion in Colorectal Cancer: A Systematic Review and Meta-Analysis of the Literature. AJR Am J Roentgenol. 2019;213(3):575-85.

[4] Lin X, Jiang H, Zhao S, Hu H, Jiang H, Li J, Jia F. MRI-based radiomics model for preoperative prediction of extramural venous invasion of rectal adenocarcinoma. Acta Radiol. 2024;65(1):68-75.

Contacts of the corresponding author:
Author: Yothin Rakvongthai
Institute: Department of Radiology, Division of Nuclear Medicine, Faculty of Medicine, Chulalongkorn University, Bangkok, Thailand
Street: Pathumwan
City: Bangkok
Country: Thailand
Email: Yothin.R@chula.ac.th

Proficiency testing program for ^{131}I and ^{99m}Tc radiopharmaceuticals using radionuclide calibrators in Thailand

Saejia Korawee[1,*], Dachviriyakij Tanapol[1,2], Thongdeelert Noppaleak[1], Luansri Kanokwan[1], Pungkun Vithit[1]

1 Ionizing Radiation Metrology Section, Office of Atomic for Peace, Ministry of Higher Education, Science, Research and Innovation, Bangkok 10900, Thailand.
2 The Korea Research Institute of Standards and Science (KRISS), Daejeon 34113, Republic of Korea.
*(*Corresponding author: korawee.s@oap.go.th)*

Abstract —**Introduction:** The Office of Atoms for Peace (OAP), the regulatory authority for radiation and nuclear energy safety in Thailand, implemented an Interlaboratory Proficiency Testing (IPT) Program to assess radionuclide activity measurements using radionuclide calibrators in nuclear medicine facilities. **Methods:** The program included 21 laboratories across Thailand for ^{131}I testing and 11 laboratories in Bangkok and nearby areas for ^{99m}Tc testing, conducted over two sessions from 2023 to 2024. Reference materials (RMs) for ^{131}I (6–12 mCi in 3 cc) and ^{99m}Tc (15–25 mCi in 3.6 cc) were prepared in 5 cc glass ampoules, with activity values determined using re-entrant ionization chambers. The RMs and calibration reports were distributed to laboratories for measurement. **Results:** The results were analyzed using percent deviation (%Δ) and normalized error (E_n). For ^{131}I, 96.77% of measurements from 31 radionuclide calibrators across 21 laboratories were within ±5% of OAP reference values. For ^{99m}Tc, 83.33% of measurements from 18 calibrators across 11 laboratories met the same criteria. E_n analysis confirmed accurate uncertainty estimations, with 96.77% of ^{131}I and 100% of ^{99m}Tc results meeting the standard. **Conclusion:** Overall, over 80% of calibrators demonstrated accuracy within ±5% of OAP reference values. Only one ^{131}I calibrator (3.2%) required recalibration to ensure accurate activity measurement.

Keywords — Proficiency testing, Radionuclide calibrator, ^{131}I, ^{99m}Tc, Radiopharmaceutical

I. INTRODUCTION

Thailand has a significant need for accurate and precise activity measurements of short-lived radionuclides used in nuclear medicine. Radionuclide calibrators (RCs), also known as activity meters, are widely used in nuclear medicine facilities to measure radiopharmaceutical activity. Their near 4π geometry ensures high detection efficiency. (Knoll, 2010).

RCs are essential instruments for measuring radiopharmaceutical doses in mCi or Bq. With doses of ^{131}I and ^{99m}Tc often exceeding 100 mCi, accurate measurement is critical for patient safety and radiation protection. The International Atomic Energy Agency (IAEA) requires source and instrument calibration to ensure accurate patient dosimetry. Standards for activity measurement accuracy typically range from ±5% to ±10%, emphasizing the importance of traceability to radiation metrology standards in nuclear medicine.

The Office of Atoms for Peace (OAP), the regulatory authority for radiation and nuclear energy safety in Thailand, has implemented an Interlaboratory Proficiency Testing (IPT) program for laboratories performing radiopharmaceutical activity measurements. This program, a collaborative effort between OAP and nuclear medicine facilities in Thailand, aims to standardize and harmonize activity measurements across the country. By collecting and analyzing results, the IPT program serves as a valuable tool for improving measurement quality and ensuring consistency among practitioners.

II. MATERIALS AND METHODS

The IPT program aimed to evaluate participants' ability to measure the activity (mCi) of two radionuclides, ^{131}I and ^{99m}Tc, using specified reference materials (RMs). To ensure a fair comparison, RC calibration factors were adjusted to values known only to the participants. Among the 23 participating centers, 10 (43%) were located in Bangkok, while the remainder were distributed across various provinces.

A. Preparation of samples

RMs were prepared in 5 cc glass ampoules (33.0 ± 1.0 mm body height, 16.5 ± 0.5 mm outer diameter, 0.55 ± 0.05 mm wall thickness), with 3 cc for ^{131}I activity (6–12 mCi) and 3.6 cc for ^{99m}Tc activity (15–25 mCi). Measurements were performed using a CENTRONIC IG12/N20 re-entrant ionization chamber filled with nitrogen gas at 2 MPa, encased in a 5 cm thick

lead shield, and housed in a temperature-controlled environment. Operating at 400V DC, the system was connected to a Keithley 6517B electrometer/high resistance meter through custom LabView software. The ionization chamber has been calibrated from the National Metrology Institute of Japan (NMIJ). RMs and calibration reports were distributed to laboratories for measurement with their own radionuclide calibrators (RCs). ^{131}I testing was conducted nationwide, while ^{99m}Tc testing was limited to Bangkok and nearby areas.

B. Stability and linearity Testing

The stability of the IPT program was evaluated through repeated measurements of a long-lived ^{166m}Ho standard source with a known activity of 1.97 MBq (0.05 ± 0.0016 mCi) and a 2.5% uncertainty. Thirty measurements were performed within a 30-minute timeframe, yielding a standard uncertainty of 0.03%. The ^{166m}Ho reference material (Serial No. 99-104, reference date: 1999-03-03, produced by JAERI) has a half-life of approximately 1,200 years, making it ideal for long-term stability assessments and statistical analysis of measurement systems.

Instrument linearity was verified prior to distribution to participants using a ^{99m}Tc source, covering an activity range of 5 to 25 mCi. The linearity curve demonstrated an absolute deviation of less than 1.5%.

C. Activity measurements with RCs

The laboratories carried out the measurements, by:

I. Measuring the RM using their own RC (hereafter referred to as the "laboratory value");
II. Measuring the background;
III. Measuring the sample ten times, prepared as outlined in point A;
IV. Measuring the background after the last value measurement;
V. Reporting the results on a data sheet provided by the OAP, including the date and time of each measurement, the corresponding result, and the model and manufacturer of the RC;
VI. Placing the samples in plastic tubes, transferring them to a lead shield, and sending them to the OAP after measurement;
VII. For ^{99m}Tc only, the OAP has recommended adjusting the dial values if the measurement deviates from the OAP reference values by more than ±5%.

All activity readings were performed in the nominal activity units of measurement (mCi) of the RC.

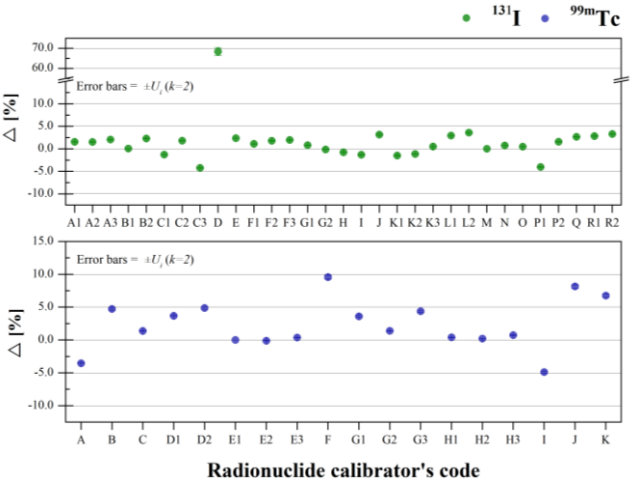

Figure 1. *The percentage deviation between the activity values of ^{131}I and ^{99m}Tc as declared by participants and the reference values provided by the OAP.*

III. RESULTS

The procedure for establishing the reference value involved several steps: The OAP calculated the average of the readings provided by each participant using their RC, then subtracted the average background readings. These values were reported at a specific reference time, with decay corrections applied by the OAP based on the half-life of each radionuclide (Bé et al., 2004). This approach allowed for a comparison of laboratory values from participants, each using their own instrumentation to measure the radioactive sources. To analyze the results of this comparison, statistical indicators commonly used in evaluation tests and interlaboratory comparisons were employed. (Iwahara et al., 2001; UNI CEI EN ISOIEC 17043:2010; International Organization for Standardization, 2015; Olivei-ra et al., 2016).

These indicators included percent deviation (%Δ) and normalized error (E_n) as defined below:

$$\%\Delta = \frac{X_{lab} - X_{ref}}{X_{ref}} \cdot 100 \quad (1)$$

$$E_n = \frac{X_{lab} - X_{ref}}{\sqrt{(U_{lab})^2 + (U_{ref})^2}} \quad (2)$$

Table 1. *Results for ^{131}I*

Lab code	X_{lab} [mCi]	U_{lab} k=2 [%]	X_{ref} [mCi]	U_{ref} k=2 [%]	E_n
A1	12.44	3.00	12.25	3.00	0.04
A2	12.43	3.00	12.25	3.00	0.04
A3	12.50	3.00	12.25	3.00	0.06
B1	12.71	3.00	12.70	3.00	0.00
B2	12.99	3.00	12.70	3.00	0.07
C1	11.62	3.21	11.77	3.00	-0.03
C2	11.98	3.21	11.77	3.00	0.04
C3	11.27	3.21	11.77	3.00	-0.10
D	19.84	3.00	11.78	3.00	1.90
E	11.68	3.00	11.41	3.00	0.06
F1	11.94	3.00	11.81	3.00	0.03
F2	12.02	3.00	11.81	3.00	0.05
F3	12.04	3.00	11.81	3.00	0.05
G1	6.45	3.27	6.40	3.00	0.01
G2	6.39	3.27	6.40	3.00	0.00
H	12.00	3.00	12.09	3.00	-0.02
I	11.30	3.29	11.45	3.00	-0.03
J	11.88	4.19	11.52	3.00	0.05
K1	11.23	3.00	11.40	3.00	-0.04
K2	11.27	3.00	11.40	3.00	-0.03
K3	11.46	3.00	11.40	3.00	0.01
L1	11.84	3.00	11.50	3.00	0.08
L2	11.91	3.00	11.50	3.00	0.10
M	11.69	3.00	11.69	3.00	0.00
N	11.03	3.00	10.95	3.00	0.02
O	11.01	3.00	10.96	3.00	0.01
P1	10.50	3.00	10.94	3.00	-0.10
P2	11.11	3.00	10.94	3.00	0.04
Q	11.07	3.00	10.78	3.00	0.07
R1	10.80	3.00	10.50	3.00	0.07
R2	10.84	3.00	10.50	3.00	0.08

Table 2. *Results for ^{99m}Tc*

Lab code	X_{lab} [mCi]	U_{lab} k=2 [%]	X_{ref} [mCi]	U_{ref} k=2 [%]	E_n
A	21.47	3.00	22.26	3.00	-0.19
B	23.99	3.20	22.91	3.00	0.25
C	16.25	1.67	16.03	3.00	0.06
D1	26.00	3.27	25.08	3.00	0.21
D2	26.30	3.27	25.08	3.00	0.28
E1	16.52	4.24	16.52	3.00	0.00
E2	16.50	4.24	16.52	3.00	0.00
E3	16.58	4.24	16.52	3.00	0.01
F	16.62	3.00	15.17	3.00	0.34
G1	22.50	3.00	21.72	3.00	0.18
G2	22.02	3.00	21.72	3.00	0.07
G3	22.67	3.00	21.72	3.00	0.22
H1	15.01	4.24	14.95	3.00	0.01
H2	14.98	4.24	14.95	3.00	0.01
H3	15.06	4.24	14.95	3.00	0.02
I	15.13	3.00	15.91	3.00	-0.18
J	26.57	3.00	24.57	3.00	0.47
K	16.61	3.00	15.56	3.00	0.25

where X_{lab} and X_{ref} represent the values from the participant (laboratory) and the OAP (reference), respectively, and U_{lab} and U_{ref} are the corresponding expanded uncertainties (k = 2).

- An $E_n \geq 1$ or $E_n \leq -1$ may indicate the need to review the uncertainty estimation or provide a correction for a measurement issue.
- An E_n between -1 and 1 should be considered an indicator of successful performance, provided that the uncertainties are reliable and the deviation ($X_{lab} - X_{ref}$) is smaller than what is required by the participant's customers.

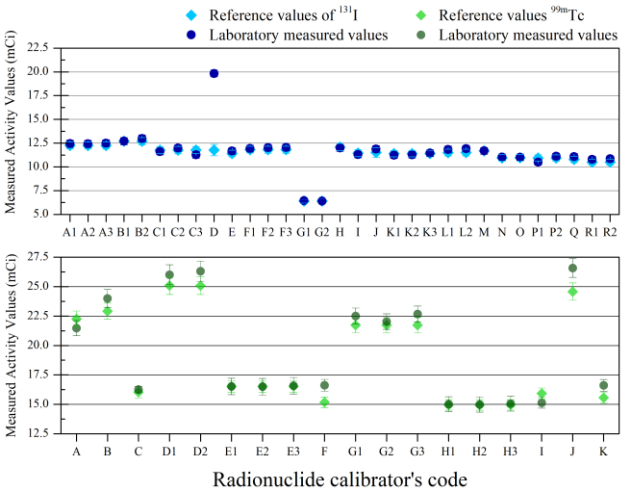

Figure 2. *Measured activity values from participants and the reference, along with their respective uncertainty for ^{131}I and ^{99m}Tc.*

A. ^{131}I

For ^{131}I, only one participant (RC's code D) exhibited a Δ(%) greater than 5%. This same participant had an E_n value greater than 1, and is therefore considered an outlier. Due to the significant discrepancy in the Δ(%) obtained by RC code D, a comparison with the OAP for this radionuclide is currently being arranged. However, it is important to note that this RC uses ^{131}I measurements in clinical practice, but the IPT scenario involved quality control with lower activity levels than typically used in clinical settings. Additionally, all participants who achieved a Δ(%) of less than 5% also had E_n values within ±1.

B. ^{99m}Tc

For ^{99m}Tc, all participants obtained results with an E_n value of less than 1. However, not all

participants achieved acceptable results in terms of Δ(%). For instance, RC codes F, J, and K did not meet the criteria, as shown in Figure 1 (>±5%). This suggests that measurements with low uncertainty might obscure underlying issues with uncertainty estimation, particularly an underestimation of uncertainty.

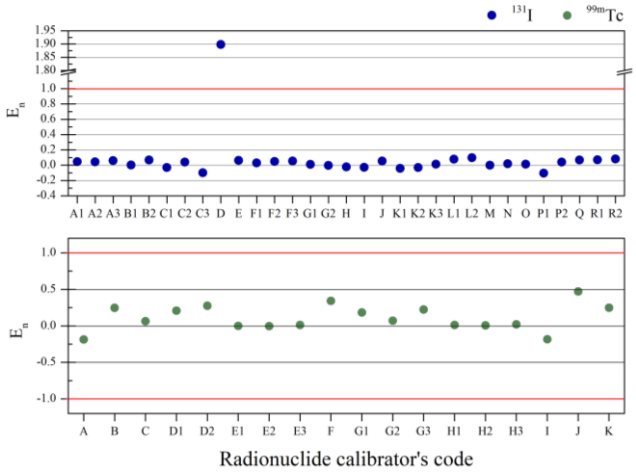

Figure 3. *^{131}I and ^{99m}Tc normalized error.*

IV. DISCUSSION

In this IPT, a result was considered acceptable if the Δ(%) was within ±5% and the E_n was within ±1. The ±5% Δ(%) boundary for the IPT was based on literature recommendations (American Association of Physicists in Medicine, 2012; Park et al., 2019), which generally suggest thresholds between 5% and 10%. Therefore, a ±5% Δ(%) threshold was applied to both radionuclides (^{131}I and ^{99m}Tc) to determine the acceptability of the results. The IPT results for ^{131}I and ^{99m}Tc are presented in Tables 1-2 and Figures 1-3, respectively.

V. CONCLUSION

All participants successfully measured both ^{131}I and ^{99m}Tc within a ±5% deviation from the reference value, achieving success rates of 96.77% and 83.33%, respectively. However, when applying a stricter criterion of E_n within ±1, the proportion of participants meeting both criteria increased significantly: 96.77% for ^{131}I and 100% for ^{99m}Tc.

This underscores the critical role of accurate uncertainty estimation in activity measurements. Participants with results exceeding the ±5% Δ(%) and ±1 E_n thresholds are strongly encouraged to reassess the calibration of their radionuclide calibrators. A comprehensive evaluation of uncertainty, particularly in routine applications, is essential to ensure reliable and accurate measurements.

ACKNOWLEDGEMENTS

The authors express their sincere gratitude to Mr. Thongchai Soodprasert of the OAP for providing calibration factors for the CENTRONIC ionization chamber. Appreciation is also extended to the Ionizing Radiation Metrology (IRM) Section of the Office of Atoms for Peace, Ministry of Higher Education, Science, Research, and Innovation, for funding the IPT program. Finally, the authors thank the Thai nuclear medicine facilities for their efforts in measuring the reference materials using their radionuclide calibrators.

REFERENCES

[1] B´e M.-M, Chist´e V, Dulieu C, Browne E, Chechev V, et al. Table Of Radionuclides, Volume 1 & 2 of Monographie BIPM-5. Bureau International des Poids et Mesures, Pavillon de Breteuil. 2004; F-92310. S`evres, France.

[2] Hino Y. Results from APMP comparisons on radioactivity measurements of ^{58}Co, ^{88}Y and ^{166m}Ho. Appl Radiat Isot. 2002; 56:421-427.

[3] Knoll, Glenn F., 2010. Radiation Detection and Measurement. John Wiley & Sons.

[4] Spagnuolo L, Capogni M, Fazio A, Felice P. National programme for the reliability of ionizing radiation measurements based on inter-laboratory comparisons (ILCs): ILC n◦2 ‘radiopharmaceutical activities. Appl Radiat Isot. 2024; 212:111449.

[5] UNI CEI EN ISOI/EC 17043:2010 Valutazione della conformit`a – Requisiti generali per prove valutative interlaboratorio, 2010.

[6] Vargas C, Pérez S, Baete K, Pommé S, Paepen J, et al. Intercomparison of ^{99m}Tc, ^{18}F and ^{111}In activity measurements with radionuclide calibrators in Belgian hospitals. Phys Med. 2018; 45:137-142

Contacts of the corresponding author:
Author: Korawee Saejia
Institute: Ionizing Radiation Metrology Section, Office of Atomic for Peace, Ministry of Higher Education, Science, Research and Innovation
Street: Vibhavadi-Rangsit
City: Bangkok
Country: Thailand
Email: korawee.s@oap.go.th

Feasibility of total-body fast SPECT imaging for optimized image quality and voxel-based dosimetry in ^{177}Lu molecular radiotherapy using ring-shaped CZT SPECT/CT

Handayani Wuri[1,2], Chantadisai Maythinee[3], Pasawang Panya[3], Noipinit Nut[3], Phromphao Benchamat[3], Damthongsen Panattha[1], Khamwan Kitiwat[1,2,4*]

[1] Department of Radiology, Medical Physics Program, Faculty of Medicine, Chulalongkorn University, Bangkok 10330, Thailand
[2]Department of Radiology, Division of Nuclear Medicine, Faculty of Medicine, Chulalongkorn University, Bangkok 10330, Thailand
[3]Department of Radiology, Division of Nuclear Medicine, King Chulalongkorn Memorial Hospital, The Thai Red Cross Society, Bangkok 10330, Thailand
[4]Department of Radiology, Chulalongkorn University Biomedical Imaging Group, Faculty of Medicine, Chulalongkorn University, Bangkok 10330, Thailand
*(*Corresponding author: kitiwat.k@chula.ac.th)*

Abstract — **Introduction:** Molecular radiotherapy dosimetry requires 3D SPECT scans for accurate absorbed dose calculation, which can be time-consuming and impacting patient comfort. This study evaluated the feasibility of ^{177}Lu therapy dosimetry and image quality based on fast-imaging protocol. **Methods:** The NEMA/IEC body phantom with six fillable spheres filled with ^{177}Lu solution at a 10:1 target-to-background ratio, was scanned for 30 min by SPECT/CT model Veriton-CT 200 with energy window of 113 keV±10%. Simulated acquisition time of 15, 10, 5, and 2 min were performed to assess the quantification accuracy. The signal-to-noise ratio (SNR) was determined by measuring the activity concentration (Bq/cc) in spheres and background. The recovery coefficient (RC) was computed as quotient of the estimated and actual activity concentration in the sphere. Retrospectively, total-body SPECT/CT image of eight ^{177}Lu therapy patients scanned for 28 min at ~4, 24, and 48-72 h post-injection were analyzed. The fast-imaging protocols were simulated by reducing acquisition time to 90%, 80%, 70%, and 60% of original. The absorbed doses in kidneys, liver, spleen, salivary glands, and tumors were calculated as the organs-at-risk (OARs) using MIM voxel-based dosimetry software. Image quality and absorbed dose difference were compared between protocols. **Results:** The phantom study demonstrated declining RC and SNR as acquisition times decreased. The difference between calculated and measured activity concentrations increased up to 38% in the largest sphere. Absorbed dose calculations in OARs revealed relative percentage differences (RPD) <10% in the liver, 13-26% in the salivary gland, spleen, and kidney, and up to 40% in tumors. Shortened acquisition times increased image noise and absorbed dose differences due to reduced counts. **Conclusion:** These results indicate that fast imaging protocol improves patient workflow, however anticipated optimization in image quality and personalized dosimetry were not fully achieved.

Keywords — ^{177}Lu, Molecular Radiotherapy Dosimetry, Shortened Acquisition Time, Ring-shaped SPECT/CT.

I. INTRODUCTION

^{177}Lutetium (^{177}Lu) molecular radiotherapy is increasingly used for targeted cancer treatments, particularly in neuroendocrine tumors (NETs) and metastatic castration-resistant prostate cancer (mCRPC), offering both therapeutic and imaging benefits with minimal toxicity and improved patient survival [1]. Despite advancements in ^{177}Lu therapy, fixed treatment protocols employing a one-size-fits-all approach constrain the achievement of optimal outcomes by disregarding individual patient-specific needs. Variations in anatomy, physiology, and metabolism can lead to underestimate or overestimate the dosimetry calculation [2]. Personalized dosimetry, can address this concerns by delivering more precise doses tailored to individual patients, minimizing side effects and improving therapeutic efficacy. Personalized dosimetry, grounded in the Medical Internal Radiation Dose (MIRD) framework, utilizes organ-level S-values to estimate radiation doses [3]. Recent advancements have introduced voxel-based dosimetry, enhancing precision by calculating doses at voxel levels using SPECT imaging [4]. However, clinical implementation is hindered by logistical challenges, such as long acquisition times, which can affect patient comfort and clinical outcomes. Recent

advances, including 360° ring-shaped CZT-based digital SPECT/CT detectors, improve imaging efficiency and accuracy [5]. These innovations reduce acquisition time while maintaining high-quality imaging, enabling faster dosimetry workflows. This study aims to evaluate the feasibility of shortened acquisition times for dosimetry and image quality in ^{177}Lu therapy using ring-shaped CZT SPECT/CT.

II. MATERIALS AND METHODS

The phantom and clinical study was performed using a SPECT/CT system model Veriton-CT 200 (Spectrum Dynamics Medical). The OSAC algorithm with 12 iterations and 8 subsets, with scatter correction via the Triple Energy Window method (113 keV ±10% energy window) were used for image reconstruction.

A. Phantom Study

An IEC/NEMA phantom was filled with a ^{177}Lu solution, with target-to-background ratio of 10:1. The phantom was scanned for 30 minutes at 2-4 hours, 24 hours, and 48-168 hours post-injection (p.i.). Simulated acquisition time of 15, 10, 5, and 2 min were performed to assess the quantification accuracy.

B. Quantification Performance Evaluation

Volumes of interest (VOI) were drawn using MIM SurePlan™ MRT software to quantify the activity concentration (AC) in term of Bq/mL in the spheres and background.

The recovery coefficient (RC) was determined by dividing the measured activity concentrations with the known activity concentration using Equation (1) as follows:

$$RC = \frac{AC_{measured}}{AC_{known}} \cdot 100 \quad (1)$$

The signal-to-noise ratio (SNR) was calculated to assess image quality, as given by Equation (2):

$$SNR = \frac{AC_{sphere} - AC_{background}}{\sigma_{background}} \quad (2)$$

where AC_{sphere} , $AC_{background}$, and $\sigma_{background}$ were the activity concentration in sphere, in background and standard deviation of the background (Bq/mL), respectively.

C. Clinical Study

Retrospective total-body SPECT/CT image of eight ^{177}Lu therapy patients scanned for 28 min (referred as Standard Scan Time (SST)) at ~4, 24, and 48-72 h post-injection was retrieved from the PACS system. To generate the fast-imaging protocol, acquisition times were simulated to 25, 22, 19, and 16 minutes at each time point (referred as Reduction Time (RT)).

D. Organ and Tumor VOI Delineation

VOIs for organs-at-risk (kidney, liver, spleen, salivary) and tumors were manually delineated on CT images using MIM software. For bone marrow, the VOIs was automatically be generated based on HU values. Delineations were verified by a nuclear medicine physician.

E. Organ and Tumor Dose Calculations

Patient absorbed dose calculations were performed based on multiple time points, using MIM software by utilizing Monte Carlo Simulation approach. The voxel-S value convolution (VSV) method (Eq. (3)) was used in line with the MIRD Pamphlet No. 17.

$$\bar{D}(voxel_k) = \sum \tilde{A}(voxel_h).S(voxel_k \leftarrow voxel_h) \quad (3)$$

Target and source voxel were represented by $voxel_k$ and $voxel_h$. $\bar{D}$ is absorbed dose in Gy. $\tilde{A}$ is time-integrated activity in source voxel in Bq.s/ml. $S(voxel_k \leftarrow voxel_h)$ is the absorbed dose per cumulated activity in Gy/(Bq.s/ml).

F. Statistical Analysis

Image quality difference was evaluated between protocols in terms of RC and SNR. To evaluate the clinical results, we presented relative percentage difference (RPD) of patient absorbed dose using standard and fast protocol.

III. RESULTS

A. Phantom study result

The RC for the largest sphere (37 mm) dropped from 0.87 to 0.75 as acquisition time decreased from 30 to 2 minutes, while SNR fell sharply from 13.9 to 3.7 as shown in Figure 1.

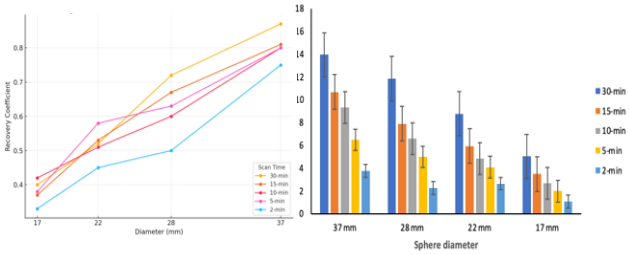

Figure 1. *(a)RC and (b)SNR for the four largest spheres in all scan time.*

B. Clinical study result

Visual assessment of patient image at different acquisition time revealed a difference in image quality (Figure 2). As the acquisition time decreases, a notable increase in image noise and degradation of lesion detectability is observed. The reduced acquisition protocols show diminished contrast and detail, especially in smaller structures.

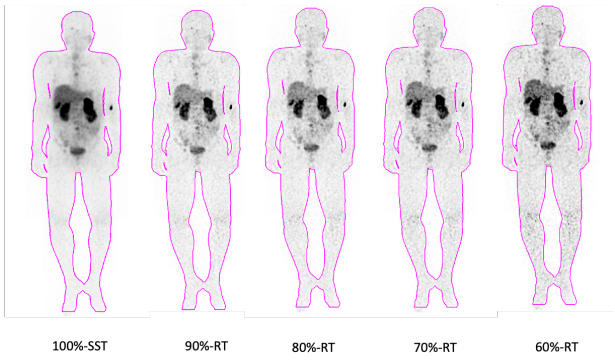

Figure 2. *Visual comparison on different acquisition time. SST = Standard Scan Time and RT = Reduction Time*

The mean absorbed dose per administered activity (Gy/GBq) for target organs and tumors were assessed at different acquisition durations, as shown in the Table 1. For most organs, including the parotid gland, submandibular gland, lacrimal gland, kidneys, spleen, and bone marrow there was a general decrease in absorbed dose as acquisition time reduced. A similar trend was observed for the tumor absorbed dose. However, an exception was noted in the liver, where the absorbed dose slightly increased at 80%-RT (0.45 ± 0.71 Gy/GBq) compared to SST (0.42 ± 0.33 Gy/GBq) before declining at shorter times.

Patient absorbed dose calculations revealed relative percentage differences (RPD) <10% in the liver, 13-26% in the salivary gland, spleen, and kidney, and up to 40% in tumors (Table 2).

IV. DISCUSSION

The findings from both the phantom and clinical studies highlight the impact of acquisition time on image quality and dosimetry accuracy, with implications for optimizing protocols in ^{177}Lu radionuclide therapy.

In the phantom study, the decreasing acquisition time was associated with a consistent reduction in recovery coefficients (RC) and signal-to-noise ratios (SNR). These results illustrate the trade-off between acquisition time and quantitative accuracy, underscoring the degradation of both activity recovery and noise characteristics with shorter imaging durations.

The clinical study reinforced these findings, as shorter acquisition times led to visible increases in image noise and reductions in lesion detectability, particularly in smaller structures. Dosimetric analysis revealed that absorbed doses generally declined with shorter acquisition times for most organs and tumors. However, the liver presented an exception, showing a slight increase in absorbed dose at 80%-RT before declining at shorter times, possibly reflecting variability in liver pharmacokinetics or reconstruction effects. These observations align with previous research, such as the study by Danieli et al.[6], which highlighted the impact of reconstruction protocols on quantitative performance in ^{177}Lu SPECT/CT imaging.

Additionally, relative percentage differences (RPD) in absorbed doses were minimal for the liver but more pronounced in smaller organ such as salivary glands, kidneys, and spleen, while tumors showed the greatest variability. Similarly, Alsarag et al.[7] demonstrated that shorter acquisition times may compromise the spatial resolution, particularly affecting smaller lesions

V. CONCLUSION

Shorter acquisition times led to declines in recovery coefficients, signal-to-noise ratios, and lesion detectability. Relative percentage differences (RPD) in absorbed dose for most organs remained below 30%, suggesting that fast imaging protocols show potential for improving patient workflow, but further tailored acquisition strategies that balance reduced scan times with accurate quantification is necessary to optimize these approaches.

Email: wuri.handayani92@gmail.com

Table 1. *Mean absorbed dose per administered activity in target organ and tumor.*

Acquisition time	Mean Absorbed dose per administered activity (Gy/GBq)					
	Salivary gland	Kidney	Liver	Spleen	Bone marrow	Tumor
SST	0.15 ± 0.13	0.72 ± 0.26	0.42 ± 0.33	0.70 ± 0.78	0.05 ± 0.04	6.48 ± 1.08
90%-RT	0.13 ± 0.13	0.57 ± 0.25	0.42 ± 0.64	0.53 ± 0.50	0.03 ± 0.01	6.08 ± 1.49
80%-RT	0.13 ± 0.14	0.66 ± 0.35	0.45 ± 0.71	0.63 ± 0.60	0.029 ± 0.01	5.39 ± 1.30
70%-RT	0.13 ± 0.13	0.58 ± 0.25	0.43 ± 0.65	0.55 ± 0.52	0.029 ± 0.01	4.86 ± 1.45
60%-RT	0.13 ± 0.13	0.57 ± 0.25	0.42 ± 0.65	0.54 ± 0.51	0.028 ±0.01	4.26 ± 1.46

Table 2. *Relative percent difference of mean absorbed dose per activity of fast acquisition protocol compare with routine protocol*

Acquisition time	Relative Percentage Difference compare to Standard Protocol (%)					
	Salivary gland	Kidney	Liver	Spleen	Bone marrow	Tumor
90%-RT	14.68	22.83	0.75	26.27	55.93	6.37
80%-RT	14.85	8.51	8.04	9.13	61.12	18.10
70%-RT	14.52	22.16	1.58	23.64	63.24	28.39
60%-RT	18.04	23.97	0.93	26.14	67.51	40.95

ACKNOWLEDGEMENTS

The authors are very grateful to all staff at the Division of Nuclear Medicine, Faculty of Medicine, Chulalongkorn University and King Chulalongkorn Memorial Hospital, who have generously supported in this work.

REFERENCES

[1] Malcolm, J., et al., Targeted Radionuclide Therapy: New Advances for Improvement of Patient Management and Response. Cancers (Basel), 2019. 11(2).

[2] Danieli, R., et al., Personalized Dosimetry in Targeted Radiation Therapy: A Look to Methods, Tools and Critical Aspects. J Pers Med, 2022. 12(2).

[3] Lee, M.S., et al., Whole-Body Voxel-Based Personalized Dosimetry: The Multiple Voxel S-Value Approach for Heterogeneous Media with Nonuniform Activity Distributions. J Nucl Med, 2018. 59(7): p. 1133-1139.

[4] Bolch, W.E., et al., MIRD pamphlet No. 17: the dosimetry of nonuniform activity distributions--radionuclide S values at the voxel level. Medical Internal Radiation Dose Committee. J Nucl Med, 1999. 40(1): p. 11S-36S.

[5] Desmonts, C., et al., Evaluation of a new multipurpose whole-body CZT-based camera: comparison with a dual-head Anger camera and first clinical images. EJNMMI Phys, 2020. 7(1): p. 18.

[6] Danieli, R., et al., Quantitative ^{177}Lu SPECT/CT imaging for personalized dosimetry using a ring-shaped CZT-based camera. EJNMMI Phys, 2023. 10(1): p. 64.

[7] Alsarag, L., et al., Reducing Lu 177-Vipivotide Tetraxetan (PSMA) Acquisition Time While Maintaining Spatial Resolution. 2023, Soc Nuclear Med.

Contacts of the corresponding author:
Author: Kitiwat Khamwan, Ph.D
Institute: Department of Radiology, Faculty of Medicine, Chulalongkorn University
Street: Rama IV Road, Phatumwan
City: Bangkok
Country: Thailand

Comparing image quality characteristics of different post-filtered Iodine-131 SPECT: A phantom study

Rattanamongkonkul Pattaravarin[1], Krisanachinda Anchali[2], Chuamsaamarkkee Krisanat[3*]

1 Department of Radiology, Maha Vajiralongkorn Thanyaburi Hospital, Pathumthani, Thailand.
2 Department of Radiology, Faculty of Medicine, Chulalongkorn University, Bangkok, Thailand.
3 Department of Diagnostic and Therapeutic Radiology, Faculty of Medicine, Ramathibodi Hospital, Mahidol University, Thailand.
*krisanat.ch@gmail.com

Abstract — **Introduction:** Single photon emission computed tomography (SPECT) Iodine-131 (^{131}I) imaging is a nuclear medicine technique that has become an important tool for diagnostic of thyroid cancer and accurately localizing treatment outcomes after high-dose thyroid ablation. However, the SPECT image quality is limited by the reconstructed images' finite spatial resolution and noise. Typically, the post-processing filter is the common method that is applied after SPECT reconstruction to suppress noise and improve the image quality. Hence, this study aims to evaluate the effect of post-filter on ^{131}I SPECT/CT using three types of filters: Butterworth, Hann, and Gaussian. **Methods:** The NEMA/IEC phantom was filled with an aqueous solution of ^{131}I with a sphere-to-background ratio of 10:1 (activity concentration in the sphere of 740 kBq/mL, background of 74 kBq/mL) acquired by the dual-head SPECT/CT GE 870 DR. The OSEM reconstruction technique (4 iterations, 8 subsets) was employed as a clinical routine, followed by applying three post-filters: Butterworth, Hann, and Gaussian with different parameter settings after reconstruction. The contrast-to-noise ratio (CNR) and relative noise were evaluated and compared for image quality analysis. **Results and Discussion**: The CNR of all spheres increased with the increasing cut-off frequency of the Butterworth filter. Similarly, the CNR generally increased with the increasing cut-off frequency of the Hann filter, except at the smallest sphere diameter showed a decreased CNR at higher cut-off frequencies. For the Gaussian filter, the CNR results decreased with increasing the filter size in sphere size from 13 mm to 37 mm. The smallest sphere showed the opposite result. In terms of noise, the noise decreased with the decreasing of the cut-off frequency of the Butterworth filter and Hann filter. While, the Gaussian filter shows decreased noise when the FWHM increases. **Conclusion:** These findings highlight the importance of optimizing filter parameters to balance image quality. Post-filtering impacts the image quality and could influence lesion detectability, especially in the smallest sphere of ^{131}I SPECT for clinical thyroid imaging.
Keywords — Butterworth filter, Hann filter, Gaussian filter, SPECT, I-131.

I. INTRODUCTION

The most commonly used radionuclide therapy for several benign and malignant thyroid diseases is radioiodine (^{131}I) [1]. The gamma camera is an imaging modality with high sensitivity which is the non-invasive modality that can provide the planar whole-body scintigraphy of ^{131}I to detect the local disease and metastasis [1-2]. Recently, SPECT/CT has been used in addition to whole-body scans, in which SPECT/CT images gain benefits over planar images regarding tumour localization by image contrast improvement and increasing quantification accuracy [2,3]. However, the quality of SPECT/CT images degrades because of the limited spatial resolution and high noise through several factors such as attenuation and scattering of radiation that passes through tissue and collimator-detector system [1-4]. Moreover, ^{131}I has a complex spectrum of emission, so after ^{131}I is penetrated through the septal collimator (HE), it causes the degradation of the image resolution and contrast and can create the image noise. These effects impact on the accuracy of the image information [2,4]. Post-filtering is necessary for the process of SPECT image reconstruction to improve image quality which, including smoothing, edge enhancement, resolution recovery, and also decreasing the noise in the image [5,6]. The smoothing filter or low pass filter is the common method to reduce the statistical noise in a SPECT image by allowing the loss frequency and blocking the high frequency [2,5].

Hence, this study aims to evaluate the effect of post-filter on ^{131}I SPECT/CT using three types of filters: Butterworth, Hann, and Gaussian.

II. MATERIALS AND METHODS

Imaging in this study was performed with dual-heads SPECT/CT (GE discovery NM/CT 870, GE Healthcare) equipped with high energy (HEGP) collimators. SPECT/CT data were collected using the NEMA IEC body phantom with six spheres with diameters of 10, 13, 17, 22, 28, 37 mm, respectively. The sodium iodide (^{131}I NaI) aqueous solution was used in which the activity concentration of the sphere-to-background ratio of 10:1, which ^{131}I activity concentration of 740 kBq/mL for the spheres and 74 kBq/mL for background [7,8].

A. Data collection

The acquisition protocol was used as a routine protocol for ^{131}I SPECT/CT in the Division of Nuclear Medicine, Department of Diagnostic Radiology, Maha Vajiralongkorn Thanyaburi Hospital. The matrix size was set at 128×128. The acquisition data were obtained by step and shoot mode with 60 views for 360º rotation and time per projection was 25 seconds. The reconstruction process used the ordered subset expectation maximization (OSEM) methods (4 iteration 8 subsets) for the reconstruction image. The data set of images evaluated the effect of post-filter in three types of low pass filters: the Butterworth filter (the cut-off frequency of 0.3, 0.7, 1.1 with the order of 10), the Hann filter (the cut-off frequency of 0.3, 0.7, 1.1), and the Gaussian filter (FWHM of 1, 3, and 6) were evaluated. The reconstruction processes were performed using the Xeleris 4.1 workstation (GE Healthcare, USA).

B. Data Analysis

The comparison of images of the data will be evaluated by quantitative analysis using the contrast-to-noise ratio (CNR) for each sphere, and relative of noise [6,11].

The contrast-to-noise ratio (CNR) is defined by equation 1.

$$CNR = \left|\frac{C - C_{BG}}{\sigma_{BG}}\right| \quad (1)$$

Where C was the average count in the interesting sphere ROI, C_{BG} was the average count in the background ROI and σ_{BG} was the standard deviation in the background ROI.

The relative of noise in the image using equation 2.

$$Noise\ (\%) = \frac{\sigma_{BG}}{C_{BG}} * 100 \quad (2)$$

Where σ_{BG} was the standard deviation in the background ROI and C_{BG} was the average count in the background ROI.

Then, the quantitative analysis was performed in which the largest dimension of spheres was selected to draw the circular ROIs with the size of about 50% of each sphere and the background sphere are center of the phantom. The count, pixel area, and standard deviation of the background were recorded which ROIs were repeatedly drawn on three separate occasions to eliminate inconsistency. The CNRs and noise were calculated and plotted.

III. RESULTS

In this study, the image quality characteristics of different filters on the detectability were evaluated using CNR and Noise related to the different sphere diameters. The Butterworth filter result is shown in Figure 1. The result of CNR shows an increase in the cut-off frequency in all spheres. Furthermore, the noise show decreased with decreasing of cut-off frequency.

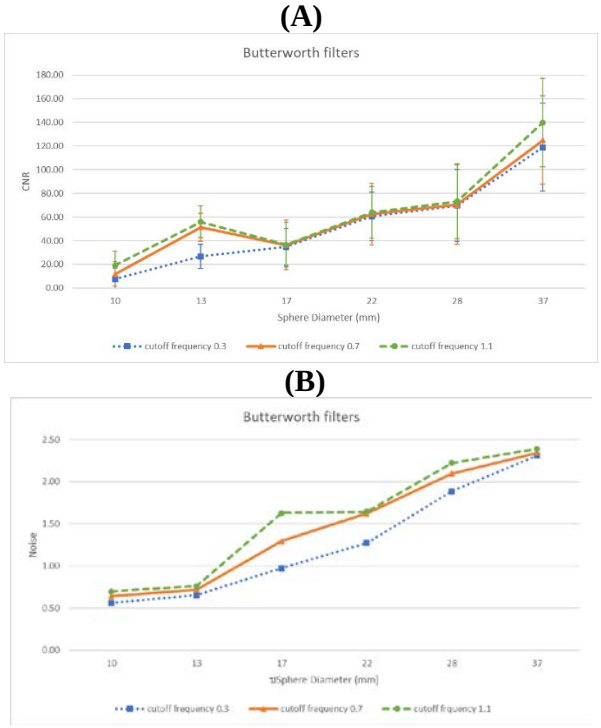

Figure 1. *(A) the CNR (mean ± SD) and (B) Noise of the Butterworth filters with the different cutoff frequency on sphere diameters.*

For the result of the Hann filter, the CNR increased as the cutoff frequency of the Hann filter increased in Figure 2, while the smallest sphere was observed to have the highest CNR

when using a cut-off frequency of 0.3 and the CNR of the smallest sphere showed a decrease in the cut-off frequency of Hann filter. Figure 2 (B) shows the noise result of the different cut-off frequencies of the Hann filter, which decreased in the cutoff frequency the noise decreased.

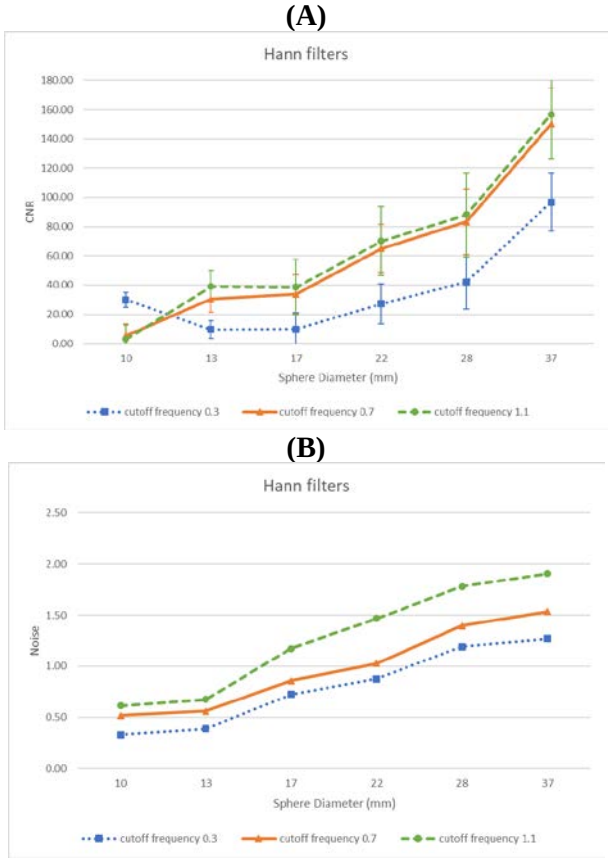

Figure 2. *(A) the CNR (mean ± SD) and (B) Noise of the Hann filters with the different cutoff frequency on sphere diameters.*

The effect of the Gaussian filter is shown in Figure 3, in which the CNR result increased as the FWHM of filter size decreased. However, the smallest sphere diameter shows an increase in CNR when the FWHM of Gaussian increased. Additionally, the noise results of the effect of the Gaussian filter are shown in Figure 3 (B). The noise decreased with increased FWHM of filter size on all the sphere diameters.

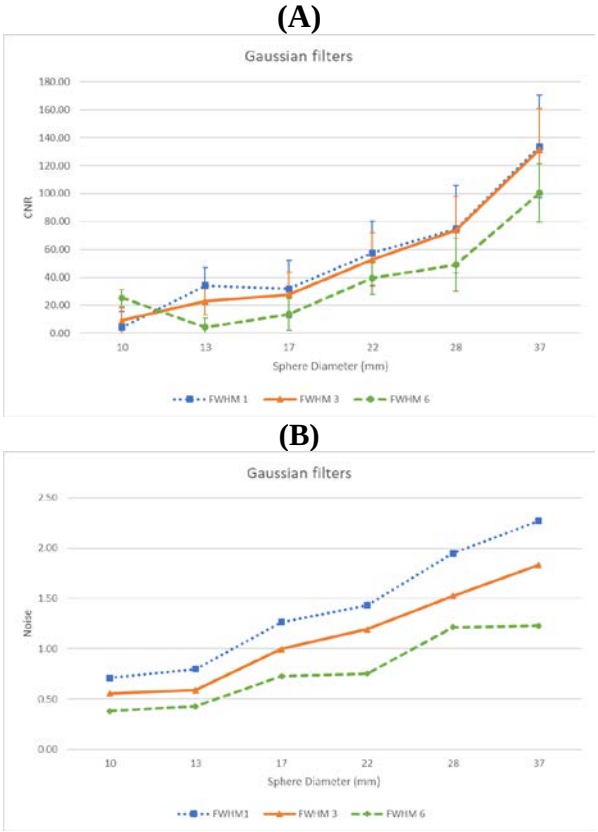

Figure 3. *(A) the CNR (mean ± SD) and (B) Noise of the Gaussian filters with the different FWHM on sphere diameters.*

IV. DISCUSSION

Based on our results, the Butterworth filter aligns with Kim, Ha Gyun et al.'s previous findings and H.I. Abdelkader et al., showing that CNR increases with higher cutoff frequencies [10,13]. Noise levels decrease as the cut-off frequency is lowered, reflecting the low-pass nature of the Butterworth filter, which smooths images by suppressing high-frequency components [5,10-13].

Similarly, the results for the Hann filter confirm previous studies, indicating its effectiveness in reducing noise, although it does not preserve edges. The Hann filter rapidly attenuates frequencies to zero by adjusting the cut-off frequency [5,9-13]. On the other hand, the Gaussian filter effectively reduces noise and smooths the background, but this smoothing leads to image blurring and reduced CNR due to spill-out effects [11-14].

When comparing the smallest spheres, the Hann filter (cut-off of 0.3) produced the highest CNR, followed by the Gaussian filter (FWHM of 6) and the Butterworth filter (cut-off of 1.1 with order 10). Noise reduction followed the same trend, with the Hann filter demonstrating

the greatest noise suppression, followed by the Gaussian and Butterworth filters. The Hann filter's ability to rapidly minimize noise highlights its effectiveness in enhancing image quality [5].

These findings underscore the importance of filter selection and parameter optimization for 131I SPECT/CT imaging. To preserve detectability, the filter must balance noise reduction, contrast, resolution, and image detail. Future studies should further evaluate the relationship between image resolution and sphere diameter to refine filter selection criteria.

V. CONCLUSION

Our results indicate that filter parameters play a crucial role in optimizing image detectability by balancing noise reduction, CNR, contrast, and image detail. To ensure accurate diagnostic imaging, especially for small lesion, careful selection and optimization of filter parameters are essential. Consideration of factors such as resolution recovery in relation to lesion size is necessary to enhance image quality and maintain diagnostic accuracy.

ACKNOWLEDGEMENTS

The authors would gratefully acknowledge the Department of Diagnostic and Therapeutic Radiology, Faculty of Medicine, Ramathibodi Hospital for supporting equipment as well as giving technical support throughout the experiment.

REFERENCES

[1] Silberstein EB, Alavi A, Balon HR, Clarke SE, Divgi C, Gelfand MJ, Goldsmith SJ, Jadvar H, Marcus CS, Martin WH, Parker JA. The SNMMI practice guideline for therapy of thyroid disease with 131I 3.0. Journal of Nuclear Medicine. 2012 Oct 1;53(10):1633-51.

[2] Cherry SR, Sorenson JA, Phelps ME. Physics in nuclear medicine. Saunders; 2013 Jul.

[3] Spanu A, Solinas ME, Chessa F, Sanna D, Nuvoli S, Madeddu G. 131I SPECT/CT in the follow-up of differentiated thyroid carcinoma: incremental value versus planar imaging. Journal of Nuclear Medicine. 2009 Feb 1;50(2):184-90.

[4] Buvat I. Quantification in emission tomography: Challenges, solutions, and performance. Nuclear Instruments and Methods in Physics Research Section A: Accelerators, Spectrometers, Detectors and Associated Equipment. 2007 Feb 1;571(1-2):10-3.

[5] Lyra M, Ploussi A. Filtering in SPECT image reconstruction. International Journal of Biomedical Imaging. 2011;2011(1):693795.

[6] Van Gils CA, Beijst C, Van Rooij R, De Jong HW. Impact of reconstruction parameters on quantitative I-131 SPECT. Physics in Medicine & Biology. 2016 Jun 28;61(14):5166.

[7] Erdi YE. Limits of tumor detectability in nuclear medicine and PET. Molecular imaging and radionuclide therapy. 2012 Apr;21(1):23.

[8] Pereira JM, Stabin MG, Lima FR, Guimarães MI, Forrester JW. Image quantification for radiation dose calculations—limitations and uncertainties. Health physics. 2010 Nov 1;99(5):688-701.

[9] Taylor D. Filter choice for reconstruction tomography. Nuclear Medicine Communications. 1994 Nov 1;15(11):857-9.

[10] Kim HG, Kim SM, Woo JR, Oh SW, Lee JS, Kim YK. The Evaluation of Images with Various Filters in I-131 SPECT/CT. The Korean Journal of Nuclear Medicine Technology. 2014;18(1):62-8.

[11] Erojo M. *Quantitative I-131 SPECT for thyroid cancer radionuclide therapy* (Master's thesis, Itä-Suomen yliopisto).

[12] Sayed IS, Ismail SS. Comparison of Low-Pass Filters for SPECT Imaging. International journal of biomedical imaging. 2020;2020(1):9239753.

[13] H.I. Abdelkader et al. Evaluating the effect of using different filters in thyroid SPECT image reconstruction. Int. J. Sci. Eng. Res. (2020).

[14] Wernick MN, Aarsvold JN. Emission tomography: the fundamentals of PET and SPECT. Elsevier; 2004 Dec 7.

Contacts of the corresponding author:
Author: Krisanat Chuamsaamarkkee
Institute: Department of Diagnostic and Therapeutic Radiology, Faculty of Medicine, Ramathibodi hospital, Mahidol University
Street: 270 Rama VI Rd, Thung Phaya Thai, Ratchathewi
City: Bangkok
Country: Thailand
Email: krisanat.ch@gmail.com

Optimization of shortening acquisition for quantitative 99mTc bone SPECT imaging with ordered subset conjugate gradient minimizer reconstruction: A phantom study

Songprakhon Rangsee[1], Krisanachinda Anchali[2], Chuamsaamarkkee Krisanat[3,*]

1 Division of Nuclear Medicine, Department of Radiology, Surin Hospital, Muang Surin, Surin, Thailand,
2 Department of Radiology, Faculty of Medicine, Chulalongkorn University, Bangkok, Thailand
3 Department of Diagnostic and Therapeutic Radiology, Faculty of Medicine, Ramathibodi Hospital, Mahidol University, Bangkok, Thailand
*(*Corresponding author: krisanat.ch@gmail.com)*

Abstract — **Introduction:** Bone Single Photon Emission Computed Tomography (SPECT) imaging with Ordered Subset Conjugate Gradient Minimizer (OSCGM) reconstruction is a modern technique to improve the image quality and quantitative accuracy of SPECT images for the diagnosis and evaluation of various skeletal disorders. However, standard protocol often suffers from long acquisition times. This study aimed to optimize protocol of shortening acquisition time for quantitative bone SPECT with OSCGM using the ACR PET phantom. **Methods:** The hot cylinders of the American College of Radiology (ACR) PET phantom were filled with a bone-equivalent solution and technetium-99m (99mTc). This phantom was acquired by SPECT system using step-and-shoot mode with time per view at 5, 8, 10, 15, 20, and 30 seconds, respectively. SPECT images were reconstructed using OSCGM. The volume of interests (VOIs) placed at the center of each hot cylinders for measuring the set of standard uptake values (SUV), the activity concentration (AC), the percent coefficient of variation (%CV), and the recovery coefficient (RC). **Results:** The AC values were independent of acquisition time for larger cylinders but significant reductions were observed in smaller cylinders. Moreover, the quantitative results of time per view below 10 second showed increased deviations in smaller cylinders. **Conclusion:** The shortened acquisition time per view at 10 seconds can be set when using the step and shoot mode for quantitative 99mTc bone SPECT imaging with OSCGM reconstruction.
Keywords — Quantitative, Bone SPECT, OSCGM

I. INTRODUCTION

Bone scintigraphy using technetium-99m methylene diphosphonate (99mTc-MDP) remains a pivotal diagnostic tool for detecting bone metastases, fractures, and other skeletal abnormalities. SPECT imaging, particularly when combined with quantitative reconstruction techniques, enhances the ability to localize and quantify tracer uptake, thereby improving diagnostic accuracy [1]. Quantitative imaging enables measurement of SUV which offer objective and reproducible metrics for assessing tracer distribution and metabolic activity. However, the accuracy of quantitative 99mTc bone SPECT heavily depends on advanced reconstruction techniques that account for attenuation, scatter, and resolution recovery [2].

The ordered subset conjugate gradient minimizer (OSCGM) reconstruction algorithm represents a significant advancement in SPECT imaging technology. OSCGM combines the speed of ordered subset techniques with the precision of gradient-based optimization, offering improved convergence and image quality for quantitative imaging [3]. By addressing limitations such as image noise and resolution artifacts commonly encountered in traditional iterative reconstruction methods, OSCGM holds the potential to enhance both visual and quantitative accuracy. Its application in bone SPECT imaging could facilitate more precise quantification of tracer uptake. However, standard protocol of OSCGM often suffers from long acquisition times.

Shortening acquisition time has been a focal point of optimization in clinical imaging due to its potential to reduce patient discomfort, motion artifacts, and overall procedural time. However, shorter acquisition durations often lead to increased noise and reduced image quality, posing challenges for accurate quantification [4]. In bone SPECT imaging, achieving a balance between acquisition time and quantitative accuracy is particularly critical, especially when using advanced reconstruction algorithms like OSCGM. This study aims to evaluate the feasibility of optimizing acquisition time in quantitative 99mTc bone SPECT imaging with OSCGM while maintaining high levels of accuracy and reproducibility.

II. MATERIALS AND METHODS

A. Phantom preparation

The phantom measurements were performed using the ACR-approved PET phantom with four

of thin-walled cylinders (8, 12, 16, and 25 mm in diameter). The phantom was filled with a bone-equivalent solution of K_2HPO_4 and technetium-99m, with specific activity of 200 kBq/ml for each of thin-walled cylinders and 8 kBq/ml for the background. The phantom was acquired with the clinical bone protocol.

B. SPECT/CT: Data acquisition and reconstruction

Imaging was acquired using a Symbia Intevo Bold SPECT/CT system, equipped with the low energy high resolution collimator (Siemens Healthcare, Erlangen, Germany). SPECT acquisitions were performed using the following parameters: energy window 15% at 140 keV with lower window 15% for scatter correction, matrix size 250 x 250 and zoom 1.0, a total of 120 projections over 360° in non-circular orbit and step-and-shoot mode. The time per view 30 second was determined as a standard protocol (STP). The image protocols were set following Table 1.

Table 1. *Image protocol*

Protocol	Time per view	Acquisition time
STP	30 sec	33 min
A	20 sec	23 min
B	15 sec	18 min
C	12 sec	15 min
D	10 sec	12 min
E	8 sec	10 min
F	5 sec	7 min

CT imaging was acquired at 110 kV and 100 reference mA using adaptive dose modulation (CAREDose 4D) with a pitch 0.8, 1 s rotation, and 2 × 1.5 mm collimation. The CT data were reconstructed with a 3.0 mm slice thickness, a 512 × 512 matrix into a 500 mm diameter field of view (FOV). The SPECT/CT images were reconstructed using OSCGM for the number of iterations and the full width at half maximum (FWHM) of the Gaussian filter depending on counts of projection data. SEPCT/CT images were reconstructed and converted to activity concentration using system sensitivity with a Cobalt-57 standard source of NIST traceable calibration.

C. Data analysis

All SPECT/CT images were analyzed by drawing the VOIs placed at the center of each cylinder by using the MM Oncology on Syngo.Via system Version 60S (Siemens Healthcare, Erlangen, Germany) for measuring the activity concentration (AC) and other quantitative values as following;

The percent coefficient of variation (%CV) was used to estimate the image noise. This value was computed from standard deviation divided by the mean of AC.

The standard uptake values (SUV) can compute by using equation (1)

$$\text{SUV} = \frac{\text{Activity concentration } (\frac{\text{MBq}}{\text{ml}})}{\frac{\text{Injected dose (MBq)}}{\text{Patient's body weight (kg)}}} \qquad (1)$$

There were three of SUV results that showed in MM Oncology including; SUVmax is the maximum SUV value in a selected ROI, representing the highest concentration of tracer uptake. Next, the SUVmean is the average SUV value within the ROI, giving a more generalized measure of tracer distribution and the SUVpeak is the average SUV in a small, high-uptake area (typically a 1 cm^3 spherical region), balancing sensitivity and reproducibility.

The recovery coefficients (RC) were determined using the mean AC in the sphere and the real activity concentration.

D. Statistical analysis

The Friedman test was used for statistical evaluations of the AC, %CV, and RC results from each protocol using IBM SPSS statistics version 20 (IBM Corp., Armonk, NY, USA).

III. RESULTS

The bone SPECT images of each protocol clearly showed all of the hot cylinder in phantom (Figure 1). The effect of acquisition time was not visually noticeable in the bone SPECT with OSCGM.

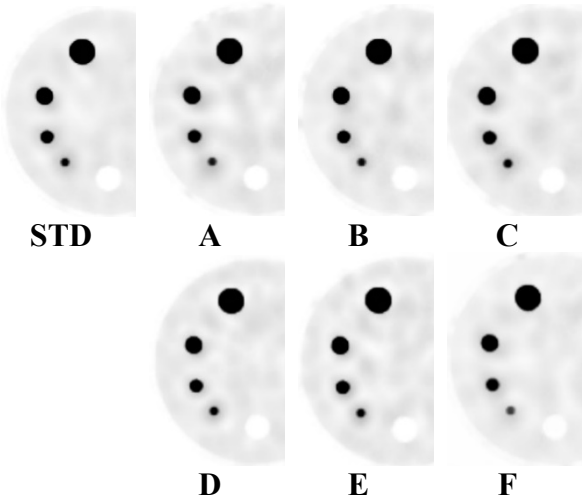

Figure 1. *Axial bone SPECT images of each protocol. The effect of acquisition time was not visually noticeable.*

The activity concentration values for each protocol and cylinder size compared to the STD protocol. The AC values of 12-, 16-, and 25-mm cylinders were independent of the acquisition time.

Protocols **E** and **F** exhibited significant reductions in activity concentration for smaller cylinders (12 mm and 8 mm), particularly in the 8 mm size where Protocol **F** had the largest deviation (-22.33%). Moreover, the statistical result showed significant differences in AC value at least two protocols from STD, $X^2 = 18.43$, $p = 0.005$. (Figure 2)

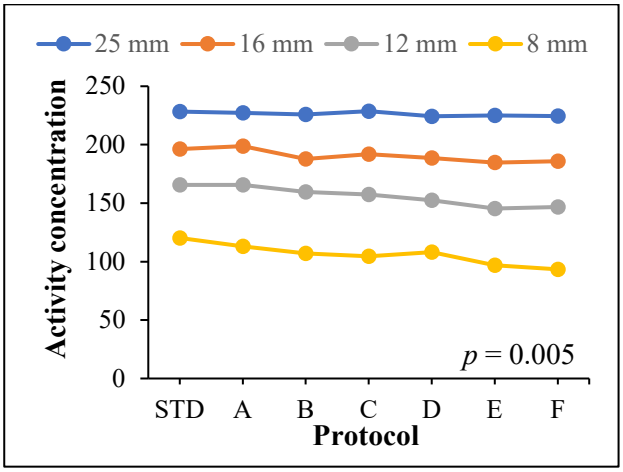

Figure 2. *The activity concentration at each protocol. There were significant differences of AC in protocol E and F from STD.*

There was no %CV of each protocol greater than 10%. The %CV decreased with an increase in acquisition time, suggesting a more stable signal for longer acquisition protocols. The statistical result showed significant differences in %CV value at least two protocols from STD, $X^2 = 13.29$, $p = 0.039$. (Figure 3)

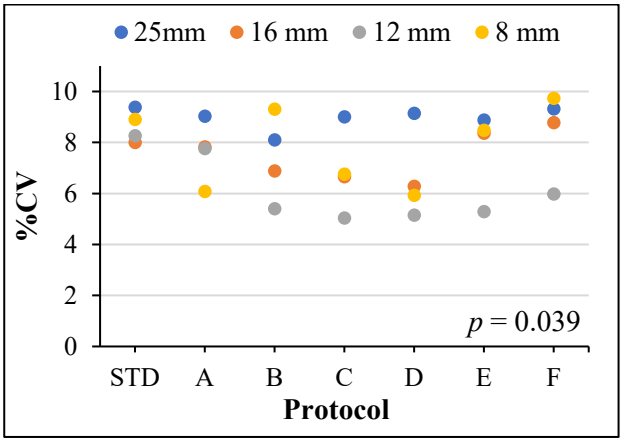

Figure 3. *The %CV at each protocol. There were significant differences of %CV values*

The SUV_{max}, SUV_{peak}, and SUV_{mean} were similar among each protocol. However, The SUV values slightly decrease in relation to the reduction in acquisition time. The percentage difference in each protocol compared with STD showed protocol E and F exhibited the largest deviations, particularly for smaller cylinders (12 mm and 8 mm), suggesting potential limitations in detecting small objects (Table 2). The percentage differences for SUV_{max}, SUV_{peak}, and SUV_{mean} increased as the cylinder size decreased across most protocols, highlighting the challenge of achieving accurate quantification in smaller objects

Table 2. *The percentage differences of SUV_{max}, SUV_{peak}, and SUV_{mean} in each protocol compared with STD protocol.*

	Protocol					
SUV_{max}	A	B	C	D	E	F
25mm	1.85	2.06	-0.03	2.46	-0.25	0.69
16mm	3.73	9.10	7.34	9.64	6.93	8.66
12mm	2.74	8.39	7.84	9.39	14.94	13.16
8mm	6.34	6.86	8.88	9.87	19.22	22.34
SUV_{peak}	A	B	C	D	E	F
25mm	1.66	1.31	-1.39	1.55	-0.78	-0.19
16mm	3.73	9.10	7.34	9.64	6.93	8.66
12mm	2.39	8.86	490	7.84	11.76	10.10
8mm	5.77	9.19	9.35	8.78	17.24	18.29
SUV_{mean}	A	B	C	D	E	F
25mm	1.58	1.64	1.00	2.32	2.02	2.23
16mm	1.52	4.00	3.41	5.04	6.66	4.59
12mm	2.19	9.89	6.49	9.61	13.75	12.98
8mm	4.75	9.11	9.45	9.33	18.27	21.15

The recovery coefficient (RC) for each protocol and cylinder size (25 mm, 16 mm, 12 mm, 8 mm) compared to the STD protocol were presented in the figure 4. The recovery coefficient decreases with smaller cylinder sizes for all protocols, highlighting the challenge of accurately recovering activity in small objects. The STD protocol remains the most consistent, with Protocol A performing comparably well, while Protocol F demonstrated the lowest recovery efficiency for smaller cylinders. The statistical result showed significant differences in RC value at least two protocols from STD, $X^2 = 20.24$, $p = 0.003$.

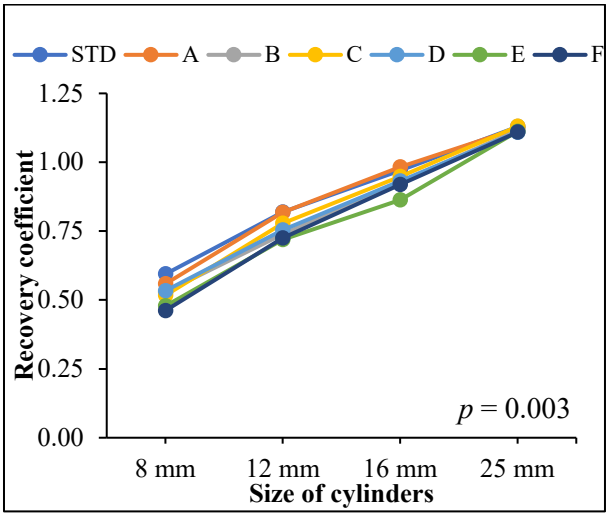

Figure 4. *The recover coefficient for each protocol and cylinder size. There were significant differences of RC in protocol E and F from STD.*

IV. DISCUSSION

This study aimed to evaluate the impact of shortened acquisition times on quantitative accuracy in 99mTc bone SPECT imaging reconstructed with the OSCGM. This study evaluated the performance of various acquisition protocols for bone SPECT imaging by analyzing key quantitative parameters, including AC, %CV, SUV values, and RC, across different cylinder sizes in a phantom.

The AC were largely consistent across protocols for larger cylinders, indicating that AC is relatively independent of acquisition time for larger objects. However, for smaller cylinders (8 mm), significant reductions in AC were observed in protocols **E** and **F**, with Protocol **F** showing the largest deviation (-22.33%) compared to the STD protocol. Statistical analysis confirmed significant differences in AC values between at least two protocols and the STD protocol. These findings suggest that protocols with shorter acquisition times may face challenges in accurately quantifying activity for smaller objects due to partial volume effects and limited resolution [5,6]. The %CV showed good reproducibility in most cases. However, %CV decreased as acquisition time increased, suggesting that longer acquisition durations provide more stable signals. shorter acquisition times may compromise quantitative stability [4,7]. Protocols **E** and **F** exhibited the largest percentage deviations in SUV values, particularly for smaller cylinders (12 mm and 8 mm). These deviations indicate that shortened acquisition times may limit the ability to accurately detect and quantify smaller objects due to noise amplification and partial volume effects in SPECT imaging [5,8]. The RC values decreased for smaller cylinder sizes across all protocols, reflecting the inherent difficulty of accurately recovering activity in small objects due to resolution limitations and noise effects [9,10].

Shortening the acquisition time for 99mTc bone SPECT imaging using OSCGM reconstruction was feasible while maintaining visual image quality and acceptable quantitative accuracy for larger objects. However, challenges arise with small objects, where shortened acquisition protocols, particularly E and F, exhibit significant limitations in terms of AC, SUV metrics, %CV, and RC. Protocol **D** demonstrated performance comparable to the STD protocol, suggesting that it could serve as an optimized alternative for reducing acquisition time without compromising quantitative accuracy.

V. CONCLUSION

The shortening acquisition time per view at 10 seconds can be set when using the step and shoot mode for quantitative 99mTc bone SPECT imaging with OSCGM reconstruction while maintaining quantitative accuracy.

ACKNOWLEDGEMENTS

We would like to thank Mrs.Sucheera and Mr.Suraphong from Bumrungrad International Hospital for ACR PET phantom and all Nuclear Medicine staff from Surin hospital for their support and assistance.

REFERENCES

[1] Even-Sapir E, Metser U, Lievshitz G, et al. The detection of bone metastases in patients with high-risk prostate cancer: 99mTc-MDP planar bone scintigraphy, SPECT, and 18F-fluoride PET. J Nucl Med. 2006;47(2):287–297.

[2] Boellaard R, Delgado-Bolton R, Oyen WJ, et al. FDG PET/CT: EANM procedure guidelines for tumor imaging. Eur J Nucl Med Mol Imaging. 2015; 42:328–354.

[3] Song X, Chen W, Hu Z. Application of OSCGM reconstruction in 99mTc bone SPECT imaging. J Nucl Med Technol. 2020;48(3):200–206.

[4] Peters SM, Schramm G, Ziegler SI, et al. Advances in SPECT/CT technology for quantitative imaging in oncology. J Nucl Med Technol. 2021;49(1):1–11.

[5] Bailey DL, Townsend DW, Valk PE, Maisey MN. Positron Emission Tomography: Basic Sciences. Springer; 2014.

[6] Boellaard R, Delgado-Bolton R, Oyen WJ, et al. FDG PET/CT: EANM procedure guidelines for tumor imaging. Eur J Nucl Med Mol Imaging. 2015; 42:328–354.

[7] Ljungberg M, Strand SE. Monte Carlo Modeling for SPECT and PET Imaging. CRC Press; 2019.

[8] Vija H, Tsui BMW, Frey EC. Advanced reconstruction algorithms in nuclear medicine. Phys Med Biol. 2019;64(12):12TR02.

[9] Soret M, Bacharach SL, Buvat I. Partial-volume effect in PET tumor imaging. J Nucl Med. 2007;48(6):932–945.

[10] Kadrmas DJ, Casey ME, Conti M, et al. Impact of time-of-flight on PET tumor detection. J Nucl Med. 2013; 54:118–123.

Contacts of the corresponding author:
Author: Krisanat Chuamsaamarkkee
Institute: Department of Diagnostic and Therapeutic Radiology, Faculty of Medicine, Ramathibodi Hospital, Mahidol University
Street: Rama VI
City: Bangkok
Country: Thailand
Email: krisanat.ch@gmail.com

Estimation of ^{18}F-FDG PET/CT effective dose associated with three different calculating methods

Thinn Thinn Myint[1], Krisanachinda Anchali[2*]

[1]*Department of Nuclear Medicine, PET/CT and Cyclotron Center Yangon General Hospital, Yangon, 11041, Myanmar*
[2]*Department of Radiology, Faculty of Medicine, Chulalongkorn University, Bangkok, Thailand*
**anchali.kris@gmail.com*

***Abstract* - Introduction**: The aim of this study is to estimate the patient effective dose from positron emission and computed tomography (PET/CT) study by three different methods. **Methods**: This retrospective study involved 89 patients (42 male, 47 female, average aged 55±15 years) undergoing whole body 18F-FDG PET/CT in 2024. Patient's demographic data and radiation metric quantities were collected from vertex to mid-thigh standard protocol. For CT parameters, tube voltage 120-140 kVp and tube current 70-120 mAs were used for patient body mass index (BMI) 19-30 kg/m^2. The algorithm adapted from ICRP Publication 106, modified for patient body weight and patient blood volume with three different methods, calculated the patient effective dose. **Results**: The CT effective doses were calculated by the multiplication of the dose length product DLP (mGy.cm) and coefficient k (mSvmGy-1 cm-1). The mean (standard deviation) of CT effective dose was 11.47(3.45) mSv based on BMI 25.05(4.57) (kg/m^2) and PET effective dose was 6.84(1.24) mSv. Therefore, the mean (standard deviation) of total effective dose PET/CT is approximately 18.09(3.95) mSv, 19.00(3.64) mSv and 19.18(3.76) mSv by ICRP method, body weight method and blood volume method respectively. The effective dose increases with the patient's body weight and BMI, regardless of injection activity per body weight of 4.4MBq/kg. **Conclusion**: The patient effective dose of PET/CT study was significantly different between three calculation methods. All three methods are related, the blood volume method was more accurate than the other two methods. The patient's body weight and BMI show the high influence on the total effective dose. The significant parameters of patient body weight, BMI, scan length influence the effective dose were reported leading to the further optimization of PET/CT study in the near future.

Keywords — Effective dose, PET/CT, DLP Dosimetry

I. INTRODUCTION

PET/CT, a hybrid imaging modality is widely used for the detection of various cancers. The hybrid PET and CT has advantages over PET or CT alone. A low kVp acquisition in PET/CT is mainly used for the purpose of patient attenuation correction. The common range of tube voltage in CT acquisition 90-120 was categorized as low dose CT and tube voltage 140 was categorized as diagnostic CT parameter.

Even though the high kVp improves the imaging accuracy, the combination of two modalities increases the organ absorbed dose and the patient effective dose significantly. Therefore, there is an urgent need to identify the lowest achievable effective dose and optimize the PET/CT imaging techniques to keep the low radiation dose while maintaining the image quality.

Whole-body PET/CT effective dose is calculated by summing effective dose from PET and CT. The validation to estimate total effective dose of PET/CT could be done by standard algorithms from ICRP Publication 106 [1]. The average total effective dose from a whole-body PET/CT study is approximately 14.5mSv using the low-dose protocols of modern PET/CT scanner [2]. However, over the years, many studies have published the wide range of total effective dose from PET/CT using various imaging parameters and techniques. Therefore, the aim of this study is to estimate effective dose in patients undergoing PET/CT imaging at the Department of Nuclear Medicine, Yangon General Hospital, Myanmar. The estimated effective dose for whole body ^{18}F-FDG PET/CT imaging uses three different calculating methods.

II. MATERIALS AND METHODS

PET/CT image set of 89 adult patients 42 male, 47 female, average age and standard deviation 55±15 years, underwent ^{18}F-FDG examinations from January to October 2024 were collected. This retrospective study involved whole body ^{18}F-FDG PET/CT by using a Philips Gemini Time of Flight (ToF) 16 slice system. The administered activity of ^{18}F-FDG in all patients based on 0.12mCikg^{-1} before 60 minutes of the whole body PET/CT examination. PET acquisition was 2 minutes per bed from vertex to the upper thigh.

For CT acquisition, the selected protocol based on the patient's BMI. Vary the tube current-time according to BMI.Tube voltage and tube current-time of three CT protocols were: for BMI (15-19 kg/m^2)-120 kVp and 70 mAs, for BMI (19-25 kg/m^2)-120 kVp and 90 mAs, for BMI (>25kg/m^2)-140kVp and 120 mAs respectively. $CTDI_{vol}$ and DLP were recorded.

A. CT Dosimetry

Effective dose from CT was calculated using the simple dose length product, DLP method (Eq.1) [3].

$$EDCT = DLP \times k \quad \text{(Eq.1)}$$

Where k is the coefficient based on empirical weighting factor proposed by ICRP 102, which is dependent on the anatomical region scanned. k has a unit of mSv.mGy^{-1}.cm^{-1} and the value 0.015 was used for the trunk region.

B. PET Dosimetry

For PET effective dose, 3 methods were utilized and compared in present study based on the algorithm published by Willowson, et al. (2012) [2]. Tissue weighting factor plays a crucial role in estimating effective dose coefficients that are multiplied by respective organ equivalent dose values and summed up in order to obtain a whole-body dose coefficient. The algorithms for CT and PET whole body coefficient are described in (Eq.2)

$$Whole\ body\ dose\ coefficient\ (PET) = \Sigma\ WT\ \times \lceil T\ FDG \quad \text{(Eq.2)}$$

WT refers to tissue weighting factor, $\lceil TFDG$ refers to organ dose coefficient of effective dose. In our study, we used the whole body dose coefficient 0.019 and 0.025 for >65 kg and <65 kg.

The dose coefficient that is derived for calculation of the effective dose according to the ICRP Recommendation can be found in ICRP a publication [4]. For PET effective dose, 3 methods were utilized and compared in present study based on the algorithm published by Willowson, et al. (2012) [8]. First method, using the standard method as described in ICRP Publication 106 was shown in Equation 3 and other two methods were presented using Equation 4 and 5. Effective Dose PET-EDICRP

$$EDICRP = (\Sigma\ WT \cdot \lceil T\ FDG) \times Activity\ Administered \quad \text{(Eq.3)}$$

Effective Dose PET- EDWS

$$EDPETWS = (\Sigma\ WT \cdot \lceil TFDG) \times Activity\ administered \times \frac{WeightICRP}{Patient\ Weigh} \quad \text{(Eq.4)}$$

Effective Dose PET BV

$$EDP\ ETBV = (\Sigma\ WT \cdot \lceil TFDG) \times Activity\ administered \times \frac{IndexBV}{70(ml/kg)} \quad \text{(Eq.5)}$$

The indexed blood volume of each patient measured by ideal BMI is considered to be 22 kg.m^{-2} and 70 ml/kg is the blood volume for a patient at ideal weight among Asian patients as shown in (Eq.6).

$$IndexBV = \frac{70\ ml/kg}{\sqrt{\frac{BMI\ patient}{Ideal\ BMI}}} \quad (Eq.6)$$

C. PET/CT Dosimetry

The total effective dose is obtained from CT and PET as shown in (Eq.7)

$$EDT = EDCT + EDPET \quad \text{(Eq 7)}$$

III. RESULTS

The collected data is categorized into four variables of patient body weight, patient height, patient injected dose, and dose length product (DLP). Effective dose estimated using three different methods were tabulated: a standard ICRP method, weight scaled method and blood volume scaled method in Table 1.

Table 1: *Patient demography and dosimetry details*

CT Dosimetry		
	Average(SD)	Range
DLP (mGy.cm)	757.19 (243.67)	477.41-1629
CTED (mSv)	11.47 (3.45)	7.16-24.49
PET Dosimetry		
PET EDICRP (mSv)	6.44 (1.20)	3.28-9.61
PET EDWS (mSv)	7.34 (1.17)	4.10-10.07
PET EDBV (mSv)	7.53 (1.46)	4.66-11.11
PET/CT Whole body Effective Dose(mSv)		
PET/CT EDICRP	18.09 (3.95)	10.76-31.69
PET/CT EDWS	19.00 (3.64)	11.58-30.54
PET/CT EDBV	19.18 (3.76)	12.14-30.25

According to the results of total effective dose PET/CT, a paired t-test two samples were performed to test the difference of the effective dose using weight scaled and blood volume scaled methods compared to standard ICRP by using SPSS software version 22. If the p-value < 0.05, there is significant difference in the means of each method in Table 2.

Table 2: *Paired Two Sample t-Test for Means for weight scaled and blood volume calculation model compared to standard ICRP*

Calculation Model	Total ED ICRP			
	Pearson Correlation	degrees of freedom (df)	t Stat	P-value (two-tailed)
Total ED ICRP WS	0.96	89	-7.43	0.000
Total ED BW	0.93	89	-7.17	0.000

In addition, the mean value of both body weight and blood volume methods associated with each other. The blood volume method was more effective than the body weight based method as shown in Table 3.

Table 3: *Paired two sample t-test for weight scaled and blood volume scaled calculation model*

Calculation Model	Total ED Body Weight			
	Pearson Correlation	degrees of freedom (df)	t Stat	P-value (two-tailed)
Total EDBV	0.98	89	-2.54	0.000

The ratio of total effective dose was evaluated for three calculating methods; body weight and BMI were presented in Figure 1, Figure 2 and Figure 3.

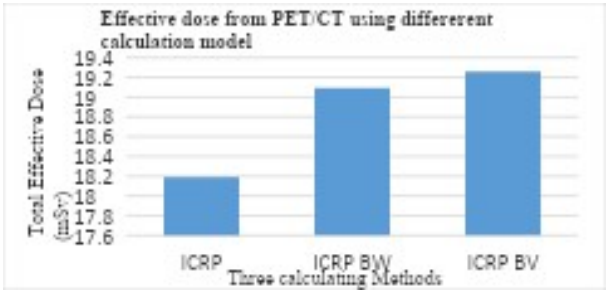

Figure 1: *Total effective dose, PET/CT calculated by three methods*

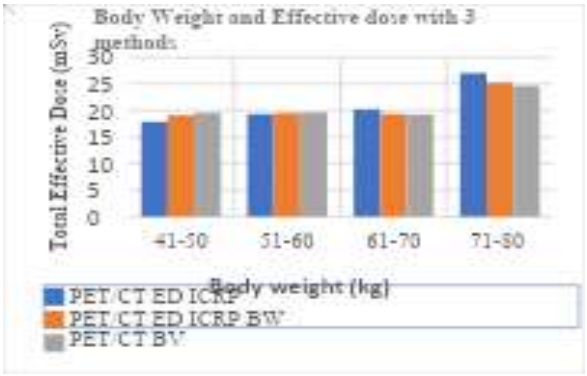

Figure 2: *PET/CT total effective dose for different patient weight ranges*

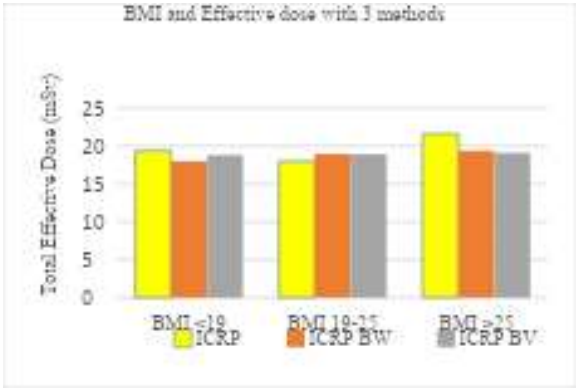

Figure 3: *PET/CT total effective for different patient weight ranges.*

IV. DISCUSSION

According to the study result, the mean effective dose for CT calculated using the DLP method was 11.35 ± 3.66 mSv averaged for 89 patients. In the present study, we evaluated the influence of BMI of patients on the total effective dose from PET/CT. The 140 kVp and 100mAs was selected for BMI >25 kg/m^2, the parameter is diagnostic CT. When BMI is

greater than 25 kg/m^2, the total effective dose increases significantly compared to other BMI ranges. In this study, 10 patients with BMI <19 kg/m^2, total effective dose was less than BMI 19 -25kg/m^2 of increased dose length product. Parimalah et al, reported body weight and BMI are associated with PET/CT effective dose [6].

For PET effective dose, average ^{18}F-FDG administered activity to the patient is only 273.69 ± 49.44 MBq that depends on patient body weight. The activity is much lower than the ^{18}F-FDG mean activity of 304 MBq [2] used by Willowson *et al*. The relationship between body weight and administered activity was directly proportional as shown in Figure 2.

According to the combination of CT and PET effective dose combination, the average effective dose(SD) for whole body PET/CT examination at our center was 18.19(4.05) mSv, 19.06(3.72) mSv and 19.29(3.85) mSv by ICRP method, body weight method and blood volume method for standard protocol respectively. The body weight scale method and blood volume methods were significant compared with standard ICRP method and association between them. Hence, the BW method and result showed that the total effective dose was more effective than the body weight method because this method based calculation on blood volume, patient BMI and ideal body weight. Therefore, we can use effective dose calculation by blood volume method to achieve specific effective dose and be more compatible with our region.

V. CONCLUSION

Total effective dose of PET/CT study is significantly different between standard ICRP, weight scaled, and blood volume scaled methods. All three methods, body weight and BMI associated with each other and blood volume method was more effective than two other methods. It can be concluded from the PET/CT effective dose study, the patient radiation dose optimization is needed to reduce the risk of cancer at later life.

ACKNOWLEDGEMENTS

The author thanks the clinical supervisor of the CQMP program, Head of Department and Nuclear Medicine team of Yangon General hospital for their cooperation and kind assistance.

REFERENCES

[1] ICRP Publication 103 2007 The 2007 Recommendations of the International Commission on Radiological Protection Ann. ICRP 37 247–332

[2] Willowson K P, Bailey E A and Bailey D L 2012. A retrospective evaluation of radiation dose

[3] ICRP Publication 102 2007 Managing patient dose in multi-detector computed tomography Ann. ICRP 102 2007

[4] Sabri, A.S.A. and Wong, J.H.D., 2019, June. Estimation of effective dose for whole body 18F-FDG PET/CT examination. In Journal of Physics: Conference Series (Vol. 1248, No. 1, p. 012006). IOP Publishing.

[5] Velo, P., Ismail, M.I., Mohandas, K.K. and Kasilingam, L., 2023. A new upper limit for effective dose in patients administered with 18F-FDG for PET/CT whole-body imaging with diagnostic CT parameters. Journal of Medical Imaging and Radiation Sciences, 54(1), pp.43-50.

Contacts of the corresponding author:
Author: Anchali Krisanachinda
Institute: Chulalongkorn University
Street: Rama IV Road
City: Bangkok
Country: Thailand
Email: anchali.kris@gmail.com

Local diagnostic reference level at nuclear medicine centers in Thailand and Myanmar

Aye Yin Moe[1], Thein May Phyu Zin[2], Krisanachinda Anchali[3,*]

1. Department of Radiology, Medical Physics Program, Faculty of Medicine, Chulalongkorn University, Bangkok, Thailand.
2. Department of Nuclear Medicine, Pinlon Hospital, Yangon, Myanmar.
3. Department of Radiology, Faculty of Medicine, Chulalongkorn University, Bangkok, Thailand.
**anchali.kris@gmail.com*

Abstract **-Introduction:** The advanced nuclear medicine technology has led to increase clinical examinations over the past decades. Diagnostic reference level (DRL) plays an important role in optimization of protection in medical exposure of patients. Local DRL represents the median value, or 50th percentile of the quantity distribution of common examinations. This study aims to establish LDRL at NM centers in Thailand and Myanmar. **Methods:** Between January 2023 and October 2024, the demographic data of adult patients with body weight range 45-75 kg, at least 20 cases per examination, radiation metric parameters including radiopharmaceutical administered activity (MBq), Volumetric CT dose index (CTDIvol, mGy), dose length product (DLP, mGy.cm) were retrospectively collected at King Chulalongkorn Memorial Hospital (KCMH), Thailand and Pinlon Hospital (PL), Myanmar. LDRL was estimated and compared to NDRL Thailand, 75th percentile of the median distribution. **Results:** LDRL of planar imaging at KCMH and PL, the activity of bone scan was 640 and 679 MBq, thyroid scan was 155 and 144 MBq, and renal scan was 96 and 153 MBq. NDRL Thailand of bone, thyroid, and renal scans was 800, 200, and 200MBq respectively. For whole-body PET/CT imaging, LDRL of administered activity, ^{18}F-FDG, at KCMH and PL was the same of 255 MBq while NDRL Thailand was 400MBq. At KCMH and PL, CTDIvol and DLP were 4.3 mGy and 424.6 mGy.cm, 4.5 mGy and 469.4 mGy.cm. NDRL Thailand was 11.28mGy and 500mGy.cm. LDRL at both centers was lower than NDRL Thailand. At PL, LDRL of some studies could not be established as the patient data is much less than 20 cases. **Conclusion:** LDRL for common NM examinations at two centers were established. LDRL should be consistently estimated together with the image quality for the optimization of radiation protection of patients.

Keywords — Dagnostic reference level, administered activity, CTDIvol, DLP

I. INTRODUCTION

Over the past few decades, the clinical use of nuclear medicine examinations has increased because of their impact on diagnosing, staging malignant disease, and identifying and localizing metastases. UNSCEAR reported that the annual number of nuclear medicine examinations increased from 24 million to 32.7 million and the corresponding annual collective effective dose has increased from 150,000 man-Sv to 200,000 man-Sv from 1985 to 2007 [1]. According to the principle of radiation protection, the medical use of radiation exposure must be justified and optimized to limit the radiation exposure risk. To achieve the optimization process, ICRP introduced the term Diagnostic reference level, DRL in publication 73 and specified the existing guidelines and considerations for establishment of DRL in publication 135. DRL is a form of investigation level used to aid in the optimization of protection in the medical exposure of patients for diagnostic and interventional radiology procedures. National DRL, NDRL is determined based on the 75th percentile of the median distribution of the DRL quantity observed at each healthcare facility throughout the country. Local DRL, LDRL represents the 50th percentile (median value) of the distribution of DRL quantity for each type of common examination at a facility. ICRP recommended that the LDRL should be compared with local, national, or regional DRL values to identify whether the 50th percentile of DRL value is substantially higher or lower than the 75th percentile. If the LDRL consistently exceeds the NDRL value, it would be recommended to investigate whether the patient will be exposed to excessive radiation or

not. If the LDRL value is substantially less than the NDRL value, the impact of image quality on diagnosis should be considered. [2,3]. This study aims to establish the LDRL for common NM examinations at NM centers in Thailand and Myanmar and compare it with NDRL Thailand.

II. MATERIALS AND METHODS

This study was carried out as a multi-center descriptive-analytical and retrospective study.

A. Data Collection

The survey from January 2023 to October 2024, consists of two parts. The first part was to collect equipment information used and identify the most common type of NM examinations at two centers. Secondly, radiopharmaceutical administered activity (MBq), Volumetric CT dose index (CTDIvol, mGy), and dose length product (DLP, mGy.cm) of standard-sized adult patients were retrospectively collected. A minimum of 20 cases for each type of common examination were collected, in line with ICRP recommendations [3]. The Institutional Review Board of the Faculty of Medicine, Chulalongkorn University, Bangkok, Thailand, and the Board of Administration (BOA) of Pinlon Hospital, Myanmar approved the submitted research proposal.

B. Data analysis and statistics

The administered activity, CTDIvol, and DLP were statistically analyzed. The minimum, maximum, mean, 25th percentile, 50th percentile, and 75th percentile values were recorded. LDRLs of each type of common examination for both centers were determined as the median value (50th percentile) of the distribution of DRL quantity. Statistical analyses were performed by using commercially available software, IBM SPSS Statistics (Version 29) and Microsoft Excel (Version 2019).

C. Effective dose calculation

The effective dose for radiopharmaceutical activity (E_P), the effective dose for CT part of the hybrid imaging system (E_{CT}), and the total effective dose (E_T) were calculated and compared for the patients who underwent SPECT/CT and PET/CT examinations. E_P was calculated by multiplying the administered activity (MBq) by the conversion factors (mSv/MBq) obtained from ICRP publications 53 and 128 [4, 5]. E_{CT} was calculated by multiplying the DLP (mGy.cm) by the conversion factors (mSv/mGy.cm) obtained from ICRP publication 102[6].

III. RESULTS

A total of 1000 standard-sized adult patients from KCMH, Thailand, and 163 from PL, Myanmar were included. At KCMH, LDRL of five planar imaging, three SPECT/CT imaging, and three PET/CT imaging was estimated. At PL, LDRL of three planar imaging, one SPECT/CT imaging, and one PET/CT imaging was established. The LDRL of planar imaging was summarized in Table 1. The LDRL of SPECT/CT and PET/CT imaging was presented in Tables 2 and 3**.**

At KCMH, ^{18}F-FDG PET/CT WB scan, E_P was 4.84 mSv, E_{CT} was 6.4 mSv and E_T was 11.24 mSv. At PL, E_P was 4.85 mSv, E_{CT} was 7 mSv and E_T was 11.85mSv. At KCMH, ^{18}F-FDG brain scan, E_P was 3.5 mSv, E_{CT} was 1.1 mSv and E_T was 4.6 mSv. In the case of the ^{18}F-FDOPA brain scan, E_P was 8.1 mSv, E_{CT} was 1.1 mSv, and E_T was 9.2 mSv. For the SPECT/CT imaging, myocardial perfusion scan (stress /rest), E_P was 5.7 mSv, E_{CT} was 0.3 mSv, and E_T was 6.0 mSv, for combined stress and rest scan, E_T was 12 mSv. For the parathyroid scan utilizing a dual-radiotracer technique, E_P was 5.8 mSv for MIBI, 1.2 mSv for ^{99m}Tc-pertechnetate, E_{CT} was 2.0 mSv, and E_T was 9 mSv. For the bone scan, E_P was 3.1 mSv, E_{CT} was 3.7 mSv, and E_T was 6.8. At PL, for the bone scan, Ep was 3.1 mSv, E_{CT} was 2.5 mSv and E_T was 5.6 mSv. E_P, E_{CT}, and E_T for SPECT/CT and PET/CT imaging at KCMH are shown in Figure 1.

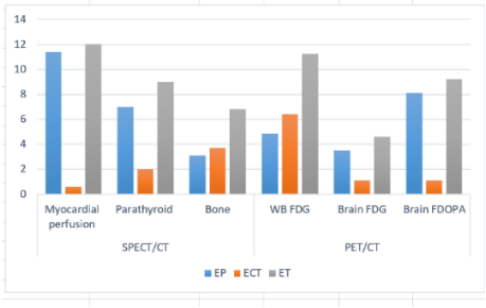

Figure 1. *E_P, blue bar, E_{CT}, orange bar, and E_T gray bar for SPECT/CT and PET/CT, at KCMH*

IV. DISCUSSION

ICRP recommended that the DRL from a single facility should be compared with local, national, or regional DRL values to identify whether the 50th percentile of DRL value is

substantially higher or lower than the 75th percentile [2,3]. Based on the survey result, the LDRL of activity of thyroid imaging at KCMH was higher than at PL. Conversely, the LDRL of activity of bone and renal imaging was lower than at PL. This result is primarily due to the patient size, the sensitivity, and the resolution of the imaging systems. For WB PET/CT scan, the LDRL of activity at KCMH and PL were comparable while LDRL of CTDIvol and DLP at KCMH was lower than at PL as the PET/CT system at KCMH is less than two years after installation while PET/CT system at PL has the longer life.

LDRL of common NM examinations from both centers was compared to the NDRL Thailand 2023 as recommended by ICRP (Tables 1, 2, and 3). The LDRLs from each center were lower than NDRL Thailand. In case of WB PET/CT, the highest $CTDI_{vol}$ and DLP values at PL is according to the CT protocols. Therefore, there is a need to optimize the radiation dose delivered from CT at PL.

The effective dose from the injected activity (E_P) and from the CT radiation metric (E_{CT}) had been compared. At KCMH, E_P of myocardial perfusion scan, parathyroid scan, brain FDG scan, and brain FDOPA scans were higher than E_{CT}. For WB PET/CT, E_{CT} was higher than E_P. (Fig 1).

At PL, E_P of bone scan was higher than E_{CT}. For WB PET/CT scan, E_{CT} is higher than Ep.

The limitation of this study, LDRL of some NM examinations at PL could not be established according the number of cases was lower than 20.

V. CONCLUSION

LDRL of eleven common NM examinations at KCMH and five examinations at PL were established. The LDRLs of both centers were slightly varied based on the examination, the patient size, and the equipment performance. Importantly, LDRLs from both centers were lower than the NDRL Thailand. The E_T from the myocardial perfusion imaging is highest**,** where the E_P contributes a notably higher effective dose than E_{CT}. Overall, the findings demonstrate that the optimization of radiation protection in NM procedures are well maintained at both centers.

ACKNOWLEDGEMENTS

I would like to express my sincere gratitude to my advisor for her invaluable guidance and support throughout this research. I also wish to extend my appreciation to the NM physicists and technologists at KCMH and PL Nuclear Medicine Department for their kind assistance to make this study become successful.

REFERENCES

[1] United Nations Scientific Committee on the Effects of Atomic Radiation. Sources, effects, and risks of ionizing radiation: UNSCEAR 2020/2021 Report. Volume I. New York: United Nations; 2021: 1-354.

[2] ICRP. Radiological protection and safety in medicine. ICRP Publication 73. Ann ICRP 1996; 26 (2):1-55.

[3] ICRP, 2017. Diagnostic reference levels in medical imaging. ICRP Publication 135. Ann. ICRP 2015;44(2S): 1-325

[4] International Commission on Radiological Protection (ICRP). Radiation dose to patients from radiopharmaceuticals: ICRP publication 53. Ann ICRP. 1987;18:1-387.

[5] International Commission on Radiological Protection (ICRP). Radiation dose to patients from radiopharmaceuticals: a compendium of current information related to frequently used substances. ICRP Publication 128. Ann ICRP. 2015 Jul;44(2 Suppl):7-321. PMID: 26069086.

[6] International Commission on Radiological Protection. Managing Patient Dose in Multi-Detector Computed Tomography (MDCT): ICRP publication 102. Ann ICRP. 2007;37(1):1-85.

Contacts of the corresponding author:
Author: Anchali Krisanachinda
Institute: Department of Radiology,
Faculty of Medicine,
Chulalongkorn University
Street: Pathumwan
City: Bangkok
Country: Thailand
Email: anchali.kris@gmail.com

***Table 1**. LDRL of the administered activity of planar imaging from KCMH and PL with NDRL Thailand*

System	Radiopharmaceutical	Administered activity (MBq)		
		Median		75th percentile
		KCMH	PL	NDRL Thailand
Cardiovascular (MUGA)	Tc-99m RBC	614	-	800
Bone	Tc-99m MDP	640	679	800
Thyroid	Tc-99m Pertechnetate	155	144	200
Renal	Tc-99m DTPA	96	153	200
	Tc-99m MAG3	100	-	100

***Table 2**. LDRLs of SPECT/CT imaging from KCMH and PL with NDRL Thailand*

System	Radiopharmaceutical	KCMH (Median)			PL (Median)			NDRL Thailand (75th percentile)		
		Activity (MBq)	CTDIvol (mGy)	DLP (mGy.cm)	Activity (MBq)	CTDIvol (mGy)	DLP (mGy.cm)	Activity (MBq)	CTDIvol (mGy)	DLP (mGy.cm)
Myocardial Perfusion	Tc-99m MIBI (stress)	636	0.86	22.7	-	-	-	1000	1.59	200
	Tc-99m MIBI (rest)	633	0.86	22.8	-	-	-	370		
Parathyroid	Tc-99m MIBI	623	5.01	179.8	-	-	-	800	10.49	468
	Tc-99m Pertechnetate	157	-	-	-	-	-	200	-	-
Bone	Tc-99m MDP	633	1.38	243.8	629	3.86	168.4	800	8	200

***Table 3.** LDRLs of PET/CT imaging from KCMH and PL with NDRL Thailand*

System	Radiopharmaceutical	KCMH			PL			NDRL Thailand		
		Activity (MBq)	CTDIvol (mGy)	DLP (mGy.cm)	Activity (MBq)	CTDIvol (mGy)	DLP (mGy.cm)	Activity (MBq)	CTDIvol (mGy)	DLP (mGy.cm)
Whole Body	^{18}F-FDG	255	4.3	424.6	255	4.5	469.4	400	11.28	500
Brain	^{18}F-FDG	186	19.6	530	-	-	-	260	35.68	688
	^{18}F-FDOPA	326	19	515	-	-	-	370	-	-

Development and Characterization of Customizable Carrageenan Bolus for Superficial Radiation Therapy

Cruzet Rhodesa[1,2*], Calma John Mc Guiller[2], Dadol Glebert[2,3], Bacabac Rommel[2]

1 Radiation Therapy Center, Cebu Doctors' University Hospital, Cebu City, Cebu, Philippines
2 Medical Biophysics Group, University of San Carlos, Cebu City, Cebu, Philippines
3 Department of Chemical Engineering, University of San Carlos, Cebu City, Cebu, Philippines
*(*Corresponding author: rhodesacruzet@gmail.com)*

Abstract — **Introduction:** In radiation therapy, a bolus is a tissue-equivalent material that alters the radiation dose distribution and resolves the skin-sparing effect of megavoltage x-ray energies. Commonly used bolus materials are non-customizable and usually result in air gaps making the bolus less effective. This project aims to develop prototypes of customizable bolus made from kappa-carrageenan for superficial radiation therapy and compare them with commercial gel-type bolus sheets using specific tests for characterization of physical, mechanical, conformity, radiation attenuation, and radiation dosimetric properties that satisfy the criteria of a good radiotherapy bolus. **Methods:** Purified Kappa-Carrageenan (PKC) powder, derived from a locally produced semi-refined kappa-carrageenan (SKC) powder, was further processed, blended with different polymers and additives, and molded into 0.5 cm and 1.0 cm-thick sheets to make carrageenan boluses. Characterization tests were performed for commercial and carrageenan boluses to determine the following: optical transmittance, conformity to curved surfaces with air gap estimation, CT numbers, relative depth doses, gel strength, and viscoelastic properties. The carrageenan gel mixture was also subjected to rheological tests to assess its potential for customized shape applications. **Results:** The carrageenan boluses have better optical transmittance and shape conformity than the commercial type. CT scan images indicate the tissue equivalence of the bolus samples with the carrageenan bolus closer to water. The relative depth doses of the boluses indicated the shift of d_{max} to shallower depths. The different additives had an effect on the mechanical and viscoelastic properties of carrageenan bolus based on indentation and rheology tests. **Discussion:** The versatility and tunability of kappa carrageenan make it suitable for use as a bolus in radiotherapy and agree with other previous studies that use kappa carrageenan in combination with other additives in tissue-mimicking applications. **Conclusion:** The developed carrageenan bolus satisfies the specific characteristics and criteria of a radiotherapy bolus.

Keywords — customized bolus, carrageenan, hydrogel, radiation therapy, dosimetry

I. INTRODUCTION

In radiation therapy, treatment machines that produce megavoltage x-rays are commonly used for the treatment of deep seated and superficial tumors which often results in insufficient skin dose due to the skin sparing effect of high energy x-rays. To resolve this, a tissue equivalent material (known as a bolus) can be applied directly to the skin to act as a tissue compensator to increase skin dose and consequently reduce the depth doses. The characteristics of a good radiotherapy bolus include tissue equivalence (or close to water), flexibility, allows visibility of set up markings, can withstand high radiation exposures, and safe to use even with close contact with the skin. Depending on the bolus' material, thickness, shape conformity, and the energy of the radiation being used, it can be used as a tissue compensator that modifies the radiation dose to an irradiated volume.

Traditional bolus materials (such as wet cloth or gauze, paraffin wax, etc.), thermoplastic and plastic wrapped gel bolus materials (which are commercially available) tend to be less effective due to air gaps with the skin when applied because they are not flexible enough. Among these bolus types, the unwrapped gel-type commercial bolus sheet conforms well to the surface contour of the treated area but cannot totally fill small crevices and skin gaps.

Kappa-carrageenan hydrogels have previously been investigated for their distinct properties, is widely used in biomedical applications as a biomaterial due to their affordability, biocompatibility, non-toxicity, and versatility making it a potential material for radiotherapy bolus with tunable properties that can be evaluated and optimized using rheology [1,2]. Crosslinkers like potassium chloride [3] and glutaraldehyde [4] can significantly improve the mechanical properties of kappa-

carrageenan by increasing its synergistic strength and elasticity. It can also be combined with co-polymers like konjac glucomannan [5] to create an interpenetrating network (IPN) hydrogel with superior toughness and elasticity in the presence of Borax ions.

Thus, this study aims to fabricate carrageenan gel bolus prototypes and compare them to commercial gel-type bolus sheets in terms of physical, mechanical, radiation attenuation, and radiation dosimetric properties that meet the criteria of a good radiotherapy bolus.

II. MATERIALS AND METHODS

A. Carrageenan Bolus Preparation

The semi-refined kappa-carrageenan (SKC) powder, produced locally by MCPI Corporation, Cebu, Philippines, was subjected to purification to remove the suspended solids and acid-insoluble matter (AIM) to obtain purified kappa-carrageenan (PKC) powder which serves as base material in the preparation of different hydrogel samples. The carrageenan hydrogel solutions were poured into 13cm x 13cm silicone molds with 0.5cm and 1.0cm thicknesses to fabricate carrageenan bolus slabs. Table 1 summarizes the different commercial gel-type bolus and synthesized carrageenan bolus samples used in this study.

***Table 1**. Compositions and Naming Conventions of Commercial and Commercial Boluses used in various experiments*

	Sample Name	Composition
Commercial Boluses	Com1 S	Polyurethane with plastic skin
	Com1 SL	Polyurethane
	Com2 S	Silicone Gel with Polyurethane skin
	Com2 SL	Silicone Gel
Carrageenan Boluses	Car	PKC
	Covalent	PKC, GA, and Glycerol
	Konjac	PKC, KG, and Glyercol
	Ionic	PKC, KCl, and Glycerol
	Combined	PKC, GA, KCl, KG, and Glycerol
	Flexible	PKC, GA, KG, and Glycerol
	Stiff	PKC, Borax, GA, KCl, KG, and Glycerol

B. Optical Transmittance Evaluation

The bolus samples were placed in a Shimadzu UV-1280 UV-Visible Spectrophotometer to determine the transmittance values at 450 nm, and 650 nm following the methods of Bertasa et al. [6] with slight modifications. An empty compartment (air) was used as a reference during each measurement and base correlation was conducted for each sample test.

C. Bulk Indentation Test and Rheological Characterization

The mechanical properties of bolus samples were obtained through indentation testing in terms of gel strength using the ThermoFisher Scientific HAAKE™ MARS™ II rheometer (Thermo Scientific, USA) with a 20-mm diameter rod moving at a speed of 1mm/s. Three trials were performed using a parallel plate geometry (35-mm diameter, 1-mm gap) with samples loaded on a preheated plate and covered with low-viscosity silicone oil. Frequency Sweep (0.1 – 100 Hz) was performed with 0.5% strain at 25°C, and strain sweeps were done from 0.1% - 1000% strain with a frequency of 1 Hz at 25°C.

D. Conformity Test (Air Gap Estimation)

To test the conformity to a curved surface, the bolus samples were placed on a specific Region of Interest (ROI) of a PET bottle water phantom (marked with rubber bands) as shown in Figure 1 and CT scanned using SIEMENS Definition Edge CT scanner with 120 kV and tube current of 108 mA settings. The CT images of the samples were imported into a Varian Eclipse treatment planning software (Varian Medical Systems, Inc.) to determine the air gap volume between the bolus samples and the water bottle using contouring tools in the TPS.

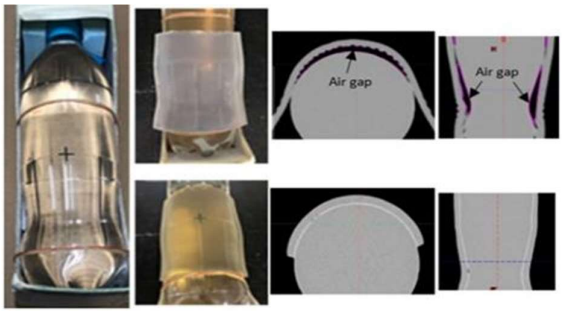

***Figure 1.** Air gap estimation using CT images of bolus sample on a PET bottle water phantom*

E. CT Numbers and Relative Depth Doses

The CT numbers of the samples were measured using the TPS based on the CT calibration data of the CT scanner being used. The mean CT number value from 50 sample points within the bolus volume represented the CT number of the sample.

For dosimetric characterization, the TPS was used to simulate irradiating 6MV x-rays to the bolus samples placed on top of a solid water phantom with a 10cm x 10cm field size at 100cm

SSD as shown in Figure 3 and the relative depth dose curves were obtained for each bolus sample and without a bolus for comparison of d_{max}.

Table 2. *Summary of Results displaying the Mean CT numbers, transmittance values, and air gap volume.*

Sample	Transmittance (%) 450 nm	Transmittance (%) 650 nm	Air Gap Volume (cm^3)	Mean CT number
0.5 Com1 S	n/a	n/a	16.9	-169.24
0.5 Com1 SL	27.58	32.39	0	-77.98
0.5 Com2 S	n/a	n/a	16.4	-162.22
0.5 Com2 SL	45.97	58.81	0.1	37.38
0.5 Car	33.77	57.61	0	-13.70
0.5 Covalent	45.96	68.10	1.9	-2.94
0.5 Konjac	27.49	52.90	6.6	-6.74
0.5 Ionic	28.17	54.54	7.5	-3.68
0.5 Combined	28.45	47.85	9.6	-5.86
0.5 Flexible	25.88	44.10	22.4	-8.52
0.5 Stiff	21.21	40.15	37.1	-8.72
1.0 Com1 S	n/a	n/a	15.5	-149.95
1.0 Com1 SL	16.44	21.27	0	-56.82
1.0 Com2 S	n/a	n/a	10.7	-125.20
1.0 Com2 SL	29.30	46.77	2.3	-56.82
1.0 Car	14.97	39.10	2.2	-10.65
1.0 Covalent	31.08	59.34	14.5	0.48
1.0 Konjac	12.08	36.49	25.4	-5.74
1.0 Ionic	12.49	37.92	50.8	-0.72
1.0 Combined	18.74	45.68	62.1	-7.14
1.0 Flexible	9.21	24.96	28.1	-1.44
1.0 Stiff	7.20	22.50	_	-2.28

III. RESULTS

A. Optical Transmittance Evaluation

The second column of Table 2 shows the transmittance of the bolus samples at 450nm and 650nm. The Covalent and Car samples have higher transmittance values than the other samples. Overall, 1.0cm samples generally have lower transmittance compared to 0.5cm thickness samples.

B. Indentation and Rheological Tests

Figure 2a shows the gel strength of 0.5-cm commercial and carrageenan bolus samples before breaking. 0.5 Com1 SL and 0.5 Com2 SL have high gel strength. For carrageenan boluses, 0.5 Ionic and 0.5 Konjac samples had the maximum gel strengths, showing effective crosslinking and structural integrity.

The Frequency Sweep Curves shown in Figure 2b depict the variation of tan δ (loss factor) with frequency. All samples are relatively stable across the frequency range indicating the dominance of elastic solid behavior. The Shear Stress-Strain curve in Figure 2c displays the mechanical strength and deformation limits of each sample formulation. At low strain, stress increases linearly in the elastic region until the yield point where it transitions to plastic deformation. Beyond this, stress may drop, indicating structural breakdown, followed by a plateau or further increase, depending on the formulation.

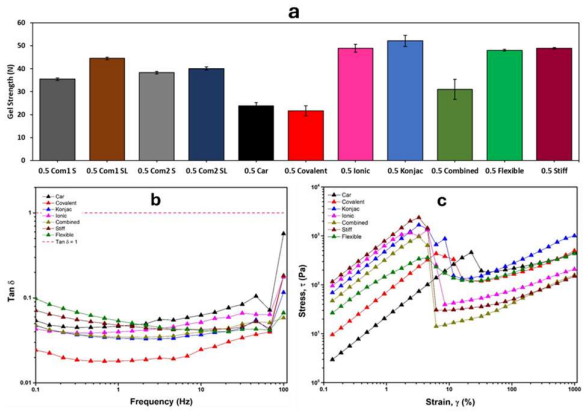

Figure 2. *Gel strength of 0.5-cm thick bolus samples (a). Frequency Sweep Curves in terms of tan δ (loss factor) (b) and Shear Stress-Strain curves (c).*

C. Conformity Test (Air Gap Estimation)

The third column of Table 2 provides estimated air gap volumes in cm^3 for all bolus samples. Skinless commercial boluses adhere well to the curved surface and do not produce air gaps, as well as soft and flexible carrageenan boluses (Car and Covalent) that have very minimal or no air gaps On the other hand, with-skin commercial gel boluses create air gaps due to their plastic wrap, while stiff carrageenan bolus samples do not easily conform to a curved surface; 0.5 Stiff and 1.0 Ionic had the highest reported air gap volumes for 0.5-cm and 1.0-cm thick samples, respectively.

D. CT Numbers and Relative Depth Doses

The mean CT numbers of the samples are displayed in the last column of Table 2. According to the classification of Kalender et al. [7], Carrageenan bolus samples have CT numbers close to water (-4 to 4 HU), bolus materials made of polyurethane (0.5/1.0 Com1 S/SL, 0.5/1.0 Com2), fall within the adipose tissue range of -200 to -20 HU, whereas silicone bolus (0.5/1.0 Com2 SL) falls within the muscle or soft tissue range of 20 to 100 HU.

Shown in Figure 3 is the relative depth doses for 0.5 and 1.0 boluses and without any bolus. The relative depth doses indicate the shift of d_{max} to shallower depths which is what is needed for superficial radiotherapy. The results also show the effect of bolus thickness in dose attenuation.

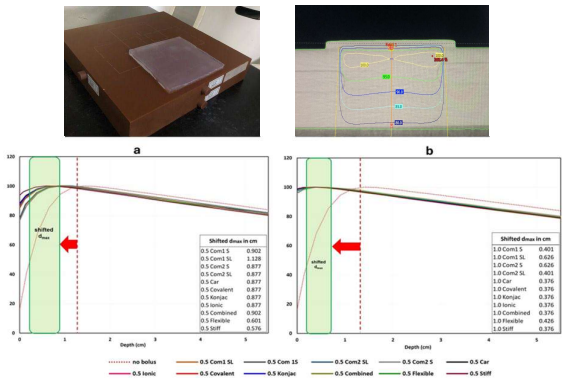

Figure 3. *Relative depth doses with and without bolus samples, 0.5 cm (a) and 1.0 cm (b).*

IV. DISCUSSION

The characterization tests used in this study serve to verify on whether kappa Carrageenan Hydrogel can be used as a tissue compensator in comparison with commercial gel bolus types. Aside from radiation field visibility and tissue equivalence, the adjustability of kappa carrageenan (in combination with additives) gives an advantage in customization of its form (flexible or rigid) depending on the need of end users. Moreover, the carrageenan bolus behaves close to water which may be useful with electron radiotherapy where water equivalence is highly applicable [8].

V. CONCLUSION

Based on the results of this study, the developed carrageenan boluses can be an alternative locally resourced material that satisfy the function of a radiotherapy bolus. Given the tunable properties of carrageenan, it can be made into a customized tissue-mimicking and biodegradable radiotherapy bolus.

DECLARATION OF CONFLICT OF INTEREST

The author(s) declared the following potential conflicts of interest with respect to the research, authorship, and/or publication of this article: a patent application relating to the fabrication and use of carrageenan bolus as a radiotherapy bolus material.

FUNDING

The author(s) disclosed receipt of the following financial support for the research, authorship, and/or publication of this article: DOST-PCIEERD NICER PROGRAM

ACKNOWLEDGEMENTS

The authors thank Ms. Teresa Simbajon of MCPI Corporation, the Medical Biophysics Laboratory of the Department of Physics, University of San Carlos, and Cebu Doctors' University Hospital for supporting this project.

REFERENCES

[1] Russo Spena S, Grizzuti N, Tammaro D. Linking Processing Parameters and Rheology to Optimize Additive Manufacturing of k-Carrageenan Gel Systems. Gels. 2022 Aug 9;8(8):493.

[2] Patel P, Mujmer K, Aswal V, Gupta S, Thareja P. Structure, rheology, and 3D printing of salt-induced κ-carrageenan gels. Materials Today Communications. 2023 Jun;35:105807.

[3] Nguyen BT, Nicolai T, Benyahia L, Chassenieux C. Synergistic effects of mixed salt on the gelation of k-carrageenan. Carbohydr Polym. 2014;112:10–5.

[4] Distantina S, Rochmadi R, Fahrurrozi M, Wiratni W. Preparation and Characterization of Glutaraldehyde-Crosslinked Kappa Carrageenan Hydrogel. Engineering Journal. 2013 Jul 1;17(3):57–66.

[5] Chen Y, Song C, Lv Y, Qian X. Konjac glucomannan/kappa carrageenan interpenetrating network hydrogels with enhanced mechanical strength and excellent self-healing capability. Polymer. 2019 Dec;184:121913.

[6] Bertasa M, Dodero A, Alloisio M, Vicini S, Riedo C, Sansonetti A, et al. Agar gel strength: A correlation study between chemical composition and rheological properties. European Polymer Journal. 2020 Jan;123:109442.

[7] Kalender WA. Computed tomography. Erlangen: Publicis Publishing; 2011.

[8] Adamson JD, Cooney T., Demehri F, et al. Characterization of Water-Clear Polymeric Gels for Use as Radiotherapy Bolus. Technology in Cancer Research & Treatment. 2017;16(6):923-929.

Contacts of the corresponding author:
Author: Rhodesa Cruzet
Institute: Radiation Therapy Center
Cebu Doctors' University Hospital
Street: Osmeña Blvd
City: Cebu City
Country: Philippines
Email: rhodesacruzet@gmail.com

Measurement of photoneutron dose rate from high energy photon beams in medical linear accelerator using neutron survey meter

Hmwe Aye Thiri[1], Ekjeen Tawatchai[1], Kakanaporn Chumpot[2], Suwannarat Achawee[1], Kittipayak Samrit[3], Damrongkijudom Nuanpen[1*]

1 Department of Radiological Technology, Faculty of Medical Technology, Mahidol University, Salaya, Nakhon Pathom, Thailand
2 Department of Radiation Oncology, Faculty of Medicine, Siriraj Hospital, Mahidol University, Bangkok-Noi, Bangkok, Thailand
3 Faculty of Health Science Technology, HRH Princess Chulabhorn College of Medical Science, Chulabhorn Royal Academy, Bangkok, Thailand
*(*Corresponding author: nuanpen.dam@mahidol.ac.th)*

Abstract — **Introduction:** Undesirable photoneutrons can be produced from a linear accelerator (LINAC) operating above 10 MV photon beam and contribute extra doses to treated patients and staff. This study aimed to measure photoneutron dose rate produced by Elekta Versa HD LINAC with different photon energies. **Methods:** Photoneutron dose rates of LINAC delivering 6 MV, 10 MV, 15 MV, 6 MV FFF (flattening filter free), and 10 MV FFF were measured using a Ludlum Model 12-4 survey meter with a He-3 neutron detector. The measurement was performed at various locations in the treatment room, and outside the front door with open and closed doors, respectively. **Results:** The highest photoneutron dose rates from LINAC operated at 6 MV, 10 MV, 15 MV, 6 MV FFF and 10 MV FFF with 10 x 10 cm^2 field size were 3.00±0.00 mSv/h, 27.80±0.45 mSv/h, 48.00±0.00 mSv/h, 1.74±0.09 mSv/h and 10.00±0.00 mSv/h respectively at radiation therapist working spot beside the patient couch. When delivered dose rates were higher than 600 MU/min, the highest photoneutron dose rates produced from 6 MV FFF and 10 MV FFF were 3.12±0.11 mSv/h and 30.00±0.00 mSv/h respectively at the same location. For 15 MV photon beam, the photoneutron dose rate measured outside the front door was 0.02±0.00 mSv/h with the door opened, and unable to detect with the door closed. **Conclusion:** The information of the photoneutron dose rates from this study is beneficial for the clinical practice in optimizing of radiation safety for the patient and radiation therapist during the procedures.

Keywords — Photoneutron, Neutron dose rate, Linear accelerator, Survey Meter

I. INTRODUCTION

Nowadays, linear accelerators (LINAC) are being utilized more and more in medical applications as the primary tool in external beam radiotherapy, delivering high-energy x-rays or electrons to conform to the shape of a tumor and destroy cancer cells while preserving the surrounding normal tissue [1]. Modern radiation therapy utilizes high-energy LINACs for cancer treatment, offering benefits such as lower skin dose, larger depth dose and reduced scattered radiation [2]. However, when using photon beams above 10 MV, undesired photoneutrons can be generated through (γ, n) reaction between bremsstrahlung photons and high-Z materials in the LINAC head, leading to therapeutic beam contamination and non-negligible neutron dose to the patients [3,4]. The useless & unwanted neutron irradiation is harmful to both patients and technologists. Therefore, this study aimed to measure photoneutron dose rate produced by Elekta Versa HD LINAC with different photon energies.

II. MATERIALS AND METHODS

In this study, a new addition of digital sophisticated Elekta Versa HD LINAC machine with various energies of flattened photon beams with the use of flattening filter (FF) and flattening filter-free (FFF) photon beams at Department of Radiation Oncology, Siriraj Hospital, Thailand was utilized to measure the photoneutron dose rate contributed by high energy photon beams. Ludlum Model 12-4 Survey Meter with He-3 Neutron Detector was applied to investigate the contamination of photoneutrons in this study. It comprises a proportional detector with 2 Atm ^{3}He tube (LND 25185 or equivalent) enclosed by 9″ diameter Polyethylene Sphere that serves as a moderator for measuring neutrons.

The irradiations were performed using the Elekta Versa HD LINAC with various photon

beams. For every irradiation exposed, the output radiation dose (MU) of 600 MU from LINAC was delivered in both FF and FFF modes. The tissue homogeneity solid phantom with a thickness of 20 cm was used as the irradiation target at the isocenter simulating the patient. The SAD treatment method was applied and the isocenter was located at the depth of 10 cm from the phantom surface. With the gantry and the collimator angle vertically oriented at 0°, the isocenter was positioned at (0,0,0) for all the measurements. The neutron survey meter was placed at different measurement locations in the treatment room:(1) radiation therapist's working spot beside the patient couch, (2) at the distal end of the couch, (3) at the patient waiting area, and (4) at the front door measured outside with open and closed protective doors respectively to record the neutron dose rate. The center of the sphere of the neutron detector was kept at the same level as the isocenter in the patient plane.

Figure 1. *The equipment set-up for measuring neutron dose rate at location 2: the distal end of the couch*

The various parameters chosen to measure the neutron dose rate for different measuring locations in this work were: (i) Different photon energies (6 MV FF, 10 MV FF, 15 MV FF, 6 MV FFF and 10 MV FFF), (ii) Various field sizes (5x5 cm^2, 10x10 cm^2 and 20x20 cm^2), and (iii) FF & FFF modes using 600 MU/min dose rate and the ultra-high dose rates 1400 MU/min and 2200 MU/min.

III. RESULTS

When irradiations were made under the condition using FF mode with radiation output dose of 600 MU and conventional dose rate of 600 MU/min to evaluate the effects of different photon energies and various field sizes, the photoneutron dose rate findings in mSv/h can be seen in (Table 1). In the table, "N/A" for certain measurements, which typically means that data for those specific photon energy, field size, location were not applicable or below detectable limit of neutron survey meter. The highest photoneutron dose rates measured for 6 MV, 10 MV and 15 MV were found to be 3.00±0.00 mSv/h, 27.80±0.45 mSv/h, and 48.00±0.00 mSv/h respectively at Location 1 when using 10 x 10 cm^2 field size. The findings from (Table 1) indicated that higher photon energies (10 MV and 15 MV) generally resulted in higher photoneutron dose rates when applying various field sizes across all locations.

Table 1. *Photoneutron dose rate (mSv/h) measured for different photon energies & field sizes in FF mode with 600 MU/min dose rate at various locations*

Photon Energy & Field size	**Neutron Dose Rate (mSv/h) (Mean±S.D.)**		
	Location 1	**Location 2**	**Location 3**
6 MV, 5x5 cm^2	3.00 ± 0.00	N/A	N/A
10 MV, 5x5 cm^2	27.20 ± 1.79	14.00 ± 0.00	0.13 ± 0.01
15 MV, 5x5 cm^2	47.80 ± 0.45	34.00 ± 0.00	0.46 ± 0.01
6 MV, 10x10 cm^2	3.00 ± 0.00	N/A	N/A
10 MV, 10x10 cm^2	27.80 ± 0.45	14.00 ± 0.00	0.13 ± 0.01
15 MV, 10x10 cm^2	48.00 ± 0.00	34.00 ± 0.00	0.46 ± 0.02
6MV, 20x20 cm^2	3.00 ± 0.00	2.16 ± 0.05	N/A
10MV, 20x20 cm^2	25.80 ± 1.10	14.00 ± 0.00	0.12 ± 0.00
15 MV, 20x20 cm^2	46.60 ± 0.89	34.00 ± 0.00	0.44 ± 0.01

For 15 MV with all field sizes at Location 4: outside the front door with open protective door, a minimal exposure 0.02±0.00 mSv/h was observed, highlighting the effectiveness of shielding barriers & the double maze design of treatment room. No experiments were performed for 6 MV & 10 MV at Location 4 due to a very low neutron dose rate recorded for 15 MV. When measurements were taken outside the front door with closed protective door and

the center of the neutron survey meter kept 30 cm away from the outer surface of the door, there were no discernible readings displayed on the device, suggesting that the protective door is safe for neutron protection.

Table 2. *Photoneutron dose rate (mSv/h) measured for 6MV FFF and 10MV FFF using 600 MU/min dose rate & 600 MU radiation dose in different field sizes at various locations*

Photon Energy & Field size	Neutron Dose Rate (mSv/h) (Mean±S.D.)		
	Location 1	Location 2	Location 3
6 MV FFF, 5x5 cm^2	1.66 ± 0.09	0.17 ± 0.01	N/A
10 MV FFF, 5x5 cm^2	10.00 ± 0.00	4.82 ± 0.04	0.08 ± 0.00
6 MV FFF, 10x10 cm^2	1.74 ± 0.09	0.37 ± 0.01	N/A
10 MV FFF, 10x10 cm^2	10.00 ±0.00	4.88 ± 0.04	0.08 ± 0.00
6MV FFF, 20x20 cm^2	1.60 ± 0.00	1.20 ± 0.00	N/A
10MV FFF, 20x20 cm^2	9.40 ± 0.55	4.71 ± 0.07	0.07 ± 0.00

Table 3. *Photoneutron dose rate (mSv/h) measured for 6MV FFF and 10MV FFF using higher dose rates with 600 MU radiation dose in different field sizes at various locations*

Photon Energy & Field size	Neutron Dose Rate (mSv/h) (Mean±S.D.)		
	Location 1	Location 2	Location 3
6 MV FFF (1400MU/min), 5x5 cm^2	3.12±0.11	0.24±0.00	N/A
10 MV FFF (2200MU/min), 5x5 cm^2	30.00±0.00	16.00±0.00	0.20±0.00
6 MV FFF (1400MU/min), 20x20 cm^2	3.00±0.00	2.00±0.00	N/A
10 MV FFF (2200MU/min), 20x20 cm^2	28.20±0.45	16.00±0.00	0.20±0.01

The photoneutron dose rate outcomes were displayed in (Table 2) when experiments on measuring the effects of 6 MV and 10 MV under the FFF mode using 600 MU/min dose rate and delivering radiation dose of 600 MU were conducted. The highest average photoneutron dose rates emitted from 6 MV FFF were found 1.74±0.09 mSv/h in 10x10 cm^2 field size at Location 1 and for 10 MV FFF, the largest photoneutron dose rate was 10.00±0.00 mSv/h in 5x5 cm^2 & 10x10 cm^2 field sizes at the same location. All the values of photoneutron dose rates in (Table 2) exhibited significant decrease with removing flattening filter, when comparing the values from (Table 1). When delivered dose rates were higher than 600 MU/min, the photoneutron dose rates produced from 6 MV FFF with 1400 MU/min and 10 MV FFF with 2200 MU/min for 5x5 cm^2 & 20x20 cm^2 field sizes were presented in (Table 3) to evaluate the effects of ultra-high dose rates.

IV. DISCUSSION

According to the findings from this study, higher photoneutron dose rates were recorded when the photon energy is increased. It is because photoneutron production via (γ, n) reactions typically becomes significant when the photon energy exceeds certain threshold energy and can interact more with nuclei in the LINAC head and surrounding materials and thus, higher photon energies increase the likelihood of these (γ, n) reactions occurring and more neutrons are produced consequently. The evaluated photoneutron dose rates in the current study (Table 1) were found to be significantly higher than the neutron dose equivalent from the study of Tai et al. [5], ranging from 0.0001 to 8.6 mSv/h, since their study used Siemens Primus M5497 electron accelerator. Different types of accelerators with different configurations of the LINAC head produce distinct neutron spectra and will result in variations in the interaction cross-sections and beam geometry of the LINAC. Thus, there could be higher different values of photoneutron dose rates in the current study with Elekta Versa HD LINAC.

Locations closer to the isocenter such as location 1 (60 cm from isocenter) typically exhibited higher neutron dose rates compared to more distant locations (e.g., location 3). The results from the present study were consistent with those of Karaman O. et al., indicating that the photoneutron dose equivalents reach their maximum at the field's center and diminish as the distance from the isocenter increases [1].

When investigating the effect of flattening filter on the photoneutron production with other parameters kept the same such as same photon energy, same field size and the same dose rate of 600 MU/min in both modes, FF mode (Table 1) indicated notably higher neutron dose rates compared to FFF mode with reduced neutron production (Table 2). The results from this work agreed with that of Li D. et al. who also found that neutron doses can be considerably lower in FFF mode than in FF mode with 10 MV utilizing the Varian Truebeam accelerator [6]. According to another research by Kry SF et al., employing the FFF mode during treatment would result in 69% reduction in the dose of neutron radiation [7]. According to the findings of the present study, the patient receives less photons of radiation, and the irradiation duration is shortened, which results in fewer neutrons in FFF mode, as opposed to the FF mode. The reduced neutron production in FFF mode is most likely because removing the flattening filter from the beam can cause the leak neutron dose to drop and the incoming photons will have fewer materials to interact with in the LINAC head. This will cause the reduced dose rate of photoneutrons in the measurements in FFF mode.

The highest photoneutron dose rates produced from 6 MV FFF with ultra-high dose rate of 1400 MU/min and 10 MV FFF with 2200 MU/min (Table 3) were 3.12±0.11 mSv/h and 30.00±0.00 mSv/h respectively at Location 1 which were slightly greater than the largest photoneutron dose rates of 6 MV FF (3.00±0.00 mSv/h) & 10 MV FF (27.80±0.45 mSv/h) with 600 MU/min dose rate at the same location and same field sizes (Table 1), indicating that even if the flattening filter was eliminated, the potential neutron dose rate will still rise when ultra-high dose rates were utilized.

V. CONCLUSION

The neutron contamination generated by Elekta Versa HD LINAC operating at high photon energy primarily depends on the photon energy, the field size and the distance from the isocenter measured in various locations of the treatment room. The photoneutron dose rate increases with increasing energies of photon beam and decreases with increasing distance from the isocenter. Moreover, the photon beam with flattening filter-free reduces the production of photoneutron, however, the potential neutron dose rate still rise when higher delivered dose rate (MU/min) were applied.

ACKNOWLEDGEMENTS

The authors would like to express their sincere thanks to the staff and medical physicists of Department of Radiation Oncology, Siriraj Hospital, Thailand for their great support and permitting the facilities in performing this research work.

REFERENCES

[1] Karaman O, Tanir A, Karaman C. Investigation of photoneutron contamination from the 18-MV photon beam in a medical linear accelerator. Materiali in tehnologije. 2019;53(5).

[2] Hashemi F, Hashemi-Malayeri B, Raisali G, Shokrani P, Sharafi A. A study of the photoneutron dose equivalent resulting from a Saturne 20 medical linac using Monte Carlo method. Nukleonika. 2007;52(1):39-43.

[3] Rajesh K, Musthafa M, Raj H, Joseph N, Raman RG. A Comparative Study of Photo-Neutron Production from Flattened and Unflattened Beams in a Medical Linear Accelerator. Indian Journal of Public Health Research &Amp; Development. 2019;10:393.

[4] Thekkedath SC, Raman RG, Musthafa MM, Bakshi AK, Pal R, Dawn S, Kummali AH, Huilgol NG, Selvam TP, Datta D. Study on the measurement of photo-neutron for 15 MV photon beam from medical linear accelerator under different irradiation geometries using passive detectors. Journal of Cancer Research and Therapeutics. 2016 Apr 1;12(2):1060-4.

[5] Tai DT, Loan TT, Sulieman A, Tamam N, Omer H, Bradley DA. Measurement of neutron dose equivalent within and outside of a linac treatment vault using a neutron survey meter. Quantum beam science. 2021 Nov 30;5(4):33.

[6] Li D, Deng X, Xue Y, Lou Z, Zhang Y, Guo W, Wang J. Neutron dose distribution in the treatment room for an accelerator in the flattening filter-free mode. Precision Radiation Oncology. 2017 Mar;1(1):13-9.

[7] Kry SF, Titt U, Pönisch F, Vassiliev ON, Salehpour M, Gillin M, Mohan R. Reduced neutron production through use of a flattening-filter–free accelerator. International Journal of Radiation Oncology* Biology* Physics. 2007 Jul 15;68(4):1260-4.

Contacts of the corresponding author:
Author: Nuanpen Damrongkijudom
Institute: Department of Radiological Technology, Faculty of Medical Technology, Mahidol University
Street: Phutthamonthon Sai 4 Rd, Salaya
City: Nakhon Pathom 73170
Country: Thailand
Email: nuanpen.dam@mahidol.ac.th

Determination of neutrons in a photon radiotherapy treatment room using CR-39 dosimeters

Rattanarungruangchai Natch[1,3], Suwanbut Pattarakan[2], Thongsawad Sangutid[1,2], Liamsuwan Thiansin[1,*]

1 Princess Srisavangavadhana College of Medicine, Chulabhorn Royal Academy, Bangkok, Thailand
2 Radiation Oncology Department, Chulabhorn Hospital, Chulabhorn Royal Academy, Bangkok, Thailand
3 Nuclear Technology Service Center, Thailand Institute of Nuclear Technology (Public Organization), Nakhonnayok, Thailand
*(*Corresponding author: thiansin.lia@cra.ac.th)*

Abstract — **Introduction:** Neutrons are undesired products in high-energy photon beam radiotherapy caused by interactions between photons and treatment head components. Neutron measurement is essential to evaluate out-of-field dose in patients and treatment room design for radiation protection purposes. This study aimed to determine neutron ambient dose equivalent, $H^*(10)$, at different locations of the 10 MV linear accelerator treatment room for different field sizes shaped by multi-leaf collimators (MLCs). **Methods:** CR-39 dosimeters were placed at 100 cm and 200 cm from the isocenter, maze junction, maze, and entrance during irradiation with 10 MV flattened photon beams from the TrueBeam machine with the field sizes of 1×1 cm^2, 2×2 cm^2, 5×5 cm^2, 10×10 cm^2, and 20×20 cm^2 for 1,800 monitor units. The CR-39 dosimeters have been calibrated free in air with ^{252}Cf for fast neutrons and ^{241}Am-Be moderated with graphite blocks for thermal neutrons. **Results:** $H^*(10)$ was highest at 100 cm from the isocenter and decreased with increasing distance from the isocenter. $H^*(10)$ at the maze and entrance were lower than neutrons at the maze junction. The different field sizes shaped by MLC affected $H^*(10)$ with decreased $H^*(10)$ as the field size was increased. **Discussion:** $H^*(10)$ at 100 cm and 200 cm from the isocenter obtained in this study were different from those obtained by a similar study, which determined $H^*(10)$ by a neutron spectrometer, potentially due to the difference of treatment room environment and dosimeter calibration using standard sources. This may suggest that standard source calibration may not be adequate for accurate neutron dose determination. **Conclusion:** Neutron ambient dose equivalent decreased with the increased distance from the isocenter and increased field size. To determine accurate neutron dose, dosimeters should be calibrated in a reference neutron field that has a similar energy spectrum as the neutron field of interest.

Keywords — CR-39 dosimeter, neutron dosimetry, photon radiotherapy, 10 MV

I. INTRODUCTION

Medical linear accelerator (LINAC) has become the tool to kill cancer cells for patients in radiotherapy. The high-energy photon beam is used in treatment to increase the penetrating distance in patient body and reduce the skin dose [1]. However, for treatment that uses high energy photon beams with energy ≥10 MV, neutrons can be generated by photonuclear reactions between high energy photons and high atomic number materials in the treatment head components [2-3].

Treatment head components, such as, flattening filter, primary collimator, secondary collimator (also called jaws), and multileaf collimators (MLCs), played important roles to modify photon beams in 3-dimension conformal radiotherapy (3D-CRT) and advanced techniques, such as, intensity modulated radiation therapy (IMRT) and volumetric modulated arc therapy (VMAT) [4]. Thus, when the LINAC is operated at high energy (≥10 MV), neutrons can be produced.

The determination of neutrons is a part of radiation protection program, including individual monitoring to measure the occupational dose and dose to patients who directly exposed to the beams, as well as workplace monitoring to measure the radiation dose in controlled areas and supervised areas for assessing and reviewing of area classification [5].

In previous studies, one field size was typically selected to demonstrate neutron production in the treatment room when operating at high energy (≥10 MV). It is interesting to study the field size dependence on neutron production.

This study aimed to determine neutron ambient dose equivalent, $H^*(10)$, at different locations of the 10 MV LINAC treatment room for different field sizes shaped by the MLCs by using CR-39 dosimeters.

II. MATERIALS AND METHODS

Varian TrueBeam (Varian Medical System, Palo Alto, CA, USA) LINAC at Radiation Oncology Department, Chulabhorn Hospital was used to study neutron generation in the treatment room with 10 MV flattened beams. The measurement locations in the treatment room were at 100 cm (A) and 200 cm (B) from isocenter, at the maze junction (C), in the maze (D), and at the room entrance (E), as shown in Figure 1.

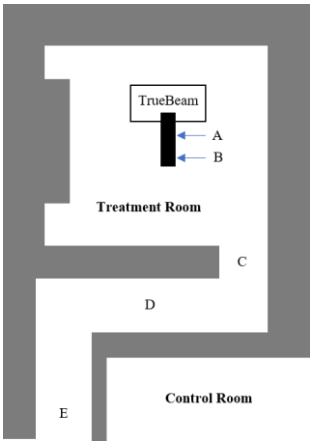

Figure 1. *Layout of the measurement locations in the treatment room.*

CR-39 dosimeters (BARYOTRAK, Fukuvi Chemical Industry, Japan), as shown in Figure 2, were used for detecting neutrons in this study. Each CR-39 dosimeter was put into a plastic holder with one side covered by a polyethylene sheet and the other by a boron sheet, to detect fast neutrons in the energy range from 24 keV to 15 MeV and thermal neutrons in the energy range from 0.025 eV to 0.5 eV, respectively. Note that the CR-39 dosimeters had lower detection limits (LLDs) of 0.1 mSv for both fast and thermal neutrons.

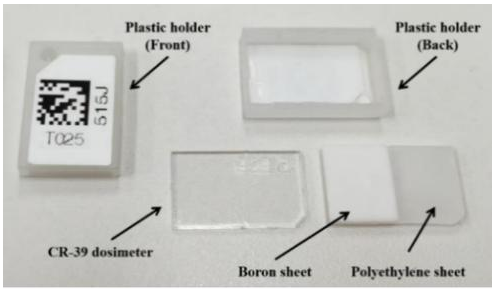

Figure 2. *A CR-39 dosimeter with a polyethylene converter, a boron converter, and a plastic holder.*

A. Irradiation set-ups

The CR-39 dosimeters were placed in air at the locations of measurement, as shown in Figure 3. The irradiation was done with 10 MV flattened beams at the gantry angle of 0°, the dose rate of 600 MU/minute, and the total dose of 1,800 MU. The field sizes of 1×1 cm^2, 2×2 cm^2, 5×5 cm^2, 10×10 cm^2, 20×20 cm^2 were shaped by the MLCs together with the field size of 20×20 cm^2 shaped by the jaws. The couch was set to the lowest position to avoid scattered radiations.

Figure 2. *Placement of CR-39 dosimeters in air in treatment room.*

To compare with other publication, the CR-39 dosimeters were also irradiated in air with 10 MV flattened beams under the following settings:

(i) Gantry angle of 270°, dose rate of 400 MU/minute, and total dose of 2,400 MU at 100 cm from the isocenter with the field size of 0.5×0.5 cm^2 shaped by the jaws [3], and

(ii) Gantry angle of 0°, dose rate of 400 MU/minute, and total dose of 2,400 MU at 100 cm and 200 cm from the isocenter with the field size of 0.5×0.5 cm^2 shaped by jaws [4].

For each measurement, 3 repetitions were performed to derive the average and standard deviations of the measurements.

B. Neutron dose evaluation process

After irradiation, CR-39 dosimeters were etched in 5.26 M NaOH solution for 15.5 hours in water bath at the temperature of 72℃ to expand the neutron tracks on the CR-39 surface. After etching, the CR-39 dosimeters were rinsed with distilled water to wash NaOH solution from the surface and were dried by a blower. The neutron tracks were counted under microscope with magnification of 400x. The example of neutron tracks has shown in Figure 3.

The CR-39 dosimeters have been calibrated in term of neutron ambient dose equivalent with ^{252}Cf for fast neutrons and ^{241}Am-Be moderated with graphite blocks for thermal neutrons. The number of neutron tracks was converted to $H^*(10)$ by using calibration coefficients obtained from the calibration.

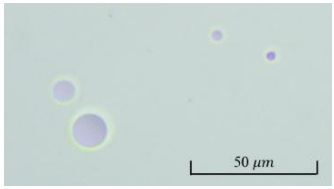

Figure 4. *The neutron tracks on the surface of a CR-39 dosimeter under the magnification of 400x.*

It is to note that thermal neutrons could be detected at all positions but the resulting *H**(10) were lower than the LLD. Thus, *H**(10) reported in this study were only those from fast neutrons.

III. RESULTS

A. H(10) at different locations in the treatment room and for different field sizes shaped by the MLCs*

Table 1 shows *H**(10) at the different locations in the treatment room for the different field sizes shaped by the MLCs. The highest neutron dose was found at point A for all field sizes and the neutron dose decreased with the increasing distance from the isocenter. Moreover, the different field sizes shaped by the MLCs affected *H**(10) with the decreased *H**(10) as the field size was increased.

Table 1. *H*(10) at different locations in the treatment room and different field sizes shaped by MLCs.*

Field size (Shaped by MLCs)	Neutron ambient dose equivalent per MU, *H**(10) (×10^{-4} mSv/MU)				
	Point A	**Point B**	**Point C**	**Point D**	**Point E**
1×1 cm^2	4.88 ± 0.47	2.20 ± 0.31	1.53 ± 0.08	0.81 ± 0.21	0.76 ± 0.14
2×2 cm^2	3.84 ± 0.17	1.89 ± 0.39	1.08 ± 0.08	0.54 ± 0.16	<LLD
5×5 cm^2	2.88 ± 0.41	1.53 ± 0.28	0.72 ± 0.08	0.54 ± 0.21	<LLD
10×10 cm^2	2.16 ± 0.31	1.35 ± 0.21	0.72 ± 0.08	<LLD	<LLD
20×20 cm^2	1.35 ± 0.16	1.12 ± 0.08	0.74 ± 0.00	<LLD	<LLD

For relatively large field sizes at point D (10×10 and 20×20 cm^2) and point E (from 2×2 to 20×20 cm^2), neutrons could be detected but the measured *H**(10) were lower than the LLD.

B. Comparison with published data

Table 2 shows the comparison of *H**(10) measured in this work with those obtained from neutron spectrum measurements of Maglieri [3] and Montgomery et al. [4] at the gantry angles of 270 and 0, respectively. At the gantry angle of 270, our result was higher than the published result by 8.37%. However, at the gantry angle of 0, our results were lower than the references by 30.00% and 19.51%, at 100 and 200 cm from the isocenter, respectively. Considering the neutron dose ratio at 100 and 200 cm, our result yielded a ratio of 1.74, about 15% higher than that obtained from the spectrum measurement.

IV. DISCUSSION

This study demonstrated the use of CR-39 dosimeters to measure *H**(10) in the treatment room at the different locations from the isocenter. The results showed that *H**(10) decreased with increasing distance from the isocenter and when the MLCs intercepted the primary photon beam with a larger surface in the photon beam, or a decreased field size. These findings were similar to those reported by Suliman et al. [6] and Howell et al. [7], respectively.

Compared to the neutron spectrometry studies of Montgomery et al. [4], we found large discrepancies from the published results. In this study, we placed the dosimeters in air and set the couch furthest down to avoid scattered radiations, but in Montgomery et al.'s study, the couch was required to place at the neutron spectrometer. The different measurement environments could cause a different degree of scatterings in the treatment room.

Furthermore, the energy response of the CR-39 dosimeters should be considered due to relatively broad neutron energy spectra in the treatment room [8]. In this study, ^{252}Cf standard source was used for calibrating the dosimeters for fast neutrons. This source yielded the average neutron energy of 2.13 MeV [9], but the average neutron energies at 100 cm and 200 cm from the isocenter were 0.13 [3] and 0.11 MeV

Table 2. *Comparison of H*(10) measured in this study and those published in the literature.*

Location	Gantry angle	Ref.	$H^*(10)$ ($\times 10^{-4}$ mSv/MU)	
			This study	Published data
100 cm from isocenter	270	[3]	4.79	4.42
100 cm from isocenter	0	[4]	2.87	4.10
200 cm from isocenter	0	[4]	1.65	2.05

[4], respectively. Thus, the standard source calibration coefficients may not be adequate for accurate neutron dose determination and the actual neutron energy spectra should be considered.

V. CONCLUSION

The neutron ambient dose equivalent decreased with increasing distance from the isocenter and was influenced by the collimated field size defined by the MLCs. Additionally, to accurately determine neutron dose, dosimeters should be calibrated in a reference neutron field that had a similar energy spectrum as the neutron field of interest.

ACKNOWLEDGEMENTS

The authors would like to thank Individual Monitoring Service Laboratory of Thailand Institute of Nuclear Technology (Public Organization) for supporting a CR-39 dosimeters and the instruments in evaluation process.

REFERENCES

[1] Banaee N, Goodarzi K, Nedaie HA. Neutron contamination in radiotherapy processes: a review study. J Radiat Res. 2021;62(6):947-54.

[2] Carlone M, Yang R, Hyde D, et al. Measurement of neutron yield for a medical linear accelerator below 10 MV. Med Phys. 2023;50(6):3338-46.

[3] Maglieri R. A study of photoneutron spectra around high-energy medical linear accelerators using Monte Carlo simulations and measurements [master's thesis on the Internet]. Quebec (CA): McGill University; 2015 [cited 2024 Dec 1] Available from: https://escholarship.mcgill.ca/concern/theses/nc580q71b.

[4] Montgomery L, Evans M, Liang L, et al. The effect of the flattening filter on photoneutron production at 10 MV in the Varian TrueBeam linear accelerator. Med Phys. 2018;45(10):4711-9.

[5] IAEA. Safety Standard Series No. GSR Part 3. International Atomic Energy Agency, Vienna, AT. 2014

[6] Suliman II, Khouqeer GA, Mayhoub FH. Photoneutrons and Gamma Capture Dose Rates at the Maze Entrance of Varian TrueBeam and Elekta Versa HD Medical Linear Accelerators. Toxics. 2023;11(1).

[7] Howell RM, Kry SF, Burgett E, et al. Effects of tertiary MLC configuration on secondary neutron spectra from 18 MV x-ray beams for the Varian 21EX linear accelerator. Med Phys. 2009;36(9):4039-46.

[8] Kry SF, Bednarz B, Howell RM, et al. AAPM TG 158: Measurement and calculation of doses outside the treated volume from external-beam radiation therapy. Med Phys. 2017;44(10):e391-e429.

[9] ISO 8529-1:2021. Neutron reference radiation fields — Part 1: Characteristics and methods of production.

Contacts of the corresponding author:
Author: Thiansin Liamsuwan
Institute: Princess Srisavangavadhana College of Medicine, Chulabhorn Royal Academy
Street: 906 Kampangpetch 6 Road, Talat Bang Khen, Lak Si
City: Bangkok
Country: Thailand
Email: thiansin.lia@cra.ac.th

Investigated radiation dose at surrounding area in real-time motion tracking system of tomotherapy: A phantom study

Kititharakun Phairot[1,2], NopNob Wannapha[2], Kongsa Anupong[2], Watcharawipha Anirut[2,*]

[1]*Department of Radiology, Medical Physics program, Faculty of Medicine, Chiang Mai University, Chiang Mai, Thailand.*
[2]*Department of Radiology, Division of Radiation Oncology, Faculty of Medicine, Chiang Mai University, Chiang Mai, Thailand.*
**anirut.watch@cmu.ac.th*

Abstract — **Introduction:** Real-time motion tracking (RTMT) is the method that delivers radiation to the moving target. The system tracks the target movement and adapts the radiation aperture corresponding to the target position. During the target movement, the surrounding organs remain in a permanent location. The organ dose may increase due to the returning target position. This study investigated the dose difference at the surrounding area in a phantom study. **Methods:** Five breathing cycles were acquired from patients diagnosed with thoracic cancer. Three treatment plans of stereotactic body radiotherapy were recruited and matched to these breathing cycles. The radiation dose was measured using ArcCHECK® with a synthetic moving target. A 0.13cm^3 ionization chamber (IC) was simulated as the target driven by dynamic platforms CIRS®. The dose difference between the static and moving target was observed and compared. **Results:** The Gamma passing rates evaluated for static target measurements were 99.6 ± 0.4% and 99.1 ± 0.9% for Gamma criteria of 3%/3mm and 3%/2mm, respectively. The percentage of detectors with percent dose difference levels within 5%, 10%, 15%, 20%, 25%, 30% and 100% were 46.4 ± 16.6%, 21.3 ± 6%, 9.2 ± 3.4%, 5.3 ± 2.3%, 4.1 ± 1.9%, 2.9 ± 2.2% and, 10.9 ± 12.3%, respectively. **Conclusion:** Using the RTMT method can increase the surrounding dose when these organs are static. The dose can be increased by up to 10% of the treatment planning dose. However, a dose difference of more than 10% appeared at the area of low dose.

Keyword: Real time motion tracking, Tomotherapy, Gamma passing rate, surrounding dose

I. INTRODUCTION

External Beam Radiotherapy (EBRT) aims to eradicate cancer cells with high-energy radiation while minimizing the impact on surrounding organs. Accurate localization and dose of radiation are critical, particularly in the target motion. The movement of target may be caused by the respiratory and other organ functions. This is the main cause which affect the size of the Planning Target Volume (PTV)[1-2].

The American Association of Physicists in Medicine (AAPM) Report Number 91 recommends motion management when the target is moving[3]. The Real-Time Motion Tracking (RTMT) is one method manages the target motion. This method was developed for the Tomotherapy after the robotic treatment machine. This tracking system consists of sweeping jaws for tracking the target in the craniocaudal direction, while the binary multi-leaf collimator (biMLC) tracks in vertical and horizontal directions. Using this system, the target can receive accurate doses and be precisely located[4-5]. However, the radiation delivers the moving target, some surrounding normal organs remained. This can result in dose differences in the normal organs compared to the target[6]. Although there is a publication investigating dose uncertainty in normal organs, the radiation was measured using a detector for image reconstruction[7-8]. This study aims to investigate the radiation dose at the surrounding area using helical detector in the phantom on the static and moving target conditions.

II. MATERIALS AND METHODS

A. Treatment planning selection

Three treatment plans for Stereotactic Ablative Body Radiotherapy (SABR) for thoracic cancer were randomly selected from treatment plans between January 2024 and August 2024. All selected plans involved a single lesion in the lung and were delivered using Radixact® Tomotherapy (Accuray® Inc., WL, USA). The plans were based on images from a Computed Tomography simulator (SOMATOM Definition AS, Siemens Inc., Healthineers, Germany) with a slice thickness of

Table 1 *Target volume and breathing cycle characteristics.*

Target volume characteristic	
PTV (cc)	28.7 ± 3.4
Width (mm)	35.0 ± 2.4
Length (mm)	36.1 ± 9.0
Height (mm)	46.1 ± 8.5
Breathing cycle characteristics	
Frequency (cycle/min)	25.0 ± 7.1
Travel distance (mm)	7.8 ± 3.0

1 mm. The Planning Target Volume (PTV) was expanded by 3 mm from the Gross Target Volume (GTV) in the phase of deep inspiration breath hold (DIBH). The targe characteristics are described in Table 1.

B. Breathing Cycle Preparation

The breathing cycles were acquired from five patients diagnosed with thoracic cancer. These breathing cycles were acquired using a surface guided system (Sentinel™, C-RAD AB, Sweden). The CSV file format from the Sentinel™ was converted to TXT file format using in-house software implemented in MATLAB® version R2021b (MathWorks Inc., MA, USA). Detailed attention was given to the characteristics of these breathing cycles, specifically the frequency and travel distance, which were on average 25.0 ± 7.1 cycles per minute and 7.8 ± 3.0 mm, respectively, as recorded in Table 1.

Table 2 *Gamma passing rate of static target condition*

Plan	Gamma passing rate (%)	
	3%/3mm	3%/2mm
Static target condition		
1	100.0	99.7
2	99.6	99.6
3	99.2	98.1
	99.6 ± 0.4	99.1 ± 0.9
Moving target condition		
1	79.4 ± 27.1	67.4 ± 26.5
2	89.1 ± 8.9	79.8 ± 13.0
3	93.7 ± 6.9	84.6 ± 12.6
	87.4 ± 16.8	77.3 ± 18.7

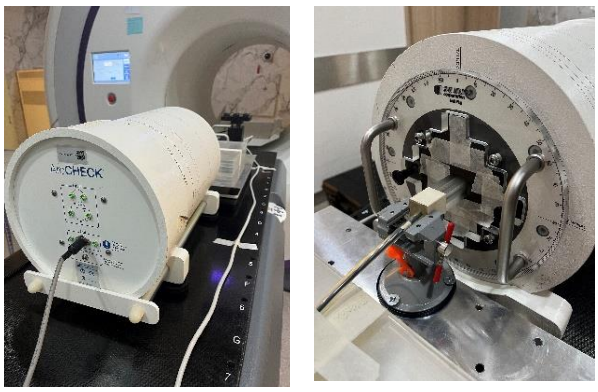

Figure 1. *Measurement setup using ArcCHECK® and Dynamic platform CIRS®.*

C. Measurement Methods

Patient specific quality assurance (PSQA) for stereotactic body radiotherapy treatment plans of three selected patients were conducted using a helical diode array phantom (ArcCHECK®, Sun Nuclear Co., FL, USA). The measurements were performed both static and moving target condition. For the moving condition, a synthetic motion marker (0.13 cc ionization chamber, Scanditronix Wellhofer Inc., MN, USA) was inserted at the center of the phantom and driven using a dynamic planform (Dynamic Platform CIRS®, Model 008PL, VA, USA) as shown in Figure 1. The motion cycles were uploaded into the computer controller and drove the platform when the measurement was performed.

D. Dose different evaluation and data analysis

The plans of static target condition were measured to confirm the plan quality using Gamma passing rate (GPR). The criterion of Gamma analysis was performed using 3%/3mm and 3%/2mm for the dose difference and distance to agreement, respectively. The dose difference between static and moving target conditions were compared from point-to-point of ArcCHECK® detectors. The levels of dose difference were classified by 5% equivalent intervals, except the dose difference larger than 30%. The number of detectors of each dose level was counted and reported. The significant correlation among dose difference level, frequency and travel distance was analyzed using Pearson correlation (SPSS version 30.0.0.0 (172), IBM Co. NY, USA).

Table 3 *Percent detector number of point-to-point dose difference between static and moving target condition*

Plan No.	Cycle No.	Freq. (c/m)	Travel distance (mm)	Percent number detector of dose different level (%)						
				< 5%	5%-10%	10% - 15%	15% - 20%	20% - 25%	25% - 30%	> 30%
1	1	15.8	5.6	9.2	18.3	8.9	8.6	6.7	3.9	44.4
	2	20.6	12.7	31.7	13.7	9.5	7.2	6.7	3.1	28.1
	3	25.1	6.2	35.3	20.1	9.6	5.1	5.3	7.8	16.8
	4	30.8	6.0	68.3	18.8	6.2	3.4	2.5	0.6	0.3
	5	32.8	8.6	38.1	23.2	9.3	6.1	4.5	4.5	14.1
2	1	15.8	5.6	54.1	34.8	5.4	2.2	1.8	0.8	0.8
	2	20.6	12.7	44.0	19.3	9.4	6.3	7.3	3.5	10.2
	3	25.1	6.2	41.1	29.5	11.2	5.4	4.8	1.6	6.4
	4	30.8	6.0	80.6	14.1	3.1	0.6	1.2	0.4	0.0
	5	32.8	8.6	50.2	13.6	6.5	3.1	4.3	6.3	15.9
3	1	15.8	5.6	51.9	18.7	7.2	5.6	3.0	2.0	11.5
	2	20.6	12.7	35.5	20.6	16.2	9.2	4.4	3.5	10.5
	3	25.1	6.2	51.7	21.5	13.0	6.8	4.5	1.5	0.9
	4	30.8	6.0	58.5	24.9	8.7	5.1	2.3	0.0	0.6
	5	32.8	8.6	46.2	28.0	13.4	4.6	2.2	3.3	2.2
Mean		25.0	7.8	46.4	21.3	9.2	5.3	4.1	2.9	10.9
SD		7.1	3.0	16.6	6.0	3.4	2.3	1.9	2.2	12.3
^{T}p-value				0.271	0.291	0.088	0.084	**0.045**	0.264	0.461
^{F}p-value				0.081	0.717	0.810	0.112	0.167	0.873	0.111

Abbrivations: SD, Standard Deviation; ^{T}p-value, p-value between range of dose level and travel distance; ^{F}p-value, p-value between range of dose level and frequency.

III. RESULTS

A. Gamma passing rates of static target condition

The measurement of the target in a static condition illustrated the results as shown in Table 2. The mean value of GPR revealed 99.6 ± 0.4% and 99.1 ± 0.9% for the criteria of 3%/3mm and 3%/2mm, respectively.

B. Gamma passing rates of moving target condition

GPR was used to evaluate the plan quality in the moving target condition. The results are revealed in Table 2 as well. The mean GPR values of 3%/3mm and 3%/2mm were 87.4 ± 16.8% and 77.3 ± 18.7%, respectively.

C. Percent detector number of point-to-point dose difference

These data were compared between static target and moving target conditions. The dose differences at point-to-point are 46.4 ± 16.6%**,** 21.3 ± 6.0%, 9.2 ± 3.4%**,** 5.3 ± 2.3%**,** 4.1 ± 1.9%**,** 2.9 ± 2.2% and 10.9 ± 12.3% for 0-5%**,** 5-10%**,** 10-15%**,** 15-20%**,** 20-25%**,** 25-30% and over 30%, respectively. The statistical analysis found a significant correlation ($p = 0.045$) only between the range of 20-25% dose difference and travel distance whereas the other dose ranges did not show a significant correlation ($p > 0.05$) to both travel distance and breathing cycle frequency.

IV. DISCUSSION

Dose difference in the surrounding area using RTMT was an area of interest for investigation. This study observed the surrounding dose in a phantom using the clinical breathing cycle. The detector of the phantom can represent the static normal tissue at the peripheral object while the radiation beam focused on the moving target. Although the detectors presented a dose difference larger than 5%, this difference in dose levels was observed in the superior and interior region of the target as shown in Figure 2. According to the International Commission on Radiation Units and measurements (ICRU) recommendation, the dose uncertainty of the target can deviate up to 5%[9]. This study then focused on the range of 5-15% dose difference. This dose difference area was a major dose deviation that depended on the amplitude of target motion while an area of larger dose difference had less impact on the surrounding treatment area as shown in Figure 2. These results confirmed the work of Ferris et. al[6].

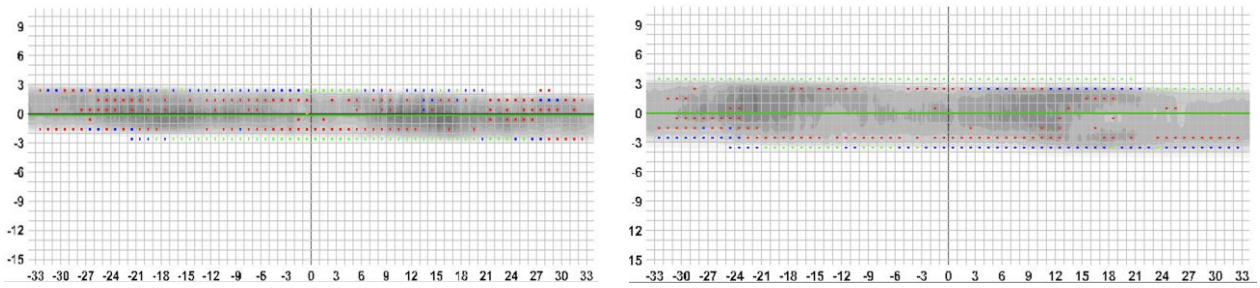

(a) (b)

Figure 2. *Dose difference comparison point-to-point between static and moving target conditions using ArcCHECK®. The color dots of by red, blue and green indicate dose differences in the ranges of < 5%, 5%-15% and 15%-30%, respectively, for example cases of patient A (a) and patient B (b).*

However, this study could not conclude the direction (over-dose or under-dose) of the dose difference due to the motion of the breathing cycle as shown in Figure 2.

The point of interest was that a dose difference level of 20-25% was found to have a significant difference impact on the travel distance. This may be influenced by the end of the target, which depends on the PTV size. Meanwhile, the detectors may not be able to measure if the end of the target cannot reach the sensitive detector area. This impact should be confirmed using a high-resolution detector device.

V. CONCLUSION

This study investigated the surrounding dose using a helical detector phantom. The result showed a dose difference up to 10% from the prescribed dose. This dose deviation found no significant correlation between the dose difference level and travel distance, and frequency of the breathing cycle. However, the interface at the end of the superior and inferior target required further investigation.

ACKNOWLEDGEMENTS

This study has no acknowledgements.

REFERENCES

[1] Choi Y, Kwak DW, Lee HS, et al. Effect of rectal enema on intrafraction prostate movement during image-guided radiotherapy Journal of medical imaging and radiation oncology. 2015;59(2):236-242.

[2] Chen GP, Tai A, Puckett L, et al. Clinical Implementation and Initial Experience of Real-Time Motion Tracking with Jaws and Multileaf Collimator During Helical Tomotherapy Delivery. Practical radiation oncology. 2021;11(5):e486-e495.

[3] American Association of Physicists in Medicine. The management of respiratory motion in radiation oncology. AAPM Report No. 91. College Park, MD

[4] Ferris WS, Culberson WS, Smilowitz JB, Bayouth JE. Effects of variable-width jaw motion on beam characteristics for Radixact Synchrony®. Journal of applied clinical medical physics. 2023 Mar; 24(3):e13883.

[5] Schnarr E, Beneke M, Casey D, et la. Feasibility of real-time motion management with helical tomotherapy. Medical physics. 2018;45(4):1329-1337.

[6] Ferris WS, Chao EH, Smilowitz JB, Kimple RJ, Bayouth JE, Culberson WS. Using 4D dose accumulation to calculate organ-at-risk dose deviations from motion-synchronized liver and lung tomotherapy treatments. Journal of applied clinical medical physics. 2022;23(7):e13627.

[7] Chen GP, Tai A, Puckett L, et al. Clinical Implementation and Initial Experience of Real-Time Motion Tracking with Jaws and Multileaf Collimator During Helical Tomotherapy Delivery. Practical radiation oncology, 2021;11(5):e486-e495.

[8] Ferris WS, Kissick MW, Bayouth JE, Culberson WS, Smilowitz JB. Evaluation of radixact motion synchrony for 3D respiratory motion: Modeling accuracy and dosimetric fidelity. Journal of Applied Clinical Medical Physics. 2020;21(9):96-106.

[9] International Commission on Radiation Units and Measurements (ICRU). Prescribing, recording, and reporting photon beam therapy. Report 50. Bethesda, MD: ICRU; 1993.

Contacts of the corresponding author:

Author: Anirut Watcharawipha
Institute: Department of Radiology, Faculty of Medicine, Chiang Mai University
Street: 110 Intawaroros Rd.
City: Mueang, Chiang Mai
Country: Thailand, 50200
Email: anirut.watch@cmu.ac.th

Investigated performance of Real-Time Motion Tracking System in Tomotherapy

Messuwan Jiraphat[1,2], Watcharawipha Anirut[2,*], Nopnob Wannapha[2] and Kongsa Anupong[2]

[1]*Medical Physics program, Department of Radiology, Faculty of Medicine, Chiang Mai University, Chiang Mai, Thailand.*

[2]*Division of Radiation Oncology, Department of Radiology, Faculty of Medicine, Chiang Mai University, Chiang Mai, Thailand.*

First author: Jiraphat_me@cmu.ac.th, First33@outlook.com

Corresponding author: anirut.watch@cmu.ac.th

Abstract — **Introduction:** Real time motion tracking (RTMT) is a sophisticated radiotherapy technique where treatment machines deliver radiation by tracking the target motion. The machine is equipped with a kV imaging system and an optical positioner to generate the motion cycles. However, the transition between the acquired signal and beam adaptation may affect the accuracy delivery. This research evaluated the performance of the RTMT system of tomotherapy using clinical breathing cycles. **Methods:** A surface detector (Sentinel™) acquired 15 breathing cycles from a patient diagnosed with thoracic cancer. Six treatment plans for stereotactic body radiotherapy in lung cancer were randomized to match these beathing cycles. Sixty pairs of measurements were performed using MapCHECK® on Dynamic platform CIRS® and compared between static target and moving target using potential difference (PD) of 3. An analysis of Gamma passing rate (GPR) evaluated the performance of RTMT with Gamma criteria of 3%/2mm, 3%/1mm, 2%/3mm, 2%/2mm and 2%/1mm. **Result:** The results illustrated that the mean value of PTV, traveling distance and frequency of these samples were 10.2 ± 7.8 cm^3, 7.5 ± 2.3 mm and 22.6 ± 6.0 cycles/min, respectively. The results of GPR for a static target revealed mean value of 100 ± 0.0%, 100 ± 0.0%, 100 ± 0.0%, 99.8 ± 0.4% and 99.5 ± 1.2% whereas a moving target showed mean value of 100 ± 0.2%, 99.9 ± 0.6%, 99.6 ± 0.6%, 99.2 ± 1.1% and 97.9 ± 2.4% in the order of Gamma criteria, respectively. However, these results demonstrated no significant correlation between GPR and travel distance and breathing frequency. **Conclusion:** The performance of the tracking system in tomotherapy showed accuracy in tracking target motion, with a DTA value as low as 1 mm for both 2% and 3% dose differences. Additionally, this accuracy was not impacted by the various traveling distance and frequencies of the breathing cycle.

Keywords — Tomotherapy, Real-time motion tracking, Motion management, Gamma passing rate.

I. INTRODUCTION

Radiation therapy is the process that delivers radiation to a lesion. Sophisticated techniques commonly used in this treatment include Intensity Modulated Radiotherapy (IMRT) and Intensity Modulated Arc Therapy (IMAT). The treatment technique requires treatment planning on a static image set of Computed Tomography (CT) or Magnetic Resonance Imaging (MRI).[1-3] Due to organ motion, particularly in the chest and abdomen, the International Commission on Radiation Units and Measurements (ICRU) recommends that the volume of the target include the traveling area of the target, in terms of *'Internal Motion (IM)'*, namely *'Internal Target Volume (ITV)'*.[4-5] Consequently, the surrounding normal tissue of the target receives the prescribed radiation dose. To reduce this impact, Real-Time Motion Tracking[6] (RTMT) is one of the motion management methods that is an interesting method of treatment. The RTMT system has recently been integrated into Tomotherapy in terms of the *'Synchrony®'* system. This system controls the position of the binary multi-leaf collimator (biMLC) and sweeping jaws to synchronize the target motion. For respiratory motion, the system requires a Light Emitting Diode (LED) to track the breathing cycle whereas a radiography is used to acquire an image for target localization.[7] Although the Synchrony® system provided high accuracy in motion tracking, the treatment time would be extended due to treatment interruptions. Potential Difference (PD) value is

Table 1. Planning Target volume and its motion characteristic.

Plan	PTV (cc)	Width (mm)	Height (mm)	Length (mm)	Travel distance (mm)	Frequency (cycle/min)
1	6.3	22.0	21.9	23.9	8.1	23.3
2	6.1	24.8	23.3	25.3	6.8	23.2
3	14.2	44.2	32.5	26.4	7.5	21.5
4	6.2	26.9	32.2	18.2	7.6	22.4
5	24.5	25.6	33.3	48.3	7.3	21.9
6	4.1	20.1	20.0	18.0	7.5	23.3
	10.2 ± 7.8	27.3 ± 8.6	27.2 ± 8.6	26.7 ± 11.2	7.5 ± 2.7	22.6 ± 6.0

one of the main parameters that trade-off between treatment time and treatment accuracy. This value allows for the range of target displacement without machine interruption. A previous study investigated the treatment accuracy using different PD value.[8] Although this previous study recommended the value of PD, the experiment was concluded using synthetic breathing cycles. This study aims to investigate the treatment accuracy of RTMT in Tomotherapy using clinical breathing cycles.

II. MATERIALS AND METHODS

A. Treatment planning selection

The retrospective study randomly recruited six treatment plans of patients with lung cancer who underwent Stereotactic Ablative Body Radiotherapy (SABR) between January 2023 and February 2024. A single lesion of Gross Target Volume (GTV) had a 3 mm expansion to the Planning Target Volume (PTV). The volume and size of the PTV were described in Table 1.

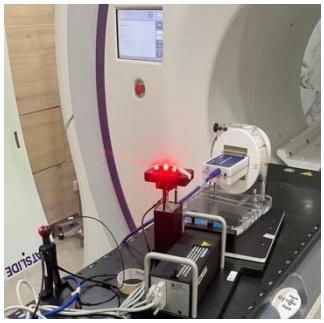

Figure 1. Phantom setup geometry for dose measurement of moving target. Dynamic Platform CIRS® aligned 30 degrees while SRS-MapCHECK® and SRSphan® aligned inline axis.

The average PTV size and its standard deviation (SD) were 10.2 ± 7.8 cm^3, while the dimensions of the PTV were 27.3 ± 8.6 mm, 27.2 ± 8.6 mm, and 26.7 ± 11.2 mm for width, height, and length, respectively.

B. Breathing cycle preparation

This study involved the clinical breathing cycle of patients who underwent treatment in the thorax region. Fifteen breathing cycles were acquired using the surface imaging system (Sentinel™, C-RAD AB, Sweden). The file format of Comma Separated Value (CSV) from the Sentinel™ was converted to the text (TXT) file format using in-house software developed using MATLAB® version R2021b (MathWorks Inc., MA, USA). The average and SD value of all breathing cycles are described in Table 1 where traveling distance (mm) and frequency (cycles/min) represent the maximum amplitude and cycle number per period of breathing cycle.

C. Measurement and motion tracking methods

Quality assurance plans for six patients were conducted using a diode array phantom (SRS-MapCHECK® and SRSphan®, Sun Nuclear Co., FL, USA). These plans were used to measure the dose distribution for static and moving target conditions. The geometry of the SRSphan® was aligned on a motion plate (Dynamic Platform CIRS®, Model 008PL, VA, USA) at a 30-degrees angle as shown in Figure 1. The measurements were performed in both static and moving target conditions. The marker of the SRSphan® was used for the motion tracking method as illustrated in Figure 2. This marker

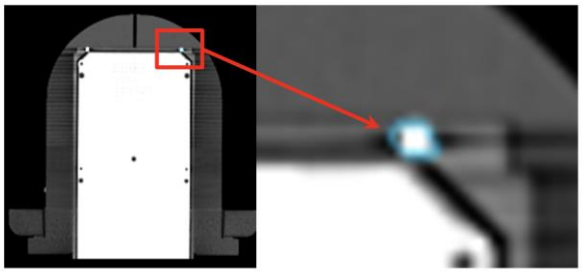

Figure 2. Marker in SRS-MapCHECK® for motion tracking.

was simulated as the target volume of a radiographic system. The kV-radiographs were captured using an energy of 120 kV and a current of 1.25 mAs for the target localization. This radiography captured the images at equivalent interval of 60 degrees. The Light Emitted Diode (LED) was used for the illuminated amplitude of the clinical breathing cycle. The values of PD measured delta and target offset were set at 3 mm, 4 mm and 30 mm, respectively.

D. Performance evaluation and statistical analysis

Gamma analysis was used to evaluate the performance of the Tomotherapy Synchrony® system. The criteria of 3%/2mm, 3%/1mm, 2%/3mm, 2%/2mm and 2%/1mm with 10% of Low Dose Threshold were used to investigate the motion tracking accuracy. The significant correlation was determined among PTV size, travel distance, breathing frequency and Gamma Passing Rate (GPR) using SPSS Statistics version 28.0 (IBM Inc., Armonk, USA). The statistic analyzed these data with 95% confidence interval where p-value < 0.05.

III. RESULTS

A. Static target condition: The plan quality of the standard target condition was assessed using Patient Specific Quality Assurance (PSQA). The results demonstrated a high accuracy of the delivery with a percentage of GPR above 99.0% for all selected Gamma analysis criteria.

B. Moving target conditions: These six PSQA plans were combined with ten random clinical breathing cycles. These measurements were performed under a mean travel distance and frequency of breathing cycle at 7.5 ± 2.3 mm and 22.6 ± 6.0 cycles/min, respectively. The results revealed the mean percentage of GPR for a Gamma criterion of 3%/2mm, 3%/1mm, 2%/3mm, 2%/2mm and 2%/1mm, were 100 ± 0.2%, 99.9 ± 0.6%, 99.6 ± 0.6%, 99.2 ± 1.1% and 97.9 ± 2.4%, respectively.

Table 2. Mean percentage Gamma passing rate and standard deviation of static and moving target conditions, and the statistical correlation analysis compared to size of PTV, travel distance and breathing frequency.

Plan	Gamma passing rate (%)				
	2%/3mm	2%/2mm	2%/1mm	3%/1mm	3%/2mm
Static target condition					
	100.0 ± 0.0	99.8 ± 0.4	99.5 ± 1.2	100.0 ± 0.0	100.0 ± 0.0
Moving target condition					
1	98.9 ± 0.7	97.9 ± 1.1	95.9 ± 2.2	99.6 ± 1.4	99.8 ± 0.5
2	99.4 ± 0.3	98.9 ± 0.5	97.0 ± 0.9	100.0 ± 0.0	100.0 ± 0.0
3	99.6 ± 0.9	99.1 ± 1.5	97.5 ± 3.5	99.8 ± 0.5	99.9 ± 0.1
4	99.8 ± 0.2	99.6 ± 0.4	98.1 ± 2.4	100.0 ± 0.0	100.0 ± 0.0
5	100.0 ± 0.2	99.9 ± 0.3	99.5 ± 1.4	100.0 ± 0.0	100.0 ± 0.0
6	100.0 ± 0.0	100.0 ± 0.0	99.8 ± 0.4	100.0 ± 0.0	100.0 ± 0.0
Mean ± SD	99.6 ± 0.6	99.2 ± 1.1	97.9 ± 2.4	99.9 ± 0.6	100.0 ± 0.2
^{P}p-value	0.631	0.876	0.871	0.412	0.412
^{T}p-value	0.063	0.440	0.577	0.067	0.067
^{F}p-value	0.252	0.286	0.400	0.586	0.586

Abbreviations: ^{P}p-value, p-value of significant correlation between GPR and size of PTV, ^{T}p-value, p-value of significant correlation between GPR and travel distance, ^{F}p-value, p-value of significant correlation between GPR and breathing frequency.

The statistical analysis found no significant difference between not only the GPR and travel distance ($p \geq 0.063$) but also the GPR and the frequency of the breathing cycle ($p \geq 0.252$). Finally, the sizes of the PTV did not significantly impact ($p \geq 0.412$) on the GPR value as well.

IV. DISCUSSION

The Synchrony® of the Tomotherapy was a treatment machine that had a RTMT system for motion management. This system has two major components: target localization and radiation beam adaptation. This study investigated the Tomotherapy tracking system, which was assessed using the GPR value. This system verifies the target localization using a least-squares minimization problem. [7] This algorithm minimizes the error in target location between the 2D position detected and breathing amplitude. However, specific tolerances should be set to minimize machine interruption. The PD of 3 was introduced in clinical practices. Although the work of Sano et. al. [8] with a PD of 3 was investigated in the synthetic breathing cycle, this study confirmed this value can be used in clinic. However, this study did not investigate the impact of GPR when the PD of 2 was used in the Synchrony® system. Finally, this study found no significant correlation between GPR and size of PTV, travel distance and breathing frequency. This may conclude that the performance of the tracking system is robust for all continuous normally breathing cycle.

V. CONCLUSION

The Tomotherapy tracking system has shown exceptional efficacy in precisely monitoring target motion, achieving a DTA value as low as 1 mm, despite variations in dose variances of 2% and 3%. This exceptional precision persisted irrespective of the trip distances or frequencies linked to the patient's respiratory cycle. The system's capacity to adapt efficiently to diverse breathing patterns guaranteed consistent and accurate dose administration, reducing exposure to healthy tissues. These findings underscore the efficacy of the tracking system in motion management, resulting in enhanced treatment precision and potentially superior outcomes.

ACKNOWLEDGEMENTS

There are no acknowledgments on this study.

REFERENCES

[1] Abdul Ghani MNH, Ng WL. Management of respiratory motion for lung radiotherapy: a review. Journal of Xiangya Medicine. 2018;3:27–7

[2] Suramo I, Päivänsalo M, Myllylä V. Cranio-caudal movements of the liver, pancreas and kidneys in respiration. Acta Radiol Diagn (Stockh). 1984;25(2):129–31.

[3] Sihono D, Ehmann M, Heitmann S. Determination of Intrafraction Prostate Motion During External Beam Radiation Therapy with a Transperineal 4-Dimensional Ultrasound Real- Time Tracking System. International Journal of Radiation Oncology*Biology*Physics. 2018;101(1):136–43.

[4] Mah D, Hanley J, Rosenzweig KE, Yorke E, Braban L, Ling CC, et al. Technical aspects of the deep inspiration breath-hold technique in the treatment of thoracic cancer. Int J Radiat Oncol Biol Phys 2000;48(4):1175–85.

[5] Wong JW, Sharpe MB, Jaffray DA, Kini VR, Robertson JM, Stromberg JS, et al. The use of active breathing control (ABC) to reduce margin for breathing motion. International Journal of Radiation Oncology Biology Physics. 1999 Jul 1;44(4):911–9.

[6] Keall PJ, Mageras GS, Balter JM. The management of respiratory motion in radiation oncology report of AAPM Task Group 76a). Medical Physics. 2006;33(10):3874–900.

[7] Schnarr E, Beneke M, Casey D, Chao E, Chappelow J, Cox A, et al. Feasibility of real-time motion management with helical tomotherapy. Med. Phys. 2018;45(4):1329-1337.

[8] Sano K, Fujiwara M, Okada W, Masao Tanooka, Takaki H, Shibata M, et al. Optimal threshold of a control parameter for tomotherapy respiratory tracking: A phantom study. Journal of Applied Clinical Medical Physics. 2023;24(5):e13901.

Contacts of the corresponding author:

Author: Asst. Prof. Anirut Watcharawipha, Ph.D.
Institute: Division of Radiation Oncology, Department of Radiology, Faculty of Medicine, Chiang Mai University.
Street: 110 Intawaroros Rd.
City: Mueang, Chiang Mai
Country: Thailand, 50200
Email: anirut.watch@cmu.ac.th

Comparison of Normal Tissue Integral Dose between Volumetric Modulated Arc Therapy and Helical Tomotherapy for Post-Mastectomy Radiation Therapy with Regional Nodal Irradiation

Tananchai Kamonwan[1], Watcharawipha Anirut[2], Onchan Wimrak[2], Nobnop Wannapha[2,*]

1 Department of Radiology, Medical Physics Program, Faculty of Medicine, Chiang Mai University, Chiang Mai, Thailand.
2 Department of Radiology, Division of Radiation Oncology, Faculty of Medicine, Chiang Mai University, Chiang Mai, Thailand.
*(*Corresponding author: wannapha.n@cmu.ac.th)*

Abstract — **Introduction:** The Volumetric Modulated Arc Therapy (VMAT) and Helical Tomotherapy (HT) techniques are widely used in breast cancer treatment. However, these techniques may increase the normal tissue integral dose (NTID), potentially leading to complications and secondary cancers. Therefore, this study aims to compare the NTID between VMAT and HT for post-mastectomy radiotherapy (PMRT). **Methods:** Thirty patients treated using VMAT were enrolled in the study. Each patient was replanned using the HT plan, with and without an L-shaped (LB) directional block. The conformity index (CI), homogeneity index (HI), integral dose (ID), ID to OARs, NTID, V_{5Gy}, and nontarget tissue receiving 10% to 75% of prescription dose were analyzed. **Results:** The HTLB plan showed significantly better CI and HI compared to VMAT, but there was no significant difference between HTLB and HT. The ID for VMAT, HT, and HTLB were 152.9+/-5.9, 162.0+/-6.5, and 152.9+/-5.8 Gy·L, respectively. The NTID values were 120.5+/-4.0, 129.9+/-4.7, and 120.0+/-4.0 Gy·L, respectively. The heart ID was 3.4+/-0.3, 3.5+/-0.2, and 3.4+/-0.2 Gy·L; the ipsilateral lung ID was 16.7+/-0.9, 16.9+/-1.0, and 16.8+/-0.9 Gy·L; the contralateral lung ID was 2.9+/-0.2, 3.8+/-0.3, and 3.5+/-0.2 Gy·L; and the contralateral breast ID was 4.2+/-0.4, 3.9+/-0.3, and 3.8+/-0.4 Gy·L, respectively. The V_{5Gy} for HTLB was not significantly different from VMAT. Additionally, HTLB showed better sparing of nontarget tissue at high doses, while VMAT performed better in sparing at low to moderate doses. **Conclusion:** The NTID showed no significant difference between VMAT and HTLB, but there were significant differences compared to HT.

Keywords: Integral Dose, VMAT, Helical Tomotherapy, PMRT

I. INTRODUCTION

The Volumetric Modulated Arc Therapy (VMAT) and Helical Tomotherapy (HT) techniques are widely used in breast cancer treatment, especially for complex targets like post-mastectomy radiotherapy (PMRT) with regional nodal irradiation (RNI), which provide highly conformal dose distribution while minimizing radiation dose to organs at risk (OARs) [1]. One concern with arc-based techniques is the spreading of low doses to large volumes of normal tissue, which leads to higher normal tissue integral doses (NTID). This simultaneously increases the risk of secondary cancer and complications [2,3]. The integral dose (ID) is the volume integral of the dose deposited in a body and calculated by the mean dose times the volume irradiated to any dose [4]. The orientation of the entrance beams may influence the extent of the low-dose volume. Thus, the VMAT technique aims to reduce the low-dose volume by using a partial arc [5]. In contrast, the HT technique, with its 360-degree gantry rotation, spreads low doses to normal tissue, thereby increasing the integral dose (ID) [6]. However, HT mitigates this by employing a directional block option, specifically the L-shaped directional block structure (HTLB), to shield the contralateral side of the target [7]. Therefore, this study aims to compare the NTID between VMAT and HT for PMRT with RNI.

II. MATERIALS AND METHODS

Thirty patients treated with PMRT and RNI using VMAT were selected for this study. The clinical target volume (CTV) included the chest wall, supraclavicular nodes, axillary nodes, and internal mammary nodes. To generate the planning target volume (PTV), the CTV was expanded to 5 mm. The PTV was cropped 3 mm below the external surface. The OARs included the heart, ipsilateral lung, contralateral lung, and contralateral breast. A normal tissue structure was generated by subtracting the PTV from the

whole-body contour. All plans were generated for a prescription dose of 42.6 Gy in 16 fractions. The criteria for the target following the International Commission on Radiation Units and Measurements (ICRU) report No. 83 and the dose constraints for OARs met the objective.

A. Volumetric modulated arc therapy planning

The VMAT plans were created using the Monaco treatment planning system (version 5.11.10). All VMAT plans were constructed for an Elekta synergy using 6 MV photons. In all VMAT plans, two partial arcs were used: for the right breast, clockwise (CW) start from about 212° (range 205° - 215°) to about 78° (range 75° - 85°), counterclockwise (CCW) start from about 75° (range 70° - 75°) to about 215° (range 205° - 220°); for the left breast, CW start from 290° to 150°, CCW start from about 147° (range 140° - 150°) to about 287° (range 280° - 290°). The partial arc range averages 220° (210° - 240°). The couch angle and the collimator angle are 0°. In the case of difficult patients whose dosimetric goal could not be achieved with two arcs, an additional arc was added.

B. Helical tomotherapy planning

The HT plans were replanned using the Precision treatment planning system (version 3.3.1.3 [2]). The HT plan parameters include a dynamic jaw mode with a jaw width of 5 cm, a pitch of about 0.229 (range 0.206 - 0.412), and a modulation factor of about 1.39 (range 1.2 - 2). The optimization iterations were completed when the planning goals were met or until the plan could no longer be improved.

C. Helical tomotherapy planning with L-shaped directional block (HTLB)

The HTLB plans were also generated using the HT plan parameters. The L-shaped directional block was added to limit the entrance dose to OARs and was created by two rectangular structures perpendicular to each other on the opposite side of the PTV. The length of the L-shape was defined based on the heart's shape in the axial plane.

D. Plan evaluation parameters

Plan quality was evaluated by the conformity index (CI) and homogeneity index (HI), defined as follows:

$$CI = \frac{TV_{95\%}}{TV} \times \frac{TV_{95\%}}{V_{95\%}}, \quad HI = \frac{D_{2\%}-D_{98\%}}{D_{50\%}}$$

where TV is the target volume, $TV_{95\%}$ is the target volume received at 95% of the prescribed dose, and $V_{95\%}$ is the volume of external contour received at 95% of the prescribed dose. The CI value of 1 was represented as ideal conformity. $D_{2\%}$, $D_{50\%}$, and $D_{98\%}$ are the doses received by 2%, 50%, and 98% of PTV, respectively. The HI value of 0 was represented as ideal homogeneity.

The integral dose [4] was classified into 3 groups, including whole body integral dose (whole body ID), normal tissue integral dose (NTID), and integral dose to OARs (ID to OARs), defined as follows:

$$ID\ (Gy{\cdot}L) = D_{mean}\ (Gy) \times V\ (L)$$

where D_{mean} is the mean dose and V is the volume irradiated. The ID was calculated as a volume integral rather than a mass integral.

Nontarget body tissue doses were evaluated by the volume of normal tissue structure receiving 10%, 20%, 25%, 30%, 40%, 50%, 55%, 60%, and 75% of the prescription dose [8].

E. Statistical analysis

All statistical analyses were performed using SPSS statistics 27.0.1. Normal distributions were investigated using the Shapiro-Wilk test. The paired sample t-test was used for normal distributions, while the Wilcoxon signed-rank test was used for cases of non-normal distributions. A *p*-value < 0.05 was considered statistically significant.

III. RESULTS

A. Plan quality

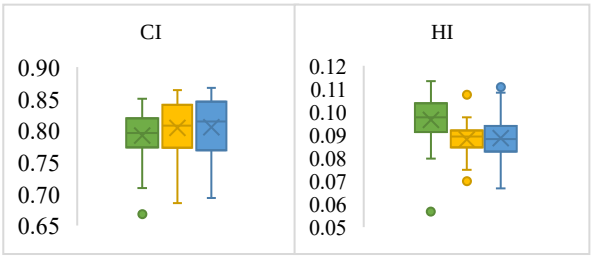

Figure 1. *Comparison of conformity index (CI) and homogeneity index (HI) between VMAT (green), HT (yellow),* and HTLB (blue).

The HT plan showed no significant difference in CI (p = 0.09) but demonstrated significantly better HI (p < 0.001) compared to VMAT. Conversely, the HTLB plan showed

significantly better CI and HI than VMAT, with *p*-values of 0.049 and < 0.001, respectively, as shown in Figure 1.

B. Integral dose

VMAT showed a significantly lower whole-body ID and NTID than HT ($p < 0.001$), while the HTLB showed no significant difference, with *p*-values of 0.985 and 0.7, respectively, as shown in Figure 2a-b.

The V_{5Gy} for VMAT was significantly better compared to HT ($p < 0.001$), with no significant differences compared to HTLB ($p = 0.301$), as shown in Figure 2c

The ID to OARs is shown in Figures 2d-e. The ID to the heart, ipsilateral lung, and contralateral breast showed no significant differences between VMAT and HT, with *p*-values of 0.163, 0.422, and 0.074, respectively. However, VMAT demonstrated significantly superior sparing of the contralateral lung ($p < 0.001$). When comparing VMAT and HTLB, the ID to the heart and ipsilateral lung showed no significant differences, with *p*-values of 0.974 and 0.632, respectively. The ID to the contralateral lung was significantly better in VMAT ($p < 0.001$). In contrast, HTLB performed significantly better for the contralateral breast ($p = 0.028$).

C. Nontarget body tissue doses

Nontarget body tissue doses are shown in Table 1. VMAT significantly decreased the mean nontarget tissue doses at V_{10Gy} through V_{40Gy} compared to HT. In contrast, HT showed significantly better sparing at V_{55Gy} through V_{75Gy}. When comparing VMAT and HTLB, VMAT showed a significant reduction in the mean nontarget tissue doses at V_{20Gy} through V_{30Gy}. On the other hand, HTLB demonstrated significant sparing of nontarget tissue at V_{50Gy} through V_{75Gy}.

IV. DISCUSSION

VMAT and HT were both clinically acceptable for patients treated with PMRT and RNI. Regarding plan quality, VMAT demonstrated significantly better CI, while HT showed significantly better HI, consistent with a previous study by Nichols et al. [3]. Nonetheless, HTLB showed significantly better CI and HI compared to VMAT. Regarding the integral dose, VMAT resulted in lower whole-body ID, NTID, and V5Gy compared to HT,

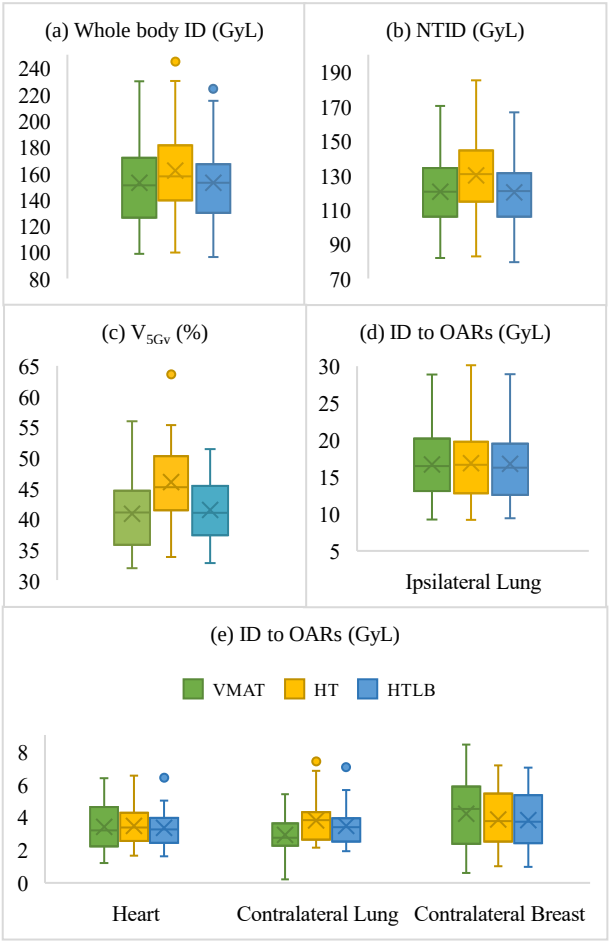

Figure 2. *Integral dose of three techniques (a) whole-body integral dose (GyL), (b) normal tissue integral dose (GyL), (c) volume received 5 Gy (%), (d) integral dose to ipsilateral lung (GyL), and (e) integral dose to organs at risk (GyL) including heart, contralateral lung, and contralateral breast.*

with no significant difference when compared to HTLB, consistent with the findings of Phurailatpam et al. [9]. However, another study [8] found that VMAT resulted in the highest NTID for prostate cancer.

The integral dose to the heart and ipsilateral lung was not significantly different between VMAT, HT, and HTLB. However, VMAT demonstrated better sparing of the contralateral lung, resulting in a lower ID. In contrast, HTLB showed better sparing of the contralateral breast. Nichols et al. reported that HT demonstrated better sparing of the contralateral breast, which they attributed to the highly modulated dose delivery at each helical slice. Additionally, HT showed better dose sparing at higher doses, while VMAT showed better sparing at lower doses. In our study, VMAT illustrated sparing of

Table 1. *Nontarget body tissue doses*

V% (mean)	VMAT (range)	HT (range)	HTLB (range)
V10	7394 cc (4822-10453)	8268 cc (5036-12154) *	7450 cc (5065-9985)
V20	4432 cc (3009-6258)	5373 cc (3317-7997) *	4675 cc (3188-6428) †
V25	3597 cc (2508-5078)	4374 cc (2765-6454) *	3871 cc (2721-5625) †
V30	2993 cc (2092-4347)	3540 cc (2236-5175) *	3215 cc (2114-4810) †
V40	2198 cc (1548-3293)	2387 cc (1332-3607) *	2246 cc (1289-3635)
V50	1623 cc (866-2555)	1601 cc (839-2416)	1526 cc (828-2488) †
V55	1431 cc (979-2222)	1327 cc (725-1999) *	1265 cc (718-2040) †
V60	1230 cc (832-1908)	1114 cc (643-1656) *	1065 cc (634-1680) †
V75	749 cc (509-1091)	692 cc (433-972) *	664 cc (429-975) †

* $P < 0.05$ for VMAT vs HT.
† $P < 0.05$ for VMAT vs HTLB.

nontarget tissue at low to moderate doses, while HT and HTLB showed better sparing at high doses.

V. CONCLUSION

Comparing VMAT and HT plans in PMRT with RNI, the HT plan showed significantly higher NTID than VMAT. In contrast, the HTLB plan showed no significant differences and achieved better conformity and homogeneity.

ACKNOWLEDGEMENTS

We would like to thank the staff of the Division of Radiation Oncology, Chiang Mai University, for their support and assistance

REFERENCES

[1] Nobnop W, Phakoetsuk P, Chitapanarux I, Tippanya D, Khamchompoo D. Dosimetric comparison of TomoDirect, helical tomotherapy, and volumetric modulated arc therapy for postmastectomy treatment. J Appl Clin Med Phys. 2020;21(9):155-62.

[2] Karpf D, Sakka M, Metzger M, Grabenbauer GG. Left breast irradiation with tangential intensity modulated radiotherapy (t-IMRT) versus tangential volumetric modulated arc therapy (t-VMAT): trade-offs between secondary cancer induction risk and optimal target coverage. Radiat Oncol. 2019;14(1):156.

[3] Nichols GP, Fontenot JD, Gibbons JP, Sanders ME. Evaluation of volumetric modulated arc therapy for postmastectomy treatment. Radiat Oncol. 2014;9:66.

[4] Aoyama H, Westerly DC, Mackie TR, Olivera GH, Bentzen SM, Patel RR, et al. Integral radiation dose to normal structures with conformal external beam radiation. Int J Radiat Oncol Biol Phys. 2006;64(3):962-7.

[5] Fogliata A, Seppala J, Reggiori G, Lobefalo F, Palumbo V, De Rose F, et al. Dosimetric trade-offs in breast treatment with VMAT technique. Br J Radiol. 2017;90(1070):20160701.

[6] Van Gestel D, Verellen D, Van De Voorde L, de Ost B, De Kerf G, Vanderveken O, et al. The potential of helical tomotherapy in the treatment of head and neck cancer. Oncologist. 2013;18(6):697-706.

[7] Chirawattana A, Chitapanarux I, Nobnop W. Improvement of helical tomotherapy treatment plan efficiency with block techniques for left-sided post-mastectomy radiation therapy. Journal of Radiotherapy in Practice. 2023;22.

[8] Grzywacz VP, Arden JD, Mankuzhy NP, Gustafson GS, Sebastian EA, Abbott VL, et al. Normal Tissue Integral Dose as a Result of Prostate Radiation Therapy: A Quantitative Comparison Between High-Dose-Rate Brachytherapy and Modern External Beam Radiation Therapy Techniques. Adv Radiat Oncol. 2023;8(3):101160.

[9] Phurailatpam R, Wadasadawala T, Chauhan K, Panda S, Sarin R. Dosimetric comparison of volumetric-modulated arc therapy and helical tomotherapy for adjuvant treatment of bilateral breast cancer. Journal of Radiotherapy in Practice. 2020;21(1):36-44.

Contacts of the corresponding author:
Author: Wannapha Nobnop
Institute: Department of Radiology, Division of Radiation Oncology, Faculty of Medicine, Chiang Mai University
Street: 110 Inthawarorot
City: Chiang Mai
Country: Thailand
Email: wannapha.n@cmu.ac.th

Dosimetric Comparison Between Images with and without Contrast Agent Using Intensity Modulated Arc Therapy in Head and Neck cancer

Wantongsuk Wilasinee[1,2], Nopnob Wannapa[2], Thongsuk Warit[2], Chakrabandhu Somvilai[2] and Watcharawipha Anirut[2,*]

[1]*Medical Physics program, Department of Radiology, Faculty of Medicine, Chiang Mai University, Chiang Mai, Thailand.*
[2]*Division of Radiation Oncology, Department of Radiology, Faculty of Medicine, Chiang Mai University, Chiang Mai, Thailand.*
*(*Corresponding author: anirut.watch@cmu.ac.th)*

Abstract — **Introduction**: Intensity Modulated Arc Therapy (IMAT) is a widely used technique for targeted radiotherapy. Accurately identifying the target's shape and location is essential for effective treatment. The use of a contrast agent is necessary to define the target during this process. However, the increased intensity in the image can impact dose calculations, especially with precise algorithms. This study aims to evaluate the impact of contrast enhancement on dose calculations and compare different dose calculation algorithms. **Methods:** This study included twenty head and neck treatment plans using Volumetric Modulated Arc Therapy (VMAT) and Helical Tomotherapy (HT) based on CT image series without contrast agent. The treatment geometry was recalculated on contrast-enhanced images, and the plans were transferred for replanning on a different treatment planning system. The doses to targets and organs at risk were analyzed and compared. **Result:** The study found that the percentage dose difference (%DD) between images with and without contrast was minimal. The doses on Planning Target Volume of 70.0 Gy, 59.4 Gy, and 54.0 Gy showed %DD 0.49%, 0.67%, and 0.75%, respectively. The doses of OARs ranged from 0.16% to 1.02%. The target dose had a lower %DD on VMAT than HT, while HT resulted in higher doses to OARs. **Conclusion:** Contrast agent can be used in the images for IMAT treatment planning, despite the dose calculation being performed with a high-accuracy algorithm. The %DD between with and without contrast images was within 1.1%. The more precise dose calculation algorithm led to a reduced impact of radiation dose on the target and OARs.

Keywords: Contrast agent, Head and Neck cancer, Volumetric modulated arc therapy, Helical Tomotherapy, Dose calculation algorithm.

I. INTRODUCTION

Intensity Modulated Arc Therapy (IMAT) is commonly used in targeted radiotherapy, particularly for head and neck cancer[1]. The Computed Tomography (CT) image is essential in this treatment technique due to the CT number. Generally, CT images do not provide excellent soft tissue detail compared to other imaging modalities such as Magnetic Resonance Imaging (MRI). Although image registration between modalities is performed, a contrast agent is still required on the CT image in the treatment simulation process. This contrast agent can increase the intensity of the lesion to confirm its area and location for the target delineation[2]. However, the enhanced intensity on the image may affect the dose calculation of the Treatment Planning System (TPS) due to the relative electron density (RED)[3]. The Compton effect is the main interaction in radiotherapy and its cross-section depended on the RED, which is related to the CT number value by calculating the mass attenuation coefficient of radiation in the medium[4]. In recent dose calculation methods, high precision in the calculation has been improved from a model-based algorithm to Monte Calo simulation. These dose calculations can precisely consider the RED in each voxel of the image.

This study aimed to investigate the impact of contrast agent enhancement on dose calculation and compare different dose calculation algorithms for IMAT in head and neck cancer (H&N).

II. MATERIALS AND METHODS

A. Data preparation and CT simulation

This study recruited twenty H&N treatment plans that had CT simulation image with and without contrast agent. These image set were acquired by the CT simulator (SOMATOM Definition AS, Siemens Inc., Healthineers, Germany). The image acquisition parameters use an energy of 120 kVp and a 3 mm slice thickness. A 100 cc of iodinated contrast agent (Omnipaque 350 mg I/cc, GE Healthcare Ireland Limited, Cork, Ireland) was injected through the patient for image enhancement using a power injector. Image set without contrast CT was set as the primary image and was registered with the image set with contrast CT. Finally, the Planning Target Volumes (PTVs) and organs at risk (OARs) were delineated for the treatment planning.

B. Treatment planning

The treatment planning technique was randomly used for these 20 cases, involving Volumetric Modulated Arc Therapy (VMAT) and Helical Tomotherapy (HT). The dose delivered to the PTVs was 70.0 Gy, 59.4 Gy and 54.0 Gy for $PTV_{70.0}$, $PTV_{59.4}$ and $PTV_{54.0}$, respectively, in 33 fractions. This dose considered the OARs, including the spinal cord, brain stem, parotid glands and submandibular glands.

To evaluate the impact of contrast enhancement, the treatment plan was transferred and recalculated on the image set with contrast agent. Dosimetric parameters of targets and OARs were recruited from both image sets.

C. Comparison of calculation-based algorithm

Twenty treatment plans were randomly used between VMAT and HT treatment techniques. To prevent the sample size bias, the treatment plan was created in the lack of each treatment technique.

- *Volumetric Modulated Arc Therapy (VMAT) plans*: The image set without contrast agent was transferred to the Monaco® ver. 6.1.3.0 (Elekta Inc., Missouri, USA) TPS. The geometry was performed using 360 gantry angle degree with 2-3 rotations. The optimization and dose calculation used Monte Carlo (MC) algorithm with 3 mm grid resolution. The dose constraints of PTVs and OARs were limited to meet the criteria of the International Commission on Radiation Units and measurements (ICRU) guideline[5]. Finally, this geometry was transferred and recalculated on the image set with contrast agent.

- *Helical Tomotherapy (HT) plans:* In the same direction, the image set without contrast from Monaco® TPS was transferred to the Precision® ver. 3.3.1.3 TPS (Accuray Inc., Sunnyvale, California, USA). The helical tomotherapy delivery technique was performed using dynamic Field width of 50 mm and modulation factor of 2 whereas the Pitch was automatically calculated by Volo™ Ultra. The optimization and dose calculation used the Collapse Cone Convolution (CCC) algorithm with Medium and High grid resolution, respectively. Dose limitations followed the ICRU guideline as well. Finally, these geometries were transferred and recalculated on the contrast enhancement image set.

D. Statistical dosimetric analysis and comparison

Dosimetric parameters were analyzed dosimetric significant difference between with and without contrast enhancement by SPSS® software ver. 27.0.1 (IBM co., New York, USA). Shapiro-Wilk test analyzed the normal distribution of the data. Student t-test evaluated the data of normal distribution while non-normal distribution data was evaluated using the Wilcoxon rank test. This data was analyzed using 95% confidence interval where p-value < 0.05.

III. RESULTS

A. Dosimetric comparison between with and without contrast again in CT image

Dosimetric comparison of PTVs and OARs demonstrated in Table 1. The statistical analysis found a significant difference of the dose between CT image with and without contrast again on all dosimetric parameters of PTVs and OARs. However, the dose difference of each organ was reported on Table 1 as well. The dose difference found within 1.1% on all organs.

B. Dosimetric comparison between MC and CCC

The CT image of each patient was replanned in the other dose calculation algorithm. The results were illustrated in Table 2. The D2 of PTV70.0Gy using CCC found to significantly

Table 1. *Dosimetric parameters of targets and organs at risk, and percent dose difference between CT image with and without contrast agent.*

Organs		Dose (Gy)		Dose difference (%)	p-value
		Without contrast	With contrast		
$PTV_{70.0}$	D_{98}	66.28 ± 1.61	65.95 ± 1.57	-0.49	**< 0.001**
	D_{50}	69.47 ± 1.79	69.15 ± 1.74	-0.46	**< 0.001**
	D_2	71.52 ± 2.04	71.27 ± 2.07	-0.35	**< 0.001**
$PTV_{59.4}$	D_{98}	57.36 ± 0.63	56.98 ± 0.64	-0.67	**< 0.001**
	D_{50}	64.29 ± 2.86	64.01 ± 2.87	-0.44	**< 0.001**
$PTV_{54.0}$	D_{98}	52.03 ± 0.42	51.64 ± 0.50	-0.75	**< 0.001**
	D_{50}	54.54 ± 0.51	54.24 ± 0.56	-0.56	**< 0.001**
Spinal cord	D_2	31.71 ± 3.99	31.66 ± 3.98	-0.16	**0.012**
Brain stem	D_2	24.26 ± 11.15	24.12 ± 11.13	-0.59	**0.035**
Lt parotid gland	D_{mean}	28.04 ± 5.36	27.95 ± 5.36	-0.35	**< 0.001**
	D_{50}	24.43 ± 6.22	24.28 ± 6.17	-0.61	**< 0.001**
Rt parotid gland	D_{mean}	34.26 ± 13.01	33.91 ± 13.07	-1.02	**0.030**
	D_{50}	31.84 ± 15.21	31.59 ± 15.10	-0.78	**< 0.001**
Lt SMB gland	D_{mean}	55.37 ± 7.82	55.02 ± 7.79	-0.65	**< 0.001**
Rt SMB gland	D_{mean}	59.74 ± 7.81	59.30 ± 7.82	-0.74	**< 0.001**

Abbreviations: PTV, Planning Target Volume; Lt, Left; Rt, Right and SMB, Submandibular.

higher than MC while the dose on spinal cord was significantly lower.

IV. DISCUSSION

A. Dosimetric comparison between with and without contrast again in CT image

The study investigated the impact of using an iodinated contrast agent for H&N cancer in the treatment plan of IMAT. The CT image with the contrast agent had a high CT number, which caused more beam attenuation, resulting in a lower dose on the CT without contrast. Several studies[6-8] observed the impact of contrast-enhanced CT images for H&N cancer of IMRT plans and found the dose difference less than 2% between CT image with/without contrast agent. These studies concluded this dose difference was not impact on a clinical treatment result. Although a significant difference was found in this study, the dose difference was within 1.1% for all organs confirmed the previous study as well [6-8].

B. Dosimetric comparison between MC and CCC

This study observed the dose difference using a different dose calculation algorithm. The dosimetric results using MC and CCC were compared. A previous study [9] found a significant sensitivity on the MC algorithm compared to other dose calculation algorithms. In contrast, this study found more sensitivity in CCC rather than MC. This may be influenced by the resolution of the dose calculation where MC used a 3 mm grid size, but CCC used a 0.98 mm grid size. Other publications[10-11] have confirmed that higher dose to organs can be found with higher resolution in dose calculation.

V. CONCLUSION

This study found a significant difference in radiation dose between images with and without contrast agent. Although a significant difference was found, the dose difference was within 1.1% which had no impact on clinical treatment results. The collapsed cone convolution algorithm was found to be more sensitive than the Monte Carlo algorithm. This may be influenced by the resolution of dose calculation grid size.

ACKNOWLEDGEMENTS

This study has no acknowledgements.

Table 2. *Absolute and percent dose differences of target and organs at risk between CT image with and without contrast agent for VMAT and HT plan.*

Organs		Dose difference (Gy)		Percentage dose differences		p-value
		VMAT	HT	VMAT	HT	
$PTV_{70.0}$	D_{98}	0.30 ± 0.14	0.36 ± 1.17	-0.44 ± 0.20	-0.54 ± 1.75	0.370
	D_{50}	0.31 ± 0.16	0.33 ± 0.15	-0.45 ± 0.23	-0.47 ± 0.29	0.550
	D_2	0.19 ± 0.21	0.31 ± 0.25	-0.26 ± 0.29	-0.43 ± 0.36	**0.016**
$PTV_{59.4}$	D_{98}	0.40 ± 0.35	0.37 ± 0.26	-0.70 ± 0.60	-0.65 ± 0.46	0.970
	D_{50}	0.27 ± 0.15	0.29 ± 0.21	-0.42 ± 0.24	-0.46 ± 1.95	0.250
$PTV_{54.0}$	D_{98}	0.33 ± 0.22	0.45 ± 0.39	-0.64 ± 0.42	-0.87 ± 0.75	0.230
	D_{50}	0.29 ± 0.15	0.32 ± 0.32	-0.52 ± 0.27	-0.59 ± 0.39	0.670
Spinal cord	D_2	0.09 ± 0.14	0.01 ± 0.16	-0.28 ± 0.43	-0.04 ± 0.52	**0.026**
Brain stem	D_2	0.01 ± 0.16	0.26 ± 1.12	-0.04 ± 0.75	-1.15 ± 6.72	0.100
Lt parotid gland	D_{mean}	0.14 ± 0.13	0.06 ± 0.18	-0.47 ± 0.44	-0.27 ± 0.7	0.930
	D_{50}	0.18 ± 0.27	0.12 ± 0.36	-0.73 ± 0.94	-0.45 ± 1.35	0.360
Rt parotid gland	D_{mean}	0.36 ± 1.06	0.25 ± 0.57	-1.36 ± 4.38	-0.68 ± 1.64	0.702
	D_{50}	0.21 ± 0.32	0.28 ± 0.9	-0.67 ± 3.33	-0.74 ± 2.60	0.575
Lt SMB gland	D_{mean}	0.43 ± 0.27	0.28 ± 0.22	-0.75 ± 0.44	-0.54 ± 0.49	0.083
Rt SMB gland	D_{mean}	0.51 ± 0.21	0.37 ± 0.27	-0.84 ± 0.37	-0.66 ± 0.61	0.074

Abbreviations: PTV, Planning Target Volume; Lt, Left; Rt, Right and SMB, Submandibular.

REFERENCES

[1] Buciuman N, Marcu LG. Adaptive Radiotherapy in Head and Neck Cancer Using Volumetric Modulated Arc Therapy. J Pers Med. 2022;12(5).

[2] Imaging in Radiotherapy. Report of Consultant's Meeting held in Vienna 15-19 October 2007. Vienna: International Atomic Energy Agency (IAEA), 2007.

[3] Shi W, Liu C, Lu B, Yeung A, Newlin HE, Amdur RJ, Olivier KR. The effect of intravenous contrast on photon radiation therapy dose calculations for lung cancer. Am J Clin Oncol. 2010;33(2):153-6.

[4] Pereira GC, Traughber M, Muzic RF, Jr. The role of imaging in radiation therapy planning: past, present, and future. Biomed Res Int. 2014.

[5] International Commission on Radiation Units and Measurements Report 83. Prescribing, recording, and reporting photon-beam intensity-modulated radiation therapy (IMRT). J ICRU. 2010;10.

[6] Liauw SL, Amdur RJ, Mendenhall WM, Palta J, Kim S. The effect of intravenous contrast on intensity-modulated radiation therapy dose calculations for head and neck cancer. Am J Clin Oncol. 2005;28(5):456-9.

[7] Choi Y, Kim JK, Lee HS, Hur WJ, Hong YS, Park S, et al. Influence of intravenous contrast agent on dose calculations of intensity modulated radiation therapy plans for head and neck cancer. Radiother Oncol. 2006;81(2):158-62.

[8] Liu AJ, Vora N, Suh S, Liu A, Schultheiss TE, Wong JY. Effect of CT contrast on volumetric arc therapy planning (RapidArc and helical tomotherapy) for head and neck cancer. Med Dosim. 2015;40(1):32-6.

[9] Zhu F, Wu W, Zhu F, Wang Y, Wang Y, Xia T. Influence of computed tomography contrast agent on radiotherapy dose calculation for pancreatic carcinoma: A dosimetric study based on tomotherapy and volumetric-modulated arc therapy techniques. Med Dosim. 2017;42(4):317-25.

[10] Srivastava SP, Cheng CW, Das IJ. The dosimetric and radiobiological impact of calculation grid size on head and neck IMRT. Pract Radiat Oncol. 2017;7(3):209-17.

[11] Kim KH, Chung JB, Suh TS, Kang SW, Kang SH, Eom KY, et al. Dosimetric and radiobiological comparison in different dose calculation grid sizes between Acuros XB and anisotropic analytical algorithm for prostate VMAT. PLoS One. 2018;13(11):e0207232.

Contacts of the corresponding author:
Author: Asst. Prof. Anirut Watcharawipha, Ph.D
Institute: Division of Radiation Oncology, Department of Radiology, Faculty of Medicine
Street: 110 Intawaroros
City: Chiang Mai
Country: Thailand
Email: anirut.watch@cmu.ac.th

Interfraction motion of wingboard and breastboard immobilization devices during postmastectomy 3D-CRT for breast cancer

Coronel Michael Ben Joseph[1,2*], Zerrudo JI[3,4], Caballar RC[1,5], Balete MJ[2,6], Mones E[2], Cereno RE[2,7,8]

1 The Graduate School, University of Santo Tomas, Manila 1008, Philippines
2 Radiation Oncology Center, Global Care Cancer Institute Inc., Bay, Laguna 4033, Philippines
3 Department of Radiation Oncology, Batangas Medical Center, Batangas City, Batangas 4200, Philippines
4 Department of Physical Sciences and Mathematics, College of Arts and Sciences, University of the Philippines – Manila 1000, Philippines
5 Department of Mathematics and Physics, College of Science, University of Santo Tomas, Manila 1008, Philippines
6 Department of Radiology, Section of Radiation Oncology, Cardinal Santos Medical Center, San Juan 1502, Philippines
7 College of Medicine, University of the Philippines Manila, Manila 1000, Philippines
8 Department of Radiology, Division of Radiation Oncology, University of the Philippines – Philippine General Hospital, Manila 1000, Philippines
**michaelben.coronel.gs@ust.edu.ph*

Abstract — **Introduction:** Postmastectomy radiotherapy includes the chestwall, axilla, and supraclavicular fossa as targets. Immobilization devices such as wingboards (WB) and breastboards (BB) are crucial to ensure precise dose delivery. The study aims to compare setup errors between WB and BB setups during three-dimensional conformal radiation therapy (3D-CRT) for breast cancer. **Methods:** Twenty WB setups and 22 BB setups were utilized for this study. Setup errors were derived by recording the lateral, longitudinal, and vertical couch shifts. These were used to calculate the clinical target volume (CTV) to planning treatment volume (PTV) margins. Doses to the target volumes and OARs were compared for the WB and BB setups in the original and shifted plans. **Results:** Interfraction setup errors were higher in the WB setup. The computed CTV-PTV margins were 2.75 mm (lateral), 2.14 mm (longitudinal), and 3.97 mm (vertical) for the WB setup, and were 2.08 mm, 1.96 mm, and 2.16 mm for the BB setup. There was less dose coverage in the shifted plans compared to the original plans for the CTV chestwall in the WB ($V_{90\%}$=91.07% vs 89.90%; $V_{95\%}$=85.75% vs 85.46%) and BB ($V_{90\%}$=89.39% vs 89.05%; $V_{95\%}$=81.58% vs 81.38%). The same was reported for the CTV supraclavicular fossa for WB ($V_{90\%}$=98.90% vs 96.31%; $V_{95\%}$=94.10% vs 91.18%) and BB ($V_{90\%}$=98.36% vs 95.11%; $V_{95\%}$=90.55% vs 84.59%). Doses to the OARs, except for the heart at V_{17Gy} (6.90% vs 7.13%) and D_{mean} (4.84 Gy vs 4.89 Gy), were lower in the shifted plans of the BB; however, ipsilateral lung dose (V_{17Gy}=33.41% vs 34%) was higher for the WB. **Conclusion:** Interfraction motion from the BB and WB setups were within the 5 mm tolerance of the study institution. Further validation of the findings in a larger sample size is recommended.

Keywords — radiation therapy, breast cancer, wingboard, breastboard, interfraction motion

I. INTRODUCTION

Radiotherapy has played a vital role in treating and preventing the recurrence of breast cancer in females. It was reported that breast cancer is the most common type of cancer worldwide, and the Philippines is the frontrunner for the high rates of breast cancer mortality in Asia. Local population cancer registries from the early 2000s showed that 97% of Stage I breast cancer underwent mastectomy instead of breast conserving surgery, hence the need for representation of post-mastectomy radiotherapy (PMRT) patients in the current literature [1-2]. Patient setup and immobilization are crucial factors in ensuring the precise delivery of radiation dose to the target [3-4]. However, setup deviations result from daily treatment execution errors, organ motion, laser misalignment, and changes in patient anatomy. These systematic and random errors gradually affect the dose delivered to the target and the OARs unless setup corrections have been made [5]. Thus, this study aims to compare setup error between wingboard (WB) and breastboard (BB) setups during three-dimensional conformal radiation therapy (3D-CRT) for breast cancer. In addition, target volume dose coverage and doses received by the organs-at-risk (OARs) are described in the paper.

II. MATERIALS AND METHODS

This retrospective study was conducted in a private cancer institute in Laguna, Philippines. Cancer staging and patient demographics were not considered in the experimental process. Breast cancer patients who received a dose of 40.05 Gy in 15 fractions of 2.67 Gy were eligible. Forty-two (42) sets of electronic portal images of breast cancer patients were acquired for offline review. These were further divided into the WB group with twenty (20) setups and the BB group with twenty-two (22) setups. The BB and WB setups were divided into two, namely the left wingboard (LWB), and left breastboard (LBB) groups to make a subanalysis of the heart dose.

A. Equipment and immobilization devices

Setup images were obtained using a Varian Clinac CX linac with a dedicated MV electronic port imaging device (EPID). Dosimetric values were obtained through the dose-volume histogram (DVH) in the external beam planning software in Eclipse. CT simulations of each patient were acquired using a Siemens SOMATOM Confidence 64-slice CT simulator. The CIVCO MT-350 breastboard and the CIVCO extended wingboard immobilization devices were used.

B. Treatment verification

Electronic port images in the AP and LAT regions were taken during the 1st, 6th, and 11th treatment fraction. Anatomical matching was done by matching the orthogonal pairs to the DRR of each patient from the CT simulation. Reference bony landmarks used were the vertebral body and spinous process [8]. Setup errors in the lateral, longitudinal, and vertical axis were categorized into systematic and random errors. The mean error over the course of the treatment for an individual patient is the individual systematic error. Population systematic error (Σ) was computed as the standard deviation (SD) of the distribution of mean errors for each individual patient. Individual random error was calculated by computing the SD of the measured errors in each patient. The mean of the individual random error resulted to the population random error (σ). Van Herk's formula was used to compute for the CTV to PTV margins [5].

$$PTV\ Margin = 2.5\Sigma + 0.7\sigma$$

Shifted plans were generated by moving the isocenter of the original plans based on the individual mean errors of each patient at the lateral, longitudinal, and vertical axis. All the other treatment plan parameters were retained from the original plans.

C. Contouring and treatment planning

The CTV chestwall and supraclavicular fossa (SCF), and the OARs were contoured by the radiation oncologist and the medical physicist, respectively, following the RTOG Breast Cancer Atlas for Radiation Therapy. Treatment planning was done through a mono-isocentric technique with two wedged, half-beam lateral 6 MV tangential fields for the lateral chestwall region as seen in (Fig 1). The axilla and the SCF were treated through opposed photon fields directed away from the esophagus and the spinal cord. An anterior electron field ranging from 6 MeV to 12 MeV was utilized to treat the anterior chestwall region. Dose constraints followed the DBCG Hypo Trials protocol [6].

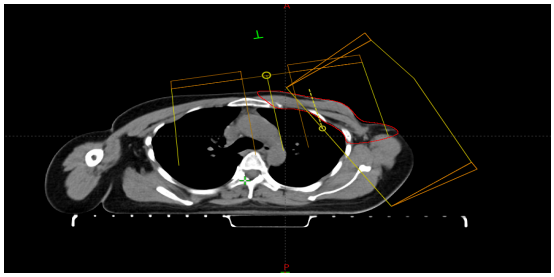

Figure 1. *The axial view shows the two wedged, half-beam tangential fields covering the lateral chestwall area. An anterior electron field was used to treat the chestwall region.*

D. Statistical treatment of data

Descriptive statistics of the setup deviations were acquired. A two-tailed, dependent t-test was also conducted with a 95% confidence interval in comparing the means of the original and shifted plans.

III. RESULTS

As shown in Table 1, higher population systematic errors (PSE) and population random errors (PRE) were found in the WB compared to BB. With this, the computed margins were higher in the WB compared to the BB when Van Herk's formula was used.

Table 1. CTV-PTV margins calculation using the population systematic errors (PSE) and population random errors (PRE)

	PSE (mm)	PRE (mm)	Margin (mm)
WB (n=20)			
Lateral	0.67	1.53	2.75
Longitudinal	0.54	1.13	2.14
Vertical	1.16	1.54	3.97
BB (n=22)			
Lateral	0.52	1.12	2.08
Longitudinal	0.51	0.98	1.96
Vertical	0.61	0.90	2.16

Table 2. Dosimetric comparison between original and shifted plans of CTV CW for WB (n=20) and BB (n=22)

	Original	Shifted
WB		
$D_{95\%}$ (Gy)	31.59	30.63
$V_{90\%}$ (%)	91.07	89.90
$V_{95\%}$ (%)	85.75	85.46
BB		
$D_{95\%}$ (Gy)	30.15	30.24
$V_{90\%}$ (%)	89.39	89.05
$V_{95\%}$ (%)	81.58	81.38

Table 2 shows the changes in the dosimetric parameters when the individual mean errors were incorporated into the original plans for the CTV chestwall. Dose coverage in the WB setups based on $D_{95\%}$ (31.59 Gy vs 30.63 Gy), $V_{90\%}$ (91.07% vs 89.90%), and $V_{95\%}$ (85.75% vs 85.46%) was reduced in the shifted plans. Better dose coverage was reported in the BB setups at $D_{95\%}$ (30.15 Gy vs 30.24 Gy); however, lower dose coverage was seen at $V_{90\%}$ (89.39% vs 89.05%) and $V_{95\%}$ (81.58% vs 81.38%).

Table 3 shows that most dosimetric parameters in the recalculated plans reported lower values in the WB setups for the CTV SCF. The decrease in dose coverage can be seen at $D_{95\%}$ (38.93 Gy vs 34.73 Gy), $V_{90\%}$ (98.90% vs 96.31%), and $V_{95\%}$ (94.10% vs 91.18%). Data from the BB setups reported similar results. All parameters had lower values in the recalculated plans compared to the original plans. Dose coverage also decreased at $D_{95\%}$ (37.35 Gy vs 34.27 Gy), $V_{90\%}$ (98.36% vs 95.11%), and $V_{95\%}$ (90.55% vs 84.59%).

Table 3. Dosimetric comparison between original and shifted plans of CTV SCF for WB (n=20) and BB (n=22)

	Original	Shifted
WB		
$D_{95\%}$ (Gy)	38.93	34.73
$V_{90\%}$ (%)	98.90	96.31
$V_{95\%}$ (%)	94.10	91.18
BB		
$D_{95\%}$ (Gy)	37.35	34.27
$V_{90\%}$ (%)	98.36	95.11
$V_{95\%}$ (%)	90.55	84.59

Table 4. Dosimetric comparison between original and shifted plans of the OARs for WB (n=20) and BB (n=22)

	Original	Shifted
WB		
Ipsi lung ($V_{17\%}$)	33.41	34.00
Lungs ($V_{17\%}$)	18.17	17.59
Cord PRV 0.5 (D_{max})	25.29	23.10
BB		
Ipsi lung ($V_{17\%}$)	37.32	36.19
Lungs ($V_{17\%}$)	20.38	18.77
Cord PRV 0.5 (D_{max})	29.13	24.81

Table 4 shows that there was a dose increase in the ipsilateral lung at V_{17Gy} (33.41% vs 34%), Less dose was received for V_{17Gy} of the bilateral lungs (18.17% vs 17.59%) and D_{max} of cord PRV (25.29 Gy vs 23.10 Gy). V_{17Gy} of the ipsilateral lung (37.32% vs 36.19%) and bilateral lungs (20.38% vs 18.77%), and cord PRV (29.13 Gy vs 24.81 Gy) reported lower doses in the shifted plans. There was an increase in the V_{17Gy} (4.27% vs 7.42%) and D_{mean} (4.43 Gy vs 5.59 Gy) of the heart in the shifted plans of the LWB setups. The same was reported for the heart dose in LBB setups at V_{17Gy} (6.90% vs 7.13%) and D_{mean} (4.84 Gy vs 4.89 Gy).

IV. DISCUSSION

A study conducted by Raza et al. [7] concluded that the WB can serve as an alternative to the BB based on the computed setup errors and CTV-PTV margins. However, a review conducted by Mast et al. revealed that there was still no consensus on the

recommended immobilization device for breast RT [3]. Population random errors were higher in the WB and BB setups compared to the population systematic errors which can be attributed to the intrafraction errors such as organ motion for both WB and BB at all axes. The same results were reported in the study of Alabedi et al. except in the lateral axis [8].

In terms of dosimetric effects, dose coverage to the CTV chestwall and SCF were reduced in the shifted plans vs the original plans. However, there is a clinically significant result at $V_{90\%}$ in the shifted plans of the WB and BB setups for the CTV chestwall and SCF. Doses received by the OARs in the BB setup were lower in the shifted plans except for the heart; however, the ipsilateral lung and spinal cord PRV dose was higher in the WB setups after recalculation. Thus, setup errors should be accounted for during treatment planning and daily execution to ensure the precise dose delivery to the CTV without increasing the dose to the OARs.

V. CONCLUSION

The study showed that the interfraction motion of utilization of breast board and wingboard were within the 5 mm tolerance. Further validation of the findings in a larger sample size is recommended, as well as the evaluation of rotational shifts on top of the translational shifts utilized in this study. Lastly, it is recommended to add two setups (1 WB and 1 BB) per patient to eliminate anatomical variations that affect doses.

ACKNOWLEDGEMENTS

The authors would like to thank the board and the radiation oncology department of the study institution for approving the conduct of this study. Special thanks to the research advisers and the research panel for giving their insightful comments and feedback.

REFERENCES

[1] Sung H, Ferlay J, Siegel RL, Laversanne M, Soerjomataram I, Jemal A, et al. Global Cancer Statistics 2020: GLOBOCAN Estimates of Incidence and Mortality Worldwide for 36 Cancers in 185 Countries. CA A Cancer J Clinicians. 2021 May;71(3):209–49.

[2] Jamora K, Cruz-Lim EM, Cereno RE, Castillo MR, Baldivia K. Hypofractionated radiotherapy in postmastectomy locally advanced breast cancer: an interim report on acute toxicities and dosimetry. Rep Pract Oncol Radiother. 2022 Dec 29;27(6):943–53.

[3] Mast ME, Leong A, Korreman SS, Lee G, Probst H, Scherer P, et al. ESTRO-ACROP guideline for positioning, immobilisation and setup verification for local and loco-regional photon breast cancer irradiation. Technical Innovations & Patient Support in Radiation Oncology. 2023 Dec;28:100219.

[4] Costin IC, Costin I, Marcu LG. PO-2059 The impact of breast board and body mass index on setup errors during breast cancer radiotherapy. Radiotherapy and Oncology. 2023 May;182:S1834–5.

[5] On target: ensuring geometric accuracy in radiotherapy. London: Royal College of Radiologists; 2008.

[6] Offersen BV, Boersma LJ, Kirkove C, Hol S, Aznar MC, Biete Sola A, et al. ESTRO consensus guideline on target volume delineation for elective radiation therapy of early stage breast cancer. Radiotherapy and Oncology. 2015 Jan;114(1):3–10.

[7] Raza W, Agarwal S, Maria Das KJ, Senthil Kumar SK, Lal P. Comparison of set-up errors by breast size on wing board by portal imaging. Reports of Practical Oncology & Radiotherapy. 2016 Sep;21(5):447–52.

[8] Alabedi H, Department of Surgery, College of Medicine, Baghdad University, Baghdad, Iraq. Assessing setup errors and shifting margins for planning target volume in head, neck, and breast cancer. JMedLife. 2023 Mar;16(3):394–8.

Contacts of the corresponding author:
Author: Michael Ben Joseph A. Coronel
Institute: Global Care Cancer Institute, Inc.
Street: National Highway, Barangay Maitim
City: Bay, Province of Laguna 4033
Country: Philippines
Email: michaelben.coronel.gs@ust.edu.ph

Evaluation of Patient-Specific Quality Assurance for Beam Matched LINAC in Stereotactic Radiosurgery and Stereotactic Radiotherapy (SRS/SRT)

Boujamrat Thanuch[1], Oonsiri Sornjarod[2], Oonsiri Puntiwa[2], Kingkaew Sakda[2], Vimolnoch Mananchaya[2], Plangpleng Nattha[2], Chatchumnan Nichakan[2], Yabsantia Sumalee[1,*]

[1] Medical Physics Program, Department of Radiological Technology, Faculty of Allied Health Sciences, Naresuan University, Muang District, Phitsanulok, Thailand
[2] Department of Radiology, Division of Radiation Oncology, King Chulalongkorn Memorial Hospital, The Thai Red Cross Society, Bangkok, Thailand
*(*Corresponding author: sumaleey@nu.ac.th)*

Abstract — **Introduction:** Beam-matching with multiple LINACs in the institution ensures consistent radiation beam characteristics across LINAC. This allows for patient switches between LINACs without the need of replanning. To ensure accuracy when switching machines, especially for complex techniques like Stereotactic Radiosurgery (SRS) and Stereotactic Radiotherapy (SRT), it is essential to evaluate patient-specific quality assurance (PSQA) to verify the consistency of radiation delivery across LINACs. Therefore, the objective of this study is to assess the feasibility of using beam-matched LINACs for Stereotactic Radiosurgery (SRS) and Stereotactic Radiotherapy (SRT) while maintaining reliable and precise dosimetric performance. **Methods:** The percentage depth dose at 10 cm depth (PDD_{10}) of 6 MV flattening filter-free (FFF) beams in two beam-matched LINACs (TrueBeam 1 and TrueBeam 2) was compared. The evaluation of 20 SRS and SRT treatment plans was conducted using 6 MV-FFF beams and the volumetric modulated arc therapy (VMAT) technique on two beam-matched LINACs. Treatment plans were created on TrueBeam 1 and assessed on both LINACs. PSQA was performed using portal dosimetry, with gamma passing rates compared at criteria of 3%/2 mm, 2%/1 mm, and 1%/1 mm. **Results:** Difference about PDD_{10} of beam-matched LINACs within ±1%. The average differences of gamma passing rate between TrueBeam 1 and 2 were within 0.5%, 3.2%, and 3.3% for the 3%/2 mm, 2%/1 mm, and 1%/1 mm criteria, respectively. All differences were not statistically significant ($P > 0.05$, paired-sample t-test), indicating consistent performance between the two LINACs. **Conclusion:** The average differences in gamma passing rate of TrueBeam 1 and 2 increases as the criteria became tighter. Beam-matched LINACs demonstrate consistent and reliable performance for SRS and SRT, with minimal and statistically insignificant differences in gamma passing rate, allowing for patient switches between LINACs without replanning in SRS and SRT using VMAT. This confirms the feasibility of delivering complex treatment plans across beam-matched LINACs.

Keywords — Beam-matching, Stereotactic Radiosurgery, Stereotactic Radiotherapy, Portal dosimetry, Patient-specific quality assurance

I. INTRODUCTION

Stereotactic radiosurgery (SRS) and stereotactic radiotherapy (SRT) are types of radiation therapy that uses a small beam of radiation to target the area with precision and accuracy. These techniques are particularly suited for treating small tumors that conventional methods such as surgery, chemotherapy, or standard radiotherapy, cannot address. SRS delivers a single high-dose fraction of radiation (12–25 Gy) to the head, while SRT divides the dose (10–50 Gy) into 2–5 fractions to minimize side effects. Both approaches use advanced delivery methods such as intensity-modulated radiotherapy (IMRT) and volumetric-modulated arc therapy (VMAT), which utilize multileaf collimators (MLCs) for precise dose shaping during beam irradiation with continuous gantry rotation. As VMAT is an evolution of IMRT, it allows for adjustment of dose rate and gantry speed during radiation [1].

Previous study recommended that stereotactic treatment should utilize flattening filter-free (FFF) beams because they allow for higher dose rates, shorter treatment times, reduced head scatter, and minimized out-of-field dose [2].

Beam Matching refers to the characteristics of multiple linear accelerators (LINACs) that are adjusted to produce identical beam characteristics in the same treatment planning system (TPS) across all LINACs. For clinical systems with multiple LINACs, beam matching ensures identical dosimetric characteristics across LINACs, allowing patients to switch

between devices without replanning in case another particle LINAC malfunctions or there are too many patients waiting for radiation treatment. Key parameters for beam matching include percentage depth dose (PDD), beam profiles, and output factors at depth of dose maximum (d_{max}) to ensure the same dose irradiation of each machine [3-5].

Patient-specific quality assurance (PSQA) is essential to verify the treatment plan accuracy and precision for complex techniques like SRS and SRT, particularly when utilizing VMAT, where achieves high dose conformality by optimizing the dose rate, gantry speed, and continuous movement of the MLC [1]. PSQA has been defined as part of the beam matching assessment [2, 6-8] to check the feasibility of delivering radiation within the same treatment plan for each LINAC, particularly for advanced techniques like SRS [9] and SRT [6, 10].

At King Chulalongkorn Memorial Hospital, a new LINAC has been installed and the beam matching characteristics of the existing LINAC should be tested. Beam matching for Varian LINACs includes tests such as PDD_{10} measurement using a water phantom and commissioning, as specified by the company uses data from the smallest field sizes of 3 × 3 cm². Studying of dosimetrics characteristics in smaller fields sizes may enhance confidence in beam-matching assessment, particularly for SRS and SRT plans. Therefore, the objective is to assess the feasibility of using beam-matched LINACs for complex techniques like SRS and SRT, by investigating PSQA of VMAT plans using portal imaging.

II. MATERIALS AND METHODS

Two Varian TrueBeam linear accelerators (Varian Medical System, Palo Alto, CA, USA) were used in this study. The first LINAC was installed in 2022 (TrueBeam 1) SN-5348 and the second in 2024 (TrueBeam 2) SN-6462, each equipped with a 120-leaf Millennium multileaf collimator. Both machines could deliver dose rates ranging from 400 to 1400 MU/min and with the capacity to deliver energies of 6 MV, 6 MV-FFF, 10 MV, and 10 MV-FFF. This study was reviewed and approved by the Human Research Ethics Committee of Naresuan University with (IRB No. P1-0145/2567).

A. Beam characteristic

The percentage depth dose at 10 cm depth (PDD_{10}) of 6 MV-FFF were measured for 2 × 2, 3 × 3, 4 × 4, 6 × 6 cm^2 and 10 × 10 cm^2 field sizes using IBA SMARTSCAN™ scanning phantom system (IBA dosimetry, Schwarzenbruck, Germany) at scanning speed of 5.0 mm/s. For beam characterization, the IBA CC04 ionization chamber (IBA dosimetry, Schwarzenbruck, Germany), with an active volume of 0.04 cm^3, was used for measurement. The difference in PDD_{10} for beam matched LINACs should be ±1% [2].

B. Patient-specific quality assurance

Twenty SRS and SRT treatment plans planned using Eclipse version 16.1 (Varian Medical System, Palo Alto, CA) with 6 MV-FFF beams and VMAT using a calculation grid size of 1.25 mm on a TrueBeam 1 treatment planning system. PSQA for all plans were performed using portal dosimetry with an aS1200 EPID (Varian Medical Systems, Palo Alto, CA), which is equipped with an amorphous silicon detector. It has 1280 × 1280 pixels matrix array (active area: 43 cm × 43 cm, pixel size: 0.34 mm × 0.34 mm). And compared in both LINACs with gamma passing rates at criteria of 3%/2 mm, 2%/1 mm, and 1%/1 mm.

C. Statistical analysis

The measured data were presented as mean values with standard deviations. Dosimetric parameter differences were expressed as percentage differences. The gamma passing rates between the two LINACs were compared using a paired sample t-test. A p-value of less than 0.05 was considered to indicate a statistically significant difference.

III. RESULTS

A. Beam characteristic

In Table 1, The PDD_{10} for 6 MV-FFF beams was analyzed across various field sizes to assess beam consistency between the two LINACs remaining within the ±1%. The smallest difference in PDD_{10} between TrueBeam 1 and TrueBeam 2 was observed in 10 × 10 cm² field size (-0.4%), and the largest

difference was -0.86% for a field size of 2 × 2 cm².

Table 1. *Difference in PDD_{10} for 6 MV-FFF of TrueBeam 1 and TrueBeam 2*

Field size (cm^2)	PDD_{10}		Difference (%)
	TrueBeam 1	TrueBeam 2	
2 × 2	55.97	55.11	- 0.86
3 × 3	57.51	56.8	- 0.71
4 × 4	58.77	57.93	- 0.84
6 × 6	60.77	60.31	- 0.46
10 × 10	63.65	63.25	- 0.4

B. Patient-specific quality assurance

Figure 1 shows the distributions of gamma passing rates for TrueBeam 1 and TrueBeam 2 under different gamma criteria. Overall, both LINACs demonstrate an average gamma passing rate exceeding 90%.

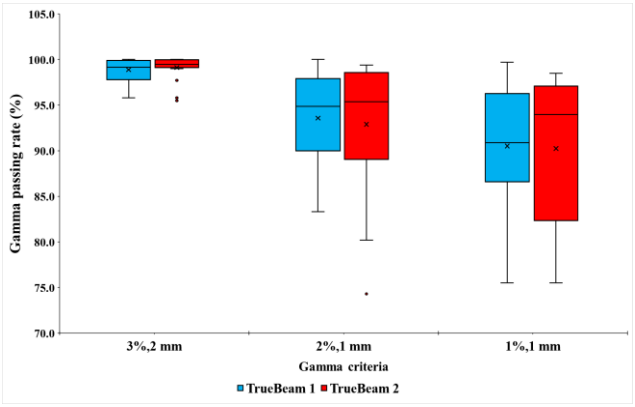

Figure 1. *Distributions of gamma passing rate of SRS/SRT VMAT plans delivered on two beam matched LINACs and different criteria.*

In Table 2, the average difference of gamma passing rate from PSQA test for SRS and SRT cases with different criteria of 3%/2 mm, 2%/1 mm, and 1%/1 mm, were 0.5 ± 0.6%, 3.2 ± 4.1%, and 3.3 ± 4.0%, respectively. The PSQA results for these criteria showed that the mean gamma passing rate decreased as the criteria became tighter.

Additionally, statistical analysis using a paired sample t-test showed no significant differences between TrueBeam 1 and TrueBeam 2, with p-value of 0.161, 0.567, and 0.816 for 3%/2 mm, 2%/1 mm, and 1%/1 mm, respectively, when performing PSQA using EPID across all SRS and SRT cases.

Table 2. *Percent difference in gamma passing rate, and paired sample t-test between TrueBeam 1 and TrueBeam 2*

Gamma criteria	Mean gamma passing rate (%) ± SD		Difference (%)	P-value
	TrueBeam 1	TrueBeam 2		
3%, 2 mm	98.9 ± 1.2	99.1 ± 1.3	0.5 ± 0.6	0.161
2%, 1 mm	93.6 ± 4.9	92.9 ± 7.1	3.2 ± 4.1	0.567
1%, 1 mm	90.5 ± 6.7	90.2 ± 8.1	3.3 ± 4.0	0.816

P-value < 0.05 is statistically significant.

IV. DISCUSSION

The results of the two LINACS demonstrated consistency and clinical reliability for SRS and SRT. In Table 1, The two LINACs have similar dosimetric characteristics remaining within the ±1%, which is consistent with tolerance from the reported data for 6 MV-FFF beams in Varian LINACs [2].

As the PSQA criteria became tighter, the mean gamma passing rate decreased. This is likely due to the increased sensitivity of the system to deviations when tighter tolerances are applied. Consistent with the findings reported in Thongsawad et al. [11] and Miri et al. [12].

The consistency in dosimetric parameters and PSQA results between the two beam-matched LINACs demonstrates their interchangeability in clinical practice. This capability is particularly useful in situations where one LINAC is unavailable due to maintenance requirements or patient overload, ensuring treatment continuity without the need to re-plan treatments.

This study has limitations that should be acknowledged, such as the evaluation focused on two specific Varian TrueBeam LINACs with beam-matched characteristics, and thus the results may not be generalized to other LINAC models or manufacturers. Furthermore, the integration of advanced measurement tools, such as Monte Carlo simulations or 3D dose verification systems could provide a more comprehensive understanding of the effects of beam matching on highly complex treatments.

V. CONCLUSION

This study evaluated the dosimetric performance and PSQA of two Varian TrueBeam LINACs. Beam characteristics showed good agreement between both machines. The average differences gamma passing rate of TrueBeam 1 and TrueBeam 2 increased as the criteria became tighter. The variations in dose and gamma passing rate between the two LINACs for SRS and SRT cases were minimal and within acceptable limits. The differences between the beam-matched LINACs are not statistically significant, allowing patient switches between LINACs without replanning in SRS and SRT using VMAT. This confirms the feasibility of delivering complex treatment plans across beam-matched LINACs.

ACKNOWLEDGEMENTS

I would like to sincerely thank the Faculty of Allied Health Sciences, Naresuan University, for providing the facilities for this research. I also deeply appreciate King Chulalongkorn Memorial Hospital for their kind support in assisting with the data collection for this study.

REFERENCES

[1] Radiation Oncology Physics. Vienna: INTERNATIONAL ATOMIC ENERGY AGENCY; 2005.

[2] Ghemiș DM, Marcu LG, Virag V, Virag A. Dosimetric characteristics of 6MV flattening filter free and flattened beams among beam-matched linacs: a three-institutional study. Radiation Oncology. 2023;18(1):126.

[3] Sjöström D, Bjelkengren U, Ottosson W, Behrens CF. A beam-matching concept for medical linear accelerators. Acta Oncologica. 2009;48(2):192-200.

[4] Beyer GP. Commissioning measurements for photon beam data on three TrueBeam linear accelerators, and comparison with Trilogy and Clinac 2100 linear accelerators. J Appl Clin Med Phys. 2013;14(1):4077.

[5] Hrbacek J, Depuydt T, Nulens A, Swinnen A, Van den Heuvel F. Quantitative evaluation of a beam-matching procedure using one-dimensional gamma analysis. Med Phys. 2007;34(7):2917-27.

[6] Goodall SK, Dunn L, Dunning J, Muñoz L, Rowshanfarzad P, Ebert MA. Matched linac stereotactic radiotherapy: An assessment of delivery similarity and distributive patient-specific quality assurance feasibility. J Appl Clin Med Phys. 2022;23(11):e13652.

[7] Rojas-López JA, Venencia D. Importance of Beam-Matching between TrueBeam STx and Novalis Tx in Pre-Treatment Quality Assurance Using Portal Dosimetry. J Med Phys. 2021;46(3):211-20.

[8] Bhangle JR, Narayanan VK, Kumar NK, Vaitheeswaran R. Dosimetric analysis of beam-matching procedure of two similar linear accelerators. J Med Phys. 2011;36(3):176-80.

[9] Muñoz L, Kron T, Petasecca M, Bucci J, Jackson M, Metcalfe P, et al. Consistency of small-field dosimetry, on and off axis, in beam-matched linacs used for stereotactic radiosurgery. Journal of Applied Clinical Medical Physics. 2021;22(2):185-93.

[10] Xu Z, Warrell G, Lee S, Colussi V, Zheng Y, Ellis R, et al. Assessment of beam-matched linacs quality/accuracy for interchanging SBRT or SRT patient using VMAT without replanning. Journal of Applied Clinical Medical Physics. 2019;20(1):68-75.

[11] Thongsawad S, Chanton T, Saiyo N, Udee N. Planar EPID-Based Dosimetry for SRS and SRT Patient-Specific QA. Life (Basel). 2021;11(11).

[12] Miri N, Keller P, Zwan BJ, Greer P. EPID-based dosimetry to verify IMRT planar dose distribution for the aS1200 EPID and FFF beams. Journal of Applied Clinical Medical Physics. 2016;17(6):292-304.

Contacts of the corresponding author:
Author: Asst. Prof. Sumalee Yabsantia, Ph.D.
Institute: Department of Radiological Technology, Faculty of Allied Health Sciences, Naresuan University
City: Phitsanulok
Country: Thailand
Email: sumaleey@nu.ac.th

Design and fabrication of a dedicated phantom for geometric verification in single-isocenter multiple-target (SIMT) stereotactic radiosurgery

Montreemanorom Warisara[1], Khamfongkhruea Chirasak[1,2], Mundee Thunpisit[2], Chanpanya Thananya[2], Suwanbut Pattarakan[2], Polee Chalermpong[3], Wonglee Sarinrat[3], Thongsawad Sangutid[1,2,*]

[1]*Princess Srisavangavadhana College of Medicine, Chulabhorn Royal Academy, Bangkok, Thailand*
[2]*Radiation Oncology Department, Chulabhorn Hospital, Chulabhorn Royal Academy, Bangkok, Thailand*
[3]*Nuclear Research and Developments, Thailand Institute of Nuclear Technology, Bangkok, Thailand*
*sangutid.tho@cra.ac.th

Abstract — **Introduction:** The Single-Isocenter Multiple-Target (SIMT) stereotactic radiosurgery (SRS) technique streamlines treatment by eliminating the need for separate isocenter setups for each target, resulting in reduced setup and treatment time. However, accurate alignment across multiple targets is essential, and a single Winston-Lutz test is inadequate for complete geometric verification. Furthermore, dosimetric verification is performed to ensure dosimetry accuracy. This study develops a dedicated phantom with multiple metallic markers to accurately identify and verify radiation isocenters for multiple targets. **Methods:** A phantom dimension of 198×198×180 mm^3 was constructed from polymethyl methacrylate (PMMA) and embedded with 13 stainless steel ball markers to define isocenter and off-isocenter positions. A geometric verification plan for SIMT was developed, which involved shaping the multileaf collimator (MLC) around the markers at the gantry, collimator, and couch angles across five separate tests. The plan was implemented on a TrueBeam linear accelerator (Linac), with the Electronic Portal Imaging Device (EPID) capturing images to assess the accuracy of isocenter and off-isocenter alignments. Positioning accuracy was evaluated by calculating the centroid deviation between the markers and the radiation beam. **Results:** For geometric verification, the beam positioning errors range from 0.4 mm to 0.9 mm at the isocenter, with the maximum being 0.9±0.20 mm. At the off-isocenter, the beam positioning errors increase, ranging from 0.2 mm to 1.8 mm, with the maximum being 1.8±0.2 mm. For dosimetric verification, the percentage dose differences ranged from 0.02% to 4.3% for the minimum and maximum values, respectively. **Conclusion:** This phantom is well-suited for verifying the geometric and dosimetric accuracy of the SIMT technique, offering a cost-effective and user-friendly solution. Integrating MATLAB script code for analysis can further streamline SIMT geometric verification workflows.
Keywords — Single-isocenter multiple-target stereotactic radiosurgery, stereotactic radiosurgery, geometric verification, and dosimetric verification.

I. INTRODUCTION

Traditional treatment for multiple brain metastases involves setting up an isocenter for each target, making the beam delivery process time-consuming. Thus, a SIMT technique is now employed to reduce treatment time and the ability to treat multiple targets in a single session [1]. Therefore, the concerns with the SIMT technique are target positioning (geometry accuracy) and radiation quantity (dosimetry accuracy). The SIMT technique requires several protocols and quality assurance (QA) to deliver accurate and precise treatment: The AAPM-RSS Medical Physics Practice Guideline 9.a. focusing on SRS & stereotactic body radiation therapy (SBRT) [2] and AAPM Task Group 142 (TG-142) report on the QA of Medical Accelerators [3] globally recognized for QA guidelines in SRS and SBRT. The TG-142 guidelines recommend beam positioning error at the isocenter position within 1 mm. However, no specific recommendation is provided for verifying the off-isocenter positions. According to a report by Yock et al. [4], off-isocenter targets' uncertainties are more significant than isocenter targets. These uncertainties may arise from various factors, including setup errors and the inherent uncertainty of the MLC.

Typically, geometry and dosimetry in SIMT SRS are conducted as separate processes.

Dosimetry verification involves measuring the radiation dose using phantoms or detector arrays. Conversely, geometry verification involves radiation isocenter for advanced techniques using the Winston-Lutz test as a standard method for evaluating the displacement between the center of the radiation field and the machine (gantry, collimator, and couch angles). However, a Winston-Lutz test evaluates only the target at the isocenter, which does not represent all targets in a SIMT. Therefore, validation of the targeting accuracy away from the isocenter (off-isocenter) is necessary. Thus, this study aims to develop a single phantom for geometric and dosimetric verification and establish the QA approach for SIMT SRS.

II. MATERIALS AND METHODS

A. TrueBeam linear accelerator

The TrueBeam Linac (Varian Medical Systems, Inc., Palo Alto, CA) was used in this study with flattened and flattening-filter-free (FFF) beams to perform the geometric and dosimetric verifications. The radiation field size was shaped using the jaws and the 120-millennium MLC model with a maximum field size of 40×40 cm^2. Additionally, the TrueBeam Linac is equipped with kV and MV imaging systems. The kV imaging features a 40×30 cm^2

B. Phantom design and fabrication

The phantom was designed using the AutoCAD program (version 2024) and the phantom was fabricated with a machine tool (milling machine FB-3; EMCO-Maier GmbH, Austria). The phantom was constructed from PMMA material with a 1.190 g/cm^3 density. The phantom size (Figure 1) is 198×198×180 mm^3 to cover all markers and contains 13 stainless steel markers (diameter 5 mm) at both isocenter (distance = 0 mm) and off-isocenter positions

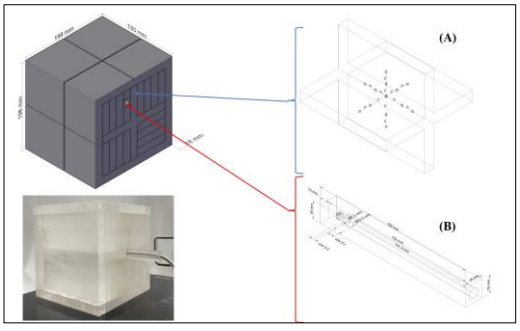

Figure 1. *Phantom design: (A) All markers in plus insert, (B) CC13 insert*

(distances = 20, 30, 40, and 50 mm from the isocenter) following Gao et al. [5], which recommended the off-isocenter distance for the SIMT should be < 6 cm. Furthermore, the phantom was designed to facilitate the insertion of the CC13 (IBA Dosimetry GmBH, Schwarzenbruck, Germany).

C. Treatment planning approach

C.1 Treatment planning system (TPS)

Varian's Eclipse TPS (Varian Medical Systems, Palo Alto, CA) was used to generate the treatment plans with the Anisotropic Analytical Algorithm (AAA) applied for dose calculation. This study utilized 10 approved treatment plans (Table 1) with the HyperArc VMAT technique for SIMT SRS using a 6 MV FFF (6FFF) beam energy for dosimetric verification. Point dose measurement was used to evaluate dosimetric verification. The treatment planning data were used to calculate the dose on the CT images of our developed phantom. These images included the detector insertion and structure contouring of both the CC13 detector's active volume and the phantom body. The QA plan was generated for Winston-Lutz analysis at the isocenter and off-isocenter for geometric verification across five separate tests. The markers were created to evaluate the alignment of the MLC shape. All QA plans generated a field size of 1×1 cm^2 with an MLC width of 5 mm to cover the marker.

C.2 Geometric verification (Winston Lutz test)

The MATLAB software version R2023a (Mathworks, Inc., Natick, MA) program receives images from digital imaging or DICOM files for WL analysis. The first step is to convert the DICOM file into a grayscale image and crop the original image at marker's region of interest (ROI). Subsequently, the detection involves two categories: (1) radiation field detection and (2) marker detection.

Table 1. *SIMT SRS plans used for dosimetric verification*

Plan	Targets	PTV volume(cm^3)	Off-iso distance (cm)
1	2	5.1,1.4	2.65, 4.92
2	4	1.3, 4.8, 3.2, 1.4	6.09, 6.42, 4.33, 5.25
3	2	0.9, 4.0	4.40, 4.40
4	2	1.0, 1.6	4.52, 4.53
5	2	2.2, 0.3	2.09, 2.09
6	3	0.8, 2.9, 4.7	2.33, 2.02, 4.82
7	2	4.9, 0.7	3.20, 3.26
8	2	1.6, 1.2	4.56, 4.56
9	2	5.3, 15.8	3.74, 3.74
10	3	1.0, 0.9, 3.0	7.74, 5.92, 4.28

Table 2. *Percentage dose difference of 10 SIMT SRS plans*

Plan	% Dose difference			
	PTV1	PTV2	PTV3	PTV4
1	1.2	1.1	-	-
2	0.6	0.2	0.6	0.2
3	3.6	0.9	-	-
4	1.5	0.02	-	-
5	0.4	2.8	-	-
6	1.3	0.3	0.5	-
7	0.3	0.5	-	-
8	3.2	4.3	-	-
9	0.1	2.8	-	-
10	0.4	3.5	2.1	-

A threshold grayscale image was created to generate a binary image. In the final step, the radiation field and marker were plotted onto the cropped image, and the distance between the centers of the radiation field and the marker was calculated to find beam positioning errors in each marker. The beam positioning error (d_{error}) was calculated as follows:

$$d_{error} = \sqrt{(x_r - x_m)^2 + (y_r - y_m)^2} \quad (1)$$

where x_r and x_m are x-axis positions of the radiation field and marker, and y_r and y_m are y-axis positions of the radiation field and marker.

C.3 Dosimetric verification

Point dose measurement was performed on the treatment plan using a CC13 ionization chamber (IC) inserted inside the phantom. The center of the sensitive volume was placed at the center of the target, as defined in the TPS. Following AAPM-RSS medical physics practice guideline 9.a. for SRS-SBRT [2], a tolerance of ±5% was applied to compare the mean calculated dose volume in the TPS with the measured point doses in the CC13 IC. The equation to calculate the percentage dose difference between measurement and TPS ($\%diff$) is as follows:

$$\%diff = \left| \frac{Measurement - calculation}{\frac{Measurement - calculation}{2}} \right| \times 100 \quad (2)$$

where $Measurement$ is the point dose measurement in CC13, and $calculation$ is dose calculated in TPS.

III. RESULTS

A. Geometric verification

The beam positioning errors reported the mean values and standard deviations of the isocenter and off-isocenter position (Figure 2) from all five measurements. Figure 2A, presents the beam positioning errors as several distinct values, with the mean values remaining below 1 mm. In Figure 2B, 2C, and 2D, the angles with a mean value exceeding 1 mm at an off-isocenter of 5 cm show maximum mean values of 1.8±0.2 mm.

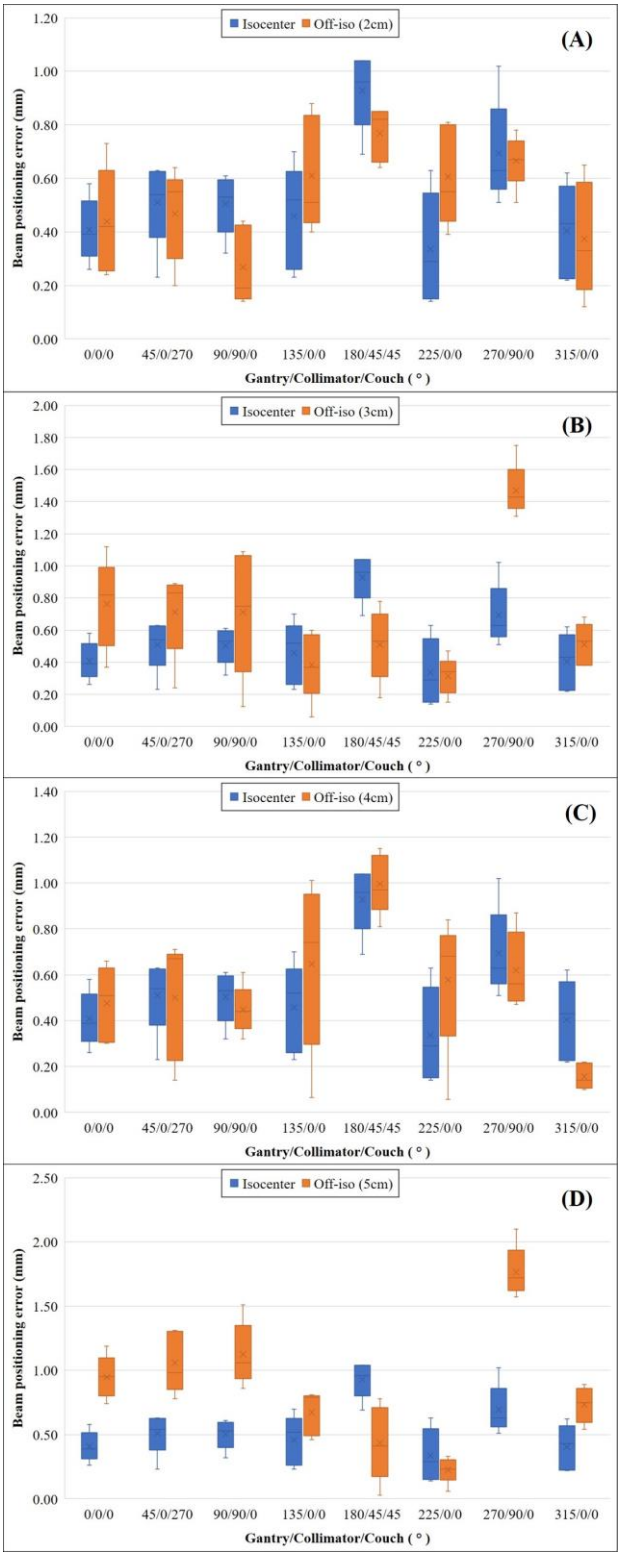

Figure 2. *Beam-positioning errors of five measurements*

B. Dosimetric verification

The percentage dose difference for each target (Table 2) was analyzed across the study's 10 SIMT SRS plans (Table 1). The percentage dose differences ranged from 0.02-4.3% at minimum (Plan 4 with PTV2) and maximum (Plan 8 with PTV2), respectively, where the results of the percentage dose difference are within ±5% tolerance.

IV. DISCUSSION

The results indicate that geometric verification increases beam positioning errors at the off-isocenter compared to the isocenter at a distance of 5 cm. This is attributed to the higher sensitivity to positional errors in the off-axis region compared to the isocenter. Additionally, this study performed dosimetric verification using percentage dose difference to evaluate the QA of SIMT SRS. The percentage dose difference observed in this study ranged from 0.02-4.3% when using the CC13 IC. When compared to the results of Capaldi et al. [6], the percentage dose difference measured by the PTW Pinpoint 31014 (PTW, Freiburg, Germany) in a OneIso phantom was reported to range from 0.05-3.06%, the results show a close similarity to this study, though with slight differences that may be attributed to the phantom settings, which could introduce uncertainty when changing the positions for each target of 0.3-15.8 cm^3. However, the Poder et al. [7] study reported a slightly higher percentage dose difference of 0.1-4.9% using a perspex Multi-Plug device with a Sun Nuclear ArcCheck phantom (Sun Nuclear, Melbourne, FL). This uncertainty may be attributed to the IC insert not being specifically designed to accommodate the PTW PinPoint 3D, potentially contributing to uncertainties in the absolute dose measurements.

V. CONCLUSION

This phantom is well-suited for verifying the geometric and dosimetric accuracy of the SIMT, offering a cost-effective and user-friendly solution. Integrating MATLAB scripts streamlines workflows and establishes QA plans for off-isocenter distance accuracy covering 5 cm. Future research will focus on developing a film holder to facilitate the analysis of dose distribution accuracy using film dosimetry.

REFERENCES

[1] Slagowski JM, Wen Z. Selection of single-isocenter for multiple-target stereotactic brain radiosurgery to minimize total margin volume. Phys Med Biol. 2020 Sep 21;65(18).

[2] Halvorsen PH, Cirino E, Das IJ, Garrett JA, Yang J, Yin FF, Fairobent LA. AAPM-RSS Medical Physics Practice Guideline 9.a. for SRS-SBRT. J Appl Clin Med Phys. 2017 Sep 1;18(5):10–21.

[3] Klein EE, Hanley J, Bayouth J, Yin FF, Simon W, Dresser S, Serago C, Aguirre F, Ma L, Arjomandy B, Liu C, Sandin C, Holmes T. Task group 142 report: Quality assurance of medical accelerators. Medical Physics. John Wiley and Sons Ltd. 2009;36:4197-212.

[4] Yock AD, Grees B, Luo G. Innovative margin design and optimized isocenter to minimize the normal tissue in target volumes for single-isocenter multi-target stereotactic radiosurgery. Phys Med Biol. 2023 Oct 7.

[5] Gao J, Liu X. Winston-Lutz-Gao Test on the True Beam STx Linear Accelerator. Int J Med Phys Clin Eng Radiat Oncol. 2019;08(01):9–20.

[6] Capaldi DPI, Skinner LB, Dubrowski P, Yu AS. An integrated quality assurance phantom for frameless single-isocenter multitarget stereotactic radiosurgery. Phys Med Biol. 2020 Jun 7;65(11).

[7] Poder J, Brown R, Porter H, Gupta R, Ralston A. Development of a dedicated phantom for multi-target single-isocentre stereotactic radiosurgery end to end testing. J Appl Clin Med Phys. 2018 Nov 1;19(6):99–108.

Contacts of the corresponding author:
Author: Sangutid Thongsawad
Institute: Chulabhorn Royal Academy
Street: Kamphaeng Phet 6 Road
City: Bangkok 10210
Country: Thailand
Email: sangutid.tho@cra.ac.th

Development of deep learning-based auto-segmentation on CT images for prostate radiotherapy

Pranee Chanaphat[1], Kummanee Patiparn[1], Deeharing Apisara[2], Khamfongkhruea Chirasak[1,2], Fuangrod Todsaporn[1*]

1 Medical Physics Program, Princess Srisavangavadhana College of Medicine, Chulabhorn Royal Academy, Bangkok, Thailand.
2 Radiation Oncology Department, Chulabhorn Hospital, Chulabhorn Royal Academy, Bangkok, Thailand.
**Corresponding author: Todsaporn.fua@cra.ac.th*

Abstract — **Introduction:** The accurate delineation of organs at risk (OARs) and clinical target volumes (CTV) is critically significant in radiotherapy; nevertheless, this undertaking is often obstructed by the resource-intensive nature of manual segmentation. This study presents the development of a deep learning-based auto-segmentation model specifically targeting lymph node clinical target volumes (CTVn) and OARs within the context of prostate radiotherapy. **Methods:** A dataset of 233 prostate Volumetric Modulated Arc Therapy (VMAT) cases, including treatment plans, structures, and computed tomography (CT) scans, was retrospectively collected from Chulabhorn Hospital between 2018 and 2024. The data were divided into training (80%) and testing (20%) subsets. An Attention U-Net architecture was employed to train CTVn and 7 OARs models, including the bladder, rectum, bowel, sigmoid, penile bulb, and left and right femurs. Model performance was assessed using the Dice Similarity Coefficient (DSC). **Results:** The mean DSC for CTVn was 0.789 ± 0.188. For OARs, DSCs were 0.921 ± 0.156 (bladder), 0.883 ± 0.130 (rectum), 0.829 ± 0.213 (bowel), 0.760 ± 0.103 (penile bulb), 0.408 ± 0.219 (left femur), and 0.468 ± 0.391 (right femur). **Conclusion:** The Attention U-Net-based auto-segmentation model demonstrates CTVn and OARs delineation capability, highlighting its potential to streamline prostate radiotherapy planning.

Keywords — Deep learning, Attention U-Net, Auto-segmentation, CT image, prostate cancer.

I. INTRODUCTION

Prostate cancer is the second most common malignancy and the fifth leading cause of cancer-related mortality in men globally, with incidence and mortality rates continuously rising. Radiation therapy plays a critical role in the management of prostate cancer, offering offering a non-invasive procedure. Advanced techniques, such as Volumetric Modulated Arc Therapy (VMAT), enables precise dose delivery to the tumor and reduces toxicity to adjacent organ. Radiation treatment planning traditionally relies on computed tomography (CT) simulation with manual segmentation of target volumes and organs at risk (OARs). This process is labor-intensive, time-consuming, and prone to inter-observer variability. While commercial auto-segmentation tools are available, their lack of institution-specific data often limits clinical applicability.

The development of deep learning-based auto-segmentation for CT images in prostate radiotherapy cancer patients indicates a significant advancement in medical imaging, aiming to enhance the precision and efficiency of treatment planning. By automating the segmentation of prostate cancer-related structures, deep learning models can potentially reduce the burden of manual delineation while improving accuracy and consistency. In general, variations of the U-Net architecture widely used for segmentation tasks have demonstrated high accuracy. For example, 2D and 3D U-Net models for prostatic urethra segmentation achieved average centerline distances of 2.07 mm and 2.05 mm, respectively (1). Incorporating attention mechanisms has further enhanced segmentation performance, with studies reporting improved consistency and reduced delineation times (2). Additionally, patient-specific models using daily fan-beam CT images have shown superior performance compared to population-based models in terms of Dice Similarity Coefficients (DSC) (3).

Applications of these deep learning models in prostate radiotherapy have included

automated segmentation of clinical target volumes (CTVs) for intact and postoperative cases, significantly reducing segmentation time and improving operator consistency (2). Moreover, these models have been successfully applied to segment OARs such as the bladder, rectum, bowel, sigmoid colon, and femurs, achieving high DSC values indicative of reliable segmentation accuracy (3,4). Evaluation metrics such as DSC, commonly used to assess segmentation accuracy, have reported values ranging from 0.83 to 0.94 for various organs, demonstrating the effectiveness of deep learning models in achieving high-quality segmentation (4,5). These advancements highlight deep learning-based auto-segmentation tools' potential to streamline and improve prostate cancer radiotherapy planning.

This study aims to develop and validate an AI-based automated segmentation tool for lymph node clinical target volumes (CTVn) and OARs, including the rectum, bladder, bowel, sigmoid colon, and femurs, using CT imaging. The tool's accuracy and efficiency were compared to manual delineation.

II. MATERIALS AND METHODS

A. Datasets

Planning CT images from 233 prostate cancer patients treated with radiotherapy using Volumetric Modulated Arc Therapy (VMAT) with a Sequential Boost plan were retrospectively collected between January 1, 2018, and September 30, 2024. The dataset was randomly divided into a training validation set (186 cases) and a test set (47 cases).

CT scans were performed following the standard pelvic protocol using the Philips Big Bore scanner (Philips Healthcare, Netherlands), the SOMATOM go.Open Pro scanner (Siemens HealthCare, USA). Patients underwent bladder and rectum preparation prior to scanning in the supine position. Scans were acquired at a tube voltage of 120 kVp with manufacture-specific tube current (mAs) settings, a matrix size of 512 × 512, a slice thickness of 3 mm, and pixel spacing of 0.67 × 0.67 mm^2. A radiation oncologist manually delineated contours for CTVn and OARs following Radiation Therapy Oncology Group (RTOG) guidelines. These manual contours served as the ground truth for training the deep learning model.

B. Model training

We developed an Attention U-Net model for CTVn and OARs segmentation, incorporating the U-Net architecture and Attention Gates (AGs). As illustrated in Figure 1, The U-Net architecture facilitates the integration of high-level and low-level features through skip connections between the encoder and decoder, enabling precise segmentation by preserving fine details. Attention Gates (AGs) are embedded within the skip connections, enhancing the model's ability to focus on the most relevant regions.

Figure 1. *Attention U-Net segmentation model.*

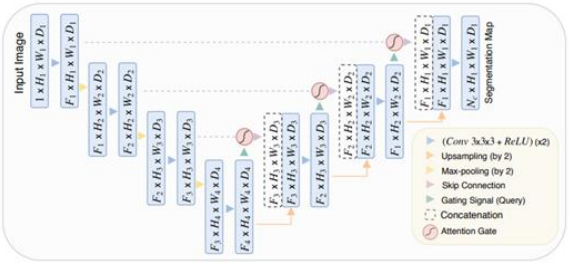

The network was implemented using PyTorch (version 3.11.2). The training was conducted separately for each region of interest (ROI), employing the Adam optimizer with an initial learning rate of 0.00001 over 50 epochs. A mini-batch size of 8 was selected to accommodate GPU memory constraints. The loss function, BCEWithLogitsLoss, combines a Sigmoid activation with Binary Cross-Entropy (BCE) loss for robust segmentation performance.

Input CT images, standardized to a resolution of 512 × 512 pixels, underwent data augmentation to improve model generalization. Augmentation techniques included rotations within a ±35-degree range, horizontal and vertical flipping, and pixel normalization (rescaling from [0, 255] to [0, 1]).

C. Quantitative evaluation

The DSC was used to evaluate the Attention U-Net model's performance quantitatively. The

DSC measures the overlap between the predicted segmentation and the manual annotation, defined as:

$$DSC = \frac{2 \times |A \cap B|}{|A| + |B|}$$

where A represents the predicted segmentation volume, and B represents the manually delineated volume. The DSC ranges from 0 to 1, with a value of 1 indicating complete overlap between the two volumes and a value of 0 indicating no overlap. This metric effectively measures the model's accuracy in replicating expert annotations.

III. RESULTS

The mean and standard deviation (SD) of the Dice Similarity Coefficient (DSC) for each region of interest (ROI) are summarized in Table 1 and visually presented in Figure 2.

Table 1. *Descriptive Statistics of DSC Performance Metrics for Attention U-Net*

ROI	Mean ± SD
CTVn	0.789 ± 0.188
Bladder	0.921 ± 0.156
Bowel	0.829 ± 0.213
Rectum	0.883 ± 0.130
Sigmoid	0.475 ± 0.352
Left. femur	0.408 ± 0.219
Right. femur	0.468 ± 0.391
Penile bulb	0.760 ± 0.103

*ROI: regions of interest

As shown in Table 1, the Attention U-Net achieved a DSC of 0.789 ± 0.188 for CTVn. Among the OARs, the bladder and rectum exhibited the highest segmentation accuracy with DSC values of 0.921 ± 0.156 and 0.883 ± 0.130, respectively. In contrast, lower DSC values were observed for the left femur (0.408 ± 0.219) and sigmoid (0.475 ± 0.352), reflecting more significant variability in these regions.

IV. DISCUSSION

The Attention U-Net model demonstrated strong performance in segmenting both CTVn and OARs, with DSCs observed for significant structures. Specifically, the bladder and rectum achieved the highest DSC values, 0.921 ± 0.156 and 0.883 ± 0.130, respectively, showcasing the model's capability to delineate critical regions accurately. However, segmentation of the left femur (0.408 ± 0.219), right femur (0.468 ± 0.391), and sigmoid (0.475 ± 0.352) displayed more significant variability, highlighting potential challenges associated with these regions.

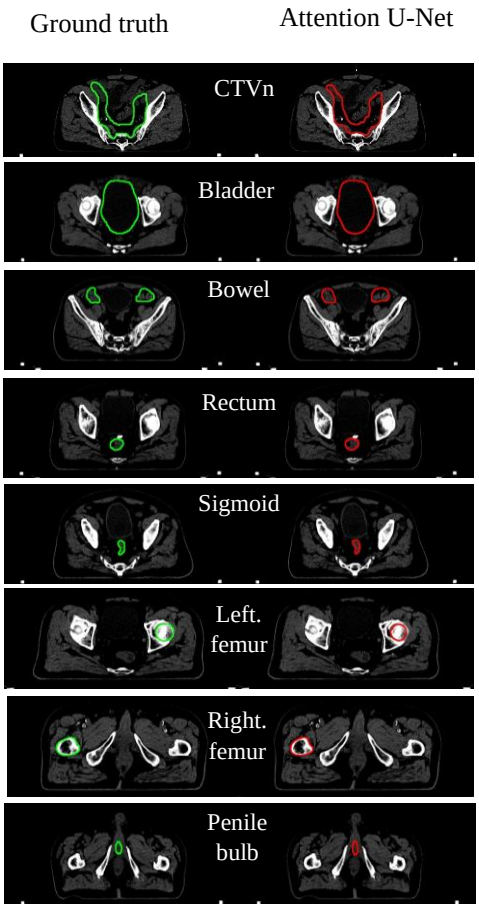

Figure 2. *Segmentation results comparing the ground truth (left) and Attention U-Net predictions (right) for CTVn and seven OARs.*

The Attention U-Net model's performance aligns with existing studies on the segmentation of anatomically complex structures. For sigmoid colon segmentation, Rahman et al. achieved a maximum DSC of 56.92% using a modified 3D U-Net with Pyramid Pooling and Channel-Spatial Squeeze and Excitation (PyP and csSE) modules, with ensemble methods further improving DSC to 88.11% (6). Our model showed high accuracy

for the bladder (0.921) and rectum (0.883) but lower performance for the sigmoid (0.475), consistent with Rahman et al., who highlighted variability in sigmoid segmentation due to its size and irregular shape.

The limitations of this study include lower performance for regions like the sigmoid and femurs, possibly due to anatomical variability or imbalanced representation in the dataset. GPU memory constraints, which restricted the mini-batch size to 8, may have limited further optimization of the training process.

In addition, using a single-institution dataset limits the model's generalizability. Incorporating multi-institutional datasets in future studies can improve robustness and performance, particularly for challenging structures like the sigmoid colon and femur. Training strategies that simultaneously segment anatomically related structures, such as the left and right femurs, may further enhance generalizability and clinical applicability.

V. CONCLUSION

This study developed an Attention U-Net model for auto-segmentation of CTVn and seven OARs in prostate cancer radiotherapy. The model achieved high accuracy for structures like the bladder (DSC 0.921) and rectum (DSC 0.883) but faced challenges with the sigmoid colon (DSC 0.475) and femurs, highlighting difficulties in segmenting anatomically variable regions. This model shows significant potential to streamline radiotherapy planning, reduce manual workloads, and improve consistency for clinical adoption.

REFERENCES

[1] Hisamichi T, Takeda K, Kadoya N, Inoue K, Endo S, Takahashi N, et al. Development of deep learning-based novel auto-segmentation for the prostatic urethra on planning CT images for prostate cancer radiotherapy. Radiol Phys Technol. 2024. doi: 10.1007/s12194-024-00832-8

[2] Feng W, Chen Z, Wang X, Dou M, Yang J, Yao Y, et al. Deep learning-based clinical target volumes contouring for prostate cancer: Easy and efficient application. J Appl Clin Med Phys. 2024. doi: 10.1002/acm2.14482

[3] Chen Y, Butler S, Xing L, Han B, Bagshaw HP. Patient-specific auto-segmentation of target and OARs via deep learning on daily fan-beam CT for adaptive prostate radiotherapy. Int J Radiat Oncol Biol Phys. 2022;114(3):e553-e554. doi: 10.1016/j.ijrobp.2022.07.2186

[4] Pemmaraju R, Song DY, Lee J. Cascaded neural network segmentation pipeline for automated delineation of prostate and organs at risk in male pelvic CT. Proc SPIE Med Imaging. 2023;12464:124641D. doi: 10.1117/12.2653387

[5] Jeong S, Cheon W, Kim S, Kim N, Han Y. Deep-learning-based segmentation using individual patient data on prostate cancer radiation therapy. PLOS ONE. 2024;19(7):e0308181. doi: 10.1371/journal.pone.0308181

[6] Rahman MA, Singh S, Shanmugalingam K, Iyer S, Blair A, Ravindran P, et al. Attention and pooling-based sigmoid colon segmentation in 3D CT images. In: Proceedings of the 2023 International Conference on Digital Image Computing: Techniques and Applications (DICTA). Piscataway (NJ): IEEE; 2023. p. [312-319]

Contacts of the corresponding author:
Author: Todsaporn Fuangrod
Institute: Medical Physics Program, Princess Srisavangavadhana College of Medicine, Chulabhorn Royal Academy
Street: Kamphaeng Phet 6
City: Bangkok
Country: Thailand
Email: Todsaporn.fua@cra.ac.th

The effect of constructing CT images from multiple MR sequences in the treatment planning of a brain tumor

Pisut Duanghatai[1], Oonsiri Sornjarod[2], Auethavekiat Supatana[3,*]

1 Department of Biomedical Engineering, Faculty of Engineering, Chulalongkorn University, Bangkok, Thailand
2 Department of Radiology, King Chulalongkorn Memorial Hospital, Bangkok, Thailand
3 Department of Electrical Engineering, Faculty of Engineering, Chulalongkorn University, Bangkok, Thailand
*(*Corresponding author: Supatana.A@chula.ac.th)*

Abstract — **Introduction:** The information from CT and MR imaging are different. Thus, the translation of a MR image to a CT image is not perfect. In most studies, a CT image is constructed from a single MR sequence. However, brain tumor patients take three MR sequences: T1W, T2W and FLAIR. Multiple MR sequences contain more information and should lead to better construction of the CT image. The effect of using multiple MR sequences to generate CT brain image was investigated. **Methods:** In this study, the MR and CT images were manually registered. Pix2Pix was used to translate an MR image to a CT image. Three Pix2Pix networks were constructed and had different types of inputs: (1) T1W image only, (2) the combination of T1W and T2W images and (3) the combination of T1W, T2W and FLAIR images. Different MR sequences were combined by putting them into different color channels. Only the slices above the eyes were used. The training set consisted of 377, 371 and 372 slices for the translation from T1W image only, the combination of T1W and T2W images and the combination of T1W, T2W and FLAIR images, respectively. 20 slices from the patient not used in the training were used to evaluate the translation efficiency. **Results:** The construction of CT images from multiple MR sequences was better. The addition of T2W image improved the translation of overall brain, while the additional FLAIR sequence improves translation for ventricles. **Conclusion:** Compared to the translation from a single sequence, the translation from multiple MR sequences produced more detailed CT images. More data was necessary to evaluate whether multiple MR sequences led to better tumor translation.

Keywords — Image translation, MR to CT images translation, Multiple MR sequences

I. INTRODUCTION

Brain tumors are the 7th most common cancer treated at the Department of Radiology, King Chulalongkorn Memorial Hospital in 2022 [1]. They are also among the most common solid tumors in children. Treatment planning involves both computed tomography (CT) and magnetic resonance (MR) scans. However, CT scans pose a radiation risk, which is more significant in children. Younger children undergoing CT scans face a higher cancer-related mortality risk [2]. MR scans are considered safer as they do not involve radiation exposure. While MR imaging provides better contrast between brain tumors and normal tissue, it has lower resolution compared to CT scanning.

The translation of MR images to CT images is challenging due to the inherent differences in the information provided by each modality. While most studies construct CT images from a single MR sequence [3][4][5], brain tumor patients typically undergo three MR sequences: T1-weighted (T1W), T2-weighted (T2W), and fluid attenuated inversion recovery (FLAIR). Since multiple MR sequences provide more comprehensive information, this study explored the impact of using them to generate CT brain images.

One of the difficulty in utilizing AI is the need for a large training dataset. Combining different MR sequences enhances tissue contrast, which may offer an additional benefit of reducing the required size of the training dataset.

II. MATERIALS AND METHODS

The dataset used in this study was provided by King Chulalongkorn Memorial Hospital and consisted of 16 cases diagnosed with primary brain tumors. Two cases were used for testing, while the remaining cases were used for training. Only axial slices above the eyes were included in the analysis and all brain images were rescaled to approximately the same size (cropped for the area of a head and resized to 256×256 pixels).

Registration is necessary due to different coordinate references between CT and MR images. 3D Slicer (https://www.slicer.org/) was used for manual aligning MR and CT scans.

In this study, Pix2Pix [6] is used to translate MR to CT images. It is a conditional generative

adversarial network (cGAN) and requires two networks to perform image-to-image translation. The generator is responsible for translating the input image into a corresponding target (output) image. Meanwhile, the discriminator is the classifier that differentiates between the real and the generated images. The training process involves a competition between these two networks, where the generator (G) aims to produce more realistic outputs, and the discriminator (D) strives to distinguish between real and generated images. The objective function is as follows

$$G^* = \arg\min_G \max_D \mathcal{L}_{GAN}(G, D) + \lambda \mathcal{L}_{L1}(G),$$

where λ is a regularization parameter, $\mathcal{L}_{GAN}(G, D)$ and $\mathcal{L}_{L1}(G)$ are the loss functions of cGAN and L1 difference between the actual CT image and the generated CT image, respectively. They are defined as follows,

$$\mathcal{L}_{GAN}(G, D) = \mathbb{E}_y[\log D(y)] + \mathbb{E}_{x,z}[\log(1 - D(G(x, z))],$$

$$\mathcal{L}_1(G) = \mathbb{E}_{x,y,z}[\|y - G(x, z)\|_1],$$

where x, y and z are the input MR image, the target CT image and noise, respectively. D(y) is 1 if y is classified as the actual CT image; otherwise it is 0. In order to compute $\mathcal{L}_1(G)$, it is required that the MR and CT images are paired. This adversarial training framework enables the Pix2Pix model to generate high-quality image translations.

Three Pix2Pix networks were constructed and had different types of inputs: (1) T1W image only, (2) the combination of T1W and T2W images (T1W-T2W) and (3) the combination of T1W, T2W and FLAIR images (T1W-T2W-FLAIR). Different MR sequences were combined by putting them into different color channels. The training set consisted of 377, 371 and 372 slices for the translation from T1W image only, T1W-T2W images and T1W-T2W-FLAIR images, respectively. 20 slices from 2 patient not used in the training were used to evaluate the translation efficiency.

Different MR sequences are combined by utilizing the multi-channel structure of color images. Since MR images are grayscale, they occupy only one channel. However, color images have three channels (red, green, and blue), allowing multiple MR sequences to be combined into a single image. This approach preserves all the information from each MR sequence and enables better visualization, as different tissues can be represented in distinct colors, facilitating easier tissue differentiation.

For the T1W-T2W combination, the T1W image, being more similar to the CT image, was assigned to two channels (R and B), while the T2W image was put into the G channel. **For the T1W-T2W-FLAIR combination**, the T1W, T2W, and FLAIR images were put into the R, G, and B channels, respectively. The combination results are shown Fig.1

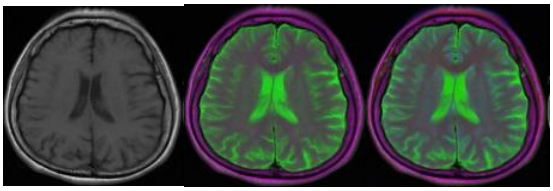

Figure 1. *Example of T1W [left], the T1W -T2W [center], and T1W-T2W-FLAIR images [right].*

The Dice Similarity Coefficient (DSC) is used to quantitatively evaluate the similarity between two images or regions, and is expressed by the equation [4]:

$$\mathrm{DSC}\,(A, B) = \frac{2 \times |A \cap B|}{|A| + |B|} \qquad (1)$$

where A and B are the regions of interest (ROI) in the actual and translated images, respectively. |A| represents the area of A.

III. RESULTS

The translation quality of Pix2Pix is greatly affected by parameter setting. In this study, λ and the learning rate were manually adjusted for the optimal translation of T1W to CT images. In all training, λ and the learning rate were set to 300 and 2×10^{-5}, respectively. The learning step was 120,000. The number of the training image pairs for the three translation were approximately the same (377, 371 and 372 pairs for the translation from T1W, T1W-T2W and T1W-T2W-FLAIR images, respectively.) 20 image pairs from 2 patients were used to evaluate the result.

Table 1. *Average DSC of the translated images.*

Types of inputs	DSC			
	Patient#1		Patient #2	
	Brain	Ventricle	Brain	Ventricle
T1W	0.922	0.525	0.918	0.630
T1W-T2W	0.940	0.637	0.940	0.610
T1-T2W-FLAIR	0.937	0.661	0.941	0.593

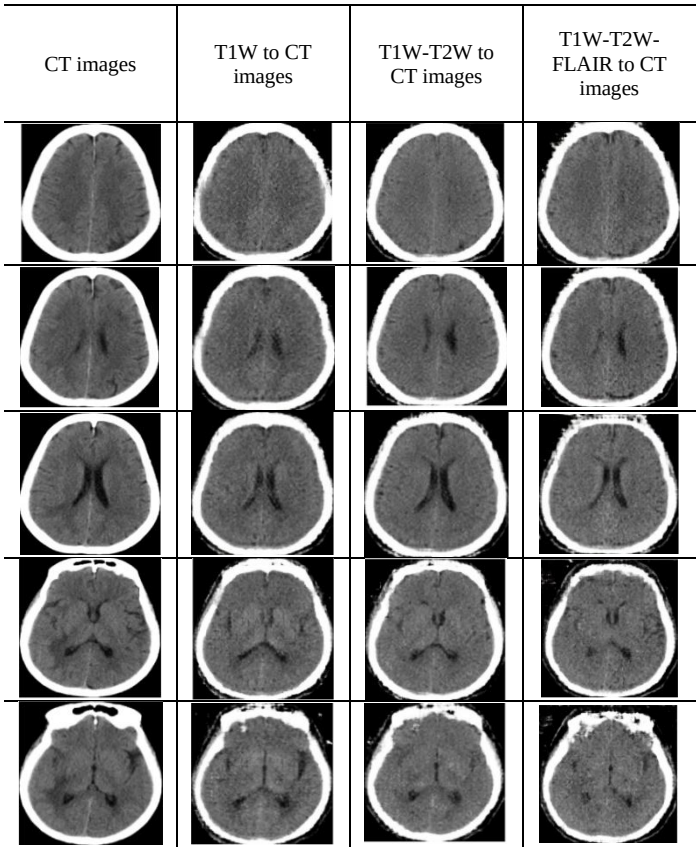

Figure 2. *Sample translation results of Patient#1. The actual CT images (1st column), translated CT images from T1W (2nd column), T1W-T2W (3rd column), T1W-T2W-FLAIR images (4th column).*

Figures 2 and 3 show the sample results. In this study, there were not enough slices to evaluate the tumor translation quality. Only the ventricle and brain excluding the ventricle were quantitatively investigated. Table 1 shows the DSC of 2 regions from the 2 test case.

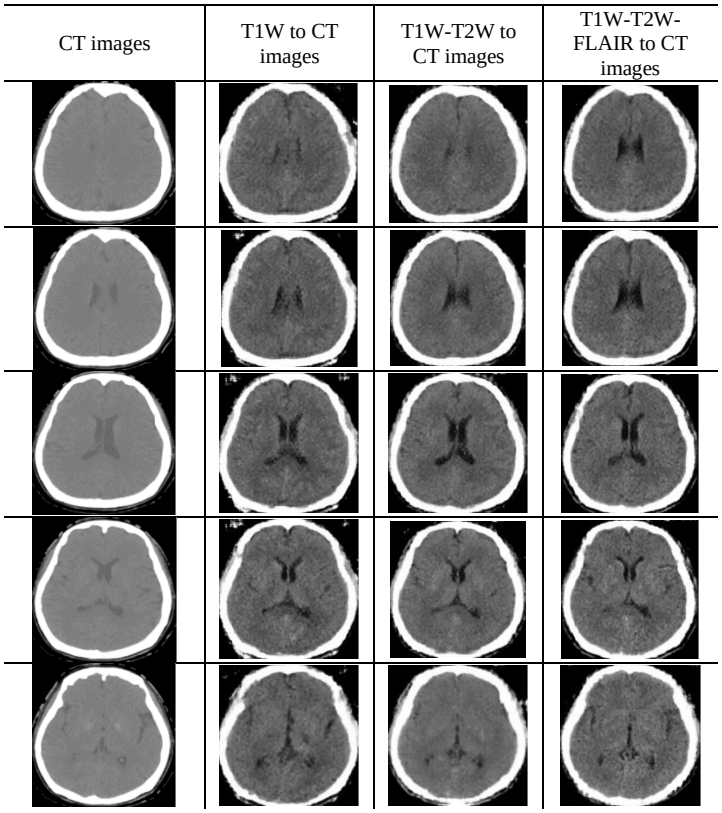

Figure 3. *Sample translation results of Patient#2. The actual CT images (1st column), translated CT images from T1W (2nd column), T1W-T2W (3rd column), T1W-T2W-FLAIR images (4th column).*

IV. DISCUSSION

The ventricle in the CT images of Patient #1 is much more pronounced. Thus, the ground truth area could be defined more accurately. That the ventricle translation was the most accurate for the translation from T1W-T2W-FLAIR images of Patient#1 (0.661) indicated that the inclusion of T2W and FLAIR images improved the translation quality. Note that when the ventricle was blurred (Patient #2), the DSC of the translated image from T1W only image was better than multiple MR inputs. This may be due to the inaccuracy in defining the blurred region.

The DSC values of the brain were high for all cases. It indicated good brain shape translation. It was found that the brain area was more accurate for the translation from multiple MR inputs in both patients. Inspecting the translated results in Figures 2 and 3, we found that the shape from multiple MR sequences was more accurate. The effect of FLAIR sequence was not found in the translation of the brain area.

Multiple MR sequence inputs provided slightly better results. It was likely due to the additional complementary information gained by combining multiple imaging modalities, which improved the model's ability to distinguish between different structures.

V. CONCLUSION

This pilot study indicated the better translation for multiple MR sequences. Though the information of FLAIR sequences was not required for the overall brain shape, it helped improve the translation of ventricle. The limitation of this study is that there were not enough slices with tumor to evaluate the tumor translation.

ACKNOWLEDGEMENTS

I would like to express my sincere gratitude to the Chulalongkorn University Graduate Scholarship on the Auspicious Occasion of Her Royal Highness Princess Maha Chakri Sirindhorn's 5th Cycle Birthday Anniversary for awarding me the tuition fee scholarship. This support has been invaluable in enabling me to pursue my education and successfully complete this research.

REFERENCES

[1] Chulalongkorn University, "Statistics of patients receiving services at the Radiology and Pathology Department," [Online]. Available: https://www.chulacancer.net/service-statistics-inner.php?id=809.

[2] National Research Council, Division on Earth and Life Studies, Board on Radiation Effects Research and Committee to Assess Health Risks from Exposure to Low Level of Ionizing Radiation, "Health risks from exposure to low levels of ionizing radiation: BEIR VII, Phase 2," National Academies Press, 2006. Chapter 12

[3] Kazemifar, S., et al., "MRI-only brain radiotherapy: Assessing the dosimetric accuracy of synthetic CT images generated using a deep learning approach". Radiother Oncol, 2019. 136: pp. 56-63. https://doi.org/10.1016/j.radonc.2019.03.026

[4] Gupta, D., et al., "Generation of Synthetic CT Images From MRI for Treatment Planning and Patient Positioning Using a 3-Channel U-Net Trained on Sagittal Images". Front Oncol, 2019. Vol. 9: 964, doi: 10.3389/fonc.2019.00964

[5] Spadea, M.F., et al., "Deep Convolution Neural Network (DCNN) Multiplane Approach to Synthetic CT Generation From MR images-Application in Brain Proton Therapy". International Journal Radiation Oncol Biol Phys,2019. Vol. 105, No. 3, pp. 495-503. https://doi.org/10.1016/j.ijrobp.2019.06.2535

[6] Isola, P., et al. "Image-to-Image Translation with Conditional Adversarial Networks". 2017 IEEE Conference on Computer Vision and Pattern Recognition (CVPR), Honolulu, HI, USA, 2017, pp. 5967-5976, doi: 10.1109/CVPR.2017.632

[7] Yeap, P.L., et al., "Predicting dice similarity coefficient of deformably registered contours using Siamese neural network". Physics in Medicine & Biology, 2023. 68(15): p. 155016. https://dx.doi.org/10.1088/1361-6560/ace6f0

Contacts of the corresponding author:
Author: Supatana Auethavekiat
Institute: Department of Electrical Engineering
Chulalongkorn University
Street: Phayathai
City: Bangkok
Country: Thailand
Email: Supatana.A@chula.ac.th

Machine learning model for predicting radiation-induced xerostomia from head and neck cancer radiotherapy

Chantarak Kiattiyot[1], Suntiwong Sawanee[2], Chamchod Sasikarn[1,2], Liamsuwan Thiansin[1,*]

[1]*Princess Srisavangavadhana College of Medicine, Chulabhorn Royal Academy, Bangkok, Thailand*
[2]*Radiation Oncology Department, Chulabhorn Hospital, Chulabhorn Royal Academy, Bangkok, Thailand*
*(*Corresponding author: thiansin.lia@cra.ac.th)*

Abstract — **Introduction:** This study aimed to develop a machine learning (ML) model for predicting radiation-induced xerostomia in head and neck cancer (HNC) patients treated with intensity modulated radiation therapy (IMRT) and volumetric modulated arc therapy (VMAT), using clinical, radiomic, and dosimetric features. **Methods:** 85 HNC patients underwent IMRT and VMAT were included. Radiomic features were extracted from the patients' computed tomography (CT) images, while dosimetric features were obtained from the dose-volume histograms (DVHs). A total of 121 features were initially considered. The endpoint of interest was grade ≥2 xerostomia at 6 months after treatment. The patients were randomly split into the training (n = 68) and test (n = 17) datasets. Machine learning (ML) models, including Random Forest (RF), Support Vector Machine (SVM), Naïve Bayes (NB), and Logistic Regression (LR) were investigated using Orange software. For these models, five-fold cross-validation was conducted with the training dataset. Feature selection on training set was achieved by ReliefF. Finally, the model performance was assessed with the test dataset using the area under precision-recall curve (AUC-PR). **Results:** ReliefF selected 2, 10, and 5 clinical, radiomics, and dosimetric features, respectively. Three models achieved the AUC-PRs above 0.60, namely RF and SVM with radiomic features (AUC-PR = 0.67 and 0.64, respectively) and RF with dosimetric features (AUC-PR = 0.60). **Conclusion:** Using only radiomics features, the ML models could predict grade ≥2 xerostomia nearly equally well as using dosimetric features, allowing for prediction of this toxicity before dose calculation in the treatment planning process.

Keywords — Radiation-induced xerostomia, head and neck cancer, radiomics, machine learning, predictive model

I. INTRODUCTION

Xerostomia is a prevalent side effect of radiotherapy (RT) for head and neck cancer (HNC), affecting 60% of patients receiving intensity modulated radiation therapy (IMRT) [1]. While advanced techniques for radiotherapy can minimize radiation exposure to healthy tissues and reduce the risk of xerostomia [2], the salivary glands often remain susceptible to radiation damage. This exposure may result in glandular injury and the onset of xerostomia [3]. In severe cases, xerostomia can lead to permanent salivary gland dysfunction and swallowing impairments, profoundly impacting patients' quality of life (QoL) [4].

The complexity of predicting normal tissue response is that the dose distributions to the surrounding normal tissues are inhomogeneous and more than one organ at risk are usually exposed to radiation. Typically, dose metrics are quantified using the maximum or mean dose value, or by the volume of a structure receiving a specified dose level (V_x) obtained from the dose-volume histogram (DVH). Therefore, the concept of normal tissue complication probability (NTCP) was developed to represent the probability that a specific dose distribution delivered to a defined tissue or structure will cause a measurable response in the patient. The Lyman-Kutcher-Burman (LKB) model is among the most well-known and frequently used models. It is an empirical model that describes dose response based on the volume of tissue exposed to radiation [5]. The LKB model uses only dosimetric parameters. To incorporate other relevant data, in particular clinical data, to the NTCP model, other functions such as a logistic regression (LR) can be used [6]. Lately, medical image data, including computed tomography (CT), magnetic resonance imaging (MRI), collected form treatment planning system (TPS), or even positron emission tomography (PET) images could be used as the input of a NTCP model in forms of radiomic features, which are quantitative features of medical images [7-8].

Machine learning algorithms have become widely adopted tools for decision support. With recent advances in image processing, informatics, and machine learning, medical

imaging is increasingly being utilized to enhance clinical decision-making [9] .

In this study, we developed a machine-learning based model to predict radiation-induced moderate-to-severe xerostomia (grade ≥2) features at 6 months after treatment using clinical factors, dosimetric parameters, and CT-based radiomic features.

II. MATERIALS AND METHODS

A. Patients and images

A retrospective analysis was conducted on HNC patients who underwent intensity modulated radiation therapy (IMRT) or volumetric modulated arc therapy (VMAT) at Chulabhorn Hospital during 2020-2022. The study was approved by the Human Research Ethics Committee, Chulabhorn Royal Academy (Project Code EC 035/2566). The inclusion criteria were 1. Completion of RT, 2. Curative aim, 3. No previous irradiation, and 4. Treated via IMRT or VMAT techniques. A total of 85 patients were included in this study and divided into a training set (68 patients) and a test set (17 patients), as shown in Table 1.

The patients' CT images were obtained using SOMATOM go.Open Pro system (Siemens Healthineers AG, Erlangen, Germany) scanner with a 3 mm slice thickness. Each CT image had a resolution of 512 × 512 pixels. Target volumes and organs at risk (OARs) were contoured by treating radiation oncologists following Radiation Therapy and Oncology Group (RTOG) guidelines. The treatment plans were created using Eclipse treatment planning system (TPS) version 13.6 with the Anisotropic Analytical Algorithm (AAA). The prescribed dose ranged from 60 to 70 Gy in 2.0 to 2.121 Gy per fractions, once daily and five days per week. The beam delivery was done using TrueBeam linear accelerators (Varian Medical Systems Inc., Palo Alto, California, USA) with 6 MV X-rays.

Patient saliva secretion performance, as documented during ward rounds, was graded in conjunction with xerostomia (XM) severity and classified according to the Radiation Therapy Oncology Group (RTOG). The grading system included three levels: mild-to-moderate xerostomia (grade≥1), moderate-to-severe (grade ≥2), and severe (grade ≥3).

CT images for the head and neck regions were extracted from the TPS. Clinical features were extracted from the Hospital Information System (HIS) of Chulabhorn Hospital, including the age, gender, subsite of the primary tumor, BMI, and chemotherapy. Dosimetric parameters were extracted from dose-volume histograms (DVHs), including, mean dose to ipsi- and contralateral of the parotid glands, ipsi- and contralateral of parotid volume, as well as minimum and maximum dose to the ipsi- and contralateral parotid glands.

Table 1. *Patient demographics and characteristics*

Characteristic	All data (n = 85)	Training data (n= 68)	Test data (n= 17)
Xerostomia			
grade ≥2	49	43	6
grade <2	36	25	11
Age (years)			
Range	25-86	30-86	25-83
Median	56	57	52
Gender			
Male	65	54	11
Female	20	14	6
Subsite			
Hypopharynx	6	5	1
Oropharynx	31	27	4
Nasopharynx	32	25	7
Larynx	4	3	1
Oral cavity	12	8	4
BMI (kg/m^2)			
Underweight (< 18.5)	16	13	3
Normal (18.5-24.9)	55	43	12
Overweight (≥ 25)	14	12	2
Chemotherapy			
Yes	72	57	15
No	13	11	2
Prescribed dose (Gy)			
60	5	4	1
66	7	5	2
70	73	59	14

B. Radiomics features extraction and model generation

The radiomics tool kit in AccuContour version 3.1 (Manteia Medical Technologies Co. Ltd., Xiamen, China) was used to extract a total of 107 radiomic features from the parotid glands. These features included 14 features related to shape, 18 features based on first-order statistics, and 75 texture features. The texture features were further divided into five subcategories: 24 features from the gray-level co-occurrence matrix (GLCM), 16 from the

gray-level run length matrix (GLRLM), 16 from the gray-level size zone matrix (GLSZM), 14 from the gray-level dependence matrix (GLDM), and five from the neighborhood gray-tone difference matrix (NGTDM).

The workflow diagram of this study is illustrated in Figure 1. All of 85 HNC patients were randomly split into the 80% for training (n = 68) and 20% for test (n = 17) datasets. Machine learning (ML) models, including Random Forest (RF), Support Vector Machine (SVM), Naïve Bayes (NB), and Logistic Regression (LR) were applied to create predictive models using Orange software version 3.38.0 (Laboratory of Bioinformatics, Faculty of Computer and Information Science, University of Ljubljana, Slovenia).

For these models, five-fold cross-validation was conducted with the training dataset. In total, 121 features were initially used, including 107 radiomic features, 6 clinical features, and 8 dosimetric features. Feature selection on the training set was achieved by ReliefF.

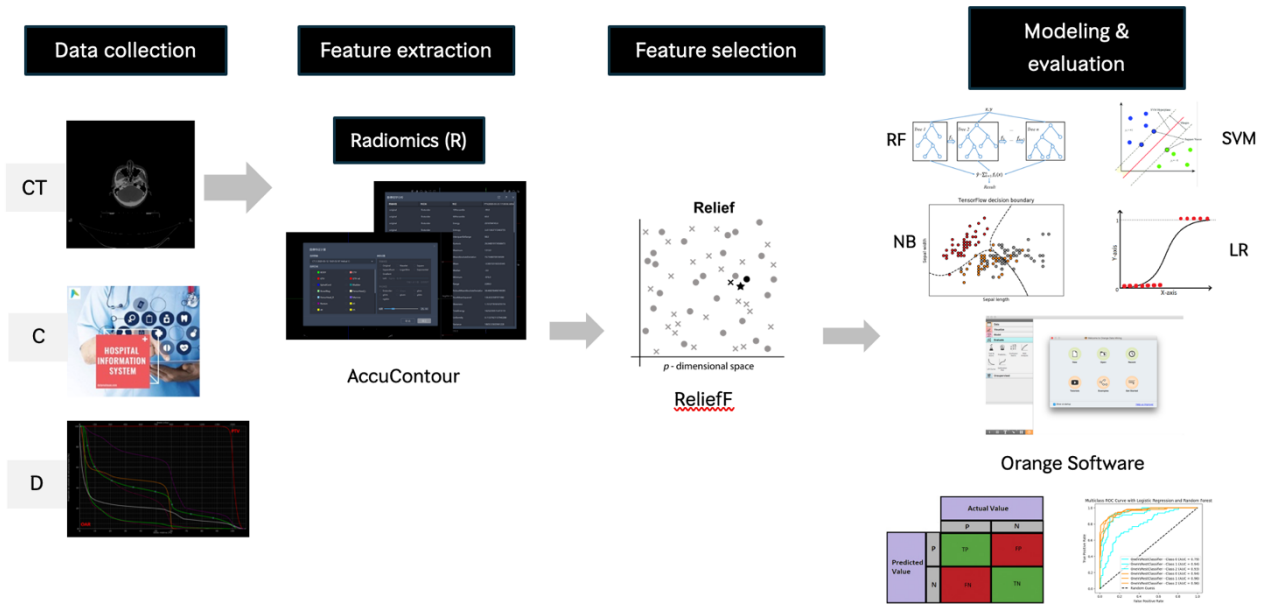

Figure 1. *The comprehensive workflow diagram of this study*

Table 2. *Predictive performance of the models*

Feature	RF					LR				
	AUCPR	AUROC	F1	Sen	Prec	AUCPR	AUROC	F1	Sen	Prec
Rad	0.67	0.78	0.64	0.65	0.68	0.64	0.55	0.37	0.53	0.28
Clin	0.55	0.69	0.50	0.56	0.54	0.53	0.64	0.50	0.56	0.53
Dos	0.60	0.73	0.51	0.60	0.77	0.53	0.57	0.61	0.67	0.64
Feature	**SVM**					**NB**				
	AUCPR	AUROC	F1	Sen	Prec	AUCPR	AUROC	F1	Sen	Prec
Rad	0.56	0.68	0.42	0.53	0.77	0.65	0.77	0.77	0.77	0.77
Clin	0.58	0.60	0.40	0.56	0.31	0.53	0.67	0.64	0.64	0.64
Dos	0.58	0.41	0.41	0.47	0.42	0.53	0.46	0.41	0.47	0.42

Abbreviations: Rad = Radiomics, Clin = Clinical, Dose = Dosimetric, RF = Random Forest, LR = Logistic Regression, SVM = Support Vector Machine, NB = Naïve Bayes, AUCPR = the area under the precision-recall curve, AUROC = the area under the receiver operating curve, Sen = Sensitivity, Prec = Precision.

C. Model Evaluation

Model evaluation was assessed by using confusion metric parameters, including the are under the precision-recall curve (AUCPR), the area under the receiver operating curve (AUROC), F1-score, sensitivity, and precision.

III. RESULTS

A. Predictive performance of radiomics, clinical, and dosimetric features

From this study, 12 models were developed. The evaluation metrics, including AUCPR, AUROC, F1-score, sensitivity, and precision for each model are shown in Table 2. Employing RF with only the radiomic features gave the best performance, with the AUCPR and AUROC of 0.67 and 0.78, respectively.

The LR model, which is one of the most commonly used NTCP model, provided the AUCPR of 0.64, 0.53, 0.53 using radiomics, clinical, and dosimetric features, respectively. From all ML models, using radiomic features produced the highest AUCPR.

IV. DISCUSSION

According to the result shown in Table 2, we found that for each feature type the RF model provided the highest AUCPR and AUROC. Similar result has been reported by Li et al. [10].

The difference of the AUC-PR in each input. From the conventional model of NTCP, LKB model [5], using only dosimetric parameter achieved an AUCPR of 0.60 in test set of RF model. After using the clinical feature and especially CT images, the model performance of radiomics feature provided the highest AUCPR of 0.67 and AUROC of 0.78 for RF model.

The use of only radiomics features based on patients' CT images was proved to be capable of predicting radiation-induced xerostomia.

V. CONCLUSION

Using only radiomics features, the ML models could acceptably predict moderate-to-severe (grade ≥ 2) xerostomia at 6 months post treatment, demonstrating the potential of radiomics-based approaches in assessing toxicity risk. This capability enables clinicians to anticipate and mitigate potential toxicities early in the treatment planning process, even before dose calculation.

ACKNOWLEDGEMENTS

I would like to express my sincere gratitude to my advisor, Thiansin Liamsuwan, for their invaluable guidance and support throughout this research. Special thanks to my family and friends for their unwavering support during this journey. Finally, I extend my appreciation to Development and Promotion of Science and Technology Talents Project (DPST) scholarship for their financial support, which made this study possible.

REFERENCES

[1] Baharudin, A et al. "Evaluation of irradiated salivary gland function in patients with head and neck tumours treated with radiotherapy." The Journal of laryngology and otology vol. 123,1 (2009): 108-13.

[2] Gupta, Tejpal et al. "Three-dimensional conformal radiotherapy (3D-CRT) versus intensity modulated radiation therapy (IMRT) in squamous cell carcinoma of the head and neck: a randomized controlled trial." Radiotherapy and oncology : journal of the European Society for Therapeutic Radiology and Oncology vol. 104,3 (2012): 343-8.

[3] Ortholan C, Benezery K, Bensadoun R-J, et al. Normal Tissue to tolerance to external beam radiation therapy: salivary gland. Cancer Radiother 2010; 14(4-5): 290-4.

[4] Jellema, A.P., et al., Impact of radiation-induced xerostomia on quality of life after primary radiotherapy among patients with head and neck cancer. International Journal of Radiation Oncology* Biology* Physics, 2007; 69(3): p. 751-760.

[5] Beetz, I., et al., Development of NTCP models for head and neck cancer patients treated with three-dimensional conformal radiotherapy for xerostomia and sticky saliva: the role of dosimetric and clinical factors. Radiotherapy and Oncology, 2012; 105(1): p. 86-93.

[6] Thomas B., et al. Predicting radiotherapy-induced xerostomia in head and neck cancer patients using day-to-day kinetics of radiomics features. Physics and Imaging in Radiation Oncology, 2022, 24: 95-101.

[7] Sheikh, K., et al., Predicting acute radiation induced xerostomia in head and neck Cancer using MR and CT Radiomics of parotid and submandibular glands. Radiation Oncology, 2019; 14(1): p. 1-11.

[8] Li Y, van Rijn-Dekker M.I, de Vette S.P.M, et al., Late-xerostomia prediction model based on 18F-FDG PET image biomarkers of the main salivary glands. Radiotherapy Oncology, 2024; 196:110319.

[9] Nardone, V., et al., Texture analysis as a predictor of radiation-induced xerostomia in head and neck patients undergoing IMRT. La radiologia medica, 2018. 123: p. 415-423.

[10] Li, M., Zhang, J., Zha, Y., et al.(2022). A prediction model for xerostomia in locoregionally advanced nasopharyngeal carcinoma patients receiving radical radiotherapy. BMC Oral Health, 22(1), 239.

Contacts of the corresponding author:
Author: Thiansin Liamsuwan
Institute: Princess Srisavangavadhana College of Medicine, Chulabhorn Royal Academy
Street: 906 Kampangpetch 6 Rd., Talat Bang Khen, Lak Si
City: Bangkok 10210
Country: Thailand
Email: thiansin.lia@cra.ac.th

Artificial intelligence-based dose prediction for optimizing treatment plans in locally advanced cervical cancer radiation therapy

Yooyen Nattawut[1], Thongsawad Sangutid[1,2], Chamchod Sasikarn[1,2], Kummanee Patiparn[2], Nimjaroen Kampheang[2], Intanin Panatda[2], Chaipanya Thitaporn[1,3], Khamfongkhruea Chirasak[1,2*]

1 Medical Physics Program, Princess Srisavangavadhana College of Medicine, Chulabhorn Royal Academy, Bangkok, Thailand.
2 Radiation Oncology Department, Chulabhorn Hospital, Chulabhorn Royal Academy, Bangkok, Thailand.
3 Division of Radiation Oncology, Lopburi Cancer Hospital, Lopburi, Thailand.
*(*Corresponding author: chirasak.kha@cra.ac.th)*

Abstract — **Introduction:** Intensity-modulated radiation therapy (IMRT) is essential for locally advanced cervical cancer, delivering precise tumor doses while sparing healthy organs. However, its complex planning relies heavily on the planner's experience, causing variability that impacts outcomes. Therefore, this study aims to develop an artificial intelligence (AI)-based dose prediction model to assist planners in achieving optimal treatment planning, thereby improving plan quality and reducing workload. **Methods:** This study utilized computed tomography (CT) images from 48 locally advanced cervical cancer patients treated with IMRT. A total of 535 radiomic features were extracted from the images and reduced to 54 significant features using the F-test algorithm. The dataset was divided into 80% training and 20% testing for machine learning in MATLAB. Five models—support vector machine (SVM), decision tree, Gaussian process regression, kernel, and ensemble—were trained to predict dose metrics, including maximum dose (D_{max}) and organ volumes receiving 50 Gy (V_{50}), 45 Gy (V_{45}) and 40 Gy (V_{40}). Model performance was evaluated using mean absolute error (MAE), accuracy, sensitivity, and specificity. **Results:** Among the models tested, the SVM model showed the best performance, achieving the lowest MAE values. For the bladder, MAE was 0.343(D_{max}), 9.48(V_{50}), and 7.76(V_{45}). For the rectum, it was 0.241(D_{max}) and 6.77(V_{40}). For the small bowel, MAE was 0.286(D_{max}) and 8.31(V_{40}). Binary classification accuracy ranged from 0.50 to 0.90, with specificity between 0.67 and 1.00, and sensitivity between 0.44 and 1.00. **Conclusion:** The AI-based dose prediction model is a promising tool that enhances IMRT planning by providing accurate dose predictions, reducing variability in treatment plans, and supporting precise and efficient decision-making. This approach improves the consistency and quality of radiotherapy planning, ultimately contributing to better treatment outcomes for patients with locally advanced cervical cancer.

Keywords — Dose prediction, Cervical cancer, Artificial intelligence, Intensity-modulated radiation therapy, Radiomics

I. INTRODUCTION

Cervical cancer is one of the most prevalent gynecologic malignancies and remains the fourth most common cancer globally (1). The International Federation of Gynecology and Obstetrics (FIGO) 2018 classification categorizes cervical cancer into early-stage, locally advanced, and metastatic (2). Treatment approaches are determined by the cancer stage and the patient's overall health. For locally advanced cervical cancer (LACC), the standard treatment is concurrent chemoradiotherapy (CCRT), which combines chemotherapy with external beam radiation therapy (EBRT), followed by brachytherapy (3). Advancements in EBRT techniques, such as the transition from three-dimensional conformal radiation therapy to intensity-modulated radiation therapy (IMRT) and volumetric-modulated arc therapy (VMAT), have improved patient survival rates and reduced treatment-related toxicity (3). IMRT is widely used in postoperative EBRT for cervical cancer, as it helps minimize radiation exposure to critical structures, including the rectum and bladder, compared to conventional methods. However, radiotherapy planning remains a complex and time-intensive process, involving multiple optimization iterations that can take hours or even days to complete.

Another significant challenge is the variability in plan quality caused by differences in how planners balance competing objectives. This variability can result in suboptimal plans and poorer clinical outcomes (1). To address these issues, accurate dose prediction is essential for improving treatment management.

In recent years, artificial intelligence (AI) has gained substantial attention in the field of medical physics. One promising application of AI is dose prediction, which can improve the consistency of treatment plan quality while significantly reducing the time and effort required by medical physicists (4). Knowledge-Based Planning (KBP), a widely used AI approach, utilizes geometric and anatomical features extracted from regions of interest (ROIs) in previously treated patients to automatically predict doses for new patients. While KBP offers many benefits, it has limitations in tailoring dose predictions for individual patients. This study aims to develop a machine learning-based dose prediction model for cervical cancer that goes beyond traditional KBP by integrating additional predictive features (1). The proposed AI-based model enhances IMRT planning by providing precise dose forecasts, reducing variability in treatment plans, and supporting more informed clinical decisions. Ultimately, this approach aims to improve outcomes for cervical cancer patients.

II. MATERIALS AND METHODS

A. Data selection and collection

This retrospective study includes 48 cases, focusing on patients with LACC treated with IMRT. All treatments were conducted at the Radiation Oncology Department of Chulabhorn Hospital between 2018 and 2024. The IMRT treatment plan was prescribed with a total dose of 50 Gy, delivered in 25 fractions at 2 Gy per fraction. CT scans were performed with a slice thickness of 3 mm using the Brilliance Big Bore system (Philips Healthcare, Best, Netherlands) and the Siemens SOMATOM go Open Pro system (Siemens Healthineers AG, Erlangen, Germany). The study methodology involves the analysis of a patient dataset comprising CT images, structure contours, doses, and dose-volume histograms (DVH) to achieve the research objectives.

B. Feature extraction and model generation

In the initial step of constructing a model to predict dose metrics, such as the maximum dose (D_{max}) and organ volumes receiving 50 Gy (V_{50}), 45 Gy (V_{45}), and 40 Gy (V_{40}) for OAR, including the bladder, rectum, and small bowel in cervical cancer patients, feature extraction was performed from CT images and structured contours. These data were obtained through radiomics analysis using AccuContour software version 3.1 (Manteia Medical Technologies, Wisconsin, MI), resulting in a total of 535 features. Subsequently, feature selection was conducted using the F-test algorithm in MATLAB software version 2024a (The Mathworks, Inc, Natick, MA), which significantly reduced the number of features to 54. The dataset was then divided into 80% for training and 20% for testing, with 5-fold cross-validation applied to minimize overfitting and improve model accuracy. Five machine learning models—support vector machine (SVM), decision tree (DT), Gaussian process regression (GPR), kernel methods (KM), and ensemble methods (EM)—were trained to predict the dose metrics.

C. Model evaluation

The performance of the model was assessed by comparing the predicted doses with the actual doses. This evaluation was conducted using the mean absolute error (MAE), calculated as outlined in Equation 1.

$$MAE = \frac{1}{n}\sum_{i=1}^{n}\left|Y_P^i - Y_c^i\right| \qquad (1)$$

Where n is the total number of pixels, Y_P^i is the i^{th} pixel value of the predicted dose, Y_c^i is the i^{th} pixel value of clinical dose.

Additionally, as outlined in Equations 2, 3, and 4, accuracy, sensitivity, and specificity were evaluated to ensure the reliability of the model in predicting doses. These metrics were analyzed to build confidence in the model's ability to enhance IMRT planning by providing accurate dose predictions for individual patients in clinical settings. The predicted doses were compared to the clinical guidelines established by RTOG and EMBRACE II.

$$Accuracy = \frac{TP+TN}{TP+TN+FP+FN} \qquad (2)$$

$$Sensitivity = \frac{TP}{TP+FN} \quad (3)$$

$$Specificity = \frac{TN}{TN+FP} \quad (4)$$

where TP is True Positive, FN is False Negative, FP is False Positive, and TN is True Negative

III. RESULTS

Figure 1 shows the MAE values for each dose prediction model. Among the models, SVM consistently achieved the lowest MAE values across most parameters, demonstrating superior accuracy in predicting doses for the bladder, rectum, and small bowel. In contrast, the EM model exhibited relatively higher MAE values, indicating lower reliability. These findings highlight the effectiveness of SVM as a dependable model for dose prediction in this study.

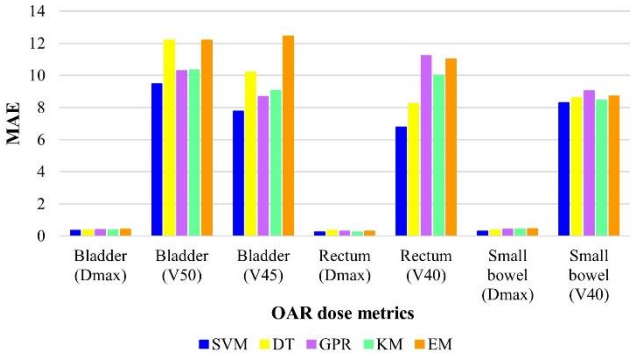

Figure 1. Comparison of MAE for prediction models and OAR dose metrics.

Table 2 compares the predicted dose metrics from the SVM model with the ground truth values, including the mean, standard deviation, and percentage differences for D_{max}, V_{50}, V_{45}, and V_{40} across OARs in 10 tested patients. The percentage differences ranged from 0.00% to 32.42%. The SVM model demonstrated reasonable accuracy, with strong agreement observed in rectum D_{max} (0.00%), small bowel D_{max} (0.06%), and small bowel V_{40} (1.45%). However, more significant deviations were identified in bladder D_{max} (32.42%) and bladder V_{45} (9.10%), indicating areas where improvements are needed. Overall, the results suggest that while the SVM model performs well for certain parameters, further refinement is required to enhance its prediction accuracy for volumetric metrics.

Table 3 presents the performance evaluation of the classification algorithms, focusing on accuracy, precision, and specificity. The accuracy ranged from 0.50 to 0.90, specificity varied between 0.67 and 1.00, and sensitivity was observed between 0.44 and 1.00.

Table 2 *Comparative analysis of predicted and ground truth results: mean, standard deviation, and percentage difference for the SVM Model.*

Parameter (Gy)	Predicted	Ground truth	%Diff (%)
Bladder (D_{max})	35.43 ± 19.59	52.43 ± 0.393	32.42
Bladder (V_{50})	40.28 ± 6.03	42.87 ± 15.98	6.04
Bladder (V_{45})	54.65 ± 6.06	60.13 ± 12.75	9.10
ectum (D_{max})	52.75 ± 0.406	52.75 ± 0.211	0.00
Rectum (V_{40})	82.50 ± 7.11	81.81 ± 11.57	0.84
Small bowel (D_{max})	53.06 ± 0.06	53.09 ± 0.39	0.06
Small bowel (V_{40})	26.57 ± 2.63	26.96 ± 12.92	1.45

Table 3 *Reliability assessment of the SVM model for each OAR, based on clinical guidelines.*

Parameter	Accuracy	Sensitivity	Specificity
Bladder (D_{max})	0.900	0.889	1.00
Bladder (V_{50})	0.700	1.00	0.625
Bladder (V_{45})	0.700	0.667	1.00
Rectum (D_{max})	0.800	0.500	0.875
Rectum (V_{40})	0.500	1.00	0.444
Small bowel (D_{max})	0.900	1.00	0.889
Small bowel (V_{40})	0.700	0.667	1.00

IV. DISCUSSION

This study developed and evaluated an AI-based model for predicting radiation dose to assist in treatment planning for patients with LACC. By utilizing radiomic features derived from CT images and structured contours, the model showed promise in enhancing the accuracy of dose predictions while reducing variability in IMRT plans. Among the five machine learning models tested, the SVM consistently achieved the lowest MAE, making it the most reliable for predicting key dose metrics, such as D_{max} and V_{40}, for organs

at OARs like the bladder, rectum, and small bowel. These findings demonstrate that AI can address critical challenges in radiotherapy planning, including time-consuming processes and variations among planners. This contribution could lead to improved plan quality and better clinical outcomes for patients.

The SVM model demonstrated lower MAE for most parameters. However, bladder Dmax showed a significantly higher deviation of 32.42% compared to small bowel D_{max} (0.06%) and rectum V_{40} (0.84%). These results highlight the need for further improvement, particularly in predicting bladder-related metrics. The challenges in these predictions may arise from the anatomical complexity of the bladder and variability in contouring practices.

This study utilized radiomics features to improve prediction accuracy compared to traditional KBP, which relies on geometric features. The SVM model outperformed other methods, including decision trees, Gaussian process regression, kernel methods, and ensemble methods. Similarly, Zhu et al. (4) reported that integrating radiomics into machine learning models enhanced dose prediction accuracy for cervical cancer, although challenges with bladder dose metrics persisted.

Deep learning approaches, such as those by Wang et al. (5), achieved high accuracy in predicting bladder and rectum doses using convolutional neural networks (CNNs). However, these studies also noted difficulties in generalizing the models across datasets. While SVM offers computational efficiency compared to CNNs, it may benefit from incorporating deep learning components to improve volumetric predictions. Additionally, Feng et al. (6) highlighted the limitations of KBP-based dose prediction for cervical cancer, further emphasizing the advantages of integrating diverse features, particularly for metrics like rectum D_{max} and small bowel dose.

This study has several limitations, including a small dataset of 48 patients, which may impact the generalizability of the findings and a significant deviation observed in bladder D_{max} predictions. Future research should address these issues by utilizing larger datasets, incorporating additional clinical data, and exploring advanced deep-learning architectures to improve model performance. Ongoing work in this area focuses on predicting accumulated doses of EBRT and brachytherapy for cervical cancer using deep learning techniques. By integrating data from multiple treatment modalities, this research aims to enhance EBRT planning and improve the sparing of OAR through cumulative dose modeling. This approach has the potential to provide a more comprehensive framework for optimizing radiotherapy treatments.

V. CONCLUSION

This study develops an AI-based dose prediction model to help planners achieve optimal IMRT treatment planning. The model accurately predicts doses for OARs, reducing variability and improving clinical decision-making. Incorporating radiomics features enhances consistency and addresses challenges in volumetric dose predictions. This approach aims to advance personalized treatment strategies and improve outcomes for patients with locally advanced cervical cancer.

ACKNOWLEDGEMENTS

The author expresses sincere gratitude to all advisors, clinical staff, and friends for their invaluable guidance and support throughout this study. Their insights, advice, and assistance were instrumental in successfully completing this research.

REFERENCES

[1] Yu W, Xiao C, Xu J, Jin J, Jin X, Shen L. Direct Dose Prediction with Deep Learning for Postoperative Cervical Cancer Underwent Volumetric Modulated Arc Therapy. Technology in Cancer Research & Treatment. 2023 Jan 1; 22:153303382311670- 153303382311670.

[2] Pang SS, Murphy M, Markham MJ. Current Management of Locally Advanced and Metastatic Cervical Cancer in the United States. JCO Oncology Practice. 2022 Mar 14.

[3] Gennigens C, De Cuypere M, Hermesse J, Kridelka F, Jerusalem G. Optimal treatment in locally advanced cervical cancer. Expert Review of Anticancer Therapy. 2021 Mar 11;21(6):657–71.

[4] Zhu X, et al. Machine learning-based dose prediction for cervical cancer IMRT: Improving accuracy with radiomics features. Radiother Oncol. 2020;149:123-130.

[5] Wang J, et al. Deep learning-based dose prediction for cervical cancer radiotherapy: A CNN approach. J Appl Clin Med Phys. 2021;22(3):45-53.

[6] Feng C, et al. Knowledge-based planning in cervical cancer radiotherapy: Challenges in volumetric dose prediction. Med Phys. 2019;46(5):2108-2116.

Contacts of the corresponding author:
Author: Chirasak Khamfongkhruea
Institute: Medical Physics Program, Princess Srisavangavadhana College of Medicine, Chulabhorn Royal Academy
Street: Kamphaeng Phet 6
City: Bangkok
Country: Thailand
Email: chirasak.kha@cra.ac.th

Dose prediction for cervical cancer brachytherapy using deep learning

Rinjan Nawarat[1], Khamfongkrue Chirasak[1, 2], Chanpanya Thananya[2], Kummanee Patiparn[1], Tannanonta Chirapha[2], Tharavichitkul Ekkasit[3], Thongsawad Sangutid[1, 2*]

1 Medical Physics Program, Princess Srisavangavadhana College of Medicine, Chulabhorn Royal Academy, Bangkok, Thailand
2 Radiation Oncology Department, Chulabhorn Hospital, Chulabhorn Royal Academy, Thailand
3 The Division of Radiation Oncology, Department of Radiology, Faculty of Medicine, Chiang Mai University
*(*Corresponding author: sangutid.tho@cra.ac.th)*

Abstract — **Introduction:** Dose distribution in brachytherapy planning is influenced by the dwell time of radioactive sources and the positioning of targets and organs at risk (OARs). Manual optimization is effective but time-consuming and varies with planner expertise. This study aims to develop a deep learning model to predict dose distribution, enhancing efficiency and standardization in treatment planning. **Methods:** Data from 54 cervical cancer patients treated with hybrid brachytherapy using three applicator types—tandem ovoids, tandem rings, and tandem cylinders —were collected for this study. The dataset was divided into training (80%), validation (10%), and testing (10%) subsets. A Cascade 3D U-Net model was implemented for dose prediction. **Results:** The model demonstrated effective dose prediction, with overall mean absolute error (MAE) across all organs was 0.334 ± 0.065 Gy, 0.321 ± 0.073 Gy, and 0.330 ± 0.078 Gy for tandem ovoids, tandem rings, and tandem cylindrical applicators, respectively. **Conclusion:** The dose prediction demonstrates strong agreement with ground truth plans. Despite the small sample size, the results for dose distribution prediction are promising. In future studies, the model will incorporate a larger sample size to enhance accuracy, with the goal of assisting planners in optimizing brachytherapy treatments.
Keywords — deep learning, dose prediction, hybrid brachytherapy, cervical cancer

I. INTRODUCTION

Cervical cancer is a significant global health challenge, ranking as the fourth most commonly diagnosed cancer among women. According to the World Health Organization (WHO), over 662,000 new cases and 350,000 deaths were reported in 2024, with most fatalities occurring in low- and middle-income countries. High-dose-rate brachytherapy (HDR) is a critical component in the treatment of cervical cancer, particularly for advanced stages [1]. This modality allows precise radiation delivery to the target while minimizing exposure to adjacent critical organs, such as the bladder, rectum, sigmoid colon, and small bowel. Despite its effectiveness, HDR brachytherapy planning is complex and requires considerable expertise, especially for large or irregularly shaped tumors, necessitating hybrid brachytherapy—a combination of intracavitary and interstitial techniques.

Traditional dose planning methods often rely on manual adjustment of dwell times, which is a time-consuming process and heavily dependent on the expertise of the planner [2]. These limitations underscore the necessity of developing automated and accurate methods for predicting dose distributions tailored to individual patients. Artificial intelligence (AI), particularly deep learning, has demonstrated significant potential in transforming this process by utilizing large datasets to rapidly and accurately predict optimal dose distributions.

Recent studies [3] have shown that deep learning models, such as Convolutional Neural Networks (CNNs) and U-Net architectures, are effective tools for automating dose predictions, both in External Beam Radiation Therapy (EBRT) and brachytherapy. However, hybrid brachytherapy presents unique challenges, particularly in capturing the intricate interactions between applicator geometry and patient anatomy. These complexities necessitate specialized models that can account for these factors to achieve clinically acceptable results.

This study focuses on developing an enhanced Cascade 3D U-Net model with a residual module for predicting dose distributions in cervical cancer patients undergoing hybrid brachytherapy. The research framework consists of four main steps: data collection and preparation, model generation, model training and validation, and model evaluation.

II. MATERIALS AND METHODS

A. Data collection

A retrospective dataset was gathered from cervical cancer patients treated with hybrid brachytherapy at the Radiation Oncology Department, Chulabhorn Hospital, between 2012 and 2024. The dataset included 54 patient datasets, categorized by applicator type: 15 with tandem and ovoid applicators, 22 with tandem and ring applicators, and 17 with tandem and cylinder applicators. Treatment plans were generated using the Eclipse treatment planning system (Varian Medical Systems, Palo Alto, CA). All CT images were acquired using Siemens SOMATOM go.Open Pro (Siemens Healthineers, Erlangen, Germany) and Philips Big Bore (Philips Healthcare, Best, The Netherlands) scanners. The structure sets include contours of the high-risk clinical target volumes (HRCTV), bladder, rectum, sigmoid colon, and small bowel. The dose distributions were derived from treatment plans with a prescribed dose of 7 Gy per fraction. All datasets were stored in DICOM format: RT images, RT structure sets, and RT dose files.

B. Data Preparation

The data preparation process was conducted to standardize input data and enhance the quality of model training. CT images were retained in their original dimensions of 512 × 512 × depth to preserve the full resolution of the scans. The Hounsfield Unit (HU) values were first adjusted to lie within the range of -1000 to 1000, representing the typical range for CT scans of the body. Pixel values were then normalized to a range of 0 to 1 to ensure consistency across the dataset, and zero padding was applied to standardize the number of slices across patients. For the structure sets, binary masks were generated for the HRCTV, bladder, rectum, sigmoid, and small bowel using the DicomRTTool library in Python (Python Software Foundation, USA). The contours of each structure were assigned a value of 1, while the background was assigned a value of 0. Regarding the dose distributions, dose values were normalized to a range of 0 to 1 while retaining the original values for future recalculations. The normalized dose distributions were aligned to match the dimensions of the corresponding CT images. Finally, the prepared datasets were split into training (80%), validation (10%), and testing (10%) subsets to ensure effective model evaluation.

C. Model architecture

Figure 1 shows the architecture of residual blocks and the cascade 3D U-Net used in this study. The proposed model is a Cascade 3D U-Net architecture optimized for brachytherapy dose prediction. The model comprises two sequential 3D U-Net networks. The first U-Net extracts anatomical features from CT images and structure sets. The second U-Net refines dose prediction outputs using the features extracted by the first network. Each U-Net uses residual blocks to prevent vanishing gradient issues, ensuring robust training. Convolutional layers in the encoder and decoder paths capture multi-scale spatial features, while skip connections preserve fine spatial details.

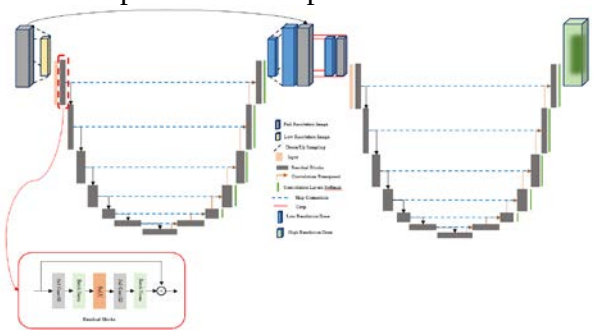

Figure 1. *The architecture of residual blocks and the cascade 3D U-Net used in this research*

D. Model training and validation

Model training was conducted using PyTorch for 200 epochs with a batch size of 4. Learning rates (1e-3, 1e-4, and 1e-5) were evaluated, and the optimal rate was selected based on validation performance. Five-fold cross-validation was used to minimize the overfitting. Smooth L1Loss was used to balance sensitivity to small and large errors.

In this study, the dataset was divided based on the type of applicator used in the brachytherapy procedure. Specifically, the applicators were classified into three types: tandem and ovoid, tandem and ring, and tandem and cylinder. Three separate models were trained to optimize model performance for each applicator type. Each model was trained on data corresponding to one specific applicator type, allowing the model to focus on learning the dose distribution characteristics and unique anatomical features. This approach ensured that

each model was specialized for the applicator it was trained on, improving accuracy and performance for each type.

E. Model evaluation

To ensure that the predicted dose distributions were aligned with clinical requirements, a post-processing step was carried out. The normalized dose values were converted back to absolute values based on the prescribed dose (e.g., 7 Gy per fraction) to represent the treatment dose accurately.

The model's performance was assessed on the test dataset, which comprised 20% of the total data and was entirely distinct from the training dataset. The evaluation was conducted using Mean Absolute Error (MAE), which quantifies the average difference between the predicted and clinical doses.

$$\mathrm{MAE} = \frac{1}{n}\sum_{i=1}^{n}\left|D^{i}_{\mathrm{prediction}} - D^{i}_{\mathrm{ground\ truth}}\right| \quad (1)$$

Where n represents the total number of pixels, $D^{i}_{\mathrm{prediction}}$ and $D^{i}_{\mathrm{ground\ truth}}$ represents the i^{th} pixel value of the prediction and ground truth dose.

III. RESULTS

The proposed models' performance was evaluated using MAE, which was calculated as the voxel-wise absolute difference between the predicted dose and the ground truth. The evaluation was done without incorporating the predictions into a treatment planning system (TPS), reflecting the models' direct predictive accuracy. The study used a hybrid approach combining intracavitary and interstitial brachytherapy applicators for comprehensive dose coverage and anatomical variation management. Table 1 shows the evaluation results for three models. Model 1, using a tandem-ovoid applicator with interstitial needles, achieved MAE values of 0.310 ± 0.066 Gy for HRCTV, 0.334 ± 0.043 Gy for the bladder, 0.335 ± 0.058 Gy for the rectum, 0.348 ± 0.086 Gy for the small bowel, and 0.342 ± 0.089 Gy for the sigmoid colon. Model 2, with tandem-ring applicators and interstitial needles, had the lowest errors: 0.282 ± 0.078 Gy for HRCTV, 0.317 ± 0.083 Gy for the bladder, 0.339 ± 0.031 Gy for the rectum, 0.336 ± 0.061 Gy for the small bowel, and 0.330 ± 0.070 Gy for the sigmoid colon. Model 3, using tandem-cylinder applicators and interstitial needles, showed slightly higher errors: 0.329 ± 0.058 Gy for HRCTV, 0.323 ± 0.065 Gy for the bladder, 0.336 ± 0.081 Gy for the rectum, 0.330 ± 0.048 Gy for the small bowel, and 0.332 ± 0.093 Gy for the sigmoid colon. Figure 2 compares the predicted dose distributions with the ground truth, highlighting the models' accuracy in capturing dose distribution. These results demonstrate the effectiveness of voxel-based dose prediction in hybrid brachytherapy cases. The MAE values represent baseline predictive accuracy; no TPS adjustments were made. Future work will focus on integrating these predictions into clinical workflows to improve high-dose-rate brachytherapy treatment planning.

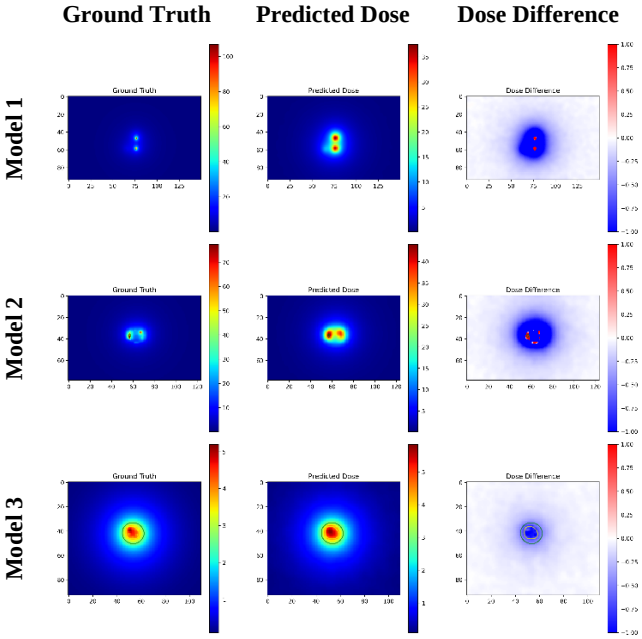

Figure 2. *Comparison of ground truth dose and predicted dose distributions.*

Table 1. *The results of evaluation metrics for three models (mean ± standard deviation).*

		MAE (Gy)
Model 1	HRCTV	0.310 ± 0.066
	Bladder	0.334 ± 0.043
	Rectum	0.335 ± 0.058
	Small bowel	0.348 ± 0.086
	Sigmoid colon	0.342 ± 0.089
Model 2	HRCTV	0.282 ± 0.078
	Bladder	0.317 ± 0.083
	Rectum	0.339 ± 0.031
	Small bowel	0.336 ± 0.061
	Sigmoid colon	0.330 ± 0.070

Model 3	HRCTV	0.329 ± 0.058
	Bladder	0.323 ± 0.065
	Rectum	0.336 ± 0.081
	Small bowel	0.330 ± 0.048
	Sigmoid colon	0.332 ± 0.093

IV. DISCUSSION

The results of this study demonstrate the effectiveness of the dose prediction model for hybrid brachytherapy treatments. The evaluation results indicate that the developed model can accurately predict dose distributions, with MAE values ranging from approximately 0.3 to 0.4 Gy across various anatomical structures, such as HRCTV, bladder, rectum, small bowel, and sigmoid colon. From the comparison image (Figure 2), the model performs well in capturing the dose distribution across anatomical structures. However, discrepancies are noticeable in regions near the applicator, where rapid dose changes occur. These differences may be due to the model's difficulty handling areas with steep dose gradients. Future work should focus on improving accuracy in these regions and expanding the dataset to include more diverse anatomical characteristics. Integrating the model into clinical workflows and refining it over time will enhance its reliability and efficiency in radiation treatment planning. Additionally, the model's ability to handle complex anatomical variations will be crucial for improving its generalizability across different patient populations. The model can be refined by incorporating continuous feedback from clinical applications to achieve greater precision in predicting dose distributions and improving treatment planning.

V. CONCLUSION

In conclusion, this study developed a dose prediction model for hybrid brachytherapy, achieving MAE values of 0.3 to 0.4 Gy across various anatomical structures. While the model performed well overall, discrepancies were observed in high-dose regions near the applicator. Future work will focus on expanding the dataset, refining the model to handle rapid dose variations, and integrating it into clinical workflows to improve the accuracy and efficiency of radiation dose delivery.

ACKNOWLEDGEMENTS

I sincerely thank my advisor, colleagues, and everyone who supported this research. Special thanks to Chulabhorn Hospital for providing the data, which greatly contributed to this work.

REFERENCES

[1] Sung H, Ferlay J, Siegel RL, Laversanne M, Soerjomataram I, Jemal A, et al. Global cancer statistics 2020: GLOBOCAN estimates of incidence and mortality worldwide for 36 cancers in 185 countries. CA Cancer J Clin. 2021; 71(3):209-249.

[2] Kirisits C, Rivard MJ, Baltas D, Ballester F, De Brabandere M, van der Laarse R, et al. Review of clinical brachytherapy uncertainties: Analysis guidelines of GEC-ESTRO and the AAPM. Radiother Oncol. 2014;110(1):199-212.

[3] Yu J, Smith R, Zhang W, et al. Deep learning-based models for predicting radiation dose distributions in high-dose rate brachytherapy. Front Oncol. 2023; 13:1285555.

[4] Cortes M, Nguyen D, Andersen M, et al. Three-dimensional convolutional neural networks for predicting radiation dose distributions in T&O brachytherapy. Phys Med Biol. 2022; 68(2):025005.

[5] Li Z, Yang Z, Lu J, Zhu Q, Wang Y, Zhao M, Li Z, Fu J. Deep learning-based dose map prediction for high-dose-rate brachytherapy. Phys Med Biol. 2023;68(17):175001.

Contacts of the corresponding author:
Author: Sangutid Thongsawad
Institute: Medical Physics Program, Princess Srisavangavadhana College of Medicine, Chulabhorn Royal Academy
Street: Kamphaeng Phet 6 Rd.
City: Bangkok
Country: Thailand
Email: sangutid.tho@cra.ac.th

Auto-segmentation for cervical cancer brachytherapy using deep learning

Wattanagul Nuttapol[1], Khamfongkruea Chirasak[1,2] , Kummanee Patiparn[1], Mundee Thunpisit[2], Tannanonta Chirapha[2], Tharavichitkul Ekkasit[3], Thongsawad Sangutid[1,2*]

[1]*Princess Srisavangavadhana College of Medicine, Chulabhorn Royal Academy, Bangkok, Thailand*
[2]*Radiation Oncology Department, Chulabhorn Hospital, Chulabhorn Royal Academy, Bangkok, Thailand*
[3]*Department of Radiology, Faculty of Medicine, Chiang Mai University, Chiang Mai, Thailand*
*(*Corresponding author: sangutid.tho@cra.ac.th)*

Abstract — **Introduction:** Manually delineating clinical target volumes (CTVs) and organs at risk (OARs) in cervical cancer brachytherapy treatment planning is a time-intensive and laborious process. Deep learning (DL) provides a promising solution to automate and accelerate this critical task. This study aims to develop and evaluate a deep learning-based model to automatically segment CTVs and OARs in cervical cancer patients from computed tomography (CT) images, thereby enhancing the efficiency of treatment planning and potentially improving clinical outcomes. **Methods:** A U-Net 3+ model with a ResNet-50 backbone was implemented on two datasets. The OARs dataset consisted of 115 cases, while the CTVs dataset was augmented to 115 cases. Segmentation performance was assessed using Dice Similarity Coefficient (DSC), 95th percentile Hausdorff distance (HD_{95}), and average surface distance (ASD). **Results:** The model achieved high accuracy for the bladder (DSC_{avg} = 0.904 ± 0.16) and rectum (DSC_{avg} = 0.868 ± 0.10), with moderate performance for HR-CTV (DSC_{avg} = 0.780 ± 0.17) and IR-CTV (DSC_{avg} = 0.787 ± 0.19). Accuracy was lower for the sigmoid colon (DSC_{avg} = 0.422 ± 0.34) and bowel (DSC_{avg} = 0.638 ± 0.23). **Conclusion:** The model demonstrates potential for auto-segmentation in cervical cancer brachytherapy, though further improvements for complex structures with poor visibility.

Keywords — Deep learning, auto-segmentation, cervical cancer, brachytherapy, U-Net 3+ with a ResNet 50 backbone

I. INTRODUCTION

Cervical cancer is a significant health concern and ranks as the third most common cancer among Thai women[1]. Combining brachytherapy (BT) and external beam radiation therapy (EBRT) is a key treatment modality with demonstrated efficiency in achieving high survival outcomes[2]. A critical step in BT is the manual delineation of CTVs and OARs on CT images, which is a time-intensive and laborious process.

Recently, deep learning (DL), a branch of artificial intelligence, especially convolutional neural networks (CNNs), has shown significant potential in automating medical image segmentation[3], offering a solution to streamline this labor-intensive process. The U-Net model, a widely used CNN architecture[4], has demonstrated robust performance in medical image segmentation due to its long skip connections of encoder-decoder that preserve spatial information during feature extraction, enhancing segmentation accuracy[5]. The U-Net 3+ model, first introduced by Huang et al.[6], extends the U-Net framework by incorporating dense skip connections to enable full-scale feature aggregation and improve segmentation accuracy in complex medical imaging tasks. Although the U-Net 3+ model has demonstrated advancements in medical image segmentation, no study has yet been implemented for segmenting the CTVs and OARs in CT-based brachytherapy for cervical cancer. To address this gap, this study develops a CNN-based model implementing the U-Net 3+ architecture for accurate and efficient segmentation of CTVs and OARs in cervical cancer CT-based brachytherapy.

II. MATERIALS AND METHODS

Dataset

The dataset in this study comprised 115 cervical cancer patients who received their first fraction of CT-based brachytherapy at Chulabhorn Hospital, Thailand, between January 2012 and October 2024. CT images were acquired using the Philips Big Bore scanner (Philips Healthcare, Netherlands) and

the SOMATOM go.Open Pro scanner (Siemens HealthCare, USA), both operating at 120 kilovoltage peak (kVp) with vendor-specific tube current (mAs) settings. Radiation oncologists delineated clinical target volumes (CTVs) and organs at risk (OARs) on each CT slice for treatment planning. The dataset included 115 cases for OARs segmentation (bladder, rectum, sigmoid colon, and bowel) and 57 cases for CTVs segmentation, including the high-risk CTV (HR-CTV) and intermediate-risk CTV (IR-CTV). Cases with contoured ovoid and ring regions in HR-CTV were excluded. Augmentation was applied to the CTVs dataset, increasing the number of cases to 115. The dataset was then divided into two portions: 80% for training and validation and 20% for independent testing, ensuring no augmented cases were included in the testing set.

Preprocessing

CT images and their corresponding radiation therapy (RT) structure sets, obtained in Digital Imaging and Communications in Medicine (DICOM) format from the Eclipse treatment planning system (Varian Medical Systems, California, USA), were processed for training and testing. The DICOMRTtool library in Python 3.9 (Python, Amsterdam, Netherlands) was used to convert the RT structures into binary masks. Both the CT images and masks were cropped to center around the gluteus maximus muscle, resized to 512×512 pixels. The pixel values of the CT images were clipped to the range of -150 to 250 (rectum: -250 to 250) to remove extreme outliers. Noise reduction was applied using 'denoise_tv_chambolle' (scikit-images), followed by normalization to a 0-1 range and linear scaling to 0-255. The processed CT images and masks were saved in Portable Network Graphics (PNG) format.

Model architecture

The model architecture is the U-Net 3+ model with a ResNet-50 backbone, as shown in Fig 1. The U-Net 3+ model improves segmentation by using multiple short skip connections. The pre-trained ResNet-50 backbone serves as the encoder, extracting spatial and semantic features from the input CT images. By leveraging pre-learned features from ImageNet, the model captures complex patterns and enhances localization and segmentation accuracy.

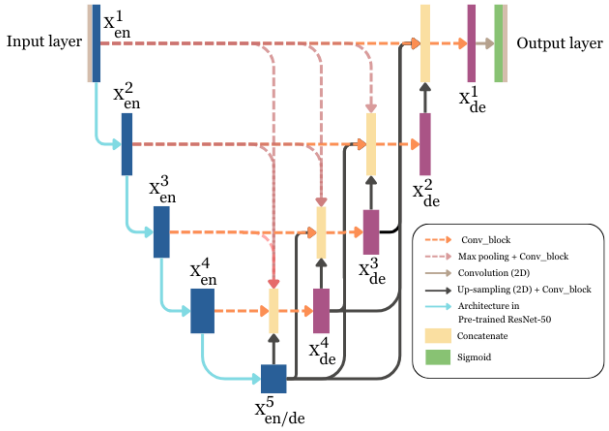

Figure 1. U-Net 3+ model with a ResNet-50 backbone architecture. *The architecture employs multiple short skip connections to merge features from the encoder and decoder, along with deeper and shallower decoder layers, enhancing localization and segmentation accuracy. The encoder layers are derived from the ResNet-50 backbone as follows:*
- 1st encoder (X^1_{en}): Output of the input layer
- 2nd encoder (X^2_{en}): Output of the 1st ReLU
- 3rd encoder (X^3_{en}): Output of the 10th ReLU
- 4th encoder (X^4_{en}): Output of the 22nd ReLU
- 5th encoder/decoder ($X^5_{en/de}$): Output of the 40th ReLU

Model training

The models were trained separately for each structure as binary segmentation task using the TensorFlow Keras framework (Google LLC, California, USA). The input data consist of pre-processed CT images and corresponding binary masks in PNG format. 5-fold CV with random shuffling was implemented to select best model based on validation loss. The adaptive moment estimation (Adam) optimizer was employed, with a starting learning rate set at 10^{-4} and a reduced learning rate to minimum learning rate = 10^{-10} based on validation loss. Each model was trained for 300 epochs and a batch size of 4, employing early stopping if validation loss did not improve for 50 consecutive epochs. To optimize performance, the loss function combined binary cross-entropy loss (BCE) and Dice loss[7], weighted at 30% and 70%, respectively. BCE, defined in Equation (1), focuses on pixel-wise classification, while Dice loss, defined in Equation (2), emphasizes overlap between the ground truth (GT) and predicted (PD) contours:

$$\mathcal{L}_{BCE} = -\frac{1}{N}\sum_{i=1}^{N} y_i \log(\hat{y}_i) + (1 - y_i)\log(1 - \hat{y}_i) \quad (1)$$

$$\mathcal{L}_{Dice} = 1 - \frac{2\sum_i^N y_i\hat{y}_i + \varepsilon}{\sum_i^N {y_i}^2 + \sum_i^N {\hat{y}_i}^2 + \varepsilon} \quad (2)$$

Where y_i represents a GT pixel value, $\hat{y}_i$ the corresponding prediction and N the total number of pixels. A small constant $\varepsilon = 10^{-15}$ is added to ensure numerical stability.

Model evaluation

The trained model was evaluated in terms of the Dice similarity coefficient (DSC), 95th percentile Hausdorff distance (HD_{95}), and average surface distance (ASD)[8]

DSC was implemented to quantify the overlapping area between the GT and PD contours, as defined in Equation (3).

$$DSC(y_i, \hat{y}_i) = \frac{2\sum_i^N y_i\hat{y}_i}{\sum_i^N {y_i}^2 + \sum_i^N {\hat{y}_i}^2} \quad (3)$$

Where y_i represents an GT pixel value, $\hat{y}_i$ the corresponding prediction.

HD_{95} was implemented to determine spatial boundary distance in mm between the GT and PD (3) contours, as defined in Equation (4)

$$HD_{95}(Y_i, \hat{Y}_i) = max\{d_{95}(Y_i, \hat{Y}_i), d_{95}(\hat{Y}_i, Y_i)\}, with$$

$$d_{95}(Y_i, \hat{Y}_i) = 95^{th}_{y_i \in Y_i}\{min_{\hat{y}_i \in \hat{Y}_i}\ d(y_i, \hat{y}_i)\} \quad (4)$$

Where y_i represents an GT pixel value, $\hat{y}_i$ the corresponding prediction.

ASD was implemented to determine same as HD_{95} but analyze the average value, as defined in Equation (5)

$$ASD(Y_i, \hat{Y}_i) = max\{d(Y_i, \hat{Y}_i), d(\hat{Y}_i, Y_i)\}, with$$

$$d(Y_i, \hat{Y}_i) = \frac{1}{N}\sum_{y_i \in Y_i} \min_{\hat{y}_i \in \hat{Y}_i} \|y_i - \hat{y}_i\| \quad (5)$$

Where y_i represents an GT pixel value, $\hat{y}_i$ the corresponding prediction.

III. RESULTS

Performance metrics for all structures are summarized in Table 1. With an example comparison of GT and PD contours illustrated in Fig 2.

Table 1. *Segmentation Performance*

Structures	DSC_{avg}	$(HD_{95})_{avg}$ (mm)	ASD_{avg} (mm)
HR-CTVs	0.780 ± 0.17	10.284 ± 10.47	4.058 ± 2.96
IR-CTVs	0.787 ± 0.19	12.072 ± 8.28	4.956 ± 3.68
Bladder	0.904 ± 0.16	5.351 ± 5.96	2.040 ± 2.01
Rectum	0.868 ± 0.10	5.482 ± 9.22	1.860 ± 2.20
Sigmoid colon	0.422 ± 0.34	54.925 ± 46.65	19.604 ± 25.98
Bowel	0.638 ± 0.23	38.884 ± 28.57	11.184 ± 9.02

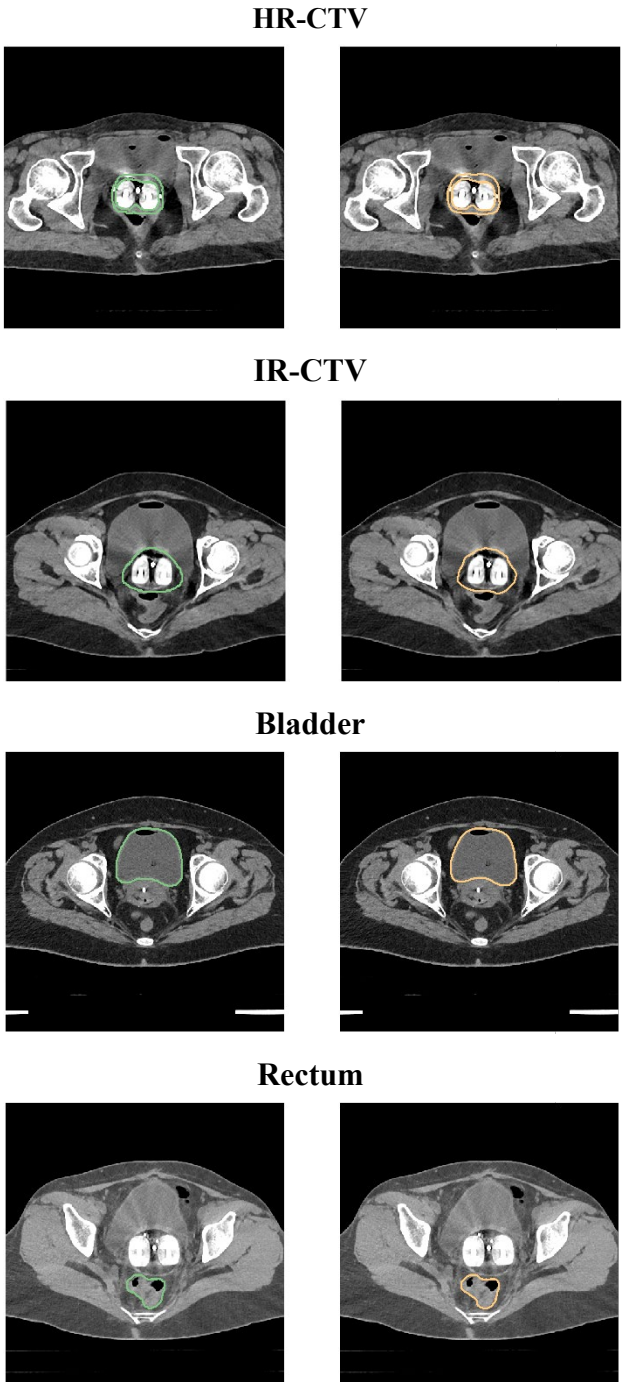

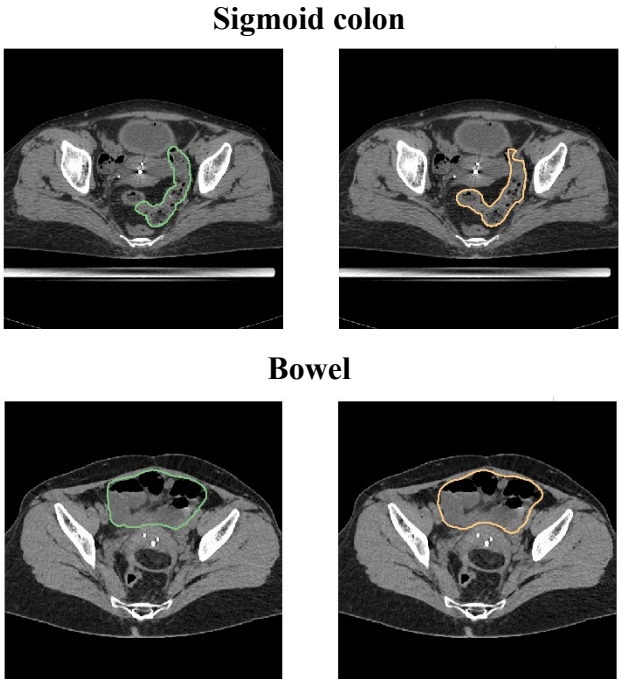

Figure 2. Comparison of GT and PD contours
The GT (green) and PD (yellow) contours are overlayed on CT images

IV. DISCUSSION

The model achieved high segmentation accuracy for the bladder and rectum, with intermediate performance for HR-CTV and IR-CTV due to their moderate complexity. Segmentation accuracy was lower for the sigmoid colon and bowel, due to their variable anatomy and less distinct boundaries on CT images. Additionally, the model struggled with poorly visualized structures in the uppermost and lowermost CT slices, which impacted segmentation accuracy, particularly for anatomically inconsistent structures.

V. CONCLUSION

The model performed well for well-defined structures (bladder and rectum) but faced challenges with complex or poorly visualized structures (sigmoid colon and bowel). Enhancing segmentation in poorly visualized slices is essential for clinical application.

ACKNOWLEDGEMENTS

I sincerely thank my advisor, **Thongsawad S**, and co-advisor, **Khamfongkruea C**, for their invaluable guidance. Thanks to **Fuangrod T** and **Kummanee P** for their consultation on model training, as well as my colleagues and everyone who contributed to this research.

REFERENCES

[1] Bruni L, Albero G, et al. Human papillomavirus and related diseases report: Thailand. ICO/IARC Information Centre on HPV and Cancer (HPV Information Centre). 2023.

[2] Sumi, et al. Radical external-beam radiotherapy in combination with high-dose-rate brachytherapy: Survival outcomes for patients with localized cervical cancer. Gynecol Oncol. 2020;157(2):380-387.

[3] Sultana S, et al. Automatic multi-organ segmentation in computed tomography images using hierarchical convolutional neural network. J Med Imaging (Bellingham). 2020;7(5):055001.

[4] Liu S, Zhang J, et al. Technical note: A cascade 3D U-Net for dose prediction in radiotherapy. Med Phys. 2021;48(9):5574–82.

[5] Ronneberger O, Fischer P, Brox T. U-Net: Convolutional networks for biomedical image segmentation. In: Navab N, Hornegger J, Wells WM, Frangi AF, editors. Med Image Comput Comput Assist Interv – MICCAI 2015. Cham: Springer; 2015: 234–41.

[6] Huang H, et al. UNet 3+: A Full-Scale Connected UNet for Medical Image Segmentation. In: Proceedings of the IEEE Int Conf Acoust, Speech Signal Process (ICASSP); 2020 May 4–8; Barcelona, Spain. IEEE; 2020:1055–9.

[7] Su J, Liu Z, et al. Robust liver vessel extraction using DV-net with D-BCE loss function. Adv Artif Intell Sec. Commun Comput Int Sci.2021;52–61.

[8] Taha AA, Hanbury A. Metrics for evaluating 3D medical image segmentation: analysis, selection, and tool. BMC Med Imaging. 2015;15(1):29.

Contacts of the corresponding author:
Author: Sangutid Thongsawad
Institute: Princess Srisavangavadhana College of Medicine, Chulabhorn Royal Academy
Street: Kampangpetch 6
City: Bangkok, Thailand
Email: sangutid.tho@cra.ac.th

Deep learning for radiation dose distribution prediction in VMAT breast cancer irradiation

Sukha Thanakorn[1], Puttanawarut Chanon[2], Sirirutbunkajorn Nat[1], Changkaew Pimolpun[1], Stansook Nauljun[1], Khachonkham Suphalak[1,*]

1 Department of Diagnostic and Therapeutic Radiology, Faculty of Medicine Ramathibodi Hospital, Mahidol University, Bangkok, Thailand.
2 Chakri Naruebodindra Medical Institute, Faculty of Medicine Ramathibodi Hospital, Mahidol University, Samut Prakan, Thailand.
*(*Corresponding author: suphalak.kha@mahidol.ac.th)*

Abstract — **Introduction:** Volumetric modulated arc therapy (VMAT) planning requires more time and expertise due to its complexity and need for repeated optimization. To address this, a deep learning (DL) model for dose prediction was developed. This study assesses the feasibility and reliability of the DL model's predictions for VMAT breast irradiation. **Methods:** A 6-channel U-Net-based network was trained and tested using data from 53 breast cancer VMAT plans. Input data included CT images, binary masks of the planning target volume (PTV), and organs at risk (OARs). The clinically accepted dose distribution served as the target for the predicted dose. Model predictions were evaluated using metrics such as mean absolute error (MAE), gamma passing rate (GPR), isodose volume dice similarity (iDSC), and dosimetric indices comparison. **Results:** Data from 8 plans were used for model testing. MAE for the PTV ranged from 1.7% to 2.6%, with an average of 2.0 ± 0.3%, while for the heart and lungs, MAE was 2.7 ± 1.0% and 3.4 ± 0.7%, respectively. The GPR at 3%/3mm ranged from 74.40% to 89.68%, with an average of 84.47 ± 0.07%. The mean of absolute difference in PTV for $D_{99\%}$, $D_{98\%}$, and $D_{2\%}$ were 0.86 ± 0.37%, 0.56 ± 0.24% and 1.12 ± 1.26%, respectively. **Conclusion:** The results show the potential of the developed DL models in enhancing the efficiency of VMAT planning, supporting advancements in personalized radiation therapy for breast cancer patients.
Keywords — Deep learning, Dose prediction, VMAT, Breast Cancer

I. INTRODUCTION

Radiation therapy has been playing a significant role in cancer treatment since 1990s, with advancements enabling personalized treatment plans and conformal dose distributions [1]. These innovations aim to improve tumor control probability (TCP) and reduce normal tissue complications probability (NTCP), enhancing patient outcomes. Radiation intensity-modulated delivery techniques such as Volumetric Modulated Arc Therapy (VMAT) deliver higher therapeutic doses to tumors while minimizing exposure to healthy tissues [2].

Breast cancer irradiation particularly benefits from these methods, improving planning target volume (PTV) coverage and reducing high-dose exposure to organs at risk (OARs). However, VMAT may increase low-dose volumes to OARs, particularly in the heart and lungs, elevating the risk of complications [3]. The complexity of VMAT planning also requires more time and expertise, potentially limiting clinical capacity [2, 3].

To address planner variability, Knowledge-Based Planning (KBP) predicts dose volume histograms (DVHs) based on prior treatment data but struggles with individual anatomical differences and spatial accuracy [4].

In recent years, deep learning (DL) has emerged as a promising tool for predicting patient-specific dose distributions. U-Net-based models have demonstrated high performance in radiation dose prediction, improving planning workflows and decision-making [5]. Despite the limited studies on DL for VMAT breast cancer irradiation, existing research suggests that DL outperforms KBP in both accuracy and planning efficiency [4, 5].

This study aims to investigate DL models for radiation dose prediction, utilizing VMAT breast cancer treatment plans from Ramathibodi Hospital to assesses its feasibility and accuracy.

II. MATERIALS AND METHODS

A. Data Collection and Pre-processing

Fifty-three clinically accepted VMAT breast cancer radiotherapy plans from the Division of Radiation Oncology, Ramathibodi Hospital, Mahidol University, were utilized as training data. The plans, developed using Varian's Eclipse system version 16.1 (Varian Oncology Systems, Palo Alto, CA, USA) from January

2021 to June 2024, employed the analytical anisotropic algorithm (AAA) for dose calculation. They included left or right breast irradiation, encompassing the chest wall and regional nodes. Coplanar VMAT arcs were manually planned for all cases, prescribing 42.56 Gy in 16 fractions, with some cases incorporating a high-risk PTV boost of 49.60 Gy using the simultaneous integrated boost (SIB) technique. All plans were evaluated based on clinically accepted dose distributions consistent with the institution's protocols. The plan typically using 6 MV photon beams, either with or without bolus, and gantry angles ranging roughly between 130°-330° for left breast and 40°-220° for right breast irradiation. Each plan ensured 95% PTV coverage at 95% of the prescribed dose, prioritizing the heart, left lung, and right lung as key OARs.

The treatment plans were exported including planning CT images, structure sets, and dose distributions. During pre-processing, all files were down-sampled to a 128 × 128 × 128 matrix with a pixel size of 3.5 × 3.5 mm^2 and a slice thickness of 3 mm. For cases with bolus, the summation dose was used as the final dose distribution. CT images were normalized using max-min scaling (-1024 HU to 3200 HU), ranging btween 0 to 1, to balance input into the model, with non-anatomical pixels set to zero. Dose distributions were normalized relative to the prescription dose of 42.56 Gy.

B. Model Architecture and Training

A 3D U-Net architecture [7] was utilized as the base network for the prediction model. The input layer received six channels: a planning CT, two binary masks for PTV (42.56 Gy and 49.60 Gy), and three binary masks for OARs (heart, left lung, right lung), while the clinically accepted dose distribution served as the target. The encoding path consisted of two 3 × 3 × 3 convolutional layers with 24, 48, 96, 192, 384, and 768 filters, followed by 2 × 2 × 2 max pooling. The decoding path mirrored this structure, with 2 × 2 × 2 transpose convolutions. Skip connections concatenated feature maps at each level, and dropout layers were added after each max pooling and transpose convolution layer to prevent overfitting. Rectified Linear Unit (ReLU) was the activation function for all convolutional layers, with mean squared error (MSE) as the loss function and the Adam optimizer.

The dataset was randomly divided into three subsets: 40 plans for training, 5 plans for validation, and 8 plans for testing. The training set was utilized to optimize the model parameters, the validation set was employed to monitor performance throughout 500 training epochs, and the test set was reserved for evaluating the model's performance after the training phase. Only PTVs prescribed with a dose of 42.56 Gy were selected for evaluation.

C. Dose Prediction and Evaluation

By utilizing the dropout layer, 30 stochastic inferences were performed for each test case, and the final dose distribution prediction was derived through voxel-wise averaging of these inferences. The accuracy of the model was evaluated by comparing the predicted dose distributions against clinically accepted dose distributions, employing a range of quantitative metrics to ensure robust assessment.

For quantitative evaluation, the mean absolute error (MAE) was calculated as $MAE = \frac{\sum_{i=0}^{128^3} |D_{pl_i} - D_{pr_i}|}{128^3}$, where D_{pl_i} and D_{pr_i} are dose at the same location i of ground truth and prediction, respectively. Dosimetric indexes (DI) at $D_{99\%}$, $D_{98\%}$, and $D_{2\%}$ of the PTV were compare using the Wilcoxon Signed-Rank test. Gamma passing rate (GPR) analysis was performed using a 3%/3mm criteria with an 80% cutoff to assess agreement between the plan and predicted dose distributions. The isodose volume dice similarity coefficient (iDSC) [12] was also calculated to measure the similarity between dose volumes at specific isodose levels, $iDSC = \frac{2|A_D \cap B_D|}{|A_D| + |B_D|}$, where A_D and B_D are the dose volumes at D Gy isodose from the clinical and predicted dose distribution, respectively. The iDSC ranges from 0 to 1, with values closer to 1 indicating stronger agreement.

III. RESULTS

The predicted dose distributions from the trained model for the 8 test cases were quantitatively compared to the ground truth. Table 1 shows the average MAE and MSE values for key ROIs, including the PTV, heart, ipsilateral lung, and contralateral lung. The highest variation occurred in the ipsilateral lung, with MAE and MSE values of 5.4 ± 1.2% and

0.67 ± 0.28%, respectively, followed by the heart, PTV, and contralateral lung. Table 2 compares the dosimetric indices ($D_{99\%}$, $D_{98\%}$, and $D_{2\%}$) between predicted (D_{pr}) and ground truth (D_{pl}) distributions, indicating no significant differences (p-value > 0.05).

For the GPR analysis using the 3%/3mm criteria with an 80% cutoff, the passing rate ranged from 74.40% to 89.68%, averaging 84.47 ± 0.07%.

Figure 1 plots the iDSC for all 8 test cases, with an average value indicated by a reference line. The coefficient demonstrates a high level of agreement between D_{pr} and D_{pl} across isodose levels peaking in high-dose regions.

Table 1. *Average MAE and MSE (±σ) of the predicted dose comparing to ground truth.*

ROI	MAE	MSE
PTV 42.56 Gy	2.0 ± 0.3%	0.07 ± 0.02%
Heart	2.7 ± 1.0%	0.17 ± 0.10%
Ipsilateral Lung	5.4 ± 1.2%	0.67 ± 0.28%
Contralateral Lung	1.3 ± 0.2%	0.04 ± 0.01%

Table 2. *Comparison of dosimetric index of D_{pr} and D_{pl} with the mean of absolute difference (Δ).*

DI	D_{pl} (Gy)	D_{pr} (Gy)	Δ (%)	*p-value*
$D_{99\%}$	38.63 ± 0.36	38.69 ± 0.16	0.86 ± 0.37	0.38
$D_{98\%}$	39.39 ± 0.23	39.44 ± 0.08	0.56 ± 0.24	0.74
$D_{2\%}$	44.33 ± 0.60	44.59 ± 0.30	1.12 ± 1.26	0.74

IV. DISCUSSION

In this study, the dose distribution of VMAT plans for breast cancer patients was predicted using a deep learning model based on a 3D U-Net architecture. The model utilized planning CT image and five binary masks (PTV, heart, left lung, right lung) as inputs to generate the predicted dose distribution. Quantitative comparisons of MAE and MSE between D_{pr} and D_{pl} in key ROIs showed accuracy levels consistent with previous studies [4, 6]. However, lower accuracy in the ipsilateral lung region was observed, aligning with prior findings. This discrepancy is attributed to significant uncertainty in dose distribution within low-density tissues, as calculated by AAA, and the proximity of the ipsilateral lung to the PTV, leading to high dose variability in the training data. DI values in Table 2 indicated no significant difference between D_{pr} and D_{pl} in the PTV. Specifically, the mean absolute difference in $D_{2\%}$ was 1.12%, which is comparable to the 1.01% reported in a similar study by Ahn et al. [4]. The gradual increase in iDSC reflects strong agreement between D_{pr} and D_{pl} in high-dose regions, while lower coefficients in lower isodose levels indicate reduced accuracy. Our model's iDSC at the 80% isodose level was 0.92, which is comparable to previous studies. For instance, Bai et al. [6] reported an iDSC of 0.94 at the 80% isodose level, and Ahn et al. [4] also noted iDSC values consistently above 0.9 for high-dose regions in their DL model.

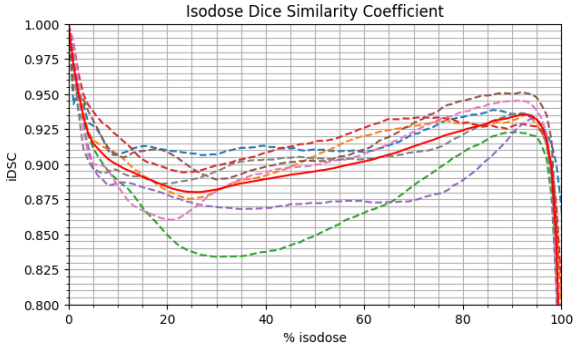

Figure 1. *Isodose dice similarity coefficient (iDSC) comparing isodose agreement between D_{pr} and D_{pl} across 8 test cases (dashed lines), with the average indicated by a red solid line.*

To improve such low accuracy in low dose region the size of training data set must increase. The size of the training dataset is a critical factor that affects the model's accuracy and generalizability. With only 40 cases, the model may not adequately capture clinical variability, particularly in the ipsilateral lung. Increasing the dataset size would improve prediction accuracy and model robustness across different patient anatomies and conditions. Additionally, refining the model architecture by incorporating features such as attention mechanisms or residual connections could enhance focus on critical regions and improve dose prediction accuracy, especially in low-density areas like the lung.

Additionally, incorporating methods to quantify prediction uncertainty, such as Monte Carlo Dropout (MCD) or Bayesian neural networks [8], is also essential for enhancing model reliability. These techniques could provide confidence intervals for predictions, enabling planners to assess the certainty of dose estimates. This approach would increase clinical safety and support oncologists in making informed decisions, particularly in high-uncertainty cases.

In conclusion, expanding the training dataset, optimizing the model architecture, and integrating uncertainty estimation methods are essential to further enhance the model's clinical

utility in VMAT dose planning for breast cancer patients. Future efforts should prioritize these aspects to achieve more accurate, robust, and clinically reliable dose predictions.

V. CONCLUSION

The study demonstrated that the developed DL model has significant potential to improve the efficiency of VMAT planning. By providing precise dose predictions, the model can streamline the treatment planning process, reduce the need for manual iteration of plan parameters adjustment, and minimize variability in treatment quality. This advancement can support the development of more personalized radiation therapy approaches, ensuring that breast cancer patients receive optimized, patient-specific treatment plans that enhance therapeutic outcomes while minimizing risks to healthy tissues. Ultimately, the integration of such models into clinical practice could lead to higher treatment consistency, reduced planning time, and improved overall patient care in radiation oncology.

ACKNOWLEDGEMENTS

The author would like to thank the Department of Diagnostic and Therapeutic Radiology, Faculty of Medicine Ramathibodi Hospital, Mahidol University for allowing us to utilize their facilities and providing access to their data.

REFERENCES

[1] Huh HD, Kim S. History of Radiation therapy technology. Prog Med Phys. 2020 9 30;31(3):124–34.

[2] Chiavassa S, Bessieres I, Edouard M, Mathot M, Moignier A. Complexity metrics for IMRT and VMAT plans: a review of current literature and applications. Br J Radiol. 2019;92(1102):20190270.

[3] Tyran M, Mailleux H, Tallet A, Fau P, Gonzague L, Minsat M, et al. Volumetric-modulated arc therapy for left-sided breast cancer and all regional nodes improves target volumes coverage and reduces treatment time and doses to the heart and left coronary artery, compared with a field-in-field technique. J Radiat Research. 2015;56(6):927–37.

[4] Ahn SH, Kim ES, Kim CK, Cheon W, Kim MS, Lee SB, et al. Deep learning method for prediction of patient-specific dose distribution in breast cancer. Radiat Oncol. 2021;16(1):154.

[5] Kui X, Liu F, Yang M, Wang H, Liu C, Huang D, et al. A review of dose prediction methods for tumor radiation therapy. Meta-Radiology. 2024;2(1):100057.

[6] Bai X, Liu Z, Zhang J, Wang S, Hou Q, Shan G, et al. Comparing of two dimensional and three dimensional fully convolutional networks for radiotherapy dose prediction in left-sided breast cancer. Sci Prog. 2021;104(3):003685042110381.

[7] Ronneberger O, Fischer P, Brox T. U-net: convolutional networks for biomedical image segmentation. In: Lecture Notes in Computer Science international conference on medical image computing and computer-assisted intervention. Cham. Springer, 2015;234–41.

[8] Abdar M, Pourpanah F, Hussain S, Rezazadegan D, Liu L, Ghavamzadeh M, et al. A review of uncertainty quantification in deep learning: techniques, applications and challenges. Inf Fusion. 2021;76:243–297.

Contacts of the corresponding author:
Author: Suphalak Khachonkham
Institute: Department of Diagnostic and Therapeutic Radiology, Faculty of Medicine Ramathibodi Hospital, Mahidol University
Street: Rama VI
City: Bangkok
Country: Thailand
Email: suphalak.kha@mahidol.ac.th

Comparative Analysis of Convolution Neural Networks (CNNs) for Automated Organ-at-Risk Delineation in Prostate Cancer Computed Tomography Images

Khuadpudsa Wanitchaya [1], Kaewlek Titipong.[1,2,3*]

[1]*Medical Physics Program, Department of Radiological Technology, Faculty of Allied Health Sciences, Naresuan University, Phitsanulok Province, Thailand.*

[2]*Department of Radiological Technology, Faculty of Allied Health Sciences, Naresuan University, Phitsanulok Province, Thailand.*

[3]*Interdisciplinary Health and Data Sciences Research Unit, Faculty of Allied Health Sciences, Naresuan University, Phitsanulok Province, Thailand.*

**Corresponding: titipongk@nu.ac.th*

Abstract — **Introduction:** The World Cancer Research Fund International ranks prostate cancer as the fourth most common cancer worldwide and the second most common cancer among men. In treatment planning, the accurate delineation of organs at risk (OARs) is crucial for optimizing treatment plans, making the process faster and more efficient. With advancements in technology, artificial intelligence (AI) has become a significant tool in medicine, helping to reduce delays and streamline treatment workflows. This study aims to investigate and compare the performance of deep learning models for the automatic delineation of OARs in CT images of prostate cancer patients undergoing radiotherapy. ***Methods****:* CT images from the Prostate-Anatomical-Edge-Cases dataset were used to test the U-Net and Dense V-Net models under identical parameters for the automatic delineation of the bladder and rectum. The models' performances were evaluated using Dice Similarity Coefficient (DSC), 95th percentile Hausdorff Distance (95HD), and Mean Surface Distance (MSD).***Results***: The Dense V-Net model achieved the best performance, with DSC, 95HD, and MSD values for the bladder of 0.99, 0.003, and 0.012, respectively. For the rectum, the corresponding values were 0.98, 0.01, and 0.02, respectively, under the same number of epochs. ***Discussion***: Dense V-Net consistently outperformed U-Net across all metrics, achieving superior DSC, 95HD, and MSD values. Although the type of GPU used did not significantly affect performance, Dense V-Net required 10 times more training time and memory compared to U-Net. ***Conclusion***: Dense V-Net demonstrated the highest accuracy in delineation tasks but required substantially greater computational resources and training time compared to U-Net when evaluated under the same batch size and number of epochs.

Keywords Deep Learning, CT, Prostate cancer, Auto-Delineation, Auto-Segmentation.

I. INTRODUCTION

The World Cancer Research Fund International(1) ranks prostate cancer as the fourth most common cancer worldwide and the second most common cancer among men, highlighting its significant global impact on public health. In treatment planning, the accurate delineation of organs at risk (OARs) is crucial for optimizing treatment plans, improving the precision of radiation delivery, and reducing adverse side effects, thereby accelerating and enhancing the treatment process. With rapid advancements in technology, artificial intelligence (AI) has emerged as a transformative tool in medicine, enabling automated processes, improving accuracy, reducing delays, and streamlining treatment workflows. Deep learning, a subset of AI, uses artificial neural networks to learn and make intelligent decisions autonomously. In radiotherapy for prostate cancer, AI facilitates automatic organ delineation to enhance precision and efficiency. AI algorithms trained on large imaging datasets can effectively distinguish between cancerous and healthy tissues. These advancements have led to the development of various medical AI applications, each with distinct algorithms, resources, and performance suited to specific needs. U-Net was selected for this study as a foundational model extensively utilized in medical image segmentation, recognized for its simplicity, computational efficiency, and effectiveness across various domains. dV-Net, on the other hand, represents an evolution of segmentation architectures, incorporating densely connected layers to enhance feature propagation, improve model learning, and minimize information loss,

making it particularly suitable for more complex segmentation tasks.Given the critical role of AI in modern healthcare.

This study aims to investigate and rigorously compare the performance of deep learning models for the automatic delineation of OARs in CT images of prostate cancer patients undergoing radiotherapy.

II. MATERIALS AND METHODS

A total of 310 CT images of the bladder and 341 images of the rectum were sourced from the Prostate – Anatomical – Edge - Cases dataset available on cancerimagingarchive.net.(2)These images consist of patients with prostate adenocarcinoma who received definitive radiotherapy between 2011 and 2019.Images were selected using specific exclusion criteria, including patients who had undergone bladder surgery or had a urinary catheter, patients with a hernia, and images affected by metal artifacts from surgical implants, such as hip replacements or other metallic devices.

A. U-Net

U-Net(3) is a convolutional neural network architecture widely used in medical image segmentation. Introduced in 2015, it has become a foundational model for tasks requiring precise localization and segmentation of objects within images, such as organs or tumors in medical imaging. U-Net is computationally efficient and relatively straightforward to implement, making it adaptable for a variety of segmentation tasks. It is highly effective in segmenting organs, tumors, and anatomical structures across modalities like CT, MRI, and ultrasound. U-Net is particularly useful for tasks requiring precise boundary detection and high-resolution outputs. Its robustness, even with limited labeled data, makes U-Net a preferred choice for automated medical segmentation tasks.

B. Dense V-net

Dense V-Net(4) is an advanced deep learning model for medical image segmentation. It enhances traditional V-Net by incorporating densely connected layers from DenseNet, which improve feature propagation, reduce redundancy, and enhance the learning of fine details. By connecting each layer to all previous layers, dV-Net improves gradient flow, retains spatial and contextual details, and enables effective learning of complex features. Additionally, its reduced parameter count makes it more compact and computationally efficient than traditional architectures.

C. Study design

The dataset was created by converting images annotated by a radiologist with over five years of experience, who delineated the boundaries of the bladder and rectum. Both the masks and corresponding images were used to train and test the models, with the data split into 70% for training and 30% for testing. The U-Net and dV-Net models were implemented, involving data preparation, CT dataset collection, and preprocessing to ensure the data was in a suitable format for training. The data was systematically organized to optimize model performance. Hyperparameters were adjusted, with the batch size set between 4 and 12 and the number of epochs fixed at 100. Model training was conducted on the Google Colaboratory platform using L4 and T4 GPUs. After training, model performance was evaluated using statistical metrics, including the Dice Similarity Coefficient (DSC), 95th percentile Hausdorff Distance (HD95), and Mean Surface Distance (MSD).

III. RESULTS

For the bladder, U-Net demonstrates consistent Dice Similarity Coefficient (DSC) values ranging from 0.90 to 0.93 across all batch sizes and GPU types. However, higher batch sizes tend to reduce performance, as reflected by an increase in the 95HD and MSD. In comparison, dV-Net shows superior DSC values, particularly at batch sizes 6 and 10 (DSC = 0.99). Additionally, dV-Net achieves significantly lower 95HD and MSD values, indicating improved boundary precision and segmentation accuracy. (Table1)

For the rectum, U-Net achieves DSC values ranging from 0.78 to 0.88, with the best performance observed at batch size 12 on the L4 GPU (DSC = 0.88). However, U-Net exhibits higher 95HD and MSD values compared to dV-Net, indicating reduced precision in boundary detection and spatial consistency.

dV-Net outperforms U-Net in all metrics, demonstrating superior segmentation accuracy and boundary precision. The best performance for dV-Net is observed on the L4 GPU at batch

size 8 (DSC = 0.99, 95HD = 0.02 mm, MSD = 0.02 mm). dV-Net remains highly consistent across different batch sizes, though a slight degradation in performance is noted at batch size 12 on the T4 GPU (95HD = 0.43 mm) (Table2).

Table1. *DSC, 95HD and MSD values of Bladder form U-net and dV-Net model*

GPU	Batch size	U-Net			dV-Net		
		DSC	95HD	MSD	DSC	95HD	MSD
L4	4	0.92	2.40	0.75	0.98	0.03	0.02
	6	0.93	1.99	0.69	0.98	0.02	0.02
	8	0.91	2.17	0.79	0.85	4.27	0.09
	10	0.90	2.97	1.25	0.98	0.01	0.01
	12	0.92	1.91	0.53	0.97	0.02	0.05
T4	4	0.92	1.85	0.64	0.79	7.74	1.80
	6	0.93	2.23	0.71	0.99	0.00	0.01
	8	0.92	2.14	0.67	0.98	0.01	0.02
	10	0.91	2.29	0.85	0.99	0.01	0.01
	12	0.90	2.97	1.17	0.98	0.17	0.05

Table2. *DSC, 95HD and MSD values of Rectum form U-net and dV-Net model*

GPU	Batch size	U-Net			dV-Net		
		DSC	95HD	MSD	DSC	95HD	MSD
L4	4	0.83	2.97	1.04	0.86	3.22	0.52
	6	0.80	3.25	0.95	0.98	0.15	0.03
	8	0.81	3.32	0.99	0.99	0.02	0.02
	10	0.85	2.44	0.68	0.98	0.02	0.02
	12	0.88	2.33	0.72	0.95	0.88	0.13
T4	4	0.78	4.93	1.79	0.83	2.85	0.53
	6	0.86	2.83	1.06	0.98	0.13	0.03
	8	0.81	4.22	1.87	0.98	0.01	0.02
	10	0.83	2.70	0.61	0.81	3.68	0.71
	12	0.87	2.05	0.53	0.96	0.43	0.07

At figure 1 shows the original image for bladder and rectum segmentation. Ground truth mask represents the manually annotated segmentation mask. Predicted mask displays the segmentation mask generated by the dV-Net with batch size 10 on an L4 GPU. The figure combines the original image with ground truth and predicted segmentation contours. The red contour outlines the ground truth mask, while the green contour depicts the predicted mask.

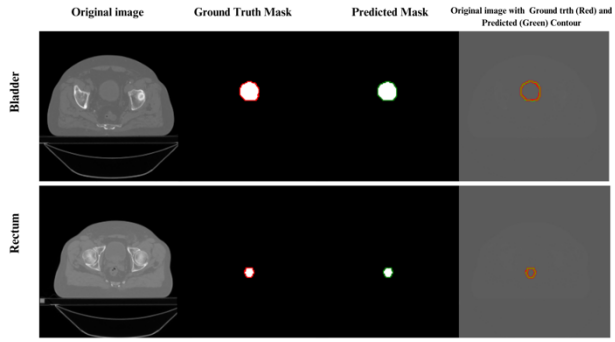

Figure1*. Image illustrates a segmentation evaluation for bladder and rectum.*

IV. DISCUSSION

This study uses CT imaging, while Savenije et al. (5) utilized MRI. The superior 95HD and MSD values observed in this study for dV-Net may be attributed to differences in imaging modality, as CT often provides clearer organ boundaries than MRI for certain structures. Variations in dataset characteristics and preprocessing methods also play a significant role in performance outcomes. Studies with smaller or less diverse datasets may exhibit lower DSC values due to overfitting or limited generalization.

A. Bladder Segmentation

In this study U-Net achieves consistent DSC values ranging from 0.90 to 0.93, closely aligning with the findings of Balagopal et al. (6) and Sultana et al. (7) However, dV-Net consistently outperforms U-Net, achieving a DSC of 0.99, which is significantly higher than the results reported by Savenije et al.

B. Rectum Segmentation

U-Net achieves DSC values ranging from 0.78 to 0.88, comparable to the findings of Balagopal et al. and Sultana et al. However, this study shows better 95HD and MSD values for U-Net, suggesting improved spatial accuracy. These improvements are likely due to the use of advanced data augmentation techniques and hyperparameter optimization during model training. And dV-Net achieves the highest DSC value for rectum segmentation in this study, surpassing the results of Savenije et al. Its superior performance demonstrates the model's capability to handle intricate anatomical boundaries, such as those of the rectum. dV-Net's densely connected layers and improved feature propagation significantly enhance its spatial accuracy and precision. The results

confirm that dV-Net is the preferred choice for bladder and rectum segmentation, offering the precision necessary for radiotherapy treatment planning. Its improved segmentation accuracy reduces the need for manual corrections, enhances workflow efficiency, and has the potential to improve patient outcomes.

Table3. *Quantitative comparison of geometric metrics with another research*

Study	Modality	Model	Bladder			Rectum		
			DSC	95HD	MSD	DSC	95HD	MSD
Balagopal et al	CT	U-Net	0.95	17.0	0.5	0.84	4.9	0.8
Sultana et al	CT	U-Net	0.88	7.20	2.34	0.83	9.2	3.91
Savenije et. al	MRI	dV-Net	0.95	3.90	1.05	0.85	7.92	2.10
This Study	CT	U-Net	0.93	1.99	0.69	0.88	2.33	0.72
		dV-Net	0.99	0.00	0.01	0.99	0.02	0.02

For GPU selection in optimizing deep learning models for bladder and rectum segmentation in CT images, Dense V-Net outperformed U-Net across all metrics, achieving higher accuracy and boundary precision, especially with the L4 GPU. The L4 GPU outperformed the T4 GPU in performance and efficiency due to its advanced architecture. Dense V-Net was robust to batch size variations, delivering its best results on the L4 GPU at batch size 8 (DSC = 0.99, 95HD = 0.02 mm, MSD = 0.02 mm). The T4 GPU showed more variability, especially at smaller batch sizes, but remains a viable option for resource-limited settings. U-Net, though consistent, showed sensitivity to larger batch sizes, resulting in higher 95HD and MSD. However, the use of high-cost GPUs like the L4 limits adoption in smaller or resource-constrained healthcare settings, reducing scalability and feasibility for widespread clinical use.

V. CONCLUSION

This study highlights the performance differences between U-Net and dV-Net for bladder and rectum segmentation in CT images. dV-Net consistently outperformed U-Net in segmentation accuracy and boundary precision, demonstrating superior results. For the bladder, dV-Net achieved higher performance than U-Net, U-Net was sensitive to larger batch sizes, resulting in reduced precision. For the rectum, dV-Net demonstrated greater consistency and accuracy compared to U-Net. Overall, dV-Net is better suited for tasks requiring high accuracy and precision, particularly for complex organs like the rectum. It is recommended for resource-intensive applications such as prostate cancer treatment planning.

REFERENCES

[1] International WCRF. Global cancer incidence in men [Web page]. 2020 [Available from: https://www.wcrf.org/cancer-trends/worldwide-cancer-data/

[2] TCIA.Cancer Imaging Archive 2024 [Available from: https://www.cancerimagingarchive.net.]

[3] Ronneberger OF, Philipp, Brox T. U-Net: Convolutional Networks for Biomedical Image Segmentation. Medical Image Computing and Computer-Assisted Intervention – MICCAI 2015. Lecture Notes in Computer Science2015. p. 234-41.

[4] Zhu Q, Du B, Yan P. Boundary-Weighted Domain Adaptive Neural Network for Prostate MR Image Segmentation. IEEE Trans Med Imaging. 2020;39(3):753-63.

[5] Savenije MHF, Maspero M, Sikkes GG, van der Voort van Zyp JRN, AN TJK, Bol GH, et al. Clinical implementation of MRI-based organs-at-risk auto-segmentation with convolutional networks for prostate radiotherapy. Radiation Oncology. 2020;15(1):104.

[6] Balagopal A KS, Nguyen D, Lin MH, Hannan R, Owrangi A, et al. Fully Automated Organ Segmentation in Male Pelvic CT Images. Phys Med Biol. 2018;63(24).

[7] Sultana S RA, Song DY, Lee J. Automatic multi-organ segmentation in computed tomography images using hierarchical convolutional

Contacts of the corresponding author:
Author: Titipong Kaewlek
Institute: Department of Radiological Technology, Faculty of Allied Health Sciences, Naresuan University
City: Phitsanulok
Country: Thailand
Email: titipongk@nu.ac.th

Prediction of radiation pneumonitis using artificial intelligence in non-small cell lung cancer patients undergoing volumetric modulated arc therapy

Chevajarassakul Wasin[1], Chamchod Sasikarn[1,2], Phonlakrai Monchai[3], Kummanee Patiparn[1], Masa-nga Wilai[2], Nimjaroen Kampheang[2], Chaipanya Thitiporn[1,4], Khamfongkhruea Chirasak[1,2,*]

1 Medical Physics Program, Princess Srisavangavadhana College of Medicine, Chulabhorn Royal Academy, Bangkok, Thailand
2 Radiation Oncology Department, Chulabhorn Hospital, Chulabhorn Royal Academy, Bangkok, Thailand
3 Faculty of Health Science Technology, HRH Princess Chulabhorn College of Medical Science, Chulabhorn Royal Academy, Bangkok, Thailand
4 Division of Radiation Therapy, Lopburi Cancer Hospital, Lopburi, Thailand
*(*Corresponding author: chirasak.kha@cra.ac.th)*

Abstract — **Introduction:** Volumetric modulated arc therapy (VMAT) has significantly improved treatment outcomes for non-small cell lung cancer (NSCLC) patients. However, radiation pneumonitis (RP) remains a critical complication. Current RP prediction models often overlook lung function variability, reducing precision. This study aims to improve RP prediction by combining artificial intelligence (AI) with four-dimensional computed tomography (4DCT) imaging to capture detailed functional variability in lung regions, enhancing model accuracy for refining treatment planning. **Methods:** This study analyzed 4DCT data from 56 NSCLC patients treated with VMAT, classifying patients by RP severity as either grade < 2 or grade ≥ 2 based on evaluations by experienced radiation oncologists. MATLAB was used for dataset preprocessing, with an 80% and 20% split for training and testing. From 535 radiomic features, the chi-square algorithm selected 54 relevant features for RP prediction. Five machine learning models—support vector machines (SVM), Naive Bayes, logistic regression (LR), linear SVM, and k-nearest neighbors (KNN)—were trained and optimized via 5-fold cross-validation on the training set. Model performance was assessed using specificity, sensitivity, precision, accuracy, and area under the precision-recall curve (AUPRC). **Results:** The SVM model was the most accurate in predicting RP, achieving an accuracy of 0.84 ± 0.08, sensitivity of 0.85 ± 0.34, specificity of 0.84 ± 0.11, and precision of 0.78 ± 0.14. The model also attained an AUPRC of 0.34. **Conclusion:** Integrating AI into RP prediction presents a promising tool for optimizing treatment planning, enabling personalized care, and reducing the risks of radiotherapy-related complications.

Keywords — Artificial intelligence (AI), Machine learning (ML), Radiation pneumonitis (RP), Non-small cell lung cancer (NSCLC), Volumetric modulated arc therapy (VMAT)

I. INTRODUCTION

Lung cancer continues to be the leading cause of cancer-related mortality worldwide, with its incidence steadily increasing across diverse populations and regions [1]. Among the various types of lung cancer, non-small cell lung cancer (NSCLC) accounts for approximately 84% of all diagnosed cases, making it the most prevalent subtype [2]. In recent years, external beam radiation therapy (EBRT) advancements have played a crucial role in improving treatment outcomes for NSCLC patients. Specifically, volumetric modulated arc therapy (VMAT) has emerged as a highly sophisticated radiation technique, offering enhanced precision in dose delivery and improved therapeutic benefits, while minimizing damage to surrounding healthy tissues [3, 4]. Despite these significant technological improvements, radiation-induced lung injuries remain a major concern. One such injury, known as radiation pneumonitis (RP), is a condition where the lungs become inflamed as a result of radiation treatment to the chest area. This inflammation can cause symptoms such as coughing, shortness of breath, and chest discomfort, which typically appear weeks to months after treatment. RP is considered a serious side effect because it limits how much radiation can be safely delivered, affecting approximately

5–36% of patients receiving chest radiation therapy. [5,6].

Traditional methods for predicting radiation pneumonitis (RP) primarily rely on dose-volume histogram (DVH) parameters, such as the lung volume receiving ≤ 5 Gy (V5) and ≤ 20 Gy (V20). However, these approaches assume uniform lung function, overlooking the functional and anatomical heterogeneity within the lungs [5]. This limitation reduces their predictive accuracy, highlighting the need for advanced imaging techniques. Four-dimensional computed tomography (4DCT) has become a valuable tool for improving RP prediction by capturing detailed spatial and temporal information about lung structure and motion during the respiratory cycle [7]. This capability enables a more precise analysis of dose distribution, addressing the limitations of uniformity assumptions in traditional methods and paving the way for more accurate and individualized RP prediction models.

In this study, we aim to develop a machine learning-based prediction model for radiation pneumonitis in NSCLC patients undergoing VMAT. Unlike previous studies incorporating functional imaging data, this research focuses exclusively on features extracted from 4DCT imaging. By leveraging machine learning algorithms, the goal is to enhance prediction accuracy, improve the clinical applicability of RP models, and ultimately support more personalized and safer radiation treatment planning for NSCLC patients.

II. MATERIALS AND METHODS

A. Data selection and collection

A total of 56 retrospective case studies focused on individuals diagnosed with NSCLC were analyzed. The studies were conducted at the Radiation Oncology Department of Chulabhorn Hospital between 2012 and 2024. The research utilized the VMAT technique, incorporating patient 4DCT images, medical records, treatment intent, and radiation transport data. The 4DCT images were acquired using the Brilliance Big Bore system (Philips Healthcare, Best, Netherlands) and the Siemens Somatom Go OpenPro system (Siemens Healthineers AG, Erlangen, Germany) with a tube voltage of 120 kV and a reconstructed slice thickness of 3 mm during simulation data acquisition. The 4DCT imaging process typically divides the respiratory cycle into 10 phases, capturing multiple time-resolved datasets that provide information about the patient's respiratory motion. 4DCT provides superior temporal resolution of respiratory-induced tumor motion, enabling precise delineation of tumor margins and facilitating accurate identification of functional lung regions, surpassing the capabilities of 3DCT. Patients were categorized into two groups based on RP grading: < 2 RP (n = 21) and ≥ 2 RP (n = 35). Prescription doses ranged between 50 Gy and 66 Gy in 1.8-2 Gy fractions

B. Feature extraction and model generation

A machine learning (ML) model was developed to predict radiation pneumonitis (RP) in lung cancer patients. The model was implemented using MATLAB 2024 (R2024a) and an ensemble approach, incorporating 535 features categorized into whole lung information, medical records, treatment intent, and radiation transport data. Feature selection was performed using the chi-square algorithm in MATLAB, reducing the dataset to 54 key features relevant to RP prediction.

The dataset underwent preprocessing in MATLAB, with an 80% split for training and 20% for testing. A total of five machine learning models—support vector machines (SVM), Naive Bayes, logistic regression (LR), linear SVM, and k-nearest neighbors (KNN)—were trained and optimized using 5-fold cross-validation on the training set. The chi-square algorithm was applied to identify the most significant radiomic features, ensuring improved model accuracy and efficiency for RP prediction.

C. Model evaluation

Model validation was conducted to ensure accuracy in RP prediction. A subset of 20 percent of the dataset was allocated for validation. Predictions of the model were compared with actual outcomes using evaluation metrics such as accuracy, sensitivity, specificity, and precision. These metrics provided a comprehensive evaluation of the predictive performance of the model.

$$\text{Accuracy} = \frac{\text{TP} + \text{TN}}{\text{TP} + \text{TN} + \text{FP} + \text{FN}} \qquad (1)$$

$$\text{Sensitivity} = \frac{\text{TP}}{\text{TP} + \text{FN}} \quad (2)$$

$$\text{Specificity} = \frac{\text{TN}}{\text{TN} + \text{FP}} \quad (3)$$

$$\text{Precision} = \frac{\text{TP}}{\text{TP} + \text{FP}} \quad (4)$$

Where TP is true positive, TN is true negative, FP is false positive, and FN is false negative.

To further assess the model's performance, the area under the receiver operating characteristic curve (AUROC) and the area under the precision-recall curve (AUPRC) were calculated, offering insights into the model's ability to distinguish between classes and its precision-recall trade-offs.

III. RESULTS

The model achieved the confusion matrix for RP prediction as Table 1, showing TP of 1, FN of 3, FP of 0, and TN of 7. This analysis reflects the model's ability to distinguish between grade < 2 RP and grade ≥ 2 RP outcomes.

Table 1. *Confusion matrix of RP prediction*

	Predicted Positive	**Predicted Negative**
Actual Positive	TP = 1	FN = 3
Actual Negative	FP = 0	TN = 7

Table 2 presents the performance metrics (mean ± S.D.) for RP prediction models. The SVM model achieved the highest accuracy (0.84 ± 0.08), sensitivity (0.85 ± 0.34), specificity (0.84 ± 0.11), and precision (0.78 ± 0.14), demonstrating its effectiveness in predicting RP outcomes.

Table 2. *Performance metrics of each RP prediction model for binary classification, including accuracy, sensitivity, specificity, and precision.*

Features	Accuracy	Sensitivity	Specificity	Precision
SVM	0.84 ± 0.08	0.85 ± 0.34	0.84 ± 0.11	0.78 ± 0.14
Naïve Bayes	0.62 ± 0.12	0.80 ± 0.27	0.54 ± 0.10	0.46 ± 0.09
LR	0.79 ± 0.08	0.48 ± 0.19	0.95 ± 0.07	0.87 ± 0.18
Linear SVM	0.75 ± 0.07	0.47 ± 0.19	0.89 ± 0.06	0.72 ± 0.18
KNN	0.82 ± 0.06	0.83 ± 0.16	0.81 ± 0.07	0.70 ± 0.08

The model, utilizing an SVM with the features that demonstrated the best performance, achieved an AUROC of 0.75, indicating effective discrimination between RP grades (< 2 RP and ≥ 2 RP). The AUPRC was 0.34, reflecting the model's performance in precision and recall. These metrics demonstrate the model's predictive performance for RP classification, as shown in Figure 1.

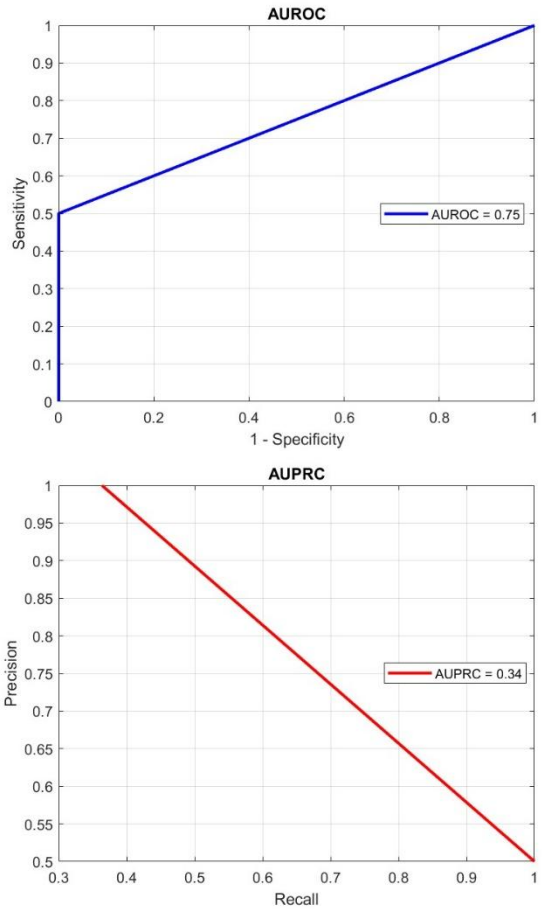

Figure 1. *Comparison AUROC and AUPRC*

IV. DISCUSSION

This study developed a machine learning model to predict RP in NSCLC patients treated with VMAT using features derived from 4DCT images. The model achieved an AUROC of 0.75 and an AUPRC of 0.34, but its performance was likely constrained by the relatively small sample size and class imbalance between RP and non-RP cases. These factors may have limited the model's predictive accuracy and generalizability. Addressing these limitations in future studies through strategies such as data augmentation or expanding dataset diversity and size is crucial for improvement.

Incorporating advanced imaging modalities, such as functional lung imaging (e.g., ventilation or perfusion images), could further enhance model performance by providing a more comprehensive representation of lung heterogeneity. Katsuta et al. [8] demonstrated that integrating dose-function features derived from 4DCT ventilation significantly improved prediction performance over traditional dose-volume metrics, achieving an AUC of 0.814. Functional imaging could also address the limitations of traditional parameters (e.g., V5, V20), which assume uniform lung function, and improve the model's ability to account for regional lung variations.

Despite these challenges, this study adds to the growing evidence that machine learning combined with imaging data has significant potential to improve RP prediction. Further work is required to enhance model precision, integrate functional lung data, and address class imbalances to achieve clinically robust outcomes.

V. CONCLUSION

The integration of ML with 4DCT imaging provides a promising framework for predicting radiation pneumonitis in NSCLC patients undergoing VMAT. The SVM model demonstrated effective predictive capabilities with substantial overall performance metrics. These findings support the potential of AI-driven approaches to aid personalized treatment planning and minimize radiation-related complications, paving the way for improved patient outcomes in clinical practice.

ACKNOWLEDGEMENTS

The author extends profound gratitude to all advisors, colleagues, and friends for their invaluable guidance, insightful contributions, and unwavering support throughout the course of this study. Particular appreciation is directed to the advisor for their expert guidance and steadfast support, which were pivotal to the successful completion of this research.

REFERENCES

[1] Cho MK, Cho YH. Factors influencing the intention for lung cancer screening in high-risk populations for lung cancer. Asia-Pacific Journal of Oncology Nursing. 2024 Jan; 11(1):100332.

[2] Kim J, Lee H, Huang BW. Lung cancer: diagnosis, treatment principles, and screening. American Academy of Family Physicians. 2022 May 1; 105(5):487-494.

[3] Alduais Y, Zhang H, Fan F, Chen J, Chen B. Non-small cell lung cancer (NSCLC): A review of risk factors, diagnosis, and treatment. Medicine. 2023 Feb 22;102(8):e32899.

[4] Lee VHF, Yang L, Jiang Y, Kong FM (Spring). Radiation Therapy for Thoracic Malignancies. Hematology/Oncology Clinics of North America. 2020 Feb;34(1):109–25.

[5] Yoshiyuki Katsuta, Noriyuki Kadoya, Kajikawa T, Shina Mouri, Kimura T, Takeda K, et al. Radiation pneumonitis prediction model with integrating multiple dose-function features on 4DCT ventilation images. Physica Medica. 2023 Jan;105:102505–5.

[6] Ye F, Xu L, Ren Y, Xia B, Chen X, Ma S, et al. Predicting radiation pneumonitis in lung cancer: a EUD-based machine learning approach for volumetric modulated arc therapy patients. Frontiers in Oncology. 2024 Jan 31;14.

[7] Huang Y, Feng A, Lin Y, Gu H, Chen H, Wang H, et al. Radiation pneumonitis prediction after stereotactic body radiation therapy based on 3D dose distribution: dosiomics and/or deep learning-based radiomics features. Radiation Oncology. 2022 Nov 17;17(1).

[8] Yoshiyuki Katsuta, Noriyuki Kadoya, Kajikawa T, Shina Mouri, Kimura T, Takeda K, et al. Radiation pneumonitis prediction model with integrating multiple dose-function features on 4DCT ventilation images. Physica Medica. 2023 Jan 1;105:102505–5.

Contacts of the corresponding author:
Author: Chirasak Khamfongkhruea
Institute: Princess Srisavangavadhana College of Medicine, Chulabhorn Royal Academy
Street: Kamphaeng Phet 6
City: Bangkok
Country: Thailand
Email: chirasak.kha@cra.ac.th

Range Comparison of Monte Carlo and Pencil Beam Algorithms in Treatment Planning System for Proton Therapy

Monkongsubsin Wiroon[1], Israngkul Na Ayuthaya Isra[2], Sanghangthum Taweap[3] ,Keawsamur Mintra[3,*]

1 Department of Radiology, Medical Physics program, Faculty of Medicine, Chulalongkorn University, Bangkok, 10330 Thailand
2 Division of Radiation Oncology, Department of Radiology, King Chulalongkorn Memorial Hospital, Bangkok, 10330 Thailand
3 Division of Radiation Oncology, Faculty of Medicine, Chulalongkorn University, Bangkok, 10330 Thailand
*(*Corresponding author: Mintra.Ke@chula.ac.th)*

Abstract — **Introduction:** The Pencil Beam Scanning technique has expanded rapidly due to its precision in targeting tumors using Bragg peak while minimizing exit dose to surrounding tissues. Proton range is determined by the energy, and reducing range uncertainties is crucial in clinical applications. Monte Carlo (MC) algorithm has demonstrated accuracy in proton dose calculations, especially in heterogeneous tissues. This study aims to compare the proton range between MC and pencil beam (PB) algorithms using experimental measurements across various tissue substitutes. **Methods:** A Gammex 467 tissue characterization phantom with 11 insertion rods and pig organs were used to study the proton range in different tissues. The range calculations were performed in RayStation treatment planning system using both MC and PB algorithms for a single proton spot with 150 MeV passing through each tissue. The range measurements were conducted using an IBA Multi-plane parallel ionization chamber (Giraffe) with a Varian ProBeam system, and the ranges were compared with the calculated ranges. **Results:** In the tissue characterization phantom, the mean R_{90} differences were -0.1 ± 2.2 mm for MC and 0.2 ± 2.2 mm for PB. In pig organs, the R_{90} differences were -1.4 ± 1.7 mm for MC and -1.2 ± 1.8 mm for PB. **Conclusion:** The limitations of PB in calculating dose for lung should be noted and considered in clinical practice.

Keywords — Monte Carlo algorithm, Pencil beam algorithm, Treatment planning system, Proton therapy.

I. INTRODUCTION

In recent years, the adoption of proton therapy, particularly the Pencil Beam Scanning (PBS) delivery technique, has significantly increased worldwide [1]. This technique allows for the precise delivery of high-dose radiation, known as the Bragg peak directly into the tumor while maintaining a lower, plateau dose in the entrance pathway and achieving a rapid dose fall-off. When interacting with matter, protons undergo processes such as stopping, scattering, and nuclear interaction [2]. The electromagnetic interactions between the proton's charge and the charge of atomic nuclei or electrons cause the protons to stop and scatter.

The American Association of Physicists in Medicine (AAPM) Task Group 224 [3] has recommended using the proton range of individual spots as a dosimetric parameter to measure R_{90}, defined as the distal depth at which 90% of the depth dose is delivered, as shown in *Figure 1*.

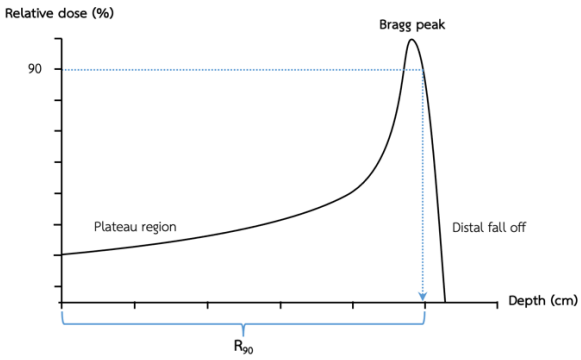

Figure 1. The proton integral depth-dose curve with R_{90} indicated.

This parameter should remain within ± 1 mm of the commissioning value. In treatment delivery systems, the radiation is delivered to patients based on the beam parameters defined by the treatment planning system (TPS), which selects the proton energy required for the desired dose at the tumor depth. Any uncertainty in the proton range can lead to deviations in the delivery depth, potentially resulting in unexpected outcomes such as compromised

tumor control or increased complications in normal tissues [4,5].

Minimizing proton range uncertainty is crucial in clinical practice. The most commonly used calculation algorithms in TPS for proton therapy are Monte Carlo (MC) and Pencil Beam (PB) algorithms. The previous study [6] showed that the MC algorithm is preferred due to its ability to simulate real interactions within the patient using probability and random number simulations. This study aims to compare the range between MC and PB algorithms with experimental measurements across various tissue substitutes.

II. MATERIALS AND METHODS

A. Tissue characterization phantom and pig organs

The Gammex 467 tissue characterization phantom (Gammex Inc., Middleton, WI, USA), containing 11 rods (70 mm thickness) representing homogeneous lung-like, soft tissue-like, and bone-like materials, and real pig organs, including the lung, liver, and bone, exhibit varying compositions within each organ were scanned using the GE Revolution Computed Tomography (CT) system (GE Healthcare, Waukesha, WI, USA) at 120 kVp.

B. Range comparison

RayStation version 2024A (RaySearch Medical Laboratories AB, Stockholm, Sweden), both MC and PB algorithms were applied within TPS. The CT images of the Gammex 467 tissue characterization phantom and pig organs, including lung, liver, and bone, were used to develop a single spot plan for each material using a proton energy of 150 MeV. The external region of interest (ROI) was extended beyond the back of the phantom and pig organs to calculate the proton range as it passed through each rod and slightly into the water. The treatment isocenter was nearly positioned behind each rod. The dose grid was applied across the entire plan to facilitate calculations using both algorithms, MC and PB.

All range measurements were conducted using the Varian ProBeam compact spot scanning system (Varian Medical System, Palo Alto, CA, USA) at Her Royal Highness Princess Maha Chakri Sirindhorn Proton Center (HPSP), King Chulalongkorn Memorial Hospital, Bangkok, Thailand. This system delivers proton energies ranging from 70 to 220 MeV, achieving water ranges from 40 to 305 mm, with a gantry capable of 360-degree rotation. The Giraffe multi-layer plane-parallel plate ionization chamber (IBA Dosimetry, Schwarzenbruck, Germany) was positioned behind the Gammex 467 tissue characterization phantom and pig organs, aligned with a 90-degree gantry beam direction (as shown in *Figure 2*), to measure the range within the water-simulated detector.

These measurements were compared with the calculated ranges from both MC and PB algorithms using

$$\Delta R_{90} = Calculated\ R_{90} - Measured\ R_{90}$$

Where ΔR_{90} was the different R_{90} in unit of millimeter (mm), measured and calculated R_{90} were the measured range by using the Giraffe detector and the calculated range from both different algorithms, respectively.

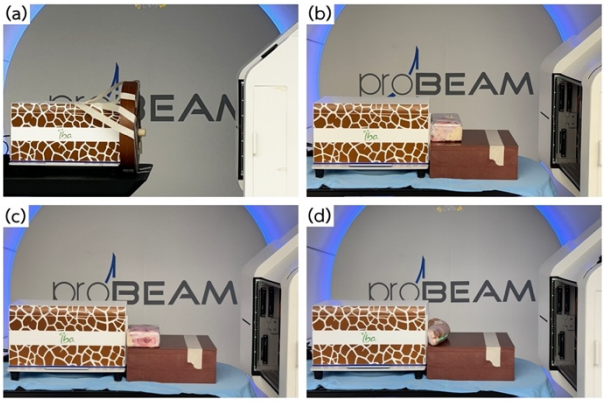

Figure 2. *R_{90} measurement using the Giraffe detector in phantom and pig organs: (a) Gammex 467 tissue characterization phantom, (b) pig lung, (c) pig liver, and (d) pig foot.*

III. RESULTS

Table 1 shows the different R_{90} in tissue characterize phantom. For lung-like materials, the range differences were -0.7 mm for both algorithms in LN-300, while in LN-450, the differences were -2.8 mm and -2.6 mm for MC and PB, respectively. In soft-tissue-like materials, the range differences were generally minimal, with ΔR_{90} ranging from -4.2 mm to 0.7 mm. The most significant discrepancy was noted in brain tissue, with a variation of -4.2 mm for MC and -3.6 mm for PB. For bone-like materials, the highest deviations were found in

cortical bone, with ΔR_{90} of 3.9 mm for MC and 4.1 mm for PB.

Overall, the mean ΔR_{90} was -0.1 mm for MC and 0.2 mm for PB, with a standard deviation of 2.2 mm for both algorithms. The minimum differences were -4.2 mm for MC and -3.6 mm for PB, whereas the maximum differences were 3.9 mm for MC and 4.1 mm for PB. The statistical analysis using the Wilcoxon Signed-Rank Test, revealed a *P*-value of .005, indicating that the ΔR_{90} between MC and PB was statistically significant ($P < .05$).

Table 1. *The different R_{90} of 11 rods between measurement and calculation.*

Rod no	Rod materials	Measured R_{90} (mm)	Calculated R_{90} (mm)		ΔR_{90} (mm)	
			MC	PB	MC	PB
	Lung like					
1	Lung (LN-300)	135.2	135.9	135.9	-0.7	-0.7
2	Lung (LN-450)	125.1	127.9	127.7	**-2.8**	**-2.6**
				Mean ± Std	-1.8 ± 1.5	-1.7 ± 1.3
	Soft-tissue like					
3	Adipose	89.3	89.1	88.9	0.2	0.4
4	Breast	86.9	86.3	86.2	0.6	0.7
5	Solid Water	85.0	85.1	84.4	-0.1	0.6
6	Brain	80.8	85.0	84.4	**-4.2**	**-3.6**
7	Liver	80.2	80.9	80.5	-0.7	-0.3
				Mean ± Std	-0.8 ± 1.9	-0.4 ± 1.8
	Bone like					
8	Inner Bone	78.6	76.7	76.4	**1.9**	**2.2**
9	Bone (CB2-30% Mineral)	66.7	67.7	67.5	-1.0	-0.8
10	Bone (CB2-50% Mineral)	55.6	53.5	53.4	**2.1**	**2.2**
11	Cortical Bone	42.4	38.5	38.3	**3.9**	**4.1**
				Mean ± Std	1.7 ± 2.0	1.9 ± 2.0
	All rod materials			Mean ± Std	-0.1 ± 2.2	0.2 ± 2.2
				Min	-4.2	-3.6
				Max	3.9	4.1
				P	**.005**	

CB: Calcium carbonate Bone

Table 2. *The different R_{90} of pig organs between measurement and calculation.*

Pig organs	Measured R_{90} (mm)	Calculated R_{90} (mm)		ΔR_{90} (mm)	
		MC	PB	MC	PB
Lung	115.1	118.4	118.3	**-3.3**	**-3.2**
Liver	41.8	42.4	42.2	-0.6	-0.4
Foot	91.0	91.2	90.9	-0.2	0.1
			Mean ± Std	-1.8 ± 1.5	-1.7 ± 1.3
			Min	-3.3	-3.2
			Max	-0.2	0.1

Table 2 also shows the different R_{90} in pig organs. For lung, the measured R_{90} was 115.1 mm, while the calculated range increased to 118.4 mm for MC and 118.3 mm for PB. This resulted in range differences of -3.3 mm and -3.2 mm for MC and PB, respectively. For liver, the measured R_{90} was 41.8 mm. The calculated range slightly increased to 42.4 mm for MC and 42.2 mm for PB, yielding ΔR_{90} of -0.6 mm and -0.4 mm, respectively. For foot, the measured R_{90} was 91.0 mm. The calculated R_{90} increased to 91.2 mm for MC and a slight decrease to 90.9 mm for PB. The corresponding ΔR_{90} were -0.2 mm for MC and 0.1 mm for PB, demonstrating minimal deviation.

Overall, the mean ΔR_{90} was -1.8 ± 1.5 mm for MC and -1.7 ± 1.3 mm for PB. The minimum differences were observed as -3.3 mm for MC

and -3.2 mm for PB, while the maximum differences reached -0.2 mm for MC and 0.1 mm for PB.

IV. DISCUSSION

Proton range is a critical parameter in clinical practice which identifies the machine stability in delivering beam energy. Range uncertainty refers to deviations in the Bragg peak position within the patient, potentially causing shifts [7] in the distal dose fall-off that affect tumor control or normal tissue complications. This uncertainty arises from patient, physics, machine, and biology factors [7,8,9]. In the physics-related, CT number conversion and dose calculation algorithms are the key contributors. Therefore, robustness optimization can be applied to mitigate uncertainties [10,11].

R_{90} is recommended for daily checks to ensure accelerator consistency. This study adopted the AAPM Task Group 224 tolerance of ± 1 mm [3], to compare the measurements with the calculation from MC and PB algorithms. Moreover, we standardized all parameters during MC optimization, to investigate the discrepancy between MC and PB calculation.

From *Table 1*, six out of eleven rods met the standard, with the mean ΔR_{90} being statistically significantly lower for MC ($p = .005$), indicating its superior accuracy. These findings align with Dae-Hyun Kim et al. [4], who compared the RayStation PB algorithm and GEANT4 MC simulation in eight different rods, confirming MC enhanced accuracy due to the model of physical interactions.

In LN-450, the differences can be affected by the porous structure within the rod material, indicating the inhomogeneity structure causes the averaged HU for voxel [7,12,13] that causes the uncertainty of CT number for dose calculation due to the resolution of scanner.

For bone-like materials, only one rod (CB2-30% Mineral) met the standard, with PB calculations algorithm underestimating R_{90} by approximately 0.1 mm compared to MC. These findings highlight the importance of accurately converting Hounsfield Units (HUs) to stopping power ratios (SPRs) in high-density regions like bone [14], as this conversion is critical for determining proton range and dose.

Moreover, ICRU78 [15] did not recommend the use of plastic phantoms due to uncertainties in fluence correction factors when scaling the absorbed dose from plastic material to water, particularly within the remaining water-equivalent depth. This discrepancy arises because proton fluences differ significantly between plastic materials and water due to variations in non-elastic nuclear cross-sections. To address this limitation, real pig organs, including lung, soft tissue, and bone, were evaluated. The results showed that range differences for the liver and bone were less than 1 mm, indicating satisfactory outcomes. However, the range difference for pig lung exceeded acceptable criteria, potentially due to organ shrinkage caused by air loss in dead tissue and averaged HU for voxel in CT imaging.

V. CONCLUSION

The limitations of PB algorithm were observed in calculating proton range when compared to MC in a tissue characterization phantom containing homogeneous material in each rod. However, in pig organs with varied compositions, the calculated range between the two algorithms showed no significant differences. In clinical practice, lung tissue should be carefully considered due to scanner resolution limitations. Beam arrangements should aim to minimize extensive paths through lung tissue to reduce uncertainties and enhance dose accuracy.

ACKNOWLEDGEMENTS

The authors acknowledge the support from the Division of Radiation Oncology, Department of Radiology, King Chulalongkorn Memorial Hospital, and extend their sincere thanks to Her Royal Highness Princess Maha Chakri Sirindhorn Proton Center for facilitating this research.

REFERENCES

[1] Hartsell WF, Simone CB, Godes D, Maggiore J, Mehta MP, Frank SJ, et al. Temporal Evolution and Diagnostic Diversification of Patients Receiving Proton Therapy in the United States: A Ten-Year Trend Analysis (2012 to 2021)

From the National Association for Proton Therapy. International Journal of Radiation Oncology Biology Physics. 2024 Jul;119(4):1069–77.
[2] Newhauser WD, Zhang R. The physics of proton therapy. Phys Med Biol. 2015 Apr 21;60(8):R155–209.
[3] Arjomandy B, Taylor P, Ainsley C, Safai S, Sahoo N, Pankuch M, et al. AAPM task group 224: Comprehensive proton therapy machine quality assurance. Medical Physics [Internet]. 2019 Aug [cited 2024 Dec 5];46(8).
[4] Kim DH, Cho S, Jo K, Shin E, Hong CS, Han Y, et al. Proton range verification in inhomogeneous tissue: Treatment planning system vs. measurement vs. Monte Carlo simulation. Depauw N, editor. PLoS ONE. 2018 Mar 5;13(3):e0193904.
[5] Bongrand A, Koumeir C, Villoing D, Guertin A, Haddad F, Métivier V, et al. A Monte Carlo Determination of Dose and Range Uncertainties for Preclinical Studies with a Proton Beam. Cancers. 2021 Apr 15;13(8):1889.
[6] Saini J, Traneus E, Maes D, Regmi R, Bowen SR, Bloch C, et al. Advanced Proton Beam Dosimetry Part I: review and performance evaluation of dose calculation algorithms. Transl Lung Cancer Res. 2018 Apr;7(2):171–9.
[7] Paganetti H. Range uncertainties in proton therapy and the role of Monte Carlo simulations. Phys Med Biol. 2012 Jun 7;57(11):R99–117.
[8] Both S. Source of uncertainty in proton therapy. Proton treatment planning in AAPM School. 2012. Available from: http://chapter.aapm.org/GLC/media/2012/Both.pdf
[9] Shanbhag NM. A Radiation Oncologist's Journey Through Technological Advancements in Oncology: Reflections on the Proton Therapy Winterschool at Paul Scherrer Institute, Switzerland. Cureus [Internet]. 2023 May 26 [cited 2024 Dec 5].
[10] Liu W, Zhang X, Li Y, Mohan R. Robust optimization of intensity modulated proton therapy: Robust optimization of IMPT. Med Phys. 2012 Feb 3;39(2):1079–91.
[11] Unkelbach J, Chan TCY, Bortfeld T. Accounting for range uncertainties in the optimization of intensity modulated proton therapy. Phys Med Biol. 2007 May 21;52(10):2755–73.
[12] Hudobivnik N, Schwarz F, Johnson T, Agolli L, Dedes G, Tessonnier T, et al. Comparison of proton therapy treatment planning for head tumors with a pencil beam algorithm on dual and single energy CT images: DECT proton therapy treatment planning for head tumors. Med Phys. 2016 Jan 4;43(1):495–504.
[13] Chirdchid T, Ruangchan S, Sanghangthum T. Dosimetric Comparison between Single-energy Computed Tomography and Dual-energy Computed Tomography Relative to Stopping Power Estimation in Proton Therapy. Journal of Medical Physics. 2023 Jul;48(3):292–7
[14] Ainsley CG, Yeager CM. Practical considerations in the calibration of CT scanners for proton therapy. J Applied Clin Med Phys. 2014 May;15(3):202–20.
[15] ICRU report 78 "Prescribing, Recording and Reporting Proton Beam Therapy" Oxford U. Press. Journal of the ICRU 7(2); 2007.

Contacts of the corresponding author:
Co-author: Mintra Keawsamur
Institute: Division of Radiation Oncology, Faculty of Medicine, Chulalongkorn University
Street: Phaya Thai Road
City: Bangkok
Country: Thailand
Email: Mintra.Ke@chula.ac.th

Comparison of kinetic repair models for protons induced DNA damage

Tikamol Natthawat [1], Nantajit D[1], Liamsuwan T[1*]

1 Princess Srisavangavadhana College of Medicine, Chulabhorn Royal Academy, Bangkok, Thailand
**thiansin.lia@cra.ac.th*

Abstract — **Introduction:** Proton therapy provides benefits over photon therapy due to its accurate dose targeting, which can spare healthy tissues. In clinical practice, the relative biological effectiveness (RBE) of protons of 1.1 is used throughout the beam path. However, cell experiments showed that the RBE varied close to the end of the proton path. Mechanistic modeling of DNA damage and repair specific for proton therapy could help to quantify the accurate RBE of protons. In this work, existing DNA repair models were systematically evaluated for therapeutic proton beams. **Methods:** The DNA double-strand break (DSB) repair models proposed by Belov (Model A) and Taleei and Nikjoo (Model B) were investigated. Both models consisted of a set of partial differential equations with repair kinetic constants specific to the mechanistic pathways proposed by each model. Initial DNA damage yields and damage complexity obtained from Monte Carlo track structure simulations were used as inputs for estimating residual DSBs over time, which was validated against experimental data. Re-optimization of the repair kinetic constants was also performed. **Results:** The root mean square (RMS) errors of Models A and B ranged from 8.6% and 17.23%, respectively. After re-optimization, the RMS errors were 1.2% and 2.37%, respectively. **Conclusion:** Model A was more suitable for predicting DNA repair kinetics for proton therapy than Model B.
Keywords — DNA double-strand break (DSB), DSB repair kinetics, proton therapy, mechanistic modeling

I. INTRODUCTION

An advantage of proton beam therapy is that it results in a low entrance dose and absence of exit dose. The constant RBE value of 1.1 was used for the absorbed dose in proton therapy treatment planning. However, based on cell experiments, it was observed that the RBE increased as the dose-averaged LET.[2] An increase in LET corresponds to a higher number of ionizations occurring over the same distance, which results in an increased yield of double-strand breaks (DSBs) and more complexity of these breaks.[1] Because LET typically increased at the distal edge of the spread-out Bragg peak (SOBP), employing a constant RBE value could lead to an underestimation of the biological effect on normal tissues and organs at risk (OARs) in that area.

DSBs are considered the most lethal type of DNA lesions, which when being mis-repaired or left unrepaired can potentially lead to mutation or cell death. The crucial processes involved in repairing DSBs in mammalian cells are primarily homologous recombination (HR) and nonhomologous end-joining (NHEJ).[3] To date, various models have been proposed to simulate DNA damage repair kinetics, such as, the utilization of biomolecular reaction rate equations[4-7] and the continuous time random walk model of sub-diffusion[8, 9]. However, these models were usually tested with different types of radiation or cell types. However, systematic comparison between proposed models were rarely done to determine which model was most suitable for proton therapy.

In this study, different DNA repair models for therapeutic proton beams were studied and compared. The aim of this study was to evaluate DNA repair models that were appropriate and had the potential to be used with therapeutic proton beams.

II. MATERIALS AND METHODS

The DNA damage yields used in this study was obtained from Chaibura[15], using Geant4-DNA Monte Carlo track structure toolkit (version 11) to simulate the physical, pre-chemical and chemical stages of the proton tracks together with an in-house developed DNA damage model. The DSBs were categorized by their complexity disregarding base damage, including a simple DSB, DSB+ (a DSB accompanied by an additional single-strand breaks (SSBs) within a 10-base-pair segment), and DSB++ (similar to DSB+ but with multiple SSBs on either strand).

A. Kinetic repair models

The DSB kinetic repair models investigated in this work were based on a system of ordinary differential equations (ODEs). The first model was proposed by Belov et al[7] (Model A). The first model was proposed by Belov et al[8] (Model A). This model consisted of four repair pathways, including non-homologous end joining (NHEJ), homologous recombination (HR), single-strand annealing (SSA), and microhomology-mediated end joining (MMEJ), altogether 52 rate constants.

The other investigated kinetic DSB repair model was proposed by Taleei and Nikjoo[6] (Model B). This model consisted of three repair pathways, including slow and fast NHEJ, and MMEJ, altogether 17 rate constants.

The DSB yields obtained from the Monte Carlo track structure simulation served as the initial DSB yield for both repair kinetic models. The solutions to the ODEs were calculated using the Scipy algorithm in Python.

B. Re-optimization of kinetic rate constants for Models A and B

The experimental data of γ-H2AX levels over time after irradiation were used for re-optimizing the kinetic rate constants for Models A and B. For Model A, the experimental data of Wu et al.[10] and Keta et al.[11] on human melanoma (HTB140) and normal human lung fibroblast (NHLF) were used to re-optimize 21 rate constants of this model. In contrast Model B did not consider HR in the model, the study by Ariungerel et al.[12] and Grosse et al.[13] on cultured hamster cells mutated in HR repair was used to re-optimize 15 rate constants of this model**.** The re-optimization of rate constants in Models A and B was performed using the Non-Linear Least-Squares Minimization and Curve-Fitting (LMFIT) algorithm in Python.

The re-optimized models were tested with the experimental data of γ-H2AX levels remaining after exposure to 3 Gy of protons on murine embryonic fibroblasts (MEF).[14]

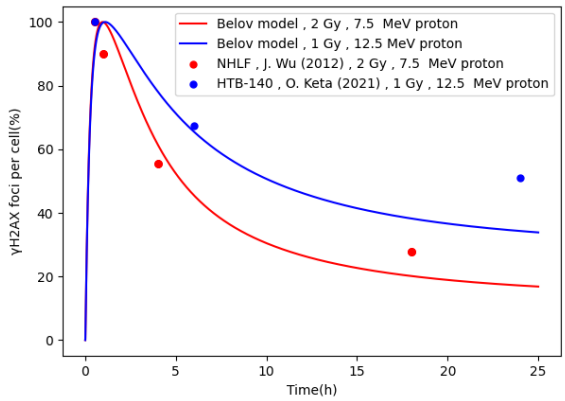

Figure.1 *Time-course of γ-H2AX levels remaining after exposure to 1 and 2 Gy of protons. The curves represent Model A after re-optimization, while the symbols correspond to experimental data of Wu et al.[10] and Keta et al.[11]*

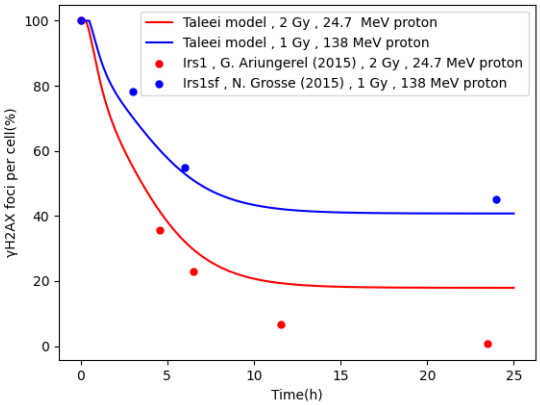

Figure.2 *Time-course of γ-H2AX levels remaining after exposure to 1 and 2 Gy of protons. The curves represent Model B after re-optimization, while the symbols correspond to experimental data of Ariungerel et al.[12] and Grosse et al.[13]*

III. RESULTS

Figures 1 and 2 show results of re-optimizing Models A and B, respectively. Figures 3 and 4 show the γ-H2AX levels remaining after exposure to proton irradiation calculated using the original and re-optimized rate constants in Models A and B, respectively. The results were compared with experimental data using the root mean square error (RMSE). For Model A, the RMSE using the original rate constants was 8.60, which decreased to 1.20 with the re-optimized rate constants. Similarly, for Model B, the RMSE using the original rate constants was 17.23, and it decreased to 2.37 with the re-optimized rate constants.

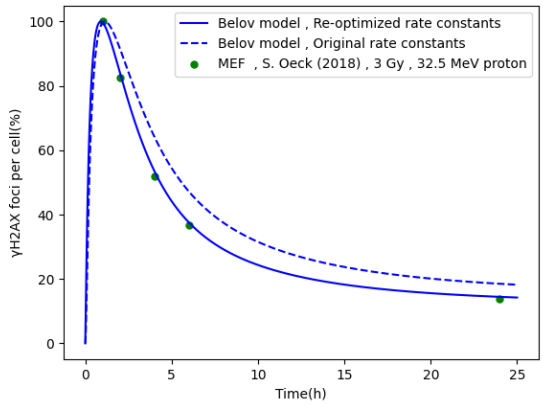

Figure.3 *Time-course of γ-H2AX levels remaining after exposure to 3 Gy of protons. The curves represent the calculated results from Model A, while the symbols correspond to experimental data derived from studies on murine embryonic fibroblasts (MEF).*[14]

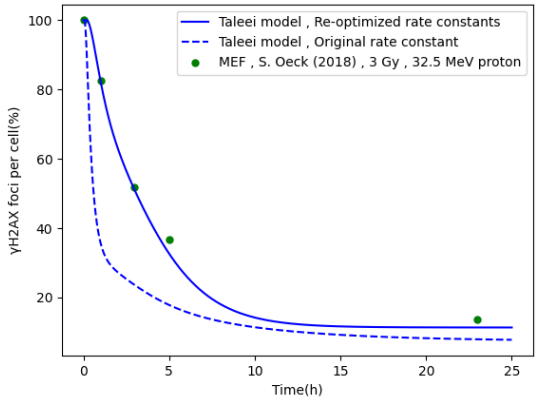

Figure.4 *Time-course of γ-H2AX levels remaining after exposure to 3 of protons. The curves represent the calculated results from Model B, while the symbols correspond to experimental data derived from studies on murine embryonic fibroblasts (MEF).*[14]

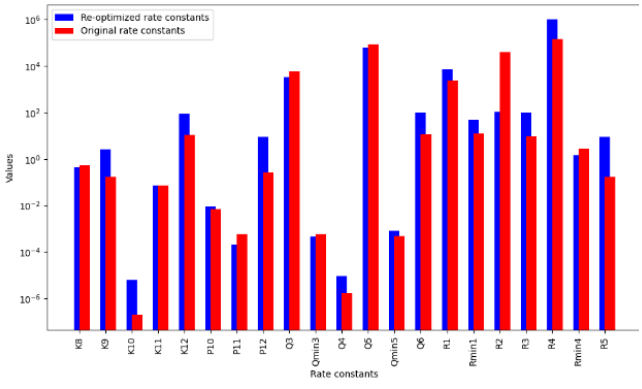

Figure.5 *Comparison of original and re-optimized rate constants used in model A.*

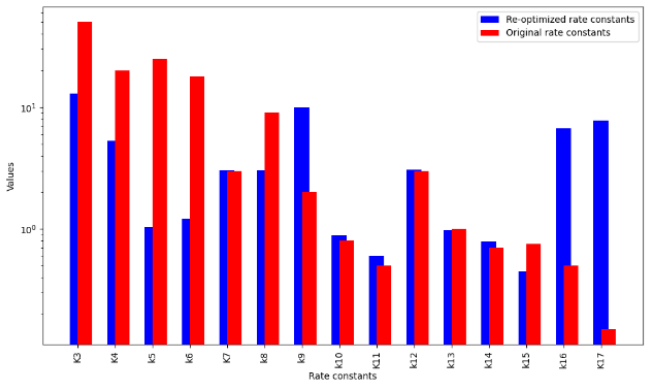

Figure.6 *Comparison of original and re-optimized rate constants used in model B.*

IV. DISCUSSION

For Model A, using the original rate constants led to an overestimation of γ-H2AX levels over time. This was because the rate constants were derived from both low and high LET radiations. For Model B, the original rate constants resulted in an underestimation of γ-H2AX levels, as its rate constants were obtained from X-ray data. However, after re-optimizing the rate constants using experimental γ-H2AX data induced by proton radiation, as shown in Figs. 1 and 2, and validating them against additional experimental γ-H2AX data not used in the re-optimization process, the results aligned more closely with the experimental γ-H2AX data. The RMSE for Model A was lower than that for Model B, indicating a higher accuracy of Model A. This was because Model A considered repair kinetics across all cell cycle phases and accounted for all possible repair pathways for DSB repair. In contrast, Model B focused only on the G1 and early S phases and considered only the fast and slow NHEJ and MMEJ repair pathways, excluding the critical HR pathway.

V. CONCLUSION

The comparison of RMSE values after re-optimizing rate constants with experimental data of proton irradiation showed that the model of Belov et al[7] (Model A) reproduced the experimental data better than the model of Taleei and Nikjoo[6] (Model B). Therefore, Model A was considered more suitable for predicting DNA repair kinetics in proton therapy than Model B. For future work, we plan to incorporate the HR repair pathway into Model B and determine the rate constants for the HR pathway to improve Model B and make it more representative of reality.

ACKNOWLEDGEMENTS

N/A

REFERENCES

[1] Watanabe R, Rahmanian S, Nikjoo H. Spectrum of Radiation-Induced Clustered Non-DSB Damage - A Monte Carlo Track Structure Modeling and Calculations. Radiat Res. 2015 May;183(5):525-40.

[2] McNamara AL, Schuemann J, Paganetti H. A phenomenological relative biological effectiveness (RBE) model for proton therapy based on all published in vitro cell survival data. Phys Med Biol. 2015 Nov 7;60(21):8399-416.

[3] Kanaar R, Wyman C, Rothstein R. Quality control of DNA break metabolism: in the 'end', it's a good thing. EMBO J. 2008 Feb 20;27(4):581-8.

[4] Mokari M, Moeini H, Farazmand S. Computational modeling and a Geant4-DNA study of the rejoining of direct and indirect DNA damage induced by low energy electrons and carbon ions. Int J Radiat Biol. 2023;99(9):1391-404.

[5] Taleei R, Nikjoo H. The non-homologous end-joining (NHEJ) pathway for the repair of DNA double- strand breaks: I. A mathematical model. Radiat Res. 2013 May;179(5):530-9.

[6] Taleei R, Nikjoo H. Biochemical DSB-repair model for mammalian cells in G1 and early S phases of the cell cycle. Mutat Res. 2013 Aug 30;756(1-2):206-12.

[7] Belov OV, Krasavin EA, Lyashko MS, Batmunkh M, Sweilam NH. A quantitative model of the major pathways for radiation-induced DNA double-strand break repair. J Theor Biol. 2015 Feb 7;366:115-30.

[8] Henthorn NT, Warmenhoven JW, Sotiropoulos M, Mackay RI, Kirkby NF, Kirkby KJ, Merchant MJ. In Silico Non-Homologous End Joining Following Ion Induced DNA Double Strand Breaks Predicts That Repair Fidelity Depends on Break Density. Sci. Rep. 2018 Feb 8;8(1):2654.

[9] Qi Y, Warmenhoven JW, Henthorn NT, Ingram SP, Xu XG, Kirkby KJ, Merchant MJ. Mechanistic Modelling of Slow and Fast NHEJ DNA Repair Pathways Following Radiation for G0/G1 Normal Tissue Cells. Cancers (Basel). 2021 May 3;13(9).

[10] Wu J, Fu Q, Quan Y, Wang W, Mei T, Li J, et al. Repair rates of DNA double-strand breaks under different doses of proton and γ-ray irradiation. Nucl. Instrum. Methods Phys. Res. B. 2012 Apr 1;276:1-6.

[11] Keta O, Petković V, Cirrone P, Petringa G, Cuttone G, Sakata D, et al. DNA double-strand breaks in cancer cells as a function of proton linear energy transfer and its variation in time. Int J Radiat Biol. 2021;97(9):1229-40.

[12] Ariungerel G, Eri M, Takaaki I, Lue S, Kazuya I, Takeji S, et al. The Major DNA Repair Pathway after Both Proton and Carbon-Ion Radiation is NHEJ, but the HR Pathway is More Relevant in Carbon Ions. Radiat Res 2015 Mar 1;183(3):345-56.

[13] Grosse N, Fontana AO, Hug EB, Lomax A, Coray A, Augsburger M, et al. Deficiency in Homologous Recombination Renders Mammalian Cells More Sensitive to Proton Versus Photon Irradiation. Int. J. Radiat. Oncol. Biol. Phys. 2014;88(1):175-81.

[14] Oeck S, Szymonowicz K, Wiel G, Krysztofiak A, Lambert J, Koska B, et al. Relating Linear Energy Transfer to the Formation and Resolution of DNA Repair Foci After Irradiation with Equal Doses of X-ray Photons, Plateau, or Bragg-Peak Protons.Int. J. Mol.Sci.2018;19(12):3779.

[15] Chaibura S. Comparison of radiation-induced DNA damage modeling approaches for proton therapy treatment planning[Thesis]: Chulabhorn Royal Academy; 2024.

Contacts of the corresponding author:
Author: : Thiansin Liamsuwan
Institute: Princess Srisavangavadhana College of Medicine, Chulabhorn Royal Academy
Street: Kamphaeng Phet
City: Bangkok
Country: Thailand
Email: *thiansin.lia@cra.ac.th*

List of Participants

Invited Speakers

Abdul Rahman, Ahmad Taufek
Amornwichet, Napapat
Angsulajit, Polawat
Ath, Vannyat
Badawy, Mohamed
Boonyaputthikul, Harit
Buppaungkul, Sakchai
Carrion, Daniel
Chotlersak, Kanjana
Chuamsaamarkkee, Krisanat
Evan, Lukmanda
Fuangrod, Todsaporn
Gibson, John Owen
Handschin Grossmann, Martin
Hardiansyah, Deni
Hidayati, Nur Rahmah
Huq, Saiful
Khorpresert, Chonlakiet
Koh, Calvin
Lin, Swe Swe
Matsubara, Kosuke
Md Ariffin, Nurmazaina
Milano, Franco
Myint, Thinn Thinn
Nakkrasae, Pitchayut
Pawiro, Supriyanto
Peralta, Agnette
Phongprapan, Wisawa
Punyanitya, Sittiporn
Puttanawarut, Chanon
Rakvongthai, Yothin
S, Somanesan
Sathitwatthanawirot, Chanida
Shintawati, Rini
Shiratori, Shuichi
Shunhavanich, Picha
Sirirutbunkajorn, Nat
Suphaphong, Sithiphong
Takatsu, Yasuo
Takemura, Akihiro
Tawara, Noriyuki
Tsujioka, Katsumi
Wanta, Arunothai
Wilkinson, Allan
Yeong, Chai Hong
Zhao, Anzi

Participants

Aekpatcha, Teerawit
Alipio, Andrea
Azimah, Alfia Faizatul
Azzi, Akbar
Boonsuan, Sasi
Boonyatulanon, Pakatip
Boujamrat, Thanuch
Buasawat, Kanyapat
Bura, Wathinee
Burasothikul, Paphawarin
Chaipanya, Thitaporn
Chaisuttee, Rusdchai
Chaiyapong, Akanit
Chaiyarith, Pornsuree
Chakrapong, Apawadee
Chalermchawalit, Wirasinee
Chanchayanon, Thanakrit
Changkaew, Pimolpun
Chantarak, Kiattiyot
Chanton, Thadpong
Chatachot, Kotchakorn
Chatchumnan, Nichakan
Chawana, Nuengruthai
Cheewakul, Jongwat
Chevajarassakul, Wasin
Choobunlap, Kanokkwan
Chow, Wendy
Chusin, Thunyarat
Coronel, Michael Ben Joseph
Cruzpero, Ramon Carlo
Dachaworakul, Kittipol
Dachviriyakij, Tanapol
Dardaranonda, Paya
Dechsupa, Patchareporn

Deeharing, Aphisara
Donmoon, Tinnagorn
Duangdaraphon, Wanwisa
Fangnok, Natnaree
Gani, M Roslan Abdul
Gumbungkai, Hempakorn
Hantragulsuk, Waraporn
Hmwe, Aye Thiri
Homkhaow, Kasama
Hompeng, Pratchayakan
Hongkham, Nattapong
Hoonghual, Thikhamporn
Huakham, Sowitchaya
Innan, Yuparak
Intanin, Panatda
Intaprom, Rudjaya
Inthibal, Pawana
Jankaew, Gadesuda
Jansawang, Sineeporn
Jarutatsanangkoon, Pasit
Jitmon, Jitlada
Jong, Wei Loong
Kaewbunperm, Urairat
Kaewpruk, Pubade
Kammak, Sunadda
Kanyakham, Kannikar
Karinchai, Piraya
Kawvised, Supannika
Keawchompoo, Rachata
Khadsiri, Patchareewan
Khamta, Nongnut
Khuadpudsa, Wanitchaya
Khuenchana, Somsak
Kim, Vladimir
Kingkaew, Sakda
Kititharakun, Phairot
Kittipayak, Samrit
Konlak, Itsaraporn
Kor-or, Kanokpong
Krongkietlearts, Komkrit
Kuibumrung, Ailada
Kulkheereeratana, Theerachon
Kulwiboonsri, Pimlada
Kummanee, Patiparn
Kyaw, Wai Lwin Lwin
Lasode, Jaravee
Liamsuwan, Thiansin
Lowong, Thanatchaya
Maknitikul, Sitanan
Malila, Wannita
Manoharn, Tamisa
Manpuen, Supamas
Masanga, Wilai
Messuwan, Jiraphat
Mockter, Tasnim
Mohd Imran, Sharmila
Mohd Zain, Azleen
Montreemanorom, Warisara
Muangkhamporn, Kanokporn
Mundee, Thunpisit
Nakpponnabutr, Wachirakorn
Nantaprae, Rutthapong
Netprasert, Sa-angtip
Ngoenthuan, Woraya
Niwa, Ayano
Niwa, Masayoshi
Niyomthai, Thida
Nobphuek, Kamonchanok
Nontachat, Siriwat
Nuntue, Chatnapa
Oh, Se An
Ohnishi, Haruki
Paduka, Sumana
Pairat, Kumutinee
Pairodsantikul, Phornpailin
Pangsai, Teerapong
Panpheng, Nichuda
Panyura, Pongpitch
Papakdee, Patumaporn
Pattanapa, Patcharaphan
Payungkulanan, Kanyawee
Phantawong, Kochakorn
Phomtum, Dararat
Piasanthia, Supakiet
Pihusut, Chonlathorn
Pimthong, Jeerawat
Pinsaitong, Natnapa
Pintakham, Chaiyaporn
Pischom, Narueporn
Pishyapan, Aiyara

Pisitjing, Siripan
Pisut, Duanghatai
Plangpleng, Nattha
Pochun, Sasiprapha
Pochun, Sasiprapha
Pojanapreecha, Pavarit
Ponkanist, Kanokvalee
Popreeda, Tippawan
Porkaew, Siriluk
Prabsattroo, Thawatchai
Prajamchuea, Kornkamol
Pranee, Chanaphat
Prasartvit, Kanogpan
Prommoon, Wararat
Promsiri, Wanlapa
Promsupap, Kronwadee
Pudsena, Pronpawee
Punlek, Nontawat
Putthaburi, Kanchana
Ratiphunpong, Phimphitcha
Rattanachayoto, Piyaporn
Rattanamongkonkul, Pattaravarin
Rattanarungruangchai, Natch
Reongsiri, Jirachai
Rinjan, Nawarat
Ritlumlert, Napat
Roonpho, Pannee
Ruediloesmethi, Namphet
Ruenjit, Sakultala
Rukthung, Kewalee
Rutchantuek, Sukanya
Saejia, Korawee
Saenchon, Phattanapong
Saiwong, Nipon
Saiyo, Nipon
Sakulsingharoj, Siwaporn
Sangsud, Nalinnipa
Santo, Taiki
Saobai, Sirawit
Sarung, Pakjira
Sawapabmongkon, Thitipong
Sawatnatee, Thunyaluk
Silambarasan, Navitha
Singusaha, Orathai
Sirichotwatcharakit, Chompunek
Sisai, Siriwan
Somboon, Siriprapa
Somboontana, Apissara
Songprakhon, Rangsee
Sornsirisakul, Natapon
Sueangamiam, Kamonrat
Suesakul, Kueakoon
Sukha, Thanakorn
Suksawang, Penpisuth
Sukumwattana, Wichasa
Suntiwong, Sawanee
Suntonkhum, Supaporn
Supapong, Napassawan
Suttho, Dutsadee
Suwan-o-pas, Siranyapong
Tananchai, Kamonwan
Tangruangkiat, Sutthirak
Tantiwetchayanon, Khajonsak
Tasomkan, Sasithorn
Teankuae, Saiwaroon
Techaphan, Apichaya
Thaiwattana, Chanchakorn
Thana, Rasalin
Thanu, Arthit
Tharavichitkul, Ekkasit
Thareeboonchai, Thamonwan
Thasasi, Phatthraporn
Thasenhod, Krisadang
Thinka, Yasumon
Thiranuntakul, Nuntawuth
Thongngam, Supaporn
Thongsuk, Warit
Thongthanom, Siwika
Thuwarojsakul, Jinjuthathip
Tikamol, Natthawat
Tohpong, Mizan
Tongngarm, Wimonmart
Treesong, Aphiram
Turathong, Suriyaporn
Uadrang, Surin
Uber, Pichet
Uchuwat, Yosita
Udomphon, Aphiyut
Utitsarn, Kananan
Viboonsak, Natkita

Vimolnoch, Mananchaya
Wankaew, Wongsakorn
Wantongsuk, Wilasinee
Wattanagul, Nuttapol
Watthanasarn, Thepphithak
Wongin, Natchana
Wongnil, Jaroonroj
Wongsa, Paramest
Yabsantia, Sumalee
Yawichai, Kannika
Yeenang, Nuttawut
Yimpak, Tongrak
Yongvithisatid, Pornpan
Yooyen, Nattawut
Zainal Abidin, Shahira Nabila
Zin, Hafiz

Committee

Aluksanasuwan, Siripat
Apipanyasopon, Lakkana
Asavaphatiboon, Sawwanee
Aye, Yin Moe
Buranavanitvong, Nalinpun
Chaiwatanarat, Tawatchai
Chaiwongkot, Napatsorn
Chi Tun Aung, Nay
Darmawan, Dimas Faisal
Funsian, Amporn
Handayani, Wuri
Hankittichai, Phateep
Htet, May Thu
Jaihow, Wanwanut
Jansawang, Joradol
Janyou, Adchara
Jittrakool, Kantida
Kakanaporn, Chumpot
Karoon, Pharewa
Keawsamur, Mintra
Khachonkham, Suphalak
Khamfongkhruea, Chirasak
Khamwan, Kitiwat
Khositharattanakool, Pathamet
Krisanachinda, Anchali
Leelasiri, Apichai
Monkongsubsin, Wiroon
Morchang, Atthapan
Narawong, Taratip
Nobnop, Wannapha
Noipairoj, Panwadee
Pasawang, Panya
Patipipittana, Supanuch
Petiraksakul, Parida
Piantham, Wannasa
Pongnapang, Napapong
Promprakob, Bharinee
Ratcha-oun, Orathai
Rueangsrisupapong, Saran
Ruengsrisupapong, Saran
Sahachjesakul, Paranee
Sanghangthum, Taweap
Shayal, Shiwani
Soe Thu, Myat
Somsuan, Keerakarn
Somwang, Puckavadee
Sontrapornpol, Tanawat
Soontranan, Preecha
Stansook, Nauljun
Suriyapee, Sivalee
Swaengdee, Yaniga
Tangboonduangjit, Puangpen
Tannanonta, Chirapha
Tansangworn, Prasit
Tanwattana, Chalisa
Tawonwong, Tanawat
Teekawong, Kamollak
Thongkam, Taitacha
Tipayamontri, Thititip
Toka, Amos
Uamsathit, Krittaphat
Watcharawipha, Anirut
Wongsirinanon, Sangsirin
Yamram, Nattaporn
Yen Nhi, Tran

Commercial Exhibitors

Archawametheekul, Kamonchanok
Buratachwatanasiri, Wirunpatch
Jirawatwanith, Titiya
Krongyuth, Khummook
Liammookda, Piyanan
Morhrasi, Pakjira
Onnomdee, Chanakarn
Polharn, Patompong
Roman, Wicha
Sangsrijan, Anchasa
Thanabordeebunsiri, Jiraporn
Wongpisarn, Sasawan

Acknowledgement

The SEACOMP 2025 organizing committee wishes to acknowledge with thanks for the contribution from:

- Business Alignment
- Varian
- Siemens Healthineers
- Elekta
- Premier Bussiness Inter
- Sukosol Healthcare
- SaintMed
- Med I
- United Imaging
- Nagase
- Brainlab
- GE HealthCare
- Abex Global Healthcare
- PT Healthcare
- BizLine
- Thailand Institute of Nuclear Technology
- Transmedic
- Dispo-Med
- RayDose


B|A
Business Alignment


varian
A Siemens Healthineers Company


MED I (Thailand) Co. Ltd.


SMDi


PBI
PREMIER BUSINESS INTER


Elekta


Biz Line

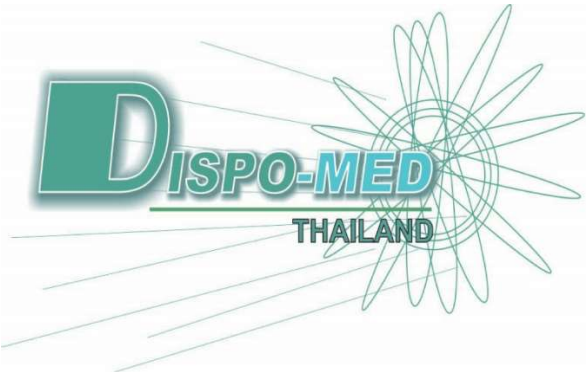
DISPO-MED
THAILAND


NAGASE


SUKOSOL
HEALTHCARE


BRAINLAB


Transmedic
Advancing Medical Technologies


anu
TINT


ABEX


SIEMENS
Healthineers


RAYDOSE®


PT
HEALTHCARE


UNITED
IMAGING